GEOPHYSICAL METHODS FOR ASSESSMENTS

OF SOIL CORROSIVITY

Ravin Navneet Deo

BSc, MSc (Physics)

A thesis submitted for the Degree of

Doctor of Philosophy

at the

School of Geosciences,
Monash University.
Melbourne, Australia.

September, 2012

ADDENDUM

p 102: delete last sentence and read:

It follows that the formation of $FeCl_2$ is unstable, which readily gets oxidized to Akaganeite (βFeOOH-Cl) and in the process releases the chloride ion to restart another reaction expressed by Eq. 4.10.

p 108: add before the last paragraph:

The galvanostatic pulse technique (GPT) advocated in this study also needs to be investigated further within the scope of current areas of interest in the discipline of soil corrosion. Firstly, as a pioneering work the present study has simulated the metal/soil interface using the simple Randle's circuit. This feature is applicable when the metal surface is completely exposed to the soil electrolyte. Future development should extend the equivalent circuit to account for pipeline surfaces coated by a protective layer which may or may not be ideal. This will further require extending the charging and discharging potential-time responses. Secondly, disturbances in uniform current distribution due to presence of strong localized corrosion, and their overall effect on the galvanostatic pulse technique needs to be investigated.

A common issue with corrosion measurements in soil environment is the reproducibility of measurements. Some issues which can lead to difficulties in reproducible measurements have been discussed in Section 4.1.1. Prior to this work, the LPR technique has been considered to be the best available method for robust measurements of instantaneous corrosion rates in soils. However, the use of either the polarization resistance method (see Section 2.4.2) or the LPR method is incapable of distinguishing and isolating soil capacitance effects from the overall measurements. It is believed this is one of the major reasons contributing to current difficulties in reproducible measurements. On the contrary, it has been clearly demonstrated that effects of soil capacitances manifesting in the overall measurements can be clearly identified in the potential-response curves (see Section 4.3.2), thereby allowing the corrosion related phenomenon to be analyzed uniquely with galvanostatic pulse techniques. Moreover as mentioned earlier, a consistent methodology has been adopted, which allows minimizing systematic errors when first initiating the metal/soil interface. This in essence improves the reproducibility of the measurements.

p 146: add before the last paragraph:

It is suggested that comparison of measurements from galvanostatic pulse technique (GPT) and SIP with weight loss measurements be given a priority for future investigation. These two important techniques from the two different disciplines (applied geophysics and applied electrochemistry) have never been integrated together for a holistic characterization of corrosive soil environment. An important aspect of the aforementioned investigation will be that the experimental design is assembled in such a way that measurements using GPT and SIP are conducted simultaneously, *i.e.*, SIP measurements are conducted on the same soil electrolytes involved in the corrosion process. In this manner any variations in soil electrolytes during the monitoring period can be captured through the SIP and GPT methods. The monitoring period can be extended to several months or years to:
    a) better obtain an overview of any important variations brought about by any abrupt changes in soil conditions.
    b) Allow sufficient corrosion to occur which can be determined through weight loss methods, especially in soils with extremely few or fairly absent from chlorides.

p 173: delete 2nd paragraph and read:

Chemical analysis for the determination of sulfate (SO_4^{2-}) salts, chloride (Cl^-) salts, and nitrate (NO_3^-) salts in the soil samples was carried out by an external commercial laboratory (Analytical Chemistry and Testing Services, located at 4 Westall Road, Springvale, VIC 3171, Australia). Electrical conductivity (EC) in 1:5 soil/water leach for each sample was also measured. This method is compliant with NEPM (1999)[*] Schedule B(3) (Method 104).

[*] NEPM. 1999. National Environment Protection (assessment of Site Contamination) Measure. Schedule B(3) Guideline on laboratory Analysis of Potentially Contaminated Soils. National Environment Protection Council, Australia.

p 191: delete 2nd sentence in last paragraph and read:

Note that the EC of 1:5 soil/water is converted from $\mu S\ cm^{-1}$ to $\Omega\ m$ (Table 7.1). To avoid confusion amongst terms, the EC of 1:5 soil/water has been converted to electrical resistivity (ER) of 1:5 soil/water.

p 192: Modify Table 7.1 as follows:

Station	Sample 1:5 soil/water [1]EC	Sample 1:5 soil/water [2]ER	Sample DC resistivity	- $\phi_{1\ Hz}$	Cole-Cole parameters		
	($\mu S\ cm^{-1}$)	($\Omega\ m$)	ρ_{DC} ($\Omega\ m$)	(mrad)	m ($\times 10^{-3}$)	c	τ (μs)
1	24	416.7	92.8 ± 0.2	6.5 ± 0.02	154 ± 6	0.3 ± 0.002	96 ± 30
3	47	212.8	48.9 ± 0.1	9.01 ± 0.03	145 ± 4	0.3 ± 0.002	482 ± 115
5	66	151.5	28.9 ± 0.1	7.2 ± 0.8	155 ± 3	0.3 ± 0.001	172 ± 29
7	55	181.8	40.9 ± 0.06	10.12 ± 0.05	175 ± 4	0.3 ± 0.002	412 ± 76
9	67	149.3	31.9 ± 0.08	10.11 ± 0.04	145 ± 2	0.3 ± 0.001	713 ± 90
11	115	87	22 ± 0.03	7 ± 0.02	162 ± 4	0.3 ± 0.001	96 ± 18
13	261	38.3	7.7 ± 0.01	2.04 ± 0.02	46 ± 2	0.3 ± 0.001	136 ± 39
15	172	58.1	10.8 ± 0.02	4.25 ± 0.01	68 ± 1	0.3 ± 0	466 ± 67
17	299	33.4	7.2 ± 0.01	2.76 ± 0.02	45 ± 1	0.3 ± 0	765 ± 94
19	213	46.9	9.2 ± 0.01	4.19 ± 0.01	74 ± 2	0.28 ± 0.001	321 ± 42
21	385	26	5.2 ± 0.01	1.44 ± 0.01	25 ± 1	0.3 ± 0	337 ± 44
23	130	76.9	16.5 ± 0.02	4.43 ± 0.02	82 ± 2	0.25 ± 0.001	225 ± 36
25	138	72.5	13.1 ± 0.02	3.2 ± 0.8	95 ± 2	0.25 ± 0	36 ± 8
27	119	84	14.3 ± 0.02	1.85 ± 0.02	56 ± 2	0.32 ± 0	42 ± 10
29	101	99	18.2 ± 0.01	3.39 ± 0.02	80 ± 2	0.3 ± 0	118 ± 17
31	115	87	9.4 ± 0.01	4.17 ± 0.02	82 ± 1	0.25 ± 0	147 ± 23
33	99	101	17.4 ± 0.01	4.94 ± 0.01	147 ± 6	0.25 ±0.001	19 ± 6
35	76	131.6	23.4 ± 0.03	2.43 ± 0.04	80 ± 1	0.3 ± 0	30 ± 3
37	63	158.7	31.6 ± 0.04	3.03 ± 0.3	88 ± 4	0.3 ± 0.001	44 ± 13
39	52	192.3	32.9 ± 0.04	2.34 ± 0.03	91 ± 5	0.3 ± 0.001	14 ± 4

NOTE: [1]EC = measured sample electrical conductivity in 1:5 soil/water.

[2]ER = calculated sample electrical resistivity in 1:5 soil/water.

Table of Contents

Chapter 1   INTRODUCTION

Chapter 2   POLARIZATION   FUNDAMENTALS   FOR   CORROSION MEASUREMENTS

Chapter 3   SURFACE GEOELECTRIC METHODS

Chapter 4   **GALVANOSTATIC   PULSE   METHOD   FOR   ASSESSING CORROSION IN SOIL ENVIRONMENT: STATE OF THE ART**

Chapter 5   **ASSESSING SOIL CORROSIVITY FROM SPECTRAL INDUCED POLARIZATION RESPONSE**

GENERAL DECLARATION

I, Ravin Navneet Deo, hereby declare that this thesis contains no material which has been accepted for the award of any other degree or diploma at any university or equivalent institution and that to the best of my knowledge and belief, this thesis contains no material previously published or written by any other person, except where due reference is given in the text of the thesis.

…………………......
Ravin Navneet Deo
28th September, 2012.

Notice 1
Under the Copyright Act 1968, this thesis must be used only under the normal conditions of scholarly fair dealing. In particular no results or conclusions should be extracted from it, nor should it be copied or closely paraphrased in whole or in part without the written consent of the author. Proper written acknowledgement should be made for any assistance obtained from this thesis.

Notice 2
I certify that I have made all reasonable efforts to secure copyright permissions for third-party content included in this thesis and have not knowingly added copyright content to my work without the owner's permission.

LIST OF FIGURES

LIST OF TABLES

LIST OF PLATES

Page

ACKNOWLEDGMENT

the first friend I made in Australia! I also wish to thank Mr. Anders Kruse, who provided the much needed field assistance within this project. He never seemed to tire and was always ready to offer his help. Thanks also to Dr. Ben Gilfedder for the interesting "corridor discussions" and assisting with requests for some of the instruments from his group.

I wish to also thank my wife Vanjalyn Deo who was always there to cheer me up especially during the stressful times. Her forever smiling face always calmed me down. This is your achievement as much as its mine. Thanks also to my mother-in-law who always provided encouragement. I pay my respect and thank my parents, brother and sister-in-law. The conclusion of this thesis marks the dreams and aspiration they have had for a long time. I am very thankful to my parents for teaching me the importance and value of education early in my life and their continued blessings. I hope that this endeavor of mine will inspire next generations of my family for higher educational aspiration. *Labor omnia vincit*.

To my Amma, Papa and Brother

for their belief and faith

ABSTRACT

Soil corrosion is a complex and multi-disciplinary problem affecting a range of engineering assets and critical civil infrastructure. Although significant efforts are being made to improve the life-time of metallic assets in the soil environment, failures continue to occur due to deterioration brought about by external corrosion. Pipelines are one such category of buried assets. As part of urban management strategies, emphasis is placed on maintaining and extending the life of these assets. Consequently, knowledge on the corrosivity of the environment in which these pipelines are embedded is considered essential. For this purpose a range of assessment methods are available, which can be conducted on either laboratory soil samples, or in-situ conditions. However, with increase in costs associated with premature failures as well as maintenance, there is an interest to deepen the scientific understanding of the pipeline corrosion phenomenon and improve existing life-time prediction models. In this regard, the present thesis has attempted to contribute to different aspects of the soil corrosion discipline, through a mixture of intensive laboratory as well as geophysical field study.

For the first time a galvanostatic pulse technique has been successfully applied to evaluate the electrical double layer properties at the metal/soil interface as well as to determine other corrosion related parameters. This has been conducted for synthetic soil samples in order to allow control over a multitude of variables. The choice of this technique is based on its ability to isolate bulk resistances from corrosion related process, as well as its ability to identify possible effects from soil capacitances. An important outcome of this study is that an experimental procedure is given, which allows consistent treatment of soils of various grain size distributions. Secondly, another detailed laboratory study has been conducted in order to illustrate the importance of integrating spectral induced polarization methods as part of normal assessment methods for identification of potentially corrosive soils. Synthetic soil samples from the aforementioned corrosion study were analyzed for their spectral responses in the frequency range $10^{-1} - 10^{3}$ Hz. Further information was extracted by fitting the acquired data using the Cole-Cole model. Overall it is shown that, apart from soil resistivities, the normalized chargeability parameter correlates with the polarization resistance, an important corrosion related parameter, when the soil physical properties manifest in the corrosion process. New ways of identifying potentially corrosive soils are also presented. This effectively extends the use of electrical characterizations for assessing soil corrosivity. Following these detailed laboratory studies, a field study is reported. Here, for the first time, the combined direct current resistivity and time-domain

induced polarization (DC-TDIP) profiling methods are used to assess site conditions along a pipeline right-of-way. Additional insights on the field results are provided by laboratory analysis of soil samples acquired systematically along the pipeline right-of-way from depths near to the buried pipeline. Following this, a methodological framework is suggested to assist in developing further capacities for the use of DC-TDIP methods for in-situ soil corrosivity assessments. In particular a distribution of self potential gradients is observed along the pipeline right-of-way suggesting zones of active electrolysis and enhanced external corrosivity.

CHAPTER 1

INTRODUCTION

1.1   Soil Corrosivity and Pipeline Failures

Soil corrosivity is a multi-disciplinary problem. It has a huge impact on the economic performance, public and environmental security, and structural integrity of metallic infrastructure; consequently soil corrosivity can be considered a hindrance to sustainable development. Most public infrastructures, also referred to as assets, are buried underground or at least in contact with soil. Consequently, their performance can be critically linked to their overall interactions within the soil environment. Pipelines are one such asset.

Pipelines are an important element of the global engine, allowing economic commodities (oil, natural gas, and water) and waste matter (sewage) to be transported over long distances from their origin to their final destination. Their ageing, as well as any accelerated deterioration, presents a serious problem. In the modern world, emphasis is always placed on maintaining and extending the life of these assets, in the larger framework of asset management strategies. However, pre-mature failures are common, and inflict substantial costs in the operating and maintenance budget of these assets. In a report by Koch *et*. *al*. (2002) it is estimated that in U.S.A, the annual cost of corrosion in the drinking water and sewer system sectors is US$36 billion, while in the gas distribution sector it stands at US$5 billion. In Australia, Cole & Marney (2012) have noted that there are 260, 000 km of pipelines used by water utilities and 80% of them are buried, with most of the critical mains constructed of ferrous metal. In order to assess the risk of failure, water utilities are actively engaged in condition and pipeline integrity assessments [Moglia *et*. *al*., 2008].

Most pipelines are constructed out of ferrous materials, and a major cause of their deterioration underground is through external corrosion [Kirmeyer *et*. *al*., 1994; Norin, 1998; Beaver & Thompson, 2006; Ricker, 2010; Benmousat & Traisnal, 2011]. To prevent significant corrosion, pipelines are usually installed with some form of protection [see Rajani & Kleiner, 2003; Baboian, 2005] including surface coatings (paint, bitumen, etc), polyethylene wraps, cathodic protection using sacrificial anodes, or impressed current cathodic protection The compound product is then installed in an engineered trench with appropriate backfill materials [Norin & Vinka, 2003]. Nevertheless, the development of point-defects along the protected asset can never be completely guaranteed, and when

present leads to corrosion. After a critical thinning of the pipeline wall due to corrosion, it becomes highly unstable and is unable to sustain active service loads, leading to a general failure. The deterioration of buried assets due to corrosion attack from its host environment in reality is a complex problem. This will be explained in the sub-sections which follow.

1.1.1 Types of Corrosion

The corrosion process involves two half-cell reactions, whereby the electron released at the anodic sites through oxidation are consumed by the reduction processes at the cathode. Hence, for the corrosion process to occur there should be an electrical continuity, provided by an electrolyte, between the anodic and cathodic site – a corrosion cell is then defined. In principle, the three major types of corrosion cells are galvanic, concentration, and electrolytic [see Garverick, 1994; Ahmad, 2006].

A galvanic cell is usually characterized by two different metals in a given electrolyte. For each metal, a corresponding corrosion potential in the electrolyte will determine whether it acts as an anode or cathode. Metal with a more positive corrosion potential will tend to act as the cathode, while adjacent metal characterized by a more negative corrosion potential will be the anode. A galvanic cell can also arise if identical metals under dissimilar conditions are placed in a given electrolyte. A classical example is when a new section of pipeline is attached to an older section [Garverick, 1994]. Provided the older section is covered by surface films (*e.g*., oxides) resulting from prior corrosion, it will tend to acquire a less active potential than the new section. This will eventually lead to a higher corrosion rate occurring on the new section.

Concentration cells develop due to differences in aeration (differential aeration cell) and other soil properties [Ahmad, 2006; Beaver & Thompson, 2006] along the pipeline. Parts of the structure in regions of high aeration have high oxygen availability and tend to become more cathodic than sections under reduced oxygen concentrations (more anodic). An example is when the pipeline traverses different lithological features, *viz*., sandy and clayey soils. Sections of the pipeline in sandy soils become more cathodic relative to the section in clayey soil, leading to a higher corrosion rate in the latter. Apart from aeration, differences in soil properties along the pipeline length, arising from different ionic compositions, local pH differences, accumulation due to ion migration, moisture content, *etc*., [Matsushima, 2011] can also give rise to similar anodic and cathodic features. Anodic and cathodic zones can be located very close to each other or can be separated by large distances giving rise to "long-line" corrosion [see Smith, 1981].

Electrolytic cells refer to the condition when any galvanic or concentration cell is acted upon by an external source of current. For buried pipelines, this is usually caused by stray currents [*e.g.*, Zakowski & Darowicki, 2000; Zhu *et. al.*, 2011], which directly lead to electrolysis and thinning of the pipewall structure. Stray currents can result from anthropogenic or natural sources and can have very detrimental effects on buried structures.

Corrosion attack on metals under the establishment of any corrosion cell can be highly variable. Generally, the attacks are characterized as localized or uniform (sometimes referred to as general) corrosion. Localized corrosion refers to the condition when the corrosion attack is confined over a smaller area. An example is pitting corrosion, which leads to small pits in the pipeline [see Doyle *et. al.*, 2003]. Pitting arises due to differences in the relative sizes of the anodic and cathodic zones. If the anodic area is very small compared to the cathodic area, then the former will be subjected to a high discharge current density [Beaver & Thompson, 2006], resulting in significant metal loss. On the contrary, uniform corrosion is characterized by corrosion attack proceeding evenly over the pipeline surface, or a large fraction of the total area. Under these circumstances, failure occurs after thinning has corrupted material integrity critical for sustaining nominal loads. It shall be noted here that the present thesis will only consider general corrosion afforded on metals by soils. Localized corrosion, in the form of pitting, is a highly complex feature which requires different testing and characterization methods [see Baboian, 2005], and is beyond the scope of the present thesis.

Another feature of pipeline corrosion is the manner in which metal loss takes place. This will usually depend on the microstructural properties of the pipeline material. For example, the two most common materials utilized in the water and sewer utilities are cast-iron and ductile-iron. In cast-iron pipes, external corrosion takes place in the form of graphitization, whereby there is selective leaching of iron from the material, leaving the graphite matrix intact [see Davis, 1996]. On the other hand, ductile-iron pipes corrode in the form of "through-hole" corrosion pits [Sadiq *et. al.*, 2004]. It will be emphasized here that the present thesis is not concerned with the microstructural effects on the overall corrosion process, and hence will not be treated further. However, studies of this nature have been carried out and can be found elsewhere [*e.g.*, Mohebbi *et. al.*, 2010; Mohebbi & Li, 2011].

1.1.2 Soil Properties Influencing its Corrosivity

Compared to other environments, soil is very difficult to classify for potential aggressivity owing to its complexity [Smith, 1981; Roberge, 2000; Ferreira & Ponciano, 2006], particularly arising from its porous and heterogeneous nature. Under field conditions and at any given time, all three types of

corrosion identified in the previous section can be occurring simultaneously on the buried pipeline. This exacerbates any appraisal of the true nature of corrosion intensity, especially with the presence of a multitude of variables [see Robinson, 1993]. However, there are some important features and properties of soils, which can at least be connected to their overall corrosiveness. Discussions on these properties are readily available in the literature [*e.g*., Romanoff, 1957; Smith, 1981; Roberge, 2000; Baboian, 2005; Stott & John, 2010], and hence a detailed treatment will not be presented here. Instead, a summary on some important properties is given as follows.

Soil texture and structure generally indicates the type of soil; soils with particulate matter in the size range (0.07 – 2 mm), (0.005 – 0.07 mm), and <0.005 mm are classified as sandy, silty, and clayey respectively [Stott & John, 2010]. Clay soils are considered to be potentially more corrosive than sandy soils [see also Oguzie *et. al*., 2004] due to their water retention properties and their contribution to formation of differential corrosion cells. The particles in clayey soils are more tightly packed and permit very low oxygen diffusion, which is a necessary component for a corrosion process [Ismail & El-Shamy, 2009]. On the contrary, tight packing also leads to poor aeration with enhanced moisture content. Soil resistivity is another important property governing the overall corrosivity. According to Stott & John (2010), soil resistivity, in the absence of microbial activity, is the dominant parameter affecting the corrosion process. It is well established that soils with higher resistivity are usually less corrosive compared to soils with very low resistivities [*e.g*., Robinson, 1993; DIPRA, 2000]. Clay and dissolved salt species can greatly reduce soil resistivities. Hence, it serves as a good indicator of the ionic current flow capability, which influences the corrosive nature of soils. Apart from this, soils with low resistivities in-situ, pose additional problems including stray current pick-up.

Chemical composition of soils further complicates the corrosivity of the media. The species notable for their corrosive attack on metals are chlorides [Garverick, 1994; Moreno *et. al*., 2004]. Apart from directly influencing the soil resistivity, chlorides participate in active dissolution of metals. Chlorides are never completely consumed in the corrosion process. They continually recycle and lead to the breakdown of any passive layer formation [Broomfield, 2007], thus leading to extensive corrosion of metal surfaces. The other chemical species, notable in soils are sulphates. Sulphate ions are believed to be more benign in terms of their corrosive attacks on metals [Roberge, 2000]. However, their contributions can become serious in the presence of sulphate-reducing bacteria (SRB), which transform the sulphates into the more aggressive sulphide components [Landolt, 2007]. The microbiologically induced corrosion (MIC) due to such bacterial activity warrants a study on its own, due to the highly detailed complex mechanisms arising from the variety of bacterial life-forms

participating in the corrosion process. It will be emphasized here that treatment and investigations into MIC are beyond the scope of the present study and thus are not dealt within this thesis.

1.2   Assessment Methods

For efficient asset management, investigations into soil properties and their relation to corrosion are important. This enables systematic inferences to be made regarding the probable asset lifetime in the soil environment. There are two ways such investigations can be carried out. Firstly, assessment can be conducted on soil samples (hand-specimens) acquired near the pipelines and subjected to physical and/or chemical analysis in order to ascertain their potential corrosivity [*e.g*., Ferreira *et. al*., 2007]. Secondly, soil conditions can be estimated in-situ from geophysical methods [*e.g*., Osella & Favetto, 2000]. It will be noted here that apart from soil investigations, inspection of excavated pipelines for surface irregularities and wall thickness also form an important part of the condition assessment. However, the present thesis is only concerned with issues from soils, and hence discussions will be restricted to this. Corrosion of utilities is known to exist within the entire pH range [Uhlig, 1981] and in the soil environment can be complicated by competing parameters such as low resistivity, redox potential (indication of degree of aeration and/or microbiological activity), high moisture content, soil type, ionic content, and stray currents [see Fitzgerald, 1993; DIPRA, 2000]. Several ranking systems and methodologies have been suggested, which can be used to ascertain whether a particular soil environment is corrosive [*e.g*., Robinson, 1993; DIPRA, 2000; Sadiq, 2004].

One such ranking system proposed by the Ductile Iron Pipe Research Association (DIPRA) and their 10-point scoring method, applicable for cast and ductile iron pipelines, is given in Table 1.1. The method assesses the magnitude of 5 soil properties including pH, redox potential, sulphide content, moisture content, and resistivity and assigns a numerical score for each property. If the sum of all scores for the 5 properties ≥ 10, then the soil is considered corrosive to pipelines, otherwise it is non-corrosive [Najjaran *et. al*., 2004]. Essentially, this system has a binary (corrosive and non-corrosive) classification, and has been noted to give mixed success [Moglia *et. al*., 2004]. Also, Najjaran *et. al*. (2004) notes that soils with scores just above and just below a value of 10 are classified as corrosive and non-corrosive respectively, albeit they may be almost identical. The DIPRA 10-point method can be applied to laboratory samples collected from the field and also to in-situ measurements of soil condition. For the relative weights conferred on each parameter, it is noted that soil resistivity is given the highest consideration. Soils with resistivities of <15 Ω m are instantly considered corrosive. This essentially indicates that high correlations generally exist between soil resistivity and its associated aggressivity [*e.g*., see Robinson, 1993; Baboian, 2005].

Table 1.**1**. Soil corrosivity evaluation for ductile/cast iron pipe using 10–point method (DIPRA, 2000).

Soil	Values and characteristics	Points
Resistivity (Ω m)	<15	10
	≥15 – 18	8
	>18 – 21	5
	>21 – 25	2
	>25 – 30	1
	>30	0
pH	0 – 2	5
	2 – 4	3
	4 – 6.5	0
	6.5 – 7.5	0
	7.5 – 8.5	0
	>8.5	3
Redox Potential (mV)	> +100	0
	(+50) – (+100)	3.5
	0 – (+50)	4
	<0	5
Sulphides	Positive	3.5
	Trace	2
	Negative	0
Moisture	Poor drainage (continually wet)	2
	Fair drainage (generally moist)	1
	Good drainage (generally dry)	0

For a further example, several more qualitative criteria are available in literature relating soil resistivity to its overall corrosiveness [*e.g*., Robinson, 1993; Baboian, 2005; Stott & John, 2010]. One particular scheme by Robinson (1993) is given in Table 1.2.

Table 1.2. Qualitative scheme for assessing soil corrosiveness from its resistivity. From Robinson (1993).

Soil Resistivity (Ω m)	Corrosiveness
0 - 5	Severely corrosive
5 – 10	Very corrosive
10 – 30	Corrosive
30 – 100	Moderately corrosive
100 – 250	Slightly corrosive
>250	Relatively corrosive

Corrosivity scale ratings, such as in Table 1.2, are usually subjective and vary slightly amongst the different scales given in the literature. Thus, there is no single scale rating, which has been universally accepted.

Apart from general classification schemes to identify potentially corrosive soils, there has been considerable interest in predicting the corrosion rates of pipelines in soils. The ASTM G162-99 (2004) standard describes the standardized procedures for conducting and evaluating laboratory corrosion tests in soils. The procedure is mainly based on laboratory weight loss measurements of test specimens embedded in saturated soil samples and monitored over a sufficient exposure time. Although useful, exposure periods required for meaningful results can become very time consuming.

Consequently, laboratory tests for estimating corrosion rates have now included more sophisticated and robust electrochemical methods [see Cole & Marney, 2012], some of which are non-destructive techniques (NDT) in nature. These techniques usually measure the instantaneous corrosion rates, which are prevalent during the time of measurement. However, corrosion rates are highly variable and will evolve with time depending upon the characteristics of the surface films or rusts on the metal surface. Hence, assessing pipeline life-time from such measurements is not a linear problem. Instead the instantaneous corrosion rates measured have to be subjected to statistical and/or probabilistic models, to account for several variabilities, in order to project mean- time-to-failure of pipelines.

One common NDT is the linear polarization resistance (LPR) method [see Scully, 2000]. Although, the drawbacks in using LPR measurements are known [*e.g*., see Kouril *et. al*., 2006], it is still utilized for estimating corrosion rates and assessing soil corrosivity under both laboratory and in-situ field conditions [*e.*g., Ferguson & Geehman, 2001; Norin & Vinka, 2003; Moglia *et. al*., 2004]. It will be noted here that at present there is no general consensus on the procedures for carrying out LPR measurements in electrochemical systems consisting of soil electrolytes.

Studies in literature have utilized different electrochemical techniques to investigate corrosion in soils [*e.g*., Kasahara & Kajiyama, 1983; Pernice *et. al*. 1990; Silva & Dick, 2008]. However, recently several electrochemical studies have focussed on soil simulating solutions [*e.g*., Liang *et. al*., 2009; Zhang *et. al*., 2009; Wu *et. al*., 2010; Benmousat & Traisnal, 2011 and the references therein] to infer the performance of different materials. These simulated solutions are especially prepared with their chemical compositions adjusted to normal groundwater conditions. It is believed that the emergence of studies involving soil simulating solutions reflects the difficulty in conducting electrochemical measurements using soil electrolytes (addressed later in the thesis). Although studies with soil simulating solutions are very important to evaluate the behaviour of different materials under the action of different chemical species, it lacks the essential feature of how the particulate matter in soils affect the overall corrosion mechanisms.

It shall be noted here that at present no electrochemical technique and accompanying procedures have been adopted as a standard for conducting tests and assessing corrosion in soils. Hence, this effectively makes it an active area of research.

1.3   Geophysical Methods in Soil Corrosivity Assessments

Geophysical methods have long been used in geotechnical and civil engineering based applications [McDowell *et*. *al*. 2002 and the references therein] and also in the context of urban geophysical problems [see Henderson, 1992]. It is not the intent of this section to provide a complete overview of all these geophysical applications, but rather to outline some important concepts and ideas which have been explored in the present thesis.

The direct current (DC) resistivity method using Wenner array is currently the accepted standard, as covered in ASTM G57-95a (2001), for determination of in-situ soil resistivities, which can be used for assessing potential soil aggressivity. This standard also describes procedures for carrying out resistivity measurements in soil samples collected from the field and analysed in a laboratory. As such, a baseline geophysical method for assessing soil corrosivity, for in-situ as well as laboratory samples does exist. However, there have been important advances in several associated aspects for characterizing soil electrical properties over the years. It has been known for a long time that apart from electrolytic conductivity, soils also possess surface conductivity mechanisms giving rise to a polarization response [*e*.*g*., Olhoeft, 1985; Ruffet *et*. *al*., 1995]. Over recent years, several important developments have taken place, at least under laboratory conditions, in understanding and characterizing this polarization phenomenon in soils under the influence of various conditions [Revil & Glover, 1998; Slater & Lesmes, 2002; Revil & Florsch, 2010; Schmutz *et*. *al*., 2010; Revil, 2012; Schwartz *et*. *al*., 2012 and the references therein]. Measurements are usually conducted in the time-domain or frequency-domain giving rise to classifications as time-domain induced polarization method or spectral induced polarization method respectively. These measurements enable characterization of extra parameters, which are somewhat electrical in nature, apart from soil resistivity determinations. This presents a unique opportunity to possibly extend the present resistivity method for laboratory soil corrosivity assessments. Also, it is now common for the time-domain induced polarization measurements to be included and carried out simultaneously with direct current resistivity measurements [*e*.*g*., Gazoty *et*. *al*., 2012]. Thus, a possibility also exists to extend the presently accepted Wenner resistivity method for soil corrosivity assessments by including time-domain induced polarization measurements. It is understood that such a work has never been carried out before in the context of pipeline integrity surveys.

Another geophysical technique gaining a lot of attention recently is the self potential method [see review by Jouniax *et. al.*, 2009 and the references therein]. It serves as a good reconnaissance tool for identifying possible anomalous features which can be connected with a multitude of ground conditions. The method bears similarity with the pipe-to-soil potential method commonly utilized in the field to map the open-circuit potential between the pipeline and a non-polarizable electrode traversed on the ground surface along the pipeline alignment [see Ahmad, 2006]. Results from pipe-to-soil potential mapping are usually used to assess pipeline integrity by identifying sections which are at high-risk of failure due to corrosion. This is usually identified by sections exhibiting large negative anomalies. Self potential methods (referred to as surface potentials) are also used in a similar manner [Ahmad, 2006; Ekine & Emujakporue, 2010]. However, results from the surface based self potential method may be difficult to interpret, compared to pipe-to-soil-potential, since anomalies can manifest due to a wide range of sources. Nevertheless, the presence of self potentials may be highly linked to the overall pipeline integrity.

1.5   Thesis Aims

The present thesis is, at its core, a multi-disciplinary study. Its overall aim is to contribute towards advances in various electrical methods, which are believed to be important to the discipline of soil-related corrosion. The thesis is mainly based in the context of pipeline corrosion in soil; it is built on a strong conviction that there is an urgent need to develop and/or identify electrochemical methods which can aid in assessing potential soil aggressivity as well as to extend the present electrical characterizations which can be further used to diagnose potentially corrosive soil environment. The specific aims formulating the thesis are to:

- Identify a suitable technique for robust measurement of corrosion rates in soil, and to assess the corrosivity of different soils.
- Identify the effects of clay and chlorides on corrosion of ferrous materials.
- Determine the feasibility of spectral induced polarization methods in assessing corrosivity of laboratory soil samples and identify any new factors which can be diagnostic of potential soil corrosivity.
- Develop capacities for the combined direct current resistivity and time-domain induced polarization method in electrical profiling for use in site condition assessments, and identify any possible implications of self potentials on pipeline integrity.

1.6   Guide to this thesis

The thesis is written to address the wider scientific community due to the implications of its multi-disciplinary nature. It consists of detailed laboratory studies in the field of applied electrochemistry and applied geophysics, as well as a field component consisting of geoelectric surveying. Hence, the thesis has been organized in a manner such that it addresses important concepts across the multi-disciplinary platform. Chapter 1 provides a brief background on the topic of soil corrosivity and outlines the overall aims of the thesis.

Chapter 2 provides a treatment of some major electrochemistry principles needed to develop an understanding of the corrosion kinetics and the various measurement techniques. Chapter 3 deals with the background and specifics of field procedures in conventional direct current resistivity, induced polarization, and self potential surveys. Formulations of Chapters 2 and 3 are essential to ensure the thesis is compatible to the wider community as mentioned.

Chapter 4 presents a laboratory study using galvanostatic pulse techniques to investigate the corrosion of different pipeline materials in synthetic soil samples. It reports the advantages and limitations of the technique, especially in soil environments. The effects of clay content and chlorides are also presented. Chapter 5 reports on the spectral induced polarization study conducted on the synthetic soil samples used in Chapter 4. It aims to illustrate the usefulness of including spectral induced polarization characterizations as part of soil corrosivity assessments. Some new characterizations, which can aid in identifying potentially corrosive soils, are also discussed.

Chapter 6 is an important outcome of the present study, which was not initially envisaged but became more obvious as the project progressed. It describes the design and implementation of a low-cost digital system for carrying out direct current resistivity and time-domain induced polarization profiling. Several advanced features of signal processing are discussed and implemented. The field component is presented in Chapter 7. Here, the combined direct current resistivity and time-domain induced polarization methods are used to perform electrical profiling along a pipeline alignment. Self potential measurements conducted along the alignment are also presented. Field results are critically assessed and further complemented with laboratory analysis. A methodological framework for interpreting field data is suggested. Chapters 4, 5, and 7 are intricately linked to each other. This, in essence, reflects the true multi-disciplinary nature of the present thesis and is unavoidable. Also, relevant literature is presented and discussed in each of the aforementioned chapters. Conclusions for each chapter are provided accordingly, where applicable.

Chapter 8 summarizes the key findings and suggests directions for further work. To avoid unnecessary redundancies, cited literature in each chapter is provided collectively in the thesis references section. Other important information as well as data relevant to provide completeness to the discussions presented in the thesis is given in the appendices accordingly.

CHAPTER 2

POLARIZATION FUNDAMENTALS FOR CORROSION MEASUREMENTS

This chapter provides a theoretical framework for understanding the electrochemistry principles in corrosion science. It presents a brief overview of some important concepts and terminologies, which are used through-out this thesis. A background on some electrochemical techniques used in this work is also presented towards the end of this chapter.

2.1   The Double Layer Theories

In a metal-electrolyte system there exists an interface, which facilitates any form of energy transfer between the two mediums. The physical structure at the interface is called the *electric double layer* (EDL). The first model explaining the behaviour of the EDL was by Helmholtz in 1853. Since then several important developments have been incorporated in this model to account for the observed more complex behaviour. To facilitate an understanding of the corrosion phenomenon and its related measurement techniques which utilize polarization phenomenon, a treatment of the properties of the metal-electrolyte interface is essential. In this section the various models developed in order to characterize the interfacial properties are visited according to their chronological order.

2.1.1   Helmholtz Model

Helmholtz in treating the EDL assumed it to behave like a simple capacitor, whereby the anionic and cationic charges were distributed across the interface as illustrated in Figure 2.1. The sign of the solvated ions at the surface will be determined by the charges on the metal surface. The layer of solvated ions manifests the so called exterior Helmholtz layer (EHL), at a distance d_H away from the metal surface. The Helmholtz model suggests rigid layers of charges separated by a planar distance d_H. The potential drop across the Helmholtz layer, $\Delta\varphi_H$, can be calculated using Gauss's Law and is given by:

$$\Delta\varphi_H = \frac{\sigma d_H}{\varepsilon_o \varepsilon_r} \tag{2.1}$$

where, σ is the charge density, ε_o and ε_r are the permittivity of free space (8.85×10^{-12} F m^{-1}) and relative permittivity respectively. The two boundary conditions for this model are a) at the metal surface, $x = 0$, the potential $U = \varphi_M$, and b) for $x \geq d_H$, $U = \varphi_S$.

Thus the potential inside the EDL varies linearly with distance away from the metal surface (see Fig. 2.1b). Using Eq. 2.1, the Helmholtz capacitance, C_H, of the EDL can be expressed as:

$$C_H = \frac{\varepsilon_o \varepsilon_r}{d_H} \tag{2.2}$$
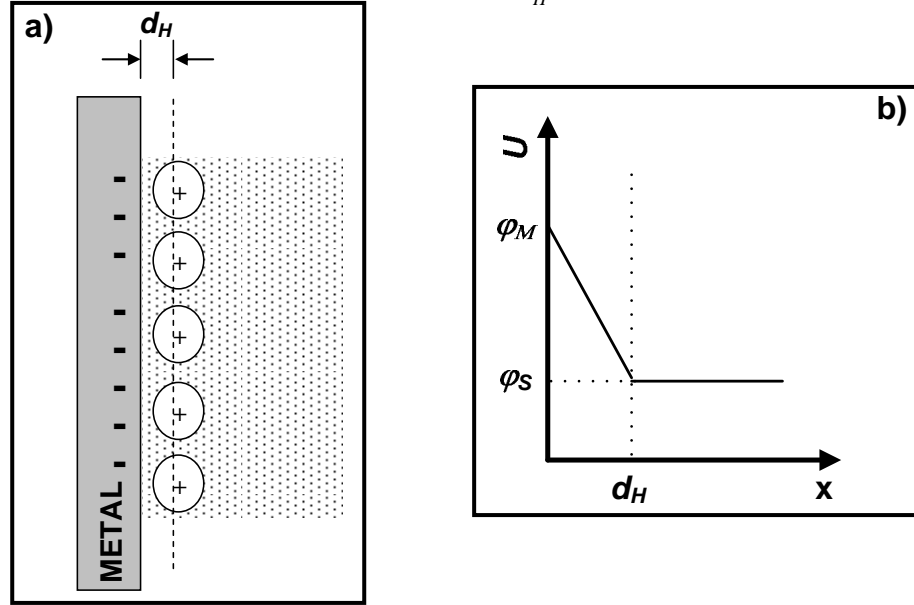
Figure 2.1. **a)** The Helmholtz model for the electric double layer and **b)** potential distribution across the interface.

Note that the capacitance C_H of the double layer is independent of any change in electrode potential. The drawback with the simple Helmholtz model is that it does not accurately describe most experimental results. This is partly addressed by the Gouy-Chapman model described next.

2.1.2 Gouy-Chapman Model

The Gouy-Chapman model deviates primarily from the Helmholtz model with the notion that the solvated ions are no longer considered to be a rigid layer of charges (see Fig. 2.2). Instead the distribution of positive or negative charges from the metal surface is approximated by the Boltzmann distribution given by:

$$N_i(x) = N_i^o \exp\left(\frac{-z_i e[\varphi_x - \varphi_S]}{kT}\right), \tag{2.3}$$

where, $N_i(x)$ is the ion concentration at a distance x from the metal surface, N_i^o is the bulk concentration, z_i is the charge on the ion, e is the electron charge (1.6×10^{-19} C), φ_x and φ_S are the potential at a distance x and the solution potential respectively, k is the Boltzmann constant (1.38×10^{-23} m^2 kg s^{-2} K^{-1}) and T is the temperature (K).
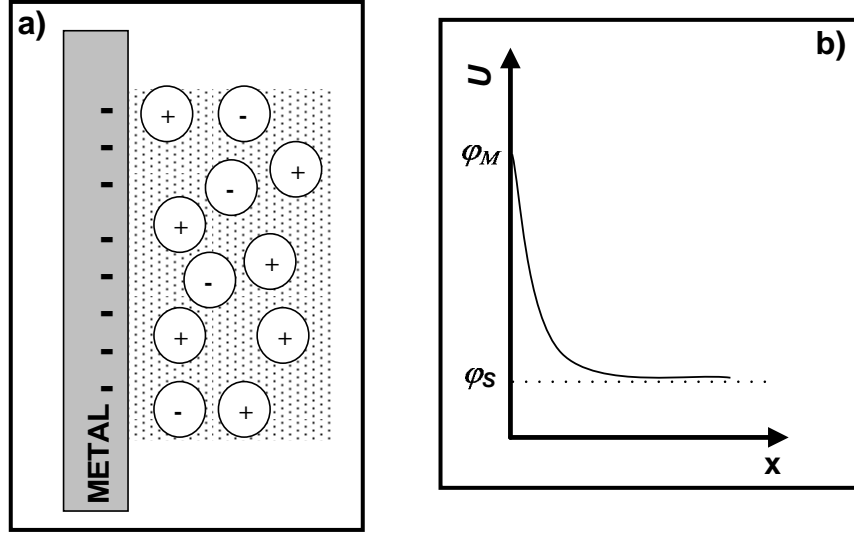
Figure 2.2. **a)** The Gouy-Chapman model for the electric double layer at the metal-electrolyte interface and **b)** potential distribution from the metal surface.

Assuming the charges can be modelled as point charges, the relationship between the electric potential φ and the volume charge density $\rho(x)$ can be expressed by Poisson's equation given by Eq. 2.4.

$$\nabla^2 \varphi(x) = -\frac{\rho(x)}{\varepsilon_o},$$ (2.4)

where,

$$p(x) = \sum z_i e N_i(x)$$ (2.5)

Equations 2.3 and 2.4 can be combined to produce the Poisson-Boltzmann equation (Eq. 2.6), which describes potential distribution away from the metal surface.

$$\frac{d^2 \Delta \varphi}{dx^2} = -\frac{1}{\varepsilon_r \varepsilon_o} \sum_i z_i e N_i^o \exp\left[\frac{z_i e \Delta \varphi(x)}{kT}\right],$$ (2.6)

where,

$$\Delta \varphi(x) = \varphi_x - \varphi_S$$ (2.7)

The Poisson-Boltzmann equation is highly non-linear. The relationship between the potential and the charge density of the diffuse layer is given by Eq. 2.8.

$$\sigma = \varepsilon_r \varepsilon_o \left(\frac{d\Delta \varphi}{dx}\right)_{x=0} = \left(8kT\varepsilon_r \varepsilon_o c^o\right)^{\frac{1}{2}} \sinh\left(\frac{ze\Delta \varphi_o}{2kT}\right),$$ (2.8)

where, c^o is the electrolyte concentration, and $\Delta \varphi_o = E - E_{PZC}$. E_{PZC} is the electric potential at the point-of-zero-charge. Using Eq. 2.8, the expression for the differential capacitor in the Gouy-Chapman model can be written as:

14

$$C_d = \frac{d\sigma}{d\Delta\varphi_o} = \frac{\varepsilon_r \varepsilon_o}{L_D} \cosh\left(\frac{ze\Delta\varphi_o}{2kT}\right) \tag{2.9}$$

Where, L_D is the Debye-length. Note that the differential capacity in the Gouy-Chapman model now varies according to $\Delta\varphi_o$. However, it predicts that for increasing $\Delta\varphi_o$, the C_d increases very rapidly without any limit. This anomaly arises in the model because of the assumption that the ions can be modelled as point charges [see Riley, 2005]. In practice, however, ions have finite radii, thus enabling only a distance of closest approach for the ions to the metal surface. This distance of closest approach is determined by the ionic radii. Thus, although the Gouy-Chapman model provides a major improvement to the Helmholtz model, it still lacks some practical considerations. These issues are addressed in the Stern model which is described next.

2.1.3 Stern Model

Improvements in the Gouy-Chapman model are provided by the Stern model, by modelling the ions not as point charges but as spheres of finite radii. This model combines the previous two models to describe the EDL as having two parts:

   a) a rigid arrangement of ions existing in the layer between the metal surface and a plane identifying the distance of closet approach of the ion to the surface. This plane is called the Outer Helmholtz Plane (OHP), and

   b) a diffuse layer extending away from the OHP.

An illustration of the above scheme is shown in Figure 2.3.
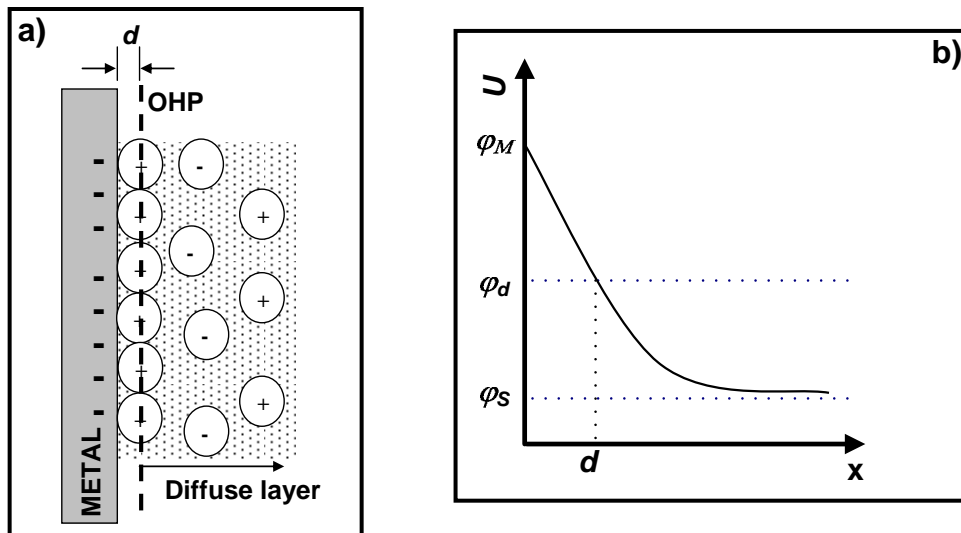
Figure 2.3. **a)** The Stern model for the electric double layer at the metal-electrolyte interface, and **b)** potential distribution from the metal surface.

The potential distribution at the interface is shown in Figure 2.3b. It consists of two distinct regions, a) a linear variation extending from the metal surface up to the OHP, followed by a non-linear variation in the diffuse region. Consequently, the two regions exhibit different capacitance. Thus, the Stern model attributes the total capacitance C_T of the interface as consisting of a series arrangement of the inner layer capacitance C_i and the diffuse layer capacitance C_d. This is equivalent to the series arrangement of the capacitances from the Helmholtz and Gouy-Chapman models [see Brett & Brett, 1994] as given:

$$C_T = \left(\frac{1}{C_i} + \frac{1}{C_d} \right)^{-1} = \left(\frac{d}{\varepsilon_r \varepsilon_o} + \frac{L_D}{\varepsilon_r \varepsilon_o \cosh\left(\frac{ze\Delta\varphi_o}{2kT} \right)} \right)^{-1} \tag{2.10}$$

Note that Eq. 2.10 identifies two special cases:

a)   For large $\Delta\varphi_o = E - E_{PZC}$, $C_i \ll C_d$, which implies $C_T \cong C_d$, and

b)   For very low $\Delta\varphi_o = E - E_{PZC}$, $C_i \gg C_d$, implying $C_T \cong C_i$.

Although the Stern model has been found to correctly predict most experimental results, it suffers from a minor drawback. In describing the distance of closest approach, it is assumed that this plane (OHP) would lay at a distance equal to the radii of the hydrated ion. In some instances, however, these ions may lose their hydration when approaching the metal surface and hence acquire smaller radii. These smaller radii ions can approach the metal surface much closer than the hydrated ions. The Grahame model accounts for this effect and is briefly described next.

2.1.4 Grahame Model

To account for specific adsorption [see Brett & Brett, 1994], Grahame in 1947 suggested some minor adjustments to the Stern model. Grahame's model adds another plane to the Stern model to account for smaller radii ions approaching much closer to the surface as shown in Figure 2.4. The model thus consists of an Inner Helmholtz Plane (IHP) and the OHP, which now accounts for ions of different radii, and the diffuse layer. The region between the IHP and the OHP is defined as the Stern layer. Note that the potential distribution exhibits three different curves, each corresponding to distinct energy considerations [Brett & Brett, 1994].
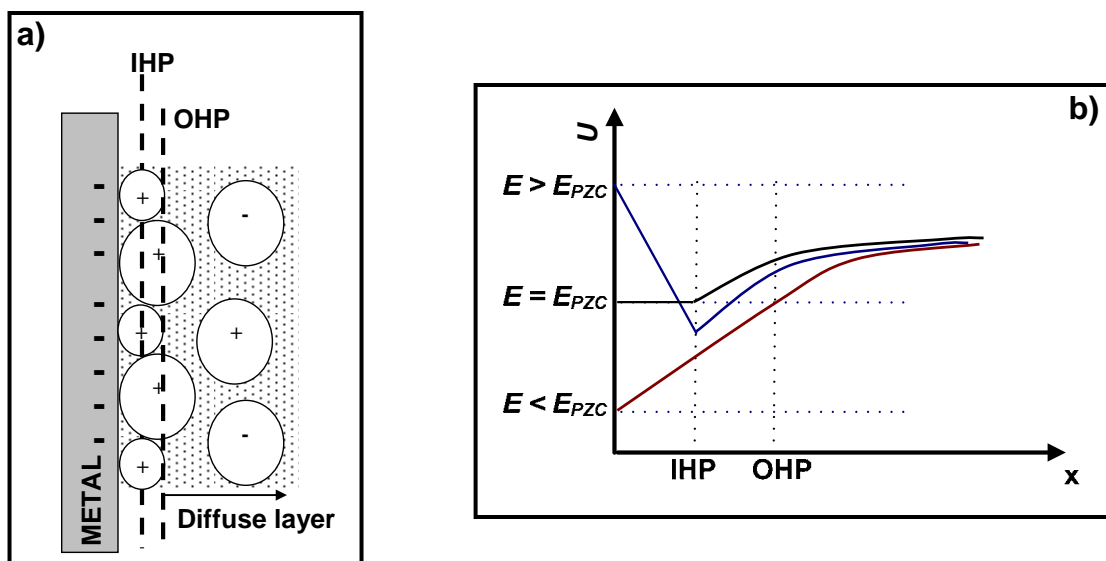
Figure 2.4. **a)** The Grahame model for the electric double layer at the metal-electrolyte interface, and **b)** potential distribution from the metal surface.

The EDL models discussed in this section is important for understanding the concepts discussed later in this thesis. Apart from their interpretative usefulness in corrosion related phenomenon, the EDL theory is also important in understanding the induced polarization phenomenon observed in soils (Chapter 3). Since a basic understanding of the interfacial properties is now established, the basics of corrosion science is treated in the next section. Detailed discussions on these basic concepts are well documented in literature [Brett & Brett; Perez, 2004; Ahmad, 2006; *etc*]. Thus only an overview summarizing important concepts is presented.

2.2   Basic Concepts of Thermodynamics in Corrosion

The Laws of Thermodynamics in corrosion science provide an insight into whether a reaction will spontaneously occur, *i.e.*, without the need for any external energy input. This is the first step in assessing corrosion processes in a given system. A basic understanding of corrosion processes requires knowledge on fundamental electrochemistry, which is well documented in literature and can be found elsewhere [Brett & Brett, 1994; Stansbury & Buchanan, 2000; Bagotsky, 2006; Hamann *et al.*, 2007; *etc*]. However for completeness, a brief overview of some important concepts and terminologies are addressed in this section.

2.2.1   Gibbs Energy and Standard Electrode Potentials

In thermodynamics, the Gibbs-Helmholtz equation provides an indication of the change in the Gibbs energy, ΔG (kJ mol^{-1}) of a system during a reaction.

$$\Delta G = \Delta H - \Delta(TS), \tag{2.11}$$

where, ΔH is the change in enthalpy of the system (kJ mol^{-1}), $\Delta(TS)$ is the change in the product of temperature, T (K) and entropy, S (J mol^{-1} K^{-1}) between the initial and final states of the system. The sign of ΔG then indicates whether the reaction is spontaneous; $\Delta G > 0$ for non-spontaneous reactions, $\Delta G < 0$ for spontaneous reactions, and $\Delta G = 0$ for reactions at equilibrium.

Consider a half-cell reaction. At the metal-electrolyte interface, under conditions of dynamic equilibrium, the ionization of the metal (Eq. 2.12) is equal to the rate of discharge across the double layer, and the double layer develops a potential difference across the interface [Ahmad, 2006].

$$M \rightarrow M^{n+} + ne$$
$$M^{n+} + ne \rightarrow M \tag{2.12}$$

This potential difference is known as the reduction potential, E_{red}. When a charge traverses the double layer, it passes through this potential difference. This leads to a change in the energy of the charge which is given by:

$$\Delta G = -nFE_{red}, \tag{2.13}$$

where, n is the number of electrons transferred in the reaction, and F is the Faraday constant (9.6485 $\times$ 10^4 C mol^{-1}). Every electrochemical reaction has its own E_{red}, which when measured under standard conditions [Perez, 2004] relative to a hydrogen reference electrode is called the standard electrode potential, E^o. Note that the total ΔG_T for the reaction will be the sum of the individual ΔG for each of the half-cell reactions in a system.

2.2.2 Nernst Equation and Pourbaix Diagram

The standard electrode potentials for different metals are well documented in literature [*e.g.*, see Ahmad, 2006]. Nevertheless, the dependence of this potential with temperature and concentrations of species involved in the half-cell reaction is given by the Nernst Equation given by Eq. 2.14.

$$E_{red} = E^o - \frac{RT}{nF} \ln \frac{a_{\mathrm{Red}}}{a_{Ox}} \tag{2.14}$$

where, R is the universal gas constant (8.31 J mol^{-1} K^{-1}), T is the temperature (K), and a_{Red} and a_{Ox} are the chemical activities of the reductant and oxidant species respectively. Note that for unit activities, $E_{red} = E^o$. Using the Nernst Equation it is possible to obtain the equilibrium potential for any practical metal-electrolyte system. In dilute electrolytes, the activity concentrations are close to unity. Hence, under this condition the Nernst equation can be directly expressed in terms of concentrations. The limitation of the Nernst equation however arises when the concentration of the species is very low;

the potential predicted by the Nernst equation then approaches $\pm\infty$, which renders the calculation meaningless.

Nevertheless, the Nernst Equation is an important tool for constructing the Pourbaix diagrams [Mccafferty, 2010]. The Pourbaix diagram is an Eh-pH diagram, which identifies possible equilibrium phases of an aqueous electrochemical system. It also reveals the conditions in which there is immunity (no corrosion), corrosion, and passivity. For example, a sketch of the Pourbaix diagram for iron in water is shown in Fig. 2.5 [accurate illustration can be found in Mccafferty, 2010].
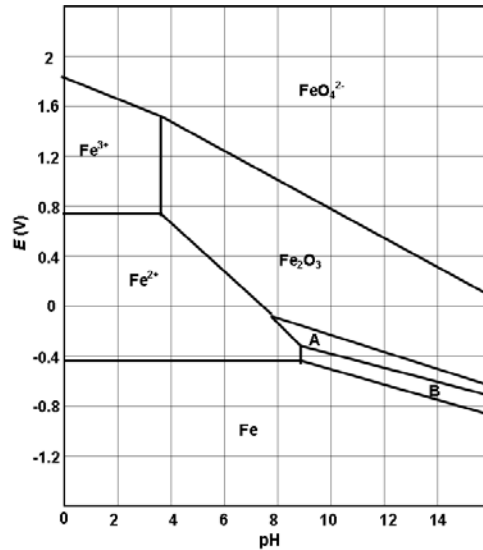
Figure 2.5. Sketch of the Pourbaix diagram for iron-water system [after information from Ahmad, 2006; Mccafferty, 2010].

The horizontal and diagonal lines in the diagram correspond to redox reactions, which are independent and dependent on pH respectively. Vertical lines correspond to non-redox reactions, which are dependent on pH. Special regions (areas) in this diagram are the:

a) immunity zone represented by Fe, which is iron in solid form absent of any corrosion,

b) corrosion zones represented by areas enclosed by
    i. Fe^{2+} and Fe^{3+}, which represents oxidation of metallic iron,
    ii. FeO_4^{2-}, which is aqueous solution of that ion.

c) passivation zones represented by areas enclosed by Fe_2O_3, region **A** (Fe_3O_4), and region B ($Fe(OH)_2$), which represent the formation of an oxide film on the surface thus preventing further corrosion.

Also, the dependency of each redox/non-redox reaction on pH can be inferred from the Pourbaix diagram. The major limitation of Pourbaix diagrams is that it is purely based on thermodynamic data, hence does not provide an indication on the rate of reaction.

Discussions so far have treated basic concepts in corrosion phenomena, which though indicating the possibility of corrosion, provide no further information on the rate of corrosion, or the metal loss. This is the classical feature of the Laws of Thermodynamics in corrosion science. In order to quantify corrosion rates, the application of electrochemical kinetics is required, which is treated in the next section.

2.3   Polarization Kinetics

The electrode potential is the most critical factor in determining the reaction rate on the electrode. This reaction rate is quantified by the number of electrons exchanged across the interface. Note that reaction rates are governed by chemical kinetics, while electrochemical kinetics govern corrosion rates [Perez, 2004]. This section provides a treatment on the effect of changing the potential of a metal in the metal-electrolyte system. It further provides a theoretical platform for understanding the potentiodynamic techniques presented in Section 2.4.

2.3.1   Activation, Concentration and Ohmic Polarizations

In order to facilitate an understanding of electrode polarization, consider the metal-electrolyte system shown in Fig 2.6.
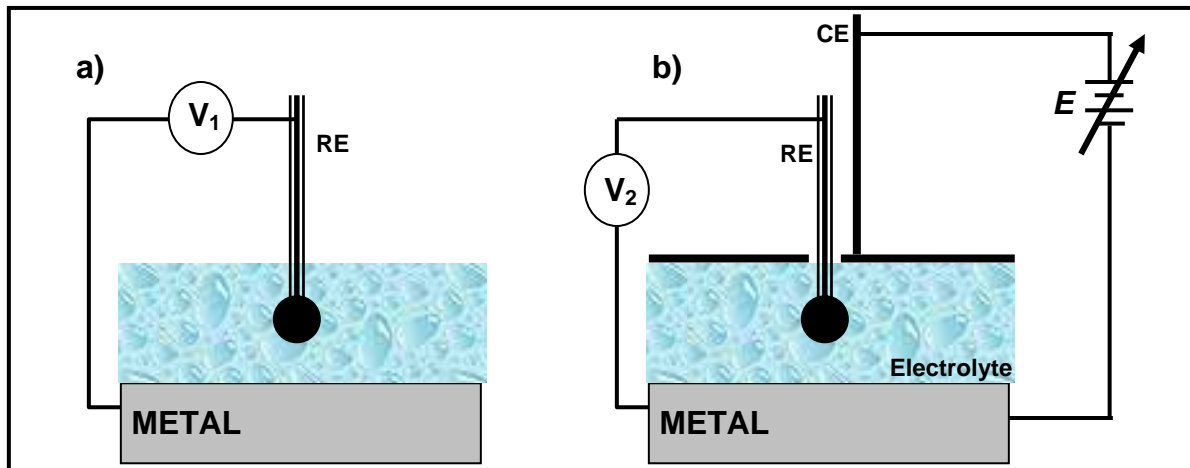
Figure 2.6. **a)** Determination of the open-circuit potential of a metal-electrolyte system, and **b)** application of an external field to a three-electrode arrangement causing a shift of the electrode potential. Note RE – reference electrode, CE – counter electrode.

In the absence of any external field (Fig 2.6a), the electrode potential measured relative to any reference electrode using a high-input impedance voltammeter is known as the open-circuit potential E_{OC} (which is a mixed potential as discussed in Section 2.3.2). This E_{OC}, is measured under steady state conditions. At equilibrium the current density in the system is the exchange current density, i_o given by:

$$i = i_o = \gamma_o \exp\left(-\frac{\Delta G^*}{RT}\right) ,$$ (2.15)

where,

i_o is the exchange current density (A cm^{-2}),

ΔG^* is the activation energy (J mol^{-1}), and

γ_o is defined as the electrochemical rate constant (A cm^{-2}).

However, this state changes when an external voltage, E is applied to the system (Fig. 2.6b). The potential of the metal (hereafter referred to as working electrode) now is shifted away from E_{OC} by an overpotential which is given by:

$$\eta = E - E_{OC}$$ (2.16)

The sign of η determines whether the working electrode is anodically ($\eta > 0$, $M \rightarrow M^{z+} + z$e) or cathodically ($\eta < 0$, $M^{z+} + z$e $\rightarrow M$) polarized. Thus, there will be a net non-zero current flowing in the system, which is no longer equal to i_o. In mathematical terms, the forward, i_F and reverse, i_R current densities for a reaction can be expressed by Eq. 2.17 and 2.18 respectively [see Perez, 2004; Ahmad, 2006].

$$i_F = k_F \exp\left(-\frac{\Delta G_A^*}{RT}\right)$$ (2.17)

$$i_R = k_R \exp\left(-\frac{\Delta G_C^*}{RT}\right)$$ (2.18)

Note:

$$\Delta G_A^* = \Delta G_A - \alpha z F \eta_a ,$$ (2.19)

$$\Delta G_c^* = \Delta G_C + (1-\alpha) z F \eta_c$$ (2.20)

where, α is a symmetry co-efficient, z is the valence number, and η_c and η_a are the cathodic and anodic overpotentials respectively. If $i_F \gg i_R$, then a net anodic current, i_a would flow and if $i_F \ll i_R$, then a net cathodic current, i_c would flow. The net current, i, flowing in the system is the difference between the two currents expressed by Eq. 2.17 and 2.18. Thus substituting Eq. 2.19 and 2.20 into Eq. 2.17 and 2.18 respectively gives:

$$i = i_F - i_R = k_F \exp\left(-\frac{\Delta G_A}{RT}\right)\exp\left(\frac{\alpha z F \eta}{RT}\right) - k_R \exp\left(-\frac{\Delta G_C}{RT}\right)\exp\left(-\frac{(1-\alpha) z F \eta}{RT}\right)$$ (2.21)

Note that the exchange current density is defined as, $i_o = i_F = -i_R$ at equilibrium:

$$i_0 = k_F \exp\left(-\frac{\Delta G_A^*}{RT}\right) = k_R \exp\left(-\frac{\Delta G_C^*}{RT}\right)$$ (2.22)

Substituting Eq. 2.22 into Eq. 2.21 yields the famous Butler-Volmer equation.

$$i = i_o \left(\exp\left[\frac{\alpha z F \eta}{RT} \right] - \exp\left[-\frac{(1-\alpha) z F \eta}{RT} \right] \right)$$

(2.23)

The Butler-Volmer equation expressed above is fundamental to electrode kinetics and, as will be shown in the next section, potentiodynamic experimental methods utilize this expression in determination of corrosion rates. However, polarization can be divided into three different types which can act separately or coexist within the system; *activation*, *concentration*, and *Ohmic* [see Fontana & Greene, 1978; Davis, 2000].

Activation polarization refers to the condition when the reaction rate is controlled by the slowest step in the electrochemical reaction series. Factors which can limit any of the reaction steps can range from the rate at which ions or electrons are transported across the interface to the rate at which reactants are transformed. The relationship between the anodic (i_a) or cathodic (i_c) current density and the anodic (η_a) or cathodic (η_a) overpotentials is given by the well known Tafel equations [Bard & Faulkner, 2001] below.

$$\eta_a = \beta_a \log \frac{i_a}{i_o}$$

(2.24)

$$\eta_c = \beta_c \log \frac{i_c}{i_o}$$

(2.25)

where, β_a and β_c are the anodic and cathodic Tafel slopes (mV), and are constant for the reaction at a fixed temperature. As will be shown in the next section, the Tafel slopes are very important in the determination of corrosion rates. Although the Tafel slopes are measured experimentally, they are usually defined as [Perez, 2004]:

$$\beta_a = \frac{2.303RT}{\alpha z F} = \frac{(1-\alpha)\beta_c}{\alpha}$$

(2.26)

$$\beta_c = \frac{2.303RT}{(1-\alpha) z F} = \frac{\alpha \beta_a}{(1-\alpha)}$$

(2.27)

Concentration polarization refers to the condition when rate of reaction is dependent upon the concentration of dissolved chemical species. When a chemical species that actively takes part in a corrosion reaction at the surface is in short supply, then the mass transport of that species to the surface starts controlling the rate at which reactions occur. A reaction for which concentration polarization dominates is referred to as mass transport controlled. The mass transport of the participating species can be a very complex mechanism as it can be influenced by diffusion due to the

molar concentration gradient, migration due to an electric field, and convection due to kinematic velocities. A complete discussion on these mechanisms is beyond the scope of this thesis and can be found elsewhere [Perez, 2004; Bagotsky, 2006; Hamann et al., 2007; etc.]. However, in terms of the corrosion process in soil, concentration polarization normally dominates and the mass transfer is mainly influenced by diffusion of oxygen. Hence, of particular interest is the diffusion limited condition. An increasing cathodic overpotential under a diffusion limited condition will not correspond to an increasing cathodic current density but give rise to a limiting current density. This limiting current density, i_L, can be derived from Fick's law of diffusion with some algebra and is given by [Perez, 2004]:

$$i_L = \frac{nFD}{\delta} C \qquad (2.28)$$

where,

D is the diffusion co-efficient (cm^2 s^{-1}),

C is the concentration of the limiting species (mol cm^{-3}), and

δ is the thickness of the diffusion double layer (mm).

Note that under conditions of concentration polarization, the Butler-Volmer equation stated in Eq. 2.23 is not directly applicable. Instead, the equation has to be modified in order to include concentration effects on the net current density as given by Eq. 2.29 [Bard & Faulkner, 2001].

$$i = i_o \left(\frac{C_o(0,t)}{C_o^*} \exp\left[\frac{\alpha zF\eta}{RT} \right] - \frac{C_r(0,t)}{C_r^*} \exp\left[-\frac{(1-\alpha)zF\eta}{RT} \right] \right) \qquad (2.29)$$

where, $C_o(0, t)$ and $C_r(0, t)$ are the time-dependent concentration of the oxidized and reduced species respectively at the surface, and C_o^* and C_r^* are the concentrations of the limiting oxidized and reduced species respectively in the electrolyte.

Finally, Ohmic polarization refers to a special condition caused by the Ohmic resistance of the electrolyte or an electrode surface oxide. For metallic corrosion in soil, this relates to the soil resistivity. Ohmic polarization is also often known as iR effect and this will be discussed in detail in section 2.4.3.

2.3.2 Mixed Potential Theory

The mixed potential theory of Wagner and Traud consists of two simple hypotheses:

    a)   any electrochemical reaction can be split into two or more partial oxidation and reduction reactions, and

b) there cannot be any net accumulation of electrical charge during any electrochemical reaction.

Under these conditions, the net current is zero and all electrons produced by the corroding metal have to be consumed by one or more cathodic processes. To understand this better, consider the schematic of Evan's diagram for pure zinc in HCl acid solution illustrated in Fig. 2.7a.
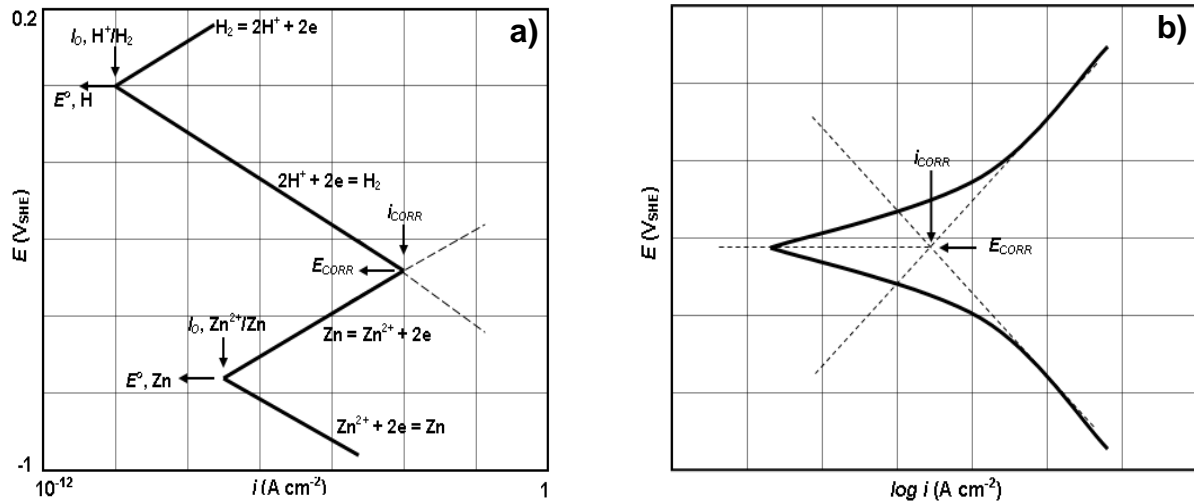
Figure 2.7. **a)** Schematic of Evan's diagram for zinc in HCl acid [redrawn after Perez, 2004], and **b)** Stern diagram for a hypothetical electrochemical system.

For zinc in acid, the two reactions are:

$$Zn = Zn^{2+} + 2e \text{ :anodic reaction}$$
$$2H^+ + 2e = H_2 \text{ :cathodic reaction}$$

(2.30)

Each has its own half-cell potentials (E^o, Zn and E^o, H) and exchange current densities (i_o, Zn^{2+}/Zn and i_o, H^+/H_2). However, each of these reactions cannot exist separately on the metal surface. Each will change potential to a common intermediate value – a mixed potential denoted by E_{CORR} (also referred to as E_{OC}), at which the exchange current density of the system is defined as the corrosion current, i_{CORR}. However, more realistic electrode kinetics for an electrochemical system are provided by Stern diagrams (*e.g.*, Fig. 2.7b), which show the non-linear anodic and cathodic curves. The Stern diagram utilizes the Butler-Volmer equation and experimentally these can be obtained using potentiostatic or potentiodynamic techniques.

The kinetic treatment and concepts in this section constitute the basic knowledge required to understand the experimental techniques which utilize the polarization concept for corrosion rate determinations. These techniques are discussed next. Note also that the calculation or corrosion rates

from knowledge of the corrosion current, i_{CORR} have been purposefully deferred to a later section (section 2.4.5).

2.4 Polarization Methods and Analysis

The (log i)–ΔE polarization curve presented in previous section (Fig. 2.7b) can be established through various means as documented in Table 1; the method type depends upon whether current or potential is monitored (single event, or continuously) or controlled. However, electrochemical measurements are often conducted by controlling the potential, rather than the current due to the theoretical relationship between potential and energy [Papavinasam, 2008].

Table 2.1. Different methods of obtaining the polarization curves [Adopted from Papavinasam, 2008].

Method Type	Potential	Current
Potentiostatic	Controlled	Monitored
Potentiodynamic	Varied at a constant rate	Continuously monitored
Galvanostatic	Monitored	Controlled
Galvanodynamic	Continuously monitored	Varied at a constant rate

Once the (log i)–ΔE relationship is established, the determination of a corrosion rate can then be performed using the mathematical framework described in the previous section. Another method, (different from the (log i)–ΔE approach), is an analysis of the potential-response in the time-domain for an electrode under a constant current stimuli – the galvanostatic pulse technique. Although there are several other techniques which can be utilized for determination of corrosion rates, the discussion in this section will be restricted to potentiodynamic and galvanostatic pulse methods as they have been used or investigated in the present work. A treatment of other techniques can be found elsewhere [Baboian, 2005; Cottis, 2008; Ekekwe, 2009; *etc*]

2.4.1 Tafel Extrapolation Method

Potentiodynamic polarization scans allow the determination of corrosion rates using two possible analytical methods, *viz.*, Tafel extrapolation and polarization resistance methods, depending upon the overpotentials applied to the working electrode. The experimental set-up is normally the three-electrode arrangement shown earlier in Fig. 2.6.

In a potentiodynamic polarization scan, the electrode potential is usually polarized from a large cathodic overpotential towards a large anodic overpotential at a particular scan rate, $\partial V/\partial t$, which is usually 0.167 mV s^{-1} as recommended in the standard ASTM G-59. The limits of the $\pm\ \eta$ scan are

usually chosen to be within the active region, unless analysis of different regions in the anodic polarization scan is also desired. In the Tafel extrapolation method, the η plotted as a function of log i will exhibit linear or quasi-linear feature at large anodic or cathodic overpotentials. Extrapolation of either the linear anodic or cathodic polarization curve to the E_{OC} ($\eta = 0$), then allow the determination of the i_{CORR} as illustrated in Fig. 2.8. The Tafel slopes β_a and β_c have already been introduced in Eq. 2.24 and 2.25. Substituting these equations into the Butler-Volmer equation given in Eq. 2.23 allows the expression of the total current in terms of the Tafel slopes and the overpotentials.

$$i = i_{CORR}\left(\exp\left[\frac{2.303(E - E_{CORR})}{\beta_a} \right] - \exp\left[-\frac{2.303(E - E_{CORR})}{\beta_c} \right] \right) \tag{2.31}$$
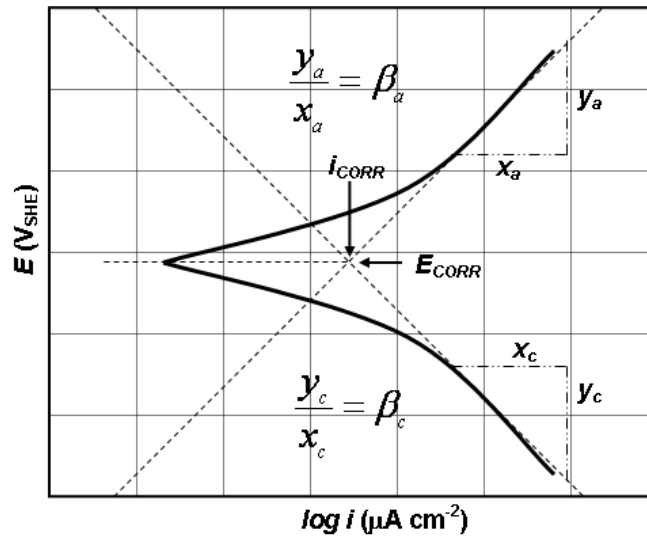
Figure 2.8. The linear region of the polarization curve is utilized for Tafel extrapolation.

Note, $\eta = E - E_{CORR}$. The feasibility of utilizing Tafel extrapolation methods appears simple, however in practical cases they are sometimes difficult to apply. This is mainly because the polarization curve depicted in Fig. 2.8 is ideal and is rarely observed; a special condition when $\beta_a = \beta_c$ and the anodic and cathodic curves are symmetrical about E_{CORR}. Instead, a range of curves are possible, which may not display the linear regions and thus the extrapolation technique becomes difficult [see Kelly, 2003]. In such situations it may also become difficult to determine the slopes β_a and β_c. In fact, at present no ASTM standard guidelines exist for this analytical method [Baboian, 2005]. The large $\pm\eta$ utilized for the Tafel extrapolation method may also damage the surface properties of the metal (destructive testing). Hence, the non-destructive polarization resistance method employing low overpotentials is usually preferred. This is discussed next.

2.4.2   Polarization Resistance Method

The Butler-Volmer equation describes the relationship between the current and the overpotential and is applicable at both low and high overpotentials. However, at low overpotentials, this equation can be simplified to the famous linear Stern-Geary relationship:

$$i_{CORR} = \frac{1}{2.303 R_p}\left(\frac{\beta_a \beta_c}{\beta_a + \beta_c}\right) = \frac{\beta}{R_p},$$ (2.32)

where,

$$\beta = \frac{\beta_a \beta_c}{2.303\left(\beta_a + \beta_c\right)}$$ (2.33)

And R_p is the polarization resistance (Ω m^{-2}) defined as:

$$R_p = \left.\frac{\Delta E}{\Delta i}\right|_{\Delta E \to 0}$$ (2.34)

The term β is defined as a constant for the electrochemical set-up. The η-range at which Eq. 2.32 is applicable (exhibits linear features) is usually ± 5 to ± 10 mV [Scully, 2000]. This choice of perturbation also ensures that the technique itself does not interfere with the corrosion reactions [Papavinasam, 2008]. The standard ASTM G-59 describes the guidelines for conducting potentiodynamic polarization resistance measurements. An illustration of this concept is shown in Fig. 2.9a. The R_p is defined as the slope of the tangent line at $i = 0$; the reason why this method is often (wrongly) referred to as *linear polarization resistance* (LPR) method. Usually, for steel under active and passive corrosion, $\beta = 26$ mV and $\beta = 52$ mV respectively are assumed [*e.g.* Garces *et. al.*, 2005]. Then the R_p value can be transformed into corrosion current easily using Eq. 2.32. This corrosion current can be further transformed into corrosion rate (see section 2.4.5) representing the instantaneous corrosion rate of the metal in the metal-electrolyte system [Scully, 2000]. Thus, the polarization resistance method enables continuous monitoring of corrosion rates in a given system.

The polarization curve shown in Fig. 2.9a is a special (rare) condition, when $\beta_a = \beta_c$. Usually, the anodic and cathodic curves are not symmetrical and the observed linearity around E_{CORR} does not exist (hence, the misnomer LPR) [see Oldham & Mansfeld, 1971; Mansfeld, 2009]. As illustrated in Fig. 2.9b, strong curvatures may be present. However, note Eq. 2.34 still applies. Mansfeld (2005) and Mansfeld (2009) showed that the presence of this non-linearity can in fact be utilized in the complete form of the Butler-Volmer equation.
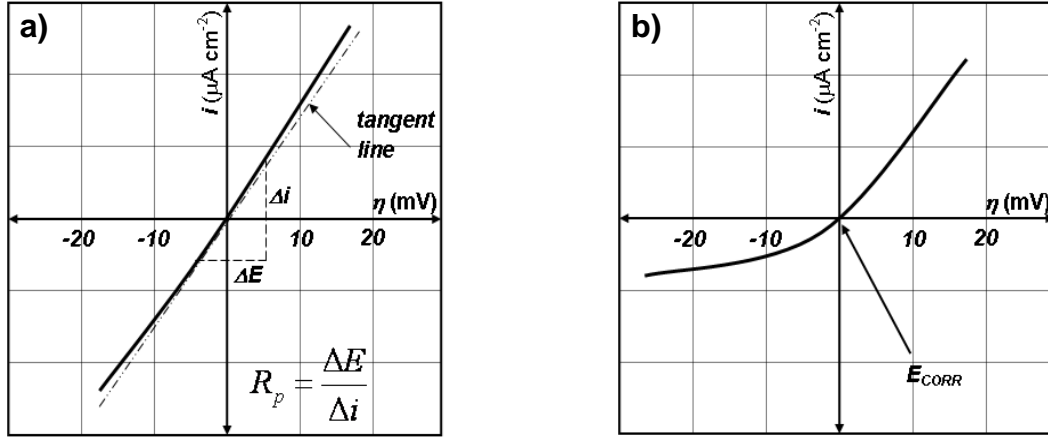
Figure 2.9. a) Schematic of the R_p determination from a potentiodynamic polarization curve, and **b)** the polarization curve in practice usually displays non-linear behavior around E_{CORR}.

Mansfeld (2005) demonstrated that a direct determination of i_{CORR} and the Tafel slopes, β_a and β_c, can be made using the Butler-Volmer equation in the vicinity of E_{CORR} using curve fitting methods. However, for the special cases $\beta_a \gg \beta_c$ (presence of a surface film on the metal), and $\beta_a \ll \beta_c$ (reaction under diffusion limited condition) some errors may arise in curve fitting especially near E_{CORR}. Nevertheless, this approach is theoretically sound as it utilizes fundamental principles.

The Tafel extrapolation and polarization resistance methods discussed so far, fall under the category of potentiodynamic methods. Although the individual difficulties associated with each method have been presented briefly, there are some collective experimental considerations and limitations which affect both these methods. These are described in the next section.

2.4.3 Some remarks on Tafel Extrapolation and Polarization Resistance Methods

The Butler Volmer equation when applied experimentally to characterize polarization curves can be expressed as:

$$i = i_{CORR}\left(\exp\left[\frac{2.303\left(E - E_{CORR}\right)}{\beta_a}\right] - \exp\left[-\frac{2.303\left(E - E_{CORR}\right)}{\beta_c}\right]\right) + \underbrace{C\frac{\partial V}{\partial t}}_{\text{scan rate term}} \quad , \quad (2.35)$$

where,

C = the capacitance of the electric double layer at the interface (μF cm^{-2}), and

$\partial V/\partial t$ = the potentiodynamic scan rate (mV s^{-1}).

Thus, the total current results from two processes, *viz.*, the Faraday current from the corrosion process, and the capacitive current due to the EDL. The capacitive current can be minimized by using very small scan rates. However, using too small a scan rate also possesses the problem that the properties of an electrochemical system being studied might vary during the measurement time, especially if a wide overpotential range is desired. The use of any scan rate has to be justified by determining the optimal condition at which there is no marked change in i_{CORR}. The effect of scan rates on the potentiodynamic polarization curves has been well documented by Mansfeld (1961) and others [Scully, 2000; Zhang *et. al.*, 2009]. Usually in potentiodynamic scans, a scan rate of 0.167 mV s^{-1} is adopted after the ASTM standard G-59.

In the discussions for the two methods, it had been assumed that the electrolyte resistance is negligible. However, in principle, electrolyte resistances, R_{Ω} (such as for soil) can be significant leading to a distortion of the polarization curves [Baboian, 2005]. The origin of these iR_{Ω} effects is the finite separation distance that exists between the working electrode and the reference electrode in a common three electrode arrangement. The separation distance consists of electrolyte of resistance R_{Ω}, which adds a potential of iR_{Ω} onto the measured overpotential of the working electrode as sensed by the reference electrode.

$$\eta = \left(E - E_{OC}\right) + iR_{\Omega} \tag{2.36}$$

The effects of electrolytic resistances are usually referred to as iR_{Ω} effects and these tend to normally overstate the applied overpotentials. The iR_{Ω} effects on polarization curves and the impact on Tafel extrapolation and polarization resistance methods are explained below using the illustration in Fig. 2.10.
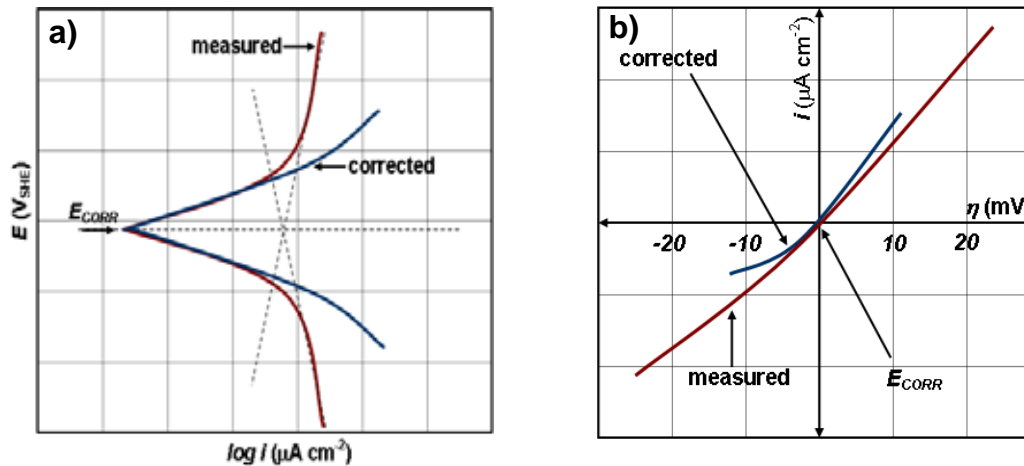
Figure 2.10. Effect of iR_{Ω} on **a)** Tafel extrapolation, and **b)** polarization resistance methods.

Since iR_Ω drops tend to overstate the true overpotential, the measured polarization curve displays incorrect overpotential limits in the cathodic and anodic sections. This affects both the Tafel extrapolation and polarization resistance methods. Extrapolation of the linear sections of the anodic or cathodic curves to E_{CORR} in this instance produces incorrect i_{CORR}. However, in some cases linear behaviour at high overpotentials may not be observed at all if the iR_Ω is extremely high. For potentiodynamic polarization resistance analysis (Fig. 2.10b), the iR_Ω tends to display a quasi-linear profile near E_{CORR} [Mansfeld, 2009]. This sometimes leads to overestimation of R_p and hence an underestimation of i_{CORR}.

Thus, the use of these two techniques requires very careful attention to the effect of iR_Ω on the overall measurement. Although, these effects can be corrected in post-acquisition analysis, they can also be minimized by placing the reference electrode as close as possible to the working electrode. However, this may not be possible in all cases and special care should be taken to ensure that the physical size of the reference electrode does not interfere with the exposed surface area of the working electrode or the potential distribution in the system. In more sophisticated experimental set-ups the R_Ω is usually compensated by the potentiostat/galvanostat using feedback mechanisms. A good discussion on iR_Ω correction schemes can be found in Oelbner *et*. *al*. (2006).

Despite their limitations, the potentiodynamic dynamic methods discussed so far provide for a firm analysis of the behaviour of an electrode when subjected to varying overpotentials. The analysis for i_{CORR} further allows the dynamics of the system to be characterized. Nevertheless, these techniques can be lengthy tasks, especially the Tafel extrapolation methods. Another method which offers much faster turnover is the galvanostatic pulse technique. This is discussed next.

2.4.4 Galvanostatic Pulse Method

In the discussions presented in section 2.1, the structure of the EDL at the metal-electrolyte was presented and was shown to have capacitive properties. The resistive component of this structure consists of the polarization resistance, R_p introduced in the previous section which simply is the resistance to charge transfer across the interface. Then a simple Randle's circuit can be used to model the metal-electrolyte interface as shown in Fig. 2.11a.
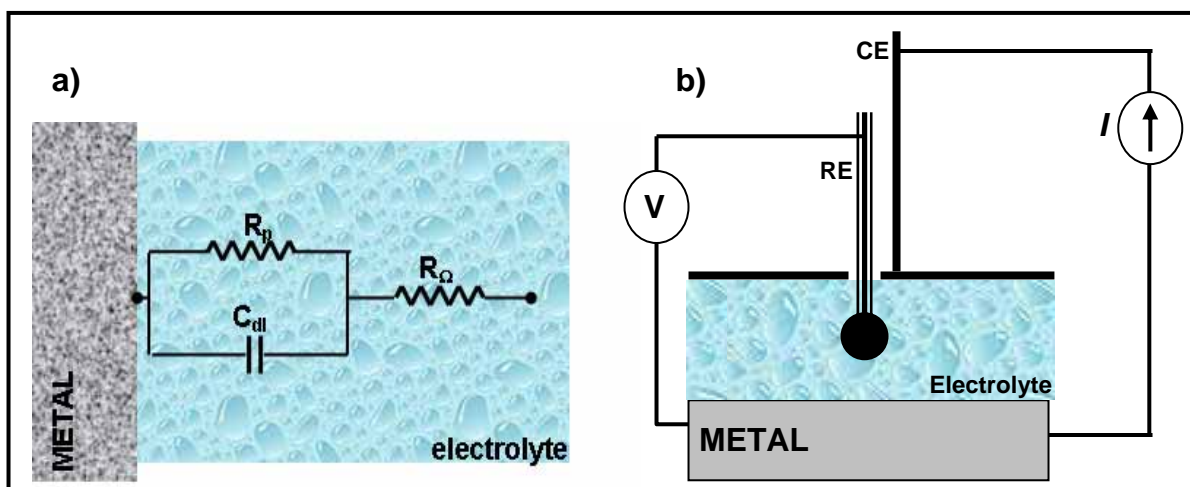
Figure 2.11.**a)** The metal-electrolyte interface can be modelled by a Randle's circuit, and **b)** schematic of a three-electrode electrochemical cell set-up using the galvanostatic pulse method.

The galvanostatic pulse method [see Sathiyanarayanan *et. al.* 2006] utilizes the concept of charging and discharging of the double layer to determine the R_p. The experimental set-up is similar to that shown in Fig. 2.11b. A square constant current pulse is usually applied for several seconds and the resulting potential-time response of the working electrode is monitored during the pulse-ON and pulse- OFF times. A typical potential-time response of the working electrode during pulse-ON period is given in Fig. 2.12.
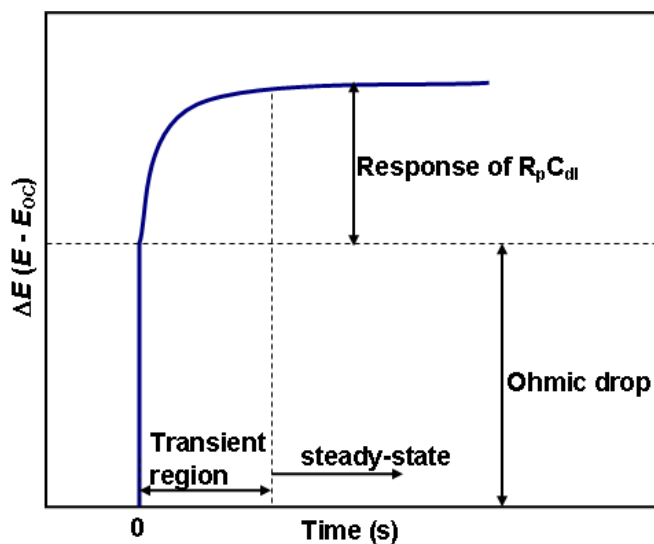
Figure 2.12. Potential-time variation of a working electrode in response to injection of a constant current.

The potential response exhibits two different sections; a) contribution from iR_Ω effects, and b) response from charging of the double layer R_pC_{dl} network. Unlike the potentiodynamic methods, the galvanostatic pulse method offers the advantage that the electrolyte resistance is measured as an integral part of the measurement. The section representing the charging of the R_pC_{dl} network can then

31

be analyzed separately to determine the R_p and C_{dl}. This is done by fitting the charging curve to the equation [Elsener, 2005]:

$$\Delta E - iR_\Omega = R_p \left(1 - \exp\left[-\frac{t}{R_p C_{dl}} \right] \right) \qquad , \tag{2.37}$$

Where, i is the applied current (mA), and ΔE is the observed overpotential (mV). The equation represents the time domain response of the Randle's circuit upon injection of a constant current. Once R_p is determined, a value of β can be assumed and the i_{CORR} can be determined. Note that the potential-response shown in Fig. 2.12 also exhibits two different regions of the charging process; a) transient region, and b) steady-state region. An important consideration in the galvanostatic method is the duration for which current is applied to the system. Large durations usually cause concentration polarization effects [Birbilis *et*. *al*., 2003], whereby the simple Randle's circuit is no longer applicable. A treatment of this and other aspects of the galvanostatic pulse method will be done in Chapter 4. For now, this covers the fundamental aspects of the galvanostatic pulse method.

2.4.5 Determination of Corrosion Rates

In all the methods discussed so far, the aim has been to determine certain parameters or carry out some transformations which can be used to determine the i_{CORR} of the system. This is because i_{CORR} is directly related to the corrosion rate, *C.R*. This relationship can be derived from Faraday's 1st Law and is expressed as [Baboian, 2005]:

$$C.R = K \frac{i_{CORR}\left(E.W\right)}{\rho} \tag{2.38}$$

where,

        $C.R$ = corrosion rate (mm y^{-1}),

        K = a constant (3.27×10^{-3} mm g μA^{-1} cm^{-1} y^{-1}),

        $E.W$ = the equivalent weight (dimensionless), and

        ρ = density of the working electrode (g cm^{-3}).

Note, i_{CORR} is in units of μA cm^{-2} (current normalized to the surface area of the working electrode). If the corrosion rate is desired in some other units, then the K value has to be changed accordingly.

The present chapter has provided a treatment of electrochemistry principles, which is required for understanding the polarization fundamentals used in measurement of metal corrosion rates. Thus, this chapter serves as a theoretical framework for understanding most of the concepts discussed in chapter 4 and provides completeness to the discussions presented elsewhere in this thesis.

CHAPTER 3

SURFACE GEOELECTRIC METHODS

The present chapter is a theoretical treatment of the fundamental concepts necessary in developing an understanding of the surface geoelectrical methods, *viz*., resistivity, induced polarization and self potential methods, routinely utilized in geophysical applications. The chapter serves as a platform for providing background information on the aforementioned techniques, which are utilized within this thesis and will be developed later.

3.1   Soil as a Conductive Media at Near-Surface Scale

Induced polarization, resistivity, and self potential techniques fall under the category of electrical methods since each of them utilize either artificial (induced polarization and resistivity) or natural energy sources to provide insight into the electrical properties of the subsurface soil. The electrical properties manifest due to a complex interaction of various components which may be physical, chemical, or biological in nature. Most geotechnical and environmental applications at near surface geophysics scale involve depths of < 30 m [Butler, 2005], although < 10 m depths are most common. At these depths the sediment electrical features are characterized by its bulk resistivity, ρ (or conductivity, σ) which is influenced by a range of parameters *viz*., porosity, saturation (location of the water table), salinity, and texture [Yungul, 1996]. In essence, however, it is the presence of the aqueous electrolyte distributed in the complex interconnected pore structure which gives rise to the current-carrying capability of the subsurface soil, with ions from dissolved salts acting as charge carriers within the electrolyte. The presence of clay further complicates the conduction mechanism due to the formation of an electric double-layer at the interfaces and the associated ion exchange processes [Schon, 1996]. Due to the heterogeneity of subsurface soil, its bulk resistivity spans a wide spectrum of values depending upon its composition and lithology as shown in Table 3.1. These values are also greatly perturbed by the amount of water in the composition matrix. It has been shown empirically however [Archie, 1942; Schon, 1996], that the bulk electrical conductivity of sediments or soil is related to its water saturation, S_w by the famous Archie's equation expressed by Eq. 3.1

$$\sigma = \left\{ \frac{\Phi^m}{a} \right\} \sigma_w S_w^n \; , \tag{3.1}$$

Table 3.1. Typical resistivities of different geological materials. Taken from Seidel & Lange (2007).

Material	Resistivity (Ω m)	
	Minimum	**Maximum**
Gravel	50 (water saturated)	$> 10^4$ (dry)
Sand	50 (water saturated)	$> 10^4$ (dry)
Silt	20	50
Loam	30	100
Clay (wet)	5	30
Clay (dry)		> 1000
Peat, humus, sludge	15	25
Sandstone	< 50 (wet, jointed)	$> 10^5$ (compact)
Limestone	100 (wet, jointed)	$> 10^5$ (compact)
Schist	50 (wet, jointed)	$> 10^5$ (compact)
Igneous and metamorphic rock	< 100 (weathered, wet)	$> 10^6$ (compact)
Natural water	10	300
Saline water (brine)	< 0.15	

where,

Φ^m = the effective porosity,

a = the tortuosity factor which is empirically determined and is usually $0.5 < a < 1$,

σ_w = the conductivity of the pore fluid,

m = the cementation factor accounting for the connectiveness of the pore space in the completely saturated cases and is usually in the range $1.5 \leq m \leq 2.5$ [Gueguen & Palciauskas, 1994],

n = the saturation exponent accounting for the pore connectiveness in the partially saturated cases and is usually in the range $1.3 < n < 2$ [Schon, 1996].

This Archie equation is valid for sediments containing negligible clay content and with no metallic minerals, thus electrolytic conduction is the major component in the whole conductivity mechanism. This in large is an oversimplification for the actual soil properties at near surface scales. Clay is abundant in near surface sediments and as mentioned earlier, they lead to formation of electric double-layers whereby there is an excess of ions in the diffuse layer at the boundary between the solid soil particle and pore fluid thereby enhancing the soil conductivity through interfacial conductivity [Lange & Seidel, 2007]. The Archie equation in this instance needs to be modified to include the extra interfacial conductivity, σ_q term generically shown in Eq. 3.2.

$$\sigma = \left\{ \frac{\Phi^m}{a} \right\} \sigma_w S_w^n + \sigma_q \ , \qquad (3.2)$$

Some extended expressions for the modified Archie's equation, which includes the interfacial conductivity mechanism has been suggested by several workers such as Waxman & Smits (1964), Juhasz (1981), Clavier *et. al.* (1984), Glover *et. al.* (2000), and recently by Revil & Florsch (2010).

Electrolytic conductivity is frequency independent over a wide range. On the contrary interfacial conductivity shows frequency dependence whereby the real and imaginary components are directly proportional to the porosity and the surface area of particles in the soil respectively [Lange & Seidel, 2007]. The interfacial conductivity mechanism briefly mentioned here will be discussed further in Section 3.3. Also, the mathematical framework of interfacial conductivities and their usefulness in assessing soil electrical properties will be developed more fundamentally later in the thesis (Chapter 5). An important parameter often utilized in petrophysical studies is the *formation factor F*, which is described by Eq. 3.3

$$F = \frac{\rho}{\rho_w} = \frac{a}{\Phi^m} \quad , \tag{3.3}$$

where, ρ_w is the resistivity of the pore fluid. It follows that the formation factor is inversely proportional to the porosity of the soil and provides an assessment of the resistivity magnification related to the saline pore fluid [Schon, 1996] in the soil matrix. It is often stated that the *F* is a constant independent of the pore fluid resistivity. However, this independence is only applicable to rocks or soils absent of interfacial conductivity arising due to conductive minerals. In the presence of conductive elements, the formation factor calculated as suggested above is the apparent formation factor F_a.

To provide qualitative information about the conductivity mechanisms in soils, different electrical methods can be utilized. Within the scope of this thesis only on-surface low frequency electrical methods are considered. Other modes of investigations such as in boreholes are not relevant within this project and hence are not discussed. The fundamental concepts and field applications of the different electrical methods utilized within the thesis are treated next. Comprehensive reviews on the concepts as well as the techniques are well covered in the literature and can be found elsewhere [*e.g.*, Telford *et*. *al*., 1990; Yungul, 1996; Sharma, 1997; Binley & Kemna, 2005; Reynolds, 2011 *etc*].

3.2   Resistivity Method

For a better treatment of the principles and field applications of the resistivity technique, they are separated into different subsections and discussed.

3.2.1 Fundamentals

For a continuous current flowing in an isotropic homogenous (ρ = constant) media, the current density, **J** (A m^{-2}) over an infinitesimal area ∂A is related to the electric field **E** (V m^{-1}) by the Ohm's Law:

$$\mathbf{J} = \sigma\mathbf{E} ,$$ (3.4)

where, σ is the conductivity in S m^{-1}. Since $\mathbf{E}$ is defined as the gradient of the potential, U [Kraus & Fleisch, 1999] it follows that:

$$\mathbf{J} = -\sigma(\nabla U)$$ (3.5)

Assuming there is no accumulation of charges over ∂A, *i.e.*, absence of a current source or sink, it follows that to maintain continuity:

$$\nabla \cdot \mathbf{J} = 0$$ (3.6)

Substituting Eq. 3.6 into Eq. 3.5,

$$(\nabla\sigma \cdot \nabla U) + \sigma\nabla^2 U = 0 ,$$ (3.7)

Since the medium is assumed to be homogenous, it follows that the term $(\nabla\sigma \cdot \nabla U)$ is negligible and can be safely ignored. Thus, the Laplace equation for a homogenous isotropic medium can be expressed as:

$$\nabla^2 U = 0$$ (3.8)

The above derivations are based on the notion that the current source is DC or very low frequency AC, in which case the displacement currents are negligible. For a current source $+I$ located on the surface of a homogenous half-space, the Laplace equation can be expressed in spherical coordinates (r, θ, ϕ). Due to the complete symmetry in the θ and ϕ directions, the potential will mainly be a function of r only [Telford *et. al*., 1990] and the Laplace equation results in [Keller & Frischknecht, 1970]:

$$\frac{1}{r^2}\frac{\partial}{\partial r}\left(r^2\frac{\partial U}{\partial r}\right) = 0$$ (3.9)

Integrating Eq. 3.9 yields the expression for U as a function of the radial distance r:

$$U = -\frac{A}{r} + B$$ (3.10)

where, A and B are constants. Since $U \to 0$ as $r \to \infty$, it follows that $B = 0$. To determine the constant A however, an expression for the total current over the Gaussian surface is needed. For the homogenous half space of surface area $2\pi r^2$ this is given by:

$$I = \oint_S \mathbf{J} \cdot d\mathbf{s} = \oint_S (-\sigma\nabla U) \cdot d\mathbf{s} = -\sigma A\oint_S \frac{1}{r^2} \cdot d\mathbf{s} = -2\pi\sigma A$$ (3.11)

Therefore, it follows that for $B = 0$:

$$U = \frac{I}{2\pi\sigma r} = \frac{I\rho}{2\pi r}$$ (3.12)

Equation 3.12 provides an expression for the potential U due to a single point current source placed above the homogenous half space. Theoretically, this is applicable when the circuit-completing second electrode (sink) is placed at some infinite distance. In the presence of multiple sources/sinks, the potentials due to each can be added arithmetically [Krauss & Fleisch, 1999] to determine the overall potential at a particular location. The use of this fundamental principle in the context of resistivity surveying is discussed next.

3.2.2 Field Applications

In field applications usually a collinear 4-electrode method is employed to determine the resistivity of the subsurface soils. Current is injected via two current-electrodes, A-B, and the potential difference on the surface is measured across two potential-electrodes, M-N. The schematic of this collinear quadrupole (AMNB) arrangement is shown in Fig. 3.1.
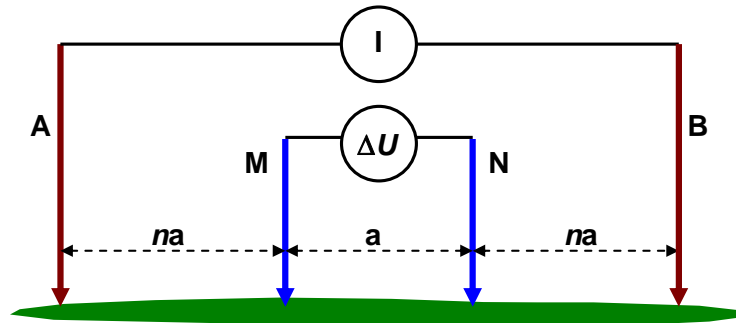
Figure 3.1. Schematic of the common collinear quadrupole system used in field employing two current-electrodes and two potential-electrodes.

For a current, I injected via electrodes A-B, the potential difference measured between M-N can be derived analytically using the superposition principle. Following Eq. 3.12, this can be expressed as:

$$\Delta U = \frac{I\rho}{2\pi}\left[\left(\frac{1}{\mathbf{AM}} - \frac{1}{\mathbf{BM}}\right) - \left(\frac{1}{\mathbf{AN}} - \frac{1}{\mathbf{BN}}\right)\right] , \tag{3.13}$$

where, AM, BM, AN, and BN represent the distance between the respective electrodes. Thus, for a homogenous half space, the uniform resistivity can be determined from knowledge of the electrode geometry, the measured potential and the injected current by re-arranging the terms in Eq. 3.13. Note Eq. 3.13 also applies to an arbitrarily arranged non-collinear quadrupole. For simplicity, it is common to denote an electrode geometry factor, K to weight the contributions arising from electrode separations. For the 4-electrode system this can be expressed as:

$$K = \frac{1}{2\pi}\left(\frac{1}{\mathbf{AM}} - \frac{1}{\mathbf{BM}}\right) - \left(\frac{1}{\mathbf{AN}} - \frac{1}{\mathbf{BN}}\right) \tag{3.14}$$

Thus, in terms of resistivity of a homogenous half space, Eq. 3.13 can be re-written as:

$$\rho = \frac{\Delta U}{I} \cdot K \qquad\qquad (3.15)$$

In reality, due to the heterogeneity of soils, the homogenous condition is very rare. Thus, in the presence of an inhomogeneous half space, the resistivity determined from Eq. 3.15 will vary depending upon the geometrical arrangement of the electrodes on the surface. Hence, the resistivities are referred to as *apparent resistivities* denoted by ρ_a. A range of electrode configurations are possible depending upon the relative locations of the current and potential electrodes and/or their separation distances in the quadrupole system. For practical applications, the adoption of a particular array type is usually assessed by the survey application and target of interest. For the discussions in this chapter, only the configuration illustrated in Fig. 3.1 (AMNB) will be considered. This type of arrangement consisting of two outer current-electrodes and two inner potential-electrodes are referred to as α-type [Szalai *et. al.*, 2009]. Reviews and treatments of other configurations (β-type, γ-type, and dipole) can be found in Telford *et. al.* (1990) and Szalai *et. al.* (2009). The Wenner-α (hereafter referred to as Wenner only) and Schlumberger are well known array configurations [Reynolds, 2011], which can be developed by considering the separation distances between the four electrodes in Fig. 3.1. These are summarized in Table 3.2.

Table 3.2. Wenner and Schlumberger electrode configurations and their geometrical factors.

Array Type	Electrode arrangement	Geometric factor
Wenner		$K = 2\pi a$
Schlumberger		$K = \pi n(n+1)a \; ; n > 3$
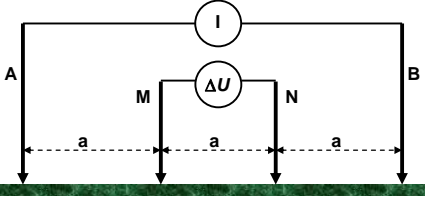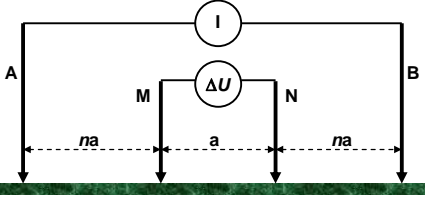
Note, that for $n = 1$ in Table 3.1, Schlumberger array simplifies to Wenner configuration. Barker (2007) has given a good summary on the comparative advantages and disadvantages of these two array configurations. For field applications, stainless steel electrodes are commonly used as current electrodes (A-B), and the potential differences are measured across another pair of stainless steel

electrodes (M-N). In some instances, non-polarizable electrodes are used instead of stainless steel for potential-electrodes. To conform to the DC-regime requirement for a current source, switched square waves usually between frequencies of 0.5 – 2 Hz [Binley & Kemna, 2005] are injected between the A-B electrodes and the resulting voltage measured between the M-N electrodes. Figure 3.2 illustrates a typical stimulus-response characteristic of this current-potential relationship.
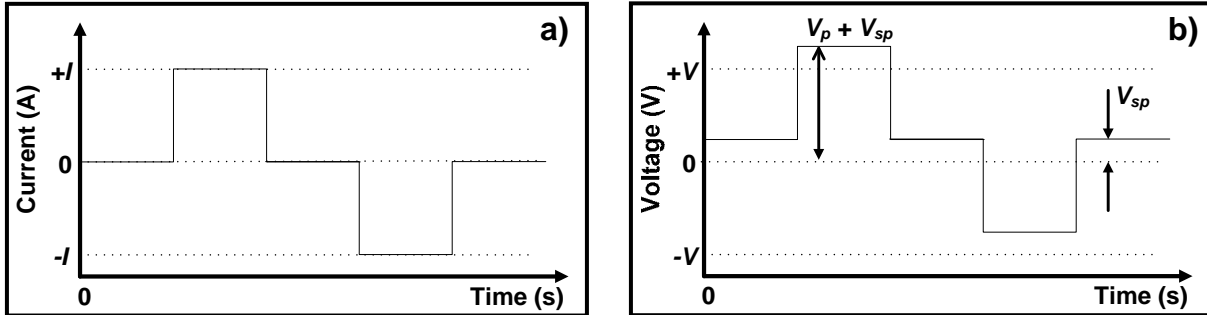
Figure 3.2. Typical characteristics of the **a)** injected current pulse and **b)** the measured potential including the self potential effect. Redrawn after Binley & Kemna (2005).

The idealized potential response shown in Fig. 3.2b is noise free and absent from any induced polarization effect (next section). However, it includes the baseline shift which arises due to the presence of self potential, V_{sp} (Section 3.4). The transfer function, $\Delta U/I$ of this system is given by V_p/I, which corresponds to the effective resistance between the M-N electrodes. Depending upon the electrode geometry, the apparent resistivity can then be calculated using Eq. 3.15. Resistivity surveying can be carried out in several modes of operation, *viz.*, profiling, vertical electrical sounding (VES), and 2-D or 3-D imaging using a combination of profiling and VES techniques [Telford *et. al.*, 1990; Parasnis, 1997; Binley & Kemna, 2005; Reynolds, 2011 *etc*]. The adoption of any of these operation modes together with the array configuration usually depends on the survey aims, region of interest and economical and time constraints. In the present thesis, the Wenner profiling technique has been utilized to determine lateral variations in soil profiles along pipeline right-of-way (ROW), which can be used as a diagnostic tool for pipeline condition assessment. Consequently, discussions hereafter will be focused on profiling techniques. Recent reviews and case studies related to other modes of operation for wide-ranging applications are well reported in literature and can be found elsewhere [*e.g.*, Tabbagh *et. al.*, 2000; Dahlin, 2001; Bentley & Gharibi, 2004; Papadopuolos *et. al.*, 2006; Ahzegbobor *et. al.*, 2010; Zeyen *et. al.*, 2011; Kaufmann *et. al.*, 2012 *etc*. and the references contained therein].

Resistivity profiling methods often referred to as *constant separation traversing* (CST) utilize a fixed electrode spacing array to map lateral variations in soil resistivity or induced polarization responses

(discussed in next section). CST techniques can be based on the four-electrode system, such as Wenner, requiring galvanic contact between the electrodes and soil or a capacitively coupled transmitter-receiver systems such as the OhmMapper [French *et. al*., 2006; Reynolds, 2011]. For CST employing Wenner configurations, the entire array is advanced along a profile after measurements have been conducted at one station. The exact station location for the measurement corresponds to the centre of the four-electrode arrangement. An important parameter in surface profiling is the depth of investigation (DOI), which is defined as the depth, z, at which a thin horizontal layer parallel to the ground surface contributes the maximum amount of total measured signal at the ground surface [Evjen, 1938]. Roy & Apparao (1971) and Roy (1972) expanded this concept and computed the depth of investigation characteristic (DIC) function for several arrays whereby their DOI corresponded to the maximum response in the DIC function. This was also utilized by Bhattacharya & Dutta (1982) to extend to other arrays. However, Edwards (1977) using the same DIC functions suggested that a better approximation for the DOI was given by the median value for the function and not the maximum, whereby the former is greater than the latter – a feature verified by Szalai *et. al*. (2009). Roy & Apparao (1971) also introduced the Normalized DIC (hereafter referred as NDIC), which is the DIC of an array normalized to the response of the homogeneous half space. Recently, the work by Szalai *et. al*. (2009) utilized the NDIC to tabulate the DOI and vertical resolutions of 30 different arrays. A schematic NDIC curve for the Wenner array illustrating the maximum and median values of the response function is shown in Fig. 3.3.
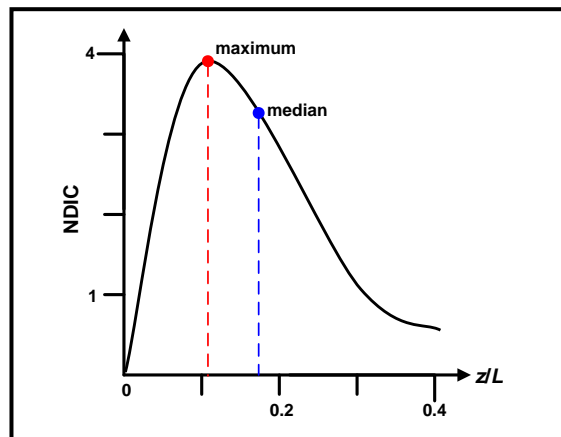
Figure 3.3. Schematic NDIC curve for a Wenner array showing the relative locations of the maximum and median response of the function, adopted from Barker (2007).

Following the response shown in Fig. 3.3, it is common that in CST techniques employing Wenner arrays, the DOI is estimated as 0.175L, where L is the separation distance between A and B electrodes (two outermost current electrodes) [Szalai *et. al*., 2009]. This computation is based on the median depth, z_e, defined as the depth at which the integral of the DIC function from the surface to z_e and

from z_e to infinity are equivalent [Edward, 1977; Szalai *et*. *al*., 2009]. However, there is also a *maximum effective depth of investigation*, z_{max}, which is defined as the depth below which only 10% of the signal manifests on the potential response [Barker, 2007] and hence is negligible. For Wenner arrays this is defined as *0.41L*. Consequently, in CST surveying the total response can be due to depths of up to *0.41L*, which can be important especially in the presence of highly conductive materials at that depth. Studies related to DOI for different array types and their application in noisy environments is presently an important area of research [see Szalai *et*. *al*., 2011].

The basic treatment and discussion of the different array types and their field applications for resistivity measurements in this section is also applicable to induced polarization methods, which forms another important diagnostic tool for subsurface characterization. This is presented next.

3.3   Induced Polarization Method

Soil resistivity as discussed previously is controlled mainly by the electrolytic conduction within the pore fluid. In contrast, the induced polarization phenomenon (IP) in soil arises due to the electrochemical reactions and charge build-up at the soil grain-fluid interfaces [Frasier, 1964; Binley & Kemna, 2005]. The mathematical treatment of this phenomenon with respect to advanced measurements will be developed later in the thesis (Chapter 5). However, in the present chapter a brief treatment of the IP phenomenon in regards to field applications will be presented.

3.3.1   Origin of the induced polarization phenomenon in soil

The early work of Marshall & Madden (1959) on the causes of the IP phenomenon was the first to introduce the distinction between the well known mechanisms of membrane and electrode polarizations as they apply to soils or rocks. At the same time Seigel (1959) in his work, which can be considered ahead of its time, developed the first mathematical formulation for the IP phenomenon in geological materials. In Section 3.1 it was discussed that the total resistivity (or conductivity) of soil consists of an electrolytic term and an interfacial term. In principle, the interfacial resistivity manifests out of the processes at the grain/fluid interface and is usually frequency dependent. The presence of interfaces indicates the formation of electric double layers (EDL), which can be described by the various models discussed earlier in Chapter 2[*]. The contribution of these (soil/fluid) EDL to polarization effects in soils will be discussed in detail in Chapter 5. In this section, however, the mechanisms of membrane and electrode polarizations [Marshall & Madden, 1959; Schon, 1996;

---

[*] The EDL in this instance will correspond to the soil particle/fluid interface properties.

Butler, 2005] will be presented. These two mechanisms form the basis of most polarization phenomenon observed in field and are illustrated schematically in Fig. 3.4.
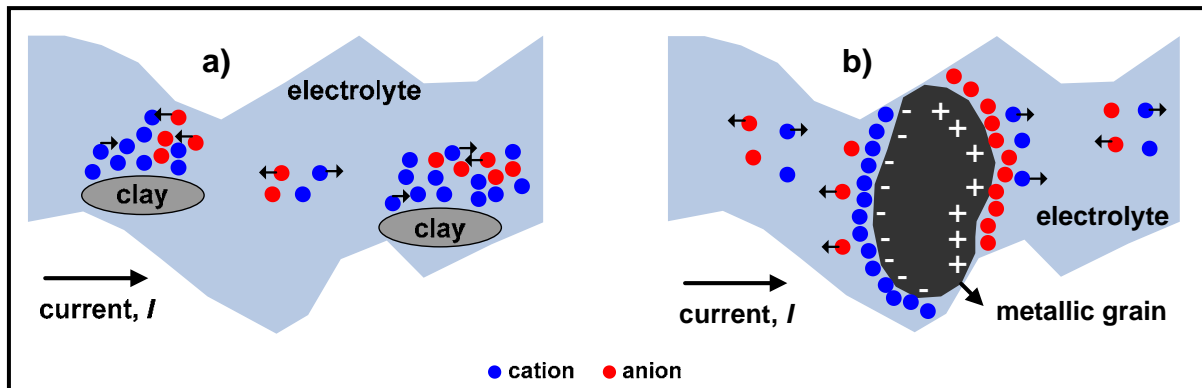
Figure 3.4. Mechanisms of **a)** membrane and **b)** electrode polarizations. Modified after Schon (1996).

In the presence of clay, cations tend to form a diffuse cloud near clay particles due to the electronegative charges on the clay surfaces. Under an applied external field, these cations tend to migrate normally through the cloud, while the transport of anions is impeded [Ward & Fraser, 1967]. Hence, the anions tend to accumulate, whereby the clay particles act as ion-selective membranes [Schon, 1996]. This membrane polarization effect is illustrated in Fig. 3.4a. When the external field is removed, the charges tend to return to their equilibrium positions. However, due to the presence of an ion concentration gradient arising from inhomogeneous charge distribution the equilibration occurs over a finite time interval resulting in the polarized effect. On the contrary, the electrode polarization mechanism requires the presence of a metallic surface as shown in Fig. 3.4b. Under the action of an external field, the conduction mechanism changes from ionic (in the electrolyte) to electronic (within the metal particle) and back to ionic. This results in distribution of opposite charges concentrated at the surfaces of the opposite ends of the metal particle respectively. The EDL structure at either surface can be described by the Grahame model. When the external field is removed, the charges do not return to equilibrium positions instantaneously but diffuse slowly thus resulting in the polarized effect. These two mechanisms form the basic sources of the polarization effect observed in field. Of course there are other important mechanisms [Revil & Glover, 1998] such as Stern layer polarization at soil grain/fluid interface (analogues to electrode polarization) which can coexist with membrane polarization. This will be developed and discussed in Chapter 5.

Field measurements of the polarization phenomenon in soils allow important information on subsurface features to be extracted, which is not possible from resistivity surveys. IP measurements in the field are conducted using a similar set-up for resistivity surveying, with the emphasis that the

potential-electrodes are non-polarizable. This non-polarizable requirement is usually realized by the use of $Cu|Cu_2SO_4$ or $Ag|AgCl$ electrodes. Nevertheless, Dahlin *et. al.* (2002) have demonstrated some promising results in measuring IP responses using more rugged polarizable electrodes, which involves correction for electrode polarizations. However, wide scale use of polarizable electrodes is still scarce in the literature. Two different types of measurements are generally utilized in the field, *viz.*, time domain or frequency domain. These measurements are explained in detail in the subsequent sections.

3.3.2 Time-domain Analysis

Time-domain induced polarization (TDIP) methods developed in early surveys are still utilized today, owing to its simplicity, relatively easy signal analysis, and survey turnover. A switched square-wave current pulse, similar to resistivity surveying, is applied across the A-B electrodes and the induced potentials are measured across the now non-polarizable M-N electrodes. It is common for the ON/OFF time for the current pulse to be equal to 1 s ($f = 0.25$ Hz). However, large times are also sometimes utilized. In the presence of a polarizable ground, it follows that the measured potential will show charging and discharging behaviour corresponding to the relaxation of the charges at the various soil-fluid interfaces in the ground. A typical stimulus-response characteristic curve neglecting baseline shifts caused by self potential effects is shown in Fig. 3.5a-b.
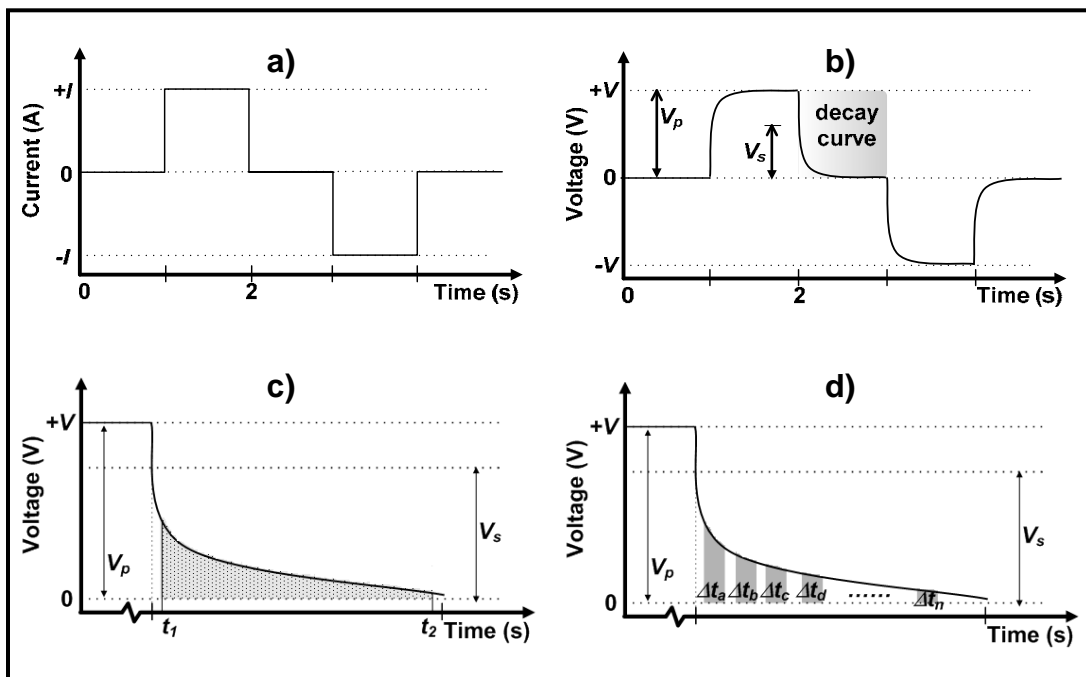
Figure 3.5. Schematic of the **a)** injected current and **b)** measured potential in a typical TDIP survey neglecting self potential effects. Analysis of the decay curve in shown in (b) can be performed by integrating over **c)** a given window or **d)** over several decay window slices.

The most basic parameter describing the polarization response is the chargeability, m defined by Seigel (1959) as:

$$m = \frac{V_s}{V_p},$$ (3.16)

where, V_s and V_p are the secondary and primary voltages respectively as illustrated in Fig. 3.4b-c. Due to the presence of noises in the field, V_s is difficult to measure accurately [Binley & Kemna, 2005]. Thus, it is common for m to be determined as an integral of the decay curve during pulse OFF time as

$$m = \underbrace{\frac{1_s}{(t_2 - t_1)}} \cdot \frac{1}{V_p} \int_{t_1}^{t_2} U(t)dt \ ,$$ (3.17)

where, t_1 and t_2 are the time boundaries of the total measured decay curve, $U(t)$. Owing to instrumental limitations or noises, the limits t_1 and t_2 are usually chosen subjectively a few ms within current switch OFF and ON as illustrated in Fig. 3.5c. This avoids any spurious spikes due to electromagnetic coupling at the instant the pulse is either switched ON or OFF to be integrated as actual responses. Noises in data can be further minimized by stacking multiple decay curves. Some commercial IP receivers utilize the Newmont window [Sumner, 1976] for reporting chargeabilities. In this instance, for a switched square wave of ON/OFF time = 2 s (f = 0.125 Hz), the decay curve is integrated between 0.45 – 1.1 s during OFF times [Butler, 2005]. These values can be transformed into the normalized Newmont standard, M331, which refers to a standard square pulse of 3 s ON and OFF times and an integration time of 1 s, using model-dependent normalization factors [Sumner, 1976; Sammis, 1987].

Note that the m determined from Eq. 3.16 and Eq. 3.17 are dimensionless. However it is common to express the m in milliseconds (ms), which is achieved by non-inclusion of the normalization factor (reciprocal of $(t_2 - t_1)$) in Eq. 3.17. Since the computed m will vary depending upon the geometrical arrangement of the electrodes on the surface of an inhomogeneous half space, the chargeability parameter calculated is in reality the *apparent chargeability* denoted by m_a. It is also common to express the chargeability connected to different window slices (Δt_a, Δt_b, Δt_c,..., Δt_n) of the complete decay curve as shown in Fig. 3.5d. Comparison of different windowed chargeabilities [see *e.g.*, Leroux & Dahlin, 2002] can then be performed amongst different locations on the profile for qualitative assessments. Note that at present there is no convention on the number of windows, their location, and the size (in seconds) which should be used for such analysis purposes.

 Chargeability itself is sensitive to bulk conduction and surface polarization effects. In order to isolate bulk conduction effects, chargeability is often normalized with soil resistivity as expressed by Eq. 3.18. According to Lesmes & Frye (2001), normalized chargeability (*MN*) is more sensitive to the surface chemical properties and is a global measure of soil polarizability.

$$MN = \frac{m_a}{\rho_a},$$

(3.18)

The determination of ρ_a is done within the scope of IP measurements by computing the transfer function $\Delta U/I$ of the system and transforming it into apparent resistivity values using Eq. 3.15. Thus, TDIP measurements permit the determination of extra information not possible within resistivity measurements alone. The other possibility of quantifying soil polarizability involves measurements in the frequency domain. This is discussed next.

3.3.3 Frequency Domain Analysis

Traditionally, frequency-domain analysis of IP response in soil has involved the *percent frequency effect* (PFE, units of %) and *metal factor* (MF, units of S m^{-1}) characterizations [Telford, *et. al.*, 1990] which are described by Eq. 3.19 and 3.20.

$$\text{PFE} = \frac{\rho_{DC} - \rho_\infty}{\rho_\infty} \cdot 100\% ,$$

(3.19)

$$\text{MF} = \frac{\left(\dfrac{\text{PFE}}{100}\right)}{\rho_{DC}} \times 2\pi \times 10^5 ,$$

(3.20)

where, ρ_{DC} and ρ_∞ are the measured resistivities at near DC ($f \to 0$ Hz) and infinitely away from DC ($f \gg 0$ Hz) frequencies respectively. In field, these conditions are normally accepted to be met within $f = 0.1$ Hz and $f \sim 8$ Hz for the former and latter respectively. Alternatively, the IP response can be characterized by the magnitude and phase difference between the current and potential waveforms [Binley & Kemna, 2005] as illustrated in Fig. 3.6 for a sinusoidal current injection across the A-B electrodes. Since soil will exhibit capacitive features, it follows that there would be a phase delay, $-\phi$ between the current and potential waveforms. Note that the magnitude $\Delta U/I$ is not a constant but will vary according to the frequency of the applied current signal. The complex impedance, *Z* thus is also a function of applied current signal frequency.

If the magnitude and phase difference response characteristic is extended over a wide frequency range, the resulting measurement forms the well known spectral induced polarization (SIP) method [Vanhala & Soininen, 1995; Lesmes & Frye, 2001; Revil & Florsch, 2010]. The SIP method is a very

important technique for IP response characterization in soils and will be developed and discussed in detail in Chapter 5.
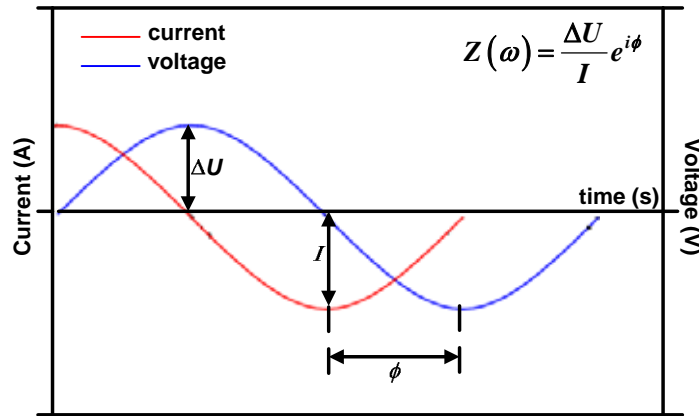
Figure 3.6. **a)** Signal analysis in frequency-domain or spectral induced polarization method.

Similar to resistivity methods, the time and frequency domain IP techniques discussed here can be used in different modes of operation, *viz*., profiling, VES, and 2-D or 3-D imaging using a combination of profiling and VES techniques. However, in the present work only profiling techniques have been used in field measurements, as will be presented later in the thesis. The DOI in induced polarization profiling are determined in the same manner as in resistivity profiling. Discussions so far has covered the necessary background material related to the concept and application of active geoelectrical methods in field. The passive self potential method will be discussed next.

3.4 Self Potential Method

The self potential (SP) sometimes referred to as spontaneous potential or natural potential, represents a passive measurement of the difference in electric potential fields on the surface of the Earth. Traditionally SP methods have been used in mineral exploration or groundwater surveys and are documented well in literature [*e.g*., John, 1963; Gay Jr, 1967; Corwin & Hoover, 1979; Revil *et. al*., 2004; Sultan *et. al*., 2009 and the references contained therein]. SP variations on the ground surface are caused by a variety of source mechanisms *viz*., electrokinetic (or streaming), thermoelectric, electrochemical, and mineralization potentials. Comprehensive discussions on these source mechanisms are also well covered in literature [*e.g*., Telford *et. al*., 1990; Sharma, 1997; Reynolds, 2011]. Hence, only brief treatments of these mechanisms are given next.

3.4.1 Sources and Mechanisms

The electrokinetic potential (E_k), also referred to as streaming or electrofiltration potential, is caused by the flow of liquid electrolyte at a constant rate through a porous media consisting of naturally charged surfaces. The E_k generated along the opposite direction to the flow path is given by the Helmholtz-Smoluchowski equation:

$$E_k = -\frac{\varepsilon \varsigma}{\eta \left(\sigma_f + \frac{2 \sum_s}{\Lambda} \right)} \cdot \Delta P \,, \tag{3.21}$$

where,

ε $\quad$ = the dielectric permittivity of pore fluid,

σ_f $\quad$ = conductivity of pore fluid (S m^{-1}),

ς $\quad$ = the Zeta potential (V),

Σ_s $\quad$ = the specific surface conductance (S),

Λ $\quad$ = characteristic length for the process,

ΔP $\quad$ = pressure difference along the flow path (Pa), and

η $\quad$ = dynamic viscosity of pore fluid. (Pa s).

The ς-potential (zeta-potential) can be best understood by the Stern model for an EDL at the soil fluid interface (see Chapter 2 for a description of Stern model). It follows that due to the difference in charges between the diffuse layer and the region inside the outer Helmholtz plane (Stern plane), relative movement of either phase with respect to the other will generate a potential difference. This relative movement occurs at the so-called shear plane, which exists away from the outer Helmholtz plane extending into the diffuse layer. The potential at the shear plane is called the ς-potential, which is largely affected by the soil composition and pH [Vane & Zang, 1997; Yukselen & Kaya, 2003]. In a strict sense, application of an electric potential can also cause the relative movement between the two phases. This coupling is described by the electrokinetic coupling coefficient, C_E (V Pa^{-1}) given by:

$$C_{EK} = \frac{E_k}{\Delta P} \tag{3.22}$$

The thermoelectric potential, E_t arises due to temperature gradients at different locations. The thermoelectric coupling coefficient, C_{TE} (V K^{-1}) for this mechanism is given by Eq. 3.23.

$$C_{TE} = \frac{E_t}{\Delta T} \tag{3.23}$$

In reality, SP generated by thermoelectric effect are of very small amplitudes except in geothermal regions [Sharma, 1997]. At near surface, these can usually manifest due to the presence of thermal fluids in fault zones. Electrochemical potentials, E_c, correspond to the sum of liquid-junction (or diffusion potentials) and the Nernst potentials. Liquid-junction potentials arise due to differences in the electrolyte concentrations in the ground. For this to remain significant, electrolyte concentration differences must be present [Sharma, 1997]. Similarly, in the presence of conductors surrounded by electrolytes of different concentrations the Nernst potential [Telford, *et. al.*, 1990] will develop. This Nernst potential can be calculated using Eq. 3.24.

$$E = \frac{RT}{zF} \ln\left(\frac{C_1}{C_2}\right),$$ (3.24)

where, all the symbols have their usual meanings and C_1 and C_2 are the different electrolyte concentrations. The combined liquid-junction and Nernst potential constitute the total electrochemical SP. Mineralization potential is usually associated with large negative SP anomalies (1 V) observed over massive sulphide ore bodies. A possible explanation on the mechanism of this phenomenon mostly cited in literature is that by Sato & Mooney (1960). However, insufficiencies arising out of Sato & Mooney (1960) model have been well discussed by Corry (1985) and Nyquist & Corry (2002).

The four basic mechanisms briefly described in this section constitute the major sources of SP in a given environment. In the absence of major geologic sources such as geothermal fields, and ore bodies, contributions from thermoelectric and mineralization mechanisms are negligible. In this instance, the manifestation of SP can be attributed to either electrokinetic or electrochemical, or the combined total of the two mechanisms. The measurement techniques usually employed in field for SP surveying will be discussed next.

3.4.2 Field Procedures

Measurement of natural potential differences on the ground surface is carried out using a pair of non-polarizable electrodes. These can be utilized in either the dipole (also referred to as leap-frog or gradient) configuration or the fixed base configuration, schematically shown in Fig. 3.7. In fixed-base configuration, one of the electrodes is kept fixed at a base station, while the other is moved along the profile route. Potentials measured at different stations (V_1, V_2, V_{n-1}, … V_n) along the route are then all referenced to the base station giving a continuous potential profile. The drawback with this technique is that it requires long reels of wires to account for long transects. This can be overcome by establishing new bases as the transect length progresses, whereby each new base accounts for

previous potential accumulations. In dipole configuration, a pair of electrodes kept a fixed distance apart (usually ~3 – 50 m) is moved along the profile route after measurement at one station; the trailing electrode occupying the spot of the leading electrode in each successive traverse. Measurements can be represented by the potential measurement at each individual station (V_{0-1}, V_{1-2}, … $V_{(n-1)-n}$), centred between the electrode pair, or can be added algebraically along the route to produce potential profiles along the route, similar to fixed-base method. The disadvantage with this technique is that zero-errors tend to accumulate as the traverse progresses [Telford *et. al*., 1990]. However, this can be minimized by measuring and correcting for the drifts between the electrodes periodically. Alternatively, the electrodes can be traversed in a leap-frog scheme to minimize zero-errors, *i.e*., the trailing electrode becomes the leading electrode and vice-versa in subsequent traverse.
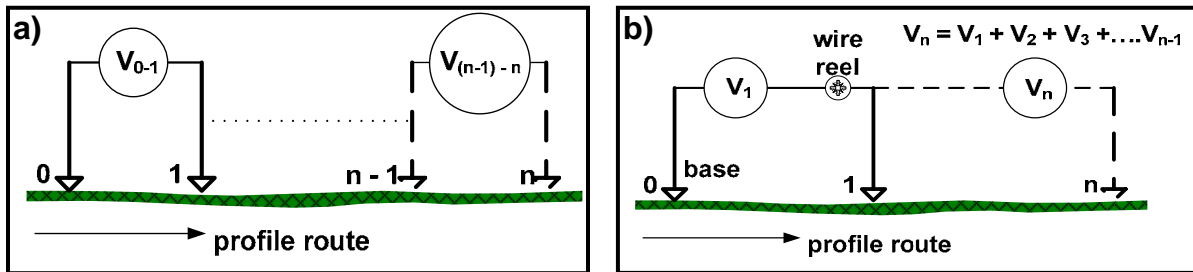
Figure 3.7. The **a)** dipole and **b)** fixed base configurations for measurement of self potentials on ground surface.

Used as a profiling tool, SP profiles along a route are interpreted qualitatively by identifying regions of positive or negative anomalies, which normally correspond to some significant processes or geological formations. Although, very useful SP profiling methods are very susceptible to noises, especially if an anomalous source generates very low amplitude potentials in a noisy environment. In such events, special signal processing functions have to be applied to reject noises in the data.

The present chapter has been a focus on brief theoretical treatments of the three surface geoelectric methods, which have been utilized in the present work. Important criteria and requirements have been discussed, which are necessary for field applications of these techniques. Specific detail on these techniques will be developed later in the thesis, and their applications in the field will be presented.

CHAPTER 4

GALVANOSTATIC PULSE METHOD FOR ASSESSING CORROSION IN SOIL ENVIRONMENT: STATE OF THE ART

The present chapter provides an investigation into the use of short galvanostatic pulse techniques as a means of assessing corrosion in a soil environment. Although the technique is well understood and has been applied in physically similar environments (*e.g.*, steel corrosion in concrete), it is believed it has never been utilized in soil environments. Thus, the chapter reports a pioneering application of the galvanostatic pulse technique for assessing corrosion in a soil environment under laboratory conditions.

4.1   Introduction

Pipeline corrosion in a soil environment is governed by a complex interaction of the physical, chemical, and biological elements which exist simultaneously on a metal leading to its subsequent deterioration. These effects can be further enhanced by other anthropogenic activities. A study by Ismail & El-Shami (2009) provides a good platform for understanding the effect of engineering soil properties on corrosion processes. They indicate that water is a prerequisite for functioning of corrosion cells and the corrosion intensity is determined by soil grain size, swelling, shrinkage and clay mineral content. In essence, these factors can be extended to any ferrous material buried in soil.

Studies aiming to understand the corrosion of pipelines in a soil environment can be generally categorized according to the methods and the scale of the investigation *e.g.*,:

a) Electrochemical or weight loss measurements in:

   i) laboratory set-ups to understand the behaviour and energy exchanges at the metal/soil interface over short or long time exposures such that some inferences on corrosion rates can be made, and

   ii) field conditions near buried pipelines to provide valuable information in condition assessment programs.

b) spatio-temporal changes in soil properties and its dynamics and consequently its influence on corrosion of buried pipelines.

Although weight loss measurements can provide "ground truth" of corrosion rates, they require long exposure times. The final corrosion rate estimates after a certain exposure time is the average corrosion rate during the exposure time. On the other hand, electrochemical measurements permit the

determination of instantaneous corrosion rates enabling a true assessment of the actual corrosion rate at a particular time. Assessments of soil corrosivity based on its composition and/or related properties is well reported in the literature [Romanoff, 1957; DIPRA, 2000; Gerwin & Baumhauer, 2000; Sadiq *et*. *al*., 2004; Ferreira *et*. *al*., 2005; Ismail & El-Shami, 2009 and the references contained therein]. Most notably soil resistivity is usually used as a first approximation for assessment of potential soil corrosivity according to the 10-point scoring method by DIPRA (2000). The early work of Romanoff (1957) laid the foundations for understanding the various soil properties which contribute towards underground corrosion. There exists however some inconsistencies in observed results in the literature. Gupta & Gupta (1979) studied the corrosion rate of mild-steel in soil samples taken from India and found that the mass loss was directly related to the moisture content. They reported that the corrosion rate increased with increasing moisture content until a critical moisture level which corresponded to 65% of the water-holding-capacity of the soil. Beyond this critical level the corrosion rate displayed an inverse relationship with moisture content. They also reported an inverse relationship between soil resistivity and corrosion rates. Likewise, Seica *et. al.* (2002) and Doyle *et. al.* (2003) reported (weak) correlations ($r^2 = 0.3$) between soil resistivity and maximum pit depths on cast iron water mains. Murray & Moran (1989) studied the effect of water content on corrosion rates and reported similar corrosion current densities for sandy and clay soils at the same moisture content levels. They reported a semi-log dependence of corrosion current densities on moisture contents. However, they did not observe any critical moisture levels as reported by Gupta & Gupta (1979). Similarly, Norin & Vinka (2003) did not observe any critical moisture levels associated with maximum corrosion rates while studying corrosion of a buried steel coupon in backfill material. Thus, there appears to be some non-consensus on the existence of any critical moisture content at which maximum corrosion occurs. Most probably the existence of any such critical limit arises due to oxygen diffusion, which is necessary for the corrosion reaction in soils [Baboian, 2005].

According to Jiang & Wang (2009) and Jiang *et*. *al*. (2009), the corrosion process in soil can be classified as a gas/liquid/solid multiphase system. The distribution of liquid on the metal surface is not necessarily continuous but depends on the size and distribution of the soil particles as illustrated in Fig. 4.1. Jiang *et*. *al*. (2009) recently investigated the gas/liquid/solid three-phase-boundary (TPB) zones in soil, which occur due to highly dispersive liquids. Their results conform well with the literature indicating that the geometry of the TPB greatly affects the cathodic limiting current density and hence the overall electrochemical corrosion rate.
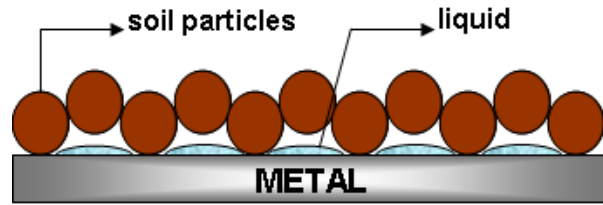
Figure 4.1. Schematic of the distribution of liquid on the metal surface in soil electrolytes [Adapted from Jiang *et*. *al*. (2009)].

In reality, natural soil will contain a size distribution of particles which will distort the liquid distribution depicted in Fig. 4.1. The presence of clay complicates this model since the size distribution of the liquid droplets in this instance will not be uniform.

The focus of most previous studies has been the measurement of various soil properties and their corresponding effects on corrosion rates. Some studies have discussed the importance of water content, which directly affects the soil resistivity, as being the major element controlling the overall corrosion strength [*eg*., Gupta & Gupta, 1979; Yahaya *et*. *al*., 2011]. Other studies involving long term measurements indicate that the soil moisture level was maintained at a specific level [Pernice *et*. *al*., 1990]. However, the homogeneity of water distribution in the soil can be very difficult to control. After the findings by Gupta & Gupta (1979), the notion of 25% w/w of moisture content or less in soils has been suggested as the optimal moisture level for maximum corrosion in some works [*e*.*g*., Yuan-hui *et*. *al*., 2005; Xiaodan *et*. *al*., 2007] Also, often overlooked, are the Atterberg Limits, which categorize the four different states of soil depending upon the water content as; solid, semi-solid, plastic, and liquid. At a given moisture level, soils with few fines content (sandy) may behave like a liquid, while those with high clay content may exhibit semi-solid to plastic response. In such a case any cross comparison should also take into consideration the different textural effects on the corrosion process. In fact the procedure used to saturate soils and their subsequent loading into the electrochemical system set-up to initiate the metal/soil interface is rarely discussed in most works. At present there is no consensus as to the moisture level at which electrochemical measurements should be conducted in laboratories, which can be used to a) grade potential corrosivity of soils and b) provide a means of comparing soil corrosivity amongst different geographical locations. The disadvantage of using a low moisture level, which results in solid to plastic states in soil, is that large errors can be encountered when initially setting up the electrochemical cell for measurements. In establishing the metal/soil interface, issues such as the optimal pressure to apply to the soil, the adherence of soil to the metal surface, uneven pressing *etc*., contribute towards several inherent systematic errors.

4.1.1 Development of the Metal-Soil Interfacial Properties

The interface which forms when soil comes in contact with a metal surface can be described by the phenomenology of a double layer. To a first approximation, the equivalent circuit for the double layer structure can be modelled by an $R_p C_{dl}$ - parallel network. This $R_p C_{dl}$ parallel arrangement in series with the soil resistance, conforming to a simple Randle's circuit, can then be used to describe the complete electrical structure at the interface and the bulk of the soil media (Fig. 4.2a). However, soil is a lossy dielectric which can be modelled by a resistor and capacitor in parallel ($R_\Omega C$). Thus a complete description may sometimes be best provided by the complete circuital structure illustrated in Fig. 4.2b. Note that the equivalent structure shown here can be applied to other metal/porous-media interfaces *e.g*., concrete/steel systems [Feliu *et. al*., 2004; Elsener, 2005]. Some works related to corrosion studies in soil using the electrochemical impedance spectroscopy (EIS) method, have reported the presence of two time constants [Pernice *et*. a*l*., 1990; Silva & Dick, 2008] in the Nyquist plot. It is noted here that the origin of these two time constants are the two parallel RC-networks arranged in series representing the corrosion and bulk processes. However, as noted by Pernice *et. al*. (1990), the corrosion process is represented by the larger time constant associated with the electrode processes. The capacitance of soil is rarely reported and discussed in the context of electrochemical corrosion investigations. Although, this phenomenon is well known in the field of soil science and applied geophysics, it has yet to be integrated as part of corrosivity assessments in soils.
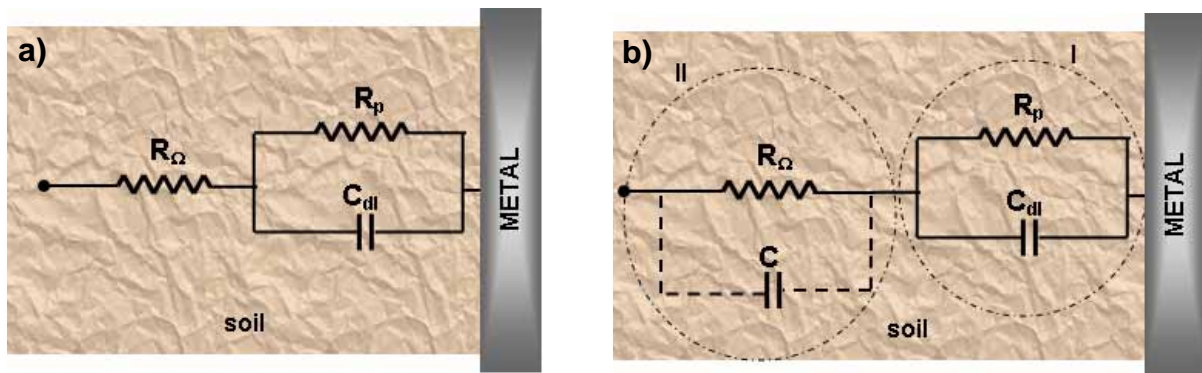
Figure 4.2. The equivalent circuit diagram at the metal/soil interface and the bulk of the soil for **a)** negligible capacitive effect from soil, and **b)** with the capacitive effect from soil.

The capacitance associated with soil will vary depending on the moisture content and clay content. It is interesting to note that although several works report higher corrosion rates in soil at some particular level of moisture content (% w/w) the effect of soil capacitances at these moisture levels on the overall measurements has not been investigated. As shown in Chapter 2 (section 2.4.3), the measured current during a potentiodynamic scan is composed of two components *viz*., the Faradaic

current related to the corrosion process and the current resulting from the charging of the EDL at the metal/electrolyte interface. For soil, there will be a third current which would originate from the charging of the soil capacitance. The magnitude of this current would strongly depend upon a) the location of the reference electrode, b) the scan rate, c) the moisture content of soil, and d) the clay content. For heavily saturated and very dry soil electrolytes, these unwanted capacitances may be lower to negligible. However at intermediate values (especially soils exhibiting plastic properties), the capacitance may be higher leading to a higher capacitive current in the overall measurements. The choice of the scan rate is also very important, since the magnitude of the capacitive current from soil will vary accordingly. This presents a difficult situation when analyzing a large number of samples, since the optimal scan rate may vary amongst the different metal/soil electrochemical cells. Trial runs to estimate this optimal scan rate for each given sample prior to proper measurements can become tedious. A comparative analysis in such situations also becomes difficult in the absence of any normalization approaches to remove any scan rate artefacts from overall measurements.

4.1.2 The Linear Polarization Resistance Technique

The economic effect of pipeline failures emanating from corrosion prompted the need for suitable field-capable corrosion monitoring and measurement techniques. This led to the implementation of the linear polarization resistance (LPR) technique for determination of the polarization resistance R_p, which can be used to infer the instantaneous corrosion rates of pipelines buried in soils. For field deployment the use of potentiodynamic scans at small overpotentials to extract information on R_p becomes tedious and cumbersome. In this regard, the assumption of linearity at small overpotentials leads to a variation in the manner in which these measurements are conducted. In essence, LPR techniques usually apply a small static overpotential of +(5-10) or -(5-10) mV and the resulting current density at the applied potential is recorded after stable conditions. The slope of the line connecting the positive or the negative overpotential to the $E_{OC} = E_{CORR}$ is then evaluated to determine the R_p as illustrated in Fig. 4.3a. Although, this method is theoretically debatable due to the errors involved in the assumed linearity (Fig. 4.3b), it has been implemented into specially designed commercial probes which are field-friendly and allow a capacity to monitor and estimate *in-situ* corrosion rates of installed pipelines.
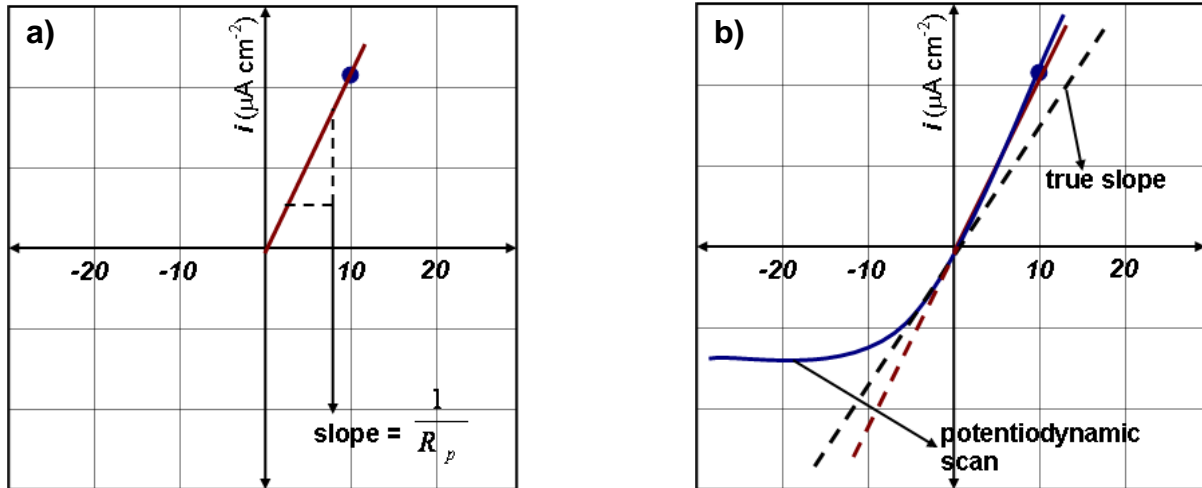
Figure 4.3. **a)** Schematic of the LPR technique employing $+\eta$, and **b)** the assumed linearity may not be present at all, in which case the true slope evaluated as the slope of the tangent to the potentiodynamic curve at E_{CORR} is not equal to the slope determined by LPR technique.

The LPR technique has been applied to analyse corrosion rates of different materials in a wide range of environments [Soleymani & Ismail, 2004; Bravo *et* al., 2006; Millard & Sadowski, 2009 *etc*]. In a soil environment, corrosion intensities of pipelines, or other buried infrastructure using the LPR technique, have been determined by various workers such as Bullard *et al*., (2005), Kear *et al.*, (2006) *etc*. Although the technique is suited for electrolytically conducting media, it has been applied in various water based environments for corrosion assessment and monitoring [Azzeri *et al*., 1981; Cigna *et al*., 1985]. In Australia, the LPR technique has been used to assess the performance of critical mains [see Dymke & Ferguson, 1999; Ferguson & Geehman, 2001]. Although the limitations of LPR have been well documented by several workers [Mansfeld, 1961; Albaya *et al*., 1973; Hilbert, 2006; Kouril *et al*., 2006], this technique is still used due to its practicality, sample turnover, and the low costs involved. Note, it is believed that the problems associated with soil capacitance and its interference on overall LPR measurements has not been studied.

4.1.3 The Galvanostatic Pulse Technique

Concerning the interferences from soil capacitances in electrochemical measurements, the electrochemical impedance spectroscopy technique (EIS) appear to be more favourable since it allows the non-corrosion related processes to be identified and separated from corrosion related processes. However, this method also requires special instruments and long times to scan from high to very low frequency limits. Also, in order to extract corrosion parameters, an equivalent circuit accurately describing the Nyquist plot has to be adopted. Birbilis *et*. *al*. (2003) while studying steel corrosion in concrete recognized similar problems associated with LPR techniques in concrete/steel systems (see

also Kouril *et. al.* (2006) and the long times associated with EIS scans. They identified a new approach to analysis of corrosion processes by using short ($\leq$ 1s) galvanostatic pulses (a deviation from the long pulses usually applied to study concrete/steel corrosion systems; Elsener, 2005), to acquire the charging and discharging curves along with some curve-fitting techniques to extract corrosion parameters, *viz.*, R_p and C_{dl}. This approach in essence bears some strategic similarity to analysing small overpotential potentiodynamic curves using the Butler-Volmer equation with curve-fitting techniques as suggested in Mansfeld (2005) and Mansfeld (2009). In their work, Birbilis *et. al.* (2003) utilized the Kohlrausch-Williams-Watts (KWW) formalism to model the charging/discharging curves as exhibiting a stretched exponential behaviour, arising due to the non-ideal behaviour of the C_{dl}. Thus, their charging and discharging curves were modelled by a Randle's type circuit shown in Fig. 4.4a. They showed that given the applied current density is small ($<$ 100 μC cm^{-2}), significant resistances due to diffusion effects can be avoided, in which case the R_D term can be ignored and the potential-time response equations for the charging and discharging sections (illustrated in Fig. 4.4b) can be described by Eq. 4.1 and 4.2 respectively.
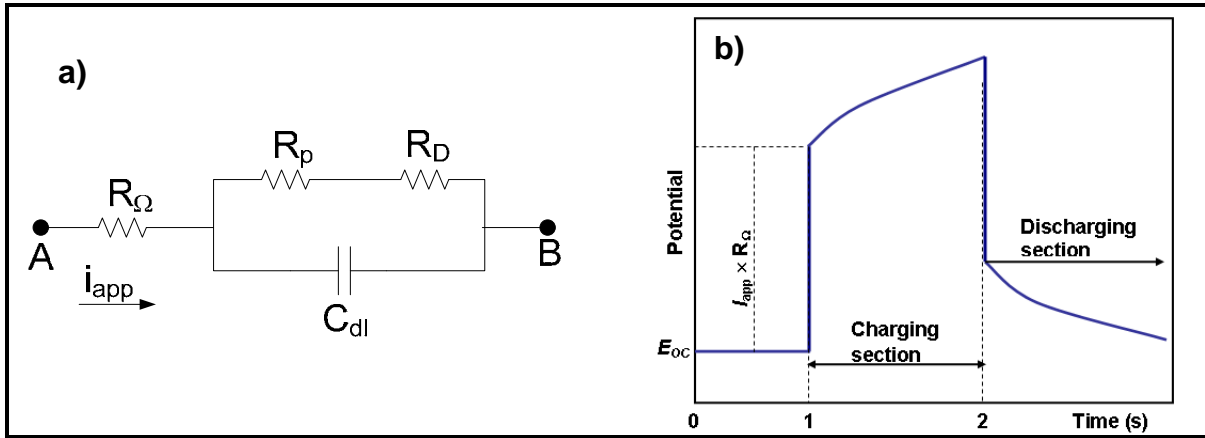
Figure 4.4. **a)** The Randle's type circuit used to model the interfacial response in concrete/steel systems, where R_D is the resistance that manifests due to significant diffusion effects [after Birbilis *et. al.*, 2004], and **b)** schematic of the charging and discharging sections on the potential-time response after application of a short (1 s) galvanostatic pulse across AB.

$$E(t) = i_{app}R_\Omega + i_{app}R_p \left(1 - \exp\left(-\left[\frac{t}{R_p C_{dl}} \right]^\beta \right) \right) \tag{4.1}$$

$$E(t) = i_{app}R_p \left(\exp\left(-\left[\frac{t}{R_p C_{dl}} \right]^\beta \right) \right), \tag{4.2}$$

where,

$E(t)$ = potential-time response (V), and

i_{app} = applied current (A), and

β = stretched exponential factor (dimensionless), where $0 < \beta \leq 1$, and

R_{Ω} = Ohmic resistance due to the electrolyte (Ω).

The term $i_{app}R_{\Omega}$ in Eq. 4.1 describes the instantaneous *jump* of the response curve corresponding to the instantaneous on-set of the charging process. In this work, a similar approach is taken to estimate the double later characteristics at the soil/metal interface. However, unlike in concrete systems, capacitances in soil (although small) can manifest in the observed results. Thus, further treatment of the data may be necessary before analyzing it using the simple Randle's circuit. Regarding Eq. 4.1 and 4.2, since the i_{app} is a constant term these equations can be expressed in terms of charging and discharging resistance-time response as given by Eq. 4.3 and 4.4 respectively.

$$R(t) = R_{\Omega} + R_p \left(1 - \exp\left(-\left[\frac{t}{R_p C_{dl}} \right]^{\beta} \right) \right) \tag{4.3}$$

$$R(t) = R_p \left(\exp\left(-\left[\frac{t}{R_p C_{dl}} \right]^{\beta} \right) \right) \tag{4.4}$$

Regarding the discharging response however, some further scaling may be required in order to correct for possible partial charging of the interfacial double layer due to the short galvanostatic pulses. This can be achieved via Eq. 4.5.

$$R(t) = \gamma * \left[R_p \left(\exp\left(-\left[\frac{t}{R_p C_{dl}} \right]^{\beta} \right) \right) \right], \tag{4.5}$$

where, γ is a dimensionless parameter limited between $0 \leq \gamma \leq 1$. To account for the partial charging effects in the discharging curves, Birbilis *et. al.* (2003) adopted a different approach by including an offset-time parameter in their equations. In a later work Birbilis *et. al.* (2004) demonstrated that the interfacial double layer parameters can be computed from analysis of the charging curve alone, without the need for any analysis of discharging curves. It is believed that the use of galvanostatic pulse techniques for assessment of corrosion rates in soil has never been conducted before in laboratory or in field. This is interesting since the technique possesses all the favourable characteristics to address the common difficulties (*e.g.*, correction for high Ohmic-drops in soils) encountered in measurements as well as being easily applied in the field. For example, one such commercial probe used for assessment of steel corrosion in concrete is the GEOCOR 6 equipment, which is based on the galvanostatic principle of operation [see Nygaard, 2009].

In the absence of any widely accepted technique for use in soil corrosion studies, the present chapter is focussed on a laboratory procedure adopted to assess corrosion in a synthetic soil environment. The contributions of this chapter to the overall thesis are mainly to:

a) Investigate the use of short galvanostatic pulse techniques for assessment of the double layer parameters at the metal/soil interface, which can be used to assess corrosion, and

b) To provide an insight into the effect of clay and chlorides on the corrosion of ferrous materials in soils.

4.2   Experiment Design and Measurements

This section describes the various procedures and methodologies which were adopted in order to qualitatively assess the levels of corrosivity of various synthetic soil samples prepared in the laboratory. For the purpose of analysis, three different pipeline materials (mild-steel, wrought-iron, and grey cast-iron) were investigated. Individual detailed analysis of the corrosion process and micro-structural effects on these different materials is beyond the scope of the present work. Instead an holistic approach is taken to understand the behaviour of ferrous materials.

4.2.1 Metal Specimen Preparations

Metal samples to be used in this investigation were furnished from mild-steel, wrought-iron and cast-iron, which were lathed using a high speed steel tip. The wrought-iron and grey cast-iron (hereafter referred to as cast-iron only) samples were cut from a previously acquired in-service sewer and water pipeline respectively. The mild-steel samples were Grade 250 materials acquired from a local commercial company. The final 45 metal specimens (15 for each material type) were circular ($\phi = 45$ mm) and 5 mm thick. For each specimen, the surface was polished using SiC paper sequentially from #600, #800, and finally with #1000 on an automatic rotating turntable. After complete polishing the specimens were degreased with ethanol in an ultrasonic bath (this was also performed between polishing with different grit sizes) and rinsed with deionized water and loaded into the flat-cell assembly with no further delay.

4.2.2 Preparation of Synthetic Soils

Soil specimens were synthetically prepared in laboratory using previously washed Mesh 30 silica sand and kaolin clay. These synthetic samples were utilized for the electrochemical experiments reported in this chapter, as well as for the experimental work reported in chapter 5. A particle size distribution for the clay utilized in this work had been previously done by Viezzoli (2006) and is given in Appendix A.1. Five different proportions by weight of sand:clay mixtures were prepared; the

relative composition by weight ranged from 75%:25% to 95%:5%. For each mix, three sets of ~1.2 kg of sample were prepared and thoroughly mixed to ensure homogeneity. Thus a total of 15 geosynthetic samples were prepared. Attempts to saturate the samples by allowing them to absorb free water proved futile. This was due to the impermeable surface layer which develops in the presence of clay preventing any penetration of water. Thus, saturation of the samples was done by progressively adding the necessary electrolyte solution while mixing until the samples were completed saturated. For increasing clay content, a larger amount of electrolyte was required to attain complete saturation. The electrolytes used for this purpose were deionized water, 0.01M NaCl, and 0.1M NaCl. A summary of the synthetic soils prepared is given in Appendix A.1. The pH levels of the synthetic samples were not controlled but allowed to evolve naturally. Note, that three different batches were prepared. After saturation, the samples were sealed in air-tight containers and kept in darkness for at least 3 weeks to ensure geochemical equilibrium.

4.2.3 Electrochemical Measurements

In order to conduct electrochemical testing, some emphasis was placed on the adoption of a specific design for the electrochemical cell. For this purpose a prototype flat-cell assembly was used. A multi-cell panel (40 cm × 40 cm) was machined from 2 cm thick high density polyethylene (HDPE) material. Sixteen cylindrical holes of diameter 4 cm were drilled on the main panel and the working electrode specimens were affixed at the bottom. Another thin sheet of supporting HDPE panel was then screwed to tightly hold the specimens against the bottom of the panel. The holes allowed the exposure of the working electrodes (area = 4π cm^2) placed at the bottom as illustrated in Fig 4.5
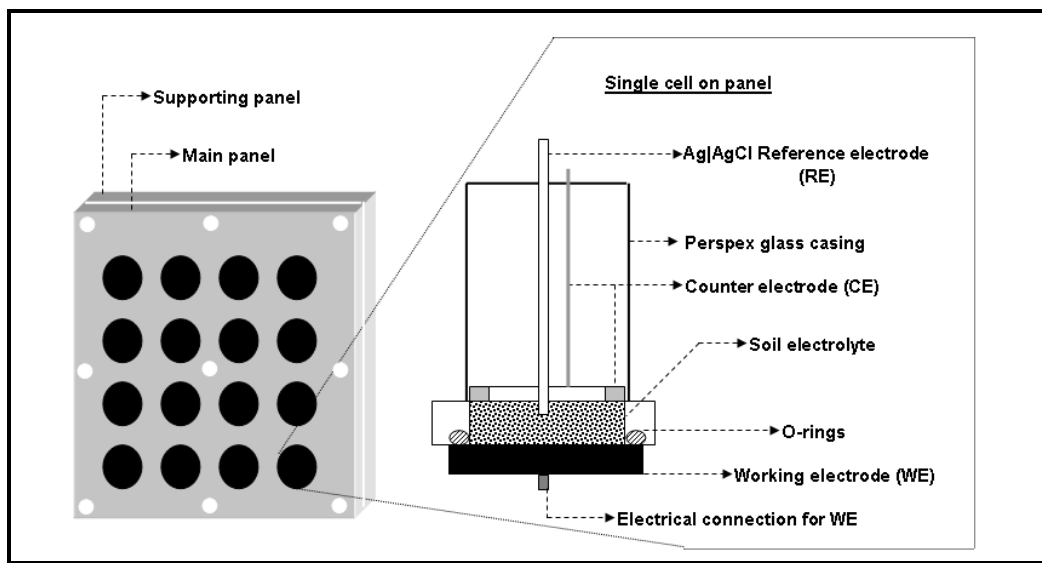
Figure 4.5. Illustration of the electrochemical cell set-up.

Three such panels were used, each loaded with Grade 250 mild-steel, cast-iron, and wrought-iron metal specimens. Each cell was loaded one at a time with the required saturated soil sample and its open circuit potential was monitored to identify the onset of steady state conditions (stable E_{OC}). This was repeated for all the 45 cells measured in the present work. Note, the complete saturation of the soil electrolytes ensured that directly pouring the soil onto the working electrode surface resulted in uniform distribution without the need for any applied pressure. However, to ensure this uniformity a small rotating blunt plastic shaft at the end of a low speed automatic drill was used to distribute soil electrolyte on the working electrode surface. The Eco-chemie microAUTOLAB III potentiostat/galvanostat accompanied by the *General Purpose Electrochemical Software* (GPES V4.6) was used to provide short (1 s) galvanostatic pulses and the resulting potential-time response was recorded internally by the instrument. The maximum recordable potential for this galvanostat is ± 10 V.

In all cases, the working electrodes were cathodically polarized in order to minimize any irreversible changes to the working electrode surface. Due to the limit on the maximum number of data acquirable by the galvanostat (10 kS), sampling frequencies were variable for different portions of the potential-time response curve, allowing sections of interest to be sampled at a higher frequency. The laboratory set-up for the experiment described in this section is shown in Plate 4.1. Particular attention was given to the quantity of charges liberated at the surface of the working electrode due to the amount of current injected.
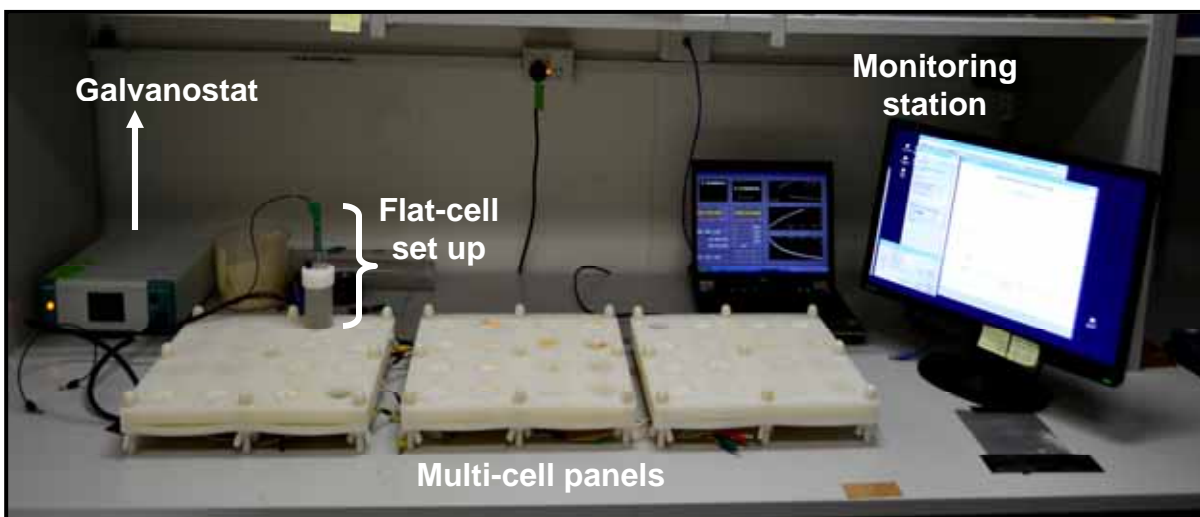
Plate 4.1. Laboratory set-up for the electrochemical measurements. Each cell is connected one at a time to the galvanostat and measurements are conducted.

To avoid significant resistances associated with diffusion effects from the technique itself, the charge densities during the application of the galvanostatic pulses were maintained below 50 μC cm^{-2}. This value was adopted after random tests on a few samples using 0.5 s and 1 s pulses; given the same current in each case, the total charge $Q = i_{app} \times t$, will be different.

The first set of measurements (BATCH 1) was conducted 2 h after loading the respective cells with soil electrolytes. For steady measurements, the counter and reference electrodes were secured on the end cap of a glass tube and allowed contact with the soil as illustrated in Plate 4.2. A circular stainless steel counter electrode with outer/inner diameter of 40 mm/20 mm and an Ag|AgCl reference electrode filled with 3M KCl solution placed in the centre of the counter electrode were used to provide the classical three-electrode configuration. The depth of penetration of the reference electrode into the soil was not strictly controlled but was not allowed to protrude > ~10 mm into the saturated soil. To ensure repeatability, each electrochemical cell in the multi-cell panel was measured three times (unless indicated otherwise), which was performed in the following manner. After each single measurement the cell was disconnected and the reference and counter electrodes were removed. After a short period the reference and counter electrodes were re-positioned on the soil surface and electrical connections were re-established. Measurements were then repeated after acquiring a stable E_{OC}. After the first set of measurements, the multi-cell panels, except those loaded with mild-steel, were left under standard room conditions and the corrosion reaction was allowed to proceed under influence of natural desaturation of the soil electrolytes. For mild-steel samples, a different approach was taken. A potential of 1.5 V was applied between the working (positive) and counter (negative) electrodes in each of the mild-steel cells for 8 hrs immediately following the BATCH 1 measurements, thus initiating an anodically activated corrosion. After 8 hrs, the mild-steels were then allowed to corrode naturally under the action of natural desaturation. The second set of measurements (BATCH 2) was conducted on the 7th day, during which time the surface layer of the soil electrolyte exhibited dry conditions. For these measurements, the counter electrode and the tip of the reference electrode was wet with distilled water and allowed to rest on the soil surface while conducting galvanostatic pulse measurements. Again, to ensure repeatability each of the cells was measured at least three times as described previously.

The purpose of the two distinct sets of measurements was to observe any differences which emanate during natural desaturation conditions. For some individual cells (especially those loaded with mild steel), the soil resistivity had increased dramatically after 7 days due to loss of moisture. This resulted in very high potential jumps corresponding to very high Ohmic-drop even for very small amounts of

injected current (*e.g.*, 10 µA). In some instances the Ohmic-drops overwhelmed the potential-time response pulses resulting in saturation of the maximum measurable voltage ($\pm$10 V). Thus, for these cases very small currents had to be utilized (10^{-9} A). To investigate if any conclusions can be drawn from the anodic curves of metals in soils, another set of experiments was carried out at the ARC Center of Excellence of Design in Light Metals located at Monash University, Clayton, Victoria, Australia. Each of the metal specimens were again polished, loaded with soil electrolytes one at a time and anodic potentiodynamic scans up to an overpotential of +0.12 V was carried out. For this purpose the BioLogic VMP3 potentiostat with Ohmic correction capability was used. The software EC-Lab was used to provide control and measurement of the potentiostat. To ensure measurements under steady E_{OC} conditions the open circuit potential was monitored for at least 30 mins for each cell prior to measurements, which were conducted 2 hrs after immersion.
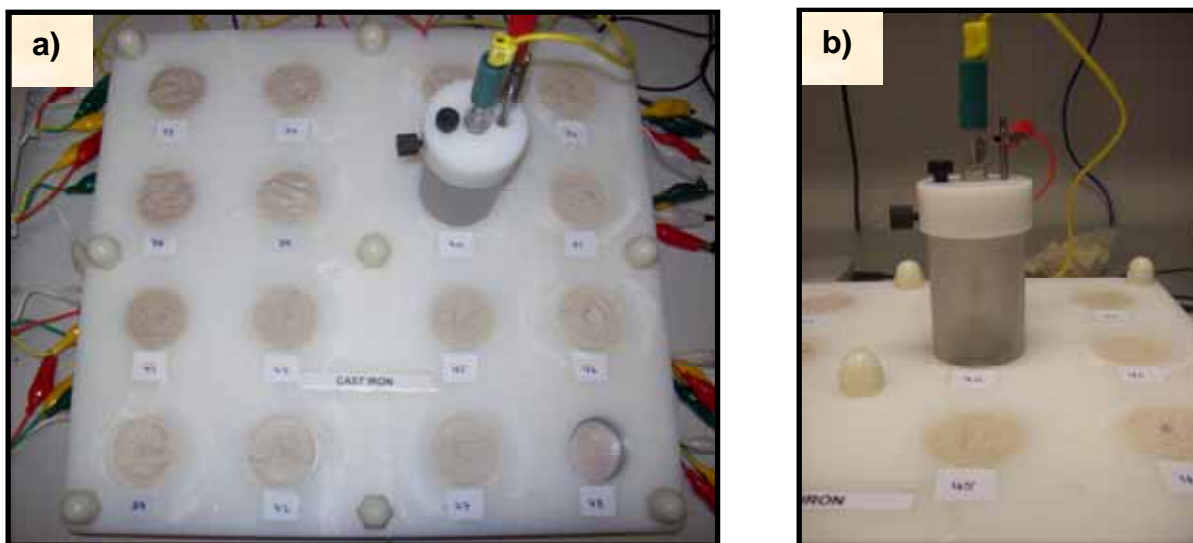
Plate 4.2. **a)** A closer look at the multi-cell panel showing the emplacement of the reference and counter electrodes affixed to a supporting Perspex glass and **b)** the exploded view.

4.2.4 Curve Fitting Routines

To extract corrosion parameters from the acquired potential-time response curves, a non-linear least squares curve fitting routine was implemented in National Instruments LabVIEW 2009 software. Programs written in LabVIEW are called *virtual instruments* (VI) and the programming language is G-code. A LabVIEW program consist of two major windows, the front panel (user interactive GUI) and the block diagram (window containing the actual codes). Similar to conventional programming, LabVIEW allows modularization of coding such that specific processing functions routinely utilized can be called for and used. Several such mathematical processing functions, called subVI's (similar to

sub routines in conventional programming), are available in LabVIEW which can be utilized. The non-linear least squares curve fitting routine developed in this work utilizes the famous Levenberg-Marquardt Algorithm (LMA). The LMA [see Levenberg, 1944; Marquardt, 1963; Press *et. al.*, 1992] is a well known technique for minimization of a given objective function and thus a detailed description is not important here. However, for completeness in the thesis, a treatment on its principles is provided in Appendix A.2. The LMA is provided in LabVIEW as a standard subVI which can be readily utilized. The user interface for the curve fitting routine developed as part of this work is shown in Fig. 4.6 and its block diagram is given in Appendix A.3. Note the routine has been modularized by the use of other subVI's, developed as part of this work or already available in LabVIEW.
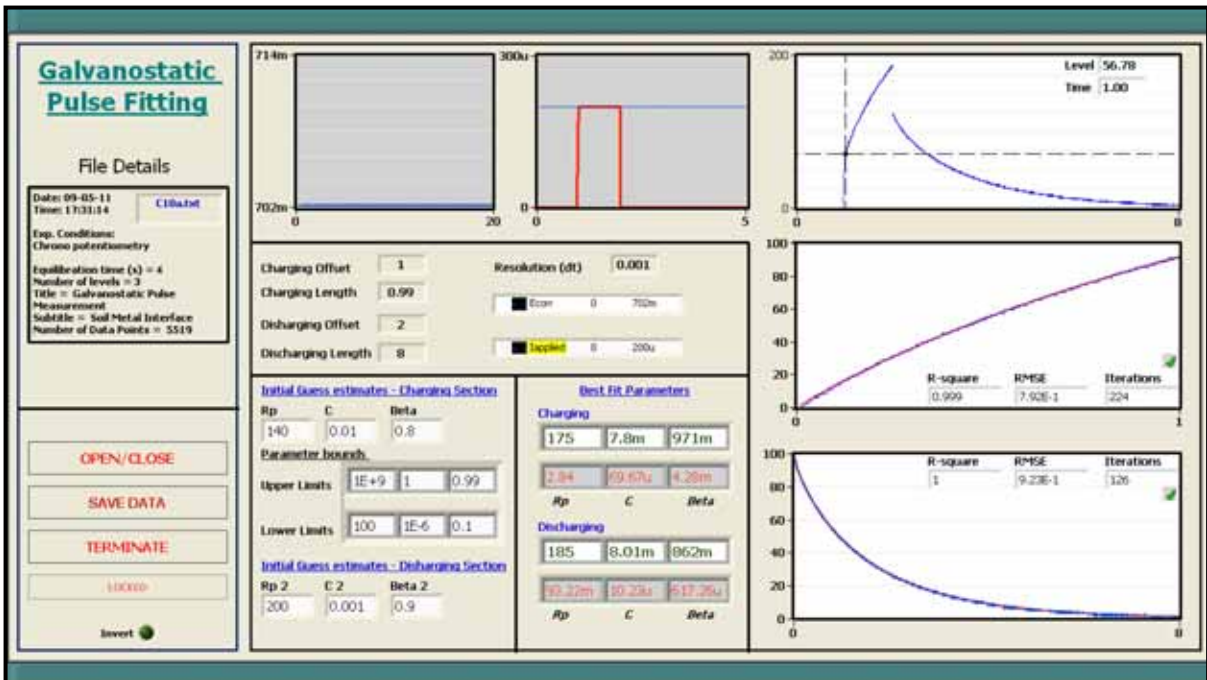
Figure 4.6. User interface for the non-linear least squares curve fitting program for extraction of corrosion parameters from the charging and discharging sections of the curve.

Although a detailed description on the operation of the routine is best provided by the block diagram (Appendix A.3), the flowchart given in Fig. 4.7 provides a basic summary on how this is achieved. It is emphasized that the advanced signal processing functions are not expanded in the flowcharts shown, but can be traced in the block diagrams. Also, the program is allowed to operate continuously for one data file. This is done in order to provide real-time observations on the changes in the fitted parameters induced by varying the initial parameter estimates. The program reads in the data which is corrected for the user specified E_{OC} and divided by the current. This converted data in terms of resistance-time pulse is displayed. This pulse can be reconstructed at the same frequency at which it

was sampled by the potentiostat or at a higher user specified rate with interpolation achieved through either FIR filter based or coerce method. The R_Ω term is evaluated manually by locating the initial jump and its magnitude on the user-interactive GUI interface using cursors. The corrected charging and/or discharging sections are then passed onto the next processing functions. The initial parameter estimates and the upper and lower limits for the parameter (constraints) are also fed into the program through the user-interactive GUI.
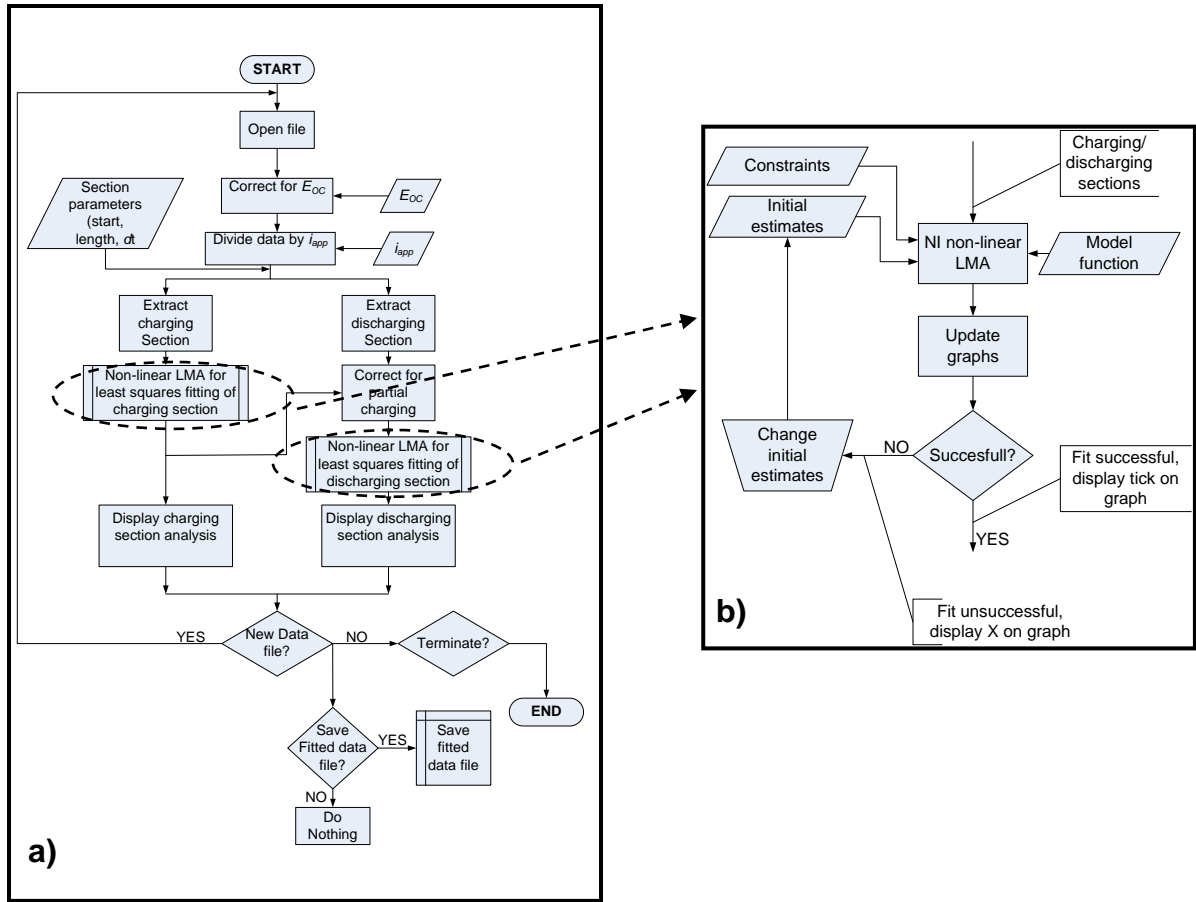
Figure 4.7. Flowchart **a)** showing the basic operation of the curve fitting routine and **b)** the implementation of the least squares fitting of charging or discharging sections employing NI non-linear LMA.

These are then passed onto the constrained LMA which separately minimizes the misfit function for both the charging and discharging cases given by:

$$\chi^2 = \sum_{n=1}^{N} \left(R_n^{\text{lab}} - R_n^{\text{model}} \right)^2 \qquad , \qquad (4.6)$$

where,

χ^2 = the objective function,

$\qquad$ N = number of data points, and

$\qquad$ $R_n^{\textbf{model}}$ = fitted value of the curve at n, and

$\qquad$ $R_n^{\textbf{lab}}$ = experimental value of the curve at n.

The summation is carried out over the entire dataset belonging to the charging (N = 500) or discharging (N = 250) sections. The final estimated parameters (R_p, C_{dl}, β) are then displayed together with a graphical display of the experimental and fitted curves. Other statistical parameters such as the root-mean-square-error (RMSE), r^2, and the number of iterations needed for convergence are also displayed. The individual errors in the data points are not known, but are believed to be equal and mostly due to any consistent instrumental errors. Thus, the uncertainties in the final parameter estimates are computed from the square-root of the diagonal elements in the final covariance matrix multiplied by the RMSE. Note the number of parameters $p \ll N$, thus there exists large degrees of freedom, ν. Since ν is high in this work, the RMSE provides a good estimate of the noises in the data. Also, the curve fitting program is capable of analyzing the charging curve without the need for the discharging curve. On the contrary, successful analysis of the discharging curve requires pre-analysis of the charging curve. This follows after the partial charging factor γ is determined from the charging curve as a simple ratio given by Eq. 4.7 below.

$$\gamma = \frac{R(t)_{\textbf{OFF}}}{R_{p(\textbf{charging})}} \qquad (4.7)$$

where, $R(t)_{\text{OFF}}$ = the maximum resistance value at the instant the pulse switches OFF, and

$\qquad$ $R_{p(\text{charging})}$ = the estimated R_p parameter from the charging curve.

This γ parameter is then used to provide corrections prior to the LMA fitting procedure on the discharging section. However, as shown by Birbilis et. al., 2004, interfacial double layer parameters (R_p, C_{dl}, β) can be computed from the charging curve only without the need for any further processing of discharging curves. Thus, the analysis of the discharging section is added as an extra feature in the curve fitting program.

4.3   Results and Discussions

In this section the results from the experiments are presented and discussions on the observed results are provided.

4.3.1 Calibration and verifications

In the absence of any standards available for electrochemical measurements with soil electrolytes, the galvanostatic pulse technique and associated curve fitting routines were calibrated and verified with

known values of resistors and capacitors arranged as a simple Randle's circuit. The potential-time response curves were acquired using the Eco-chemie microAUTOLAB III after a current injection of -100 μA. The charging and discharging curves were extracted and analyzed after manual correction for the R_Ω term. Although the fitting parameters can be obtained from either the charging or discharging curve alone, both have been analyzed separately for the fitted parameters and their respective uncertainties. The uncertainties associated with each parameter are not equal in the charging and discharging sections. Thus, a weighted scheme is utilized to determine the mean values for the parameters and their uncertainties from the two curves. The results from this exercise are presented in Table 4.1 – 4.2. Note that for testing the curve fitting routines, the constraint $\beta = 1$ was applied; ideal capacitor behaviour.

Table 4.1. Comparison between the true and fitted components in the simple Randle's circuit for verification purposes. Note R_Ω is not a fitting parameter, but is calculated manually on the user interactive curve fitting program.

C#	True Values			Fitted: charging			Fitted: discharging	
	R_Ω (Ω)	R_p (Ω)	C_{dl} (mF)	R_Ω (Ω)	R_p (Ω)	C_{dl} (mF)	R_p (Ω)	C_{dl} (mF)
1	2700	680	1	2740	641 ± 2.2	1.06 ± 0.001	678 ± 0.4	0.981 ± 0.001
2	1000	680	1	1040	641 ± 1.1	1.06 ± 0.001	677 ± 0.3	0.981 ± 0.001
3	680	560	1	720	519.1 ± 0.8	1.08 ± 0.002	552 ± 0.3	0.995 ± 0.001
4	470	680	1	512	640 ± 1.1	1.06 ± 0.001	676 ± 0.6	1.01 ± 0.002
5	68	390	5.6	76	377 ± 1.9	5.90 ± 0.006	388 ± 0.9	5.68 ± 0.003
6	22	150	5.6	29	140 ± 0.3	6.04 ± 0.006	145 ± 0.7	5.90 ± 0.007

Table 4.2. Mean values of the fitting parameters after weighted computations on the charging and discharging curve results.

C#	True values		Mean values	
	R_p (Ω)	C_{dl} (mF)	R_p (Ω)	C_{dl} (mF)
1	680	1	677 ± 0.4	1.01 ± 0.0009
2	680	1	674 ± 0.3	1.01 ± 0.0008
3	560	1	547 ± 0.3	1.03 ± 0.001
4	680	1	667 ± 0.5	1.04 ± 0.001
5	390	5.6	388 ± 0.1	5.72 ± 0.003
6	150	5.6	145 ± 0.1	5.98 ± 0.005

Good agreements are observed between the true and manually determined values for R_Ω . The charging and discharging sections extracted from the complete pulses are illustrated in Fig. 4.8. Note also that the time-scale for the charging and discharging sections are referenced from their respective onset-time. Particular attention is made to the fitted parameter values from the charging and discharging sections. It is noted that the deviations between the true and fitted R_p are generally

between 3 – 7% (charging) and 0.3 – 3% (discharging), while for C_{dl} these deviations normally fall within 5.1 – 7.3% (charging) and 0.5 – 5.1% (discharging). These further indicate that the experimental and analytical methods in the present work are sound. Nevertheless, the deviations are slightly higher in the charging curve analysis. This is also reflected in the weighted uncertainties of the fitted parameters for the two sections. The weighted means and uncertainties computed and presented in Table 4.2 conform well with the true values. These weighted means have been calculated to demonstrate that although either curve can be used to estimate the interfacial parameters, the analyzed discharge curve with the least weighted error appears to be more reflective of the true values. To further demonstrate the robustness of the curve fitting routine, experimental results from one of the circuits (C# =1), was mixed with Gaussian noise and analyzed. The results for the noisy charging and discharging section are presented in Fig. 4.9.
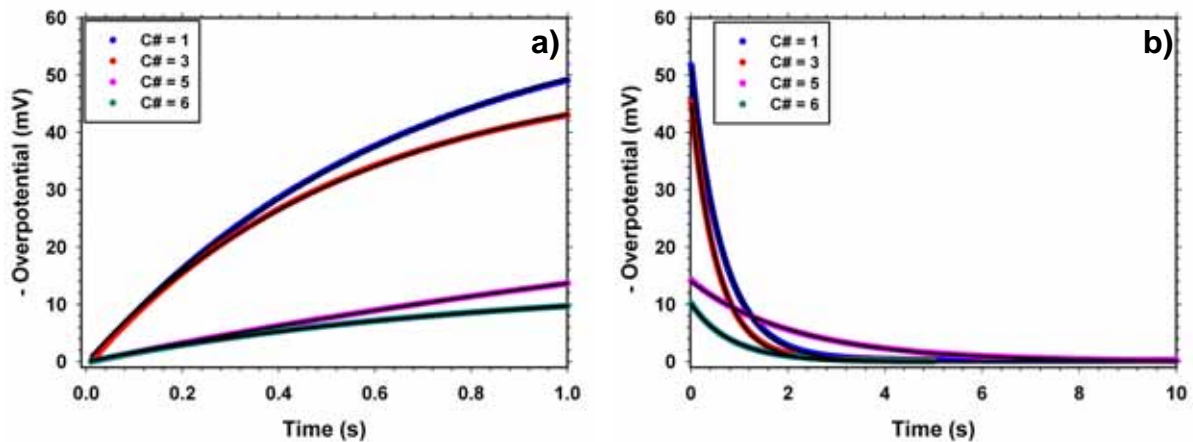
Figure 4.8. Experimental and fitted curves for the **a)** charging and **b)** discharging sections after the simulated Randle's circuit. Each curve corresponds to different circuit number (C#) and its respective model fit is illustrated by a black curve.
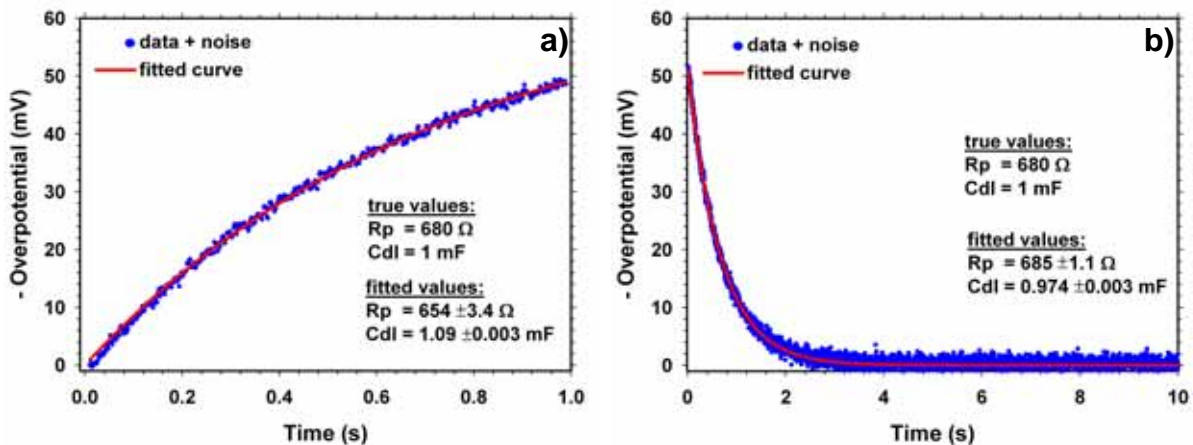
Figure 4.9. Fitting results in the presence of noise in experimental data for **a)** charging and **b)** discharging section of C# =1.

In the presence of noise, the fitting procedure adopted in this work still manages to find optimal solutions. The same can be shown for the other circuits but is not necessary here. As previously noted, it is observed here that the weighted mean of the fitted parameters for the two curves from Fig. 4.9 ($R_p = 682 \pm 1\ \Omega$, and $C_{dl} = 1.03 \pm 0.002$ mF) appears to closely resemble the true values. Overall, the curve fitting exercise demonstrated in this section reveals very good agreement between the measured and fitted data.

4.3.2 Potential-Time Responses in Soil: Simulation Remarks

Since this is believed to be the first time galvanostatic pulse techniques are being applied to derive corrosion related parameters in soils, some theoretical development and understanding is necessary. Much of the theoretical development presented in section 4.1 has been on the metal/soil structure and the basis of the short galvanostatic pulse technique. This section presents some simulation results conducted in LTspice IV electrical simulation software in order to understand the response characteristics of the equivalent electrical circuit shown in Fig. 4.2b. The implementation of this model is shown in Fig. 4.10, which in essence reflects the type of measurement carried out within the scope of this thesis concerning galvanostatic pulse methods.
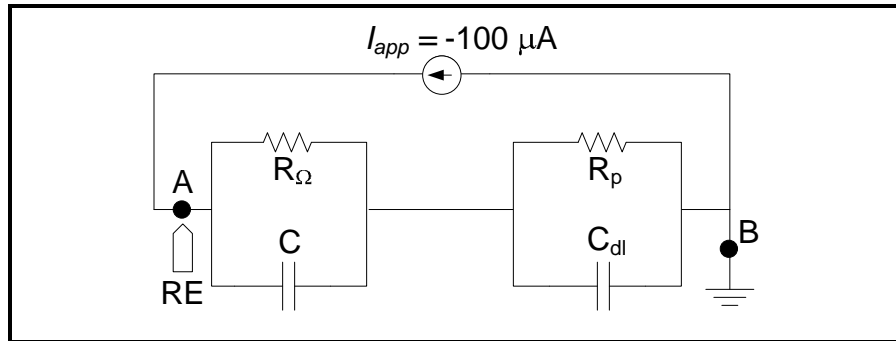
Figure 4.10. Implementation of the metal/soil bulk electrolyte equivalent circuit for simulation. The simulated current (-100 µA) perturbs the working electrode to cathodic overpotentials. Note: RE is the position of the reference electrode (probe).

The potential-time response curves for different values of soil capacitance, C, and fixed values of R_Ω (500 Ω), R_p (300 Ω), and C_{dl} (3 mF) under the application of a galvanostatic pulse is presented in Fig. 4.11. The aim here is to understand the manifestation of soil capacitance in the time constant related to the relaxation process in soil, and its overall effect on the potential-time response curve following application of a 1 s galvanostatic pulse.
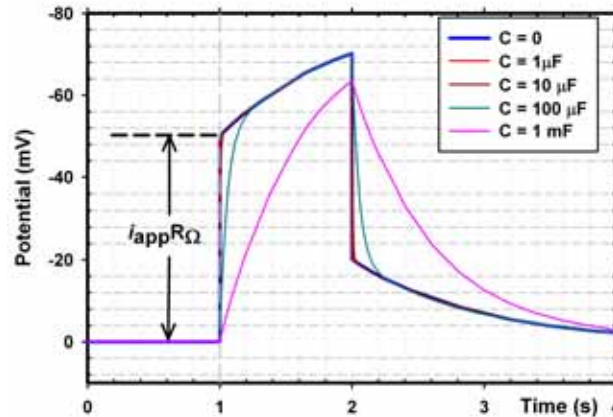
Figure 4.11. Effect of different C values according to the circuit in Fig. 4.10, on the potential-time response, measured between AB, after application of a short (1 s) galvanostatic pulse.

In principle, the double RC-network represents the response from the metal/soil and bulk electrolyte at any time. Different C values lead to different time constants associated with relaxation processes in soil electrolytes, which tend to distort the potential-time response as shown in Fig. 4.11. However, there appears to be certain conditions under which effects arising from soil capacitances can be neglected and Eqs. 4.1 – 4.4 can be applied directly for analysis. This condition is met when the product $RC << 1$ and $RC << R_pC_{dl}$, whereby the time constant of the relaxation processes in soil (RC) is negligible compared to the time constant associated with the corrosion process (R_pC_{dl}). It is observed in the simulation results that when $RC << 1$ and $RC << R_pC_{dl}$, the potential-time response exhibits non-distinguishable characteristics for the condition that $C = 0$. The quasi-instantaneous jump related to the Ohmic effect is clearly identifiable in this case. Of course, the important requirement for the presence of this feature (quasi-instantaneous jump) is that the magnitude of RC is small (~ less than a few ms). In the event that RC is in the order of a few seconds, the 1 s galvanostatic pulse technique is inappropriate and no instantaneous jumps will be observed.

Furthermore, the sharp instantaneous jump at $\Delta t = 1$ disappears when RC gets relatively comparable to R_pC_{dl} ($C = 100 \mu F$). This feature becomes most distinct when $C = 1$ mF, in which case RC and RC_{dl} are comparable in magnitude, hence yielding comparable time constants amongst soil bulk electrolyte and corrosion processes. Similar comments are applicable during the discharging process, where the increasing nature of C is clearly seen. Thus, given that the measured potential-time response exhibits sharp or quasi instantaneous jump at the time when the applied pulse is switched on, effects from soil capacitance can be assumed to be very small and can be safely ignored. Even in the presence of some intermediate C, parts of the charging/discharging sections can be removed and analysis can be carried out normally, as observed in the simulation results for $C = 100 \mu F$, where after some delay the curve

acquires non-distinguishable feature with the $C = 0$ curve. This delay corresponds to the time taken to reach steady-state conditions in soil. The technique suggested here is applicable when the time constant for the bulk electrolyte is much smaller than the time constant related to the interfacial double layer, the former having magnitudes of less than a few ms.

In the extreme case, when the two time constants are comparable in magnitude, Eqs. 4.1 – 4.4 are no longer applicable and will require modifications to account for significant relaxation processes in the bulk soil electrolyte. These modifications may lead to very highly-non linear equations, especially if the relaxation in soil is also considered to occur in some non-ideal manner. However, as has been shown elsewhere [*e.g.*, Pernice *et. al.*, 1990], the time constant related to the corrosion process is higher than that related to the bulk properties. Thus, the occurrence of the extreme case mentioned here may be very rare, unless the reference electrode is placed at some abnormal distance away from the working electrode.

The simulation exercise here provides an understanding of the cases when the soil capacitance can be safely ignored and/or its effects can be removed from the measured responses. The non-presence of a sharp or quasi instantaneous jump at the time when the pulse is switched on reflects that the potential-time response is distinctly affected by the relaxation processes in soil.

4.3.3 Galvanostatic Pulse Measurements

In this section results from the short galvanostatic pulse measurements for the different material type/synthetic soil systems will be presented. Measurements conducted 2 hours and 7 days after immersion will be referred to as Day 1 and Day 7 measurements respectively. Some important aspects of the data analysis feature in this work and will be discussed before presenting the final results.

4.3.3.1   Use of Short Galvanostatic Pulses

The simple Randle's circuit adopted for the analysis of potential-time responses requires that there is no significant resistance (R_D) due to concentration polarization. The magnitude of R_D varies as a function of the total charge, $Q = i_{app} \times t$, liberated at the electrode surface during application of the pulse. Note in essence, R_D is an artefact of the technique itself since it manifests from the applied current. However, below some specific level for Q, the manifestation of R_D is negligible and can be ignored [Birbilis *et. al.*, 2003]. Unfortunately, such limiting values of Q are unknown in soil. Since the present work is a pioneering attempt with regards to galvanostatic pulse measurements in soils,

several trials measurements were conducted in order to first understand the system. For demonstration in this section, galvanostatic measurements for 0.5 s and 1 s pulse times were conducted for the mild-steel/B15 soil sample (see Appendix A.1 for information on B15 and other soil sample designates) system under saturated conditions (Day 1). Both the charging and discharging curves from these measurements have been utilized for the estimation of the corrosion parameters (R_p, C_{dl}, β). Since the time duration for which the current is injected into the system is different, it follows that the Q will be different also. The curve fitting results for the 0.5 s pulse is shown in Fig. 4.12.
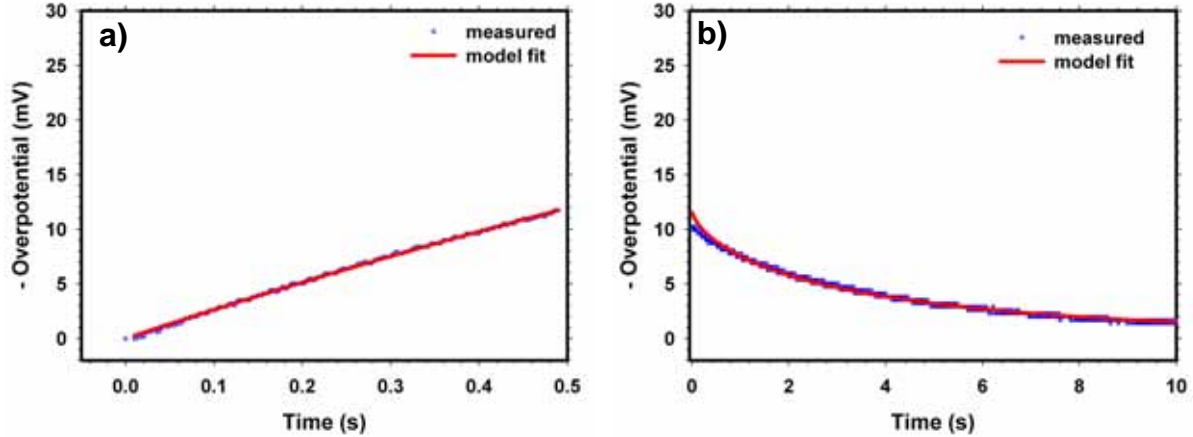
Figure 4.12. Charging and discharging curves acquired after application of **a** 0.5 s galvanostatic pulse on the mild-steel/B15 soil system.

Curve fitting results indicate good agreement between the measured and fitted values. The weighted corrosion parameters following curve fitting analysis of the single charging and discharging sections are given in Table 4.3 and compared with those obtained from weighted analysis of a repeated 1 s pulse. To avoid duplication, curve fitting results for the 1 s pulse are presented in a later section.

Table 4.3. Comparison of corrosion parameters from analysis of 0.5 s and 1 s galvanostatic pulse measurements.

Pulse width (s)	weighted mean and error		
	R_p (Ω)	C_{dl} (mF)	β
0.5	270 ± 0.6	8.9 ± 0.01	0.67 ± 0.001
1.0	286 ± 0.1	10.3 ± 0.001	0.79 ± 0.0001

The aim here is to demonstrate the close proximity of the corrosion parameters from the two different pulse-length galvanostatic pulses providing an indication that R_D can be safely ignored. For the 0.5 s and 1 s pulses, the Q liberated at the electrode surface corresponds to 7.93 μC cm^{-2} and 15.8 μC cm^{-2} respectively. It is noted here that within the scope of this thesis, similar Q (~10 – 40 μC cm^{-2}) were

71

utilized, which is much smaller than the reported values for ferrous materials in other porous electrolytes (*e.g.*, concrete, see Birbilis *et. al.*(2003)). Concerning the demonstration presented here together with the utilization of very small Q it can be safely assumed that significant resistances arising from diffusion effects can be ignored in the present work. Moreover, according to Birbilis *et. al.* (2003) the presence of significant concentration polarization effects can also be recognized from a poor agreement between the estimated parameters from the charging and discharging curves separately. In their work, however, they did not consider the errors in the associated parameter estimates.

4.3.3.2   Computation of the Corrosion Related Parameters

In this section the curve fitting analysis for the estimation of the corrosion parameters *viz.*, R_p, C_{dl}, and β are presented. A typical result within the scope of the measurements in this work is shown in Fig. 4.13. The two responses here correspond to the Day 1 measurement of the mild-steel/A20 soil and mild-steel/C20 soil systems.
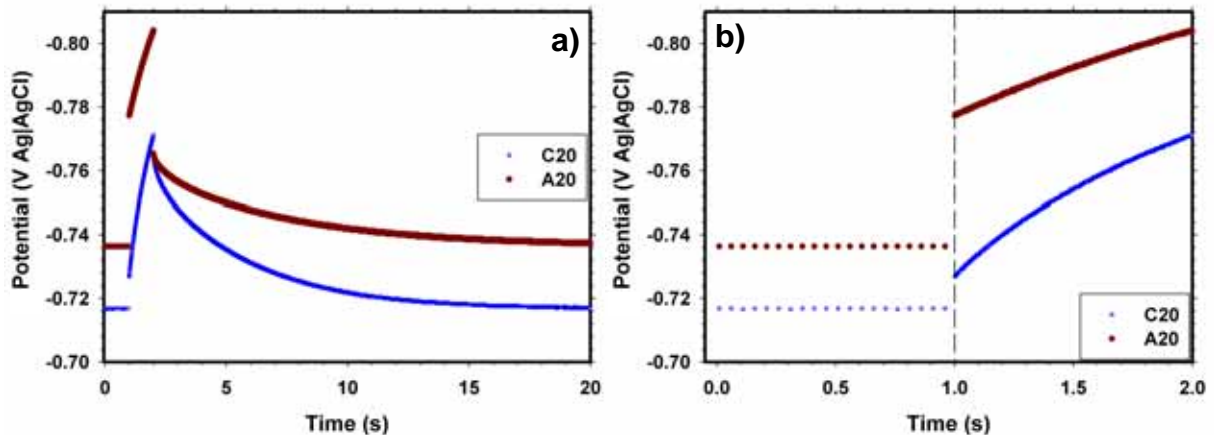
Figure 4.13. **a)** Examples of the potential-time response measured in this work, exhibiting instantaneous jump at $\Delta t = 1$ as shown in **b)**.

Although the acquired data in this work is of the form shown in Fig. 4.13, the charging and/or discharging sections have been extracted during data analysis and curve fitting. For a cohesive treatment of the results in this thesis, the following approach is taken. Results from Day 1 measurements consist of analysis of both the charging and discharging curves while for Day 7 measurements only the charging curves were acquired and analyzed (as will be discussed later). For two electrochemical systems (wrought-iron/A25, and wrought-iron/B25 systems) in Day 7 measurements, some distortions were observed in the charging section following the instantaneous jump at $\Delta t = 1$. Estimations of corrosion parameters for these systems were approximated by a reduced charging section. For this purpose, ~100 ms of the curve from $\Delta t = 1$ was subtracted from the full

charging section prior to curve fitting analysis. This effect was only observed for the two metal-soil systems with high clay content (20-25%) and initially saturated with deionized water and 0.01M NaCl. It is believed that the distortions originate from within the dryer soil, plausibly due to uneven lateral drying of the soil samples leading to layered resistivity features and complex relaxation processes in soil. It is noted here that an understanding of relaxation processes in soils due to clay and saline pore fluid is an active area of research in applied geophysics (see Chapter 5). Nevertheless, given the data is well described by the model equation, the removal of ~100 ms of the section does not affect the overall curve fitting results. Also, since this distinct observation is made only on wrought iron-soil systems, it plausibly indicates a different degree of dryness in wrought-iron/soil systems as compared to cast iron-soil and mild steel-soil systems.

The computed parameters with their uncertainties, from the curve fitting, for each measurement and its repeats were used to determine the weighted means and errors. For Day 1 measurements, the discharging curve analyses were included in the weighted mean calculations due to the high errors computed in the β parameter ($> 50\%$) from the charging section analysis. The low uncertainties for β in the discharging sections allowed reduction of errors in the overall weighted parameter computation. For Day 1 measurement analyses, a total of 265 curves were analyzed (charging, discharging and their repeats). On the contrary, for Day 7 measurements, low errors were observed for the computed parameters from analysis of the charging sections. Hence, all Day 7 analyses were conducted from the charging sections alone. For Day 7 measurements a total of 76 curves were analyzed. Thus, in the present work about 341 sets of data have been separately analyzed. A sample calculation for the analyses process described here is presented in Appendix A.4. The computed parameters for each measurement are given in Appendix A.5 and the overall weighted means and errors for each system studied in this work are given in Table 4.4. To illustrate the results from the curve fitting exercise, the following organization is adopted. Curve fitting results from the first set of measurements from Day 1 and Day 7 are shown in Fig. 4.14 – 4.22. The curve fitting analyses of the repeated measurements for Day 1 and Day 7 are given in Appendix A.6.
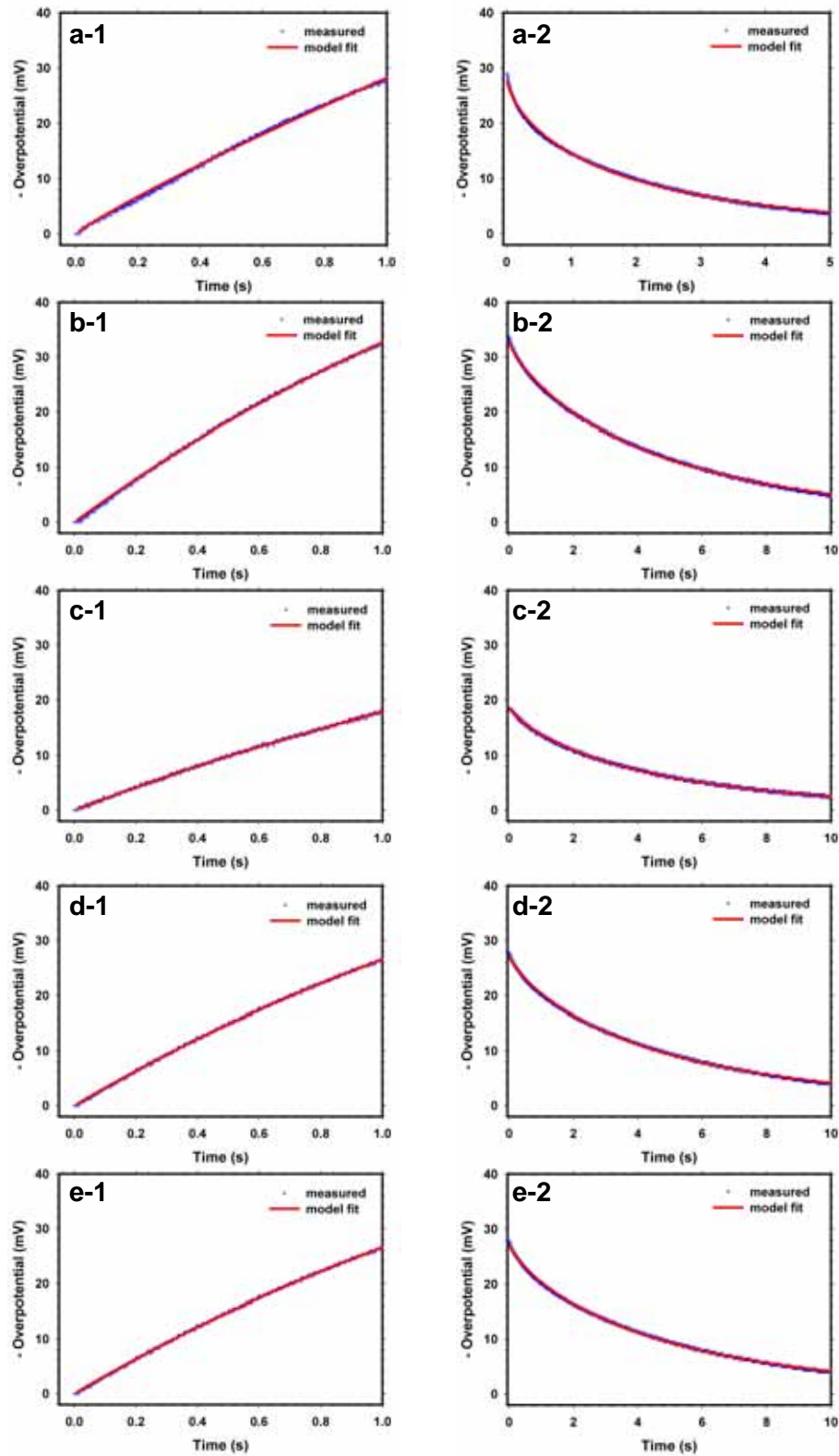
Figure 4.14. Curve fitting results for mild-steel/soil samples saturated with deionized water. The labels **a**, **b**, **c**, **d** and **e** correspond to soil electrolytes with 5%, 10%, 15%, 20%, and 25% clay respectively. The labels **1** and **2** correspond to charging and discharging sections respectively from Day 1.
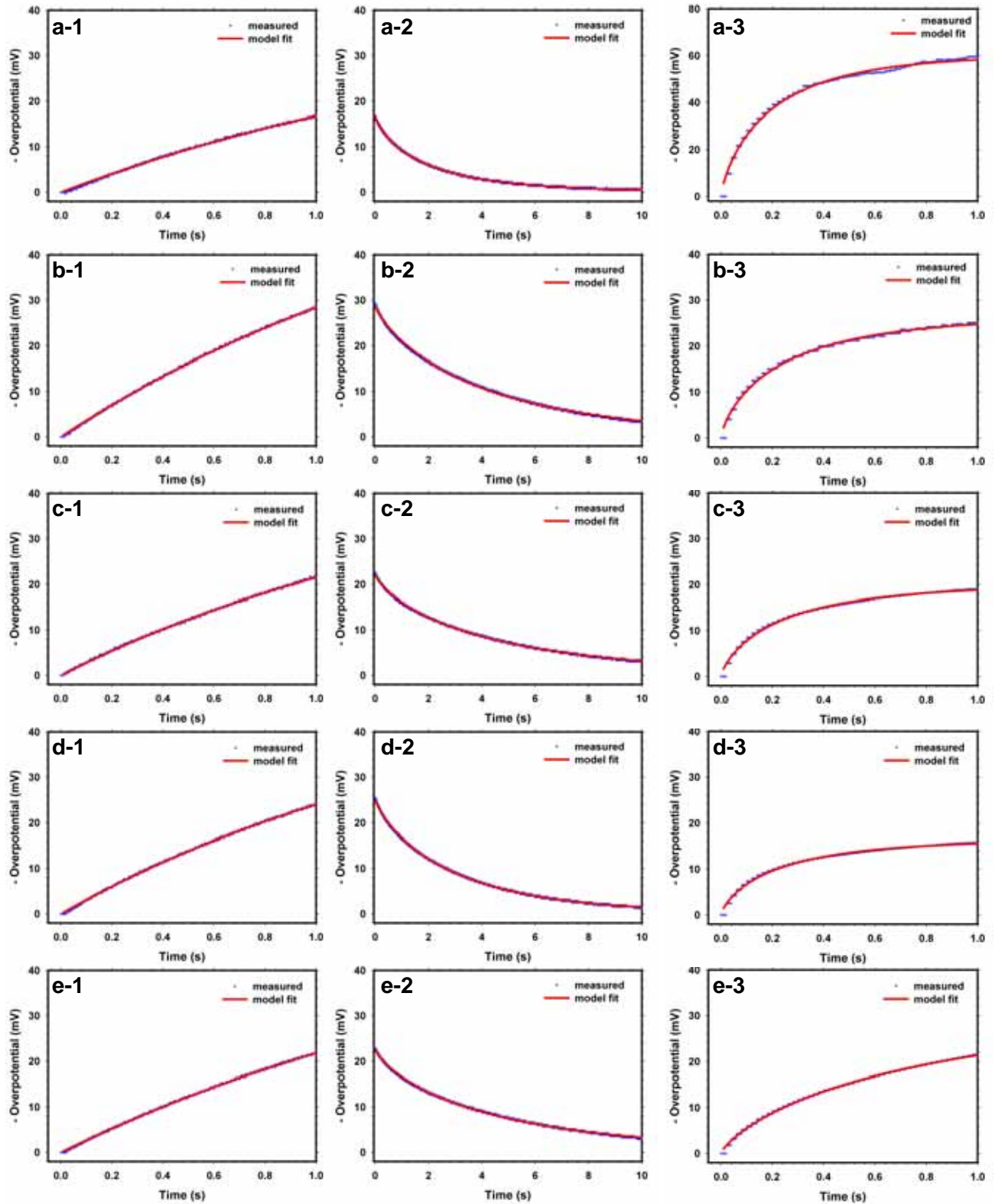
Figure 4.15. Curve fitting results for mild-steel/soil samples saturated with 0.01M NaCl. The labels **a**, **b**, **c**, **d** and **e** correspond to soil electrolytes with 5%, 10%, 15%, 20%, and 25% clay respectively. The labels **1**, **2**, and **3** correspond to charging section from Day 1, discharging section from Day 1 and charging section from Day 7 respectively.
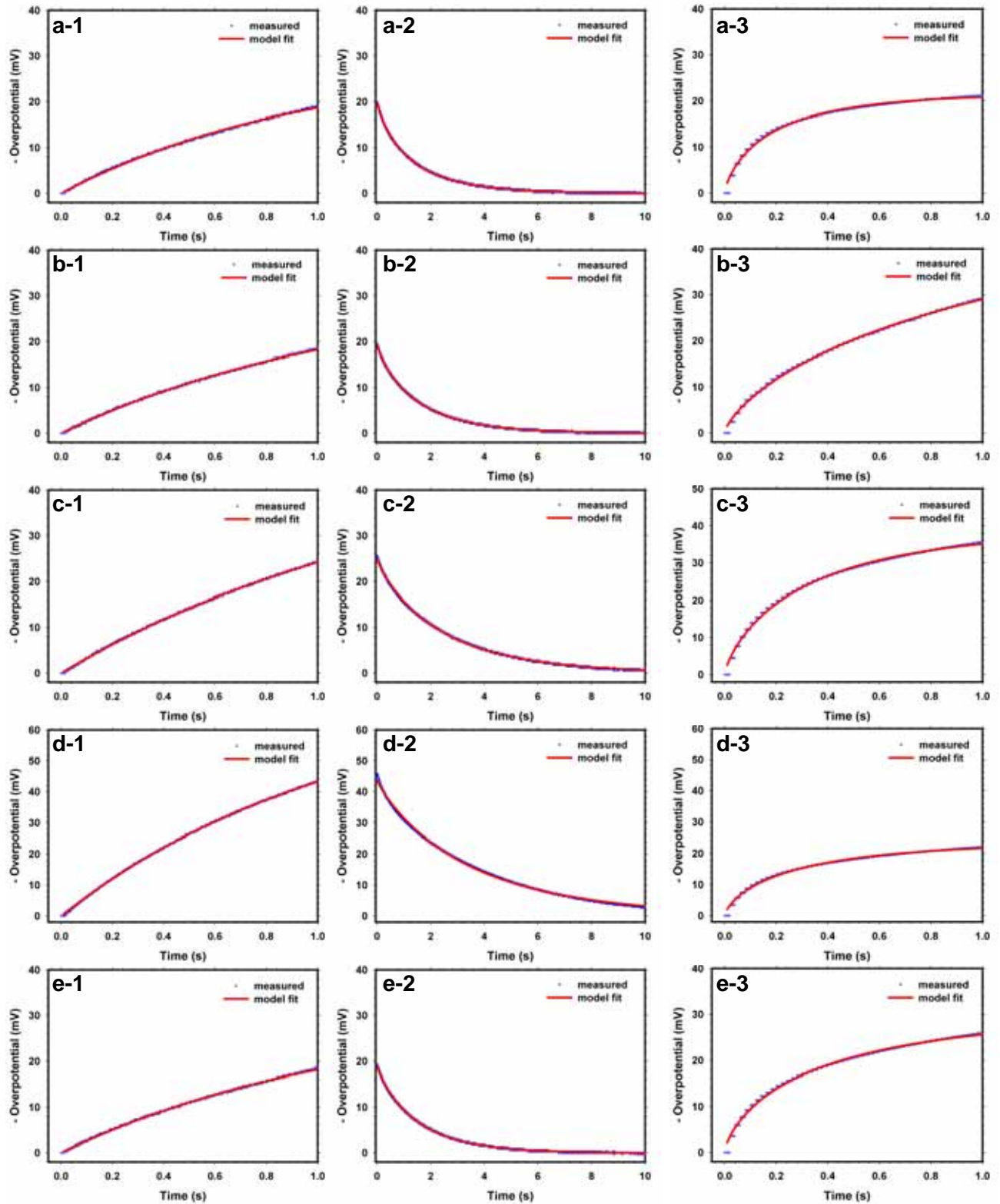
Figure 4.16. Curve fitting results for mild-steel/soil samples saturated with 0.1M NaCl. The labels **a**, **b**, **c**, **d** and **e** correspond to soil electrolytes with 5%, 10%, 15%, 20%, and 25% clay respectively. The labels **1**, **2**, and **3** correspond to charging section from Day 1, discharging section from Day 1 and charging section from Day 7 respectively.
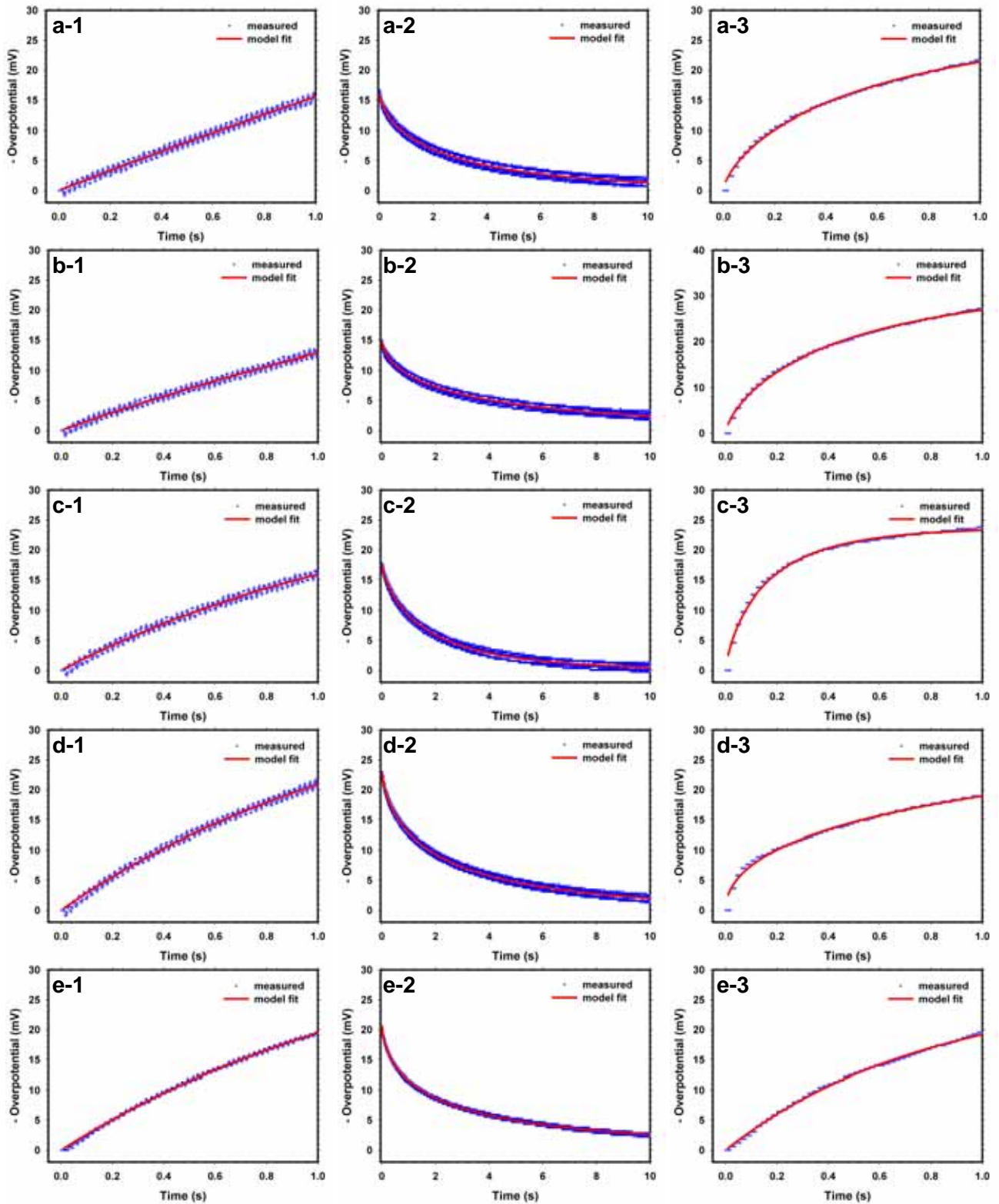
Figure 4.17. Curve fitting results for cast-iron/soil samples saturated with deionized water. The labels **a**, **b**, **c**, **d** and **e** correspond to soil electrolytes with 5%, 10%, 15%, 20%, and 25% clay respectively. The labels **1**, **2**, and **3** correspond to charging section from Day 1, discharging section from Day 1 and charging section from Day 7 respectively.
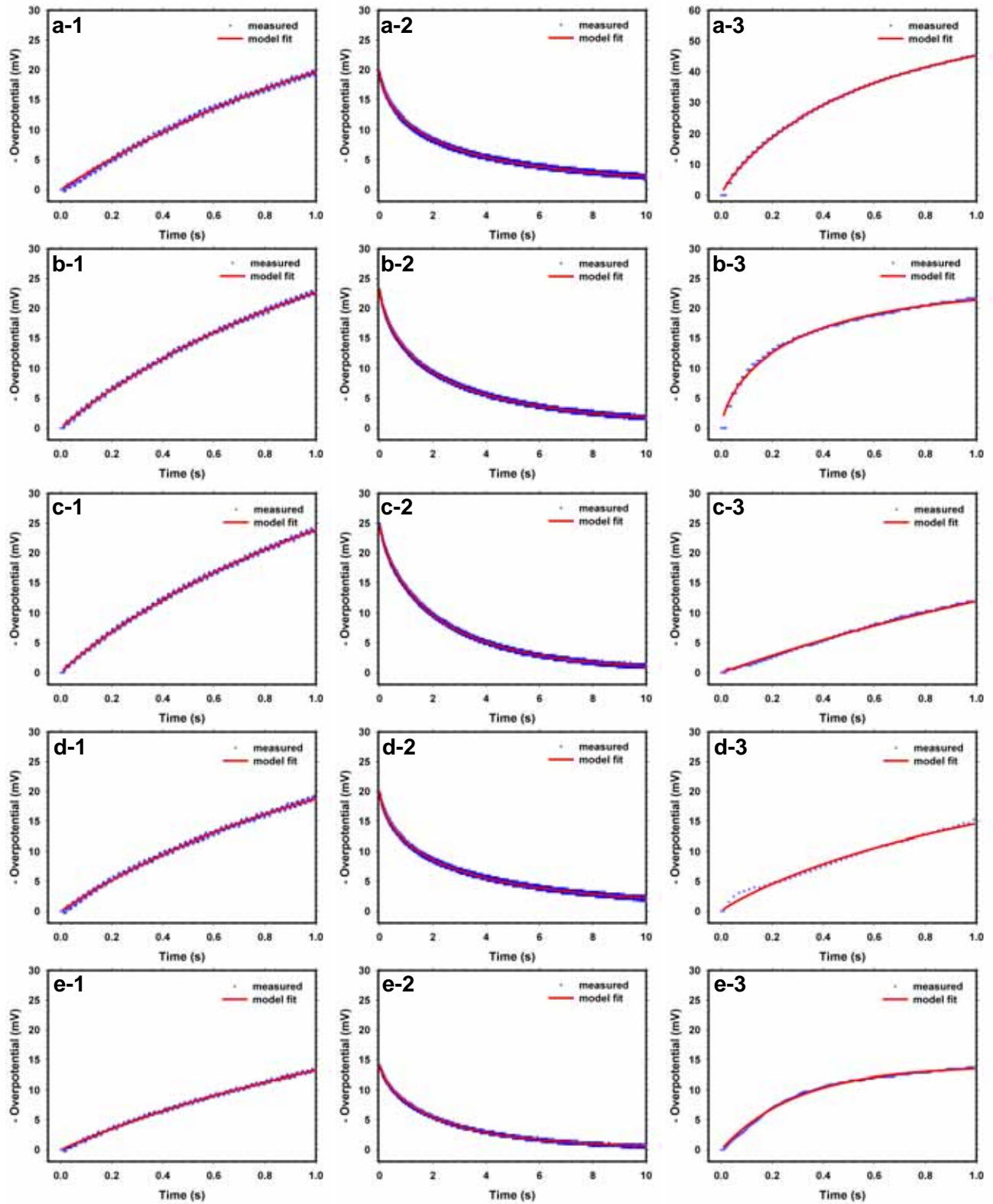
Figure 4.18. Curve fitting results for cast-iron/soil samples saturated with 0.01M NaCl. The labels **a**, **b**, **c**, **d** and **e** correspond to soil electrolytes with 5%, 10%, 15%, 20%, and 25% clay respectively. The labels **1**, **2**, and **3** correspond to charging section from Day 1, discharging section from Day 1 and charging section from Day 7 respectively.
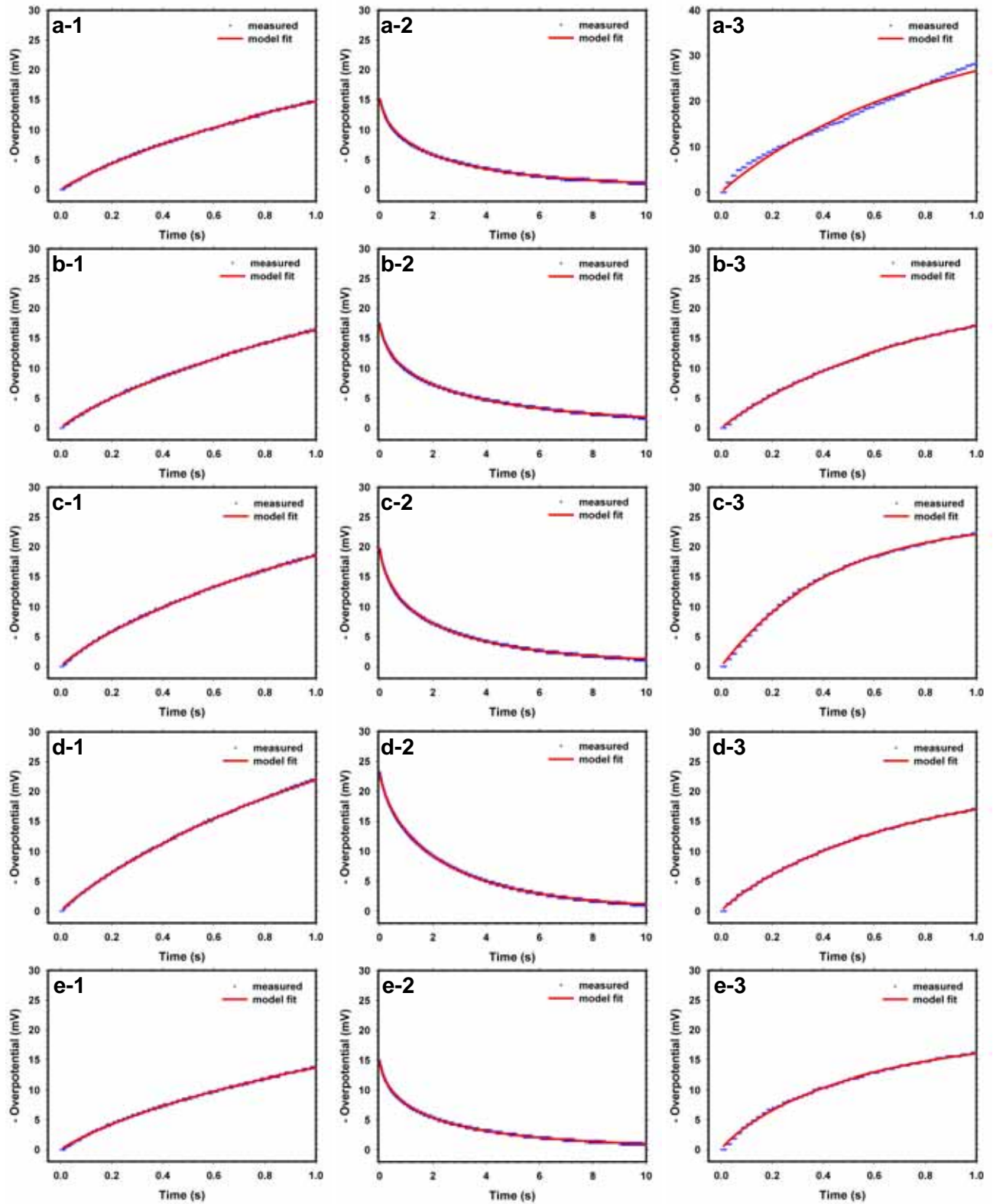
Figure 4.19. Curve fitting results for cast-iron/soil samples saturated with 0.1M NaCl. The labels **a**, **b**, **c**, **d** and **e** correspond to soil electrolytes with 5%, 10%, 15%, 20%, and 25% clay respectively. The labels **1**, **2**, and **3** correspond to charging section from Day 1, discharging section from Day 1 and charging section from Day 7 respectively.
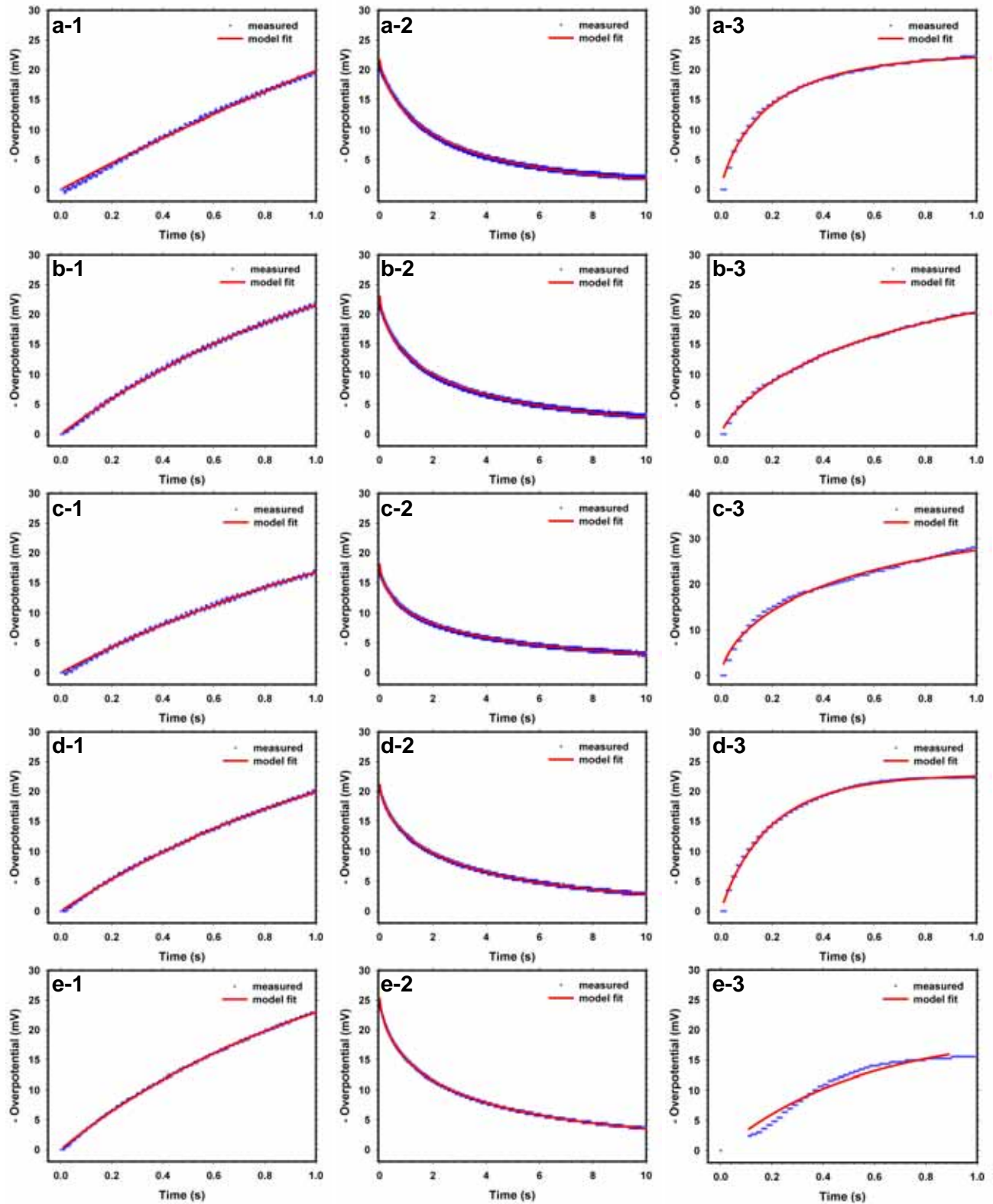
Figure 4.20. Curve fitting results for wrought-iron/soil samples saturated with deionized water. The labels **a**, **b**, **c**, **d** and **e** correspond to soil electrolytes with 5%, 10%, 15%, 20%, and 25% clay respectively. The labels **1**, **2**, and **3** correspond to charging section from Day 1, discharging section from Day 1 and charging section from Day 7 respectively.
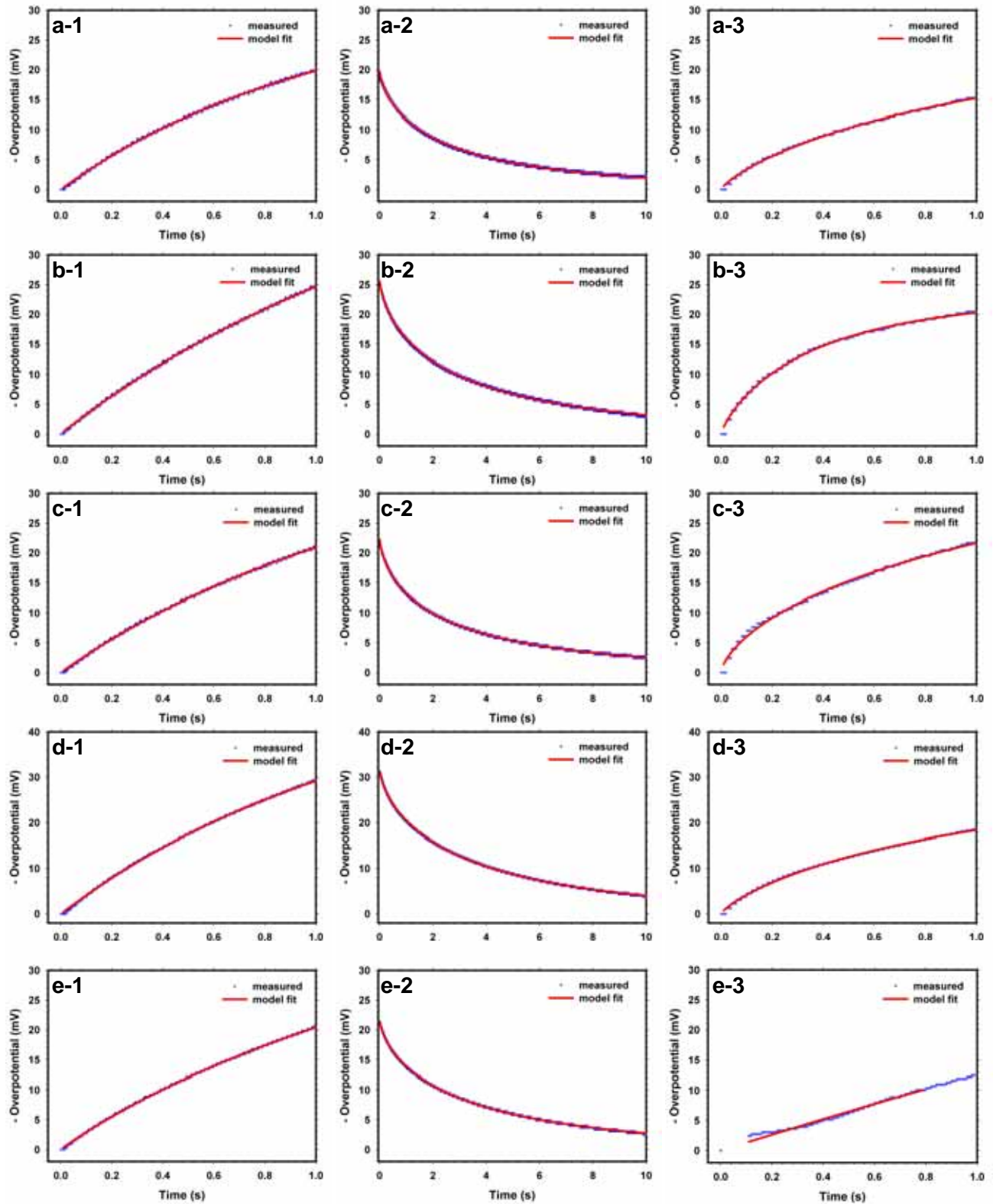
Figure 4.21. Curve fitting results for wrought-iron/soil samples saturated with 0.01M NaCl. The labels **a**, **b**, **c**, **d** and **e** correspond to soil electrolytes with 5%, 10%, 15%, 20%, and 25% clay respectively. The labels **1**, **2**, and **3** correspond to charging section from Day 1, discharging section from Day 1 and charging section from Day 7 respectively.
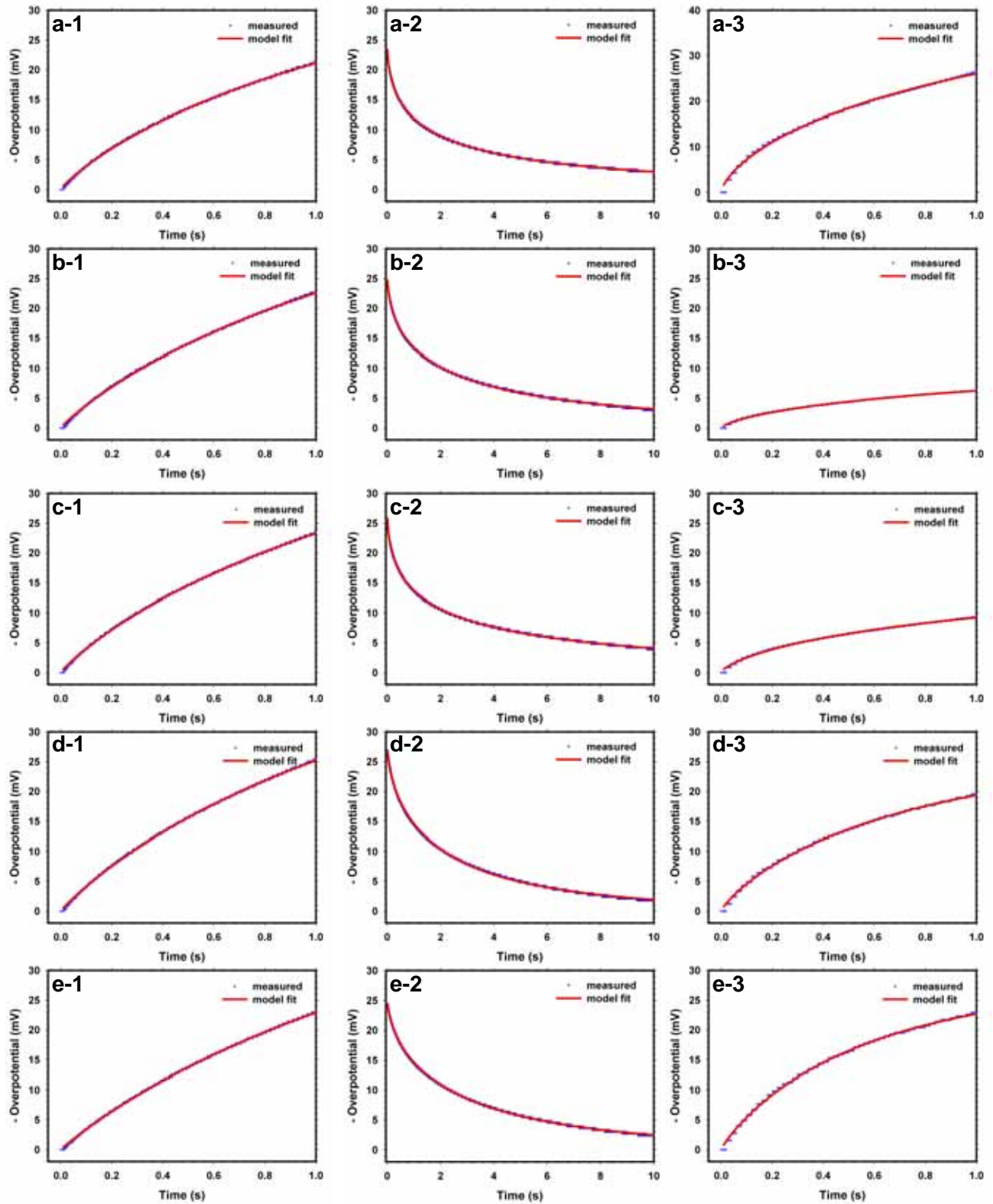
Figure 4.22. Curve fitting results for wrought-iron/soil samples saturated with 0.1M NaCl. The labels **a**, **b**, **c**, **d** and **e** correspond to soil electrolytes with 5%, 10%, 15%, 20%, and 25% clay respectively. The labels **1**, **2**, and **3** correspond to charging section from Day 1, discharging section from Day 1 and charging section from Day 7 respectively.

Table 4.4. Corrosion parameters for mild steel in different synthetic soil samples studied in this work. E_{CORR} and R_Ω are averages determined from repeated measurements and are stated to $\pm 1\sigma$. Other parameters determined from weighted methods. Note Soil compositions A5-C25 described in Appendix A.1.

Soil	DAY 1								DAY 7									
	E_{CORR} (-mV)*	R_Ω (kΩ)*	R_p (kΩ cm^2)		C_{dl} (μF cm^{-2})		β		E_{CORR} (-mV)		R_Ω (kΩ)		R_p (kΩ cm^2)		C_{dl} (μF cm^{-2})		β	
	μ	μ	μ	$\pm\sigma$	μ	$\pm\sigma$	μ	$\pm\sigma$	μ	$\pm\sigma$	μ	$\pm\sigma$	μ	$\pm\sigma$	μ	$\pm\sigma$	μ	$\pm\sigma$
A5	724	0.687	2.44	0.002	816.5	0.88	0.699	0.0006	NM	NM	NM	NM	NM	NM	NM	NM	NM	NM
A10	734	0.354	5.08	0.002	485.5	0.36	0.812	0.0005	NM	NM	NM	NM	NM	NM	NM	NM	NM	NM
A15	736	0.249	4.13	0.002	841.8	0.82	0.816	0.0006	NM	NM	NM	NM	NM	NM	NM	NM	NM	NM
A20	736	0.207	4.95	0.002	624.7	0.47	0.807	0.0005	NM	NM	NM	NM	NM	NM	NM	NM	NM	NM
A25	740	0.174	3.66	0.002	909.9	0.90	0.791	0.0006	NM	NM	NM	NM	NM	NM	NM	NM	NM	NM
B5	721	0.335	2.36	0.001	750.5	0.86	0.765	0.0006	26.3	1.2	10037	225	18198	87	0.012	0.0001	0.766	0.005
B10	731	0.218	4.41	0.002	547.8	0.40	0.828	0.0005	-47.0	0	2916	70	17005	97	0.017	0.0001	0.730	0.004
B15	736	0.178	3.60	0.002	819.6	0.91	0.790	0.0007	-23.3	0.6	1522	37	6255	39	0.040	0.0001	0.766	0.005
B20	724	0.145	3.46	0.002	672.4	0.69	0.860	0.0006	-22.3	0.6	687	11	2054	9	0.113	0.001	0.762	0.005
B25	736	0.124	3.57	0.001	760.0	0.66	0.804	0.0006	17.0	0	107.1	0.15	193.4	0.8	4.138	0.005	0.785	0.002
C5	699	0.081	2.35	0.002	546.2	0.95	0.837	0.0008	50.3	11.5	1563	51	1297	5	0.154	0.001	0.741	0.007
C10	702	0.056	2.29	0.001	647.3	0.89	0.900	0.0007	10.0	0	101.7	0.23	160.6	3.3	7.987	0.187	0.732	0.005
C15	715	0.052	3.26	0.001	623.4	0.54	0.885	0.0005	23.0	0	90.5	0.35	122.8	0.8	2.906	0.007	0.804	0.003
C20	717	0.055	4.65	0.002	698.9	0.26	0.911	0.0006	38.0	1.7	73.8	0.55	74.6	0.6	3.785	0.019	0.718	0.003
C25	705	0.041	2.44	0.002	816.5	0.88	0.699	0.0006	88.7	1.2	44.7	0.06	46.9	0.4	8.285	0.032	0.705	0.004

* - Standard deviations from repeated measurements are very small and are generally negligible.

NM - not measured.

Table 4.5. Corrosion parameters for cast iron in different synthetic soil samples studied in this work. E_{CORR} and R_Ω are averages determined from repeated measurements and are stated to $\pm 1\sigma$. Other parameters determined from weighted methods. Note Soil compositions A5-C25 described in Appendix A.1.

Soil	DAY 1										DAY 7									
	E_{CORR} (-mV)*	R_Ω (kΩ)*	R_p (kΩ cm²)		C_{dl} (μF cm⁻²)		β		E_{CORR} (-mV)		R_Ω (kΩ)		R_p (kΩ cm²)		C_{dl} (μF cm⁻²)		β	
	μ	μ	μ	±σ	μ	±σ	μ	±σ	μ	±σ	μ	±σ	μ	±σ	μ	±σ	μ	±σ
A5	643	0.455	3.07	0.012	1029.7	7.5	0.645	0.0033	-165	11	909	20.8	469.5	4.9	0.97	0.01	0.747	0.006
A10	660	0.274	1.52	0.006	1870.9	12.5	0.532	0.0030	-115	0	499	14.3	466.5	4.7	1.22	0.02	0.729	0.005
A15	654	0.223	2.16	0.005	749.9	3.6	0.732	0.0023	324	0	72.5	1	30.02	0.08	5.33	0.04	0.769	0.007
A20	654	0.171	1.37	0.003	1257.4	5.6	0.626	0.0015	136	0	65.2	0.94	16.68	0.08	21.05	0.14	0.798	0.005
A25	660	0.167	1.22	0.002	1186.6	2.4	0.522	0.0008	482	0	22.7	0.78	12.10	0.09	65.64	0.25	1.000	0.635
B5	653	0.308	1.15	0.002	1369.7	4.8	0.584	0.0012	194	0	738	0	73.2	0.8	8.44	0.11	0.836	0.007
B10	657	0.193	1.37	0.001	1493.9	4.4	0.649	0.0008	18	0	123.8	1.95	38.9	0.3	8.20	0.11	0.685	0.007
B15	650	0.152	1.46	0.001	1408.7	3.2	0.766	0.0009	425	0	7.08	0.03	5.25	0.17	393.7	2.6	1.000	0.793
B20	663	0.132	1.20	0.002	1734.0	7.2	0.604	0.0011	425	0	18.7	0.13	3.20	0.04	395.4	7.3	0.913	0.016
B25	663	0.118	1.65	0.002	1251.5	3.6	0.763	0.0011	487	0	3.04	0.13	0.46	0.00	915.61	6.50	1.000	0.672
C5	669	0.068	0.96	0.001	2062.5	4.8	0.605	0.0006	18	0	144.6	4.10	25.1	0.4	36.22	0.17	0.912	0.007
C10	671	0.054	1.19	0.001	1871.9	4.3	0.580	0.0005	392	2	4.80	0.06	3.03	0.02	269.4	0.5	0.941	0.003
C15	661	0.047	1.13	0.001	1481.8	2.8	0.614	0.0005	469	0	1.29	0.02	0.76	0.00	562.1	1.8	0.986	0.006
C20	667	0.042	1.49	0.001	1455.5	1.8	0.740	0.0005	469	2	0.79	0.01	0.75	0.01	944.2	7.6	0.928	0.005
C25	662	0.037	0.89	0.001	1998.2	5.0	0.609	0.0006	459	0	0.55	0	0.50	0.01	1104.9	12.8	0.865	0.007

* - Standard deviations from repeated measurements are very small and are generally negligible.

Table 4.6. Corrosion parameters for wrought iron in different synthetic soil samples studied in this work. E_{CORR} and R_Ω are averages determined from repeated measurements and are stated to $\pm$ 1σ. Other parameters determined from weighted methods. Note Soil compositions A5-C25 described in Appendix A.1.

Soil	DAY 1										DAY 7									
	E_{CORR} (-mV)[*]	R_Ω (kΩ)[*]	R_p (kΩ cm²)		C_{dl} (μF cm⁻²)		β				E_{CORR} (-mV)		R_Ω (kΩ)		R_p (kΩ cm²)		C_{dl} (μF cm⁻²)		β	
	μ	μ	μ	±σ	μ	±σ	μ	±σ			μ	±σ	μ	±σ	μ	±σ	μ	±σ	μ	±σ
A5	677	0.575	3.73	0.004	594.6	1.2	0.657	0.0009			-116	1	1044.1	3.2	942.1	2.6	0.211	0.001	0.791	0.006
A10	686	0.294	2.66	0.003	542.4	1.0	0.552	0.0009			-136	0	331.7	0.2	214.3	1.7	1.835	0.003	0.778	0.002
A15	696	0.219	1.94	0.003	988.7	3.5	0.479	0.0010			-136	0	196.6	0.2	156.7	2.2	3.986	0.023	0.650	0.005
A20	687	0.177	1.98	0.002	866.9	1.7	0.586	0.0006			-88	0	144.6	0.4	146.5	0.3	1.479	0.005	0.879	0.004
A25	687	0.150	2.50	0.001	1038.4	1.7	0.569	0.0004			107	4	53.56	0.15	12.8	0.1	39.5	0.3	1.000	0.000
B5	673	0.322	1.54	0.001	961.6	1.7	0.633	0.0006			-108	0	327.0	1.6	166.4	2.5	5.29	0.07	0.842	0.006
B10	695	0.200	2.74	0.001	710.4	0.9	0.625	0.0005			-106	2	204.9	1.4	159.5	0.9	4.44	0.01	0.765	0.003
B15	683	0.151	2.26	0.001	1082.6	1.7	0.614	0.0004			-31	2	130.6	0.8	108.2	0.6	15.63	0.07	0.651	0.002
B20	686	0.135	3.00	0.001	692.4	0.6	0.682	0.0004			61	0	49.31	0.04	63.6	0.3	18.08	0.06	0.798	0.002
B25	694	0.114	2.38	0.001	1341.4	1.6	0.670	0.0004			244	0	16.37	0.03	12.81	0.05	315.3	0.7	1.000	0.000
C5	675	0.064	1.40	0.001	1263.7	2.9	0.462	0.0004			-15	0	117.1	1.1	59.4	1.6	21.9	0.7	0.683	0.006
C10	682	0.048	1.33	0.001	1616.7	3.2	0.508	0.0004			37	0	45.6	0.14	34.3	0.8	35.6	1.1	0.687	0.006
C15	703	0.042	1.27	0.001	1561.01	3.8	0.434	0.0004			113	0	14.9	0.02	9.8	0.2	116.6	2.9	0.712	0.005
C20	685	0.040	1.64	0.001	1212.2	1.8	0.619	0.0004			275	0	3.17	0.00	4.27	0.03	178.4	0.4	0.841	0.003
C25	694	0.041	2.65	0.001	960.3	1.2	0.639	0.0004			357	1	1.04	0.00	1.77	0.01	332.3	0.6	0.876	0.003

[*] - Standard deviations from repeated measurements are very small and are generally negligible.

Unlike cast iron and wrought iron systems, analyses of mild steels loaded with synthetic soils initially saturated with deionized water could not be performed after 7 days. This was due to the development of high Ohmic-drops after 7 days, which overwhelmed the maximum workable voltage of the instrument (± 10 V). The high Ohmic drops in mild steel systems resulted from the high level of dryness in the soil samples which was inflicted by the 8 hrs of applied potential (1.5 V) across the working and counter electrodes. The use of small currents ($>10^{-9}$ A) also proved futile to obtain any measurable charging processes for the said systems. Not withstanding this fact, results for the other systems indicate a very good agreement between the measured and modelled data as shown in the Fig. 4.14 – 4.22.

For the corrosion parameters presented in Table 4.4 – 4.6, the R_p and C_{dl} are reported in their conventional units ($k\Omega$ cm^2 and μF cm^{-2} respectively), which is normalized to the area of the working electrode. Errors in the parameters are generally very low due to the weighted method scheme adopted in the present work. Normally within the discipline of soil corrosion, the reproducibility of results within acceptable levels of errors is of very much concern. However, in this work it is demonstrated that the use of short galvanostatic methods offers very good reproducible results in terms of characterizing the double layer parameters as shown in Appendix A.5.

4.3.3.3   Effect of Clay and Chlorides

The variation in R_p and C_{dl} as a function of clay content for the three different ferrous materials are illustrated in Fig. 4.23. These variations correspond to Day 1 measurements (measured 2 hrs after immersion). Since the pH of the soil electrolytes are generally between 4.2 – 5.0 (see Appendix A.1), the metal surfaces do not passivate instantly. For the discussions presented in this section, R_p will be used interchangeably with the corrosion current densities and hence the corrosion rates (see chapter 2), since corrosion current densities are inversely proportional to R_p. This approach is taken in order to provide a deeper evaluation of the observed results rather than just reporting the corrosion rates. The results indicate strong complexities in the double layer characteristics when considering the effect of clay and chlorides on the overall corrosion under saturated conditions. Firstly, R_p and C_{dl} appear to be similar in magnitude across the different material type, although there are some indications that R_p is slightly higher in mild steel-soil systems. This similarity is expected since the materials are mainly ferrous with a few other elements present.
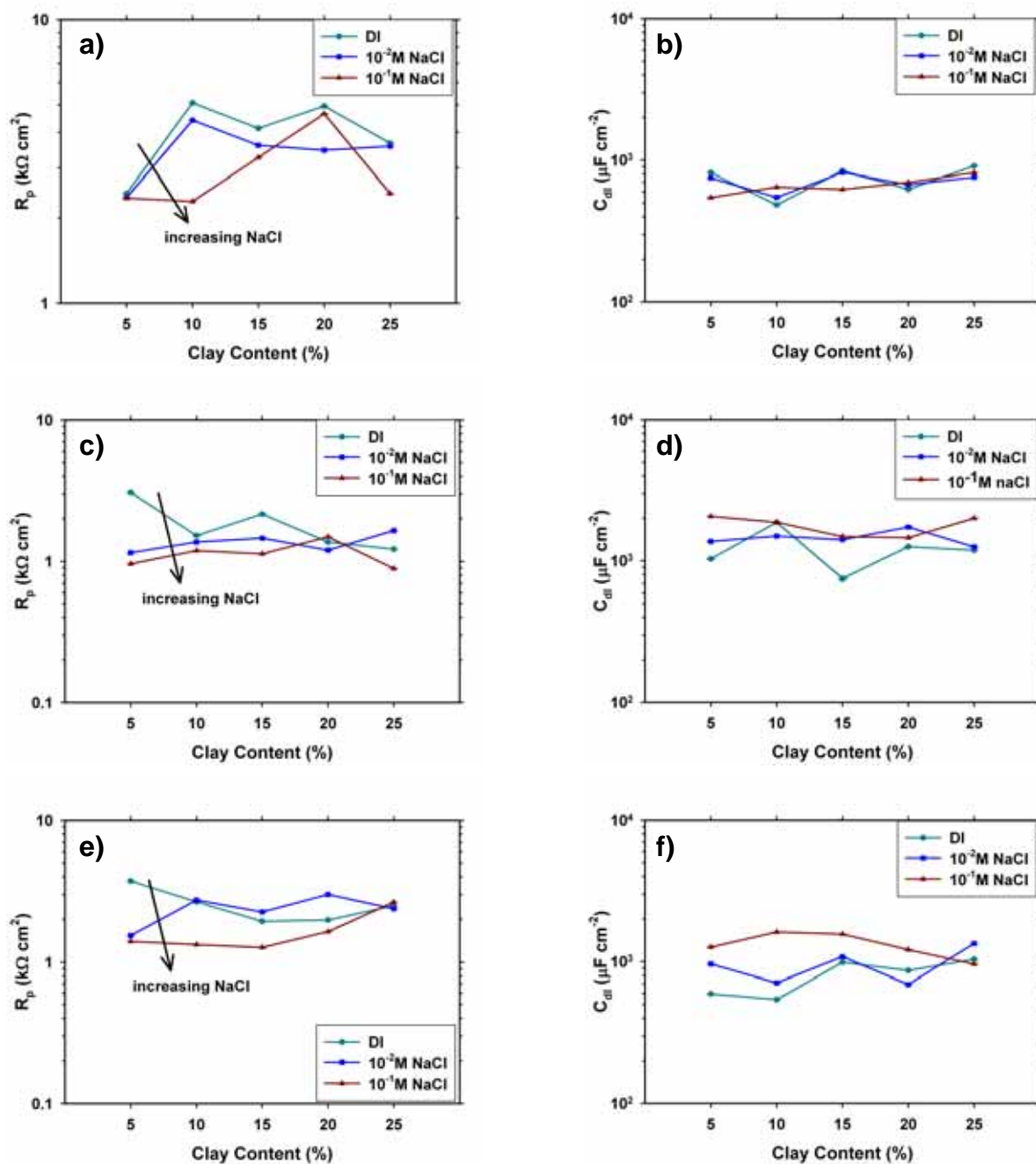
Figure 4.23. Variation of polarization resistance and double layer capacitance with clay content for **a)** – **b)** mild steel, **c)** – **d)** cast iron, and **e)** – **f)** wrought iron soil systems saturated with different pore fluids and measured on Day 1.

For completeness in the thesis, the compositions of some trace elements in the three metals were measured using inductively-coupled plasma (ICP) method and are given in Table 4.7.

Table 4.7. Some major elements present in the different ferrous materials used in this work. Mean and standard deviation stated after duplicate measurements.

Element ($\times 10^{-2}$ %)	Al	Cr	Cu	Ni	Mn	Zn
Grade 250 Mild Steel	4 ± 0.02	2 ± 0.09	1 ± 0.09	0.6 ± 0.5	23 ± 0.02	0.3 ± 0.03
Cast Iron	0.02 ± 0.02	0.5 ± 0.05	3 ± 0.4	0.09 ± 0.04	32 ± 0.06	0.2 ± 0.01
Wrought Iron	0.6 ± 0.6	0.5 ± 0.4	4 ± 0.06	3 ± 0.1	12 ± 0.08	0.6 ± 0.6

Generally, the reduction in R_p due to increase in NaCl concentration is well observed for all three metals. This is expected since corrosion proceeds relatively faster in the presence of chlorides [see Lopez *et. al.*, 2011]. The absence of any strong effect on R_p brought about by clay content at a constant pore fluid type possibly indicates that the corrosion reaction is more influenced by the pore fluid itself rather than the soil grain size distribution under saturated conditions. Most studies [*e.g.*, Liang *et. al.* (2009); Zhang *et. al.* (2009); Wu *et. al.* (2010); Benmoussat & Traisnel (2011) *etc.*,] designed to understand various aspects of pipeline corrosion have utilized simulated or natural soil solutions instead of the soil electrolyte itself. The results observed here provide justifications for the use of such solutions to simulate soil environments at least in saturated conditions. However, there is some minor indication that under saturated conditions, higher clay content leads to slight increases in R_p. This possibly indicates that the cathodic reaction is mostly oxygen reduction. In completely saturated soils the diffusion of oxygen is already very low. An increase in clay content leads to blocking of available pores and increasing tortuosity thereby suppressing the already restricted flow of oxygen to the metal surface. The anodic and cathodic reactions can thus be represented by Eqs. 4.8 and 4.9 respectively.

$$Fe \rightarrow Fe^{2+} + 2e^- \qquad (4.8)$$

$$1/2O_2 + H_2O + 2e^- \rightarrow 2OH^- \qquad (4.9)$$
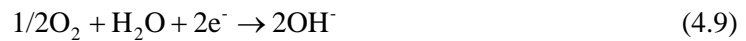
The double layer capacitance C_{dl} also displays, though very weakly, increasing values with an increase in pore fluid chloride concentration. However, no definite clayey effect on C_{dl} under saturated conditions can be identified. This suggests that the interfacial double layer capacitance is mainly influenced by the moisture content of the soil. Control of C_{dl} by the amount of clay present is either negligible or outweighed by the water content under completely saturated conditions. The present work differs from most other works related to soil corrosion in the sense that a direct evaluation of double layer capacitance is provided herein, which in most cases are rarely stated and discussed. Under completely saturated conditions, at the metal/soil interface there exists a continuous stratum of liquid, which facilitates all forms of exchanges to and from the metal surface. In principle, there exists a range of interactions amongst the different interfaces which are present, *viz*., metal/dry soil grain, metal/liquid-coated soil grain, metal/liquid, soil grain/soil grain, and soil grain/liquid.

However, the interface which determines the overall corrosion reaction is specifically that between the metal/liquid or metal/liquid coated soil grain. In completely saturated conditions both the former and latter coexist together providing the continuous strata. The EDL structure can then be somewhat approximated by the Grahame model. The evolution of R_p and C_{dl} after a period a natural desaturation of the soil electrolytes is illustrated in Fig. 4.24. The clayey effect on R_p and C_{dl}, initially absent from Day 1 measurements, manifest strongly on Day 7 measurements.
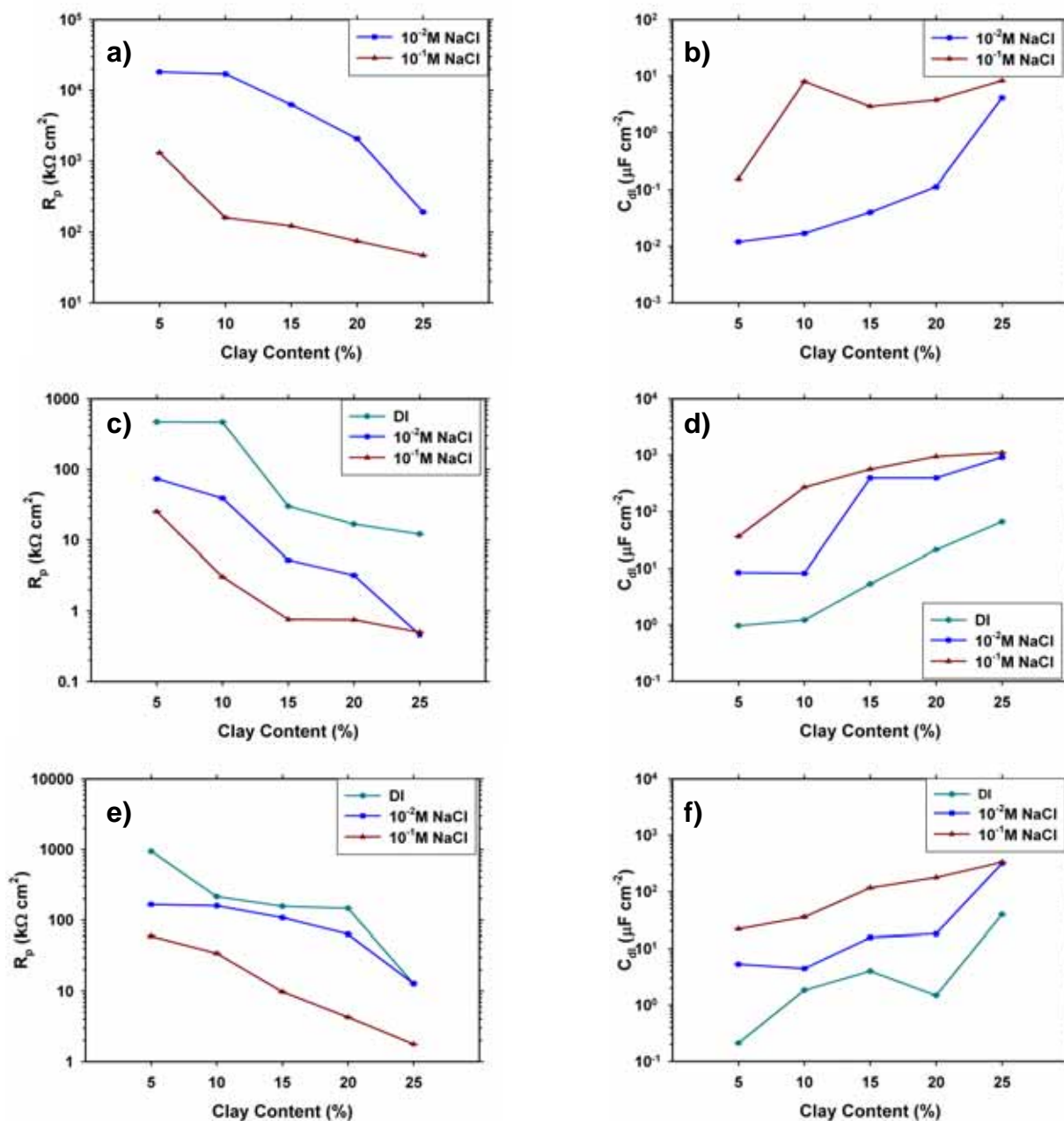
Figure 4.24. Variation of polarization resistance and double layer capacitance with clay content for **a) – b)** mild steel, **c) – d)** cast iron, and **e) – f)** wrought iron soil systems initially saturated with different pore fluids and measured after natural desaturation of the soil electrolytes on Day 7.

All three metal/soil systems exhibit similar features in terms of the variations in R_p and C_{dl} for different clay content as well as for the different pore fluid initially utilized to saturate the soil samples. The R_p is seen to decrease with increasing clay content indicating that the corrosion current density in increasing clay content soils is higher. In fact for each material type, large reductions in R_p are induced by increasing clay content. Also, the pore fluid initially used to saturate the soil electrolytes is seen to induce in some cases almost an order of magnitude reduction in R_p, corresponding to almost an order of magnitude increase in corrosion current densities, and likewise C_{dl}. Mild steel loaded systems show very high R_p values (46.9 – 18198 kΩ cm^2), reminiscent of the anodic activated corrosion these cells were subjected to. These are followed by the wrought iron-soil systems (1.77 – 942.1 kΩ cm^2) and finally the cast iron-soil systems (0.46 – 469.5 kΩ cm^2).

To explain the behaviour observed on Day 7, however, a careful consideration of the properties of the soil electrolytes is essential. During the initial saturation of the soil samples, it was observed that increasing clay content soils required larger amount of fluids in order to attain complete saturation. For the case of soils saturated with 0.01M NaCl and 0.1M NaCl, this would mean a progressive increase of chloride ions will be present in the soil matrix with increasing clay content. This feature appears to inflict minimal effects during saturated conditions on Day 1, where corrosion appears to be strongly influenced by the molar concentration of the pore fluid and hence proceeds in a manner similar to simple aqueous corrosion on a fresh metal surface. However, as the moisture evaporates during the desaturation period, the effect of higher chloride contents in soils with increasing clay content becomes stronger. Hence, the characteristic features shown in Fig. 4.24, are not solely due to moisture effects, but rather suggest a coupled moisture-chloride effect, controlled by the clay content. This is further exemplified by the fact that for soil initially saturated with deionized water, characteristic reductions are also observed with increasing clay content. However, the absence of chloride ions in these cases indicates a stronger moisture control.

Variabilities in R_p amongst different materials do not necessarily indicate the relative resistance to corrosion of the different materials across the different soil samples. It is more reflective of the different degrees of partial saturation of the soil electrolytes amongst the multi-cell panels after 7 days as reflected in the Ohmic drops presented in Tables 4.4 – 4.6. Although the multi-cell panels were kept in similar conditions during the desaturation period, the difference in drying rates could have arisen from slight differences in room conditions as each panel was measured in different weeks. Thus, a direct comparison of the corrosion parameters amongst the different material types is misleading. Instead, a comparison of the corrosion parameters within the same material exposed to

different soil electrolytes is more appropriate since the soils in each of the cells in the multi-cell panel were allowed to desaturate under same conditions. Likewise, a wide range of values for the double layer capacitance is observed between mild steel-soil systems ($0.012 - 8.29$ μF cm^{-2}), wrought iron-soil systems ($0.21 - 332.3$ μF cm^{-2}) and cast iron-soil systems ($0.97 - 1104$ μF cm^{-2}), whereby the upper limits are observed in clayey (25% content) soil initially saturated with 0.1 M NaCl. Benmoussat & Traisnel (2001) studied the corrosion properties of some gas pipelines in simulated soil solutions using EIS techniques and have reported similar high values for the double layer capacitance. However, the lower values of the double layer capacitances ($\sim 10^{-2} - 10^{-1}$ μF cm^{-2}) have not been previously reported. These low values manifest in dryer soils, which are impossible to achieve in simulated soil solutions.

Although most systems show an increase in R_p values from Day 1 to Day 7, a few systems exhibit a reduction in R_p. This trend is only observed in the following systems: cast iron-B25, cast iron-C15, cast iron-C20, cast iron-C25, and wrought iron-C25. Since the soils in these systems are either of high clay content and/or saturated with pore fluid containing different concentrations of NaCl, the high corrosive nature may be arising from the coupled effect due to clay and NaCl. It is emphasized here that the difference in the systems exhibiting these features between cast iron and wrought iron are mainly due to the different levels of drying in the two metal systems, as discussed previously. This is further supported by the fact that these observations are not made on mild steel-soil systems. However, concerning the reductions mentioned, it appears that given there is liquid immediately at the metal-soil interface, corrosion will continue regardless of the overall saturation property of the soil electrolyte. However, the strength of the corrosion process will depend on the mobilities of the chloride ions near the electrode surface and also if a larger concentration of these ions are tightly bound within the dry bulk electrolyte. It appears safe to state that gravity effects may be very important in the settling of the chloride ions within the soil matrix.

To an extent, R_p and C_{dl} variations exhibit a semi-log dependence with clay content as can be inferred from Fig. 4.24. The emergence of this behaviour can be explained by the natural desaturation rates in the different soil samples. Soil water retention is greater in clayey soils [Schaetzl & Anderson, 2005] due to the strong attraction between water and negatively charged clay particles, which can lead to either absorption or adsorption. In comparison, sandy soils have larger pores which loosely hold the water leading to rapid water losses. Hence, the partial saturation levels on Day 7 in sandy soils are lower than in clayey soils, as reflected in the E_{CORR} values. In fact E_{CORR} values in low clay content soils $>\sim 0$ mV indicating the soil electrolytes are mostly dry after Day 7. The fact that the R_p and C_{dl}

show characteristic variations with clay content during Day 7 can thus be attributed to a combined interaction of the amount of moisture and chlorides present in the soil samples as discussed previously. Indeed Murray & Moran (1989) have reported semi-log dependence of corrosion current densities (inversely proportional to R_p) with moisture contents. However, the coupled effect arising due to clay has never been addressed.

An understanding of the EDL structure during Day 7 becomes much more complicated. This occurs since the soil electrolytes are no longer completely saturated and hence the important corrosion related interfaces are now metal/liquid, metal/dry-soil grain, and metal/liquid-coated soil grain. Corrosion in this instance can be understood by making analogies to the physical model of Jiang *et. al*. (2009), whereby the dispersion of the liquid plays an important role in the corrosion current density. Nevertheless, the following argument is presented. It follows that there will be many locations on the metal surface whereby the aforementioned interfaces will develop. The metal/dry-soil grain interface will not induce any corrosion due to the absence of any ionization processes. On the contrary, the other two interfaces will involve a corrosion reaction. Each of these two (metal/liquid, and metal/liquid-coated soil grain) interfaces may exist in isolation surrounded by metal/dry-soil grain interfaces, or they may exist as an interconnected chain of individual interfaces. This will depend on the homogeneity of the water distribution induced by the natural desaturation. Thus, the EDL structure may no longer be continuous over the entire metal surface in the sense that there may be isolated cases of dry zones.

For the discussion presented so far, the double layer parameters *viz*., R_p and C_{dl} have been used to identify the effects of clay and increasing salinity (more specifically the chlorides). It is observed that in freshly exposed metal surfaces (Day 1) the corrosion reaction proceeds more strongly and especially under completely saturated conditions, corrosion in soil is analogous to aqueous corrosion. The effects of clay and chlorides becomes prominent after corrosion is allowed to proceed under conditions of natural desaturation of the soil electrolytes as reflected in the magnitudes of R_p and C_{dl} for Day 7 measurements. After the period of natural desaturation however, the initial surface conditions of the metal also change. Thus, in the strictest sense a direct comparison between R_p and C_{dl} from Day 1 and 7 measurements does not necessarily mean that the difference is due to the variations in the water and chloride contents alone. Rather differences may also arise due to the change in metal surface conditions during the natural desaturation period. The idea of conducting the measurements for saturated conditions followed by a period of natural desaturation was twofold as follows:

a) In the presence of different soil particle size distributions, several soil states are possible depending upon the amount of water present. These can become problematic especially when the metal/soil interface is first initiated. This situation can be avoided if all the soils are completely saturated in the first instance and then the interface is established. This approach also minimizes any errors arising out of state-differences and provides a treatment of the soil samples in a consistent manner.

b) Once the corrosion process has started, any further addition of water to maintain complete saturation also induces errors. It follows that a homogenous distribution of water within the soil electrolyte cannot be guaranteed if water is added periodically to maintain any specific moisture levels. Moreover, it is the presence of water at the interface which will determine the sustainability of the corrosion process. Hence, the addition of water may only lead to perturbations within the actual soil matrix giving rise to apparent behaviours with water levels. Instead the emergence of the behaviour after a period of natural desaturation allows probing the physical properties (size distribution) of soils in relation to its effect on the corrosion process.

This process to an extent simulates one end of the natural environment since the soil is continuously under some form of moisture cycling [see Hillel, 1998]. This is usually overlooked when conducting laboratory measurements of soil corrosion. Overall, it is observed here that clay has a significant impact on the corrosion process, whereby it has capabilities to allow larger amounts of salt accumulation together with longer retention times of soil moisture. Thus, it has the ability to maintain significant corrosion levels over longer periods of time compared to sandy soils. The effects of chlorides conform well to available literature in that they tend to reduce the polarization resistance thereby allowing higher levels of corrosion. Moreover, based on the analysis of R_p and C_{dl}, there is strong indication that the potential corrosivity of a given soil should be assessed in terms of:

a) its ability to retain water over long periods of time, *i.e.*, the clay or fines content, and

b) the amount of dissolved salts present, which again can be affected by clay content.

The current practice of assessing soil corrosivity based on its resistivity is correct in the sense that the aforementioned characteristics have a direct influence on soil resistivity. However, as is evident in the results presented in this section, high clay contents have the tendency to indirectly force relatively large levels of corrosion over longer periods than when lower clay contents are present. This together with the fact that in a natural environment clay soils are continuously under ion-exchange processes with groundwater makes them of particular interest in soil corrosivity assessments. For the range of synthetic soil samples prepared in this work, it is seen that their corrosivity can be regarded to

increase from sample A5 towards sample C25, *i.e.*, increasing with clay content and also with molar concentration of NaCl as indicated by Fig. 4.24.

In the discussions so far, the polarization resistance and the double layer capacitance have been treated to understand the corrosion processes in the presence of different clay contents and salinities. As noted earlier in the section, R_p values can be used to project corrosion rate estimates for each of the cells. Assuming active corrosion, a reasonable value of B = 26 mV (see Chapter 2, section 2.4.2) can then be used to transform the R_p into corrosion current densities. This is justified since the pH range of all the soils in the present work conform to slightly below neutral conditions, while some soils contain chloride additives. Following this, and on the assumption that the density of iron = 7.86 g cm^{-3}, and that the equivalent weight of the iron species mainly responsible in the corrosion process is 27.92 (Ahmad, 2006), the range of the corrosion rates corresponding to the range of R_p observed in the work fall between 0.017 – 656.5 μm yr^{-1}. Regarding these small corrosion rates, and the fact that the exposure period was only 7 days, weight loss analysis could not be performed especially owing to the physical size of the working electrodes. However, as has been shown elsewhere in a physically similar environment (steel in concrete) [*e.g.*, So & Millard, 2007], galvanostatic pulse techniques offer very good corrosion rate estimates compared to LPR methods. Another important aspect of the present work has been the use of the *β*-parameter to model the double layer capacitance when exhibiting non-ideal characteristics. A treatment of *β*-parameter within the context of the observed results is given in the next section.

4.3.3.4   The Significance of the β-Parameter

The significance of the *β*-parameter as discussed by Birbilis *et*. *al*. (2004) is very complex. They pointed out that *β* is generally associated with the intensity of corrosion and can be used to distinguish between active and passive steel corrosion in concrete. In the present work, only a small part of the entire pH spectrum has been studied. As such the discussions presented hereafter pertain to the observations within the studied pH range. The variations in *β* between Day 1 and Day 7 measurements for all the three metals are illustrated in Fig. 4.25. For simplicity, each of the synthetic soil samples from A15 – C25 have been sequentially assigned a number between 1- 15, which is used to identify a given soil electrolyte in the respective metal-soil system.

Several interesting observation are made from the variations in *β* shown in Fig. 4.25. Firstly, for both cast-iron/soil and wrought-iron/soil systems an increase in *β* is noticed from Day 1 and Day 7. However, a different picture emerges when mild-steel/soil systems are considered, whereby a

decrease in β is evident from Day 1 to Day 7. To develop an understanding of these observations, a consideration on the origin of β is required, which is explained as follows. The metal/soil interface consists of a distribution of simple capacitances, which in combination with R_p can be assumed to exhibit pure Debye relaxation characteristics. The individual capacitances within the distributions are not necessarily of equal magnitudes but can be highly variable depending upon the state of the metal surface and the interface properties. The total capacitance of the complete metal/soil interface therefore will contain a superposition of these capacitance distributions giving rise to a dispersion of capacitive features, which can be considered to be in parallel with R_p. This dispersion effect on the overall total capacitance is described by the β-parameter, which is reflective of the size distribution of the multitude of capacitances.

It has been shown elsewhere [Birbilis *et. al.*, 2003; Birbilis *et. al.*, 2004] that the β-parameter may be an index to the distribution of active and passive sites upon corroding steel in a concrete environment under conditions of lower and higher pH respectively. However, as mentioned earlier, in the present work only a narrow pH window was studied; hence, the fact that β increases for cast-iron/soil and wrought-iron/soil systems from Day 1 to Day 7 is perhaps indicative of the reduced saturation levels. It follows that in the presence of water coated soil particles there will be a range of interfaces with an associated range of capacitances.
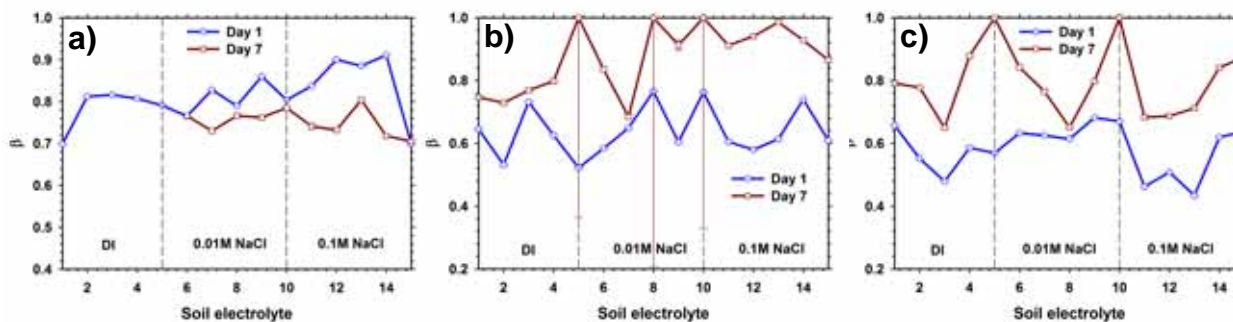
Figure 4.25. Variations in β between Day 1 and Day 7 for **a)** mild-steel/soil, **b)** cast-iron/soil, and **c)** wrought-iron/soil systems. Each of the soil electrolytes from A5 – C25 are represented by the soil electrolyte number between 1 – 15. Note the large error bars in cast-iron/soil system for 3 β values.

This size distribution of capacitances may correspond to areas on the metal surfaces which are corroding relatively faster than some other locations. Since the β values are lower during Day 1, it suggests the presence of large dispersions associated with a large size distribution of capacitances and hence the observed lower β values. During Day 7, most of the water evaporates under natural conditions and hence the corrosion levels are lower. This is associated with much smaller capacitances and hence the size distribution of these capacitances appears to be narrower leading to

higher β values. Indeed, if β is only associated with corrosion intensity as suggested by Birbilis *et. al.*, 2004 then these should be reflected in some of the cast-iron/soil systems (discussed in previous section) which tend to acquire lower R_p values on Day 7. However, the β values for these systems are still higher on Day 7 in accordance with reduced C_{dl} values from Day 1 to Day 7 further confirming that β is associated with size distribution of the capacitances. It also appears safe here to suggest that the soil characteristics has some influences on β.

To account for the opposite observations made in mild-steel/soil systems, it is first emphasized here that the mild-steel samples were subjected to an anodic activated corrosion initially. Thus, the surface properties of the mild-steel are mainly influenced by all the corrosion reactions which would have occurred during that process. As such, the degree of corrosion in mild-steel/soil systems will be higher and there will be a large distribution of surface properties consisting of either bare metal or oxide scales of variable thickness. This in turn will also give rise to a large size distribution of capacitances on the metal surface, thus increasing the dispersion in the overall total capacitance, *i.e.*, a decrease in β. The argument presented here has some very important ramifications. Similar to many other rapid techniques for corrosion measurement, the galvanostatic method in this work allows the determination of instantaneous corrosion rates via estimation of the polarization resistance. Although very useful, these techniques cannot provide any information on the state of the underlying metal, *i.e.*, if it has undergone severe corrosion. However, as discussed here it appears that the β-parameter provides some indications on the possible state of the metal surface. The fact that the β values are reduced on mild-steel/soil systems after the anodic activated corrosion indicates that it has the potential to be utilized as a possible indicator of actual pipeline surface condition in field surveys. However, following observations from cast-iron/soil and wrought-iron/soil systems, there appears to be a range of interactions which can increase or decrease the β values. Thus, the usage of β as an indicator for the metal surface condition needs to be investigated further.

4.3.3.5   On the Importance of Some Inter-Relationships

The wide range of systems studied in the present work offers a good opportunity to identify some important inter-relationships between corrosion parameters. Since the materials that have been utilized in the work are ferrous, it is believed that any such inter-relationships will be similar for each metal type. The relationships between R_p and C_{dl}, and between R_p and E_{CORR} are illustrated in Fig. 4.26. It is observed that there is a strong inverse relationship between R_p and C_{dl}, in log-log space (r^2 = 0.959) following all the three metal/soil systems as mentioned before. It follows that the total

double layer capacitance that develops at the metal/soil interface greatly influences the corrosion rate. Low C_{dl} generally indicates the absence of sufficient moisture in the soil to initiate any significant corrosion rates and hence involves large R_p values.

An important aspect of the present work is the range of R_p and C_{dl} values which are reported here for the first time in a soil environment. Usually, these values are reported for corrosion of ferrous metals in simulated soil solutions [*e.g.*, Zhang *et. al.*, 2009, and Liang *et. al.*, 2009], and hence the 'soil-factor' in terms of the grain effects are absent. Concerning the values obtained here, large variations are observed across the entire range of studied soils as well as across the different metal types; (0.46 – 18198) kΩ cm^2 for R_p and (0.012 – 2062.5) µF cm^{-2} for C_{dl}. This in essence indicates the variabilities in R_p and C_{dl}, which can be expected in metal-soil systems.
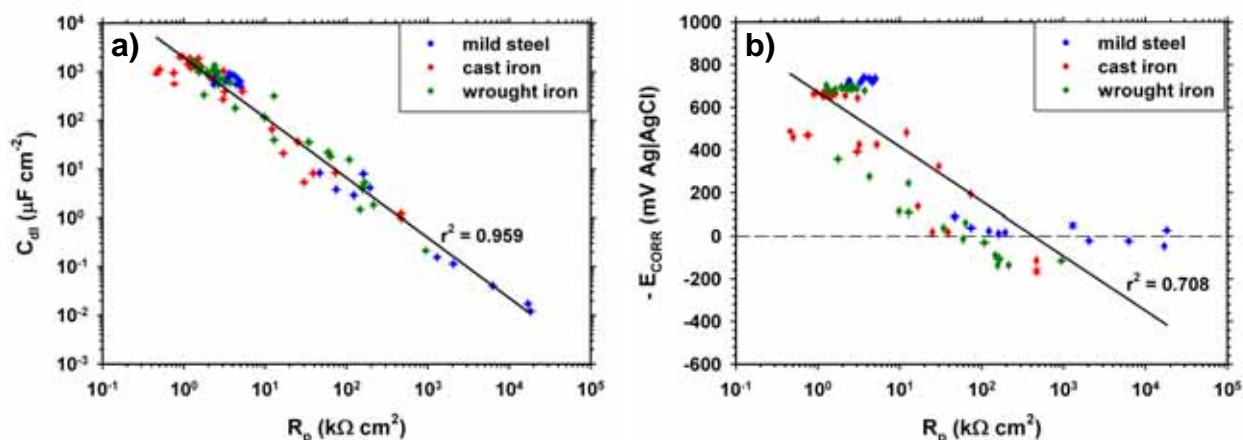
Figure 4.26. Variations between polarization resistance and **a)** double layer capacitance, and **b)** corrosion potential for the different systems from Day 1 and Day 7 analysis.

Of course, the range reported here corresponds to only a narrow window of the entire pH spectrum in soils. Furthermore, the E_{CORR} exhibits a linear regression ($r^2 = 0.708$) with R_p in the semi-log plane, which is an important aspect of the overall measurements. It follows that as the E_{CORR} becomes more negative, the corrosion current increases [Birbilis & Cherry, 2005]. The increase in corrosion current should lead to reduced R_p values since both are inversely proportional to each other by the Tafel constant. The absence of this behaviour in R_p would indicate that the corrosion system is largely affected by diffusion. Figure 4.26b shows that E_{CORR} and R_p are inversely related to each other thereby indicating that the effects of R_D can be largely ignored. This further validates the notion in the present work that significant resistances arising due to diffusion can be ignored.

Another important measurement in the present work has been the Ohmic resistances, which contains information on the soil resistivities. The experimental set-up itself had been designed such that this information can be easily extracted. For discussions which follow, the Ohmic resistances are presented and discussed. Although these can be easily transferred into the more intrinsic resistivity values, this is avoided here. A discussion of such electrical properties is reserved for the next chapter. Also, the depth of protrusion by the reference electrode was not strictly controlled but managed within 10 mm in saturated soil electrolytes (Day 1). Consequently, a correction is needed to extend the measured Ohmic resistances in order to correctly compare the Ohmic resistances measured during Day 7. Following these corrections, the relationships between the soil resistances across all the metal systems and R_p, and C_{dl} is presented in Fig. 4.27.
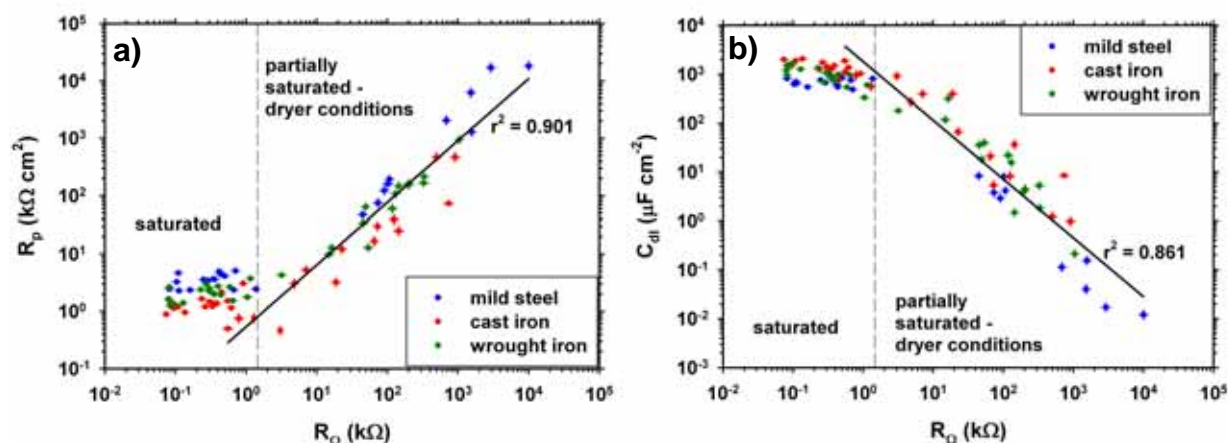
Figure 4.27. Variations of the soil resistance with **a**) the polarization resistance, and **b**) the double layer capacitance. In both cases, regression line shown corresponds to results from partially saturated-dryer conditions.

Two conclusions can instantly be drawn from the variations shown above. Firstly, both R_p and C_{dl} display relatively nominal variations when R_Ω is low, *i.e.*, < ~1.5 kΩ, contrary to when they are higher. These resistances correspond to completely saturated conditions, indicating that corrosion under these conditions is mostly driven by pore fluid. This has already been discussed for Day 1 measurements. Secondly, in dryer conditions both R_p and C_{dl} appear to display strong log-log dependence (r^2 = 0.901 and 0.861 respectively) with R_Ω, indicating the coupled effect of moisture-chloride due to clay. These effects are also somewhat reflected in the variation of E_{CORR} with R_Ω as shown in Fig. 4.28.

The fact that there are many inter-relationships between the corrosion parameters offers the possibility of identifying a corrosive soil environment through a range of investigations. The use of soil resistivity and pipe-to-soil potentials are already used as field techniques for the evaluation of

ground conditions where pipelines are embedded [Baboian, 2005; Ahmad, 2006]. The results presented herein confirm that these techniques are suitable. However, in a dynamic natural environment the use of these techniques may only be indicative of the present conditions at the time of measurement. So the natural question arises as to how to project the potential corrosivity over longer times? Results from the present work do provide an answer to this question in the sense that it is observed that the effects of clay and chlorides on the overall corrosion mechanism can be sustained over longer periods of time. In regards to clay, it has been shown that it can retain moisture as well as higher accumulation of chlorides over longer periods which can contribute towards nominal corrosion over longer times. It is also emphasized that in the natural environment clay media has the ability to undergo an ion-exchange process with groundwater [Ingebritsen *et. al.*, 2006]. These can contribute towards variable surface conditions near buried pipelines leading to more localized corrosion attacks.
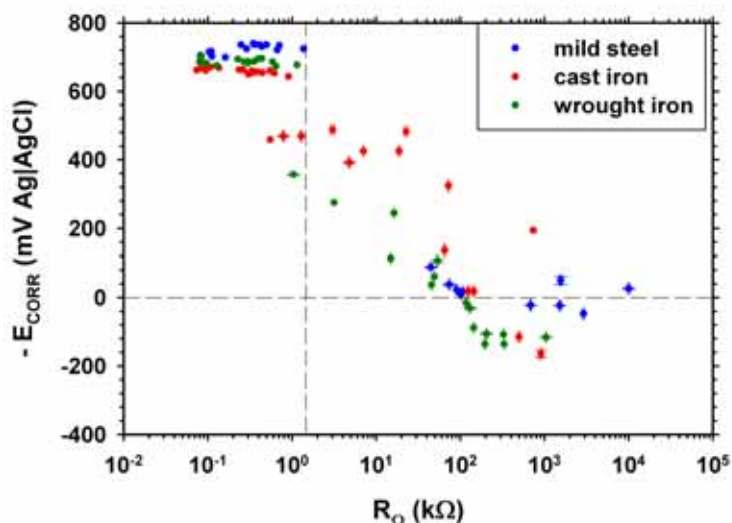
Figure 4.28. Variation of E_{CORR} with the soil resistances.

The use of the relatively new short galvanostatic pulse technique in this work demonstrates its usefulness in terms of being able to provide a deeper evaluation of the double layer structure which forms at the metal/soil interface. The successful application of this technique at small-scale laboratory levels reported in this work breaks ground in the sense that the non-destructive nature of the technique is directly applicable to field conditions. It is envisaged that the methodology and results presented in this work will form a baseline for any future investigations involving short galvanostatic pulse methods in a soil environment.

Also, the focus in the present work has been an evaluation of the transformations in the double layer characteristics brought about by varying clay content and chloride levels under conditions of saturated and desaturated soil electrolytes. Such a work in a soil environment has never been attempted before.

Thus, the present work contributes to the on-going attempt to develop a complete soil corrosivity model [Cole & Marney, 2012], which is able to explain the micro as well as macro effects. The intent in this section has been to present a physical assessment of the double layer which forms at the metal-soil interface. These physical assessments comprise of the characteristic variations in R_p, C_{dl}, and β due to the presence of clay and chlorides under saturated and desaturated conditions. Since studies in this regard are absent in the literature, a stronger focus is made in understanding the physical features of the interface in the presence of conflicting variables. However, to provide completeness to the work reported in this section, observations from visual inspections on the exposed metal samples are presented in the next sub-section.

4.3.3.6   Observations from Visual Inspection

The intent of this section is to provide an illustration of the extent to which corrosion effects were observed (visually) in the 45 metal/soil systems studied in this work. Detailed chemical treatments and phase compositions of the corrosion products for iron dissolution in clay media forms a study on its own and can be found elsewhere [*e.g.* Jeannin et. al., 2010; Schlegel *et*. *al*., 2010]. Instead a more qualitative approach is taken here to report the observations made on the exposed metal specimens. Each of the metal specimens was removed after 10 days and the corrosion products at the surfaces were dry pickled with a hard bristle brush. For some specimens, the clay particles adhered to the surface were difficult to remove. This was mostly observed for soils saturated with deionized water and in some cases 0.01 M NaCl. Owing to the size of these specimens, only photographs were taken and these are presented in Plates 4.3 – 4.5.

Generally, there are visible effects for variable clay content at fixed pore fluid salinity/chloride, as well as for fixed clay content at different pore fluid/salinities. For specimens exposed to soils with lower clay content (usually < 15%) and saturated with deionized water and 0.01 M NaCl, a quasi-uniform layer of dry soil deposit was seen on the surfaces. In some cases these deposits adhered strongly to the metal surface. However, there was a clear indication of red/brown oxides distributed in the deposit matrix, as well as in the region between the deposit and the metal surface. This is consistent with the formation of crystallized hematite (Fe_2O_3).
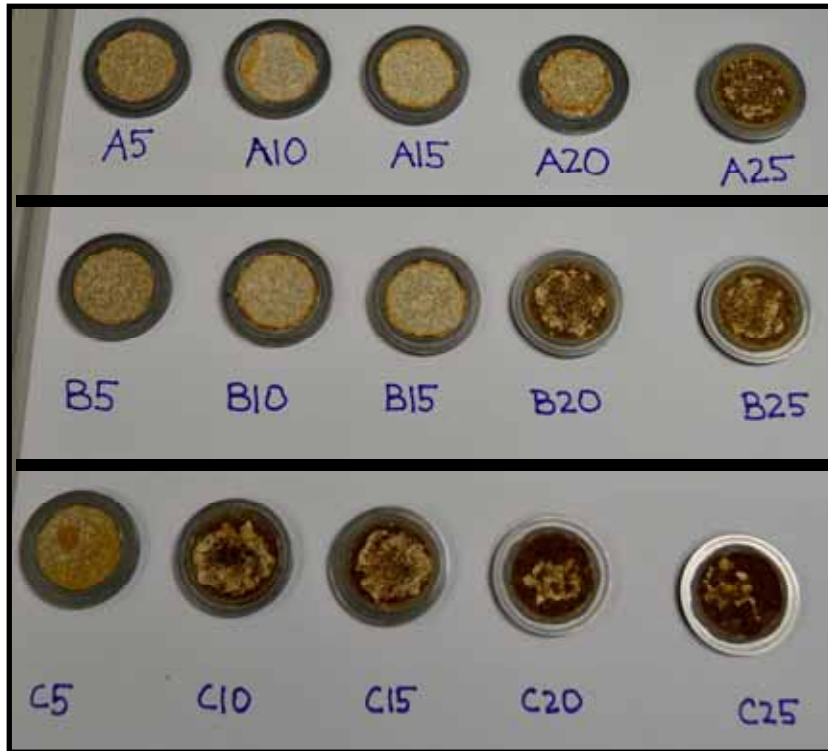
Plate 4.3. Exposed mild-steel specimens after 10 days identified by the soil electrolytes they were exposed in.
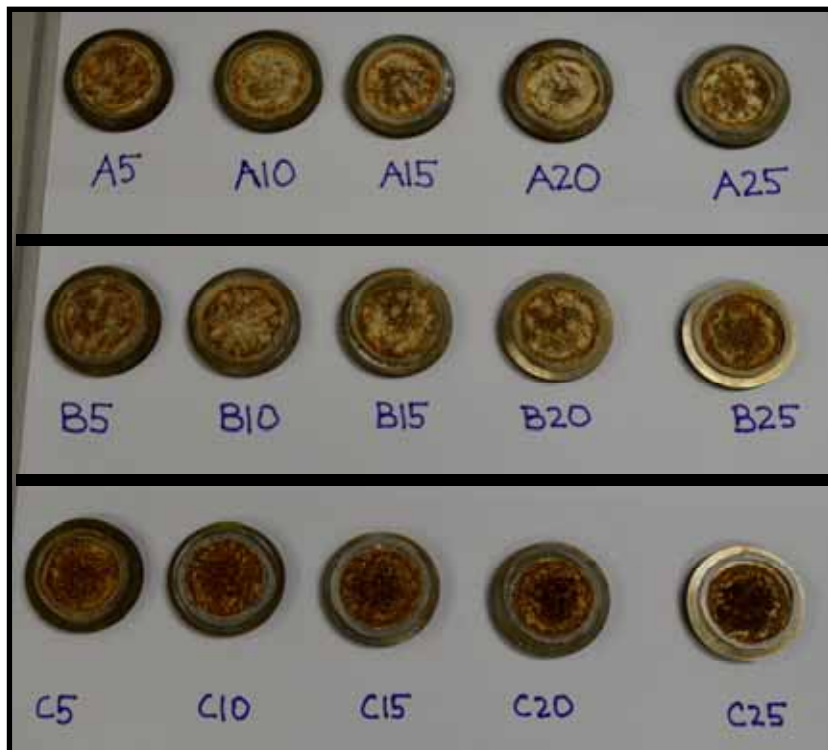
Plate 4.4. Exposed cast-iron specimens after 10 days identified by the soil electrolytes they were exposed in.
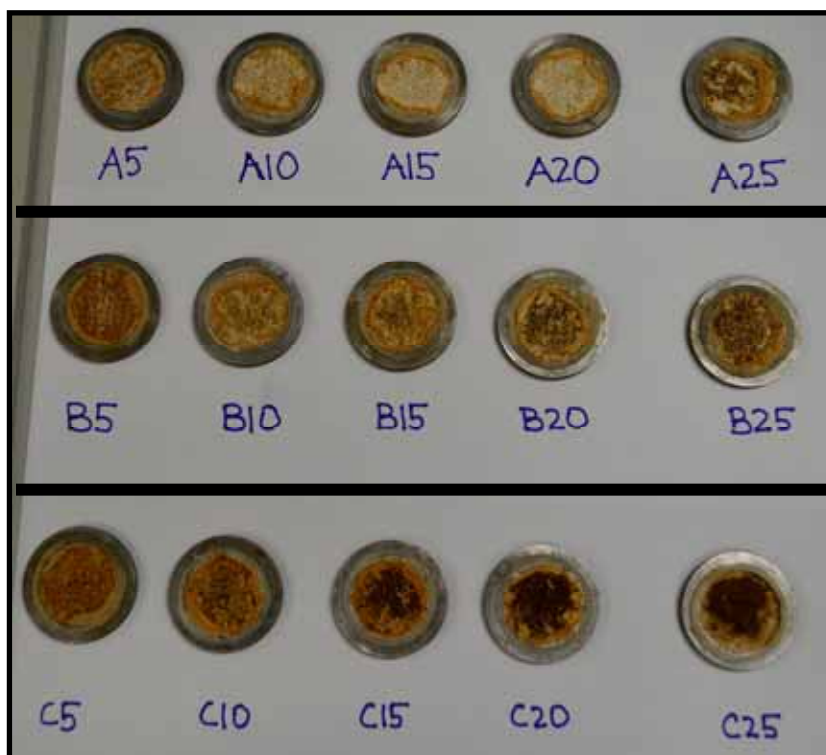
Plate 4.5. Exposed wrought-iron specimens after 10 days identified by the soil electrolytes they were exposed in.

All three metals exposed to soils saturated with 0.1 M NaCl revealed a greater depth of oxide layer on the surface. Especially for soils with clay content > 10%, a combination of red/brown and black oxides were observed. The black oxides possibly correspond to the formation of magnetite (Fe_3O_4), which develops when corrosion occurs under restricted oxygen conditions [Balasubramaniam & Kumar, 2000]. The thickness of the oxide layer in these specimens was also relatively higher than in others. However, the occurrence of magnetite did not appear to be uniform as there were isolated zones on the metal surface where areas of magnetite deposits were observed. Since magnetite has the ability to reduce oxygen to a greater extent than the underlying metal itself [Cornell & Schwertmann, 2003], it probably suggests that pitting corrosion is most probable in these conditions (clayey and high chloride contents). The presence of relatively larger degrees of corrosion inferred from the presence of higher oxides on metal surfaces immersed in soils containing > 15% clay content and initially saturated with 0.1M NaCl also indicates the cyclic effect of chloride ions in the deterioration of iron as expressed by Eqs. 4.10 and 4.11 [Lopez *et. al*., 2011]. It follows that the formation of $FeCl_2$ is unstable, which readily gets oxidized to FeOOH and in the process releases the chloride ion to restart another reaction expressed by Eq. 4.10.

$$Fe + 2Cl^- \rightarrow FeCl_2 + 2e^- \tag{4.10}$$

$$4FeCl_2 + 8OH^- + O_2 \rightarrow 4FeOOH + 2Cl^- + 2H_2O \tag{4.11}$$
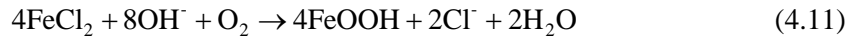
Concerning the mild-steel specimens, greater oxide scales were observed on its surfaces compared to the cast-iron and wrought-iron. This is mainly due to the anodic activated corrosion these were subjected to during Day 1. For mild-steel/soil systems, a distinct observation was made. There was evidence of a high rate of iron precipitates in the soil, due to the anodic activated dissolution of the mild-steel specimens during Day 1. These precipitates were observed within the dry electrolyte matrix and also on the surface layer of the soil, as shown in Plate 4.6. The fact that some of the dissolved iron species are oxidised away from the metal surface has some very significant implications for corrosion in soil.
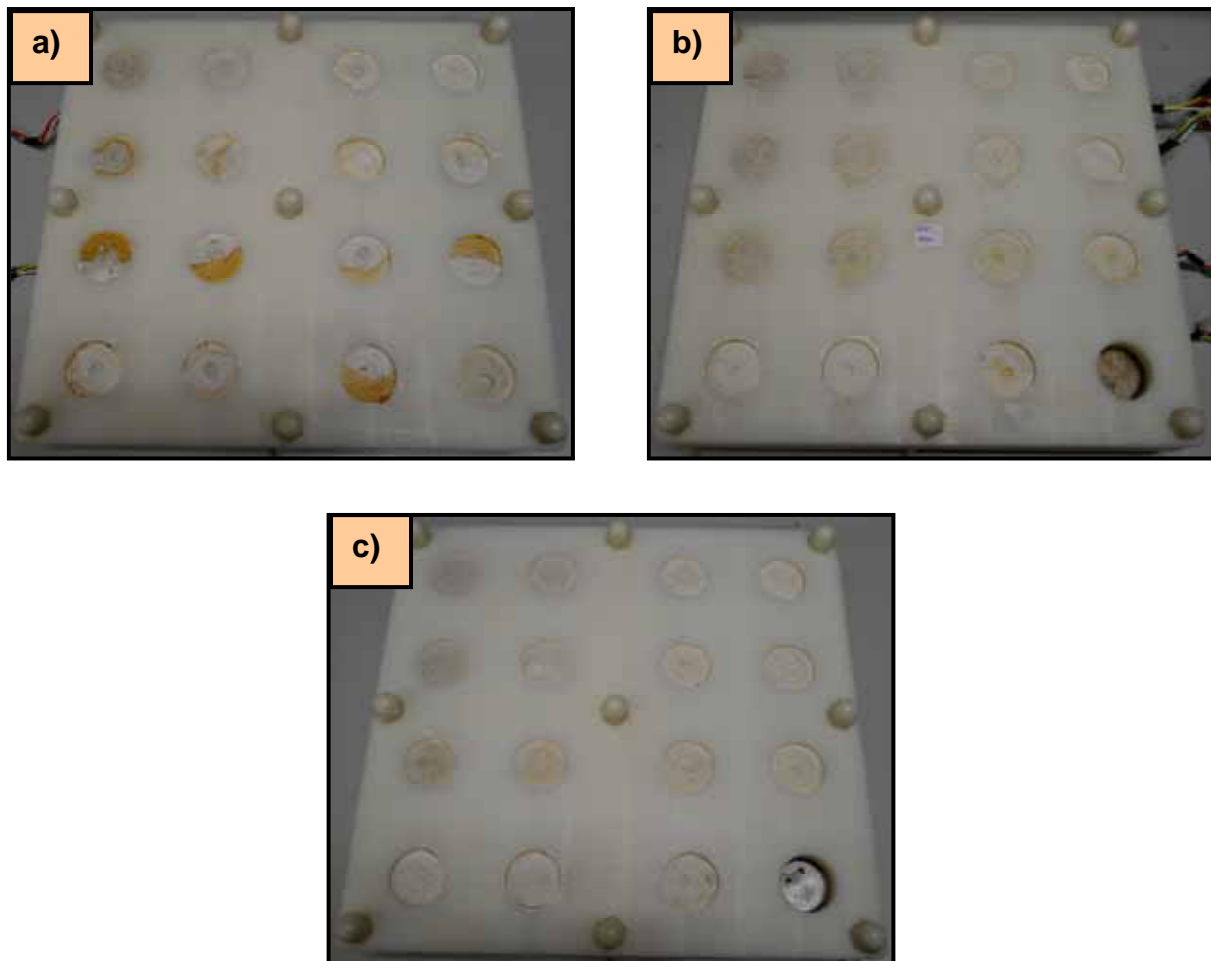
Plate 4.6. Soils in **a)** mild-steel/soil systems showed greater extent of iron precipitates compared to **b)** cast-iron/soil systems and **c)** wrought-iron/soil systems after 8 days.

It follows that the dissolved Fe^{2+} species is transported by advection or diffusion by the clay particles, whereby they can rise through the soil profile. Given that the oxygen levels towards the top layers of the soil electrolytes are higher than at the metal/soil interface, these dissolved species can then readily form oxides far away from the metal surface. Thus, in this manner clay, at least in saturated conditions, can lead to increased loss of metal from the surface. It is noted that a detailed analysis on the structural properties of the corrosion products and/or its effect on the microstructural properties of the metals is beyond the scope of this thesis and merits a project on its own. However, the inferences reported here provide some indication on the dissolution behaviour of iron across different soil compositions.

The next section presents results from the investigations carried out on the anodic curve characteristics of the metal/soil systems in the present work. Although it does not form an immediate objective of the thesis, these are included in an attempt to provide further insight on the metal/soil properties during Day 1.

4.3.4 Anodic Polarization Measurements.

The corrosion of unprotected pipelines in a soil environment rarely occurs under the mechanism of free corrosion (at E_{CORR}). Instead due to the dynamic nature of the environment, the true potential between the metal surface and the surrounding distribution of soil is usually offset away from the E_{CORR} that would exist in the absence of any external forcing. It follows that if the overall effect produces an offset towards a more negative direction from E_{CORR} then the pipeline can be considered to be somewhat protected, unless it gives rise to significant hydrogen embrittlement [Shipilov & May, 2006]. However, if the offset is towards a more positive direction relative to the equilibrium potential then the pipeline is subjected to an accelerated form of corrosion. Of course there can be multiple cathodic and anodic forcing occurring over a small area of the pipeline, which in effect can lead to severe corrosion due to pitting.

The small anodic overpotential curves measured for each of the 45 metal/soil systems in this work are illustrated in Fig. 4.29. Measurement in each cell was commenced 2 hrs after introduction of the soil electrolytes to the freshly polished metal surface at a scan rate of 0.167 mV s^{-1}. Thus the measurement time in each cell was ~12 mins. The BioLogic VMP3 potentiostat used in this experiment was used to apply 'on-the-fly' Ohmic corrections corresponding to 85% of the R_{Ω} determined by the instrument. The remainder (15%) corrections were done post acquisition to remove any Ohmic artefacts on the acquired polarization curves. Since the anodic overpotentials can inflict irreversible changes to the

surface of the electrodes, repeated measurements on the same cell were not conducted. To demonstrate repeatability however, the mild-steel/C25 system was measured twice and this is illustrated as an insert in Fig. 4.29a-3. The repeated measurement in this instance involved re-polishing the metal surface and introduction of fresh soil electrolyte. It is emphasized here, that the anodic overpotential measurements have been conducted to identify if any qualitative conclusions can be drawn from their profiles. Some observations made on these anodic overpotentials profiles are addressed next.
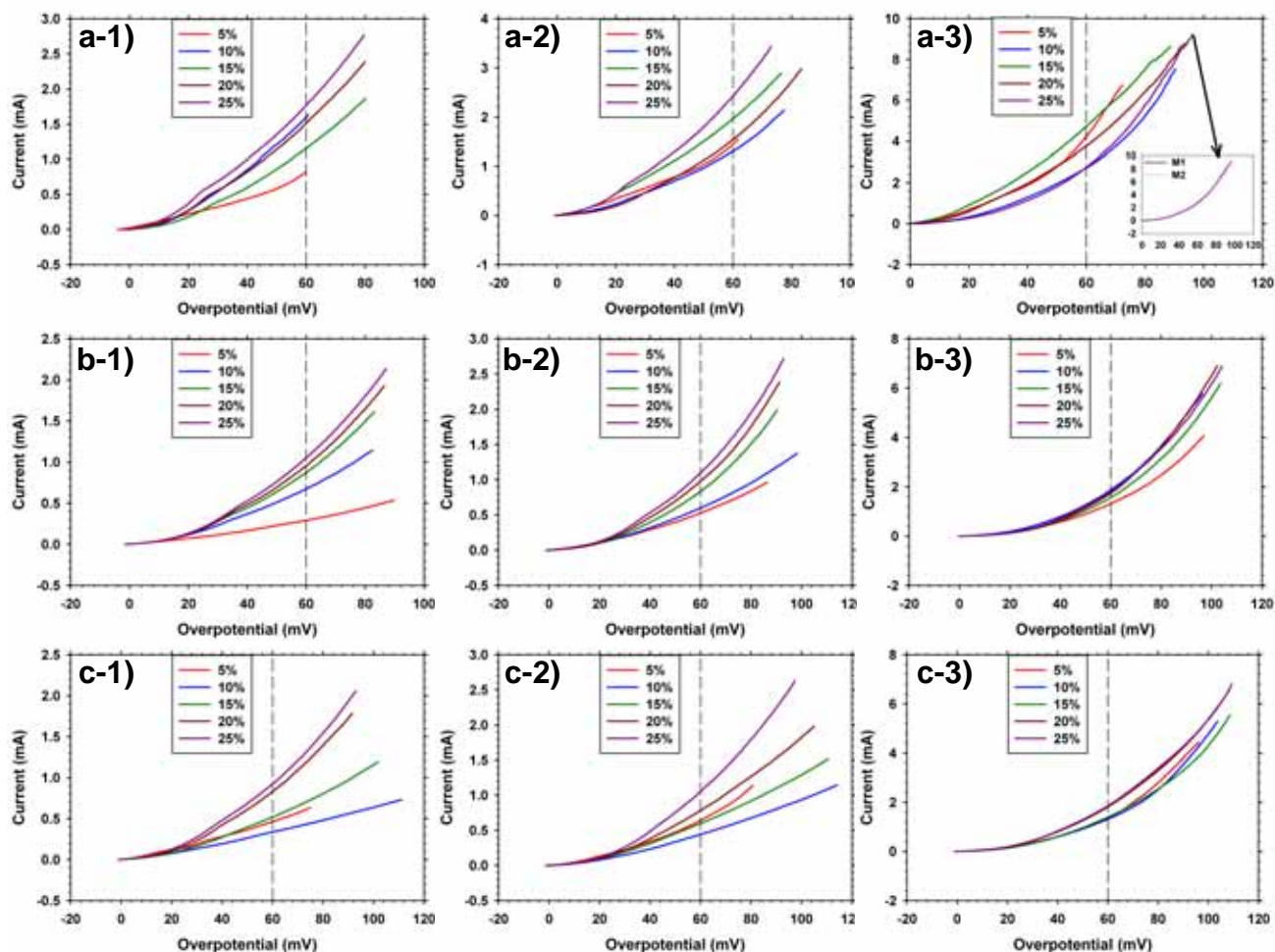
Figure 4.29. Anodic overpotential profiles for different clay contents of the various metal/soil systems studied in this work. The labels **a**, **b**, and **c** correspond to mild-steel, cast-iron, and wrought-iron respectively, while the labels **1**, **2**, and **3** correspond to soils saturated with deionized water, 0.01M NaCl and 0.1M NaCl respectively.

It is seen that even though measurements comprised of apparent anodic overpotentials up to +120 mV, the necessary Ohmic corrections reduced the true overpotential range to +60 – 110 mV. In each of the illustrations shown above, the line drawn at an arbitrary overpotential of 60 mV is given as an

aid to trace the effect of increasing clay content. In some instances, it is observed that increase in clay content leads to a slightly larger anodic current density at relatively higher overpotentials (mostly > 60 mV). This effect is significant in soils saturated with deionized water and 0.01M NaCl compared to those saturated with 0.1M NaCl. Moreover, at low overpotentials (< ~20 mV), these effects disappear, except for mild-steel/soil systems which exhibit some differences in the anodic current densities with varying clay content. It follows that as the overpotential increases, the dissolution of iron increases. Assuming that all Ohmic contributions are corrected and accounted for, the increase in anodic current densities at higher overpotential with clay content suggests the presence of some complex interactions which occur at the metal surface. A possible reason can be the strong affinity of clay particles for the ferrous ions. It follows that since the clay particles are negatively charged, the Fe^{2+} ions produced at the metal can get quickly adsorbed on its surfaces. With increasing overpotentials the rate at which these ions get adsorbed on clay particles are higher leading to exposure of fresher metal surfaces. Of course in the presence of $(OH)^-$ and weak levels of Cl^-, the Fe^{2+} ions can combine with them to form ferrous hydroxides and chlorides respectively. However, the presence of strong clayey effects for soils saturated with deionized water and 0.01M NaCl suggests that the adsorption phenomenon is stronger. In contrast the clayey effect at higher overpotentials becomes relatively weaker for soils saturated with 0.1 M NaCl. This perhaps indicates that in the presence of strong Cl^- concentrations, there are formations of corrosion products which get deposited on the metal surface, thus decreasing the dissolution rate. This is further supported by the fact that there is no clear monotonic increase in anodic current densities with increasing clay content. Instead, any such differences are minimal, except for mild-steel/soil systems. For mild-steel/soil systems saturated with 0.1 M NaCl, a significant difference is observed compared to the observations on cast-iron/soil and wrought-iron/soil systems. The erratic behaviour of anodic current densities with clay content in mild-steel/soil systems is plausibly indicative of the composition of the metal itself.

Although the present work is not concerned with analysis of anodic curves in soils, these are briefly discussed here since there are indications that it can be used to understand soil as a corrosive environment. In fact a complete and thorough investigation of anodic dissolution study merits a project on its own accord. As mentioned earlier, in the natural environment a corrosion process seldom occurs under equilibrium conditions. Thus, there is a need to develop methods in order to be able to quantify the corrosion levels, which exist under these conditions. The anodic curve does provide some hint on the iron dissolution rate in a particular environment in the event that the metal-soil potential is shifted towards an anodic direction. Overall, it is demonstrated here that under

conditions of weak Cl⁻ concentrations in soils, the presence of clay, at least in saturated phases, has the ability to increase the anodic current densities.

4.4 Conclusions

The present work provides a pioneering application of the short galvanostatic pulse technique to characterize the electrical double layer electrical properties at the metal/soil interface. In view of the current difficulties and potential errors in using the potentiodynamic or linear polarization resistance methods to grade potential soil corrosivity, it is demonstrated that the use of short galvanostatic pulse method is much more suitable and provides a non-destructive analytical probe into the double layer characteristic. This technique has been used to identify the effects of clay and chlorides on the corrosion of ferrous materials *viz*., mild steel, grey cast iron, and wrought iron under saturated and partially saturated conditions.

Under saturated conditions, the corrosion styles of these ferrous metals are similar and are mostly controlled by the concentration of the dissolved chlorides in the pore fluid. However, as the corrosion process continues under conditions of natural desaturation of the soil electrolytes, several important features emerge. Firstly, it is seen that soils with increasing clay content tend to induce large degrees of corrosion relative to soils with lower clay content, as inferred from R_p. This can be attributed to a coupled moisture-chloride effect influenced by the clay content. It follows that the amount of chlorides which can be accumulated by soil increases as the clay content increases in the presence of a given pore fluid with dissolved chloride species. This is an indirect effect from the affinity to water by clay particles. Secondly, clayey soils tend to dry out very slowly compared to sandy soils, thus sustaining moderate corrosion levels over a longer duration. Thus, the potential corrosivity of soils increases with increasing clay content and with increasing dissolved chloride levels. The double layer capacitance C_{dl} has also been found to depend on the clay content of soil as well as the concentration of the chlorides. In fact the range of values reported in this work for C_{dl} has previously never been reported. This emanates from the fact that for the first time the R_p and C_{dl} values are being reported across a range of synthetic soil electrolytes under saturated and partially saturated conditions. Moreover, the non-ideal relaxation of the electric double layer as characterized by the β-parameter, appears to reflect the moisture level at the metal-soil interface. However, it has also been seen to vary with the state of the metal surface as in the case of mild steel-soils systems which were anodically activated for 8 hrs. Thus, there is some indication that the β-parameter can be used as a diagnostic

parameter to offer some insight into the conditions of the metal surface. This needs to be investigated further since the β-parameter is seen to be affected by a range of soil conditions.

A major attempt in the present work has been to demonstrate an adoption of a consistent methodology in order to grade potential soil corrosivity. Since soils can acquire different states, *viz.*, solid, semi-solid, plastic, and liquid at given water content, it can lead to systematic errors when comparing soils with different clay contents. These errors normally will arise when the metal/soil interface is initiated. Thus, in order to normalize these effects, it is appropriate to completely saturate a given soil sample prior to introduction of the metal electrodes for electrochemical testing. These can be followed by a second set of measurements conducted after a period of natural desaturation, which will allow the water retention properties of the soils to manifest in the corrosion process. Most importantly, in the absence of any available standards for verification of soil corrosion measurements, results for the synthetic soil samples utilized in this work serve as baseline reference values for any future work aiming to calibrate a given soil corrosion measurement system.

Overall, the use of the short galvanostatic pulse technique is very useful especially for assessment of corrosion in a soil environment as has been discussed in the present work. It has been shown that significant resistances due to diffusion can be safely ignored using the electrochemical set-up used in this work. The technique itself is directly applicable under field conditions, assuming the criteria for field usage of galvanostatic methods (current confinement) are met. It is envisaged that the present work will open a new area of investigations concerning the use of short galvanostatic pulse methods for accurate laboratory as well as in-situ soil corrosion studies.

CHAPTER 5

ASSESSING SOIL CORROSIVITY FROM SPECTRAL INDUCED POLARIZATION RESPONSE

The present chapter focuses on a laboratory study investigating the spectral induced polarization response of soil samples. This study is important in order to advance the understanding of soil electrical parameters which can be used diagnostically to assess soil corrosivity. Presently, soil resistivity is the only such (electrical) parameter, which is routinely used to identify soil corrosiveness. The chapter makes an original contribution by identifying other electrical characterizations, which can advance soil corrosivity classification methods.

5.1   Introduction

Spectral induced polarization (SIP) or complex resistivity (CR) studies of geological materials were originally developed for exploration of mineral deposits [Pelton *et*. *al*., 1978; Pelton *et*. *al*., 1983]. However, the ability of this method to identify contaminated soils [Olhoeft, 1985; Vanhala, 1997], and for estimation of hydraulic properties [de Lima & Niswas, 2000; Hordt *et*. *al*., 2007; Revil & Florsch, 2010; Koch *et*. *al*., 2011], and *etc*., [*e*.*g*., Borner *et*. *al*., 1996] has allowed the technique to become an important tool in environmental and related investigations [Weller & Borner, 1996; Kemna *et*. *al*. 2000; Slater & Lesmes, 2002; Vaudelet *et*. *al*., 2011]. It has been demonstrated by Ntarlagiannis & Ferguson (2009) that SIP measurements are sensitive to biofilm development in porous media, while Slater *et*. *al*. (2007) and Personna *et*. *al*. (2008) have shown that SIP response evolutions are associated with FeS biomineralization by sulphate reducing bacteria. Moreover, Boadu & Owusu-Nimo (2010) and Boadu (2011) have reported relationships between SIP responses and geotechnical and/or engineering properties of soils, further demonstrating the feasibility of this technique in the wider field of environmental and engineering applications. The important observation from all these studies is that the surface conductivities [Schon, 1996], which give rise to the IP effect in geological materials can be perturbed by a range of physical, chemical, and biological elements. This surface conductivity phenomenon in materials of geological origins is addressed in the subsequent sections.

5.1.1   Fundamental Basis from Maxwell's Equations

To facilitate an understanding of the polarization phenomenon in soils a first look at some fundamental principles concerning physics of disordered media is necessary. Regarding electrical

properties of soils, Dias (1972), Olhoeft (1985), Chelidze & Gueguen (1999), and Borner (2006) have provided a thorough discussion on this matter, thus a brief treatment is provided in this section.

The polarization density, $\mathbf{P}$ (C m^{-2}) is defined as the density of the permanent or induced electric dipole moments in a dielectric medium such as soil under the action of an applied harmonic ($e^{-i\omega t}$ dependence) field $\mathbf{E}$ (V m^{-1}). $\mathbf{P}$ is an important component of the total electric displacement field $\mathbf{D}$ (C m^{-2}) described by:

$$\mathbf{D} = \varepsilon_o \mathbf{E} + \mathbf{P} = \varepsilon \mathbf{E} , \tag{5.1}$$

where all the symbols have their usual meanings. In electrodynamics, Maxwell's fourth equation describes the influence of the curl operator on the magnetic field intensity $\mathbf{H}$ (A m^{-1}) as given by Eq. 5.2.

$$\nabla \times \mathbf{H} = \mathbf{J_a} + \frac{\partial \mathbf{D}}{\partial t} \tag{5.2}$$

where, $\mathbf{J_a}$ (A m^{-2}) in this discussion corresponds to the average transport current density due to the drift of charged particles [Dias, 1972]. Under the influence of a small harmonic field, $\mathbf{J_a}$ and $\mathbf{P}$ follow a linear dependence with $\mathbf{E}$. Under these conditions, Eq. 5.2 can be developed as:

$$\nabla \times \mathbf{H} = \mathbf{J_a} + \frac{\partial (\varepsilon_0 \mathbf{E} + \mathbf{P})}{\partial t} = \mathbf{J_a} + \frac{\partial (\varepsilon \mathbf{E})}{\partial t} = \sigma_a \mathbf{E} - i\omega\varepsilon \mathbf{E} , \tag{5.3}$$

leading to:

$$\nabla \times \mathbf{H} = (\sigma_a - i\omega\varepsilon) \mathbf{E} , \tag{5.4}$$

where,

$$\sigma^* = (\sigma_a - i\omega\varepsilon) , \tag{5.5}$$

where, σ^* is the <u>total</u> complex conductivity of the soil arising due to charge conduction and polarization mechanisms, and σ_a and ε are the frequency dependent complex conductivity and complex permittivity of the soil (lossy dielectric) respectively and can be further expressed by their real and imaginary parts as shown in Eq. 5.6 and 5.7.

$$\sigma_a = \sigma_a^{'} + i\sigma_a^{''} \tag{5.6}$$

$$\varepsilon = \varepsilon' + i\varepsilon'' \tag{5.7}$$

where, the superscripts $'$ and $''$ correspond to real and imaginary components respectively. The σ_a is a complex quantity since it includes the electrolytic as well as surface conduction mechanisms (see Chapter 3). Following Eq. 5.6 and 5.7, the real and imaginary components of this total complex conductivity can also be written respectively by Eq. 5.8 and 5.9.

$$\text{Re}\left[\sigma^*\right] = \sigma_a' + \omega\varepsilon'' \tag{5.8}$$

$$\text{Im}\left[\sigma^*\right] = \sigma_a'' - \omega\varepsilon' \tag{5.9}$$

Regarding Eq. 5.5, two limiting conditions can be identified, *i.e.*,

  a) when $\omega \to 0$, the total conductivity is mainly controlled by the complex quantity σ_a consisting of electrolytic and surface conduction mechanisms, and

  b) when $\omega \to \infty$, the complex dielectric permittivity has a significant effect on the total conductivity.

Consequently, depending on the frequency of the applied **E** field, a range of polarization mechanisms is possible. At high frequencies these include electronic, atomic, dipolar, and ionic polarization mechanisms [see Kremer & Schonhals, 2003; Chen & Or, 2005], which are not of interest in this work and hence will not be discussed further. At lower frequencies ($< 10^3$ Hz), which are common in spectral induced polarization (SIP) studies of soil [Slater & Lesmes, 2002], the membrane and Stern layer polarizations are the most dominant mechanisms while the Maxwell-Wagner-Sillars (MWS)[*] effect at interfaces [Schwartz *et. al.*, 2012] can manifest at the high-end of the frequency spectrum. A treatment of the polarization phenomenon at these low frequencies is given next.

5.1.2 Low Frequency Polarization

The complex conductivity (σ_a) of soils arising due to electrolytic and surface conduction mechanisms have three major components, *viz.*, the bulk conductivity, σ_{bulk}, and the real and imaginary components of the surface conductivity, $\sigma_{surf}'(\omega)$ and $i\sigma_{surf}''(\omega)$ respectively. It follows that in regards to Eq. 5.8 and 5.9, at low frequencies, $\omega\varepsilon'' << \sigma_a'$ and likewise $\omega\varepsilon' << \sigma_a''$. Under these conditions, the total complex conductivity (σ^*) can then be represented by [Lesmes & Frye, 2001]:

$$\sigma^* = \sigma_a' + i\sigma_a'' = \left(\sigma_{bulk} + \sigma_{surf}'(\omega)\right) + i\sigma_{surf}''(\omega) \tag{5.10}$$

where, the in-phase conductivity is defined as the sum of the bulk and real component of the surface conductivities ($\sigma_{bulk} + \sigma_{surf}'(\omega)$), while the quadrature conductivity is equal to the imaginary component of the surface conductivity ($\sigma_{surf}''(\omega)$). The σ_{bulk} is independent of frequency and is derivable from the Hanai-Bruggerman effective medium theory [Sen *et. al.*, 1981; Lesmes & Frye, 2001], which results in the Archie equation discussed in Chapter 3 (Eq. 3.1). On the contrary,

---

[*] In literature the Maxwell-Wagner-Sillars (MWS) polarization is usually referred to as Maxwell-Wagner polarization. However, in the thesis this mechanism will be referred to as the former (MWS).

$\sigma'_{surf}(\omega)$ and $i\sigma''_{surf}(\omega)$ are frequency dependent parameters. The complex conductivity σ^* can also be represented in its polar form by Eq. 5.11.

$$\sigma^* = |\sigma| \exp^{(i\phi)} \tag{5.11}$$

where, ϕ (rad) is the phase shift between the current and potential signals (see Chapter 3, section 3.3.3). It follows that in the event that phase angles are small (< 100 mrad) [Ulrich & Slater, 2004], a condition which is common for non-metallic soils, the phase angle can be defined by:

$$\phi(\omega) = \tan^{-1}\left(\frac{\text{Im}[\sigma']}{\text{Re}[\sigma'']}\right) = \tan^{-1}\left(\frac{\sigma''_{surf}(\omega)}{\sigma_{bulk} + \sigma'_{surf}(\omega)}\right) \simeq \frac{\sigma''_{surf}(\omega)}{\sigma_{bulk} + \sigma'_{surf}(\omega)} \tag{5.12}$$

It is noted that when the σ_{bulk} is very high, *i.e.*, at high salinities, ϕ will decrease in magnitude. Thus, ϕ is directly influenced by the relative weights of the bulk and surface conductivities and is usually used as an indication of the degree of polarization in soils. The origin and causes of the surface conductivities at low frequencies for non-metallic soils are mainly attributed to membrane, Stern layer, and the MWS (at higher frequency) polarization mechanisms [Revil & Glover, 1998; Leroy & Revil, 2004; Leroy & Revil, 2009; Revil & Florsch, 2010; Schmutz *et. al.*, 2010; Revil, 2012]. The membrane polarization mechanism was discussed in Chapter 3, where it was shown that clay acts as an ion-selective membrane impeding the transport of anions and thereby creating a concentration gradient. These concentration gradients can also be caused by difference in ionic mobilities at the interfacial regions between wide and narrow pores [Titov *et. al.*, 2002], contributing towards the polarization effect in soils.

Stern layer polarization can be understood by considering the electrical conduction in the EDL [*e.g.*, Revil & Florsch, 2010; Schmutz *et. al.*, 2010] at the soil grain/fluid interface. The Stern layer, which is responsible for the excess surface conductivity, can be assumed to be discontinuous amongst individual grain/fluid interfaces and its polarization normally manifests in the frequency range 10^{-3} – 10^2 Hz [Leroy *et. al.*, 2008]. Assuming the net charge on the soil grain surface is negative, the Stern layer will consist of hydrated cations adsorbed on the surfaces. Under an applied **E** field, the EDL gets polarized and in the Stern layer the loosely held cations migrate in the direction of the field, predominantly tangentially along the surface of the soil grain [Revil & Florsch, 2010]. Some of these ions also accumulate at the location of discontinuities and back-diffuse in the concentration gradient. Further details can be found in Revil & Florsch (2010). Concerning the other important region of the EDL, the diffuse layer, Leroy & Revil (2004) showed that the Stern layer contribution to surface conductivity is much more significant than contributions arising from the diffuse layer. Recently,

Revil (2012) developed a model for the polarization response of shaly sands and showed that the in-phase conductivity is influenced by pore fluid conductivity as well as the contribution arising from the diffuse layer. However, the polarization response of the shaly sands is mainly influenced by the polarization of the Stern layer at the soil grain/fluid interface. The MWS polarization effect results from the accumulation of charges at the interfaces between two different phases of different conductivities and permittivities [Chelidze & Gueguen, 1999; Leroy *et*. *al*., 2008]. The accumulation of charges leads to an increase in the dielectric permittivity of the soil [Chen & Or, 2006] and hence it manifests strongly at higher frequencies ($> 10^2$ Hz).

The frequency dependent complex conductivity of soils/rocks has been an active field of study spanning decades. Consequently, literature is replete with studies describing various models to describe the complex conductivity of porous materials. Some of these models are based on effective medium approaches and complex electrochemical processes which occur at the soil grain/fluid interface [Wong & Strangway, 1981; Wait, 1982; Leroy *et*. *al*., 2008; Zhdanov, 2008 and the references therein]. Other formulations based on equivalent circuit models have also been suggested [*e*.*g*., Pelton *et*. *al*., 1978; Dias, 2000] amongst which the Cole-Cole model [see Kemna, 2000] remains the most highly utilized formulation to describe the frequency dependence of the complex conductivity of soils/rocks. It is not intent of this chapter to provide a detailed review on the various models which exist to characterize the complex conductivity of geological materials. Such comprehensive reviews and discussions are well covered in literature can be found elsewhere [*e*.*g*., Ruffet *et*. *al*., 1995; Chelidze & Gueguen, 1999; Dias, 2000; Borner, 2006 and the references therein]. However, the Cole-Cole model, which is of importance to the present work, is discussed next.

5.1.3 The Cole-Cole Relaxation Model

The Cole-Cole model [Cole & Cole, 1941] was initially developed as an extension to Debye's formula to explain the stretched dispersion phenomenon in dielectrics. However, Pelton *et*. *al*. (1978) showed that a model based on a modification to the original Cole-Cole model used to describe the frequency dependence of dielectric permittivity could also be used to describe the frequency dependent complex resistivity, ρ (ω), of mineralized rocks. In geophysics, this model is also referred to as the empirical or phenomenological Cole-Cole model and can also be expressed in terms of the complex conductivity ($\sigma = 1/\rho$). However, it is common in literature for the model to be expressed in terms of the complex resistivity; hence this notation will be maintained in the thesis hereafter. The Cole-Cole model can be understood by the illustration presented in Fig. 5.1a, and its equivalent circuit model given in Fig. 5.1b.
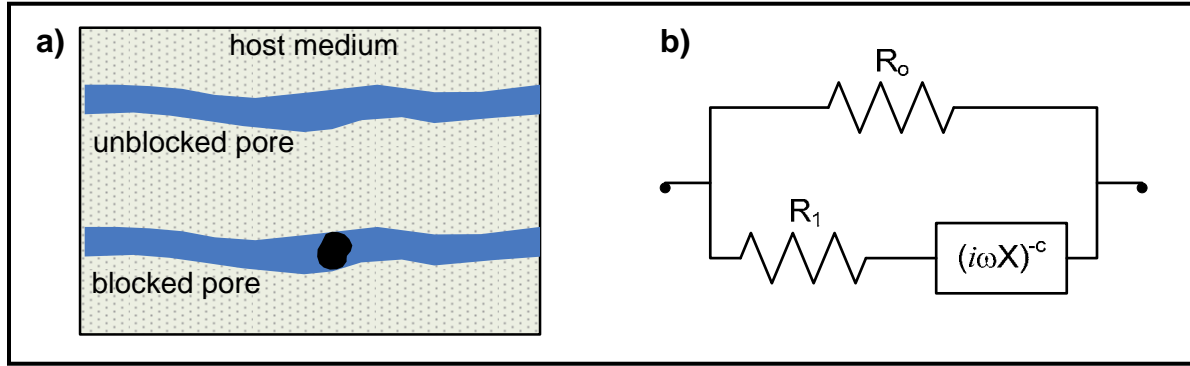
Figure 5.1. **a)** Representative element of a mineralized rock, and **b)** its equivalent circuit model. Redrawn after Pelton *et. al.* (1978).

It follows that a polarizable element of a mineralized rock can be considered to be composed of blocked and unblocked pore paths. The resistance of the unblocked path is denoted by R_o, while the resistance of the electrolyte in the blocked path is represented by R_1. The term $(i\omega X)^{-c}$ represents the complex interfacial impedance due to the reactive component X, which manifests due to the presence of a conducting mineral grain [Luo & Zhang, 1998] blocking the pore path. Following this, the equivalent circuit model given in Fig. 5.1b then represents the conduction mechanisms in the polarizable element. The impedance of this equivalent circuit after some algebra [see Pelton *et. al.*, 1978; Lou & Zhang, 1998] can then be written as:

$$\rho(\omega) = \rho_{DC}\left[1 - m\left(\frac{1}{1+(i\omega\tau)^c}\right)\right] = \rho_{DC} - m\rho_{DC} - \frac{m\rho_{DC}}{1+(i\omega\tau)^c}, \tag{5.13}$$

where, ρ_{DC} is the DC resistivity recovered when $\omega \to 0$ (Ω m), m is the chargeability (dimensionless), τ is the relaxation time (s), and c is the frequency dependence (dimensionless). The τ is usually connected to the mean size of the polarizable element giving rise to the polarization effect, while c is related to the width of the size distribution of the polarizable elements. It is noted here that the Cole-Cole model can be considered a special case of the Havriliak-Negami type model [see Havriliak & Negami, 1967], which occurs when $\beta = 1$ in the latter. Also, when $c = 1$, the Cole-Cole model reduces to the simple Debye relaxation. However, experimental evidence suggests that the value of c usually varies between $0.1 \leq c \leq 0.6$ [Pelton *et. al.*, 1978]. Note, since the IP effect in the frequency-domain as captured by the Cole-Cole model is connected to the charging/discharging effect in the time-domain, the latter can be synthesized by an inverse Fourier transform of the former [see Duckworth & Calvert, 1995; Duckworth & Brown, 1996].

The important feature of the Cole-Cole model is the magnitude ($|\rho|$) and phase (ϕ) response it describes in the frequency domain. A typical response plot is given in Fig. 5.2a.
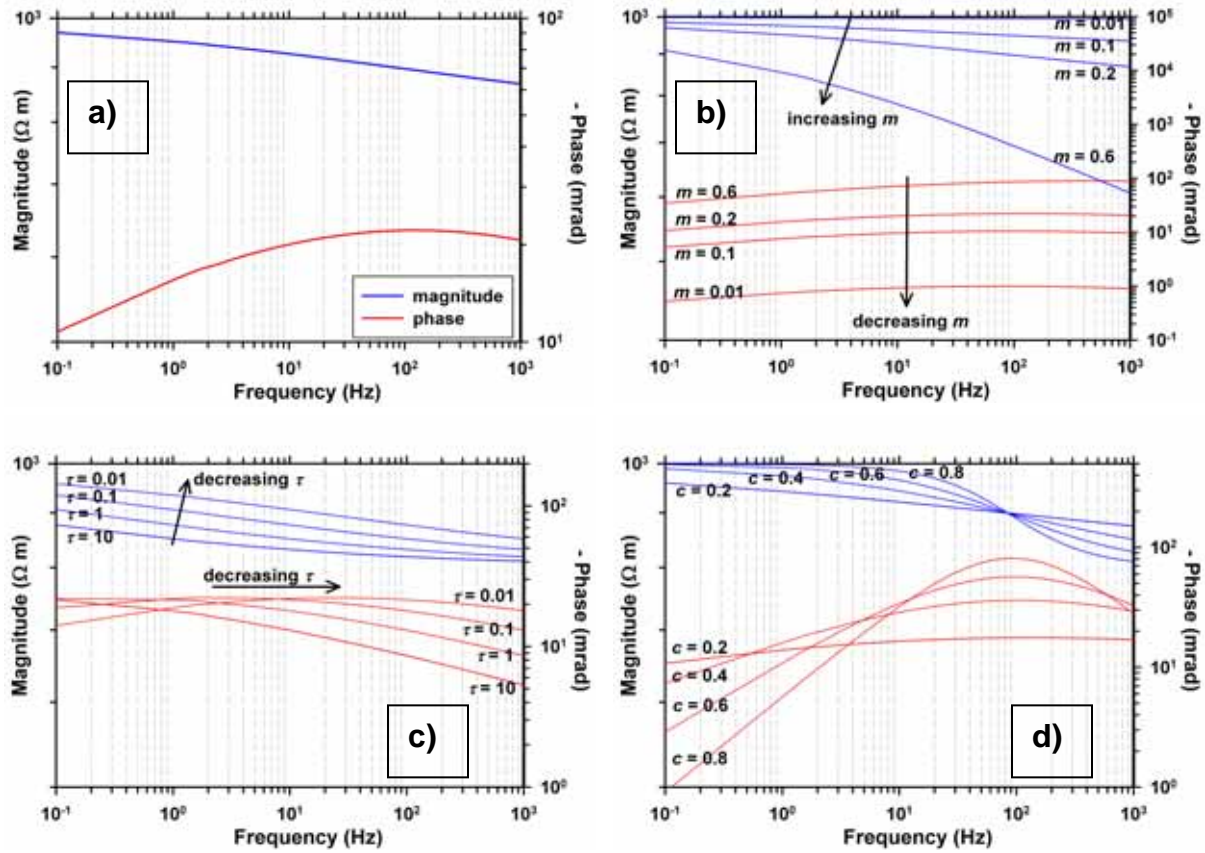
Figure 5.2. **a)** Typical plot of the magnitude and phase response of geological materials in SIP studies, numerically generated for $\rho_{DC} = 1$ kΩ, $m = 0.2$, $\tau = 2 \times 10^{-3}$ s, and $c = 0.25$. The perturbations in the magnitude and phase response caused by the individual arbitrary values of Cole-Cole parameters m, τ, and c when all other variables are kept fixed to the above mentioned values are shown in **b)**, **c)**, and **d)** respectively. Blue and red coloured curves are for magnitude and phase respectively.

The magnitude and phase response shown in Fig.5.2a represents the scope of laboratory SIP studies of geological materials in the frequency range 10^{-1} – 10^{3} Hz as these are the responses which are measured experimentally. The phase response or the joint magnitude/phase responses can then be inverted to retrieve the so-called Cole-Cole parameters $\{m, c, t\}$ [Lou & Zhang, 1998]. The magnitude and phase spectra can exhibit different shape features depending upon the values of the Cole-Cole parameters as illustrated in Fig. 5b – 5d. Regarding Fig. 5.2b, it is seen that the chargeability parameter has a huge impact on the amplitudes of the magnitude as well as the phase spectra. Considering the magnitude response, the chargeability can also be defined as:

115

$$m = 1 - \frac{\rho_\infty}{\rho_{DC}} \quad , \tag{5.14}$$

where, ρ_∞ is the resistivity measured at some infinite frequency. Hence, m can be estimated from the shape of the magnitude spectra by considering the asymptotic resistivity values in the low and high frequency ranges. Different relaxation times affect the phase spectra significantly by translating the spectra horizontally towards higher frequencies with decreasing values of τ. This feature exists due to the inverse connectivity between τ and the frequency (f_{peak},) [Pelton *et. al*., 1983; Volkman & Klitzch, 2010] at which the peak in the phase spectra occurs; corresponding to the minimum ϕ (since ϕ is negative). This inverse relationship is given by [see Pelton *et. al*., 1983; Kemna, 2000]:

$$2\pi f_{peak} = \left(\frac{\rho_{DC}}{\rho_\infty} \right)^{\frac{1}{2c}} \times \frac{1}{\tau} \tag{5.15}$$

The frequency dependence c accounts for the broadness of the phase spectra and can be estimated as the slope of the phase spectrum on the log-log plane. Due to the symmetrical nature of the phase spectrum, this slope can be evaluated at either the lower end (slope of c) or higher end (slope of $-c$) of the frequencies [Pelton *et. al*. 1978; Jaggar & Fell, 1988].

Although the SIP measurements can be represented as magnitude and phase responses across the frequency range, it is also common to report the real and imaginary components of the complex resistivity (or conductivity) across the frequency range. The real and imaginary components can be calculated from the magnitude and phase values at each frequency by the simple relationships given in Eq. 5.16 and 5.17 respectively.

$$\mathrm{Re}\left[\rho(\omega) \right] = |\rho| \cos(\phi) \tag{5.16}$$

$$\mathrm{Im}\left[\rho(\omega) \right] = |\rho| \sin(\phi) \tag{5.17}$$

It follows that since the phase is always negative the imaginary component is also always negative and both the real and imaginary components are connected to each other by the Kramer-Kronig relations [see Lucarini *et. al*., 2005]. Moreover, the frequency response of the imaginary component always maintains the shape of the phase spectra.

Although the Cole-Cole model has been found in many studies to be able to accurately characterize the low frequency phase response of various geological materials in laboratories as well as in field studies [*e.g*., Pelton *et. al*., 1978; Slater *et. al*. 2006], there are instances in which a single dispersion formulation is not sufficient [*e.g*., Ghorbani *et. al*., 2009]. These cases arise especially in the presence

of multiple dispersion peaks connected with different polarization mechanisms, complex grain size distributions or the presence of inductive coupling. In this regard, the multi Cole-Cole model formulation by Kemna (2000) can be used. This formulation is expressed in Eq. 5.18.

$$\rho(\omega) = \rho_{DC} \left[1 - \sum_{k=1}^{N} m_k \left(\frac{1}{1 + (i\omega\tau_k)^{c_k}} \right) \right] \tag{5.18}$$

In most cases, three Cole-Cole dispersion terms ($N = 3$) are sufficient to completely describe the phase response [see Kemna, 2000]. It is noted here that the although the Cole-Cole model is an empirical model originally developed by Pelton *et. al.* (1978) for discrimination of mineralized rocks, Revil & Florsch (2010) in their recent work have suggested that a theoretical justification can be given due to the ability of the Cole-Cole probability distribution to describe the grain size distribution.

5.1.4 Scope of Present Work

After the successful proven application of the Cole-Cole model in field applications by Pelton *et. al.* (1978), multitudes of laboratory studies concerned with connecting the Cole-Cole parameters with different soil properties have been described in the literature. Some recent studies (but not in any way limited to) have reported inverse and direct relationships between chargeability and porosity and effective stress on sands respectively [Seabrook & Boadu, 2002], direct relationships between normalized chargeability and specific surface area normalized to pore volume in sandstones and metal-sand and clay-sand mixtures [Scott & Barker, 2005; Slater *et. al.*, 2006], direct relationship between normalized chargeability and certain salinity range of pore fluid in sandstones [see Lesmes & Frye, 2001; Scott & Barker, 2005], and biomineralization growth during anaerobic transition [see Slater *et. al.*, 2007], inverse relationships between chargeability and water content for argillites [Cosenza *et. al.*, 2007], sands [Breede *et. al.*, 2011] and for sediments with low clay content [Cassiani *et. al.*, 2009]. Also, direct and inverse relationships between the relaxation time and pore throat diameter, and surface area normalized to pore volume for sandstones respectively have been reported by Binley *et. al.* (2005). Other studies [*e.g.*, Binley *et. al.*, 2005; Cosenza *et. al.*, 2007; Koch *et. al.*, 2011] have reported inverse and direct relationships between relaxation time and water content and hydraulic conductivity respectively. Also, Scott & Barker (2005) have shown that the relaxation time exhibits inverse relationships with pore fluid salinity.

Apart from Cole-Cole parameters, it has also been demonstrated that the phase angle or the imaginary component of the surface conductivity at some particular frequency (*e.g.*, 1 Hz) can also be connected

with different soil properties [*e.g*., Ulrich & Slater, 2004; Abdel Aal *et. al*., 2006; Slater *et. al*., 2006]. Thus, SIP measurements permit a range of soil properties to be identified, which can then be further investigated for possible relationships with physical, chemical, or biological origins. Since these physical, chemical, or biological elements can enhance corrosion activities occurring on buried metal surfaces, there is a strong possibility that an investigation of the surface conductivity phenomenon or at least a characterization of its effects can provide new electrical methods of classifying soil corrosivity. Current practice of soil corrosivity assessments is mainly based on the 10-point DIPRA criteria; this involves assessments of resistivity, pH and redox potentials, sulphide composition, and qualitative moisture content properties of soils [see DIPRA, 2000]. Contributions of other parameters, which are electrical in nature, to this current spectrum of variables for assessing laboratory soil samples for potential corrosivity may enable advances in an understanding of macroscopic and/or microscopic properties relevant to corrosion in a soil environment. It shall be noted here that soil resistivity is the only electrical parameter currently used to assess soil corrosivity and its standard measurement procedures are covered in the ASTM G57-95a (2001) standard.

In view of this potential, a laboratory study was undertaken to understand the effect of clay and salinity on the SIP response characteristics. Influences of these variables were sought after the findings reported in the previous chapter, where it was shown that clay and chlorides have a significant impact on corrosion. For the purpose of standardization, the SIP responses of sand/clay mixtures at different salinities were measured under saturated conditions. Since soil electrical properties can vary depending upon moisture content, measurements under saturated conditions enables a common platform for any comparisons amongst soils. The present chapter makes an original contribution by identifying other features of soil electrical properties, which can be used to assess potential corrosivity. The contributions of this chapter to the overall thesis are mainly to:

   a)   Identify the effect of clay and salinity on the SIP response of soils
   b)   Investigate the efficacy of SIP measurements for possible soil aggresivity analysis, and
   c)   Identify other possible electrical parameters which are diagnostic of soil corrosivity.

5.2   Experiment Design and Measurements

This section provides an overview of the experimental procedures and methodologies that were adopted for SIP measurements of sand/clay mixtures in the laboratory. For clarity each aspect of the complete experimental procedure is categorized into sections.

5.2.1 Synthetic Soil Samples

The synthetic soil samples which were prepared for this work have already been described in Chapter 4 (Section 4.2.2) and a summary of their compositions are given in Appendix A.1. These soils have already been used to understand corrosion process properties through assessment of the EDL at the metal/soil interface. In the present work, variations in soil spectral electrical response as well as other formative properties due to clay and salinity were measured under completely saturated conditions. The sand used was quartz (silica), with an angular form. The kaolin clay, which has typical cation exchange capacity of 30 – 150 meq kg^{-1} [Grim, 1968], was obtained from a local supplier.

5.2.2 Impedance Spectrometer for SIP measurements

In order to conduct SIP measurements, a sample-hold assembly along with electronic data acquisition and control is required, which in a strict sense is an impedance spectrometer [see Zimmermann *et*. *al*., 2008]. Thus, the SIP method is sometimes also referred to as impedance spectrometry. For convenience purpose, the impedance spectrometer (IS) for SIP measurements will be referred to as SIP-IS hereafter. Some of the different types of SIP-IS for characterization of geological materials in laboratories have been reported by Vinegar & Waxman (1984), Olhoeft (1985), Vanhala & Soininen (1995), Ulrich & Slater (2004), Scott & Barker (2005), Zimmermann *et*. *al*. (2008), and *etc*. The experimental set-up by Vanhala & Soininen (1995) laid the foundations for accurate laboratory based SIP measurements systems which followed. Presently, the SIP-IS system described by Zimmermann *et*. *al*. (2008) is the most accurate system available for polarizability measurements in sediments (resolutions of < 0.1mrad). In the present work, a laboratory SIP-IS system with measurement and control provided by National Instruments (NI) LabVIEW 2009 software was developed for characterization of polarization responses of non-metallic soil samples. This SIP-IS system consists of a sample holder with associated current and potential electrodes, a data acquisition (DAQ) card, and a computer based GUI program. A schematic of this experimental set-up is given in Fig. 5.3. Although the development of the SIP-IS system does not constitute an immediate aim of the overall thesis, it is an important aspect of the present work aimed at investigating SIP responses in soils. Thus, each important element of the SIP-IS system is described in detail in the subsequent sections which follow.
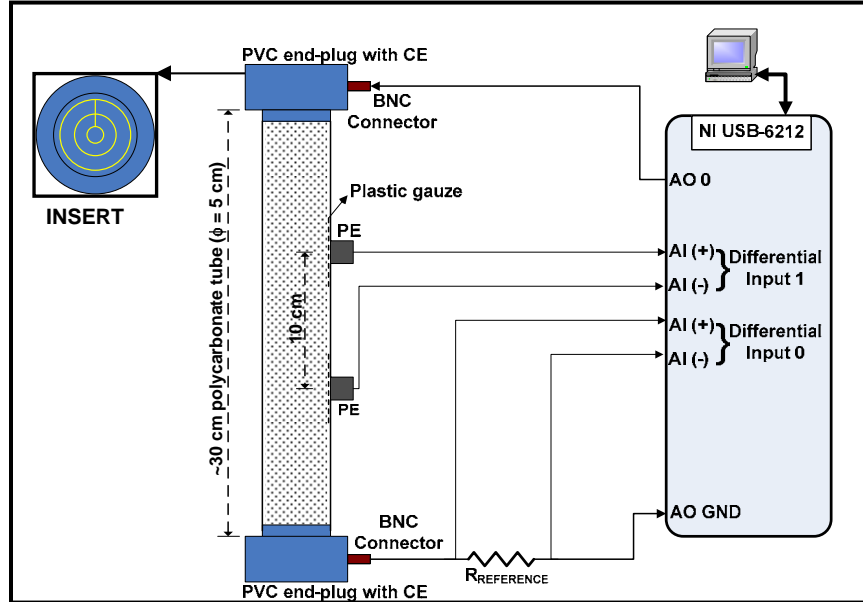
Figure 5.3. a) Schematic of the SIP-IS system for impedance spectrometry of soil samples. Insert shows the front view of the end-plugs with the coiled copper rods (shown with yellow colour) acting as CE.

5.2.2.1   Sample Holder

The sample holder consists of a transparent ~30 cm polycarbonate tube with an inner diameter of 5 cm. The end-caps are solid PVC plugs with the inner faces etched with grooves to hold the current electrodes (CE) for injecting current into the sample. Two materials *viz*., stainless steel and copper, of different geometries *viz*., coiled and flat cylindrical disks, were tested for their feasibility as current electrodes. Finally, coiled copper rods (diameter 3 mm) were utilized (and hence the grooves on the end-caps). The potential electrodes (PE) were placed 5 cm away from the centre of the tube on either side, thus an effective separation distance of 10 cm between the two PE. The distance between each of the CE and the nearest PE was 10 cm, corresponding to PE positions of ~33% and 66% of the length of the sample holder. This criterion has been shown to reduce the impact of sample impedance between either CE and nearest PE on the impedance measured between the two PE (Zimmermann *et*. *al*., 2008). Initially, stainless steel was used as a candidate material for potential electrodes. However, significant errors arising due to electrode polarization were encountered. These were then replaced by 3M™ Red Dot™ non-polarizable Ag|AgCl medical electrodes [see Ghorbani *et*. *al*., 2009] available from a commercial supplier. These electrodes, used in electrocardiogram monitoring, consist of solid buttons of Ag (diameter of 8 mm) covered with a sponge fused with AgCl hard gel. The potential electrodes were placed on top of the sample holder, with small drilled holes to allow the sponge to make contact with the soil sample. Since in the present work saturated samples were measured, care was taken not to allow direct contact between the sponge and the water laden soil. This was achieved

by attaching small mats of plastic gauze [see Slater & Lesmes, 2002] inside the sample holder at the hole-locations and sprinkling dry soils corresponding to the respective saturated soil sample inside. This allows a stable and moist contact between the soil and the sponge and also avoids any formation of bubbles, which can introduce spurious polarizations.

5.2.2.2   DAQ Card Interfacing

The sample holder and related CE and PE were interfaced to the National Instruments 16-bit DAQ card USB-6212 using separate shielded cables. The DAQ card allows non-simultaneous sampling of its channels at a maximum rate of 400 kHz. It has a maximum working voltage of ±10 V and the crosstalk between non-adjacent channels is -90 dB. Current was injected into the sample via the coiled Cu-electrodes using the analog output channel (A0 0) of the DAQ card, which has an output drive current of ±2 mA. Connections to the end-plugs housing the current electrodes were done via BNC terminations to ensure robust attachment and removal of the sample holder to the DAQ card. Differential voltages across a reference resistor, $R_{REFERENCE}$ (2 kΩ) and across the non-polarizable potential electrodes were measured on two separate input channels, *viz*., 0 and 1 respectively, configured for differential mode of operation (see Fig. 5.3). The voltage drop across the $R_{REFERENCE}$ was used to determine the current signal flowing through the sample since current injection is achieved by an applied potential, usually between 5 – 8 V. Thus in this manner the current density is not strictly constant but controlled to be <20 μA cm^{-2}, which falls in the range of linearity specified by Vanhala & Soininen (1995). External pre-amplifier circuitry usually employed to boost the input impedance [*e.g*., Vanhala & Soininen; 1995; Ulrich & Slater, 2004; Abdel Aal *et*. *al*., 2006] is not needed in this set-up due to the existing high input impedance of the analog input channels, which is >10^9 Ω in parallel with a 100 pF capacitor. Consequently, inherent system responses [see Vanhala & Soininen; 1995] which usually manifest due to external signal conditioning units are absent from the set-up.

5.2.2.3   Measurement and Control Software

A custom built LabVIEW GUI program allowed the control and measurement of stimulus (current) and response (potential) respectively from the sample holder via the DAQ. The program allows user inputs for sampling rates, value of $R_{REFERENCE}$, the amplitude of the sinusoidal voltage to be applied to the sample, and the geometrical factor, K for the sample. For the laboratory set-up, K is simply the ratio of the surface area, A ($6.25\pi \times 10^{-4}$ m^2), of one of the cylindrical ends of the sample holder to the separation distance, l (0.1 m) between the two potential electrodes *i.e*., $K = A/l = 1.9625 \times 10^{-2}$ m. The

user interface for this program is shown in Fig. 5.4 and its block diagram (coding) is given in Appendix B.1. A flowchart is provided in Fig. 5.5 to aid in understanding the spectral acquisition operation.
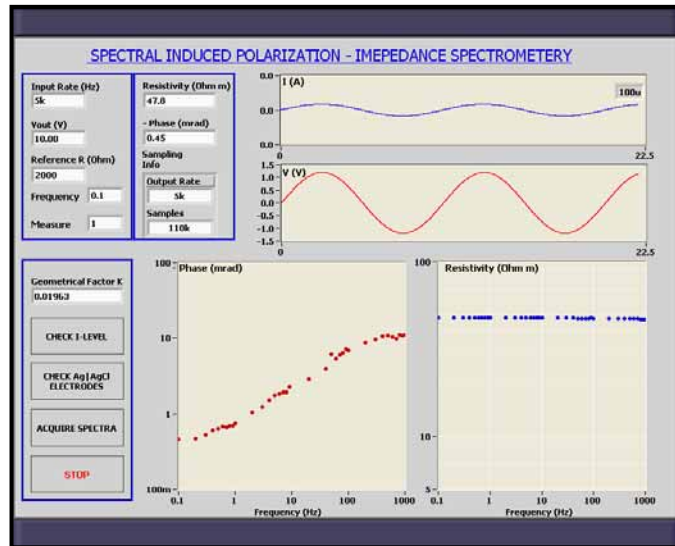
Figure 5.4. User interface of the measurement and control program for the SIP-IS system developed in this work. For illustration purposes, an arbitrary acquisition is shown.
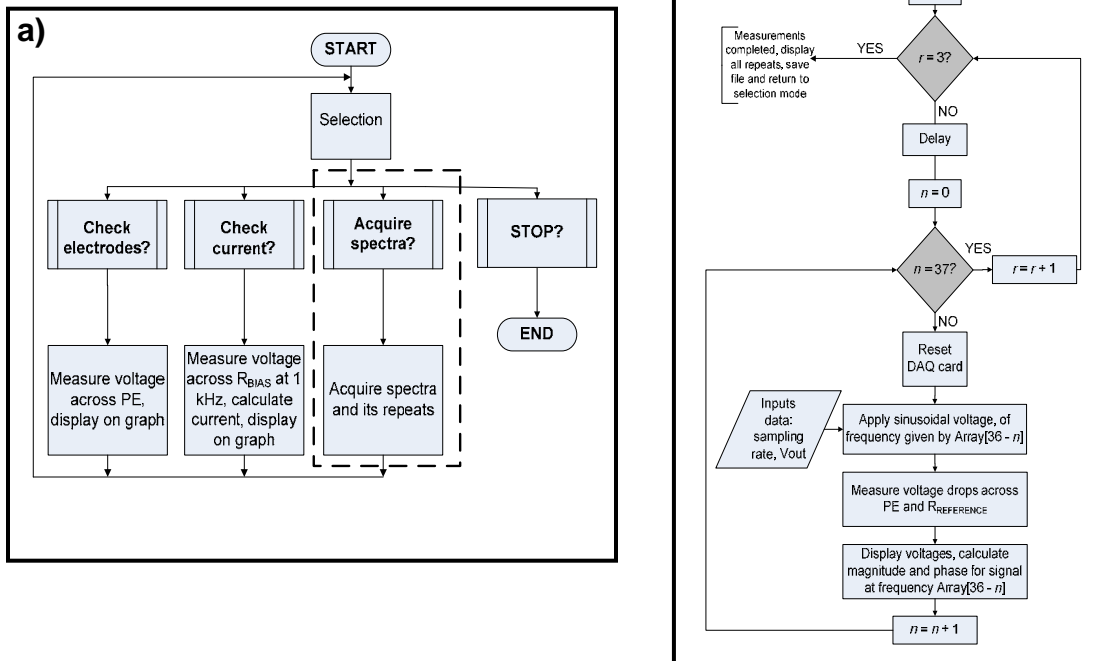
Figure 5.5. Flowchart for **a)** the SIP-IS measurement and control program, and **b)** the execution of spectral acquisition procedure following selection of the 'ACQUIRE SPECTRA' option.

Once these are initialized the current amplitude, and hence the current density can be checked by one of the options on the program ('CHECK I-LEVEL'). This option measures the voltage drop across the $R_{REFERENCE}$ for an applied sinusoidal signal at a frequency of 1 kHz and uses the simple Ohm's Law to transform the measured signal into current signal. The peak current amplitude is displayed, which depending upon the required value can then be changed by varying the amplitude of the applied voltage (V_{out} on the program). The measured current at this applied frequency (I kHz) allows an assessment of the maximum current, which will flow through the sample during measurement time. The other option, 'CHECK Ag|AgCl ELECTRODES' measures the voltage drop across the two potential electrodes when no measurements are being performed. This allows an assessment of any offsets or errors in the electrodes to be identified. Once these options are utilized, the 'ACQUIRE SPECTRA' option can then be chosen to conduct the SIP measurements, details of which are as follows.

The acquisition is conducted in an iterative manner, where measurements for each of the 37 frequencies in the range $10^{-1} - 10^{3}$ Hz, spread evenly over the logarithmic scale, are carried out one-at-a-time in a descending order. Firstly, there is a finite delay (programmable) which determines the delay between each repeat measurement. This is also encountered during the first measurement. After this delay period, the program enters a nested for-loop. Here, the DAQ card is reset, which effectively sets the analog output channel to 0 V and removes memory of prior applied voltages. Following this, a sinusoidal voltage signal at the frequency of interest is applied to the sample. This is conducted in order to energize the analog input channels to the voltage levels which will be measured. This is also optional as it was noticed that the presence of this feature makes no difference in measured voltages. After this stage, the analog input and output channels are configured according to the specified sampling rate, and amplitude of the applied voltage. In the present work, a sampling rate of 5 kHz was used for measurements. This satisfies the Nyquist criterion for the maximum frequency (1 kHz) of the signal to be measured and also avoids ghosting-effects usually encountered for high sampling rates. The applied voltage to the sample is a sinusoidal signal configured to generate two complete periods of data at the frequency of interest plus an extra 2 s of data, to compensate for a small and finite delay between read and write. Thus, the total length (in time) of the signal transmitted at each frequency, f was ($2/f + 2$) s. The output voltage is applied to the sample first, and the measurement of the voltage drops across the potential electrodes and across $R_{REFERENCE}$ follows with a finite delay, which is machine based (see Fig. B.1). This ensures that the cause-effect is satisfied, *i.e.*, measurements are not conducted before application of the current stimulus. Following these measurements, the current flowing in the sample and the voltage drop across the two potential

electrodes is displayed on the program. Phase angles for the current and voltage waveforms are then computed and their difference ϕ is calculated. The peak to peak levels of both waveforms are also computed to determine drift corrected (if present) current and voltage amplitudes, which are then transformed by the geometrical factor to determine the magnitude $|\rho|$. Following this, the process starts again for another frequency and continues until measurements at all 37 frequencies are completed. Once completed, the first set of measurement in terms of ϕ and $|\rho|$ spectra are displayed on a log-log plane. The routine then again begins the process starting from the delay to acquire another set of measurements. This is continued until the required numbers of repeat measurements have been conducted. Finally, upon competition of all repeats a dialogue allows saving the data file which consists of ϕ and $|\rho|$ spectra data for all repeat measurements as well as information on the sampling rates, and the peak amplitudes of the current and voltage waveforms. In this manner, all measurement and control of the SIP-IS system is carried out in LabVIEW. Analysis of all signals for extraction of phase and magnitude information are also conducted and saved by the program as described above, thus saving time on post processing of waveform data.

5.2.3 Measurement of Soil Samples

Samples of ~0.95 kg were taken from each of the saturated synthetic soils prepared (see Appendix A.1) and loaded into the sample holder one at a time and their spectral response was measured in the frequency range $10^{-1} – 10^{3}$ Hz. Before commencing measurements, a stabilization time of atleast 2 hrs was given during which time the soil sample inside the sample holder was allowed to attain steady state condition. To ensure reproducibility, each sample was measured three times, with a delay of ~10 min between each repeat. This was done to identify any possible non-equilibrated state of the saturated soil samples inside. For each new sample, a new pair of disposable Ag|AgCl electrodes was utilized. Cross contamination between samples was avoided by thoroughly washing the sample holder with deionized water between loading of each new sample. Hence, in the present work, a total of 45 SIP responses (inclusive of repeats) were acquired for the 15 synthetic soils. To minimize any external interference, all measurements were performed inside a Faraday cage. The laboratory set-up is shown in Plate 5.1.

For verification purposes, responses from known values of resistors and capacitors arranged in a network, as well as strong brine solutions were also measured. This was done to investigate the inherent responses which can arise from either the sample holder assembly or the data processing routines. Post data acquisition, the ϕ-spectrum for each sample was inverted to estimate the Cole-Cole

parameters The inversion program (used interchangeably with curve fitting) developed for this task is described in the next section.
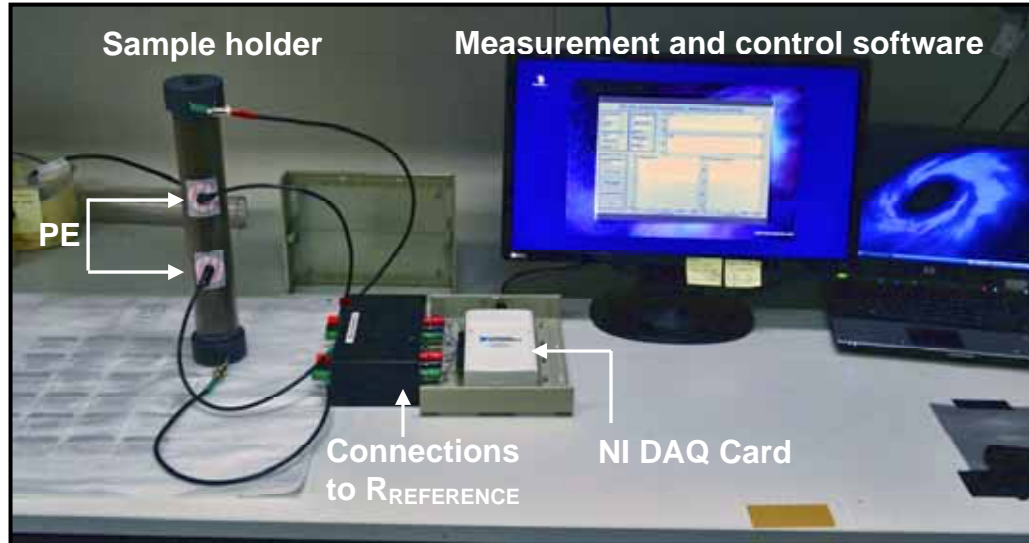
Plate 5.1. Laboratory apparatus for SIP measurement of soil samples. Note PE are potential electrodes.

5.2.4 Inversion of Phase Spectra

Measurements on soil samples indicated that a single Cole-Cole model described by Eq. 5.13 was sufficient to describe the ϕ-spectra in the frequency range studied in this work. Thus, in order to extract the three Cole-Cole parameters $\{m, c, \tau\}$ from the spectral responses of the soil samples, a program employing the Levenberg-Marquardt (LM) algorithm (see Appendix A.2) was developed in NI LabVIEW 2009 to invert the ϕ-spectrum. The choice of using the ϕ-spectrum for inversion here is based on the notion by Luo & Zhang (1998) that the Cole-Cole parameters from inversion of the ϕ-spectrum is generally very close to that of joint inversion of ϕ and $|\rho|$ spectra. It has also been pointed out by Luo & Zhang (1998) that reasonable restrictions on some parameters can be made in order to improve the efficacy of the inversion process. From the forward model for Cole-Cole dispersion (Eq. 5.13) it can be shown that the ϕ-spectrum is invariant with respect to ρ_{DC}. Hence, the following conclusions can be drawn:

a) the ϕ-spectrum is not unique to a single DC resistivity, *i.e.*, it's feature is solely due to the parameters that describe the surface conduction, *viz.*, m, c, τ.

b) as $\omega \to 0$, $\rho \to \rho_{DC}$, thus, a measured value of $|\rho|$ as $\omega \to 0$ can be reasonably regarded as the ρ_{DC} for the sample.

In the present work, it has been assumed that $|\rho(\omega)|$ at 0.1 Hz $= \rho_{DC}$ and is fixed at this value for each spectrum during inversion. In this manner, inversion is carried out to obtain the Cole-Cole

parameters, *i.e.*, *m*, *c*, τ only. The inversion program and its block diagram (codes) developed as part

of this work are given in Fig. 5.6 and Appendix B.2 respectively. Note the procedure used is similar

to the curve fitting routine discussed in the work reported in Chapter 4.
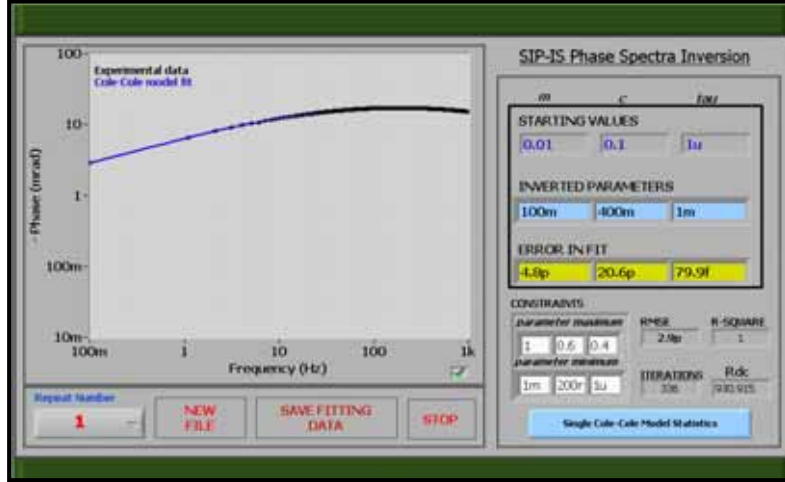
Figure 5.6. Inversion program for inverting the ϕ-spectra of soil samples in order to extract characteristic Cole-Cole parameters. Above inversion was for a theoretical spectra generated for *m* = 0.1, *c* = 0.4, $\tau = 10^{-3}$ s at an arbitrary value for ρ_{DC} = 930.915 Ω m.

The program utilizes the starting values input from the user to search for the best fit parameters.

Spectral data for a sample is loaded for each repeat measurement and the ϕ-spectrum and the $|\rho|$ at 0.1

Hz is acquired. Constrained fitting of the ϕ-spectrum is carried out iteratively using NI *Nonlinear*

Curve Fit LM bound subVI, minimizing the misfit function given by:

$$\chi^2 = \sum_{n=1}^{N} \left(\phi_n^{\mathbf{lab}} - \phi_n^{\mathbf{model}} \right)^2 , \tag{5.19}$$

where,

χ^2 = the chi-square,

N = number of data points, and

$\phi_n^{\mathbf{model}}$ = fitted value of the curve at *n*, and

$\phi_n^{\mathbf{lab}}$ = experimental value of the curve at *n*.

The model function implemented is the Cole-Cole model in its complete complex form, which is then

decomposed into its polar form to extract the $\phi_n^{\mathbf{model}}$ (see Appendix B.2). The non-weighted

summation is carried out over the entire dataset of the ϕ-spectrum. The final estimated parameters are

then displayed together with a graphical display of the experimental and fitted curves. Other statistical

parameters such as the root-mean-square-error (RMSE), r^2, and the number of iterations needed for

convergence are also displayed. Inversions which are successful are indicated on the graph. Success is achieved when the misfit function is minimized with acceptable tolerance within the maximum number of iterations (10000). Unsuccessful inversions are indicated by an 'X' on the graph. In such situations the starting values are varied until inversion process is successful. However, in the present work unsuccessful inversions were absent provided the starting values were reasonable. The standard errors for the final parameters are computed from the square-root of the diagonal elements in the final covariance matrix multiplied by the square root of SSE normalized with degrees of freedom (see Appendix A.2). This process was conducted for each repeat measurement separately. From the repeat measurements, the weighted means and weighted standard deviations for the Cole-Cole parameters were computed for each sample. For fast and efficient inversions, the starting values for the parameters were reasonably estimated from synthetic generated ϕ-spectra from the forward Cole-Cole model. Nevertheless, these starting values can also be estimated from the shape of the phase curve. The flowchart in Fig 5.7 summarizes the inversion routine scheme for understanding the basic dataflow.
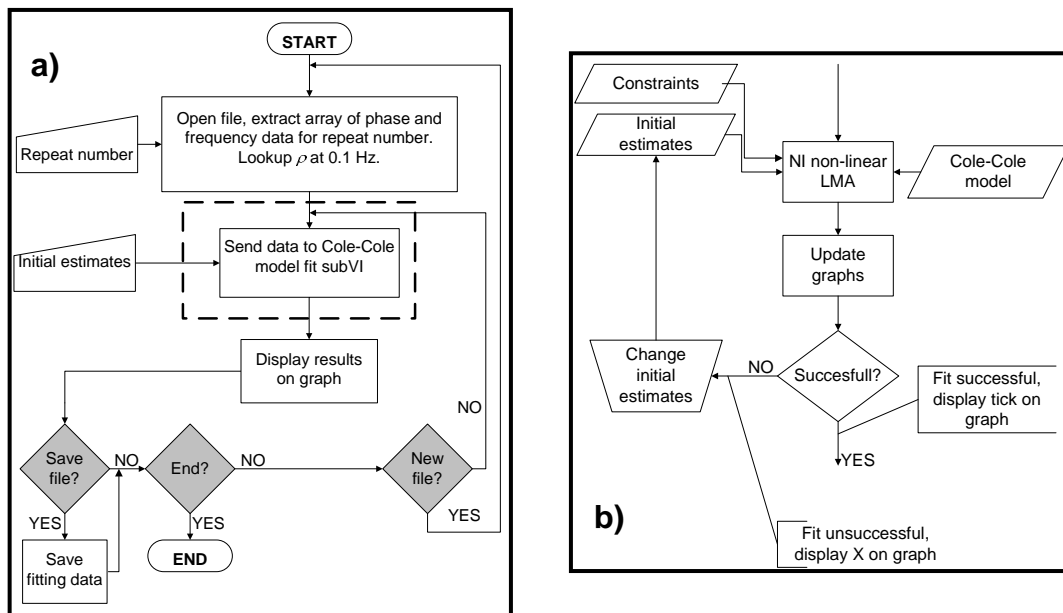
Figure 5.7. Flowchart showing **a)** the basic operation of the main inversion routine, and **b)** inside the Cole-Cole model fit subVI. For details see the block diagram in Appendix B.2.

5.3   Results and Discussions

In this section, an interpretation on the SIP responses as well as other electrical parameters of sand/clay mixtures at different pore fluid salinities is first presented. Importance of these characterizations in the context of assessing soil corrosivity is then discussed.

5.3.1 SIP-IS System Verifications

Before an integrated assessment of the SIP-IS system, the DAQ card with the measurement and control software was tested for their contributions to any distortions in the ϕ-spectrum. For this purpose, responses for networks of known values of resistors and capacitors were measured. Results from these exercises are presented in Fig. 5.8. Fig. 5.8a shows the response for multiple repeat measurements for a range of R_2 values generally between 2 k$\Omega \leq R_2 \leq 80$ kΩ, the upper end being greater than the maximum resistance of the sample (20 kΩ) measured in this work. Two important observations can be instantly made; a) there is no persistent significant system response in the frequency range $10^{-1} - 10^3$ Hz, and b) error response is generally ~0 mrad with maximum random responses <0.2 mrad attributed due to interferences and/or couplings in connecting wires. This is an important feature especially since the DAQ card performs non-simultaneous sampling. It follows that phase manifestation due to channel delays and/or connecting wires are low. Regarding the former, this is avoided through high density sampling as well as acquiring ($2f + 2$) complete cycles of waveforms for signals at frequency f, which are analyzed separately using Fast Fourier Transform methods (NI's *Extract Single Tone* subVI, see Appendix B.1) immediately after acquisition. This preserves signal integrity, which is lost when analysis is performed on saved files referenced to a common start time. Of course there are other methods, which can be used for channel delay corrections during post processing.
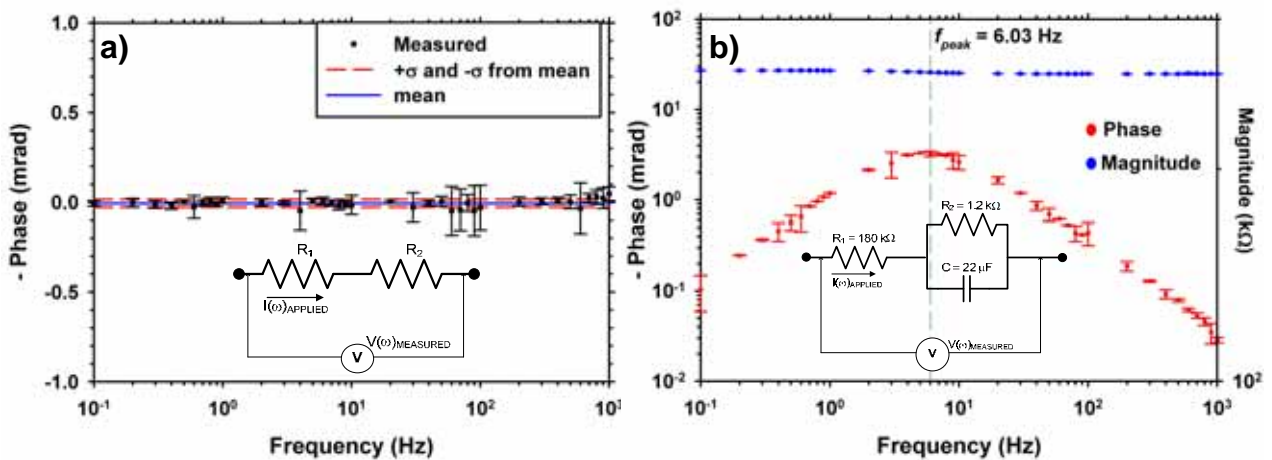
Figure 5.8. Phase response for **a) a** pure resistive network and **b)** an R-RC network.

Measurement of response for an R_1-R_2C network shown in Fig. 5.8b reveals the accuracy of the measurement and signal processing techniques used in this work. Signal processing techniques are able to resolve very small phase differences (<0.1 mrad) as shown. The relaxation peak is clearly visible in the mean phase response from three repeated measurements identifying the resonance frequency (6.03 Hz), at which the capacitive reactance of C, $X_c = R_2$. The magnitude response is also

128

given to demonstrate the correct measurement of resistance in the circuit. These measurements, although very important, do not incorporate errors arising from the sample holder assembly. To provide insight into the response arising from the integrated SIP-IS system, the phase response of a sand sample completely saturated with strong brine solution was measured and is given in Fig. 5.9.
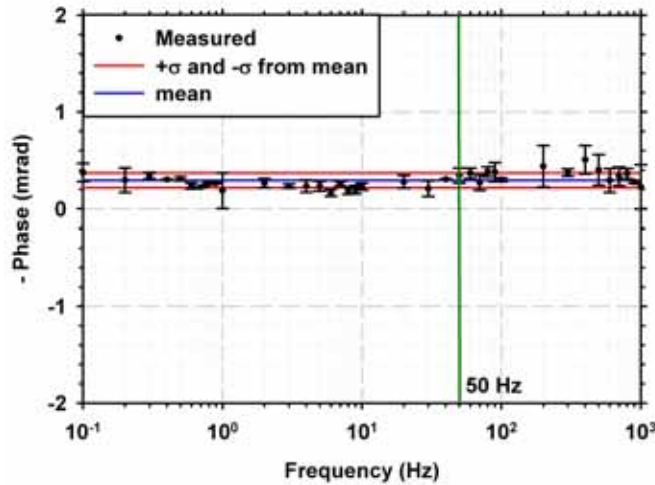
Figure 5.9. Phase response of sand completely saturated with strong brine solution.

The error bars correspond to $\pm\sigma$, computed from three sets of repeated measurements. The brine saturated clay-free sand simulates a pure resistive load, which ideally should not exhibit any polarizations. Thus, the presence of the phase artefacts measured in the frequency range $10^{-1} – 10^{3}$ Hz corresponds to polarizations, which can be attributed to the sample holder assembly incorporating the current and potential electrodes. In essence this represents the errors arising in the measurements [see Lesmes & Frye, 2001; Cosenza *et*. *al*., 2007]. For the SIP-IS system developed in this work, this error is equal to (0.29 ± 0.08) mrad in the frequency range $10^{-1} – 10^{3}$ Hz. It is meaningless to state the error of an error, thus the error can be stated as $\sim \pm 0.3$ mrad. This value compares well with errors reported in other studies [*e.g*., Lesmes & Frye, 2001; Cosenza *et*. *al*. 2007] for measurements of complex conductivities.

It is known that the phase responses of most sediments are generally low, typically <10 mrad or sometimes <1 mrad [Zimmermann *et*. *al*., 2008]. A characterization of the system error in this instance enables identification of sections of the response curve which are prone to noises. To investigate the performance of the SIP-IS system for a well defined phase response sample, a small stainless steel cylinder of diameter 15 cm and width 10 cm was placed inside a sand sample saturated with deionized water (DI) and its response was measured. The stainless steel cylinder was positioned in such a way that it lay between the two potential electrodes and concentric to the sample holder. The

phase response for this arrangement is illustrated in Fig. 5.10. Note, this particular response manifests from the electrode polarization mechanism, which occurs at the stainless steel/soil interface.
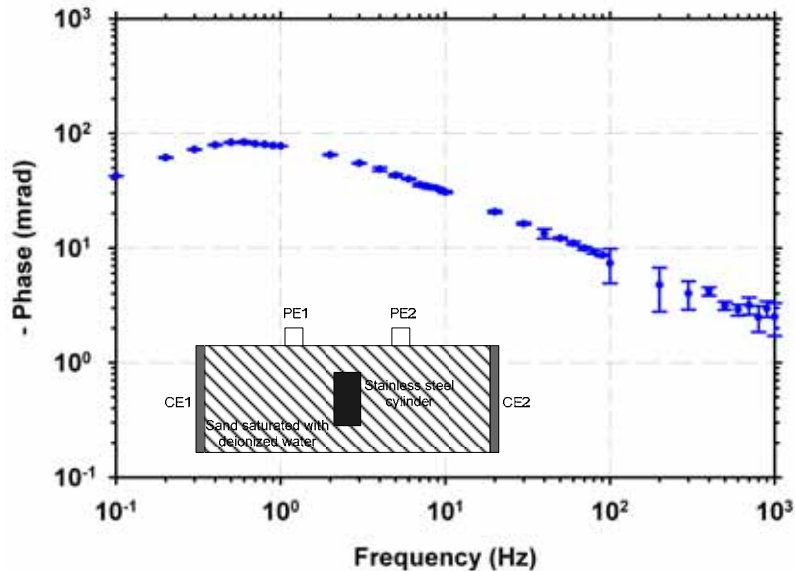
Figure 5.10. Phase response of a sand sample consisting of a stainless steel cylinder embedded between the potential electrodes (PE1 and PE2). Note the schematic shown.

Regarding the response shown in Fig. 5.10, two important remarks can be made regarding the system:

   a) the 3M™ Red Dot™ non-polarizable Ag|AgCl electrodes is robust in measurements of saturated samples as long as the contact is kept moist and not laden with water, and

   b) measurements have good reproducibility as indicated by the error bars corresponding to $\pm\sigma$, computed from three sets of repeated measurements.

Indeed, the well defined response due to electrode polarization shows good behaviour since the phase values are large. Unfortunately, such large phase values are not encountered in sediments with low polarizability [see Zimmermann *et. al.*, 2008]. Nevertheless, it is demonstrated in this section that the SIP-IS system allows reproducible measurements of samples. Verifications with a brine saturated sand sample demonstrates that the system is absent from significant inherent polarizations and any errors manifesting in the phase response is generally within ±0.3 mrad. In regards to the relatively small phase values measured for the sand/clay mixtures in this work, this is very important and will be discussed further in later sections.

5.3.2 Validations with Synthetic Spectra

In order to accurately extract Cole-Cole parameters from the phase response of various sand/clay mixtures studied in this work, it is imperative to ensure that the inversion procedures are sound. To demonstrate the effectiveness of the inversion scheme, several numerically generated ϕ-spectra mixed

with Gaussian noise were inverted and their true and estimated Cole-Cole parameters were compared. These spectra were generated for the same frequencies utilized during sample measurements. The results from this exercise are summarized in Table 5.1.

Table 5.1. Comparison of true and estimated Cole-Cole parameters obtained from inversion of different synthetically generated phase spectra.

Curve #	ρ_{DC} (Ω m)	True Cole-Cole parameters			Estimated Cole-Cole parameters		
		m	c	τ^*	m	c	τ^*
1	100	0.080	0.400	100	0.0814 ± 0.0072	0.3991 ± 0.0209	81 ± 31
2	100	0.080	0.420	1	0.0068 ± 0.0133	0.424 ± 0.0098	1.7 ± 1
3	100	0.004	0.452	205	0.004 ± 0.0001	0.4424 ± 0.0086	208 ± 20
4	100	0.002	0.512	5	0.002 ± 0.0002	0.5086 ± 0.0054	4.5 ± 1
5	100	0.040	0.435	54	0.039 ± 0.0031	0.4442 ± 0.0184	63.5 ± 20
6[**]	100	0.040	0.435	1	0.04 ± 10^{-7}	0.435 ± 10^{-7}	1 ± 10^{-12}

* - τ is in μs. ** - noise free spectra, error in fit is negligible but stated to demonstrate the accuracy.

The inversion mechanism determines three Cole-Cole parameters required to explain the shape of the ϕ-spectra at arbitrary values of ρ_{DC}, hence the values for the latter are irrelevant. Regarding the correspondence between the true and estimated parameters, a good agreement is observed. Indeed, in the absence of noises, the estimated and true values are equal (Curve# 6). However, the noises simulate the experimental conditions under which data is acquired. The inversion technique displays robust properties for extracting the small m and τ values in the presence of noises. This effectively provides validation to the inversion approach adopted in this work. The synthetic curves (with noises) and its model fit are given in Fig. 5.11 to demonstrate the effectiveness of the inversion routine to extract the Cole-Cole parameters in the presence of noise.
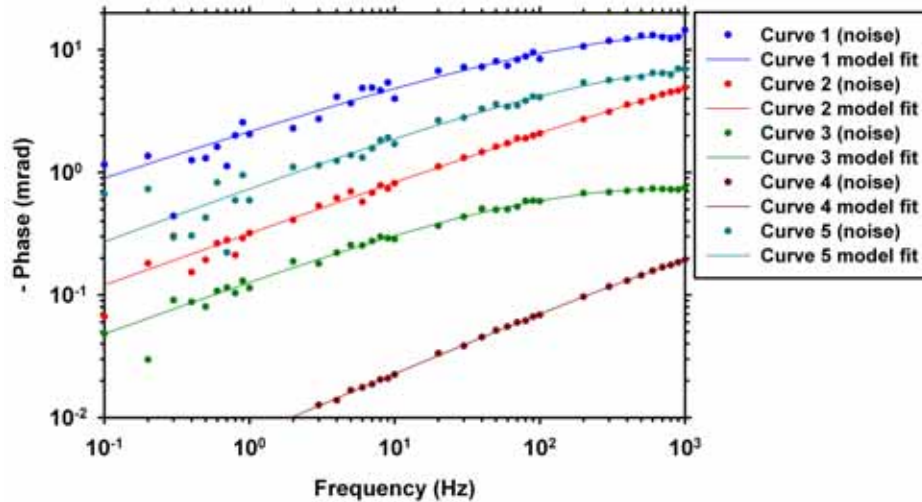
Figure 5.11. Fitting of Cole-Cole model to synthetically generated noisy ϕ-spectra.

5.3.3 SIP Responses of Sand Clay Mixtures

Results from SIP measurements on the various sand clay mixtures are presented in Fig. 5.12 – 5.16. For a coherent treatment of experimental results, the following organization is implemented. The mean phase and magnitude responses at particular clay content for different pore fluids are grouped together and shown. For each ϕ-spectrum, its model fit is calculated using the forward Cole-Cole model after computation of the weighted Cole-Cole parameters obtained from inversion. For soils saturated with 0.1M NaCl, measurement of phase values for frequencies <10 Hz, were prone to large errors. This is mainly because of the small phase values for these soils, which tend to approach system error (0.3 mrad) below 10 Hz. Consequently, this section of the spectra was truncated and not used in the inversion process. Nevertheless, the complete spectral data for each soil is given in Appendix B.3.
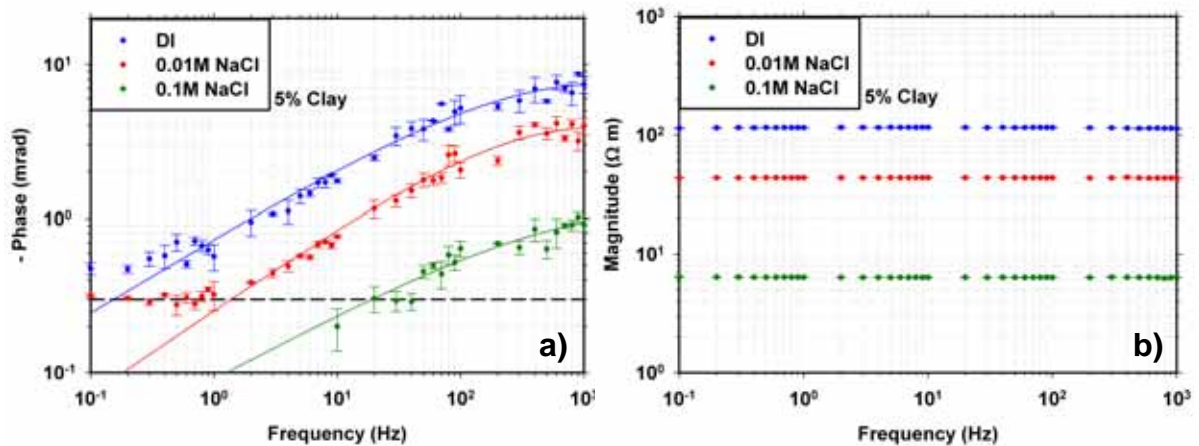
Figure 5.12. Phase (**a**) and magnitude (**b**) spectra for soils with 5% clay content saturated with different pore fluids.
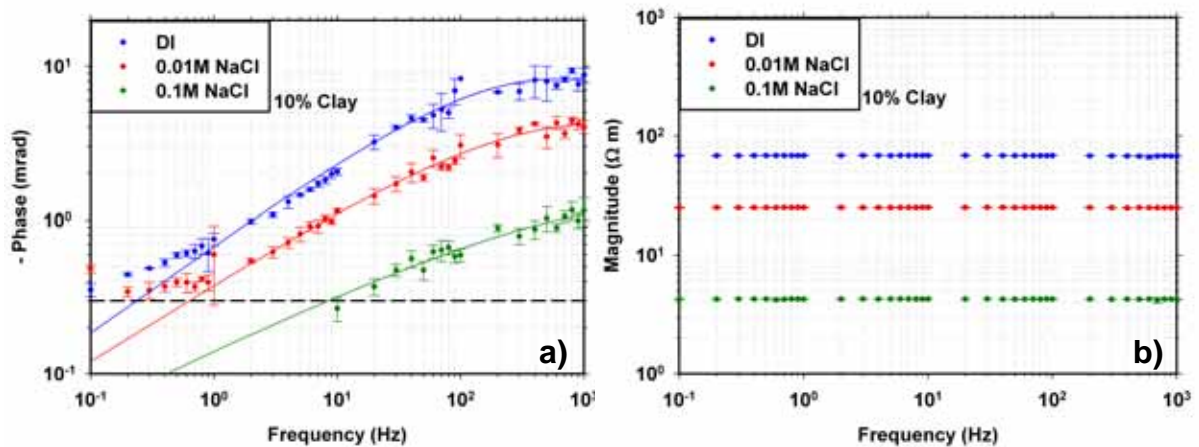
Figure 5.13. Phase (**a**) and magnitude (**b**) spectra for soils with 10% clay content saturated with different pore fluids.
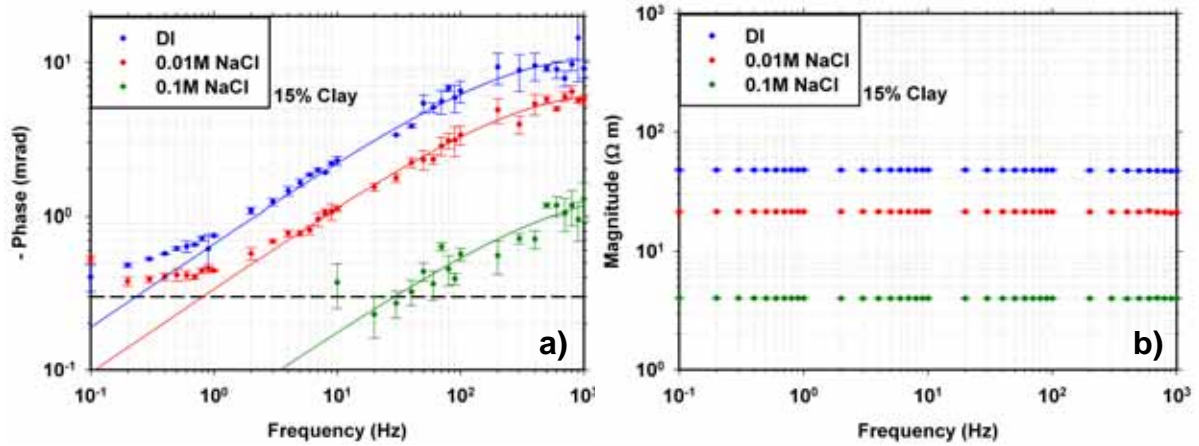
Figure 5.14. Phase (**a**) and magnitude (**b**) spectra for soils with 15% clay content saturated with different pore fluids.
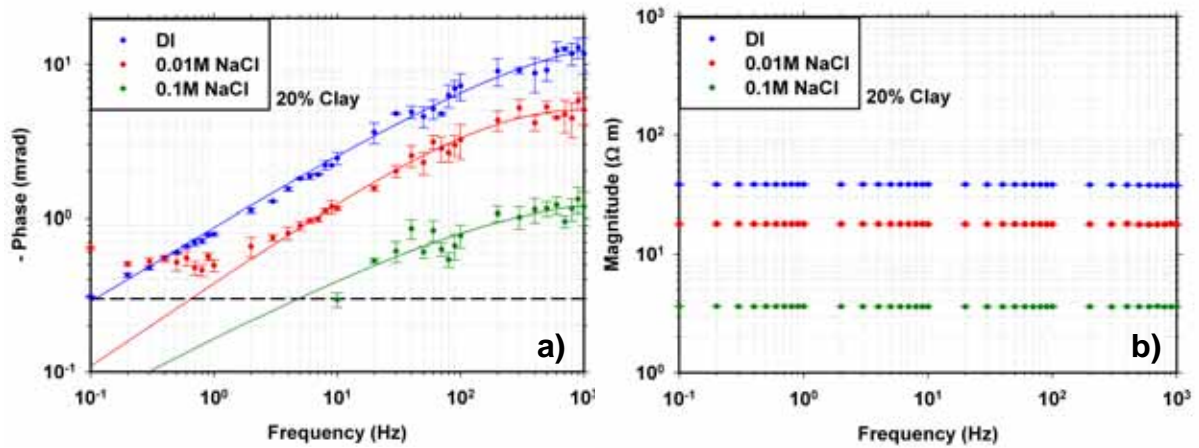
Figure 5.15. Phase (**a**) and magnitude (**b**) spectra for soils with 20% clay content saturated with different pore fluids.
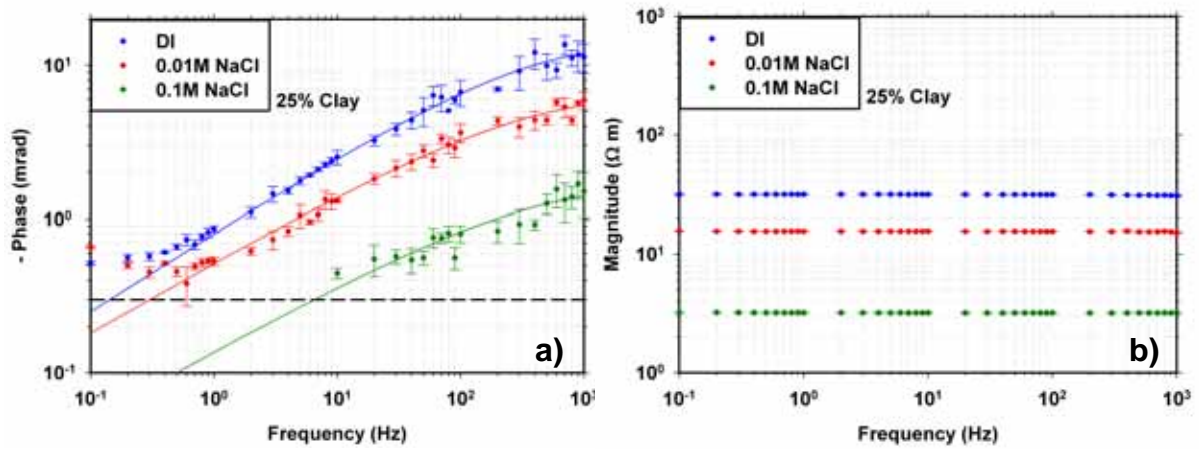
Figure 5.16. Phase (**a**) and magnitude (**b**) spectra for soils with 25% clay content saturated with different pore fluids.

Firstly, it is noted here that as ϕ approaches the system error (~0.3 mrad), errors in the ϕ-spectra begin to manifest forcing deviations from pure Cole-Cole behaviour at the lower ends of the frequency spectrum. As such, the uses of these sections of the spectra were strictly constrained during inversions as will be discussed in the next section. Error bars for each measurement also indicate the importance of an equilibrated state of the saturated soils during measurements. Unlike rocks, soils do not possess a solid matrix under saturated conditions. The dynamic collapse and re-creation of pores and kinetics of pore fluids during the measurement procedure contribute to perturbations in the responses. However, with the ~10 min delays between repeat measurements in the work, both (phase and magnitude) spectra reveal good repeatability confirming a quasi-equilibrated state of the soil samples. Results indicate that phase spectra are depressed with increasing pore fluid salinities for all soils at fixed clay contents. Because of this behaviour, accurate phase measurements of soils saturated with 0.1M NaCl become difficult. All spectra exhibit similar features, consistent with the fact that the same sand and clay are used in all synthetic soils. Observations made here are consistent with the simulations of Volkmann & Klitzsch (2010), who have shown that a decreasing SIP effect occurs with increasing electrolytic concentrations in pore fluids [see also Lesmes & Frye, 2001]. The ϕ-spectra acquired in this work bears resemblance with those reported by Boadu & Seabrook (2006) whereby they measured the SIP responses of sand clay mixtures under applied stress with variations of 0%, 5%, and 10% of the latter saturated with freshwater, 0.01M NaCl, and 1M NaCl. Following corrections for spurious polarizations from steel potential electrodes, their results exhibited similar features below ~10^3 Hz, while there was an indication of MWS effect at higher frequencies. However, Boadu & Seabrook (2006) did not make any distinctions as such and interpreted their results using the model by Dias (2000).

The effect of pore fluid salinities on the magnitude spectra is also well observed at all clay contents. Increasing clay content at a fixed pore fluid salinity also gave small enhancements of the phase spectra, *i.e.*, SIP effect increases. To enable a systematic interpretation of the results presented here, the coupled effect of clay and salinity are evaluated in terms of the electrical properties, as well as the Cole-Cole parameters, in the next section.

5.3.4 Effect of Clay and Salinity on Soil Electrical Properties

Inversions of each single ϕ-spectrum for obtaining the Cole-Cole parameters were performed under constrained conditions. In particular the *c* value was constrained to fit within 0.4 – 0.6, which is within the range often encountered for geological materials [see Kemna, 2000]. This approach also allowed the influences from deviations in ϕ values for soils saturated with deionized water and 0.01M

NaCl at the low end of the frequency spectrum to be controlled. For soils saturated with 0.1M NaCl, sections of the spectra corresponding to <10 Hz were truncated during the inversion process. This was necessary to eliminate high level of noises present in the spectra due to the already small SIP effects in these samples. Note that the maximum ϕ values measured for these soils were ~1 mrad at 10^3 Hz. However, for completeness spectral data for each sample are given in Appendix B.3, while Appendix B.4 presents the Cole-Cole parameters from inversion on each repeated measurement of the samples. For the discussions which follow, Table 5.2 summarizes the weighted Cole-Cole parameters for each sample computed from repeat analysis along with other electrical characterizations.

Table 5.2. Summary of Cole-Cole parameters and other electrical properties of the sand clay mixtures. Details of samples can be found in Appendix A.1.

Sample	Pore fluid resistivity	Sample DC resistivity	Apparent formation factor	- $\phi_{1\,Hz}$	Cole-Cole parameters		
	ρ_W (Ω m)	ρ_{DC} (Ω m)	F_a ($\times 10^{-3}$)	(mrad)	m ($\times 10^{-3}$)	c	τ (μs)
A5	7300	114.1 ± 0.3	15.63 ± 0.04	0.73	31 ± 3	0.489 ± 0.036	93.1 ± 38.8
A10	7300	67.9 ± 0.4	9.3 ± 0.05	0.68	34 ± 2	0.504 ± 0.023	220.2 ± 51.5
A15	7300	47.6 ± 0.2	6.52 ± 0.03	0.66	34 ± 1	0.6 ± 0.001	227.7 ± 37.9
A20	7300	38.1 ± 0.1	5.22 ± 0.01	0.87	45 ± 2	0.6 ± 0.001	113.8 ± 49.4
A25	7300	31.4 ± 0.1	4.3 ± 0.01	0.80	47 ± 6	0.634 ± 0.041	85.9 ± 39
B5	8.25	43.4 ± 0.1	5260 ± 12	0.25	15 ± 1	0.6 ± 0.0001	176.6 ± 29.2
B10	8.25	24.8 ± 0.2	3006 ± 24	0.38	18 ± 1	0.509 ± 0.027	109.9 ± 31
B15	8.25	21.2 ± 0.01	2569 ± 1	0.34	24 ± 2	0.564 ± 0.03	108.9 ± 30.1
B20	8.25	17.9 ± 0.04	2169 ± 5	0.38	24 ± 4	0.596 ± 0.01	201.1 ± 31.5
B25	8.25	15.6 ± 0.04	1890 ± 5	0.52	25 ± 1	0.510 ± 0.020	115.9 ± 38.1
C5	1.01	6.42 ± 0.02	6356 ± 20	0.09	6 ± 1	0.4 ± 0.0001	22.4 ± 12.9
C10	1.01	4.26 ± 0.02	4217 ± 20	0.14	7 ± 0.2	0.427 ± 0.027	38.4 ± 7.3
C15	1.01	4.02 ± 0.01	3980 ± 10	0.05	7 ± 0.1	0.5 ± 0.0001	26.7 ± 2.9
C20	1.01	3.63 ± 0.01	3594 ± 10	0.16	8 ± 0.1	0.4 ± 0.0001	56.1 ± 16.1
C25	1.01	3.21 ± 0.001	3178 ± 1	0.14	9 ± 0.1	0.465 ± 0.024	32.6 ± 4

Note the scaling factor for F_a in Table 5.2. The - $\phi_{1\,Hz}$ corresponds to the phase of the sample at 1 Hz, and is computed from the forward Cole-Cole model after inversions. This is necessary due to the difficulty in measuring ϕ below 10 Hz for soils saturated with 0.1M NaCl. Thus, for consistent treatment, ϕ values for all soils are reported in this manner. Several important observations can be made regarding the various electrical parameters reported in Table 5.2. With regards to the parameter c, the results vary between $0.4 – 0.6$, which is reflective of the constraints it was subjected to.

Firstly, the chargeability, *m* parameter for all samples is <0.1, which is characteristic of non-metallic saturated samples. The range of chargeabilities for samples saturated with DI, 0.01M NaCl, and 0.1M NaCl are (0.031 – 0.047), (0.015 – 0.025), and (0.006 – 0.009) respectively. It is seen to vary with clay content as well as with salinity, the latter producing the strongest effect as illustrated in Fig. 5.17a.
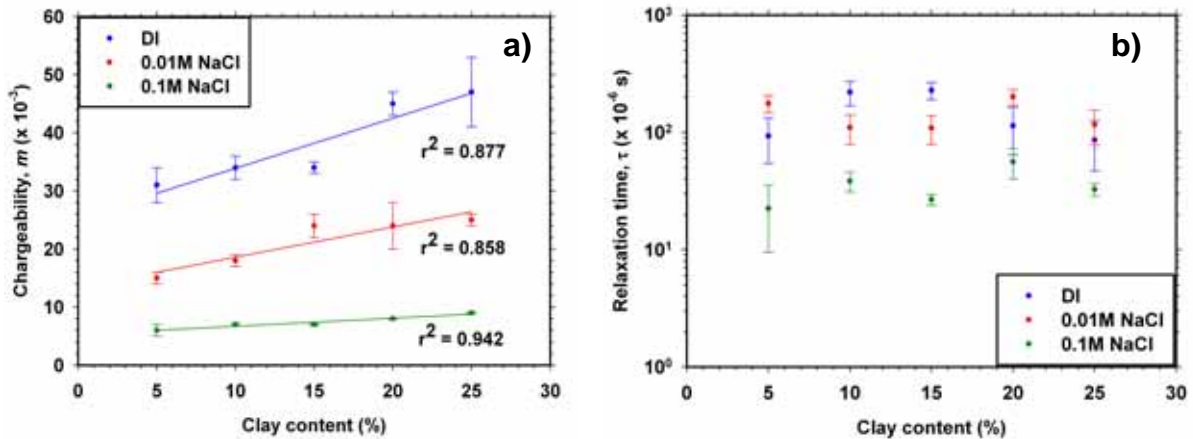
Figure 5.17. Variations in (**a**) chargeabilities and (**b**) relaxation time with clay content and different pore fluids.

Samples saturated with deionized water (DI) exhibit a strong increase in *m* with increasing clay content in the range 5-25%. This behaviour becomes weaker as the salinity of the pore fluid increases, which also drastically reduces *m*. Regression analysis reveal good dependence between clay content and *m* for all pore fluids albeit there are indications that at higher salinities, increase in clay content has minimal effect on *m*. Chargeability depends upon the distribution of polarizable elements in soil, in this case the number of clay particles, which leads to a direct relationship between clay content and chargeability. An essential requirement for this behaviour is also that the clay particles remain dispersed within the soil matrix and do not flocculate and achieve contiguity. It shall be noted here that the water content in each soil is not constant but varies depending upon the amount of clay present (see Appendix A.1). Most importantly, it is observed that the chargeability profile illustrated in Fig. 5.17a clearly distinguish between varying clay and salinity. The relaxation time, τ displays similar values within errors, for samples saturated with DI and 0.01M NaCl. This is somewhat expected [*e.g*., Boadu $ Seabrook, 2006] since the size of the sand and clay particles are the same in all samples. However, with pore fluid as 0.1M NaCl (salinity of 1.01 Ω m) τ is notably reduced by a magnitude. This reduction suggests there is some influence of pore fluid chemistry on the relaxation processes. Indeed, Klein & Sill (1982) showed that fluid conductivity has some control on τ, whereby the effect is stronger in medium-fine grain size samples relative to fine grain size samples. However,

Kruschwitz *et. al*. (2010) suggest that pore fluid chemistry has second-order effects on relaxation time. It follows that the saline pore fluid will depress the electrical double layer leading to a reduction in the effective relaxation diffusion length, *L* in pore throats. Since the relaxation time is proportional to *L* [see Titov *et. al*., 2002], a reduction in τ is observed.

Overall, the Cole-Cole parameters, *viz*., *m* and τ are observed to provide some indications on clay content and salinity variations in soils. However, the former displays a stronger ability to distinguish clayey and saline samples than the latter. The use of this parameter for assessing potential soil corrosivity will be discussed later. The resolution of the relaxation time in terms of its ability to change with varying clay contents is poor, although there are indications that it has some capability to indicate relatively strong saline samples. Other parameters which reveal strong correspondence with clay content and salinity are the DC resistivity (ρ_{DC}) and apparent formation factor (F_a), which are illustrated in Fig. 5.18.
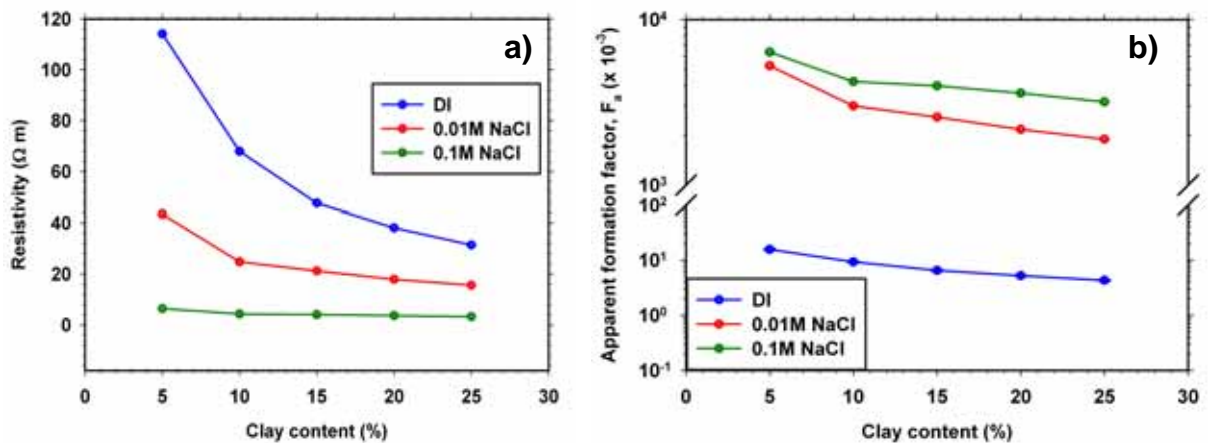
Figure 5.18. Variations in (**a**) DC resistivities and (**b**) apparent formation factor with clay content and different pore fluids. Note, error bars are too small to register.

Contrary to chargeability variations, ρ_{DC} exhibits inverse relationships with clay content and salinity. Under conditions of very low salinity (DI = 7300 Ω m), an increase in clay content from 5% to 10% leads to a strong reduction in ρ_{DC}. However, upon further addition of clay, the ρ_{DC} appears to asymptote towards a limiting ρ_{DC}, a feature which is present across all pore fluid concentrations. It follows that the addition of clay particles increases the interconnected pore structure and allows greater conduction pathways leading to attenuated resistivities. However, the asymptotic resistivity feature also indicates that there is an optimal pore structure beyond which any further increase in clay will have minimal effect on resistivity. On the contrary, the initial strong reduction in ρ_{DC} due to increase in clay content from 5% to 10% becomes weaker when the samples are saturated with 0.01M

and weakest with 0.1M NaCl albeit the asymptotic features still appear. The pore fluid consisting of the dissolved ions are the dominant carriers of electrical current in saturated samples. As the salinity of the pore fluid increases, there are more electrical current carriers leading to enhanced conductivities and hence reduced resistivities. The absence of any strong clay effect on ρ_{DC} for samples saturated with 0.1M NaCl is symptomatic of a stronger salinity control on resistivities due to enhanced levels of dissolved ions. With regards to the apparent formation factor, F_a, similar trends as with ρ_{DC} are observed. Of course this is expected since F_a is directly proportional to ρ_{DC}. However, F_a displays increasing values with increasing pore fluid salinities. This also indicates that F_a is not the intrinsic formation factor, F of the sample. Usually, F can be determined with strong pore fluid salinities such that $\sigma_{bulk} \gg \sigma_{surf}$. At other salinities, such as those used in this work, only the apparent formation factor can be calculated since surface conductivity mechanisms are present. Nevertheless, F_a exhibits variations with clay content as well as with relatively low saline fluids. This effectively indicates a strong possibility of using F_a for potential soil aggressivity assessments.

The other important parameter is $-\phi_{1\,Hz}$. Slater *et. al.* (2006) suggests that $\sigma''_{1\,Hz}$ is a measure of polarization magnitude. Since $\sigma''_{1\,Hz} \approx \phi_{1\,Hz}$, it follows that $-\phi_{1\,Hz}$ can also be used as a measure of polarizability. Following this notion, the variations of $-\phi_{1\,Hz}$ with clay content and salinity are illustrated in Fig. 5.19a.
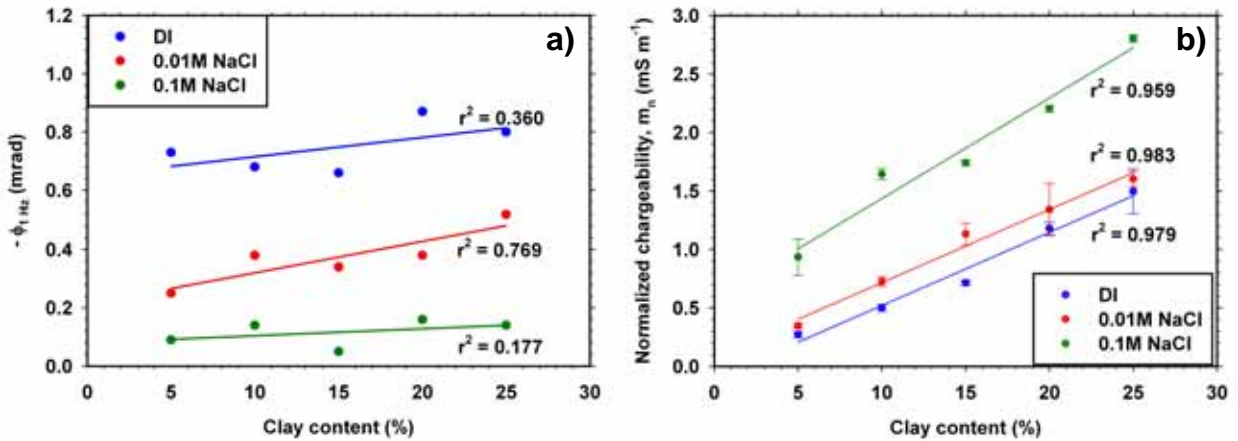
Figure 5.19. Variations in (**a**) $-\phi_{1\,Hz}$ and (**b**) normalized chargeability with clay content and different pore fluids.

The $-\phi_{1\,Hz}$ is seen to correspond to an extent with increasing clay content in the range 5-25%, although regression analysis reveals weak dependence of $-\phi_{1\,Hz}$ with clay content for samples saturated with deionized water and 0.1M NaCl. The lowest regression is observed for the latter ($r^2 = 0.177$). This is mainly due to the fact that at high salinities, the $-\phi_{1\,Hz}$ exhibits quasi-constant dependence with clay

content in the range 5 – 25%. This behaviour arises from the enhanced presence of dissolved ions in the pore fluid giving rise to stronger conduction control by pore fluid rather than clay content. Indeed, as shown earlier, ρ_{DC} also displays a relatively weak dependence on clay content when saturated with 0.1M NaCl. However, it is worthy to note that a variation in pore fluid salinity does affect the magnitudes of $-\phi_{1\ Hz}$. This is consistent with the vertical depression of the ϕ-spectra with increasing pore fluid salinity as already illustrated for Fig. 5.12 – 5.16. Discussions so far have revealed that clay and salinity have a coupled effect [see Boadu & Seabrook, 2006] on soil SIP responses. There are instances in which clay has a strong effect on controlling a certain parameter, *e.g.*, m and ρ_{DC}, while in some cases the bulk effect due to salinity masks any strong perturbations caused by clay. To normalize the bulk conduction effects, Lesmes & Frye (2001) suggested the use of a normalized chargeability, m_n (sometimes abbreviated as *MN*), which is simply the chargeability normalized by the ρ_{DC} (see Chapter 3, section 3.3.2). This m_n is considered to be a global measure of polarizability [Slater & Lesmes, 2002] directly related to the complex surface conductivity processes. Variations in m_n for the sand clay mixtures studied in this work are illustrated in Fig. 5.19b. Two important observations can be made regarding these variations:

a) m_n shows strong linear dependence with clay content ($r^2 > 0.95$) regardless of pore fluid salinity. Of course this feature is present in variations of m with clay content also (Fig. 5.17a). However, unlike m, m_n shows stronger increases with clay content even in the presence of 0.1M NaCl pore fluid.

b) m_n is seen to increase with increasing pore fluid salinity; a feature directly opposite to that exhibited by variations in m.

The direct relationship between m_n and clay content corresponds to the overall increase in polarizability of soils with increasing polarizable elements (clay particles). Indeed, Slater *et. al.* (2006) has shown that m_n bears a direct relationship with specific surface area to pore volume ratio (S_p). An increase in m_n with pore fluid salinity is consistent with the work on Berea sandstones by Lesmes & Frye (2001), who showed that m_n tends to increase with pore fluid salinity up to 0.1M NaCl, beyond which they tend to decrease. In this work the maximum pore fluid salinity corresponded to the limiting value (0.1M NaCl) of their work, and hence the observed increases. According to Lesmes & Frye (2001), the increasing m_n with pore fluid salinity up to a limiting value arises due to an increase in surface conductivity resulting from enhanced surface charge densities in the presence of high concentrations of dissolved ions.

In the previous section the SIP responses were presented and some qualitative assessments were made on the ϕ-spectra. In this section, the ϕ-spectra have been used to obtain and assess quantitative

information in terms of the Cole-Cole parameters. Specifically, the chargeability parameter has been identified to very well differentiate between clayey and saline samples. Moreover, the normalized chargeability parameter is seen to have strong dependence on clay content as well as salinity (within the range studied in this work). Apart from these, the ρ_{DC},, F_a, also reveals good dependence on clay and salinity. Observations made here reveal that there are now several parameters which could be used diagnostically to identify potential corrosivity. These are investigated further in the next section.

5.3.5 Soil Spectral Response and Potential Corrosivity

The standard procedure for assessment of soil corrosivity using resistivity determinations is covered by the ASTM G57-95a (2001) document. It suggests the use of conventional Wenner array methods for determination of *in-situ* soil resistivity using AC sources at 97 Hz. For laboratory measurements, it suggests the use of a conventional four-electrode soil box method whereby the soil resistivity is determined under completely saturated (slurry) conditions in order to ascertain the minimum resistivity of the sample. The target of the present work is to extend the paradigm of this electrical characterization of laboratory samples under completely saturated conditions. Apart from ensuring minimum resistivity conditions, measurements under completely saturated conditions define a common reference along which different soil samples can be compared. To provide an investigation into the connections between different soil electrical properties and potential corrosivity, measurements of polarization resistance R_p conducted in the previous chapter for cast iron-soil and wrought iron-soil systems are investigated for any possible relationships with the electrical parameters measured in this work.

Firstly, determinations of soil resistivity from galvanostatic pulse measurements are compared with the resistivities measured in this work. Here soil resistances measured for all three systems (mild-steel/soil, cast-iron/soil, and wrought-iron/soil) during Day 1 are corrected for length of protrusion (~10 mm) by the reference electrode and converted to resistivity values using the known geometrical factor. These results are presented in Fig. 5.20. The error bars correspond to $\pm\sigma$ from the mean soil resistivities measured in the three different systems (inclusive of mild-steel/soil system).
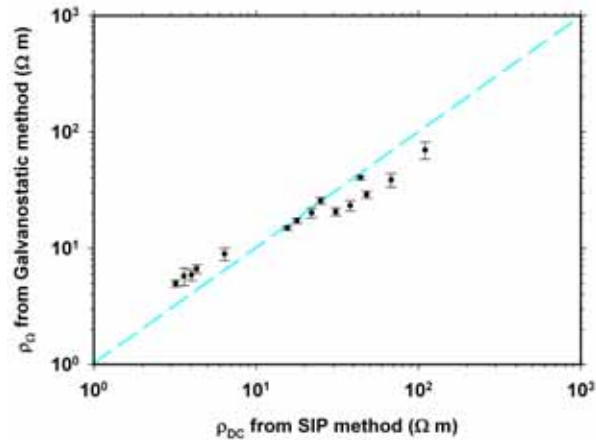
Figure 5.20. Comparison of soil resistivities measured using galvanostatic and SIP methods. Dashed line corresponds to the ideal situation when both methods yield the same resistivities.

Generally, a good correspondence between the soil resistivities determined using the two different techniques are observed providing cross validation. Soils saturated with deionized water show relatively higher deviations from the ideal condition. It shall be noted here that the soil samples in the two different measurements were exposed to two different conditions. In galvanostatic pulse measurements (GP), the soils were exposed in open air for 2 hours, while in SIP measurements the soils were allowed to settle inside the tight sample holder for the same duration. Moreover, the quantity of samples in the two methods was significantly different, *viz.*, 25.1 cm^3 in GP and 235.6 cm^3 in SIP. Thus, variables such as different rates of moisture loss, paths of least resistance between reference and working electrodes especially in soils absent of dissolved salts in GP methods can result in characteristic resistivity differences. Another important observation from SIP measurements is that the relaxation time in all the soils studied in this work is <1 ms under saturated conditions. This provides complementary validation to the criterion in the GP method that the time constant related to the relaxation processes in soils are very small. In fact they are smaller than the sampling resolution (1 ms) in GP methods. Moreover, soil capacitances in dryer conditions are very small since the dielectric constant gets significantly reduced in the absence of water [see Hillel, 2004]. This effectively results in the quasi-instantaneous jumps observed on the GP methods on Day 7, *i.e.*, capacitive effects from soil bulk properties are negligible.

In the previous chapter, following experimental results it was suggested that potential soil corrosivity should be assessed in terms of a) the ability of the soil to retain water over long periods of time, *i.e.*, the clay or fines content, and b) the amount of dissolved salts present, which can also be affected by clay content. Qualitatively, it can be seen that the ϕ-spectra from SIP measurements can be used to isolate these two features amongst soils. It is reasonably seen that clay content enhances the ϕ-spectra

141

(upward vertical translation), while increasing salinity leads to depression of ϕ-spectra (downward vertical translation). This simple ability to delineate clayey and salinity effects lays the foundation for the use of SIP measurements in soil corrosivity assessments.

The first relationship investigation between SIP measurements and soil corrosivity is between the ρ_{DC} and R_p, illustrated in Fig. 5.21.
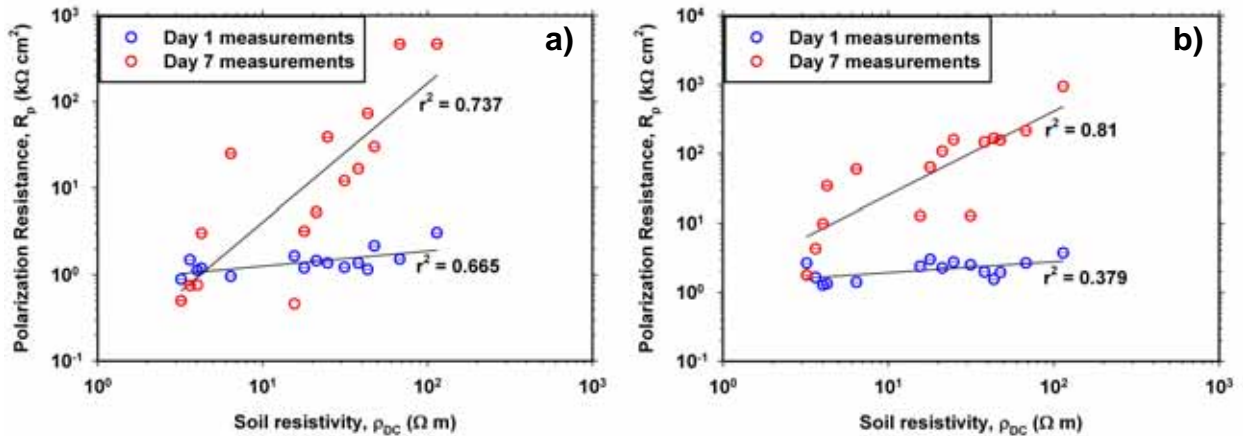
Figure 5.21. Variations in R_p for Day 1 and Day 7 and its relationship with soil ρ_{DC} measured under completely saturated conditions for **a)** cast-iron/soil and **b)** wrought-iron/soil systems.

Here, the ρ_{DC} is determined only under completely saturated conditions and compared with R_p values for the two metal-soil systems determined on Day 1 and 7. Good correspondence is observed between the two variables. On Day 1, R_p shows fair regression with ρ_{DC} on log-log plane in both cast-iron/soil (r^2 =0.665) and wrought-iron/soil (r^2 =0.379) systems. However, this feature becomes stronger on Day 7, whereby r^2 of 0.737 and 0.81 are observed in the two aforementioned systems respectively. The difference in the behaviour can be attributed to the kinetics of corrosion on the two different days. On Day 1, corrosion proceeds faster on the freshly exposed metal surfaces aided by the presence of high moisture contents. On the contrary, the reactions get impeded by Day 7 due to the loss of moisture from the soil and changes on the metal surfaces. Since the loss of moisture depends upon the clay content of soil, soil properties exert a second-order effect on the corrosion process on Day 7. Thus, the ρ_{DC}, which is a characteristic property of soil, shows prominent correspondence with Day 7 R_p values. Nevertheless, the important observation here is that the determination of ρ_{DC} at a single referenced condition enables identification of soils with potentially high corrosiveness, *viz.*, lower ρ_{DC} corresponds to relatively higher corrosive soils. Of course, this characterization is the standard practice of assessing soil corrosiveness currently utilized. A more detailed characterization

procedure, however, is achieved with the use of m_n measured under completely saturated conditions. Analysis of m_n with R_p revealed striking ln-ln relationships, which are given in Fig. 5.22.
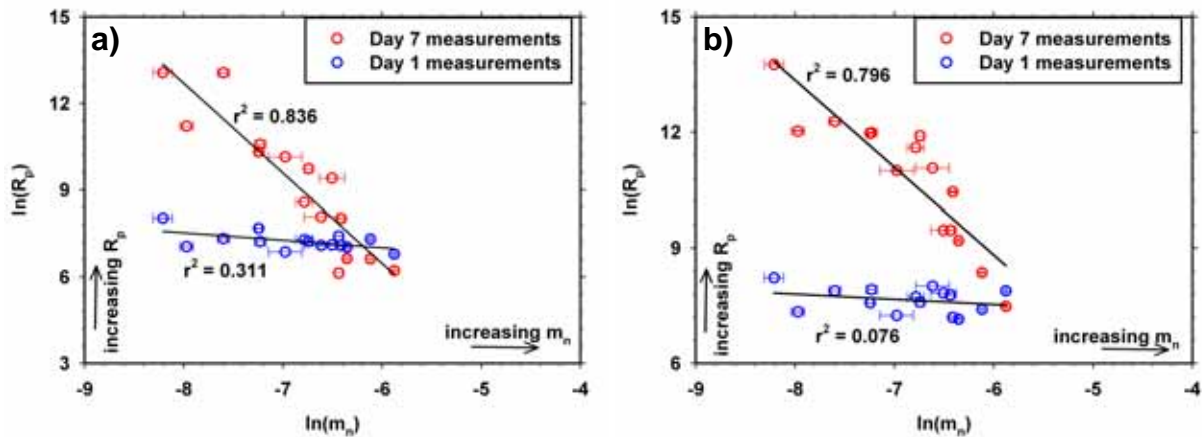
Figure 5.22. Variations in $\ln(R_p)$ for Day 1 and Day 7 and its relationship with $\ln(m_n)$ measured under completely saturated conditions for **a)** cast-iron/soil and **b)** wrought-iron/soil systems. Natural logarithms of R_p computed after conversion to units of Ω cm^2.

Plots of $\ln(R_p)$-$\ln(m_n)$ reveal some important observations, which are as follows. Correspondence between $\ln(m_n)$ and Day 1 $\ln(R_p)$ values reveal weak inverse relationship in both the cast-iron/soil ($r^2 = 0.311$) and wrought-iron/soil ($r^2 = 0.076$) systems. However, these relationships increase dramatically on Day 7, whereby r^2 of 0.836 and 0.796 are observed in the cast-iron/soil and wrought-iron/soil systems respectively. To explain these features, the following is noted. The R_p measurements on Day 1 and 7 revealed that clay effects were absent in the former, while it was significantly observed in the latter. Corrosion on Day 1 proceeded with strong presence of abundant moisture aided by salinity variations on freshly exposed metal surfaces. However, loss of moisture through to Day 7 allowed soil properties to manifest in the corrosion process. The weak correlations on Day 1 indicate the weak influence of soil (grains) on the overall corrosion process. Comparatively, the relatively higher correlations between ρ_{DC} and R_p on Day 1 are indicative of the strong salinity influences of the pore fluid as captured by the former. However, on Day 7 the clay and salinity effects are both present strongly. This constitutes the strong relationship between m_n and R_p on Day 7. Note, these influences are also captured by ρ_{DC}, but the normalized chargeability provides information on the overall soil properties and explains the coupled clay and salinity effects better because of its ability to contrast electrolytic and structural factors in soils. It shall be noted here that for high saline soils, m_n may exhibit reduced values [see Lesmes & Frye, 2001]. However, high saline soils can be identified by measurement of ρ_{DC} alone avoiding the need for any further assessments. The present scope of characterization using m_n allows segregation of corrosive and non-corrosive soils with low to

moderate levels of dissolved salts. Similar to ρ_{DC} assessments, it is observed here that the characterization of m_n under completely saturated conditions allows identification of potential soil corrosivity. Higher normalized chargeabilities correspond to relatively more corrosive soils. Most importantly, it is seen that the long term corrosion sustainability property of soil, arising due to coupled clay salinity effects, can be better evaluated from m_n measured under completely saturated conditions.

Other soil parameters exhibiting significance with clay content and salinity are F_a and $-\phi_{1\ Hz}$. Cross-plots of F_a with $-\phi_{1\ Hz}$ and ρ_{DC} provides information on different features of soil properties as illustrated in Fig. 5.23. The $(-\phi_{1\ Hz})$- F_a plot for example distinguishes soils based on the pore fluid salinity as shown in Fig. 5.23a. Of course computations of F_a in the first instance require prior measurement of pore fluid salinity. Nevertheless, it is demonstrated here that in $(-\phi_{1\ Hz})$- F_a plots, there are different regions (I, II, and III in Fig. 5.23a) which can be used to qualitatively assess coupled clay salinity effects in soils. It is emphasized here that highly corrosive soils can be immediately recognized from small values of $-\phi_{1\ Hz}$.
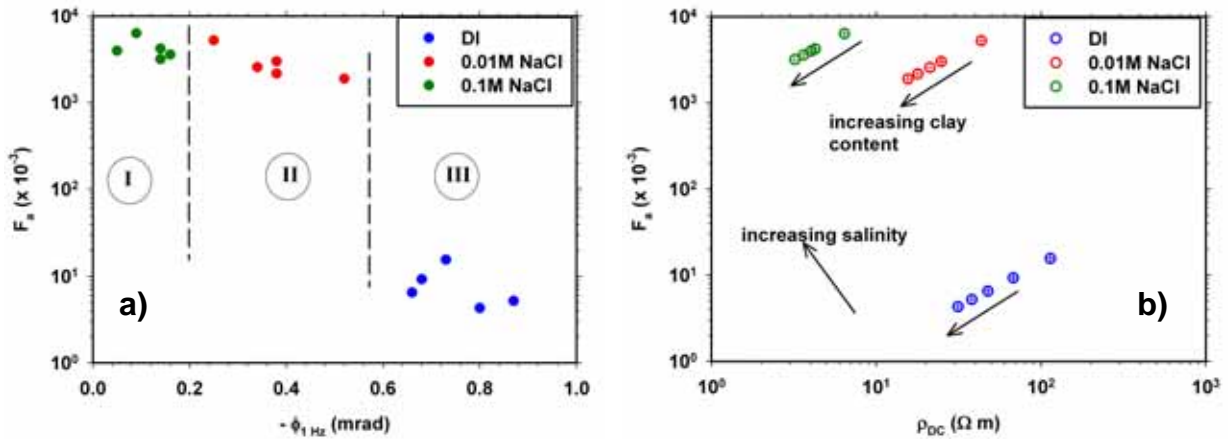
Figure 5.23. Variation of F_a with **a)** $-\phi_{1\ Hz}$ and **b)** ρ_{DC} for assessing different soil properties.

On the other hand, cross-plots of ρ_{DC} - F_a on a log-log scale allows a better distinction between clay content and salinity than $(-\phi_{1\ Hz})$- F_a. High saline pore fluids exhibit lower ρ_{DC} and tend to cluster at relatively higher F_a values. Increasing clay content at a constant pore fluid salinity leads to a reduction in F_a values due to enhanced surface conductivities. For soils with similar pore fluid salinities, ρ_{DC} - F_a plots on a log-log scale can be used to distinguish clay rich soils. It is emphasized here that these are qualitative assessments, which can be obtained from the two cross-plots, *viz.*, $(-\phi_{1\ Hz})$- F_a and ρ_{DC} - F_a mentioned here to aid in identifying potentially corrosive soils.

It has been demonstrated here that measurements of low frequency soil spectral properties can be useful in assessing potentially corrosive soils. A range of electrical characterizations have been presented, which show significant capabilities for the assessment of soil corrosiveness. This development in electrical characterizations can greatly aid in laboratory assessment of potentially corrosive soils.

5.4   Conclusions

The present work has been an attempt to extend the paradigm of electrical characterizations in assessing soil corrosivity. For this purpose, the possibility of rapid assessments of laboratory soil samples in referenced states has been investigated. The referenced states here refer to completely saturated conditions. Several important findings have been made, which are summarized as follows.

Firstly, a soil impedance spectrometer was developed to investigate the perturbations caused by clay and salinity on soil SIP responses. It was observed that clay increases the polarization phenomenon in soils, while pore fluid salinity tends to produce a decreasing effect. These effects are generally well captured by the apparent formation factors and resistivities of soils, whereby the former reveal decreasing values with increasing clay content and strong increases with increasing salinity. On the contrary, soil resistivity shows decreasing values with both increasing clay content as well as salinity. The effects of clay and salinity can be further qualitatively identified through the ϕ-spectra from SIP measurements. Interpretations of ϕ-spectra using Cole-Cole parameters allow further distinctions to be made regarding clayey and saline soils. Most notably in the present work, the Cole-Cole chargeability parameter has been found suitable to distinguish between clay and saline soils. Apart from these parameters, phase angles at 1 Hz reveal a strong dependence on salinity. The coupled clay and salinity effects on soils can be explained well by the normalized chargeability parameter, which reveals a monotonous increase with increasing clay content as well as salinity within the salinity range typical of groundwater studied in this work. These parameters were further investigated for possible connections with the polarization resistances in metal/soil systems measured in the previous chapter.

Soil resistivities measured under completely saturated conditions revealed good relationships with the polarization resistances measured on two separate days. These are consistent with the current practice of weighting corrosive strength of soils with a single determination of its resistivity under completely saturated conditions. However, it has been shown in this work that soil corrosivity characterization can be extended with single SIP measurements conducted under completely saturated conditions. The

normalized chargeability parameter is seen to provide a good indication on the corrosive strength of soil. Clay and salinity both play significant roles in the overall soil corrosion process. It has been found that soils with higher values of normalized chargeabilities are indicative of relatively more corrosive soils than those with lower values. Importantly, it has been revealed that normalized chargeabilities are more connected with the 'soil factor' during the corrosion process. Indeed, the normalized chargeability parameter depends on the specific surface area, surface densities, and surface ionic mobility, all of which are affected by the clay content and pore fluid salinity. Consequently, connections between normalized chargeabilities and corrosion strength parameters (polarization resistances) are of a fundamental nature. It is noted here that SIP measurements offer a good perspective in assessing potential soil corrosivity.

Apart from these, it is clear that qualitative assessments of apparent formation factors and $-\phi_{1\ Hz}$ can also aid in distinguishing potentially corrosive soils. It has also been highlighted that coupled effect of clay and salinity can be qualitatively isolated by comparing cross plots of ρ_{DC} - F_a and $(-\phi_{1\ Hz})$ - F_a. These new characterizations offer additional tools for diagnosing potential soil corrosivity.

It has been demonstrated in this work that a single SIP measurement of soils in a consistent state enables characterization of various electrical features, which can be used diagnostically to assess soil corrosivity. SIP responses are influenced by clay content and salinity of pore fluid both of which are significant parameters controlling corrosion in a soil environment. The present study provides an extension to the paradigm of soil corrosivity assessments using electrical characterizations. Although the present work is concerned with assessing laboratory soil samples, it is noted that findings made here suggest ramifications for field scale interpretations. This will be further elaborated later in the thesis.

CHAPTER 6

DESIGN AND IMPLEMENTATION OF A 1kHz TIME-DOMAIN INDUCED POLARIZATION SYSTEM

The present chapter provides a detailed description of the time-domain induced polarization (TDIP) transmitter/receiver system, which was developed as part of this work. Although not forming an immediate aim of the overall thesis, the development of this system is a by-product in the project and demonstrates the efficacy of low-cost digital systems. The system presented here has been used for DC resistivity and TDIP measurements (DC-TDIP) in the field, reported in the next chapter.

6.1 Importance of Full-Waveform Acquisition

In most standard TDIP systems raw data measured in the field are not stored and are unavailable for detailed investigations for the noise characteristics in the signals. This perhaps is not important in TDIP measurements related to mineral explorations provided strong IP signatures are present and noises are minimal. However, with the emergence of new applications in environmental and engineering-related investigations [*e.g.*, Slater & Lesmes, 2002; Dahlin, 2003; Kemna *et*. *al*., 2004; Vaudelet *et*. *al*., 2011 and the references therein] it becomes imperative to minimize noises [*e.g*., Paine & Copeland, 2003] and identify distortions caused by the system [*e.g*., Fiandaca *et*. *al*. 2012] since IP signatures in such environments may not be as strong as those encountered in mineral regions. Paine & Copeland (2003) have shown the robustness of suppressing noises in TDIP data, when the full-time series waveforms are acquired by the receiver. Problems at the electrodes and other interferences can easily be identified and bad repeat data can be removed prior to stacking. Moreover, the signal-to-noise-ratio (SNR) can be greatly improved with this approach. The use of full-waveform analysis thus permits stronger control on data integrity, which may not be present if only summary information on stacked waveforms is recorded. Presently, commercial TDIP receiver systems are available allowing recording of full-waveforms, which can be scrutinized during post-analysis for noise and system distortion effects on pre-stacked data.

An important aspect of the present thesis was to develop a full-waveform single channel TDIP system in order to perform resistivity and chargeability profiling along the pipeline right-of-way. The intent of this work is to contribute to the design of low-cost TDIP systems, with good noise reduction capacities. The software controlling the system was fully implemented on the NI LabVIEW 2009 environment and is described in the subsequent sections.

6.2   System Architecture and Operation Overview

The TDIP system consists of a NI USB-6212 data acquisition (DAQ) card and a power amplifier unit (PAU) built by an external company (to required specification) whereby measurement and control functions are provided by custom-built programs. The system architecture is conceptualized in Fig. 6.1.
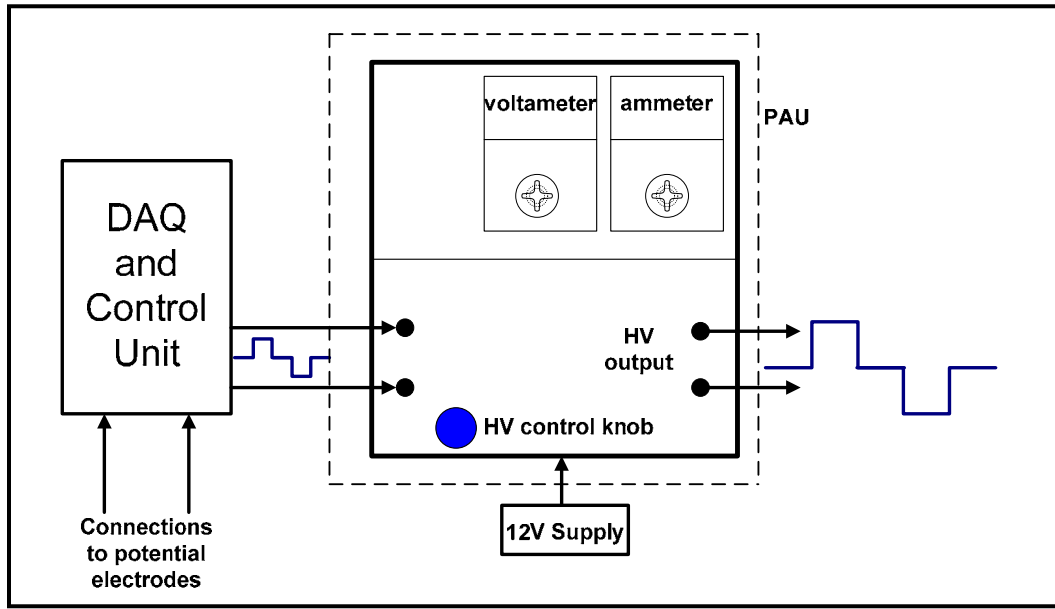
Figure 6.1. TDIP system architecture. The DAQ and Control Unit represent the NI's ADC card USB-6212. Note, HV = high-voltage.

The DAQ card is used to generate a typical 50% duty cycle TDIP waveform with amplitudes of ±5 V. This command signal is sent to the PAU, which amplifies it to a user-set output voltage typically between 27.5 – 280 V. A high Amperage power supply (12 V) is required for the operation of the power amplifier. The amplified voltage from the PAU is then used to inject currents between two current-electrodes. This feature forms the transmitter aspects of the TDIP system. The potential-electrodes are connected to the analog inputs AI0 and AI1 of the DAQ card, which are configured to operate in differential mode. To ensure that the common-mode voltage level of the signal remains in the common-mode input range, bias resistors (100 kΩ) are connected on each input line and tied to the analog input ground (AI GND) of the DAQ card. Note the input impedance of the 16-bit DAQ card used in this work is very high (>10^9 Ω). The command signal (output) and measurement of the differential voltage across the two potential-electrodes (input) are synchronized to satisfy cause-effect conditions. The maximum current drive from the PAU is 250 mA, which is sufficient for the type of profiling of interest in the present thesis (depths < 2 m). The output voltage and current levels during the pulse ON-time from the PAU are displayed on two separate multimeters. These multimeters are

connected internally to the power amplifier unit. For safety purposes, with the PAU switched on, the HV output is activated/deactivated by a manual ON/OFF switch. Hence, it only generates the HV output when the switch is ON, regardless of the state of the active command signal from the DAQ card. The inputs for the power supply and command signal from the DAQ card are isolated from each other as well as from the output of the PAU. Measurement and control of the TDIP system is provided by a custom-built LabVIEW program running on a rugged hand-held ALGIZ 7 tablet PC, which is interfaced to the DAQ card.

The main program (Fig. 6.2a) allows access to different sub-programs. Specifically, these sub-programs are for i) checking the current output levels from the PAU, ii) conducting TDIP measurements, iii) processing of raw data and computations of electrical parameters, iv) transferring data files to external device, and v) exiting the system. This window also displays pre-configured data of the survey.
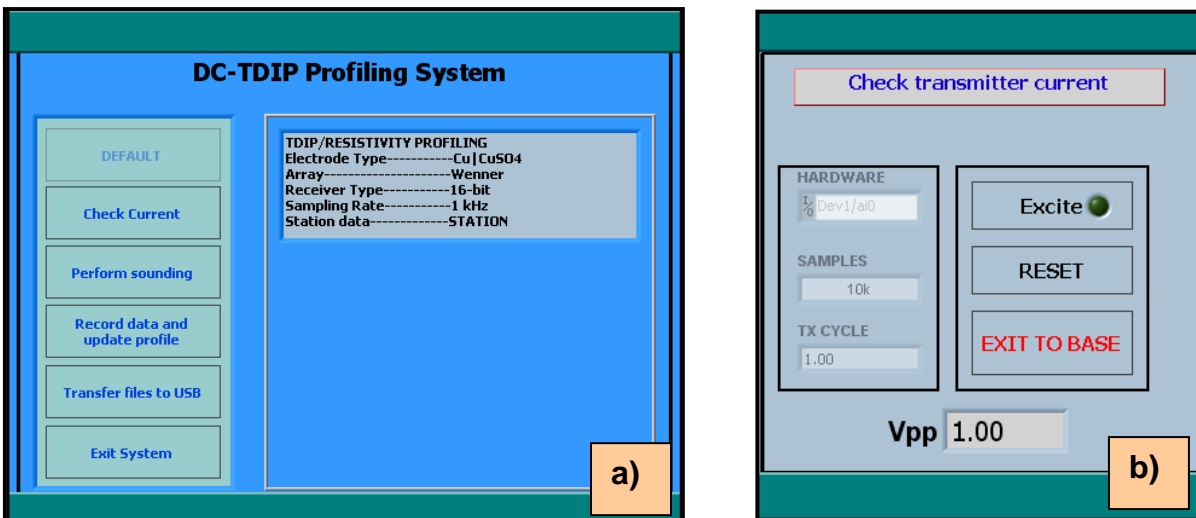
Figure 6.2. **a)** Main program providing different functions for the TDIP system, and **b)** sub-program allowing determination of output current level from the power amplifier unit.

The following basic sets of procedures facilitate an understanding of data collection using the TDIP system:

a) Firstly, with the PAU switched on and under deactivated mode, the "Check Current" option is selected from the main program. This opens up the sub-program shown in Fig. 6.2b. The "Excite" option is selected to send a 10 s long command signal to the PAU. The green indicator on the program lights up at the end of this duration. This procedure is required to correct for the zero-error of the current output readings on the ammeter and to set the display

on the correct range. This correction is only required when the system is first switched on by connecting it to the power supply. Subsequent activation and deactivation of the PAU does not require any corrections to the ammeter. Once the ammeter is corrected, the PAU is activated and the desired output voltage (displayed on the voltameter) is set using the HV control knob. The "Excite" option is again selected and the corrected current output level from the PAU is displayed on the ammeter. Once the current is noted, the "Reset" option is selected to reset the DAQ card and finally the option "Exit to Base" closes the sub-program and control returns to the main program.
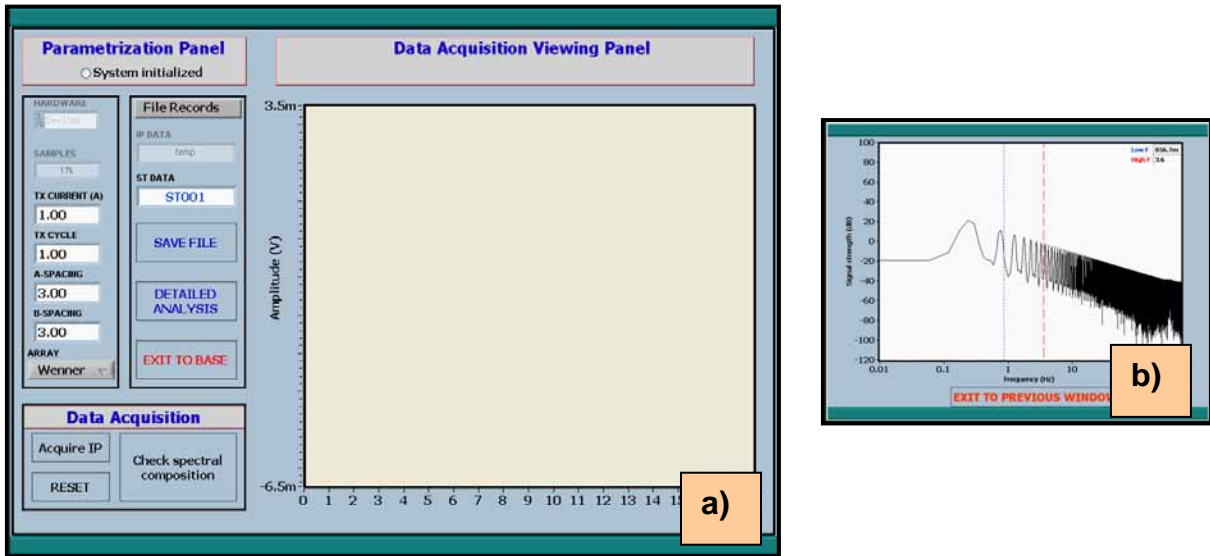
Figure 6.3. **a)** Program for making synchronous current injection and induced polarization measurements. The spectral contents of the acquired data can be easily checked using **b)** another sub-program accessible from a).

b) The next procedure is "Perform Sounding". This leads to the data acquisition sub-program shown in Fig. 6.3a. Here, the measurement parameters *viz.*, length of ON/OFF pulse (s), information on electrode geometry, the transmitter output current (A), and file details are first initialized. Once completed, the "Acquire IP" option is selected, which engages the PAU to transmit the amplified TDIP signal. Simultaneously, the induced voltage across the potential electrodes is sampled at a rate of 1 kHz. The TDIP measurements in the thesis were conducted for 1 s ON/OFF bipolar pulses and as such are the default pulse length for the TDIP system. Usually, 17 s of data is collected, allowing averaging from 8 stacks. At the end of the acquisition process, the measured voltages are displayed on the graph, which also has options for low and high pass filtering. The "Save File" option saves the raw data as well as all other relevant information displayed on the program. The "Check spectral composition"

option opens another sub-program shown in Fig. 6.3b, which displays the spectral contents of the acquired voltage. This becomes useful when working in a noisy environment to assess potential noise sources. For verification purposes, the "Reset" option can be selected and data acquired again to check the integrity of the acquired data. Following these, the data processing sub-program can be accessed using the "Detailed Analysis" option or control can be returned to the main program through the "Exit to Base" option.

The next logical step following data acquisition is the analysis process. For this purpose another program was developed with advanced signal processing capabilities. This is accessed via the "Record data and update profile" selection in the main program. The analysis process implemented is described in the next section.

6.3   Full-Waveform Data Processing

A major aim in any geophysical profiling is to quickly identify trends in parameter behaviour along a given transect. For this purpose, it is essential that all data acquired is accurately transformed into meaningful information as the profiling progresses. For the TDIP system developed in this chapter, this was achieved via the data analysis program shown in Fig. 6.4. To aid in identifying the 'noisiness' of the environment, spectral composition of raw data is also illustrated in the program.
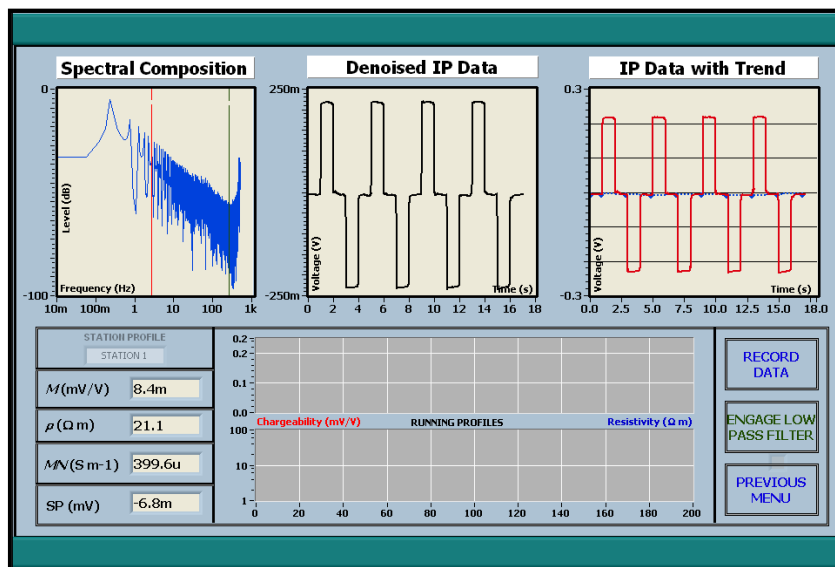
Figure 6.4. Data analysis and profiling sub-program of the TDIP system. The program shows previous stations apparent resistivity and integral chargeability values allowing identification of trends as the survey progresses. Full-time series of raw and processed data are viewable on-site for data integrity purposes.

The program processes the complete 17 s of raw data to produce the final stacked data, from which apparent resistivity, apparent integral chargeability (hereafter, mention of resistivity and integral chargeability implies apparent values) and self potential information are extracted. For each station this information is stored in a local file structure. The program continuously displays the resistivity and chargeability profiles along the transect from previously processed station data. Different stages of data processing required to achieve this task are summarized in the flowchart given in Fig. 6.5.
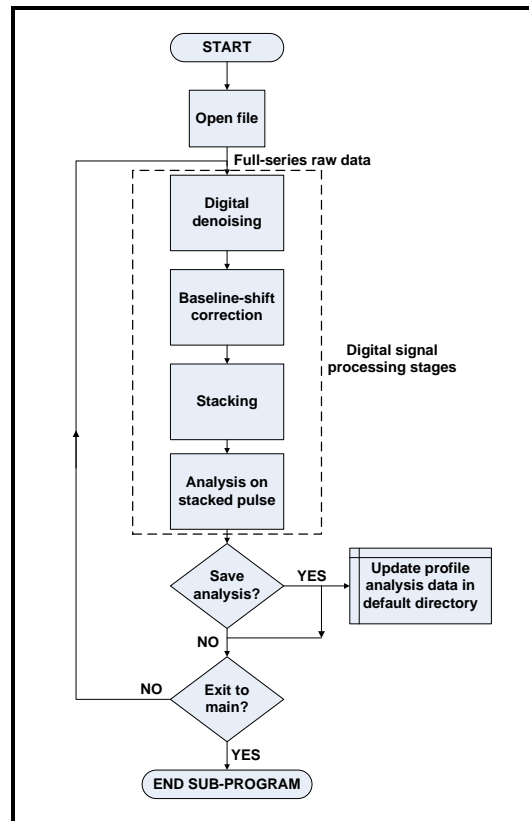
Figure 6.5. Flow chart for the data analysis sub-program for the TDIP system. Different signal processing schemes are implemented for managing noises and applying corrections in the data.

Measurement and reporting of final electrical parameters, *viz.*, resistivities and chargeabilities, constitute the end-features of the TDIP system. The important stage is the implementation of the digital signal processing methods, which perform denoising and baseline correction of raw data into meaningful information. In the present work, the signal processing methods were explored in detail for practical treatment of raw data.

Usually TDIP systems are implemented with an analog low-pass filter circuitry to minimize noises associated with power lines and other cultural anomalies. The acquired data are then stacked with baseline correction to produce the final decay curve from which sub-surface information is extracted.

Alternatively, the low-pass filters can also be implemented digitally. However, as shown by Dahlin *et*. *al*. (2002) and Fiandaca *et*. *al*. (2012), low-pass filters induce a strong distortion in the acquired data and dilute the discontinuity present during current turn-OFF and turn-ON events. This feature is illustrated in Fig. 6.6a for a purely resistive response filtered by a Butterworth 3rd order low-pass filter with a cut-off frequency, F_c, of 10 Hz.
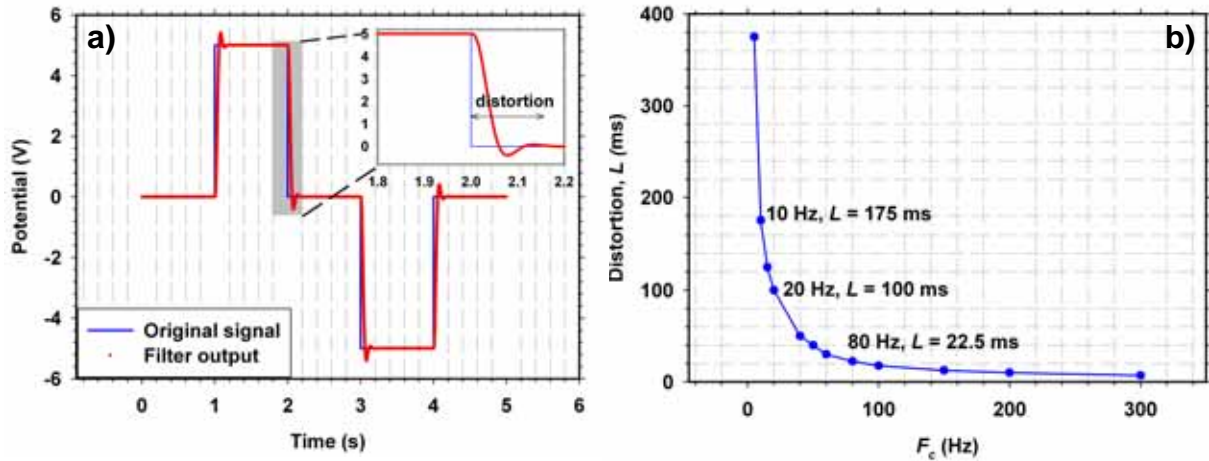
Figure 6.6. **a)** Distortion of a purely resistive signal by a Butterworth 3rd order low-pass filter with a cut-off frequency of 10 Hz. The discontinuous region (grey shaded region) is shown in an exploded view to better identify the ringing-effect. **b)** Variation of the distortion length with the filter cut-off frequency.

The low F_c produces a ringing-effect, also known as the Gibbs phenomenon, which is significant up to a period of ~175 ms. The effect of different F_c on the distortion time, L was simulated for a range of F_c values and the results are presented in Fig. 6.6b. Here, L is estimated as the total time over which the ringing-effect is present. It is clear that as the F_c of the low-pass filter increases, the distortion time decreases exponentially. Conventionally, TDIP data immediately after current turn-OFF and turn-ON are ignored due to EM coupling effects. The duration of the data (in seconds) ignored is usually subjective and is based on the data quality. It follows that the duration of the data being ignored should also cater for any distortions caused by low-pass filters. This can lead to a difficult situation, especially if the F_c of the low-pass filter is purposefully set to a low value, in order to remove power line and high frequency cultural noises. Features associated with early decay times are lost and long pulse ON and OFF times may be required for quality analysis.

A conceptual illustration of the different noise sources present in field data is shown in Fig. 6.7. It is clear that the TDIP data is affected by a range of noises, from the low to the high end of the frequency spectrum. Low frequency tellurics generally lead to baseline wandering in the TDIP data and can

pose significant difficulties during analysis (see Section 6.3.2). The use of low-pass filters appears justified since it can remove all such noises provided the F_c is set very low. On the contrary, it may appear feasible to set the F_c to a relatively high value, *e.g*., >100 Hz, which results in distortion times of ~<20 ms thereby maintaining information associated with early decay times. However, this will not remove any artefacts arising due to fundamental power line interferences. Note, if data is only affected by the power line fundamental frequency, then it can be processed using a notch filter. However, the distortions will still arise even if a notch filter is utilized.
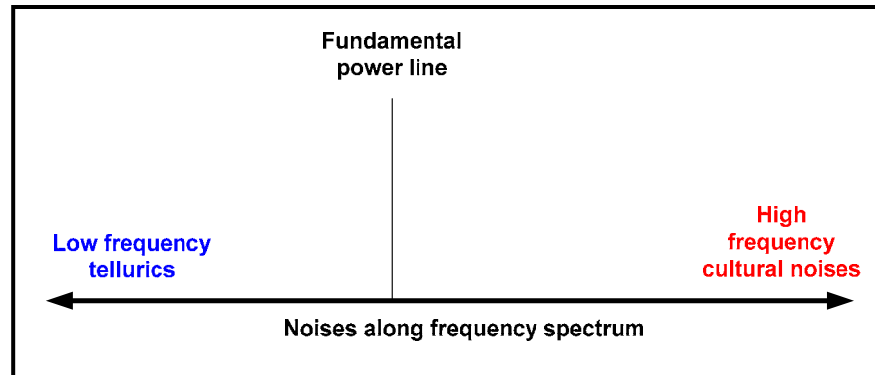
Figure 6.7. TDIP data is affected by a range of noises from low frequency tellurics to high frequency cultural sources, together with interferences from power lines.

To circumvent the problems associated with using low-pass filters, another methodology is needed. From the discussions so far, this methodology should possess two important characteristics: a) it should be able to filter out noises associated with the low to the high end of the frequency spectrum, and b) it should induce minimal artefacts on the final processed data. These two characteristics are elementary (and important) features of the wavelet transform based denoising methods [see Donoho & Johnstone, 1994; Donoho & Johnstone, 1995; Donoho *et. al*., 1995], which are becoming useful tools for image and signal processing, and has been utilized for denoising of IP data in this work. In the geophysical context, wavelet analysis started in the field of analyzing seismic signals [Morlet *et. al*., 1982; Praveen & Foufoula-Georgiou, 1997] but has since been adopted for a wide range of other applications [see Li & Oldenburg, 1997; Leblanc *et. al*., 1998; Ridsdill-Smith & Dentith, 1999; Tsivouraki-Papafotiou *et. al*., 2005; To *et. al*., 2009 and the references therein]. However, it is believed that denoising of TDIP field data by wavelet transform methods has never been reported.

6.3.1 Wavelet Denoising

To provide continuity to the discussions and description of signal processing in the TDIP system, an overview of wavelet transform methods in terms of the important equations and concepts relevant here are given in Appendix C.1. Rigorous treatment on wavelet analysis is well covered in literature and can be found elsewhere [*e.g.*, Donoho *et. al.*, 1995; Donoho *et. al.*, 1995; Lang *et. al.*, 1996; Jansen, 2001; Mallat, 2009; Jianbo *et. al.*, 2010 and the references therein].

The wavelet transform is a mathematical tool, which allows multi-resolution analysis of non-stationary signals such as TDIP data. For processing of raw TDIP data, the undecimated wavelet transform (UWT) based denoising scheme has been utilized. Denoising functionality based on UWT is available as a subVI in LabVIEW and has been preferred in the present work due to better handling of the Gibbs phenomenon and its translational-invariance property compared to the discrete wavelet transform (DWT) methods. The important aspects of the wavelet based denoising techniques are: a) the choice of the mother wavelet, b) thresholding techniques, and c) the rescaling method. There is not a single best solution to either of these choices, and the adoption of any particular setting depends upon the signal being denoised and its noise levels. For the TDIP system, settings for these parameters were chosen after several tests on synthetic as well as real data. Figure 6.8 summarizes the final choice of parameters adopted. Notably, the Haar wavelet has been used due to its similarity with the TDIP signals.
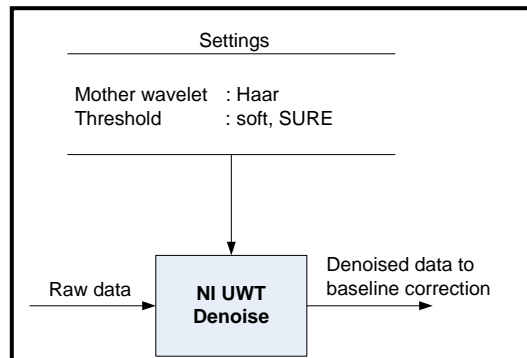
Figure 6.8. Settings for the wavelet based denoising scheme applied to TDIP data.

Basically, the UWT based denoising scheme achieves its task in the following manner:
  a) applies the UWT to the noisy TDIP data to produce the noisy wavelet coefficients,
  b) estimates the threshold using SURE algorithm and applies soft thresholding to remove the noises, and finally
  c) Reconstructs the denoised TDIP data using inverse UWT.

The denoised reconstructed signal is then passed onto the baseline correction procedures. The important characteristic of this denoising method is its ability to preserve important signal features. To demonstrate this, the original purely resistive response signal from Fig. 6.6a was subjected to the UWT based denoising technique employed in the TDIP system. Here an investigation was made to identify any distortions, which can result from this method. Figure 6.9a shows that the output appears unattenuated both along time and amplitude scales. It is virtually absent of Gibbs phenomenon – a trait which is inherent with low-pass filters and in general with any Fourier based techniques.
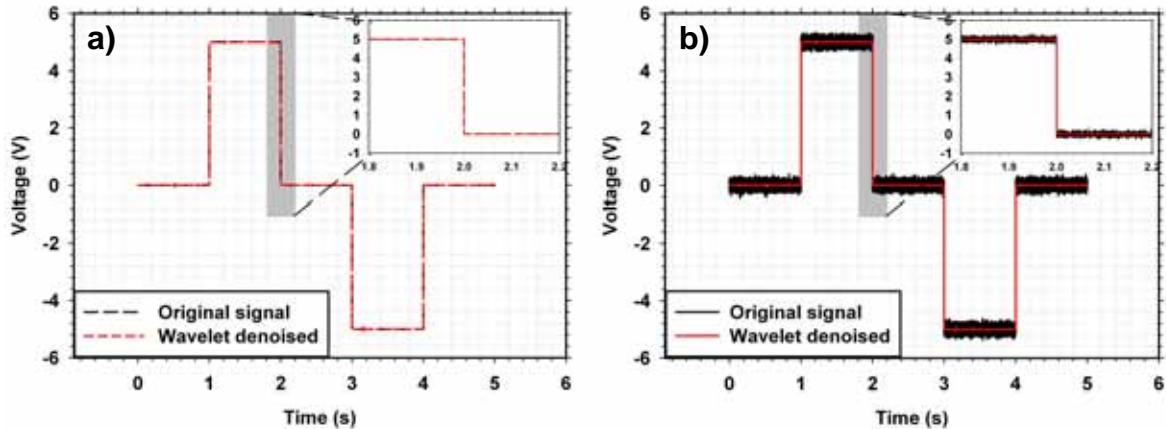
Figure 6.9. UWT based denoising for **a)** a purely resistive signal, and **b)** the same original signal in (a) mixed with Gaussian noise are free from Gibbs phenomenon and discontinuity features are well preserved. Note the improvement in SNR in (b).

On the other hand, Fig. 6.9b shows the ability of the technique to correctly extract the signal component from a noise affected data. Here, the same original signal mixed with Gaussian noise was subjected to UWT based denoising. Again, the denoised signal is free from Gibb's phenomenon and exhibits translation-invariance features. It is clear that the soft thresholding, in this application leads to good improvements in SNR. This is an important requirement of TDIP data since field data are mostly affected by a range of noise sources and extraction and analysis of decay curves becomes problematic, especially if the decay is significantly masked by high frequency noises.

For the TDIP system, wavelet based denoising is used by default. However, for flexibility, an option for low-pass filtering ($F_c = 100$ Hz) is also given on the data analysis program (see Fig. 6.4). This is done purely for data visualizations for highly noisy data in the field. After denoising, the TDIP data is passed onto the next stage, which involves corrections for baseline wandering.

6.3.2 Baseline Correction

Baseline shifts and/or wandering in TDIP data can arise mainly due to: a) self potential, and b) presence of low frequency telluric noises. Either of these sources causes a shift in the full time-series data towards a positive or negative direction from the true baseline (zero-level). To eliminate the low frequency tellurics, it may appear reasonable to use low-pass filters with very low F_c. However, it has already been shown that low-pass filters result in strong distortions, which can result in incorrect analysis. In the TDIP system the spline interpolation method has been implemented to correct for any baseline shifts in the data. This is conducted in the following manner:

a) In the full-time series data, several knots are marked in the OFF-time sections. These knots are strategically placed 0.15 s before the transmitter switches ON to avoid any EM-coupling effects. For reference purpose, a knot at the origin ($t = 0$) is also marked.

b) Interpolation between each successive knot is then carried out using the NI *Interpolate 1D* subVI configured for spline method, which interpolates each of the above intervals using the cubic polynomial function. The final resolution between each successive interpolated point is the same as the resolution of the TDIP data (1 ms).

c) The interpolated signal, which represents the baseline wander, is then subtracted from the TDIP data to produce the baseline-corrected signal.

The feasibility of the baseline correction algorithm is demonstrated in Fig. 6.10. Here, the purely resistive original signal (from Fig. 6.9a) was mixed with a 0.1 Hz sinusoidal signal (30 mV peak amplitude) and then subjected to baseline correction.
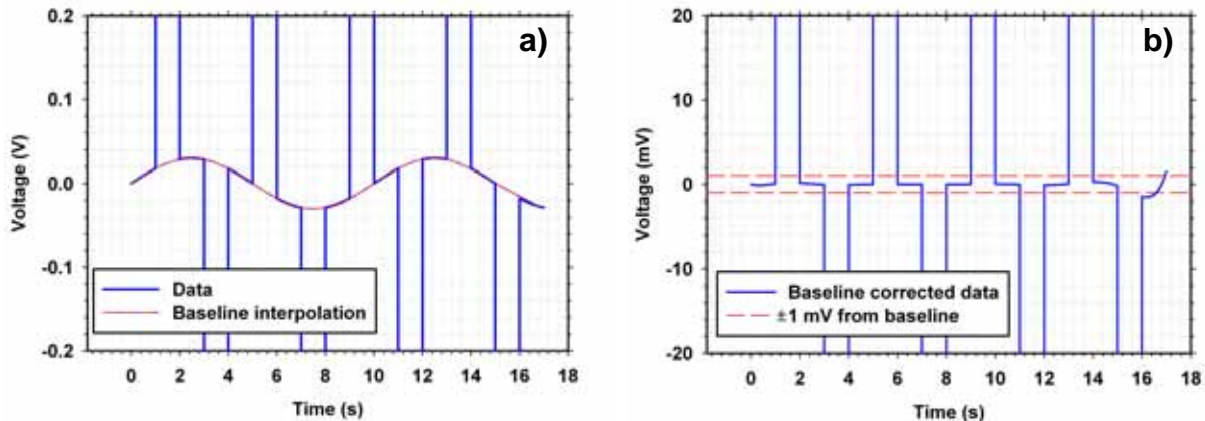
Figure 6.10. **a)** Cubic spline interpolation for estimation of baseline wander in the TDIP data. Note that the TDIP data is expanded within ±200 mV to clearly identify the trend, and **b)** shows the TDIP data with baseline wander removed.

It is noted that the cubic spline interpolation works well in identifying baseline wandering. The corrected data shown in Fig. 6.10b reveals that the procedure is able to correct baseline shift to within

<±1 mV of the true baseline. Note the difference in voltage scales between Fig. 6.10a and Fig.6.10b. This is an important feature, since computation of integral chargeabilities requires that the TDIP is accurately corrected for any baseline shifts. There are some minor incomplete corrections, which appear at the end-boundary of the TDIP data as shown in Fig. 6.10b. However, it is still <±1 mV and can be easily minimized through stacking.

After baseline corrections, the full-time series TDIP data is then analysed to retrieve information on resistivities and chargeabilities. The analysis procedure is described in the next section.

6.3.3 Integrating Window

Once the TDIP is corrected for any baseline wandering, it is passed onto the final analysis stage. Here, the successive ON and OFF sections are stacked together to produce an average pulse. The first section corresponding to the transmitter OFF-time between $0 \text{ s} \leq t < 1 \text{ s}$ is not used in the stacking process. This is necessary since this section does not result from intended causality (current injection). The amplitude of the stacked pulse and the integral of the decay curve between $0.02 \text{ s} \leq t \leq 0.85 \text{ s}$ are then calculated. From these, the apparent resistivity, apparent integral chargeability, M (mV/V), and normalized chargeability are determined. The analysis procedure is summarized in the block diagram given below in Fig. 6.11.
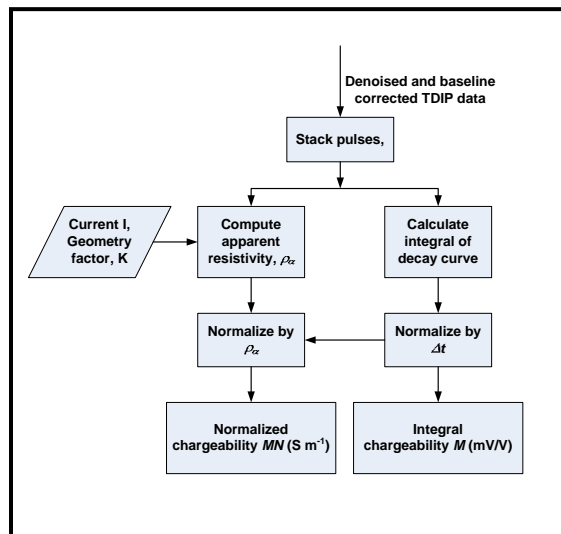
Figure 6.11. Block diagram summarizing the analysis on the stacked pulse. Note that current and geometry factor information are stored in station data files.

Of particular importance is the choice of the limits for the integrating window of the decay curve. It follows that immediately following the transmitter OFF and ON events, there will be some EM

coupling. The early decay times immediately following transmitter OFF-event are important since most information is contained in this region. Hence, the lower limit for the window should be as near as possible to the transmitter OFF-event. Measurements with the TDIP system revealed that EM coupling is short-lived in the OFF-time sections. To avoid integrating EM couplings as a valid response, an offset of 20 ms immediately following transmitter OFF-event was used. This choice allows all data to be analysed consistently and avoids analysis on a case-by-case basis. On the contrary, apart from effects of EM couplings, late time decays are usually indistinguishable from baseline noises in the data. Including late time decay sections in analysis only tend to include any effects of noises on the overall results. Consequently, the upper limit of the integrating window was kept at 0.85 s resulting in a total window length of 0.83 s over which the integral chargeability was calculated. This upper limit coincides with the positions of the knots used for baseline corrections. It is also noted here that the amplitude of the stacked pulse was calculated in such a manner that influences from EM couplings were not included.

Upon completion of analysis, the final parameters are displayed on the data analysis program (see Fig. 6.4). The self potential is also displayed for diagnostic purposes and is estimated from the mean baseline wandering. The "Record Data" option is then selected, which updates the running profiles and stores the analysis results in the local file. Following this, the electrode array is moved to the next station and the whole data acquisition and analysis procedure is repeated.

6.4   Laboratory Tests and Summary

Illustration of the denoising and baseline correction procedures on the data has already been shown in earlier sections. These identify the effectiveness of the digital signal processing schemes implemented in the TDIP system. In this section, the integrated response of the complete TDIP system is presented to allow identification and quantification of any errors. For this purpose a purely resistive network and a capacitive network were connected across the transmitter and the potential response across a 1 kΩ resistor in the network was measured using the TDIP system. Figure 6.12 summarizes the observed results. It is noted here that these responses also encompass any effects arising from the hardware and connecting wires. For the latter, the same connecting wires used in the field were used in this laboratory exercise.
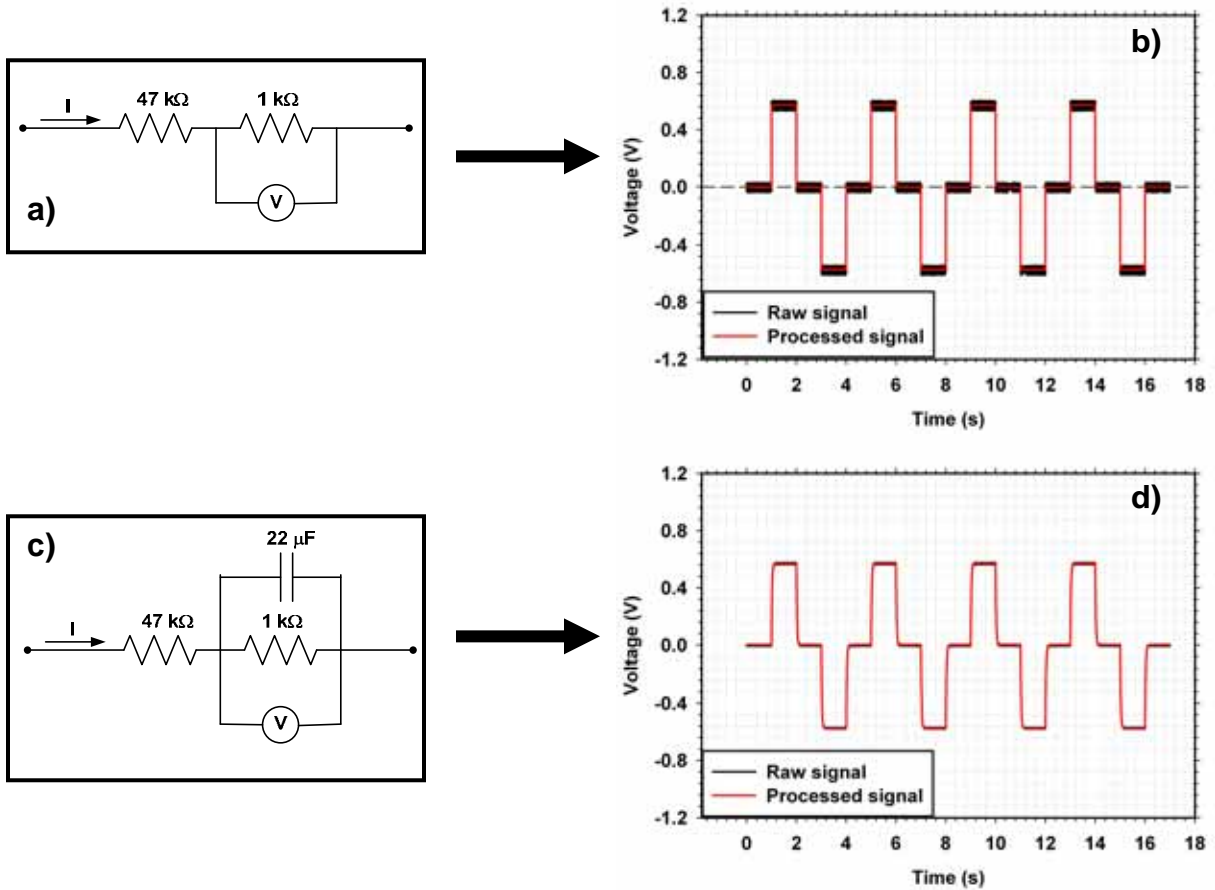
Figure 6.12. Test results of the complete TDIP system with **a)** a purely resistive network, and **c)** a capacitive network connected to the transmitter. The potential responses, measured across the 1 kΩ resistor, for both networks are shown in **(b)** and **(d)** respectively.

Firstly, for the purely resistive network shown in Fig. 6.12a a good reduction in noise and improvement in SNR is achieved with the signal processing methods as shown in Fig. 6.12b. This has already been addressed in Section 6.3.1. Since the PAU can display a minimum current of 1 mA, the current in the circuit was measured using an external multimeter and was 0.56 mA. From this, the measured load resistance is ~1.026 kΩ, which agrees well with the true value of 1 kΩ. Of course, the important characterization is the integral chargeability observed for the purely resistive response. This was calculated after stacking and was found to be 977 µV/V. Ideally, this value should be zero. However, artefacts can arise due to manifestation of stray capacitances from different elements of the TDIP system. Nevertheless, it is noted here that for the TDIP system, these artefacts are very low and contribute only ~1 mV/V. This can be considered to be the error in the computation of the integral chargeabilities. Secondly, for the response shown in Fig. 6.12d, there is clear evidence of capacitive effects occurring during the instance the transmitter is switched ON and OFF. The integral

chargeability computed from the stacked pulse is equal to 9 mV/V. The aim here is to demonstrate the effectiveness of the complete TDIP system in identifying the presence of any small capacitive effect in the data. Again, it is noted that the processed data has better SNR than the raw data. The laboratory exercises reported here reveal the accuracy of the TDIP system, which has been found to be good.

The low-cost TDIP system reported in this chapter is an important development in the overall project. A major contribution of this work is the application of wavelet based denoising method to remove extraneous signals from TDIP data. Field data is usually affected by a range of noise sources across the entire frequency spectrum and the use of low-pass filters becomes essential to eliminate their influences on the overall data. However, low-pass filtering induces large distortions in the processed data. It has been shown that these distortions can be avoided with the use of wavelet based denoising techniques. It is believed that wavelet techniques to denoise noisy TDIP data have not been attempted before. Based on the demonstration presented, it is envisaged that the use of wavelet techniques for digital signal processing can have significant ramifications on TDIP surveying in terms of turnover. Currently, TDIP surveying is hindered by long data acquisition times required to collect several pulses in order to improve the SNR through stacking procedures. However, there is an indication that the SNR can be greatly improved on single pulses through wavelet based denoising methods, thereby directly reducing the large number of pulses required for conventional stacking.

Laboratory tests on the complete TDIP system have shown that the inherent errors are generally very low. Most importantly, the errors in integral chargeabilities can be considered to be generally < 1 mV/V. Concerning these low errors, the system is suitable for environmental related investigations. The analysis aspects of the TDIP system will be further demonstrated in the next chapter, where it has been used to perform electrical profiling along the buried pipeline right-of-way.

CHAPTER 7

GEOELECTRIC METHODS IN SOIL CORROSIVITY PROFILING: NEW APPLICATIONS

The present chapter is an integrated geophysical study aiming to provide insights on the application of geoelectrical methods, *viz.*, direct current resistivity, and time-domain induced polarization surveys for soil corrosivity assessments; additional data are presented to investigate the role of self potential effects on pipeline integrity. A pioneering application of the combined direct current resistivity and time-domain induced polarization (DC-TDIP) methods for soil corrosivity assessments is presented. Although the former method is an acceptable practice for evaluation of soil corrosivity in field, it is believed that the latter technique is being utilized for the first time in this application area.

7.1   Introduction

Geophysical characterizations of subsurface conditions are being used as non-invasive, and non-destructive techniques for a range of investigations in the context of environmental and/or geotechnical studies [*e.g.*, Leroux & Dahlin, 2002; Slater & Binley, 2003; Hiltunen & Roth, 2004; Butler, 2005; Viezzoli & Cull, 2005; Soupios *et. al.*, 2007; Vaudelet *et. al.*, 2011; Gazoty *et. al.*, 2012 and the references therein]. Generally, the overall aim in such investigations is for site characterizations, which for civil engineering in particular, is important for site risk evaluations, product testing, and remedial studies [Hallenburg, 1998]. These site characterizations can be extended to make qualitative assessments on soil conditions, *i.e.*, their corrosiveness, along pipeline-rights-of-way (ROW), important in pipeline integrity assessments. For example, Fenning & Hasan (1995) have provided a list of various geophysical techniques, which can be used specifically for investigation of proposed pipeline routes.

It has been established earlier in the thesis (Chapter 4) that clay and salinity (chlorides) have a significant impact on corrosion of ferrous materials in soils. It has also been shown that enhanced levels of these variables can be captured by their perturbations in soil electrical properties (Chapter 5). Amongst the multitude of available geophysical techniques, the results from previous chapters suggests that geoelectric measurements, *viz.*, direct current resistivity and time-domain induced polarization (DC-TDIP) methods (or equivalent in the frequency-domain), possess good qualities for assessing site conditions of buried metallic pipelines (unless stated otherwise, mention of pipelines hereafter implies metallic form). It has been pointed out elsewhere in this thesis that the ASTM G57-95a (2001) document provides standard procedures for measuring soil resistivities at pipeline

installations using the Wenner method. It is noted here that resistivity profiling is a common [*e.g.*, Ekine & Emujakporue, 2010] and an accepted technique for soil corrosivity assessments in the field. However, it is believed that TDIP methods have never been used in this context before. The DC-TDIP techniques can be applied under two different scenarios, *viz.*, assessment of site conditions prior to pipeline installation and assessment after installation for monitoring purposes. DC-TDIP profiling can be carried out at proposed locations, where pipelines are to be installed. Sections of proposed pipeline assets, which will be under high corrosion risk, can be immediately evaluated from anomalous chargeability and resistivity features, which can be associated *inter alia* with clay lenses and salinity. Information such as these can readily assist in planning and implementation of external corrosion control procedures, *e.g.*, use of sacrificial anodes, or impressed current methods [McDowell *et. al.*, 2002].

However, owing to the dynamical nature of the environment, several changes can occur at sites where pipelines were previously installed. Pre-installation DC-TDIP survey data may no longer be applicable and consequently, assessment of site conditions for buried assets becomes a necessity in order to identify sections under high corrosion risks. However, buried assets constitute one of the cultural sources of noises, which as a norm are avoided in conventional DC-TDIP measurements. In their presence, survey lines are usually oriented perpendicular to the buried structures and dipole-dipole array configurations are used. An important study concerning pipeline effects on frequency-domain measurements has been conducted by Parra (1984). For assessing soil corrosivity along the pipeline ROW, it is obvious that a shift in the conventional data collection procedure is required since pipelines, viewed commonly as sources of noises, constitute the important element in the overall measurement objective. More specifically DC-TDIP profiling parallel to the pipeline ROW is required to allow identification of anomalous sections, which are possibly under high corrosion risks, and at the same time optimize data acquisition processes. Here, the electrode spacing can be arranged in such a manner that the depth of investigation is less than or equal to the depth of the pipeline crown. In such profiling, a range of electrode geometries can be utilized, including the Wenner array [McDowell *et. al.*, 2002], which provides the maximum SNR in a given environment [Sharma, 1997]. However, in contrast to normal geoelectric measurements in ground free of buried pipelines, significant current channelling effects need to be considered.

The current channelling effect is not properly addressed in the ASTM G57-95a (2001) standard nor in the limited literature concerned with resistivity profiling along pipeline ROW. For the discussions which follow, it will be assumed that the only protection mechanism employed is plastic insulation

used to isolate the pipeline from the host soil. Other modes of protection such as the use of sacrificial anodes, or impressed current methods will not be considered, since the present work relates to corrosion under native soil conditions. It follows that for a pipeline, there can be two ideal cases describing their galvanic coupling to the host soil medium:

a) If the pipeline is wrapped with an insulating material, then under ideal conditions it can be considered to be electrically insulated from the host soil, and

b) If it is completely exposed, then it behaves as a perfect conductor in the soil-pipe system.

These ideal cases have different impacts on the current flow between the outer pair of current electrodes in the Wenner array arranged parallel to the pipeline as illustrated in Fig. 7.1. For argument purposes here, it is assumed that the host medium is homogenous with resistivity ρ (Ω m).
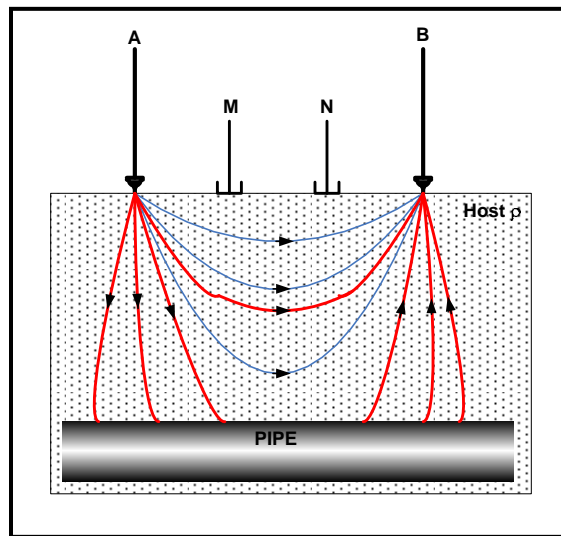
Figure 7.1. A schematic illustration of current flow between the two outer current electrodes (AB) of a Wenner array for soil containing insulated pipeline (blue lines) or exposed pipeline (red lines). Note, drawing is not to scale.

Firstly, for case (a), outlined previously, since the pipeline is electrically insulated from the host soil, the majority of the current will flow through the top layer of soil as illustrated in Fig. 7.1 by the blue lines. On the other hand, for case (b) if the electrode spacing is very close such that the depth of investigation << the depth of pipeline crown, then the majority of the current again would flow through most of the top layer soil. However, if the depth of investigation is increased, then the majority of the current will channel through the pipeline, *i.e.*, shorting along the pipeline as portrayed in Fig. 7.1 by the red lines. The implication of this is that the resistivity measured will not be the actual resistivity of the host soil (ρ) but will depend upon the coupling between the pipeline and soil as well as the density of current flowing through the pipeline. In fact, it may be very low due to the channelling effect. In this manner, interpreting the measured resistivity as the soil resistivity and

projecting this to assess soil corrosivity will be incorrect. This important fact still eludes most studies related to field scale soil corrosivity assessments from resistivity measurements. The same concepts as above can be extended to understand the overall effect on TDIP measurements. If the pipeline is completely isolated from the host soil by insulation, then the polarization response will arise from the host soil. However, in the event the pipeline is completely exposed, a response due to the electrode polarization mechanism will be observed. The strength of this response may depend upon many factors, some of which are the rate of oxidation-reduction reactions at the metal/soil interface, the exposed area, current density *etc*.

In practice, it is common for pipelines to be coated or wrapped with an insulating material to prevent deterioration due to corrosion. However, due to defects and interactions within the host medium, some insulation between the pipeline and the soil may eventually be lost or damaged over time. This will lead to several localized areas on the pipeline surface, where the pipe surface can become exposed or isolated from the host soil medium. The exposed area does not necessarily have to be extensive, as minute "spots" are sufficient for any electrical continuity between the pipeline and soil. Under these conditions, the simple ideal conditions mentioned before cannot be used to assess site conditions since there will be different zones of anodes and cathodes (point defects) along the pipeline. This in essence complicates the characterization of the complete pipeline-soil system.

From the discussions presented so far, it is clear that in the presence of buried pipelines, conventional DC-TDIP profiling may be affected by the overall pipeline-soil system. Consequently, work is needed to develop capabilities for data interpretation from pipeline ROW DC-TDIP surveys. Apart from these active electrical techniques, another important geophysical technique is the passive self potential method. [*e.g*., Naudet *et. al*., 2003; Jardani *et. al*., 2008; Jouniax *et. al*., 2009 and the references therein], which allows characterization of potential distributions over a region. Self potentials due to oxidation-reduction reactions occurring at the metal/soil interfaces are well known [*e.g*., Corwin, 1990; Castermant *et. al*., 2008; Ekine & Emujakporue, 2010] and are usually characterized by large negative anomalies, especially in the case of exposed metals [see Corwin, 1990]. In the case of a pipeline, ideally protected by insulation, it may be safe to assume that such self potential anomalies will not be present. However, the manifestation and effect of these potentials under practical considerations, when the pipeline is encased within an imperfect insulating material remains unknown.

In considering all of the discussions so far, the present chapter is aimed at a systematic study to understand the reliability of DC-TDIP profiling in the overall scope of pipeline assessment. The contributions of this chapter to the overall thesis are to:

a) Develop capacities for DC-TDIP methods in soil corrosivity assessment for pipeline integrity purposes, and

b) Identify any possible implications of self potentials on the overall pipeline integrity.

Studies reported in this chapter will make frequent reference to laboratory observations from previous chapters for efficient interpretation of field data.

7.2   Experiment Design and Measurements

A systematic description of the experimental design for the present work is given in the sub-sections which follow.

7.2.1 Field Site

The external corrosion of any ferrous pipeline depends upon the host soil material. The contents conveyed in the pipeline (water, sewer, gas, oil *etc*) are somewhat irrelevant to the overall external corrosion process provided there is no leakage from the pipeline. Hence, in the present study the selection of a field site based on the contents transported by the pipeline is not necessary. Instead, the choice of the field site for the pipeline investigation was based on the following criteria:

i)   the respective pipeline network should have a history of external corrosion,

ii)   the pipeline section should be located away from major urban influences (road-side traffic, underground cabling *etc*), and should also be easily accessible.

The South East Water (SEW) Corporation, which is based in Melbourne and provides water, sewerage, trade waste, and water saving services to the regions of south-east Melbourne to south Gippsland, was approached for a list of possible sites, which were then evaluated according to these criteria. The site eventually selected from this list was Mount Eliza, which is an outer suburb located to the south-east of greater Melbourne in the state of Victoria, Australia. The site consisted of an abandoned ductile iron cement-lined (DICL) pressurized sewer main (diameter of 375 mm) commissioned in 1987, which had a significant failure history arising from external corrosion. Due to this, the DICL sewer line was replaced in 2010 by polyethylene (PE) pipelines running 3 meters away and parallel to the former. The abandoned DICL network however was not removed from the ground. Consequently, a part of this abandoned network was chosen for investigation. From the large abandoned network, two short transects, SITE 1 and SITE 2, were then further identified for

geophysical investigations in this study. Figure 7.2 provides an illustration of the study area and the two sections mentioned.
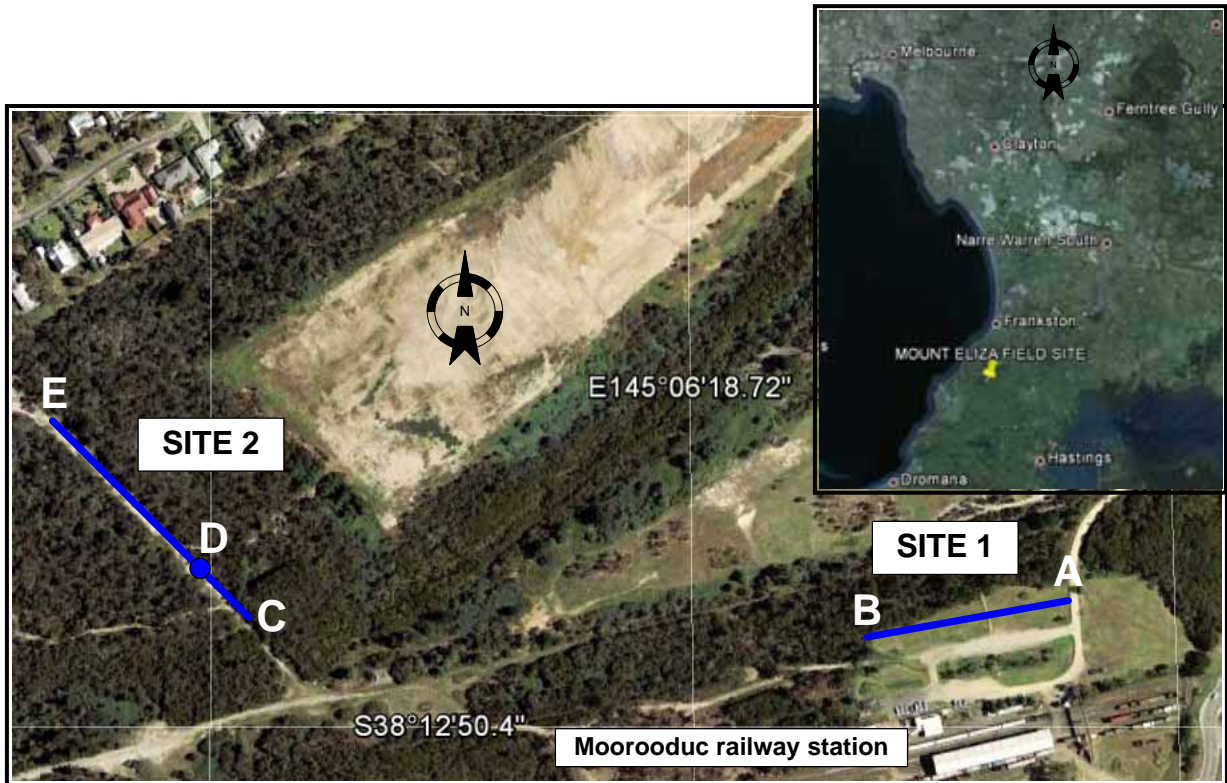
Figure 7.2. Location of transects (blue lines) for SITE 1 (AB) and SITE 2 (CE) in Mount Eliza. For SITE 2, the section CD corresponds to the section where abandoned DICL pipelines still reside, while section DE are absent of any metallic pipelines. Insert shows the location of Mount Eliza field site from the city of Melbourne. Note, images are edited after Google Earth.

SITE 1 is located in the vicinity of the Moorooduc Railway Station, which is a heritage railway. The railway lines run ~75 m away and nearly parallel to the pipeline ROW, where the abandoned DICL pipelines reside in flatbed topography. The length of SITE 1 transect is 123 m between points AB as shown in Fig. 7.2. On the contrary, SITE 2 transect is located on a hilly slope towards the north-west of SITE 1. The total length of SITE 2 transect (between points CE, see Fig. 7.2) is 162 m. However, the abandoned DICL pipelines here do not cover the entire length. Instead, they are only existent over a short span of ~30 m (between points CD); the rest of transect is free from metallic pipelines. Unlike SITE 1, the SITE 2 transect is located within a running wire fence (~1.5 m offset) with wooden posts. The site features described here are also illustrated in the schematic diagram shown in Fig. 7.3. According to the architectural blueprints provided by SEW, the depth of the pipeline crown for SITE 1 and part of the section at SITE 2 is ~0.85 m. However, due to build variations and soil transport over the years, actual depths are estimated to be within 1 – 2 meters at present. The plans also indicate

that the pipelines were wrapped in plastic for insulation purposes. The same blueprints were used to identify the pipeline alignment, and corresponding marks were made at the surface prior to conducting the geophysical survey described next. It should be noted here that the SITE 2 transect was included in the present study to provide an insight on whether any contrasting features could be observed from partial existence of buried pipelines
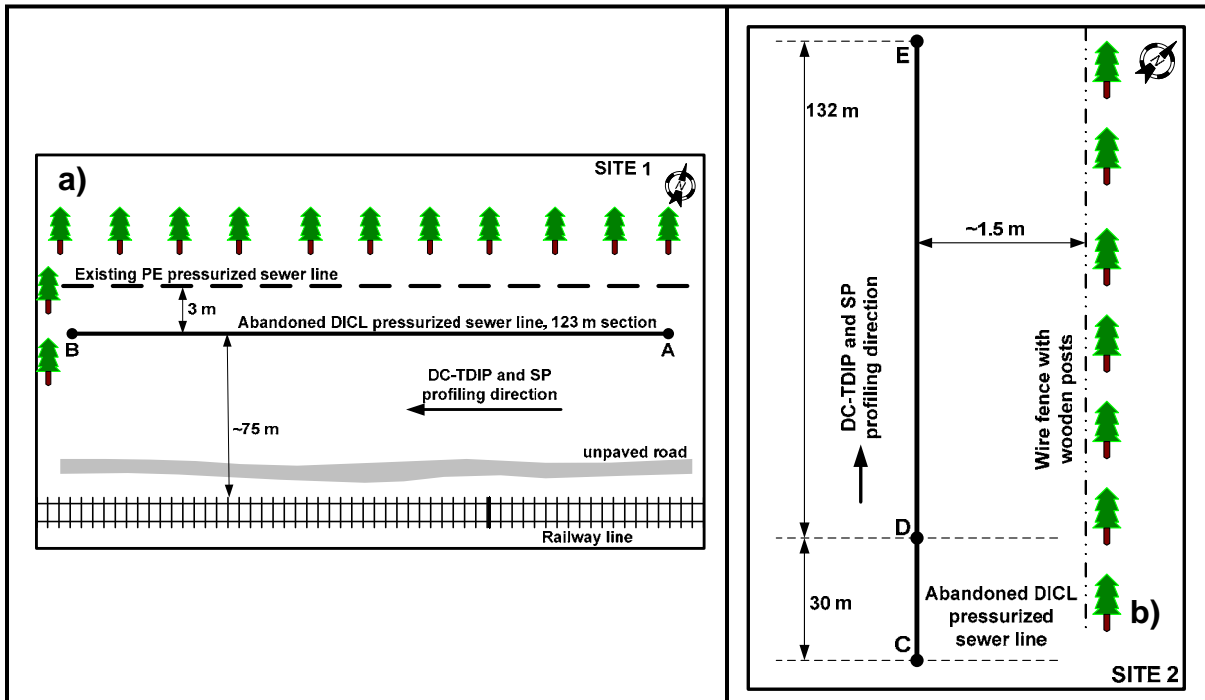
Figure 7.3. Schematic views of site conditions for **a)** SITE 1 transect, and **b)** SITE 2 transect showing the locations of different landmarks. Note, drawing is not to scale. The markers AB for SITE 1 and CDE for SITE 2 are shown in Fig. 7.2. Approximate North is also given.

7.2.2 Geoelectrical Measurements

Relevant procedures for conducting DC-TDIP and SP profiling are presented in this section. To avoid diversion from topic at hand, details for SP surveying, in particular, are presented in a brief manner and further details are provided in appendices and referenced as appropriate.

For SP surveying, the 3M™ Red Dot™ Ag|AgCl electrodes were used as the non-polarizable electrodes. The manner in which these electrodes were used, and their calibrations are provided in Appendix D.1. SP measurements were completed along the SITE 1 and SITE 2 transects using gradient and fixed-based configurations during November and December of 2010 respectively, each under favourable weather conditions. Firstly, individual stations were installed along each transect with a separation of 3 m between each point. The first and last stations coincide with markers A and

168

B respectively for SITE 1, and C and E respectively for SITE 2 as identified in Fig. 7.2 and 7.3. Measurements were then conducted as follows. At both sites the gradient method was used with an electrode spacing of 3 m to traverse the transect from the first to the last station as outlined in Fig. 7.3. The measured potential differences were then integrated and referenced to the starting point (defined as 0 mV) at each site. Fixed-base measurements conducted at SITE 1 and SITE 2 transects were referenced to a base station located well away from the pipeline ROW (>20 m). This was done to identify if any trends could be associated between the pipeline ROW and a "quiet location". The base station for SITE 2 in particular was located at the base of the slope, with normal offset (~25 m away) to the marker C on the pipeline ROW. Further details on ground preparations and measurements are given in Appendix D.1.

DC-TDIP profiling along SITE 1 and SITE 2 transects were carried out during May of 2011 under favourable weather conditions using the TDIP system described in the previous chapter. Preliminary investigations were first conducted using the Wenner configuration for its favourable SNR. In the present work, a constant-separation traversing method was used. For both sites, a station spacing of 3 m was used, resulting in 42 stations for SITE 1 and 55 stations for SITE 2; each station purposefully set to coincide with the stations in the SP surveys. Some important aspects of the measurements, which were kept consistent amongst the two sites, are as follows. At each station, current was injected using a pair of stainless steel electrodes, each of which is 60 cm in length, driven ~3 cm into the ground. By the virtue of its design (corrosion resistant), stainless steel electrodes have very high contact impedances. This can become highly problematic, when they are used to inject currents into the ground. To overcome this situation, a mixture of sand/clay slurry saturated with a strong brine solution was poured onto the surface where the current electrode was driven into the ground. This reduced the contact impedance and allowed injection of reasonable amounts of current. In the present work, currents of <200 mA have been used. Induced voltages were measured using a pair of non-polarizable Cu|CuSO$_4$ electrodes, which were constructed and cross-calibrated in the present work (see Appendix D.2). The potential electrodes were placed in small holes (depth of <5 cm), which were dug into the ground and filled with the salty sand/clay slurry. Apart from reducing the contact impedance, the slurry ensured that the interface between the electrode end-plug and ground surface were not affected by any surface irregularities.

Electrical connections from the TDIP system to the current and potential electrodes were completed using separate insulated copper wires and separate shielded cables respectively. The TDIP system was installed on a roving trolley for easier transport during the constant-separation traversing work.

Plate 7.1 shows the different elements for the field work carried out in this survey. Note also that the metal based roving trolley is decoupled from the ground by the rubber tyres. For both sites, ON-OFF periods of 1 s each, corresponding to a base frequency of 0.25 Hz, was used for DC-TDIP measurements. At each station data was collected for 17 seconds, allowing stacking of 8 decay curves for computation of integral chargeabilities. As a precautionary measure, a waiting period of 10 mins was allowed prior to data acquisition at each station in order to ensure steady-state conditions at the electrode/soil interface. DC resistivity was computed from the final stacked pulse in such a manner that effects arising due to EM-coupling were ignored. Further details on the data processing procedures of the TDIP system have already been discussed in Chapter 6, and thus will not be repeated here.

For the SITE 1 transect, the DC-TDIP profiling was done from the east to the west direction for a-spacings of 1 m and 3 m. This corresponds to a median depth of investigation of 0.525 m and 1.575 m respectively (see Chapter 3). Regarding these depths, it can be assumed that if the plastic insulation has deteriorated over the years, the measurements will incorporate any current channelling effect. On the contrary, SITE 2 profiling was conducted from south-east to north-west direction for a-spacing of 3 m only. Here, the SNR was very poor and TDIP analysis on decay curves could not be performed at most stations. It shall be mentioned here that SITE 1 transect has been studied in detail due to the large section of abandoned pipeline at this location, which is the focus of the present work. The detailed study mentioned here includes analysis of soil samples collected along the transect for further analysis in the laboratory. The types of analysis conducted are described in the next section.
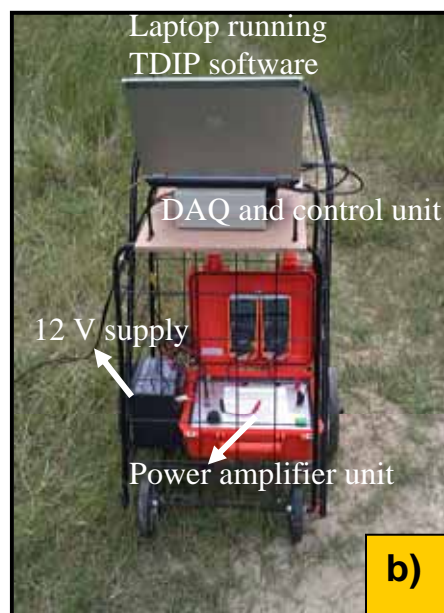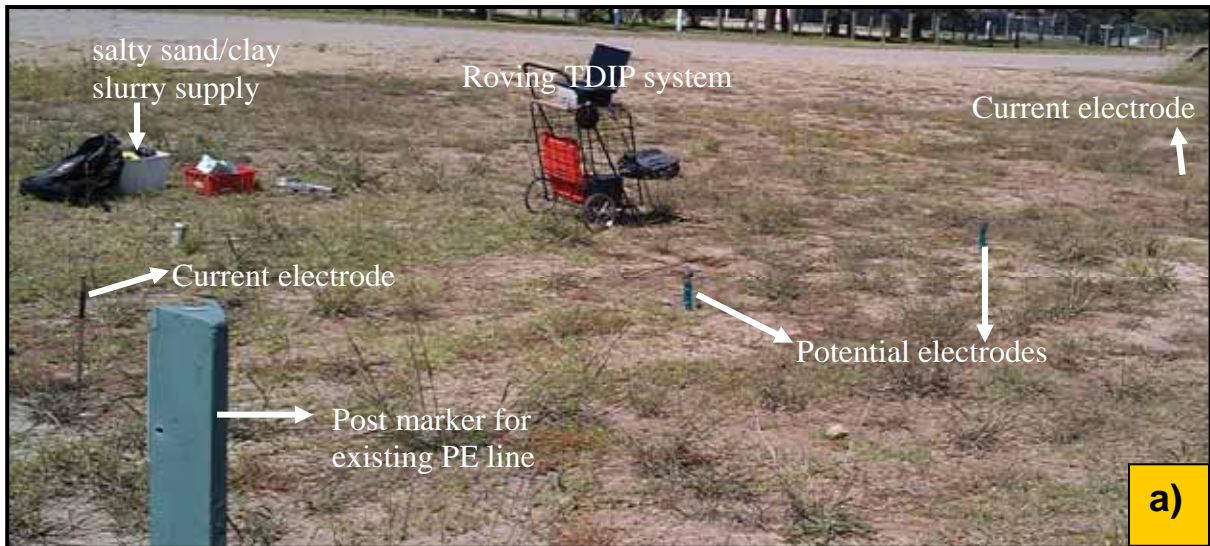
Plate 7.1. **a)** A typical measurement set-up at each station showing the electrodes lay-out and the roving TDIP system. This particular measurement is for an arbitrary station on SITE 1 transect with *a*-spacing of 3 m. Note the post marker in the foreground. **b)** The roving TDIP system showing the important elements of the complete data acquisition and control system. The DAQ and control unit is housed inside a rugged case. All connections to and from the unit is through BNC terminals.

7.2.3 Soil Sampling and Laboratory Measurements

To provide ground truthing of geophysical data collected for SITE 1 transect, core samples were collected every 6 m starting from station 1 (0 m) up to station 39 (114 m). Hence, a total of 20 core samples were collected. At each location, a drill-rig attached at the back of a vehicle was first used to drill to a depth of ~1.2 m. Upon reaching this depth, undisturbed core samples were then acquired using a core-holder (inner diameter of 4 cm) upto a depth of ~1.5 m; thus a total core length of 0.3 m. Plate 7.2 illustrates the acquisition of a typical core sample from the field.

Plate 7.2. A drill-rig attached at the back of a vehicle was used to acquire 0.3 m long core sample between the depths of 1.2 – 1.5 m to provide ground truthing of geophysical data from SITE 1. Note, it is estimated that the present depth of pipeline crown is between 1-2 m.

In order to acquire undisturbed samples as near as possible to the pipelines, a nominal value of 1.5 m was taken as a representative crown depth across the entire transect. This depth also compares well with the depth of investigation for *a*-spacing of 3 m.

The 20 core samples, each measuring ~1 kg, were brought to the laboratory, where they were broken into pieces. Large stones and foreign matter were removed and the samples were completely dried. The samples were then completely saturated with deionized water. Saturation was achieved by adding the deionized water periodically followed by light mixing, which was continued for a week. After one week, the samples were thoroughly mixed to ensure homogeneity. From each soil mixture, two sub-samples of 150 g and 50 g were obtained, which were then subjected to chemical analysis and soil

corrosivity testing using the galvanostatic pulse technique respectively. The rest of the sample (~800 g) was analyzed for their SIP responses. For galvanostatic pulse measurements, the experimental procedure described in Chapter 4 (Section 4.2.3) was used. Here, cast-iron was used as the working electrode. The corrosion-related parameters (R_p, C_{dl}, β, R_Ω, and E_{CORR}) were determined during Day 1 and Day 7 as described in the aforementioned section. Likewise, SIP measurements were conducted on saturated samples (with deionized water) using the impedance spectrometer and experimental procedures given in Chapter 5 (Section 5.2.3).

Chemical analysis for the determination of sulphates (SO_4^{2-}), chlorides (Cl^-), and nitrate (NO_3^-) contents in the soil sample was carried out by an external commercial laboratory. SO_4^{2-} content in the sample was determined using inductively coupled plasma atomic emission spectroscopy following extraction of the sample with a calcium phosphate solution. The Cl^-, and NO_3^- contents were measured with a discrete analyser under procedures conforming to the American Public Health Association (APHA) 21st Edition standards. Electrical conductivity (EC) of 1:5 soil/water leaches for each sample was also measured.

The range of laboratory soil analysis conducted enabled a detailed evaluation of the observed results from the geophysical surveying carried out for the pipeline ROW at SITE 1.

7.3   Results and Discussions

Systematic treatment of the various experimental results will be given in separate sub-sections. For clarity purposes, SP and DC-TDIP results are treated in separate sections. Philosophical discourses on the use of DC-TDIP for pipeline site condition assessment will be successively given based on the various laboratory investigations on soil samples from the SITE 1 transect in later sections.

7.3.1   Self Potential Profiling

The SP profiles at SITE 1 conducted using the gradient and fixed-base methods are illustrated in Fig. 7.4a and 7.4b respectively. Note the interpolation of the SP profile shown has no fundamental basis and is only meant to aid the eye. Measurements corresponding to gradient methods in Fig. 7.4a have been integrated along the transect and referenced to marker A as per usual practice.
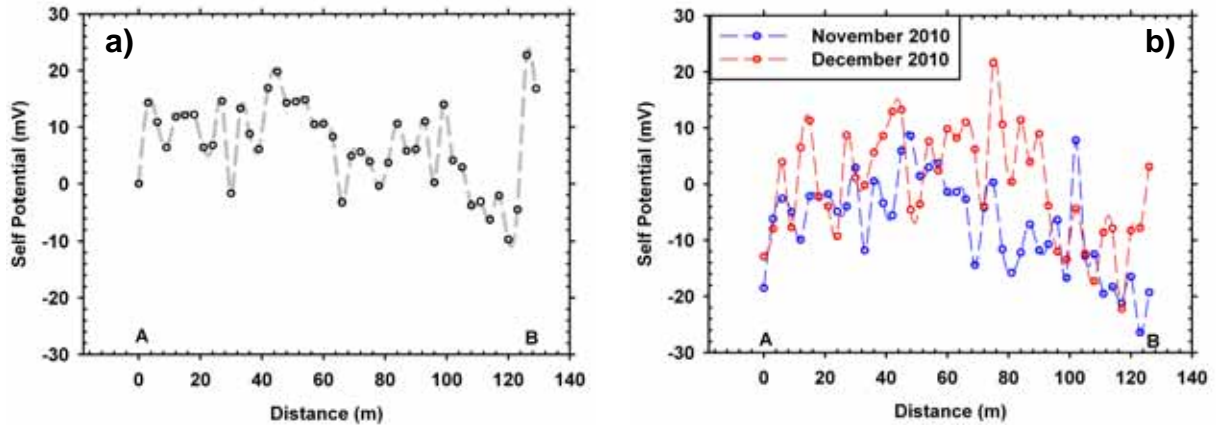
Figure 7.4. Self potential profiles at SITE 1 transect using **a)** gradient method, and **b)** fixed-base method whereby the base station is remotely located at a "quiet location".

The SP data acquired during November of 2010 using gradient methods provides a profile generally bound within ±20 mV, while for most part of the transect, SP values are generally positive. However, there is some indication that the SP starts decreasing from marker A towards B. Since all potentials are integrated along the pipeline ROW and referenced from marker A, the interpretation of the SP profile can be difficult. This is because marker A (the first station) itself lies immediately above the pipeline ROW. On the other hand, Fig. 7.4b shows the SP profile along the transect measured with respect to a base station, located well away from any buried infrastructure. The two sets of measurements conducted during November 2010 and December 2010 (separated by ~30 days) show similar features; potentials within the middle region of the transect appear relatively higher compared to either end of the transect. There is some indication that the November profile is slightly depressed in amplitude compared to the December profile. Such characteristics can possibly arise due to systematic differences in ground conditions. The important aspect of measurements with respect to a base station located well away from the pipeline ROW is as follows.

Large negative anomalies usually associated with bare steel pipes are absent. In contrast, Corwin (1990) has reported large negative (< -100 mV) anomalies at locations containing bare steel pipelines and steel well casings. The absence of such large anomalies along the transect with respect to a "quiet location" perhaps indicate that the insulating material protecting the pipelines from host soil is somewhat intact. There maybe isolated zones where the protective casing has deteriorated or failed, however the exposed area of such defects may be relatively small. Under these conditions potentials due to oxidation-reduction processes at the pipeline/soil interface, measured on the ground surface, can be small to negligible. Of course, this will ultimately depend upon several other factors such as resistivity of the soil, source strength, *etc*. [see Revil *et*. *al*., 2010; Goto *et*. *al*., 2012]. In view of this,

174

any contribution to self potentials from reactions occurring at the pipeline/soil interfaces cannot be easily distinguished from other competing sources (vegetation, bacterial activity, water filled pores, geochemical reactions in soils itself *etc*.). Notwithstanding this possibility, measurements using a base station located away from the pipeline ROW enable a better evaluation since large areas of pipeline may be identified if they are completely exposed.

The presence of several high and low potentials in close proximity merits concern. These features, exhibited with gradient as well as fixed-base measurements, indicate the distribution of several different potential gradients between stations along the transect. Such features can arise due to surface heterogeneities. Nevertheless, in the event that the sources of these potential gradients are due to some processes and/or features within the soils, these can have detrimental effects on the pipelines especially at any point defects. There is a possibility that such potential gradients can actively lead to electrolysis of localized sections of the pipeline, thereby accelerating any general corrosion process. This in essence represents the complexity of the natural environment in assessing potential corrosivity. This is further demonstrated in the SP profile for SITE 2 transect, given in Fig. 7.5.
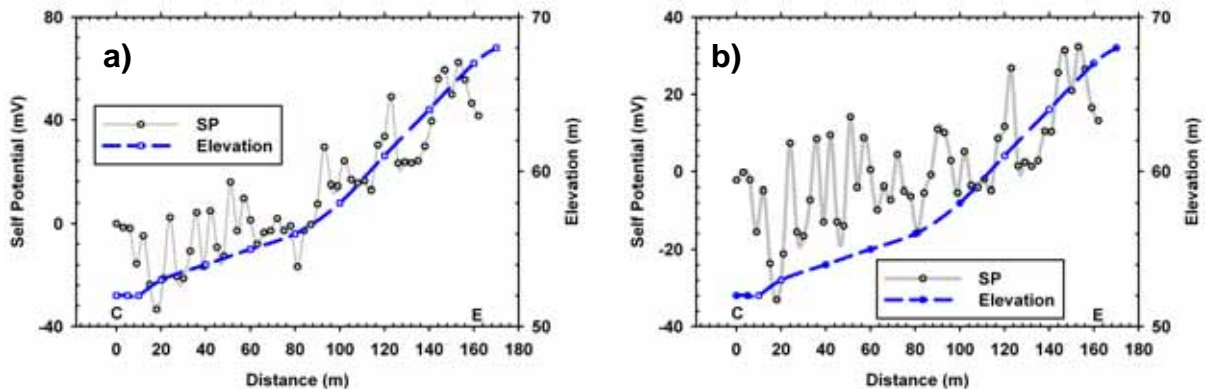
Figure 7.5. Self potential profile for SITE 2 transect using **a)** gradient scheme, and **b)** fixed-base method whereby the base station is remotely located at a "quiet location".

Firstly, unlike SITE 1, the SITE 2 transect is along a slope whereby the first and last stations (C and E respectively) are at an altitude of 52 m and 68 m above sea level respectively. Figure 7.5 shows that the self potential along the transect varies positively with the elevation. Potentials in Fig. 7.5a are referenced to marker C, at the low altitude, which is directly above the abandoned pipeline. Here, a large gradient is observed between the two ends of the transect. Usually, self potentials exhibit a negative correlation with topography due to groundwater flow [Wanfang *et. al*., 1999], whereby the resulting potentials are influenced by the vadose zone thickness [Jackson & Kauahikaua, 1987]. In this regard, Figure 7.5a may suggest that there is a pipeline effect on the SP feature since the

referenced point is immediately above the pipeline. However, measurements with a base station located well away from the pipeline also reveal a positive relationship between self potential and elevation. Such positive features have been reported by Bedrosian *et*. *al*. (2006), who attribute the effect to a vadose zone of relatively uniform thickness. Likewise Goto *et*. *al*. (2012) showed through numerical modelling that different SP features can manifest along slopes with different vadose zone properties. Although a possible pipeline effect towards the bottom slope (<30 m) in the fixed-base measurement cannot be totally ignored, the SP feature in general for SITE 2 appears to be arising due to a complicated mechanism related to elevation.

In spite of any complications it is clear that significant potential gradients can exist along a slope. Given that the pipe-to-soil potentials along a slope are affected by the self potentials from external sources, this can lead to significant electrolytic corrosion occurring along the pipeline due to the emergence of anodic and cathodic zones spread across the pipeline surfaces whereby the conduction pathway is provided by the host soil medium. In the event that these self potentials are large, they can lead to accelerated corrosion processes and ultimately to pre-mature failures, especially if there are significant resistivity contrasts linking zones of anodes and cathodes. In spite of these possibilities, self potential surveys are not usually incorporated in routine site condition assessments; for both pre and post pipeline instalment cases.

The general aim of SP profiling for each transect has been to detect possible electrolytic impacts on the overall pipeline integrity. Interpretation of these measurements can be difficult if there are competing sources in the environment. However, the presence of a distribution of potential gradients is of special concern to the integrity of pipelines. Although, SP anomalies arising due to corrosion of metallic entities are known [*e*.*g*., Castermant *et*. *al*., 2008] the effects of SP gradients due to external sources on pipeline integrity are not known. This effectively extends the paradigm of pipeline corrosion mechanisms in the natural environment, especially with varying topography, and merits a detailed further study.

7.3.2 DC-TDIP Profiling

In this section, DC-TDIP survey results will be presented for both sites (SITE 1 and SITE 2).

7.3.2.1 Noise Reduction in the DC-TDIP Data

Presentation and thorough investigation of raw DC-TDIP data is not commonly reported in the literature. This is mainly attributed to the manner in which data is usually acquired; using specialized

instruments with in-built analog and digital signal processing features. It is well-known that geophysical data is prone to background environmental noises [see Butler, 2005] and this has been treated in the previous chapter. An important aspect of the present work was to acquire the raw data in order to ascertain the noise characteristics. This allows a clear contrast to be made between noise/distortions and actual data, which is important since this is believed to be the first time the combined DC-TDIP methods have been used for the kind of geophysical work reported in this study.

A particular DC-TDIP dataset acquired in this work is illustrated in Fig. 7.6a. This dataset was collected on the SITE 1 transect, at Station 1 (location A on the map given in Fig. 7.2) for *a*-spacing of 3 m and was seen to exhibit relatively large noise levels compared to all the remaining station data acquired along this transect. The raw and wavelet denoised data are now both considered to illustrate the effectiveness of the digital signal processing techniques. The power spectral density (psd) of the raw data shown in Fig. 7.6b reveals the multitude of noise sources in this area. There is clear evidence of significant noise levels associated with very high frequencies between 400 – 500 Hz. This was observed in most datasets collected from this site and probably indicates cultural effects arising from the nearby railway station. Nevertheless, the denoised psd reveals the ability of the wavelet based technique to suppress the high frequency noise content. Other significant noises in the raw data were due to interferences from the 50 Hz mains frequency, as well as its first harmonic (100 Hz). This is attributed to the power lines at the nearby railway station as well as possibly arising from any power line coupling to the pipeline.

Although, the wavelet denoising method was able to significantly improve the SNR in most cases, there were some datasets which could not be denoised in this manner. These datasets mostly correspond to station data collected on the SITE 2 transect. One such noisy dataset collected from SITE 2, Station 1 (location C on the map given in Fig. 7.2) for *a*-spacing of 3 m is shown in Fig. 7.7.
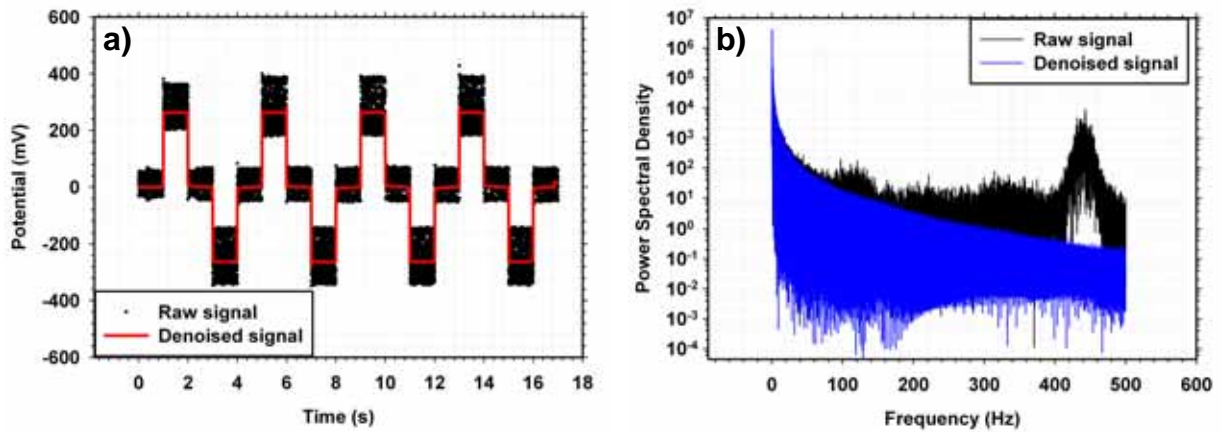
Figure 7.6. **a)** Typical noise reduction for DC-TDIP data using wavelet techniques. The raw data is for SITE 1, Station 1 collected for *a*-spacing of 3 m. Note the denoised data has been corrected for baseline shift also. **b)** Power spectral density of the raw and denoised signals reveals the suppression of high-frequency noises in the latter.
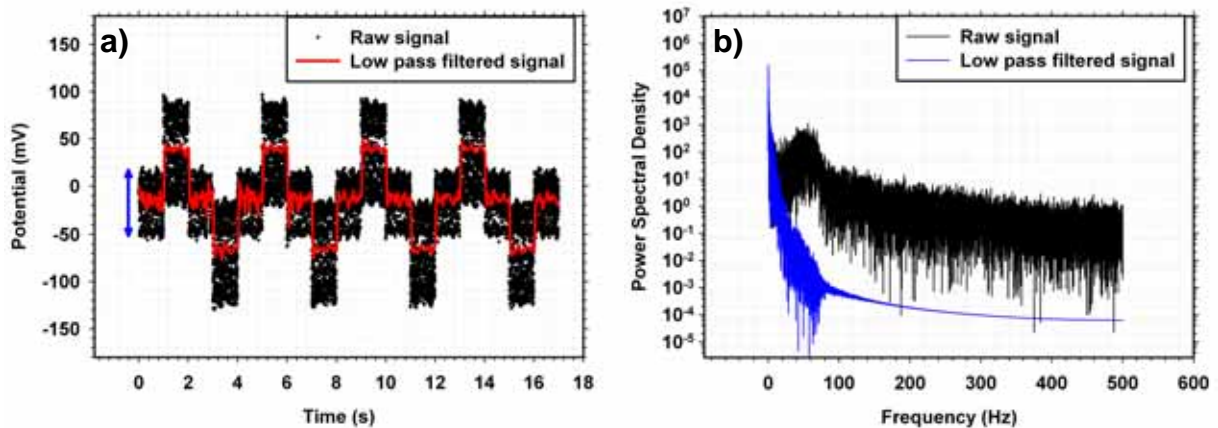
Figure 7.7. **a)** Some DC-TDIP data with very poor SNR were filtered by a low-pass filter set at F_c = 10 Hz. This data was collected at SITE 2, Station 1 for *a*-spacing of 3 m. Note the relative noise amplitudes indicated by the blue arrow. **b)** Power spectral density of the raw and low-pass filtered signal.

The wavelet denoising scheme was inefficient in removing the high frequency noise in this data set due to the poor SNR. The section of the dataset for the time (*t*) $0 \leq t < 1$ corresponds to the background noise, which is present in the locality. It is clearly seen in Fig. 7.7a that the peak-to-peak amplitude of the background noise, indicated by the length of the blue arrow, is relatively large. These high amplitudes render the small signal level changes, brought about due to current injection, almost indistinguishable. The psd of the raw dataset shown in Fig. 7.7b reveals that this particular data is affected mainly by the 50 Hz mains frequency, albeit some datasets along SITE 2 transect, with poor SNR, also showed higher frequency (>200 Hz) contents. It has already been pointed out

that SITE 2 has a wire fence running alongside the transect. It is believed that the strong 50 Hz mains and/or other higher frequency noises are arising through coupling to the fence, which can behave as an antenna. Thus, all datasets with very poor SNR were filtered by a low-pass filter with $F_c = 10$ Hz. This allowed much of the noise to be removed as shown in Fig. 7.7a, permitting determination of resistivities at these stations. However, due to the large distortions arising from low-pass filtering TDIP computations were impossible.

From the datasets presented in Fig. 7.6a and 7.7a, it is clear that the induced potentials are relatively of low amplitude (<1 V). It shall be emphasized here again that the maximum current injections used in the present work is <200 mA. It can be argued that the SNR of acquired data can be improved if large currents are used for the DC-TDIP profiling. New transmitters are required for this purpose but the results presented here demonstrate the importance of acquiring full-time raw data so that further evaluations can be made regarding the character of any noise source. This is necessary in order to avoid interpreting noisy and distorted data as actual signal, which would be the case in the event data is acquired through hardwired filters. Wavelet denoising schemes used in the present work are efficient as long as the data has reasonable SNR. Data with very poor SNR has been filtered with low-pass filters to allow computation of resistivity values. Following treatment of raw data as described in this section, the DC-TDIP profiles for the two transects were constructed and are presented next.

7.3.2.2 Observations from DC-TDIP Profiles

The apparent resistivity, ρ_a, profiling results at SITE 1 for a-spacings of 1 m and 3 m, and at SITE 2 for a-spacing of 3 m are given in Fig. 7.8. The markers A and B in Fig. 7.8a and C, D, and E in Fig. 7.8b correspond to the locations identified earlier in Fig. 7.2 and Fig. 7.3. The SITE 1 transect is of flat topography at an altitude of ~55 m above sea level. On the contrary, the SITE 2 transect is located on a slope with mean altitudes of 52 m and 68 m at the beginning and end of the transect respectively. For completeness, numerical data for each station at the two sites are given in Appendix D.3. Note that a total of 84 and 55 raw full-time series data were collected and analysed at SITE 1 and SITE 2 respectively.
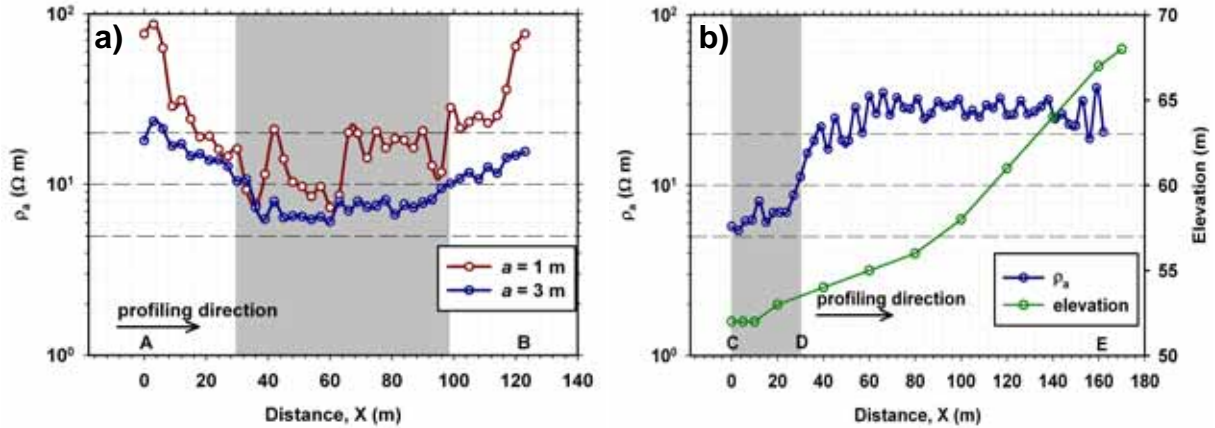
Figure 7.8. Apparent resistivity profiles for **a)** SITE 1 transect, and **b)** SITE 2 transect. The grey shaded region highlights very low apparent resistivity (<10 Ω m) section, which for SITE 2 also coincides with the presence of a short section (CD) of the pipeline.

At SITE 1, ρ_a profiles for the two a-spacings ($a = 1$ m, and $a = 3$ m) along the 123 m length exhibit variations of (7.4 – 86.8) Ω m and (6.1 – 23.4) Ω m respectively. Here, profiling using $a = 1$ m was also included to investigate if any qualitative assessments could be made using shorter array length. The profiles in Fig. 7.8a generally suggest a high-over-low ρ_a feature with lateral variations. The two ρ_a profiles decrease along the profiling direction with the minima occurring approximately within the mid-point of the length, followed by a gradual increase. Variations in ρ_a for $a = 1$ m seem to reflect possible shallow surface heterogeneities. On the contrary, ρ_a for $a = 3$ m exhibit smooth variations, which can be associated with good continuity along the transect length. On the other hand, at SITE 2, the ρ_a profile exhibits variations of (5.4 – 37.3) Ω m. Lower resistivities are observed over the short section between CD, coinciding with the partial pipeline coverage. The variation in elevation of the ground surface along the transect length is also illustrated in Fig. 7.8b.

At both sites, profiling results for $a = 3$ m is intended to provide insights on conditions as near as possible to the pipeline. If SITE 1 results are assessed using the DIPRA (2000) soil corrosivity classifications, then the buried pipelines over the entire transect can be considered to be under a corrosive environment. Likewise, at SITE 2 the section between CD ($0 \leq X \leq 30$ m) can be considered to be under highly corrosive situations. Similar comments can also be made using the corrosivity rating of Robinson (1993), whereby soils with resistivities of <10 Ω m can be considered to be very or severely corrosive. Section of the transect at both sites, which exhibit such low resistivities (<10 Ω m) have been highlighted in Fig. 7.8. However, the resistivities measured in any geophysical profiling, such as this work, are only apparent values. Moreover, it is emphasized that the presence of

the pipelines can lead to anomalous low resistivities measured using the Wenner array. This is somewhat exemplified in results from SITE 2 as shown in Fig. 7.8b. Here, two distinct sections are observed; section CD corresponding to the buried pipeline with ρ_a generally <10 Ω m, and section DE lacking buried pipeline and showing a relatively consistent ρ_a. The low ρ_a between CD can be attributed to possible effects due to the pipeline. Nevertheless, it can be equally argued that the topography of the site is responsible for the low resistivity features at the slope base. However, if so, this effect should also be present along the entire transect, whereby a steady behaviour in ρ_a consistent with elevation should be observed similar to the SP profile presented earlier. On the contrary, the contrasting ρ_a features appear consistent with the location of pipelines suggesting electrical continuity in spite of insulation applied during the initial installation. Thus, an immediate assessment of site conditions based on the absolute values of ρ_a may not be directly related to soil condition.

Evaluations of site conditions can be also made from the M_a profiles shown in Fig. 7.9. Here, the M_a is calculated as the integral of the decay curve normalized to the integral period and the primary voltage (see Section 3.3.2, Chapter 3, and Section 6.3.3, Chapter 6) and is specified in units of mV/V. Discontinuities in the M_a profiles correspond to station data, where the SNR was very poor and consequently TDIP analysis could not be performed (see data in Appendix D.3). Such situations were encountered for a few stations at SITE 1, while it was very common at SITE 2 shown in Fig. 7.9b.
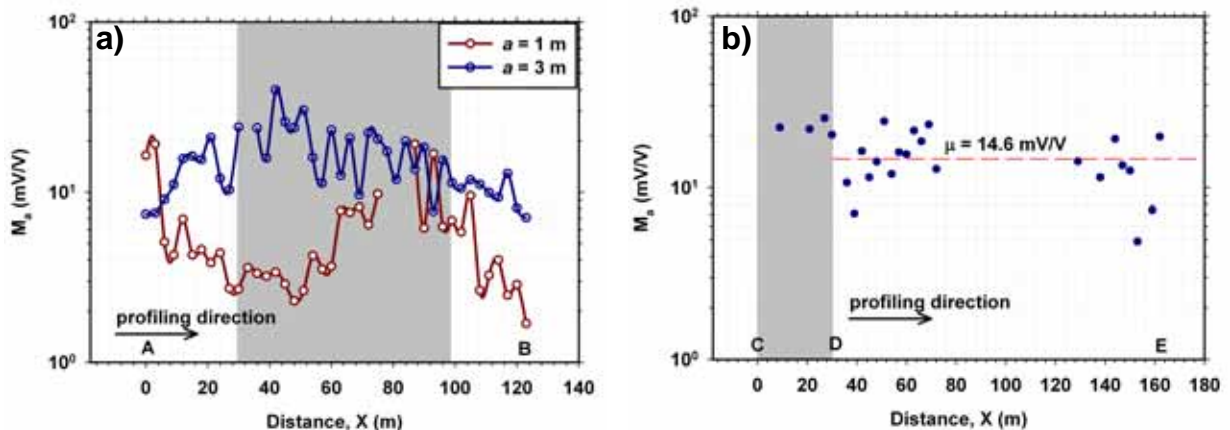
Figure 7.9. Apparent chargeability profiles for **a)** SITE 1 transect, and **b)** SITE 2 transect. The grey shaded region highlights sections with low apparent resistivity.

At SITE 1, M_a profiles for $a = 1$ m and $a = 3$ m exhibit variations of (1.7 – 19.2) mV/V and (7.1 – 39.8) mV/V respectively. The profile for $a = 3$ m appear inversely proportional to ρ_a variations.

However, for $a = 1$ m, the proportionality between ρ_a and M_a profiles is less significant. Towards the beginning of the transect, the high ρ_a coincides with relatively higher M_a, while towards the end, high ρ_a coincides with relatively smaller M_a. On the other hand, from the TDIP analysis which could be performed from the list of all station data at SITE 2, M_a exhibit variations of (4.9 – 25.4) mV/V. However, a clear distinction between the two sections CD and DE cannot be made from these variations. The mean M_a for the section DE is 14.6 mV/V.

The absence of any significant M_a anomaly (>100 mV/V) suggests some complex mechanisms occurring in the pipe-soil system, which is explained as follows. Although the soil and the pipeline/soil interface can both contribute towards the polarization response, the response from the pipeline will not necessarily be high. Provided the pipeline is exposed, the strength of the polarization response will depend on the area of the exposed surface, the locations of the anodic and cathodic zones, *i.e.*, the length over which current is channelled, the current picked up by the pipeline (and hence the amount of charge liberated at the surface), and moisture content. In addition, the surface may be under active dissolution or the pipeline/soil interface may be characterized by a compact layer of corrosion products impeding corrosion; all factors impact on the electrochemical reaction rate at the interface. Since the pipelines at the two sites have been present for ~24 yrs, it may appear safe to assume that any exposed pipeline surface would be covered by compact layers of corrosion products and be in a passive state. This may also explain the non-presence of large self potentials along the sections where pipelines are buried.

Considering the M_a variations at SITE 1 for $a = 3$ m, it is clear that the profile is highly chaotic compared to the ρ_a variations. This possibly indicates that chargeability is very sensitive to the underlying subsurface features. The location of the maxima in M_a variations appears to coincide with the minimas observed in ρ_a variations. This low resistivity/high chargeability anomaly is a classical feature, which is usually indicative of clayey lenses [Sharma, 1997]. However, in this case contributions from pipeline/soil effects cannot be totally ignored, albeit it may be small. The M_a profile associated with $a = 1$ m generally indicates that the minimum chargeability is between 2 – 3 mV/V. Here the M_a anomaly present between $60 < X < 100$ m is also present in the ρ_a profiles. However, it manifests much more strongly in the former, demonstrating again the sensitivity of M_a to underlying features. To isolate the bulk conduction effects [Slater & Lesmes, 2002], the apparent normalized chargeability, MN, variations for the two sites were determined and are shown in Fig. 7.10.
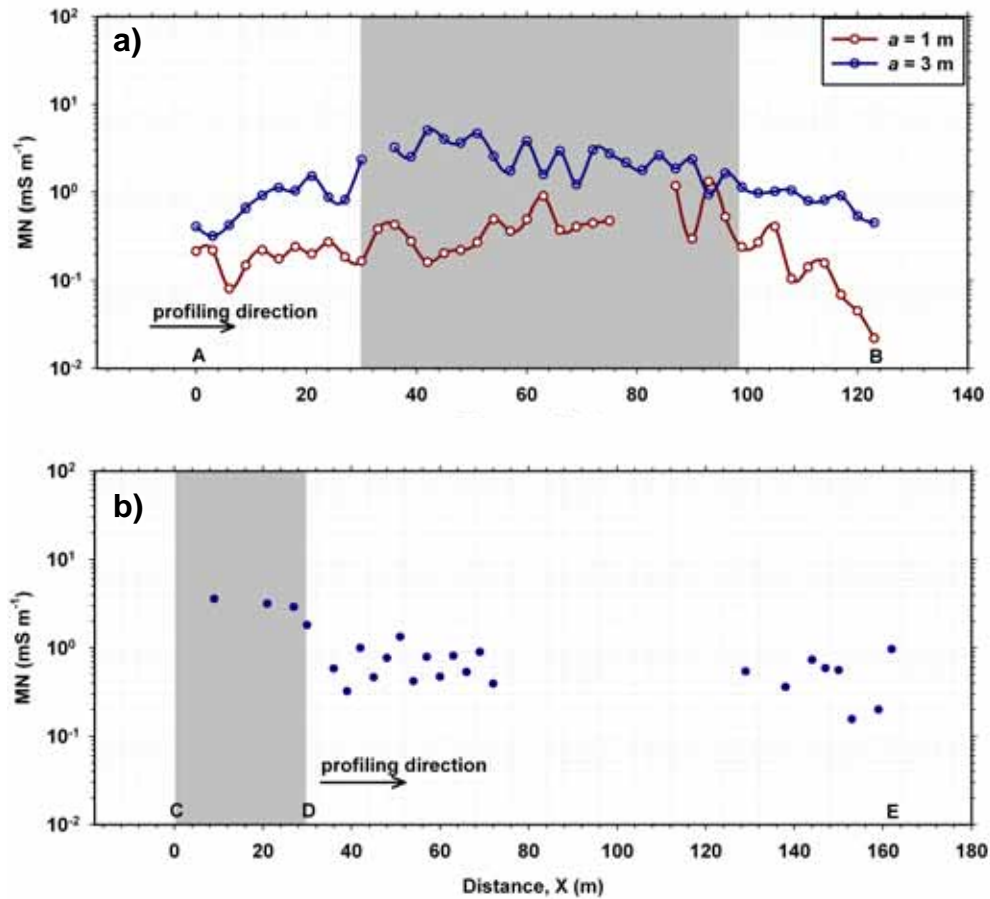
Figure 7.10. Profiles of apparent normalized chargeability at **a)** SITE 1, and **b)** SITE 2. The grey shaded region is included here to highlight sections where very low (<10 Ω m) apparent resistivities were measured.

At SITE 1, the *MN* profiles for $a = 1$ m and $a = 3$ m exhibit relatively smoother trends compared to M_a profiles. The *MN* range for the two different electrode separation are (0.02 – 1.3) mS m^{-1} and (0.3 – 5) mS m^{-1} respectively. Enhanced *MN* profiles nearer to the buried pipelines ($a = 3$ m) is well contrasted from the profile ($a = 1$ m) further away from the pipeline and nearer to the surface. Nevertheless, the two profiles exhibit relatively similar behaviour along the entire length. At SITE 2, enhanced *MN* levels (1.8 – 3.5 mS m^{-1}) are also prevalent on the section CD compared to the rest of the transect (DE), where a somewhat consistent *MN* level (0.2 – 1.3 mS m^{-1}) is observed.

It has already been discussed elsewhere that the *MN* profile is strongly related to the specific surface area, surface densities, and surface ionic mobility (see Chapter 5) as suggested by Slater & Lesmes (2002). As a measure of global polarizability [Slater & Lesmes, 2002], the *MN* profile here allows qualitative assessments on the locations where the clay content is high or there are possible zones of

electrochemical reaction at the pipeline/soil interface; both of which will result in relatively higher *MN* values. Since both these variables are also directly responsible for enhanced corrosion rates, sections with higher *MN* values can be considered under high-risk situations. Regarding this, however, the following will be emphasized. Similar to M_a, the normalized *MN* parameter does not reveal any significant anomaly, which can be associated with pipeline phenomenon; suggesting that the *MN* feature might be directly related to subsurface soils. This will be discussed further in Section 7.3.4. Notwithstanding this, evaluation of *MN* can greatly aid in isolating sections of pipelines, which are prone to corrosion risks. Note here that such isolations are not based on any quantitative scales (as for resistivity), but is purely based on qualitative assessments. For example, at SITE 1 for $a = 3$ m, relatively higher *MN* values ($> \sim 2$ mS m^{-1}) are generally observed between $30 < X < 99$ m, which coincides with the low ρ_a recorded compared to the rest of the transect. Since each of the stations is located 3 m apart, several short sections in this region, characterized by high *MN*, can be marked as possibly under high-risk situations. Similar identification can be done using the *MN* profile for $a = 1$ m. However, it appears that the profile with a depth of investigation as near as possible to the pipeline is more suitable for such qualitative assessments.

Slater & Binley (2003) while evaluating the performance of a permeable reactive barrier using conductivity and IP methods raised an important question as to the additional benefit of using IP methods in the event that simple resistivity surveys can provide quick and accurate information. They argued that since the barriers are an active IP target, the use of IP methods will be a better indicator over long term monitoring than simple conductivity evaluations. Similar views are applicable here. The ρ_a exhibit trends, which can be used to at least isolate sections of possible abnormal activity. However, the application area being conveyed here is complicated by the pipeline, which is an active IP target. The use of *MN* also has a certain advantage over ρ_a in assessing corrosivity at field scale. It follows that both ρ_a and M_a profiles may vary according to the meteorological conditions prevalent around the time that measurements are conducted. Weather conditions can alter ground water migration rates, which can manifest in ρ_a and M_a profiles. However, since *MN* is a ratio of M_a and ρ_a, it is believed that this parameter will vary slightly in different conditions. This is especially important if the pipeline ROW being surveyed is hundreds of kilometres long, in which case routine seasonal measurements are virtually impractical and non-economical. Thus, the use of *MN* has a much more practical appeal.

It appears that pipeline effects manifest differently in ρ_a and M_a measurements. Absence of significant M_a anomalies suggests that response from any defect is occurring through complex

mechanism, the strength of which maybe governed by the surface properties of the exposed pipeline as discussed earlier. Moreover, another possible condition, which can give rise to different effects on ρ_a and M_a is if the point of induced current entry and exit are characterized by moisture accumulation between the pipeline/insulation and insulation/soil interfaces, giving rise to an indirect electrolytic pathway between pipeline and soil but at the same time keeping them in a non-contact manner. This, of course will lead to current channelling.

The application area presented in this work is believed to be the first of its kind. It appears that there is much work needed to develop the understanding of polarization responses from an active or passive, partly exposed ferrous material in the natural environment, especially for any long term emplacements.

The SITE 1 transect has been further evaluated for various other laboratory based measurements as discussed earlier. Here, the soil samples collected systematically along the transect have been analysed for their various chemical and electrical properties and compared to the field DC-TDIP profiles for $a = 3$ m. Since it cannot be ascertained the degree to which the field profiles, especially ρ_a, are affected by pipelines based solely on the field results, laboratory investigations might provide additional insights on the origins of ρ_a and MN variations. Results from the various laboratory investigations will be presented and discussed in subsequent sections, aiming to provide such further insights.

7.3.3 Chemical Analysis of Soil Samples

The composition of sulphates, chlorides, and nitrates were determined (in mg kg^{-1}), as mentioned earlier. Differences in duplicate measurements on selected samples were indicated to be very small (<1%) in most instances. The minimum detectable limit, specified as the limit of reporting (LOR) for the measurement of sulphates, chlorides, and nitrates in the samples were specified as 50 mg kg^{-1}, 10 mg kg^{-1}, and 0.1 mg kg^{-1} respectively. The variation of sulphates, chlorides, and nitrates measured in the 20 samples collected at intervals of 6 m spread across the SITE 1 transect ($0 \leq X \leq 114$ m) is illustrated in Fig. 7.11.
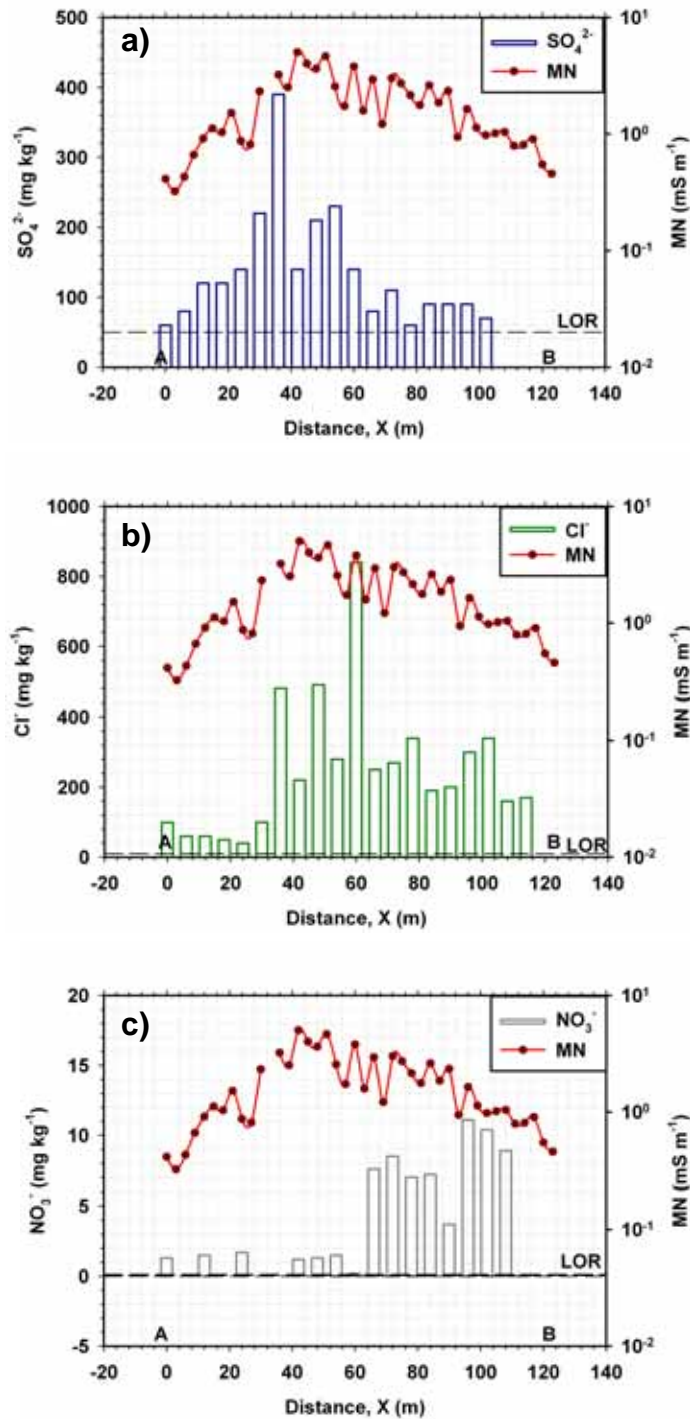
Figure 7.11. Variations of **a)** sulphates, **b)** chlorides, and **c)** nitrates in the soil samples collected from a depth of $1.2 – 1.5$ m along the SITE 1 transect. The *MN* profile for $a = 3$ m is repeated in all three illustrations to aid the eye. Note the LOR is the limit of reporting for the different species.

For some soil samples, the concentration of chemical species was below its LOR and hence was not measurable. These are reflected in Fig. 7.11. Sulphate and chloride concentrations are seen to vary between (60 – 390) mg kg^{-1} and (40 – 800) mg kg^{-1} respectively between $0 \leq X \leq 114$ m. Lower concentrations are usually present in regions with relatively lower MN. The location of the several high levels of sulphates and chlorides are seen to exist within the relatively higher levels of MN. The highest concentration of chlorides (800 mg kg^{-1}) is recorded at $X = 60$ m, which coincides with the relative location of the ρ_a minima measured at the site. On the other hand, concentrations of nitrates were generally insignificant or below the LOR for the first half of the section ($0 \leq X \leq 60$ m). They were mainly present in soil samples beyond $X > 60$ m. From the results shown in Fig. 7.11c, it is clear that the nitrate concentration show no similar features with MN.

Sulphates and chlorides are significant in soils sampled along the transect. Based on the variations observed in Fig. 7.11a and Fig. 7.11b, it appears that a superposition of the variations in sulphates and chlorides is a better reflection of the variations in MN. This is important since both of these chemical species can reduce local ground resistivities allowing higher chances of corrosion. They are also acid-forming elements and can lead to significant levels of corrosion activity occurring at any exposed pipeline surface. It has already been shown and discussed in Chapter 4 that chlorides are very aggressive towards corrosion of ferrous materials.

It is emphasized that in the present work a relatively smaller section (123 m) of pipeline ROW has been studied in detail. Indeed the strength of the technique under consideration (DC-TDIP) lies in its ability to identify very small sections which are under high-risk situations. Results from the chemical analysis indicate that DC-TDIP looks promising for this purpose. These results will be further used in the interpretation of SIP analysis and corrosion related parameters of the soil samples presented next.

7.3.4 Evaluation of DC-TDIP Results with Laboratory SIP Analysis

SIP measurements, in terms of phase and magnitude spectra, for the 20 samples in the frequency range $10^{-1} – 10^3$ Hz are presented in Fig. 7.12 – 7.15. Spectral data for each sample are also given in Appendix D.4 for completeness. All samples exhibited $-\phi$ values >1 mrad at the lowest end of the frequency spectrum and the magnitude contrasts are well observed. Error bars for the phase spectra correspond to one standard deviation of 3 repeated measurements (see Appendix D.4) carried out at intervals of 10 mins. For magnitude spectra, the error bars are too small to register; indicating their high reproducibility.
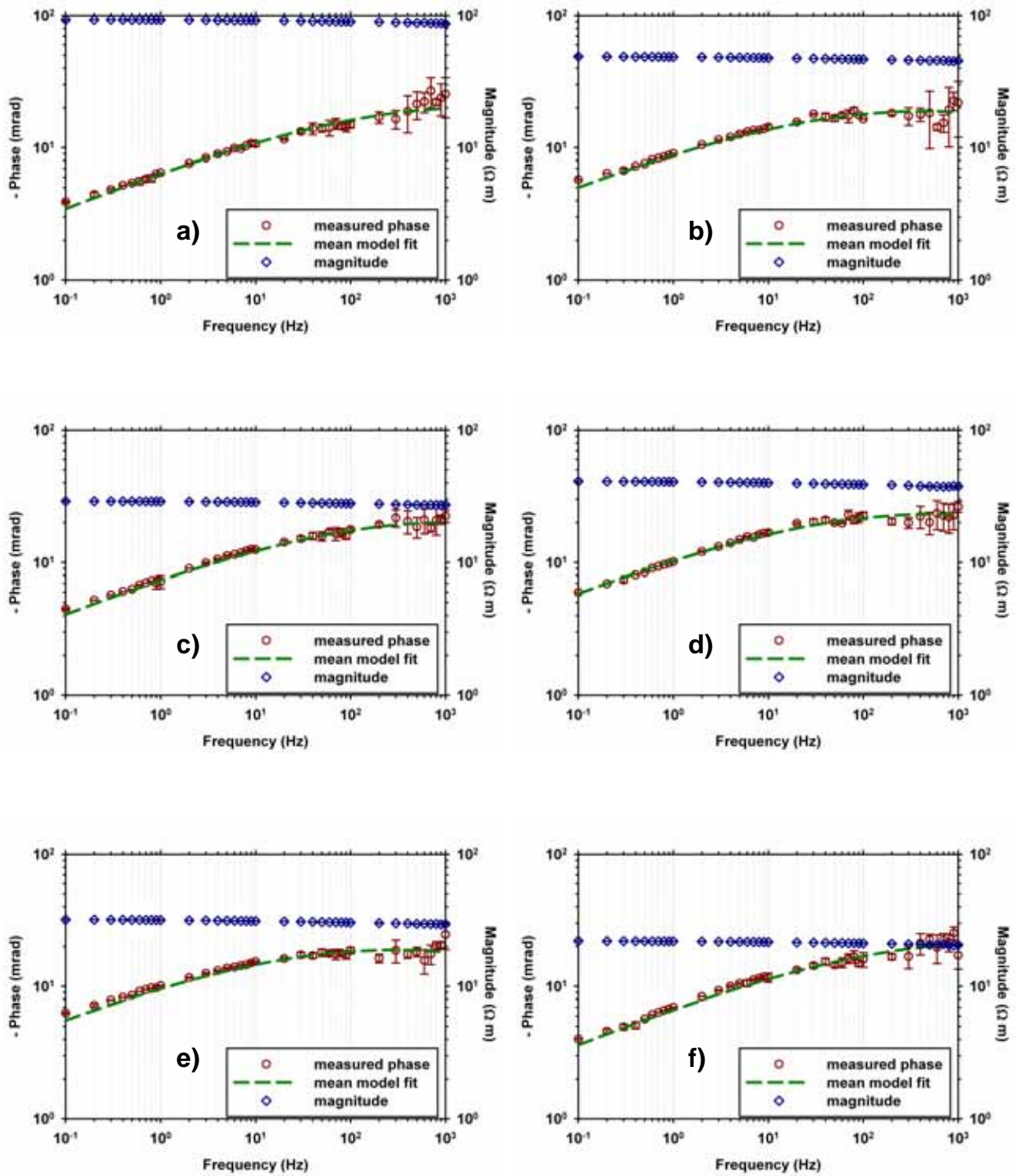
Figure 7.12. Phase and magnitude spectra for soils from Stations **a)** 1, **b)** 3, **c)** 5, **d)** 7, **e)** 9, and **f)** 11. The mean Cole-Cole model fit to each of the phase spectra is also given.
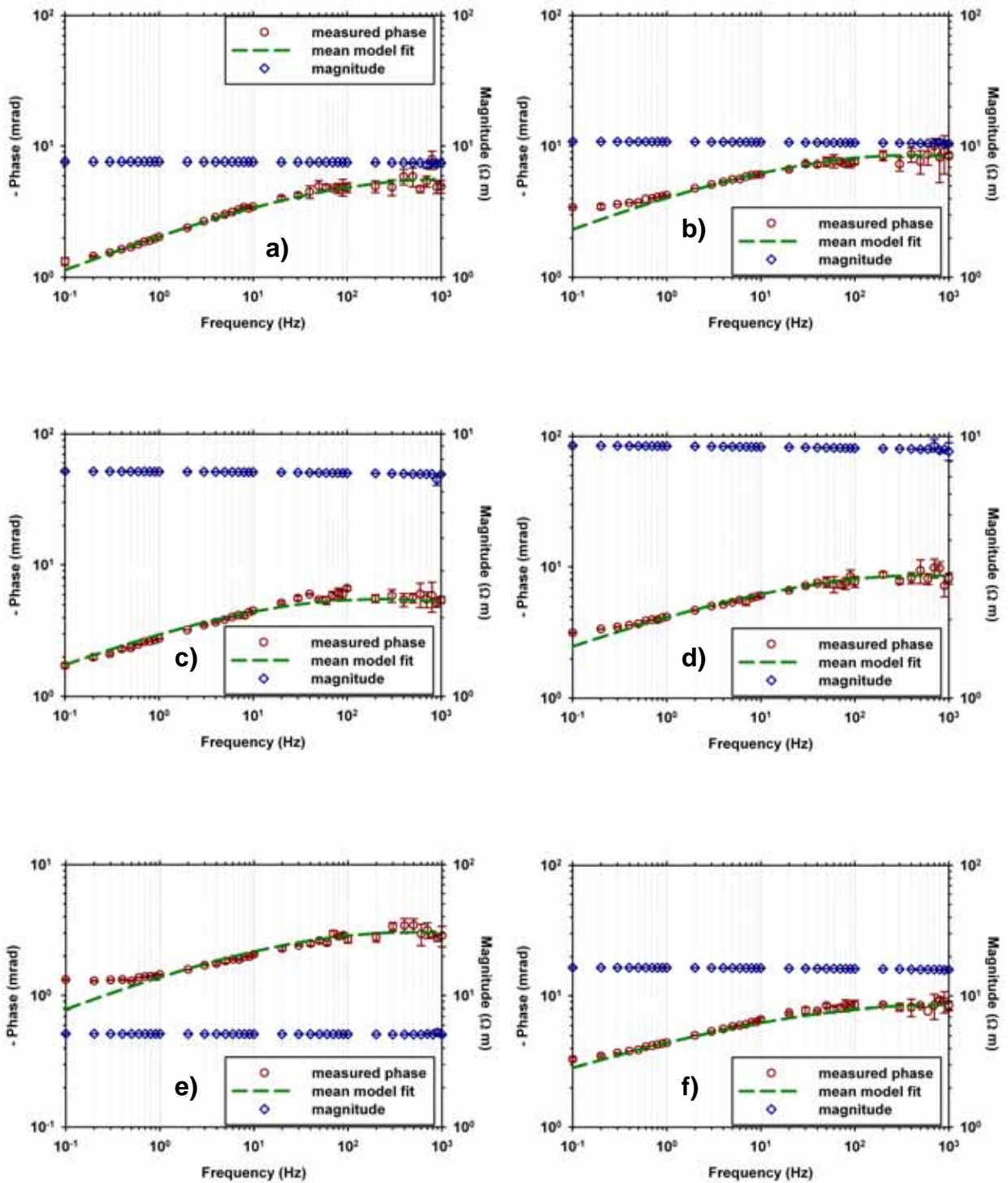
Figure 7.13. Phase and magnitude spectra for soils from Stations **a)** 13, **b)** 15, **c)** 17, **d)** 19, **e)** 21, and **f)** 23. The mean Cole-Cole model fit to each of the phase spectra is also given.
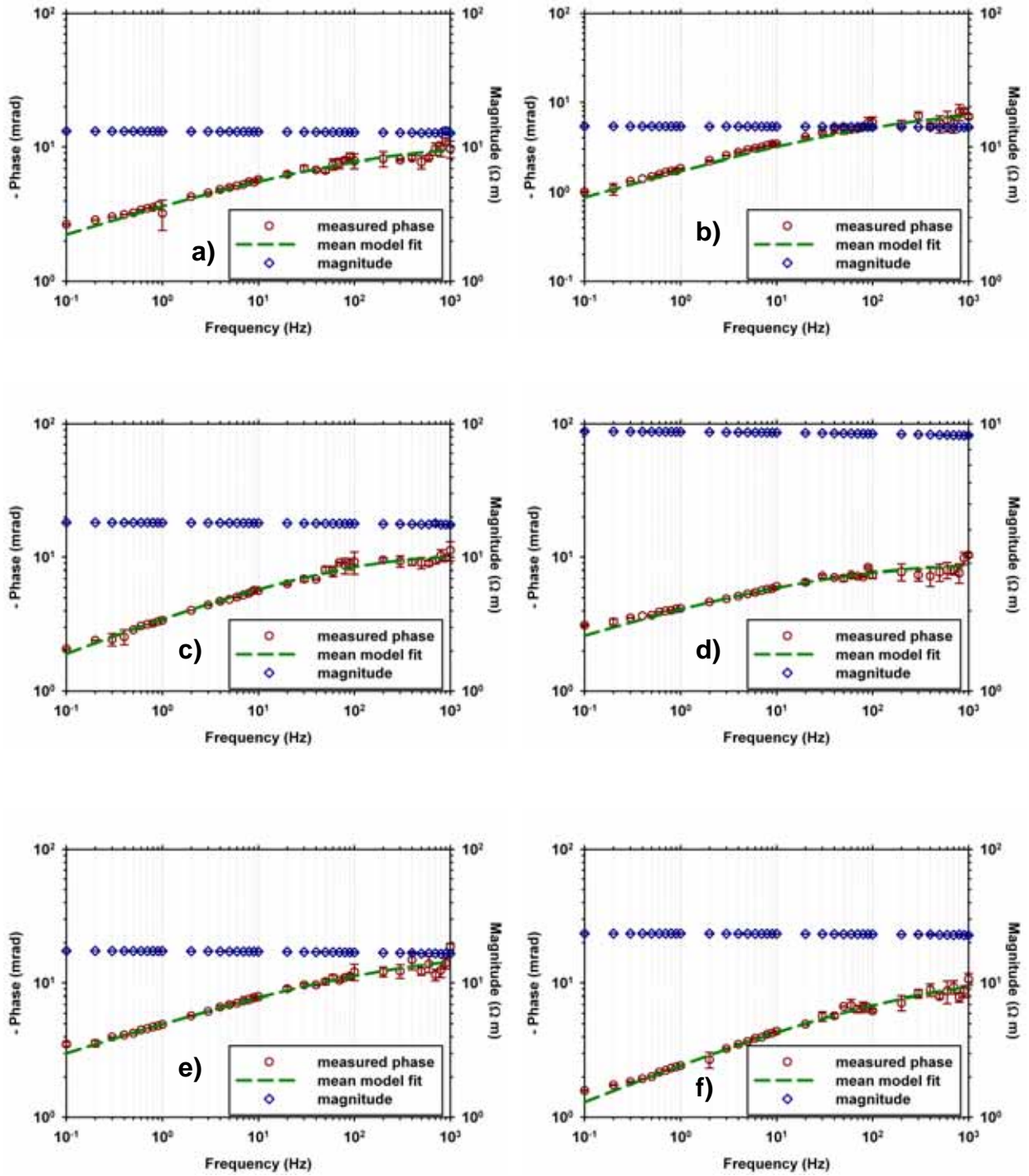
Figure 7.14. Phase and magnitude spectra for soils from Stations **a)** 25, **b)** 27, **c)** 29, **d)** 31, **e)** 33, and **f)** 35. The mean Cole-Cole model fit to each of the phase spectra is also given.
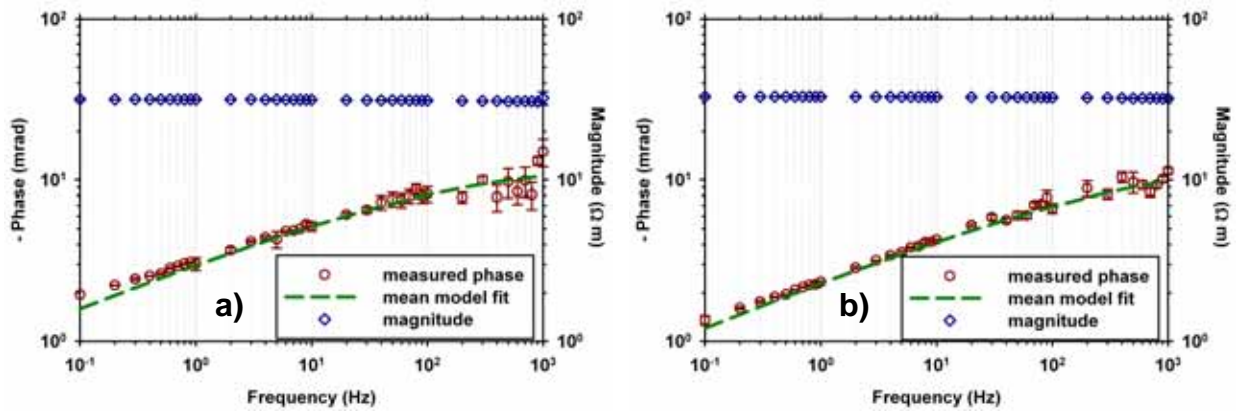
Figure 7.15. Phase and magnitude spectra for soils from Stations **a)** 37, and **b)** 39. The mean Cole-Cole model fit to each of the phase spectra is also given.

Generally, it was noticed that all ϕ-spectra could be very well described by a single Cole-Cole model. Hence, Cole-Cole parameters from the ϕ-spectra were determined using the method already described in Chapter 5. For a few selected samples (*e.g*., sample from Station 1 in Fig. 7.12a) there was an indication of a secondary mechanism, *viz*., MWS effect, at higher frequencies (>800 Hz). High-end frequency data suspected of displaying this behaviour were not included in the inversion procedure. These effects were generally observed for frequencies >~800 Hz, resulting in 3 sets of experimental data points. The omission of this data from the complete dataset did not affect the inversion procedure. The ϕ-spectra for each measurement and its repeat were individually inverted. This was done to ensure identification of any spurious measurements. Note a total of 60 ϕ-spectra were thus analyzed and these results are summarized in Appendix D.5. From these, the weighted means and standard deviations for each of the Cole-Cole parameters for all samples were computed as described elsewhere in the thesis (Chapter 5). For illustration purposes, the model fit for all ϕ-spectra were calculated using the forward Cole-Cole model from the weighted Cole-Cole parameters and are shown in Fig. 7.12 – 7.15 accordingly.

A summary of these weighted Cole-Cole parameters together with other electrical characterizations for all 20 samples are presented in Table 7.1. Note that the EC of 1:5 soil/water is stated in Ω m. To avoid confusion amongst terms, the EC of 1:5 soil/water will be referred hereafter as the electrical resistivity (ER). In a strict sense, this ER does not correspond to the resistivity of the pore fluid completely saturating the samples. This is due to the different proportions of soil/water ratios in a) the completely saturated samples for SIP analysis, and b) the soil/water leach in which the ER was determined. Nevertheless, the ER here, due to consistency, indicates the soil salinity, which is found

191

to vary considerably amongst the samples $(26 - 416.7 \; \Omega$ m). On the other hand, significant variations are observed in ρ_{DC} amongst the samples collected from SITE 1; varying between $(5.2 - 92.8) \; \Omega$ m, with a mean of $(24.1 \pm 20) \; \Omega$ m, stated to one standard deviation. The Cole-Cole parameter c appears to vary in a narrow window of $0.25 - 0.32$, possibly suggesting similar distribution of polarizable sources in the soils. However, the other Cole-Cole parameters (m and τ) show large variabilities, indicating the complexities present amongst the samples. Note the $-\phi_{1 \; Hz}$ is the experimentally measured phase value at the frequency of 1 Hz.

Table 7.1. Summary of weighted Cole-Cole parameters and other electrical characterizations of soil samples collected from different stations along SITE 1 transect.

Station	ER 1:5 soil/water	Sample DC resistivity	$- \phi_{1 \; Hz}$	Cole-Cole parameters		
	(Ω m)	ρ_{DC} (Ω m)	(mrad)	m ($\times 10^{-3}$)	c	τ (μs)
1	416.7	92.8 ± 0.2	6.5 ± 0.02	154 ± 6	0.3 ± 0.002	96 ± 30
3	212.8	48.9 ± 0.1	9.01 ± 0.03	145 ± 4	0.3 ± 0.002	482 ± 115
5	151.5	28.9 ± 0.1	7.2 ± 0.8	155 ± 3	0.3 ± 0.001	172 ± 29
7	181.8	40.9 ± 0.06	10.12 ± 0.05	175 ± 4	0.3 ± 0.002	412 ± 76
9	149.3	31.9 ± 0.08	10.11 ± 0.04	145 ± 2	0.3 ± 0.001	713 ± 90
11	87	22 ± 0.03	7 ± 0.02	162 ± 4	0.3 ± 0.001	96 ± 18
13	38.3	7.7 ± 0.01	2.04 ± 0.02	46 ± 2	0.3 ± 0.001	136 ± 39
15	58.1	10.8 ± 0.02	4.25 ± 0.01	68 ± 1	0.3 ± 0	466 ± 67
17	33.4	7.2 ± 0.01	2.76 ± 0.02	45 ± 1	0.3 ± 0	765 ± 94
19	46.9	9.2 ± 0.01	4.19 ± 0.01	74 ± 2	0.28 ± 0.001	321 ± 42
21	26	5.2 ± 0.01	1.44 ± 0.01	25 ± 1	0.3 ± 0	337 ± 44
23	76.9	16.5 ± 0.02	4.43 ± 0.02	82 ± 2	0.25 ± 0.001	225 ± 36
25	72.5	13.1 ± 0.02	3.2 ± 0.8	95 ± 2	0.25 ± 0	36 ± 8
27	84	14.3 ± 0.02	1.85 ± 0.02	56 ± 2	0.32 ± 0	42 ± 10
29	99	18.2 ± 0.01	3.39 ± 0.02	80 ± 2	0.3 ± 0	118 ± 17
31	87	9.4 ± 0.01	4.17 ± 0.02	82 ± 1	0.25 ± 0	147 ± 23
33	101	17.4 ± 0.01	4.94 ± 0.01	147 ± 6	0.25 ± 0.001	19 ± 6
35	131.6	23.4 ± 0.03	2.43 ± 0.04	80 ± 1	0.3 ± 0	30 ± 3
37	158.7	31.6 ± 0.04	3.03 ± 0.3	88 ± 4	0.3 ± 0.001	44 ± 13
39	192.3	32.9 ± 0.04	2.34 ± 0.03	91 ± 5	0.3 ± 0.001	14 ± 4

It is emphasized here that the idea of these characterizations is to investigate if the trends observed during DC-TDIP profiling are also reflected in the soil samples collected strategically along the transect. Nevertheless, some investigation is necessary in order to understand the manifestation of the electrical features in these samples as well as to honour any possible inter-relationship within the laboratory dataset so far. In view of this, the effects of sulphates and chlorides (due to their significant compositions relative to nitrates) on ρ_{DC}, the Cole-Cole chargeability parameter, m, were investigated and the results are illustrated in Fig. 7.16a and 7.16b.

Regression analysis between chloride content exhibits good inverse correlations with ρ_{DC} ($r^2 = 0.6$) and m ($r^2 = 0.81$) on a semi-log scale. On the other hand, variations in sulphate contents appear to display much weaker inverse linear correlations with ρ_{DC} ($r^2 = 0.22$) and m ($r^2 = 0.11$). Dissolved salts are known to decrease soil resistivity due to enhanced electrolytic conduction, while reductions in m with chlorides as well as with sulphates indicate the reduced surface conductivity in the soils due to the presence of enhanced ionic species. In both cases, it appears that chlorides, at least in these samples, have a more profound effect on the bulk and surface conductivity mechanisms. In the case of bulk conductivities, this is further evidenced by the relatively strong regression between ER and chloride content ($r^2 = 0.63$) than sulphate content ($r^2 = 0.33$) as shown in Fig. 7.16c.
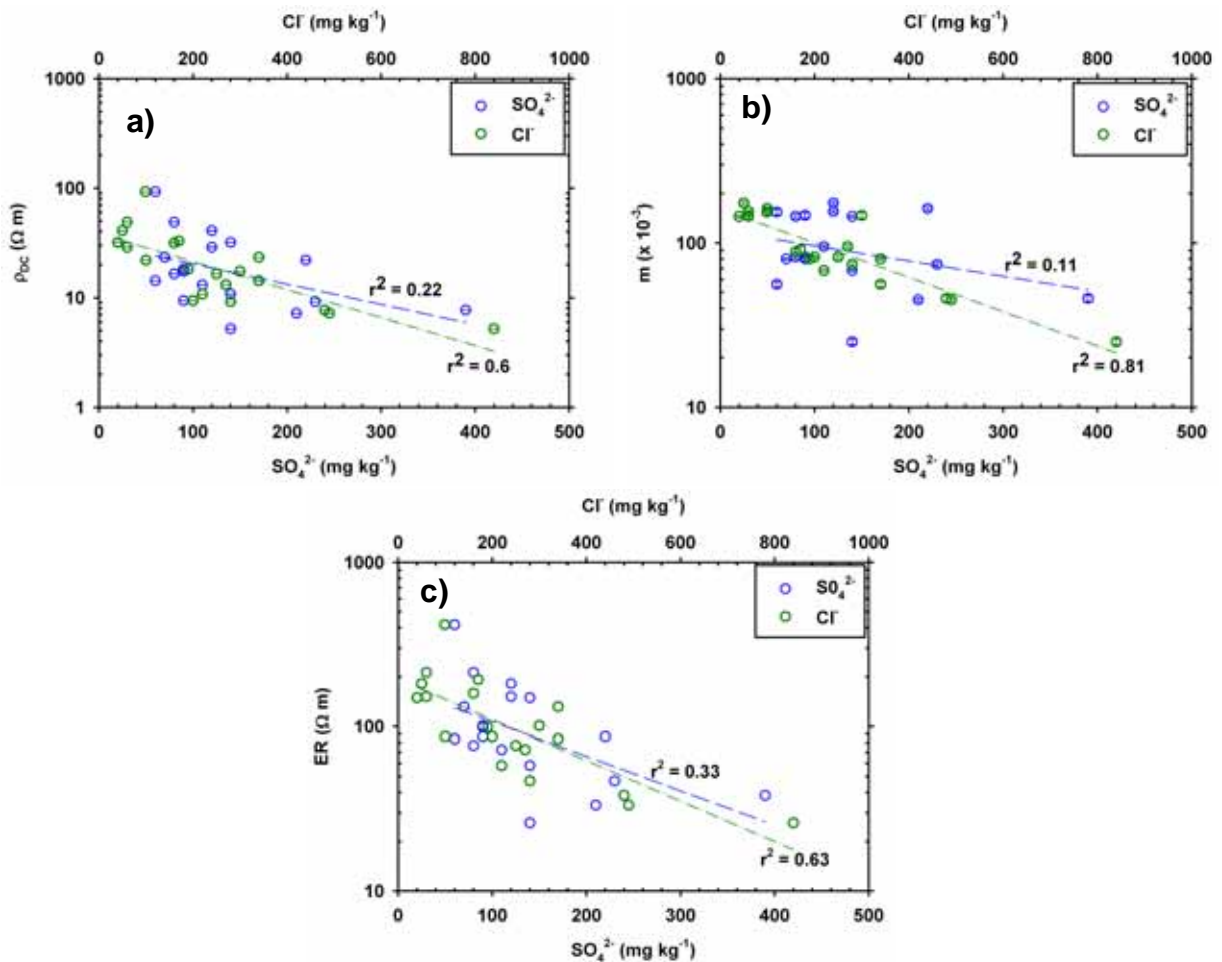
Figure 7.16. Regression analysis between **a)** ρ_{DC} **b)** m, and **c)** ER with sulphates and chlorides content in the soil samples. Note the scaling in m.

The relationships presented above so far are of course one aspect of local perturbations in ρ_{DC} and m brought about by dissolved sulphate and chloride contents. Another important feature, which can cause systematic differences in ρ_{DC} and m is varying clay content. Slater & Lesmes (2002) have

shown that identification of clayey soils can usually be carried out through cross-plots of MN and σ_{DC} (inverse of ρ_{DC}). This cross-plot represented in terms of the normalized Cole-Cole chargeability parameter (m_n) with ρ_{DC} for the soil samples is given in Fig.7.19.

Figure 7.17 reveals that the clay content amongst the soil samples is not uniform. Clustering of data points at higher m_n values with low ρ_{DC} is generally indicative of enhanced clay content in the soil samples. The most distinguishable sample amongst all appears to be that from Station 1 characterized by the highest ρ_{DC} (92.8 ± 0.2 Ω m) and lowest m_n (1.66 ± 0.07 mS m^{-1}). Note the gradual increase in m_n as ρ_{DC} decreases.
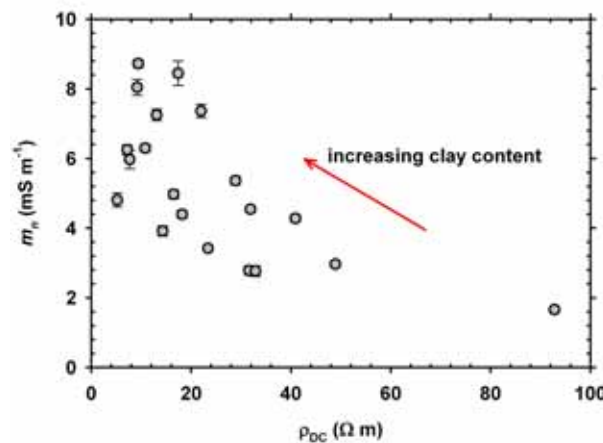
Figure 7.17. Plot of ρ_{DC} against m_n of different soils aids distinguishing soils with higher clay contents.

So how do these electrical characterizations aid in the interpretation of the DC-TDIP profiling results? Figure 7.18 shows the usefulness of ground truthing data in understanding and providing further insights of the DC-TDIP profiles. Here, the ρ_{DC} and m_n of the soil samples collected over the transect is illustrated with the ρ_a and MN respectively, measured for a-spacings of 3 m, respectively. Note the interpolation shown is to aid the eye and does not represent any physical basis.

The ρ_{DC} of the soil samples have been measured under completely saturated conditions and represent to some extent the minimum resistivity the soil samples can acquire. On the contrary, ρ_a are apparent values measured in the field and represent the average resistivity of the representative volume of the soil material for a-spacing of 3 m. In this manner a direct comparison between the two values is not appropriate. Nevertheless, it is worthy to note that in general ρ_a appears less than the ρ_{DC}. It can be argued that the soil samples collected along single cores do not strictly represent overall resistivity of the soil volume averaged by ρ_a. However, such behaviour is also indicative of conductive elements,

which can cause low apparent resistivity values. It is believed that these conductive elements include the pipelines giving rise to lower ρ_a values. On the other hand, variations in ρ_{DC} appear to mimic the ρ_a observed in field; higher towards the start and end of the transect and lower towards the middle of the transect. This feature indicates that ρ_a does reflect variations in soil properties along the transect. Owing to these facts, there is an indication that the overall measurements are indeed affected in a complex manner by the buried pipelines. The pipeline-soil system appears to inflict a coupled response on the overall ρ_a measurements.
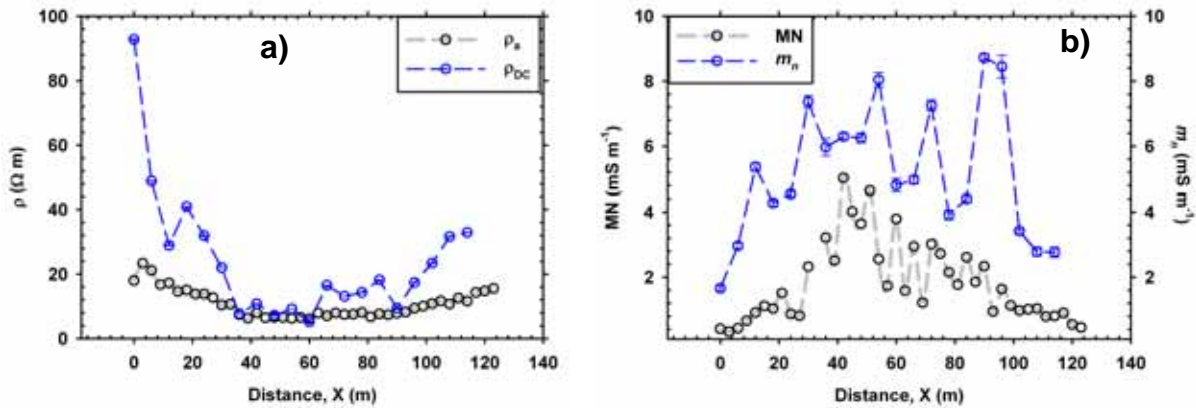
Figure 7.18. Variations in **a)** ρ_{DC} and **b)** m_n in the soil samples collected along SITE 1 transect. For illustration purposes the apparent resistivity and apparent normalized chargeability variations from DC-TDIP at a-spacing of 3 m are also given.

The m_n variations amongst stations and their overall comparison with MN profiles acquired in DC-TDIP profiling is shown in Fig. 7.18b. Regarding these variations, however, the following is emphasized. The m_n values specifically correspond to normalization of the Cole-Cole chargeability parameter, while MN is computed from the normalization of the apparent integral chargeability parameter. Thus, a direct comparison of their magnitudes is irrelevant. There is a notable high m_n feature displayed by soils collected from Stations 31 and 33 ($X = 90$ m and 96 m respectively), which is absent in the MN profile. This is attributed to the complex chemistry of the soil samples and its manifestation in the SIP signatures. Indeed, samples from these locations were relatively higher in nitrates content and the SIP responses appear to be sensitive to complicated electrolytic chemistry. However, it is interesting to note that the trends displayed in the field by MN and in the laboratory soil samples by m_n are similar. The relative change in amplitude for both m_n and MN from the start of the transect towards the middle also appear somewhat similar, unlike between ρ_{DC} and ρ_a.

The general similarity between m_n and MN suggests that the polarization magnitude captured by the latter in the field is mainly arising due to surface conductivity phenomena in the subsurface soils. This

has been mentioned in previous discussions (Section 7.3.2). Comparison of field results to laboratory measurements on soil samples further suggest that the presence of any exposed surface area (allowing current entry and exits on the pipeline) is relatively small and insufficient to induce a large polarization response, distinguishable from normal polarization processes in soils. Nevertheless, there does appear to be a conductive pathway along which current can travel along the pipeline in order to lower the ρ_a values. The relatively higher values of MN, between 40 m $< X <$ 60 m, can be generally associated with higher clay contents, allowing this section to be considered under high-risk as discussed previously.

Further insights on soils from the transect is provided by the variations of $-\phi_{1\,Hz}$ and the Cole-Cole τ parameter given in Figure. 7.19.
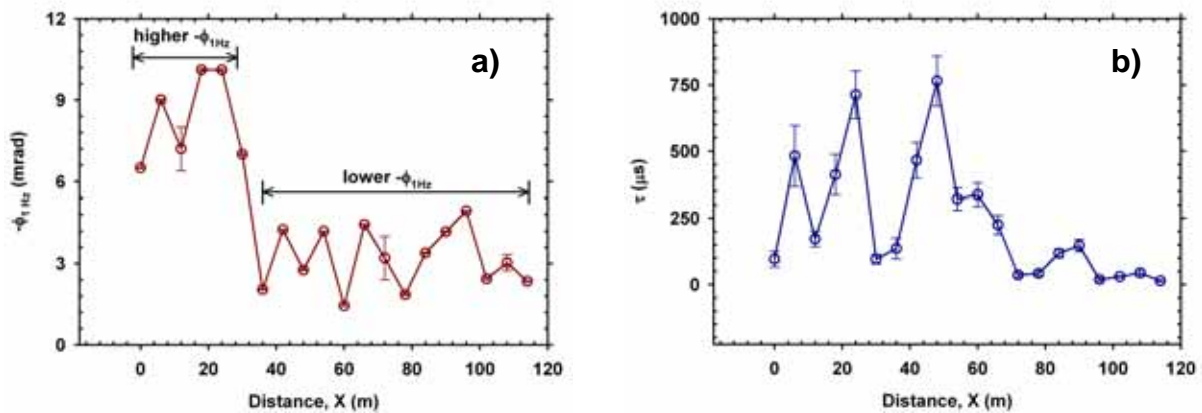
Figure 7.19. Variations in **a)** $-\phi_{1\,Hz}$ and **b)** τ in the soil samples collected from different stations along SITE 1 transect. Note the interpolation is given to aid the eye.

Generally, soils collected from the beginning of the transect exhibit large $-\phi_{1\,Hz}$, while those acquired from $X >$ 36 m appear to have lower values. This onset of lower $-\phi_{1\,Hz}$ values appears to correspond well with the onset of relatively higher chloride contents in the soil sample (see Fig. 7.11). As an indicator of polarizability, $-\phi_{1\,Hz}$ tends to indicate the relative strengths of bulk and surface conduction mechanisms which are present amongst the soil samples. On the other hand, the variation of Cole-Cole τ parameter for the soil samples along the transect display a much more complicated characteristic. There is some indication that the τ values are much lower towards the end of the transect. However, some low values are also obtained for soils collected towards the start and middle of the transect. The relaxation time constant generally is indicative of the size of the polarisable sources but can equally be affected by the salinity of the pore fluid. Hence, features observed here is a combination of grain size and salinity effects.

Following the discourses presented here, it can be safely assumed that the profiling results from the field can be used to identify high-risk sections. This is especially true with *MN* profiles, which appear to be related mainly to subsurface soils. The next logical assessment is to investigate if the soils associated with higher *MN* are indeed corrosive as characterized by their influences on metal surfaces. Soil corrosiveness in terms of R_p and other corrosion related parameters have been measured to provide further insight on the applicability of assessing soil corrosivity using DC-TDIP profiles. These are presented next.

7.3.5 Analysis of Corrosion related Parameters

The galvanostatic pulse technique was used to investigate the double layer characteristics of the interface established between each of the soil samples and a cast-iron working electrode. Although the abandoned pipelines at the site are made out of ductile-iron, the use of a cast-iron standard contact provides an indication for the corrosivity ranking of all ferrous materials in the acquired soil samples.

A total of 20 cast-iron/soil systems were studied and each measurement was repeated at least 3 times to ensure reproducibility. For Day 1 analysis, both charging and discharging curves were analysed to compute the overall weighted corrosion related parameters, while for Day 7 only charging curves were sufficient. Note a total of 167 charging and discharging curves were collected and analysed (includes repeated measurements). The analytical scheme using galvanostatic pulse techniques has been well discussed in Chapter 4, and hence will not be repeated here. To maintain continuity within this section, the charging and discharging curves for all analysis are not given here but are provided in Appendix D.6. Following curve fitting of the charging and discharging sections using the model discussed in Chapter 4, the various corrosion related parameters describing the double layer characteristics at the cast-iron/soil interface (E_{CORR}, R_p, C_{dl}, and β) as well as the Ohmic-drop in the system were estimated. These parameters for each respective measurement and its repeat are given in Appendix D.7, in their raw form. The weighted means and standard deviations computed from the repeated measurements and converted to their conventional units are summarized in Table 7.2. For completeness purposes, the pH of each soil electrolyte, measured on Day 1 is also given. For a few systems (consisting of soil electrolytes from Stations 1, 3, and 37), Day 7 measurements could not be performed due to the presence of large Ohmic-drops which overwhelmed the working voltage (± 10 V) of the Eco-chemie microAUTOLAB III galvanostat.

Table 7.2. Summary of corrosion related parameters for cast-iron exposed to the soil samples from different stations. Note the pH of the soil samples are also given. E_{CORR} and R_{Ω} are averages determined from repeated measurements and are stated to $\pm$ 1σ (except for Day 1 E_{CORR}, whereby the errors were generally very small, <0.1%, and hence are negligible). Other parameters are determined from weighted methods (See Appendix A.4).

Station	Soil pH	DAY 1										DAY 7										
		E_{CORR} (-mV)*	R_{Ω} (kΩ)		R_p (kΩ cm²)		C_{dl} (μF cm⁻²)		β			E_{CORR} (-mV)		R_{Ω} (kΩ)		R_p (kΩ cm²)		C_{dl} (μF cm⁻²)		β	
		μ	μ	±σ	μ	±σ	μ	±σ	μ	±σ		μ	±σ	μ	±σ	μ	±σ	μ	±σ	μ	±σ
1	5.6	700	1.18	0.012	8.32	0.07	99.6	0.9	0.616	0.002		NM	NM	NM	NM	NM	NM	NM	NM	NM	NM
3	5.34	687	0.576	-	11.14	0.05	117.1	1.7	0.548	0.003		NM	NM	NM	NM	NM	NM	NM	NM	NM	NM
5	6.06	692	0.372	0.005	5.12	0.01	190.4	1.2	0.671	0.002		173	-	38	-	195	2	1.64	0.04	0.48	0.005
7	5.4	697	0.519	0.007	4.24	0.01	316.8	0.7	0.565	0.001		-19	8	20	4	135	2	8.6	0.2	0.585	0.004
9	5.47	709	0.428	0.001	4.55	0.01	362	1.9	0.638	0.001		34	50	5.7	0.8	35.3	0.3	34.2	0.6	0.541	0.002
11	5.81	705	0.273	0.004	3.51	0.006	488.6	1.9	0.665	0.002		26	25	4	0.1	15.1	0.1	9	0.2	0.548	0.008
13	5.07	693	0.1	0.000	3.71	0.005	310.2	1.2	0.742	0.001		510	0	0.22	0	1.3	0.01	461	1	0.606	0.002
15	5.18	680	0.137	0.004	3.03	0.003	206	0.4	0.747	0.001		134	16	6.8	0.1	99.7	0.1	2.1	0.01	0.666	0.002
17	5.46	702	0.086	0.004	2.62	0.002	220.9	0.3	0.724	0.001		178	3	7.5	0.4	241	1	1.3	0.01	0.578	0.003
19	5.46	688	0.116	0.003	3.96	0.005	291.5	0.9	0.74	0.001		283	8	2.8	0.04	28.7	0.1	4.5	0.03	0.586	0.004
21	5.28	691	0.067	0.003	2.59	0.002	326.1	0.6	0.758	0.001		267	6	2.4	0.04	7.6	0.1	107	1	0.571	0.002
23	6.1	701	0.199	0.005	5.68	0.005	247.4	0.6	0.715	0.001		112	5	27.4	0.6	190	6	17	1	0.512	0.003
25	5.04	699	0.169	0.005	2.92	0.003	346.4	0.8	0.762	0.001		165	1	37.2	0.9	139	2	8.1	0.2	0.558	0.004
27	5.35	699	0.179	0.003	4.11	0.003	291.6	0.7	0.732	0.001		137	6	24.5	0.3	204	1	4.2	0.1	0.599	0.002
29	6.01	698	0.235	0.003	4.27	0.005	240.4	0.7	0.65	0.001		-14	2	18.2	0.8	162.3	3	10.8	0.4	0.512	0.003
31	5.23	690	0.185	0.007	4.01	0.005	328.2	1.1	0.74	0.001		28	1	22.5	0.2	336	4	6.8	0.1	0.571	0.002
33	5.1	688	0.218	0.005	3.29	0.007	302.5	1.7	0.773	0.002		130	17	19.9	0.2	54	2	8.2	0.7	0.417	0.009
35	4.9	684	0.33	0.001	5.09	0.006	281.2	0.9	0.677	0.001		-29	17	64	17	960	8	1.2	0.03	0.552	0.002
37	5.64	692	0.429	0.002	3.97	0.007	371.8	1.9	0.645	0.001		NM	NM	NM	NM	NM	NM	NM	NM	NM	NM
39	5.95	699	0.447	0.004	5.11	0.005	276.3	0.8	0.681	0.001		324	18	4.9	0.3	25.5	0.1	7.8	0.1	0.542	0.002

NOTE: NM – not measured due to large Ohmic drops.

Before discussing the results in context of the site characteristics, an evaluation of the various parameters and any inter-relationship is necessary. Here, it is noted that the pH of the soil samples were generally similar and confined in the range 4. 9 – 6.1. Also, E_{CORR} and R_p appear to exhibit an inverse relationship with each other as shown in Fig. 7.20a. The significance of this feature on the overall analysis using galvanostatic pulse techniques and the adopted circuit model has already been identified in Chapter 4. It is again emphasized here that the presence of this inverse behaviour amongst E_{CORR} and R_p validates the assumption that significant resistances owing to diffusion can be ignored in the cast-iron/soil systems.
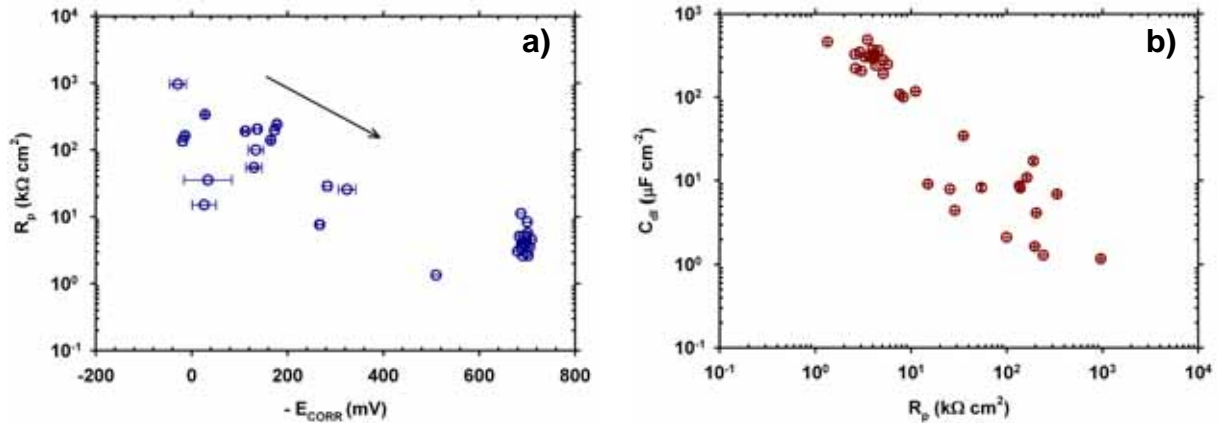
Figure 7.20. Variation of R_p with **a)** -E_{CORR}, and **b)** C_{dl}. Note that R_p exhibits a decreasing trend with -E_{CORR}.

Likewise, R_p and C_{dl} also display an expected inverse relationship as shown in Fig. 7.20b. The range of values observed for R_p and C_{dl} were (2.59 – 11.14) kΩ cm^2 and (99.6 – 488.6) μF cm^{-2} respectively during Day 1, and (1.34 – 960.1) kΩ cm^2 and (1.17 – 461.1) μF cm^{-2} respectively during Day 7. As R_p is sufficient on its own to provide indication of potential soil corrosivity, it has been investigated further as follows. Figure 7.21 shows the spatial distributions of the soil corrosivity, in terms of R_p, over the SITE 1 transect determined for Day 1 and Day 7.

Several important observations are made regarding the spatial distribution of measured R_p values along the transect. Firstly, Day 1 variations appear to agree well with the trends observed in ρ_a and MN profiles for a-spacing of 3 m. Mainly, the soil appears to be more corrosive towards the middle and becomes less corrosive towards the start and end of the transect. The lowest R_p measured for Day 1 coincides with $X = 48$ m and $X = 60$ m, both of which can be considered as high-risk regions in the MN profile. Samples from these two locations also exhibited the highest levels of chloride contents (490 mg kg^{-1} and 840 mg kg^{-1} respectively).
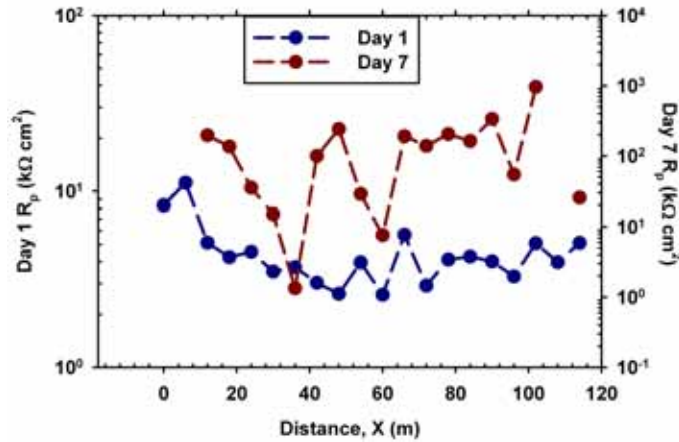
Figure 7.21. Day 1 and Day 7 polarization resistances for cast-iron/soil systems have been used to infer the spatial distribution of soil corrosivity shown by the filled circles along SITE 1 transect. Note that the interpolation is meant to aid the eye as usual.

However, measurements of cast-iron/soil systems on Day 7 display a different feature. There is some indication of enhanced contrasts in R_p values in soil samples collected from nearby stations. These features are also present in Day 1 distributions, but with less contrast. Nevertheless, the lowest R_p still appears to be in the high-risk region. The emergence of enhanced contrasts in these features can be associated with the different factors governing the corrosion rates, when the soil electrolytes have undergone natural desaturation. To understand these factors, cross-plots of ρ_{DC} against R_p, and $\ln(m_n)$ against $\ln(R_p)$ were investigated, and are presented in Fig. 7.22.
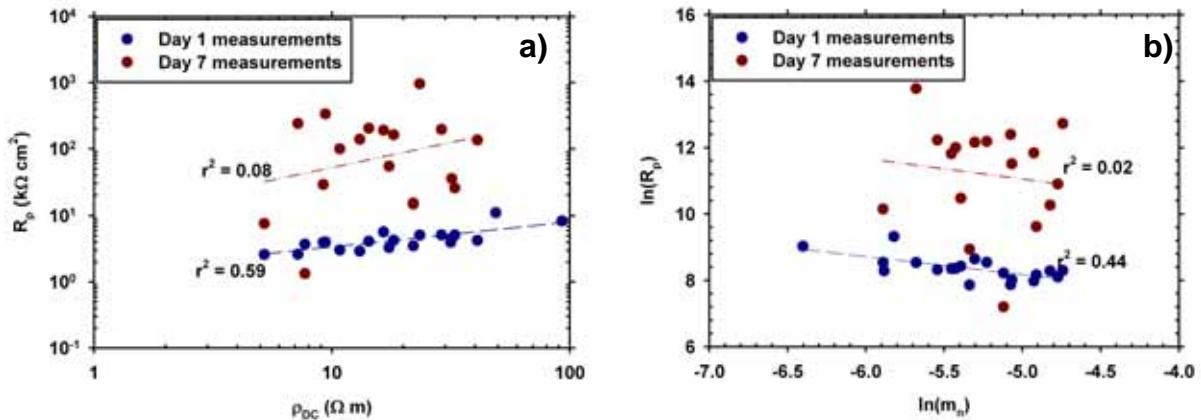
Figure 7.22. Regression analysis between **a)** ρ_{DC} and R_p, and **b)** $\ln(m_n)$ and $\ln(R_p)$.

It has been shown elsewhere in the thesis that corrosion on Day 1 is governed by the pore fluid while soil factors tend to manifest strongly during Day 7 corrosion processes. For the soil samples collected from the field, however, some anomalous features were observed, which are as follows. Day 1 corrosion processes, quantified by R_p, appears to exhibit relatively good correlation with ρ_{DC} ($r^2 =$

0.59) and m_n ($r^2 = 0.44$) as shown in Fig. 7.24. Soils showing higher ρ_{DC} are generally associated with high R_p, while soil with high m_n generally have lower R_p values. However, these features disappear during the Day 7 corrosion process. Regression analysis reveals poor correspondence between R_p and ρ_{DC} ($r^2 = 0.08$), and m_n ($r^2 = 0.02$).

The fact that m_n shows relatively good regression with R_p on Day 1 indicates that there are some effects originating from soil grains on the overall corrosion process. However, the absence of any strong correlations between ρ_{DC} and R_p, and between m_n and R_p on Day 7 plausibly indicates a change in soil physical and/or chemical properties. The fact that m_n is a normalized parameter, suggests that m and ρ_{DC} vary non-linearly over the period of natural desaturation. In terms of soil resistivity, this is evidenced by the poor correspondence between the R_Ω, which in essence represents the bulk soil resistance, measured during Day 1 and Day 7 as shown in Fig. 7.23a.
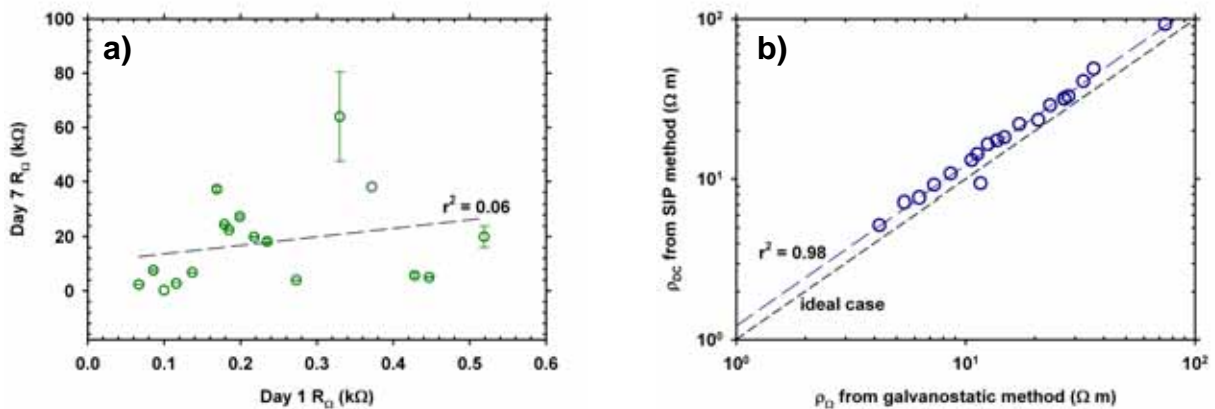
Figure 7.23. **a)** Variations in R_p between Day 1 and Day 7 display poor correspondence, and **b)** comparison between soil resistivities determined in SIP and galvanostatic pulse methods. Note the dashed black line in **(b)** corresponds to the ideal situation**.**

The correspondence between soil resistivities determined in SIP and galvanostatic methods are also shown in Fig. 7.23b. Generally, they agree well, though SIP measurements indicate enhanced values, which can be attributed to the different conditions the soils were subjected to in the two different methods. In Fig. 7.23a, the absence of any monotonic behaviour between the bulk soil resistances on the two different days indicate mechanisms apart from salinity and clay content are causing different transformations within the soil electrolytes. Consequently, the ρ_{DC} and m_n measured on Day 1 under a consistent state (completely saturated) is uncorrelated with those values, which would be present on Day 7. A possible explanation for this behaviour is that there are chemical transformations occurring over the natural desaturation period caused possibly by bacterial activity in the presence of sulphates. An evidence of this attribution is that the lowest R_p (1.34 ± 0.01 kΩ cm^2) measured on Day 7

corresponded to a sample collected from $X = 36$ m, which had the highest level of sulphate content amongst all samples (390 mg kg^{-1}). Such activities can lead to changes in the associated soil electrolytes, which are being characterized. In essence, this represents the complexities of any corrosion behaviour in soils. Apart from this, it is worth mentioning here that in general the β parameter determined for all the cast-iron/soil systems appears to decrease from Day 1 to Day 7 (see Table 7.2). Complexities involving this parameter have already been discussed elsewhere in the thesis (Section 4.3..3.4, Chapter 4) and hence will not be repeated here. Nevertheless, results from this section suggest that the β parameter is indeed affected by various factors at the metal/soil interface.

As has been stated elsewhere (Chapter 1) in the thesis, corrosion due to microbiological activity merits an investigation on its own since it can complicate the physical and chemical properties of soils governing corrosion process over time. Notwithstanding this, the location of the most corrosive soils, based on Fig. 7.23, can still be associated within the section of the transect as highlighted in the *MN* profile ($> \sim 2$ mS m^{-1}) for *a*-spacing of 3 m.

Analyses presented in this section generally indicate that the DC-TDIP profiling can be used to ascertain soil corrosivity along a given pipeline ROW. This follows since the *MN* profile appears to relate to subsurface soil features; evidenced by integrated field and laboratory measurements whereby similar features between spatial distribution of Day 1 R_p, m_n, and *MN* have been observed.

7.4   Conclusions

The present chapter reports a first of its kind application of DC-TDIP methods for the purpose of assessing site conditions for pipeline integrity purposes. Firstly, digital signal processing based on wavelet denoising methods allow improved signal interpretation provided moderate SNR is present. However, signals with poor SNR still need to be treated differently in order to allow some information to be gathered. The important demonstration here, however, has been the ability to carry out DC-TDIP profiling along the pipeline ROW at two sites where a) a continuous pipeline section is present, and b) the pipeline section covers only a part of the transect.

Survey results generally indicate that any effects arising directly from the pipeline compound on the apparent resistivities and apparent integral chargeabilities measurements differently. This is evidenced by the absence of any strong M_a anomaly along the partial pipeline section (showing contrasting ρ_a features consistent with pipeline sections). Much of the observed response is attributed to the fact that the pipelines were initially installed with plastic insulating material possibly

containing defects. The interaction of injected current with any exposed surface and the manner in which this current is channelled appears to manifest differently in ρ_a and M_a, especially considering the age of the pipeline. It is also proposed that due to its normalization nature, the *MN* profiles are practically and economically suited for condition assessment in pipeline ROW studies.

Further insights have been provided by a detailed investigation on the transect where a continuous pipeline section is available. Here, the DC-TDIP profiling, with depths of investigation as near as possible to the pipelines, have been compared with various laboratory analyses carried out on soil samples collected within these depths. Results indicate that the *MN* profiles observed in the field can be generally associated with subsurface soils, while there are indications that ρ_a values are somewhat affected by the pipelines; the ρ_a profile appears to be affected in a complex manner by a combination of the pipeline as well as subsurface soils. Distribution of potential corrosivity of the soil samples in terms of R_p generally agree well with the *MN* profiles, further providing evidence that this parameter is well connected with the soils in the field. However, some possible effects of bacterial activity on soil samples are suspected which are seen to give rise to manifestation of different features in the soil samples over time, thereby influencing the corrosion process after a period of natural desaturation. This is evidenced by poor correspondence between the soil SIP parameters measured under completely saturated conditions and Day 7 R_p, as well as between the soil electrolytes resistances measured over the two different days. Corrosion processes in the presence of bacterial activity can become very complicated and requires a study on its own right.

The important objective of the present study has been to develop capacities for DC-TDIP methods in soil corrosivity assessments along a given pipeline ROW. Although anomalies associated with strong electrochemical reactions at pipeline/soil interfaces have not been observed, the methodology adopted in this study can be used to suggest the following general framework, for carrying out soil corrosivity investigations based on DC-TDIP profiling:

     a) DC-TDIP measurements to be carried out with depths of investigations as near as possible to the pipelines,

     b) Sections of pipeline ROW exhibiting higher *MN* values should be highlighted as possible regions of significant activity or high-risk regions,

     c) Soil samples collected along the high-risk regions should be characterized in laboratories for their electrical properties, to observe if similar distributions are observed in the soil samples. In particular, absence of similar distributions between normalized chargeabilities of laboratory samples and field *MN* profiles can generally be indicative of significant pipeline

effects. This may also appear as significant anomalies in *MN*. In this manner, significant defects along pipelines may be directly identified.

d) In the event that similar distributions between the two parameters mentioned above are observed, then the *MN* profiles are indicative of the subsurface soil features. These soils can then be further evaluated for their corrosivity using the galvanostatic pulse method, suggested in this thesis.

It is envisaged that this framework will lead to a new area of investigation concerning soil corrosivity assessments.

A secondary objective has been to identify possible implications of SP on pipeline integrity. In this regard, the presence of several different potential gradients along a pipeline ROW is of concern. Provided these gradients are caused by external sources and are effectively coupling onto the pipelines, an accelerated corrosion process may be anticipated with serious implications for pipeline integrity surveys.

CHAPTER 8

SUMMARY OF CONCLUSIONS AND FUTURE DIRECTIONS

8.1   Contributions from this Work

The present thesis has been an attempt to provide advances in various electrical methods, ranging from laboratory electrochemical measurements, electrical characterizations of laboratory soil samples, and site condition assessments using geoelectrical surveying in the context of pipeline corrosion in the soil environment. Although specific conclusions have already been provided in their respective chapters, it is desirable to summarize the key findings, and highlight the significance of the outcomes from this thesis.

- A pioneering application of the galvanostatic pulse technique to characterize the electrical double layer properties (polarization resistance, double layer capacitance) at the metal/soil interface, as well as other corrosion related parameters (E_{CORR}, R_{Ω}, and β) has been conducted. In view of the difficulties generally associated with conducting electrochemical studies with soil electrolytes, it is demonstrated that the use of the galvanostatic pulse method is robust and suitable to ascertain soil aggressivity in laboratory samples. A consistent methodology has been implemented, which describes the manner in which the metal/soil system should be initially set-up in order to minimize errors and for conducting efficient measurements. The study has been conducted with synthetic soil samples, which in a manner serves as a reference for any future studies aiming for cross-calibration. The study has also identified the effects of clay and chlorides on the corrosion of different ferrous materials. Measurements conducted for metal/soil systems under saturated conditions, followed by measurements after a period of natural desaturation, reveal different features are controlling the corrosion processes during the two different states of the soil electrolytes. It has been shown that clay produces a coupled moisture-chloride effect in the overall corrosion process, whereby increasing clay content generally coincides with increasing corrosion rates. Also, any increase in chlorides is seen to inflict higher corrosion rates. These effects have been studied mainly through perturbations on the polarization resistance of the electric double layer at the metal/soil interfaces. Factors related to physical soil properties appear to manifest strongly when corrosion proceeds with a period of natural desaturation.

- The synthetic soils used in the aforementioned corrosion study have also been analyzed for their spectral properties using the spectral induced polarization (SIP) method under saturated conditions. The potential application of SIP characterizations to evaluate soil electrical properties is due to the recent interests and advances in this technique in the literature. It has been shown that low-frequency (10^{-1} – 10^3 Hz) soil spectral properties can be used to differentiate clayey and saline soils. In this regards, it stands as a good candidate for extending the current paradigm of assessing soil corrosivity based on its resistivity alone. The low-frequency soil spectral properties were analyzed with the Cole-Cole model. Further investigation using regression analysis between polarization resistances from the galvanostatic pulse based corrosion study and soil resistivities, and as well as the normalized chargeabilities showed some important characteristics. Soil resistivities generally exhibited good linear relationships with polarization resistances, measured under saturated as well as under desaturated conditions, on a log-log scale. This has been attributed to the ability of the soil resistivity to respond to changes in clay as well as salinity levels. The normalized chargeability, on the other hand, revealed very good regression with polarization resistances measured under desaturated conditions, while poor regressions were observed with the polarization resistances measured under saturated conditions. This effectively shows the ability of the normalized chargeability parameter to correspond with the soil conditions, which have been observed to dominate the corrosion processes after a period of natural desaturation. The important result obtained here was that a single SIP measurement of soils in a consistent state allows for characterization of electrical features, which can be used diagnostically to assess soil corrosivity. Consequently, it is suggested that the SIP method be adopted as a standard for assessing soil electrical properties for soil corrosivity investigations. This will effectively shift the paradigm to a more detailed analysis. Finally, cross-plots of formation factor and a) phase measured at a particular frequency, *viz.*, 1 Hz, and b) soil resistivity have been shown to allow identification of corrosive soils. These cross-plots enable new ways of characterizing soil samples for their potential aggressivity.

- Following the intensive laboratory studies, a field investigation was carried out to ascertain the use of the combined direct current resistivity and time-domain induced polarization (DC-TDIP) profiling methods for pipeline site condition assessment. Since this is the first time such an application has been explored, several practical considerations regarding the complete soil-pipe system have been discussed. Results suggest that the influence of pipelines manifest differently in resistivity and TDIP measurements. This can cause difficulties in data

interpretations. Additional insight was provided by detailed laboratory analysis of soil samples collected along the surveyed transect. Results suggested that there is some complex mechanism by which pipelines influence the resistivity and TDIP measurements in-situ. This is partly attributed to the age of the pipeline as well as possibly the non-ideal insulating plastic wrap it is encased in. Nevertheless, the importance of the combined DC-TDIP methods is demonstrated, whereby sections with higher normalized chargeabilities can be attributed to presence of clayey soils. Interestingly, these sections also exhibited high levels of chlorides indicating that such soils are indeed corrosive due to their ability to also accumulate highly corrosive chemical species. An anomalous feature, however, was observed which did not appear in the SIP studies of the laboratory synthetic soil samples. Correspondence between the polarization resistances, measured after a period of natural desaturation, and soil resistivity and as well as normalized Cole-Cole chargeability were very poor as noted through regression analysis. This is attributed to the complexities surrounding the corrosion process in the presence of possible bacterial activity. In a manner, the limitation of the SIP method conducted after saturated conditions are imposed; for soil corrosivity analysis it is applicable for soils free of bacterial activity. Nevertheless, the major outcome from this study is that a methodological framework has been suggested, which can allow identification of completely exposed pipelines or the presence of highly corrosive soils; both of which enable identification of high-risk sections. Apart from developing capacities for DC-TDIP methods in soil corrosivity profiling, a secondary objective was to identify implications of self potentials on pipeline integrity. Here, the distribution of several self potential gradients along the pipeline right-of-way merits concern. In the event these potentials are originating from external sources, there is the possibility for accelerated corrosion processes through electrolysis. Such a situation can be further aggravated by topographic profiles where pipelines are embedded.

- Apart from these major findings, a few important developments were made during the project which were not initially envisaged. These were mainly associated with the design and implementation of a low-cost DC-TDIP profiling system with capability to record full-time series data. The use of wavelet denoising methods were explored for better signal processing capabilities with a view to minimize distortions on acquired data. It has been demonstrated that wavelet based methods look very promising for efficient processing of field data as they induce minimal distortions, as compared to the use of normal low-pass filters.

The present thesis is a testimony to the multi-disciplinary approach necessary for investigations in soil corrosion. The techniques and characterizations suggested in this thesis have immediate practical applications and should greatly contribute to the overall framework of pipeline integrity and condition assessment. Although the thesis is based in the overall context of pipeline corrosion in soil environment, it can be extended to any ferrous structures in a soil environment. This is especially the case concerning applications of the galvanostatic pulse method for determination of corrosion-related parameters and hence the corrosion rate in soils, as well as the characterization of soil corrosiveness using SIP methods.

Apart from practical significance, it is envisaged that the galvanostatic pulse method suggested in this thesis will allow more detailed laboratory studies to be carried out in order to understand the corrosion dynamics in soils. The present research also opens a new area of application for DC-TDIP methods and it is envisaged that the results and framework suggested will provide a drive for further studies.

The thesis has achieved all of the aims initially set-out during the start of the project. There are, however, several issues and room for extension which have been recognized within this research. These have been discussed in the thesis, where applicable. Nevertheless, some of these are also outlined in the next section aiming to suggest directions for future work.

8.2   Future Developments

Within the highly complex phenomenon of soil-related corrosion, the present study attempted to provide developments in methods ranging from electrochemical techniques to electrical techniques for soil characterization and field assessments. All of them essentially are focused on aspects of improving measurement techniques and assessing soil corrosivity. Some important features which will aid in advancing the methods further are:

- The electrical circuit model used in the interpretation of the galvanostatic pulse method can be developed further to include responses from soil capacitances. This will allow the method to be uniquely applied to any given system with any state of the soil media.
- The non-ideal, corrosion related, β parameter needs to be investigated further to resolve any physical limitations. Although discussions on its manifestations are provided, there are indications that it is sensitive to a variety of variables, including the state of the underlying metal.

- The galvanostatic pulse technique and SIP characterizations suggested in this work should be carried out to include soils with extensive varieties of particle size distribution. This will provide indications on the effects from a distribution of liquid geometry on the corrosion process.

- DC-TDIP measurements must be conducted extensively to ascertain the range of responses so that the methodological framework suggested in the present thesis can be developed further. Especially, a study aimed to understand the interaction and polarization of the pipeline when surveys are conducted immediately parallel to the right-of-way should be conducted. Such a study should include practical considerations in terms of the pipeline exposed surface area, its age, incident current density, *etc*., as discussed in the thesis.

- Distribution of self potentials along a pipeline right-of-way should be investigated further for their possible implications on pipeline electrolysis.

- Finally, the role of bacterial activity on corrosion and its effect on the SIP response needs to be addressed. Although the present thesis is not concerned with microbiologically induced corrosion, its effect on overall corrosion cannot be ignored. In this regard, the laboratory experimental set-up will need to be improved in order to simultaneously conduct galvanostatic pulse measurements on metal/soil systems and SIP measurements using the same soil electrolytes in the presence of bacterial activity. This will require an extensive study since it has been established in the literature that SIP is sensitive to bacterial activity.

Apart from these specific recommendations, there is also a possibility that the galvanostatic pulse method adopted in the study can be applied in-situ to assess the corrosion rates of pipelines. This also warrants a detailed study, and if successful will provide robust capabilities for detailed risk analysis in the field.

REFERENCES

Abdel Aal, G., Slater, L.D., Atekwana, E. 2006. Induced Polarization Measurements on Unconsolidated Sediments from a Site of Active Hydrocarbon Biodegradation. *Geophysics*, **71(2)**:H13-H24.

Ahmad, Z. 2006. Principles of Corrosion Engineering and Corrosion Control. 1st edition. Butterworth-Heinemann. Oxford, U.K.

Ahzegbobor, P., Aizebeokhai, A., Olayinka, I., Singh, V.S. 2010. Application of 2D and 3D Geoelectric Imaging for Engineering Site Investigation in a Crystalline Basement Terrain, Southwestern Nigeria. *Environmental earth Sciences*, **61(7)**:1481-1492.

Albaya, H.C., Cobo, O.A., Bessone, J.B. 1973. Some Consideration in Determining Corrosion Rates from Linear Polarization Measurements. *Corrosion Science*, **13(4)**:287-293.

Ashworth, V. 1994. Principles of Cathodic Protection. In: "Corrosion Control". 3rd Edition. (Ed). Shreir, L.L., Jarman, R.A., Burstein, G.T. Butterworth-Heinemann. Oxford, U.K.

ASTM G57-95a. 2001. ASTM Standard G57-95a. Standard Test Method for Field Measurement of Soil Resistivity Using the Wenner Four-Electrode Method. ASTM International, West Conshohocken, PA, U.S.A. doi: 10.1520/G0057-95A.

ASTM G162-99. 2004. Standard Practice for Conducting and Evaluating Laboratory Corrosion Tests in Soils. ASTM International. West Conshohocken, PA, U.S.A.

Archie, G.E. 1942. The Electrical Resistivity Log as an Aid in Determining Some Reservoir Characteristics. *Petroleum Transactions of AIME*, **146**:54-62.

Azzeri, N., Bruno, R., Splendorini, L. 1981. Assessment of Corrosion Rate of Steel in Sea Water by Polarization Resistance Technique. *Corrosion Science*, **21(11)**:781-787.

Baboian, R. (Ed). 2005. Corrosion Tests and Standards: Application and Interpretation. 2nd Edition. ASTM International. U.S.A.

Bagotsky, V.S. 2006. Fundamentals of Electrochemistry. 2nd Edition. John Wiley & Sons. New Jersey, U.S.A.

Balasubramaniam, R., Kumar, A.V.R. 2000. Characterization of Delhi Iron Pillar Rust by X-Ray Diffraction, Fourier Transform Infrared Spectroscopy and Mossbauer Spectroscopy. *Corrosion Science*, **12**:2086-2101.

Bard, A., Faulkner, L. 2001. Electrochemical Methods: Fundamentals and Applications. 2nd Edition. John Wiley & Sons, U.S.A.

Barker, R.D. 2007. Electrical Resistivity Methods for Borehole Siting in Hardrock Region. In: "Groundwater: Resource Evaluation, Augmentation, Contamination, Restoration, Modelling and Management". (Ed). Thangarajan, M. Springer. New Delhi, India.

Beck, A.E. 1991. Physical Principles of Exploration Methods. 2nd Edition. Wuerz Publishing Ltd, Winnipeg, Canada.

Beavers, J.A., Thompson, N.G. 2006. External Corrosion of Oil and Natural Gas Pipeline. ASM Handbook Volume 13C, Corrosion: Environments and Industries. ASM International.

Bedrosian, P.A. Unsworth, M.J., Johnston, M.J.S. Hydrothermal Circulation at Mount St. Helens Determined by Self-Potential Measurements. *Journal of Volcanology and Geothermal Research*, **160(1-2)**:137-146.

Benmoussat, A., Traisnel, M. 2011. Corrosion Study of API 560 Pipelines Steels in NS4 Simulated Soil. In *Integrity of Pipelines Transporting Hydrocarbons*. Ed. Bolzon, G., Boukharouba, T., Gabetta, G., Elboujdaini, M., Mellas, M. NATO Science for Peace and Security Series C: Environmental Security. **1**:167-179. Springer, Netherlands.

Bentley, L.R., Gharibi, M. 2004. Two- and Three-Dimensional Electrical Resistivity Imaging at a Heterogeneous Remediation Site. *Geophysics*, **69(3)**:674-680.

Bhattacharya, B.B., Dutta, I. 1982. Depth of Investigation Studies for Gradient Array over Homogeneous Isotropic Half Space. *Geophysics*, **48**:1248-1251.

Binley, A., Kemna, A. 2005. DC Resistivity and Induced Polarization Methods. In: "Hydrogeophysics. Water Science and Technology Library". (Ed). Rubin, Y., Hubbard, S.S. Springer. Netherlands.

Binley, A., Slater, L.D., Fukes, M., Cassiani, G. 2005. Relationship between Spectral Induced Polarization and Hydraulic Properties of Saturated and Unsaturated Sandstone. *Water Resources Research*, **41**:W12417. doi:10.1029/2005WR004202.

Birbilis, N., Nairn, K.M., Forsyth, M. 2003. Transient Response Analysis of Steel in Concrete. *Corrosion Science*, **45**:1895-1902.

Birbilis, N., Nairn, K.M., Forsyth, M. 2004. On the Electrochemical Response and Interfacial Properties of Steel-Ca(OH)$_2$ and the Steel-Concrete System Measured Using Galvanostatic Pulses. *Electrochimica Acta*, **49**:4331-4339.

Birbilis, N., Cherry, B.W. 2005. Monitoring the Corrosion and Remediation of Reinforced Concrete On-Site: An Alternative Approach. *Materials and Corrosion*, **56(4)**:237-243.

Boadu, F.K., Seabrook, B.C. 2006. Effects of Clay Content and Salinity on the Spectral Electrical Response of Soils. *Journal of Environmental and Engineering Geophysics*, **11(3)**:161-170.

References

Boadu, F.K., Owusu-Nimo, F. 2010. Influence of Petrophysical and Geotechnical Engineering Properties on the Electrical Response of Unconsolidated Earth Materials. *Geophysics*, **75(3)**:21-29.

Boadu, F.K. 2011. Predicting the Engineering and Transport Properties of Soils Using Fractal Equivalent Circuit Model: Laboratory Experiments. *Geophysics*, **76(5)**:329-338.

Bonds, R.W., Barnard, L.M., Horton, A.M., Oliver, G.L. 2005. Corrosion and Corrosion Control of Iron Pipe: 75 Years of Research. *Journal of the American Water Works Association*, **97(6)**:88-98.

Borner, F.D., Schopper, J.R., Weller, A. 1996. Evaluation of Transport and Storage Properties in the Soil and Groundwater Zone from Induced Polarization Measurements. *Geophysical Prospecting*, **44(4)**:583-601.

Borner, F. 2006. Complex Conductivity Measurements. In: "Groundwater Geophysics". (Ed). Kirsch, R. Springer-Verlag. Heidelberg, Germany.

Bravo, V.M.S., Calderon, J.P., Rodriguez, J.G.G. 2006. Corrosion Monitoring using Electrochemical Noise and Linear Polarization Resistance in Fuel Oil Combustion Gas Environment. *Russian Journal of Electrochemistry*, **42(5)**:560-565.

Breede, K., Kemna, A., Esser, O., Zimmermann, E., Vereecken, H., Huisman, J.A. 2011. Joint measurement Setup for Determining Spectral Induced Polarization and Soil Hydraulic Properties. *Vadose Zone Journal*, **10**:716-726.

Brett, C.M.A., Brett, A.M.O. 1994. Electrochemistry. Principles, Methods, and Applications. Oxford Science Publications. NY, U.S.A.

Broomfield, J.P. 2007. Corrosion of Steel in Concrete. Understanding, Investigation and Repair. 2nd Edition. Taylor & Francis. New York, U.S.A.

Bullard, S.J., Jr Covino, B.S., Cramer, S.D., Holcomb, G.R., Ziomek-Moroz, M. 2005. Soil Corrosion Monitoring Near a Pipeline under CP. Albany Research Center, U.S DoE. Research Report DOE/ARC-2005-082. Available online at http://www.osti.gov/bridge/servlets/purl/899243-aAEsXt/899243.pdf Last accessed 6th March 2010.

Butler, D.K. 2005. Near-Surface Geophysics. (Investigations in Geophysics No 13). The Society of Exploration Geophysicists. Tulsa, U.S.A.

Callow, L.M., Richardson, J.A., Dawson, J.L. 1976. Corrosion Monitoring Using Polarization Resistance Measurements. *British Corrosion Journal*, **11**:132-139.

Cassiani, G., Kemna, A., Villa, A., Zimmermann, E. 2009. Spectral Induced Polarization for the Characterization of Free-Phase Hydrocarbon Contamination of Sediments with Low Clay Content. *Near Surface Geophysics*, **7**:547-562.

Chen, Y., Or, D. 2006. Effects of Maxwell-Wagner Polarization on Soil Complex Dielectric Permittivity Under Variable Temperature and Electrical Conductivity. *Water Resources Research*, **42**. W06424. doi:10.1029/2005WR004590.

Clavier, C., Coates, G., Dumanoir, J. 1984. Theoretical and Experimental Bases for the Dual-Water Model for the Interpretation of Shaley Sands. *Society of Petroleum Engineers Journal*, **24**:153-168.

Cigna, R., Giuliani, L., Gusmano, G. 1985. Continuous Corrosion Monitoring in Desalination Plants. *Desalination*, **55**:219-227.

Coifman, R.R., Donoho, D. 1995. Translation-Invariant Denoising in Antoniadis and Oppenheim: *Wavelets and Statistics, Lecture Notes in Statistics*, **103**:125-150.

Cole, K.S., Cole, R.H. 1941. Dispersion and Absorption in Dielectrics - I Alternating Current Characteristics. *Journal of Chemical Physics*,. **9**:341–352

Cole, I.S., Marney, D. 2012. The Science of Pipe Corrosion: A Review of the Literature on the Corrosion of Ferrous Metals in Soils. *Corrosion Science*, **56**:5-16.

Corry, C.E. 1985. Spontaneous Polarization Associated with Porphyry Sulfide Mineralization. *Geophysics*, **50**:1020-1034.

Cornell, R.M., Schwertmann, U. 2003. the iron oxides: structure, properties, Reactions, Occurrences and Uses. 2nd Edition. Wiley-VCH Verlag GmbH & Co. Germany.

Corwin, R.F., Hoover, D.B. 1979. The Self-Potential Method in Geothermal Exploration. *Geophysics*, **44**:226-245.

Corwin, R.F. 1990. The Self Potential Method for Environmental and Engineering Applications. In: "Geotechnical and Environmental Geophysics". (Ed). Ward, S. The Society of Exploration Geophysicists. Tulsa, U.S.A.

Cosenza, P. Ghorbani, A., Florsch, N., Revil, A. 2007. Effects of Drying on the Low-Frequency Electrical properties of Tournemire Argillites. *Pure and Applied Geophysics*, **164**:2043-2066.

Cottis, R. 2008. Electrochemical noise methods and harmonic analysis. In: "Techniques for Corrosion Monitoring. Part 1 Electrochemical Techniques for Corrosion Monitoring". (Ed). Yang, L. Woodhead Publishing Limited, Cambridge. England.

Dahlin, T. 2001. The Development of DC Resistivity Imaging Techniques. *Computers and Geosciences*, **27(9)**:1019-1029.

Dahlin, T. Leroux, V., Nissen, J. 2002. Measuring Techniques in Induced Polarization Imaging. *Journal of Applied Geophysics*, **50**:279-298.

Dahlin, T., Bernstone, C., Loke, M.H. 2003. A 3-D Resistivity Investigation of a Contaminated Site at Lemacken, Sweden. *Geophysics*, **68**:1692-1700.

Davis, J.R. 1996. ASM Specialty Handbook: Cast Iron. ASM International. Materials Park, U.S.A.

Davis, J.R. 2000. Corrosion: Understanding the Basics. ASM International. Materials Park, U.S.A.

Daubechies, I. 1992. Ten Lectures on Wavelets. CBMS – NSF Regional Conference Series in Applied Mathematics, 61. SIAM.

De Lima, O.A.L., Niswas, S. 2000. Estimation of Hydraulic parameters of Shaly Sandstone Aquifers from Geoelectrical Measurements. *Journal of Hydrology*, **235(1-2)**:12-26.

Deo, R.N. 2005. Concentrations of Heavy Metals and Other Trace Elements in Air at Suva by the Method of Neutron Activation Analysis (NAA). Master of Science Thesis. School of Pure and Applied Sciences, University of the South Pacific. Fiji.

DIPRA, 2000. Polyethylene encasement – Effective Economical Protection for Ductile Iron Pipe in Corrosive Environments. Company Internet Website. Ductile Iron Pipe Research Association. http://www.dipra.org/pdf/polyEncasement.pdf. Last accessed 20th December, 2010.

Donoho, D.L., Johnstone, I.M. 1994. Ideal Spatial Adaptation by Wavelet Shrinkage. *Biometrika*, **81**:425-455.

Donoho, D.L., Johnstone, I.M. 1995. Adapting to Unknown Smoothness via Wavelet Shrinkage. *Journal of the American Statistical Association*, **90**:1200-1224.

Donoho, D.L., Johnstone, I.M., Kerkyacharian, G., Picard, D. 1995. Wavelet Shrinkage: Asymptopia? *Journal of the Royal Statistical Society Series B*: **57**:301-369.

Doyle, G., Seica, M.V., Grainsky, M.W.F. 2003. The role of soil in the external corrosion of cast iron water mains in Toronto, Canada. *Canadian Journal of Civil Engineering*, **40**:225-236.

Duckworth, K., Calvert, H.T. 1995. An Examination of the Relationship between Time-Domain Integral Chargeability and the Cole-Cole Impedance Model. *Geophysics*, **60(4)**:1249-1252.

Duckworth, K., Brown, R.J. 1996. A Program for Fourier Series Synthesis of Induced Polarization Waveforms. *Computers and Geosciences*, **22(10)**:1133-1136.

Dymke, J., Ferguson, P. 1999. Condition Assessment of Large Diameter Water Mains. *Water*, 15-19. September/October.

Edward, L.S. 1977. A Modified Pseudosection for Resistivity and IP. *Geophysics*, **42**:1020-1036.

Eiswirth, M., Heske, C., Burn, L.S., Desilva, D. 2001. New Methods for Water Pipeline Assessment. *IWA 2. World Water Congress*, 15 – 19 October, 2001. Berlin, Germany.

Ekekwe, N. 2009. Electrochemical Impedance Spectroscopy: Corrosion Behaviour Application. VDM Verlag Dr. Muller, Germany.

Elsener, B. 2005. Corrosion Rate of Steel in Concrete – Measurements beyond the Tafel Law. *Corrosion Science*, **47(12)**:3019-3033.

Ekine, A.S., Emujakporue, G.O. 2010. Investigation of Corrosion of Buried Oil Pipeline by the Electrical Geophysical Methods. *Journal of Applied Science and Environmental Management*, **14(1)**:63-65.

Evjen, H.M. 1938. Depth Factor and Resolving Power of Electrical Measurements. *Geophysics*, **3**:78-95.

Feliu, V., Gonzalez, J.A., Feliu, S. 2004. Algorithm for Extraction of Corrosion Parameters from the Response of the Steel-Concrete System to a Current Pulse. *Journal of the Electrochemical Society*, **151(3)**:B134-B140.

Ferguson, P., Geehman, C. 2001. Assessing the Performance of Unprotected Cast Iron Sewer Rising Mains. In: "Proceedings of the Australian Water Association 19th Federal Convention". 1st – 5th April, 2001. Canberra, Australia.

Ferreira, C.A.M., Ponciano, J.A.C., Vaitsman, D.S., Perez, D.V. 2007. Evaluation of the Corrosivity of the Soil through its Chemical Composition. *Science of the Total Environment*, **388**:250-255.

Fiandaca, G. Auken, E., Christiansen, A.V., Gazoty, A. 2012. Time-Domain Induced Polarization: Full-Decay Forward Modelling and 1D Laterally Constrained Inversion of Cole-Cole Parameters. *Geophysics*, **77(3)**:E213-E225.

Fitzgerald III, J.H. Evaluating Soil Corrosivity – Then and Now. *Materials Performance*, **32(10)**:17-19.

Fontana, M.G., Greene, N.D. 1978. Corrosion engineering. 2nd Edition. McGraw-Hill. New York, U.S.A.

Frasier, D.C. 1964. Conductivity Spectra of Rocks from the Craigmont Ore Environment. *Geophysics*, **29**:832-847.

French, H.K., Binley, A., Kharkhordin, I., Kulessa, B., Krylov, S.S. 2006. Cold Regions Hydrogeophysics: Physical characterization and Monitoring. In: "Applied Hydrogeophysics". (Ed). Vereecken, H., Binley, A., Cassiani, G., Revil, A., Titov, K. NATO Science Series IV: Earth and Environmental Sciences – Vol 71. Springer. Netherlands.

Garces, P., Andrade, M.C., Saez, A., Alonso, M.C. 2005. Corrosion of Reinforcing Steel in Neutral and Acidic Solutions Simulating the Electrolytic Environments in the Micropores of Concrete in the Propagation Period. *Corrosion Science*, **47(2)**:289-306.

Garverick, L. 1994. Corrosion in the Petrochemical Industry. ASM International. U.S.A.

Gay Jr, S.P. 1967. A 1,800 Millivolt Self-Potential Anomaly Near HualGayoc, Peru. *Geophysical Prospecting*, **15(2)**:236-245.

Gazoty, A., Fiandaca, G., Pedersen, J., Auken, E., Christiansen, A.V., Pedersen, J.K. 2012. Application of Time Domain Induced Polarization to the Mapping of Lithotypes in a Landfill Site. *Hydrology and Earth System Sciences*, **16**:1793-1804.

Gerwin, W., Baumhauer, R. 2000. Effect of Soil Parameters on the Corrosion of Archaeological Metal Finds. *Geoderma*, **96(1-2)**:63-80.

Ghorbani, A., Cosenza, P., Revil, A., Zamora, M., Schmutz, M., Florsch, N., Jougnot, D. 2009. Non-Invasive Monitoring of Water Content and Textural Changes in Clay-Rocks Using Spectral Induced Polarization: A Laboratory Investigation. *Applied Clay Science*, **43(3-4)**:493-502.

Glover, P.W.J., Hole, M.J., Pous, J. 2000. A Modified Archie's Law for Two Conducting Phases. *Earth and Planetary Science Letters*, **180(3-4)**:369-383.

Goto, T., Kondo, K., Ito, R., Esaki, K., Oouchi, Y., Abe, Y., Tsujimura, M. 2012. Implications of Self-Potential Distribution for Groundwater Flow System in a Nonvolcanic Mountain Slope. *International Journal of Geophysics*, **2012:**ID 640250.

Grim, R.E. 1968. Clay Mineralogy. 2nd Edition. McGraw-Hill. New York, U.S.A.

Gueguen, Y., Palciauskas, V. 1994. Introduction to the Physics of Rocks. Princeton University Press. Princeton, New Jersey. U.S.A.

Gupta, S.K., Gupta, B.K. 1979. Critical Soil-Moisture Content in the Underground Corrosion of Mild-Steel. *Corrosion Science*, **19**:171-178.

Hallenburg, J.K. 1998. Non-Hydrocarbon Methods of Geophysical Formation Evaluation. Lewis Publishers, U.S.A.

Hamann, C.H., Hamnett, A., Vielstich, W. 2007. Electrochemistry. 2nd Edition. Wiley-VCH. Weinheim, Germany.

Havriliak, S., Negami, S. 1967. A Complex Plane Representation of Dielectric and Mechanical Relaxation Processes in Some Polymers. *Polymer*, **8**:161-210.

Henderson, R.J. 1992. Urban Geophysics – A Review. *Exploration Geophysics*, **23**:531-542.

Hilbert, L.R. 2006. Monitoring Corrosion Rates and Localised Corrosion in Low Conductivity Water. *Corrosion Science*, **48(12)**:3907-3923.

Hillel, D. 1998. Environmental Soil Physics. Academic Press. San Diego, California. U.S.A.

Hillel, D. 2004. Introduction to Environmental Soil Physics. Academic Press. San Diego, California. U.S.A.

Hiltunen, D.R., Roth, M.J.S. 2004. Investigation of Bridge Foundation Sites in Karst Terrane Via Multi-Electrode Electrical Resistivity. *Proceedings of the 2nd International Conference on Geotechnical and Geophysical Site Characterization*. Porto, Portugal. 19th – 22nd September. (Ed). Fonsesca, A.V da., Mayne, P.W. Millpress Publishers. Rotterdam, Netherlands.

Hoar, T.P., Farrer, T.W. 1961. The anodic Characteristics of Mild Steel in Dilute Aqueous Soil Electrolytes. *Corrosion Science*, **1**:49-61.

Hordt, A., Blaschek, R., Kemna, A., Zisser, N. 2007. Hydraulic Conductivity Estimation from Induced Polarization Data at the Field Scale – the Krauthausen Case History. *Journal of Applied Geophysics*, **62(1)**:33-46.

Ingebritsen, S.E. Sanford, W.E. Neuzil, C.E. 2006. Groundwater in Geologic Processes. 2nd edition. Cambridge University Press. New York, U.S.A.

Ismail, A.I.M., El-Shamy, A.M. 2009. Engineering Behaviour of Soil Materials on the Corrosion of Mild Steel. *Applied Clay Science*, **42**:356-362.

Jackson, D.B., Kauahikau, J. 1987. Regional Self-Potential Anomalies at Kilauea Volcano. "Volcanism in Hawaii". USGS Professional Paper, Volume 1350.

Jaggar, S.R., Fell, P.A. 1988. Forward and Inverse Cole-Cole Modelling in the Analysis of Frequency Domain Spectral Impedance Data. *Exploration Geophysics*, **19**:463-470.

Jansen, M. 2001. Noise Reduction by Wavelet Thresholding. Lecture Notes in Statistics 161. Springer-Verlag, Ney York. U.S.A.

Jardani, A., Revil, A., Boleve, A., Dupont, J.P. 2008. Three-Dimensional Inversion of Self-Potential Data Used to Constrain the Pattern of Groundwater Flow in Geothermal Fields. *Journal of Geophysical Research*, **113**:ID B09204. doi: 10.129/2007JB005302.

Jianbo, G., Sultan, H., Jing, H., Wen-Wen, T. Denoising Nonlinear Time Series by Adaptive Filtering and Wavelet Shrinkage: A Comparison. *IEEE Signal Processing Letters*, **17(3)**:237-240.

Jiang, J., Wang, J. 2009. The Role of cathodic Distribution in Gas/Liquid/Solid multiphase Corrosion Systems. *Journal of Solid State Electrochemistry*, **13**:1723-1728.

Jiang, J., Wang, J., Wang, W., Zhang, W. 2009. Modelling Influence of Gas/Liquid/Solid Three-Phase Boundary Zone on cathodic process of Soil Corrosion. *Electrochimica Acta*, **13(1)**:3623-3629.

Jeannin, M., Calonnec, D., Sabot, R., Refait, Ph. 2010. Role of Clay Sediment Deposit on the Corrosion of Carbon Steel in 0.5 mol L^{-1} NaCl Solutions. *Corrosion Science*, **52**:2026-2034.

John, T.U. 1963. Geology and Mineral Deposits of East-Central Balabac Island, Palawan Province, Philippines. *Economic Geology*, **58(1)**:107-130.

Jouniax, L., Maineult, A., Naudet, V., Pessel, M., Sailhac, P. 2009. Review of Self-Potential Methods in Hydrogeophysics. *Comptes Rendus Geoscience*, **341(10)**:928-936.

Juhasz, I. 1981. Normalized Q – The key to Shaly Sand Evaluation Using the Waxman-Smits Equation in the Absence of Core Data. Presented at *The Society of Professional Well Log Analysts, 22nd Annual Logging Symposium*. Paper Z.

Kasahara, K., Kajiyama, F. 1983. Determination of Underground Corrosion Rates from Polarization Resistance Measurements. *Corrosion*, **39**:475-480.

Kaufmann, O., Deceuster, J., Quinif, Y. 2012. An Electrical Resistivity Imaging-Based Strategy to Enable Site-Scale Planning Over Covered Palaeokarst Features in the Tournaisis Area (Belgium). *Engineering Geology*, **133-134**:49-65.

Kear, G., Flatley, I., Jones, S. 2006. Application of Polarization Resistance Measurements for the estimation of Corrosion Rates of Galvanised Steel structures in Soils. *Corrosion and Protection Conference*, 19th – 22nd, November, 2006. Grand Chancellor Hotel, Hobart Australia.

Keller, G.V., Frischknecht, F.C. 1970. Electrical Methods in Geophysical Prospecting. International Series of Monographs in Electromagnetic Waves Volume 10. 1st Edition. Pergamon Press.

Kelly, R.G. 2003. Electrochemical Thermodynamics and Kinetics of Relevance to Corrosion. In *Electrochemical Techniques in Corrosion Science and Engineering*. Marcel Dekker, Inc. New York, U.S.A.

Kemna, A. 2000. Tomographic Inversion of Complex Resistivity: Theory and Application. PhD Thesis. Berichte des Instituts für Geophysik. Ruhr-University, Bochum.

Kemna, A., Binley, A., Slater, L.D. 2004. Crosshole IP Imaging for Engineering and Environmental Applications. *Geophysics*, **69(1)**:97-107.

Kirmeyer, G.J., Richards, W., Smith, C.D. 1994. An Assessment of the Water Distribution System and Associated Research Needs. American Water Works Research Foundation, Denver, U.S.A.

Knodel, K., Lange, G., Voigt, A.-J. Environmental Geology: Handbook of Field Methods and Case Studies. Schon, J.H. 1996. Physical properties of Rocks: Fundamentals and principles of Petrophysics. Pergamon. New York, U.S.A.

Knoll, G.F. 2000. Radiation Detection and Measurement. 3rd Edition. John Wiley & Sons Inc. U.S.A.

Koch, G., Brongers, M.P.H., Thompson, N.G., Virmani, Y.P., Payer, J.H. Corrosion Costs and Preventative Strategies in the United States. Publication No. FHWA-RD-01-156. U.S. Federal Highway Administration Washington, U.S.A.

Koch, K., Kemna, A., Irving, J., Holliger, K. 2011. Impact of Changes in Grain Size and Pore Space on the Hydraulic Conductivity and Spectral Induced Polarization Response of Sand. *Hydrology and Earth System Sciences*, **15**:1785-1794.

Kouril, M., Novak, P., Bojko, M. 2006. Limitations of the Linear Polarization Method to determine Stainless Steel Corrosion Rate in Concrete Environment. *Cement and Concrete Composites*, **28(3)**:220-225.

References

Kraus, J.D., Fleisch, D.A. 1999. Electromagnetics with Applications. 5th Edition. McGraw-Hill Inc. U.S.A.

Kremer, F., Schonhals, A. 2003. Broadband Dielectric Spectroscopy. Springer-Verlag. Heidelberg, Germany.

Kruschwitz, S., Binley, A., Lesmes, D., Elshenawy, A. 2010. Textural Controls on Low-Frequency Electrical Spectra of Porous Media. *Geophysics*, **75(4)**:WA113-WA123.

Kumar, P., Foufoula-Georgiou, E. 1997. Wavelet Analysis for Geophysical Applications. *Review of Geophysics*, **35(4)**:385-412.

Landolt, D. 2007. Corrosion and Surface Chemistry of Metals. CRC Press. Florida, U.S.A.

Lang, M., Guo, H., Odegard, J.E., Burrus, C.S., Wells, R.O. Jr. Noise Reduction Using an Undecimated Discrete Wavelet Transform. *IEEE Signal Processing Letters*, **3(1)**:10-12.

Lange, G., Seidel, K. 2007. Direct Current Resistivity Methods. In: "Environmental Geology. Handbook of Field Methods and Case Studies". (Eds). Knodel, K., Lange, G., Voigt, H.-J. Springer-Verlag. Berlin, Germany.

Leblanc, G.E., Morris, W.A., Robinson, B. 1998. Wavelet Analysis Approach to Denoising of Magnetic Data. *68th International Annual Meeting of the Society of Exploration Geophysicists*. Expanded Abstracts, 554-557.

Leroux, V., Dahlin, T. 2002. Induced Polarization Survey at a waste Site in Southern Sweden. Proceedings of the *8th Annual Meeting of the Environmental and Engineering Geophysical Society – European Section.* 207-210.

Leroy, P., Revil, A. 2004. A Triple-Layer Model of the Surface Electrochemical Properties of Clay Minerals. *Journal of Colloid and Interface Science*, **270(2)**:371-380.

Leroy, P., Revil, A., Kemna, A., Cosenza, P., Ghorbani, A. 2008. Complex Conductivity of Water-Saturated Packs of Glass Beads. *Journal of Colloid and Interface Science*, **321**:103-117.

Leroy, P., Revil, A. 2009. A Mechanistic Model for the Spectral Induced Polarization of Clay Materials. *Journal of Geophysical Research*, **114**. B10202. doi:10.1029/2008JB006114.

Lesmes, D.P., Frye, K.M. 2001. Influence of Pore Fluid Chemistry on the Complex Conductivity and Induced Polarization Responses of Berea Sandstones. *Journal of Geophysical Research*, **106(B3)**:4079-4090.

Levenberg, K. 1944. A Method for the Solution of Certain Non-Linear Problems in Least Squares. *Quarterly of Applied Mathematics*, **2**:164-168.

Li, Y., Oldenburg, D.W. 1997. Fast Inversion of Large Scale magnetic Data Using Wavelets. *67th Annual International Meeting of the Society of Exploration Geophysicists*. Expanded Abstracts, 490-493.

Liang, P., Li, X., Du, C., Chen, X. 2009. Stress Corrosion Cracking of X80 Pipeline Steel in Simulated Alkaline Soil Solution. *Materials and Design*, **30**:1712-1717.

Lin, Y.W. Huang, J.H., Yu, G.P. 2010. Microstructure and Corrosion Resistance of Nanocrystalline TiZrN Films on AISI 304 Stainless Steel Substrate. *Journal of Vacuum Science and Technology*, **28(4)**:774-778.

Lopez, L.J.C., Arce, E., Torres, J., Vazquez-Arenas, J., Hallen, J.M., Cabrera-Siera, R. 2011. Corrosion process of API X52 Carbon Steel Immersed in Aqueous Solution Simulating Clay Soil Corrosion. *Corrosion, The Journal of Science and Engineering*, **67(11)**:116001-116010.

Lucarini, A., Peiponen, K. Saarinen, J.J., Vartiainen, E.M. 2005. Kramers-Kronig Relations in Optical Materials Research. Springer. Heidelberg, Germany.

Luo, Y., Zhang, G. 1998. Theory and Application of Spectral Induced Polarization. Number 8 in Geophysical Monograph Series. Society of Exploration Geophysicists.

Mallat, S.G. A 2009. Wavelet Tour of Signal processing: The Sparse Way. 3rd Edition. Elsevier Academic Press.

Mansfeld, F. 2005. Tafel Slopes and Corrosion Rates Obtained in the Pre-Tafel Region of Polarization Curves. *Corrosion Science*, **47**:3178-3186.

Mansfeld, F. 2009. Fundamental Aspects of the Polarization Resistance Technique – the Early Days. *Journal of Solid State Electrochemistry*, **13**:515-520.

Marquardt, D. 1963. An Algorithm for Least-Squares Estimation of Nonlinear Parameters. *SIAM Journal on Applied Mathematics*, **11(2)**:431-441.

Marshall, D.J., Madden, T.R. Induced Polarization, A Study of its Causes. *Geophysics*, **24(4)**:790-816.

Matsushima, I. 2011. Localized Corrosion of Iron and Steel. In: "Uhlig's Corrosion handbook". 3rd Edition. (Ed). Revie, R.W. John Wiley & sons, Inc. Hoboken, U.S.A.

Mccafferty, E. 2010. Introduction to Corrosion Science. 1st Edition. Springer Science + Business Media. New York, U.S.A.

McDowell, P.W., Barker, R.D., Butcher, A.P., Culshaw, M.G., Jackson, P.D., McCann, D.M., Skipp, B.O., Matthews, S.L., Arthur, J.C.R. 2002. Geophysics in Engineering Investigations. CIRIA Publishers. Westminster, London.

Millard, S., Sadowski, L. 2009. Novel Method for Linear Polarization Resistance Corrosion Measurement. *Proceedings of the 7th International Symposium on Non-destructive Testing in Civil Engineering*. 30th June – 3rd July, 2009. Nantes, France.

Moglia, M., Davis, P., Burn, S. 2008. Strong Exploration of a Cast Iron Pipe Failure Model. *Reliability Engineering and System Safety*, **93(6)**:885-896.

Moglia, M., Davis, P., Farlie, M., Burn, L.S. 2004. Estimating Corrosion Rates in Wrought Iron Pipelines: An Application of Linear Polarization Resistance. *Proceedings of the 6th National Conference, Australian Society of Trenchless Technology*. 27th – 29th September, 2004. Melbourne, Victoria, Australia.

Mohebbi, H., Li, C.Q. 2011. Experimental Investigation of Corrosion of Cast Iron Pipes. *International Journal of Corrosion*, **2011**. Article ID 506501. doi:10.1155/2011/506501.

Mohebbi, H., Jesson, D.A., Mulheron, M.J., Smith, P.A. 2010. The Fracture and Fatigue Properties of Cast Irons Used For Trunk Mains in the Water Industry. *Material Science and Engineering: A*, **527(21-22)**:5915-5923.

Moreno, M., Morris, W., Alvarez, M.G., Duffo, G.S. 2004. Corrosion of Reinforcing Steel in Simulated Concrete Pore Solutions: Effect of Carbonation and Chloride Content. *Corrosion Science*, **46(11)**:2681-2699.

Morlet, J., Arens, G., Fourgeau, E., Giard, D. 1982. Wave Propagation and Sampling Theory, Part1: Complex Signal Land Scattering in Multilayer Media. *Geophysics,* **47**:203-221.

Murray, J.N., Moran, P.J. 1989. Influence of Moisture on Corrosion of Pipeline Steel in Soils Using In-Situ Impedance Spectroscopy. *Corrosion*, **45**:34-43.

Najjaran, H., Sadiq, R., Rajani, B. 2004. Modelling Pipe Deterioration using Soil Properties – An Application of Fuzzy Logic Expert System. *ACSE International Conference on Pipeline Engineering and Construction*. 1st – 4th August, 2004. San Diego, CA, U.S.A.

Naudet, V., Revil, A., Bottero, J.-Y. 2003. Relationship Between Self-Potential (SP) Signals and Redox Conditions in Contaminated Groundwater. *Geophysical Research Letters*, **30(21)**: 2091. doi: 10.1029/2003GL018096.

Newton, J.G., Sykes, J.M. 1988. A Galvanostatic Pulse Technique for Investigation of Steel Corrosion in Concrete. *Corrosion Science*, **28**:1051-1074.

Norin, M. 1998. Groundwater and Soil Properties in an urban Environment and their effects on the Corrosion of Soil Buried Constructions of Carbon, Steel, and Zinc. Department of Geology, Chalmers University of Technology. Goteborg.

Norin, M., Vinka, T.G. 2003. Corrosion of Carbon Steel in Filling Material in an Urban Environment. *Materials and Corrosion*, **54**:641-651.

Ntarlagiannis, D., Ferguson, A. 2009. SIP Response of Artificial Biofilms. *Geophysics*, **74(1)**:1-5.

Nygaard, P.V. 2009. Corrosion Rate of Steel in Concrete: Evaluation of Confinement Techniques for On-Site Corrosion Rate Measurements. *Materials and Structures*, **42**:1059-1076.

Nyquist, J.E., Corry, C.E. 2002. Tutorial. Self-Potential: The Ugly Duckling of Environmental Geophysics. *The Leading Edge*, **21**:446-451.

Oelbner, W., Berthoid, F., Guth, U. 2006. The iR Drop – Well-Known but Often Underestimated in Electrochemical Polarization Measurements and Testing. *Materials and Corrosion*, **57(6)**:455-466.

Ogden, R.T. 1997. Essential Wavelets for Statistical Applications and Data Analysis. Birkhauser. York, U.S.A.

Oldham, K.B., Mansfeld, F. 1971. On the so-called Linear Polarization Method for Measurements of Corrosion Rates. *Corrosion*, **27**:434.

Olhoeft, G.R. 1985. Low Frequency Electrical Properties. *Geophysics*, **50(12)**:2492-2503.

Osella, A., Favetto, A. 2000. Effects of Soil Resistivity On Currents Induced on Pipelines. *Journal of Applied Geophysics*, **44**:303-312.

Papadopuolos, N.G., Tsourios, P., Tsokas, G.N., Sarris, A. 2006. Two-Dimension and Three-Dimension Resistivity Imaging in Archaeological Site Investigation. *Archaeological Prospection*, **13(3)**:163-181.

Papavinasam, S. 2008. Electrochemical Polarization Technique. In *Techniques for Corrosion Monitoring*. Part 1 Electrochemical Techniques for Corrosion Monitoring. Ed. Yang, L. Woodhead Publishing Limited, Cambridge. England.

Parasnis, D.S. 1997. Principles of Applied Geophysics. 5th Edition. Chapman & Hall. London, U.K.

Parra, J.O. 1984. Effects of Pipelines on Spectral Induced Polarization Surveys. *Geophysics*, **49(11)**:1979-1192.

Pelton, W.H., Ward, S.H., Hallof, P.G., Sill, W.R., Nelson, P.H. 1978. Mineral Discrimination and Removal of Inductive Coupling with Multifrequency IP. *Geophysics*, **43**:588-609.

Pelton, W.H., Sill, W.R., Smith, B.D. 1983. Interpretation of Complex Resistivity and Dielectric data, Part I. *Geophysical Transactions*, **29**:297-330.

Perez, N. 2004. Electrochemistry and Corrosion science. Kluwer Academic Publishers. Massachusetts, U.S.A.

Pernice, P., Arpaia, M., Constantini, A. 1990. Steel Corrosion rates in Soils by A.C and D.C Electrochemical Methods. *Materials Chemistry and Physics*, **26**:323-330.

Personna, Y.R., Ntarlagiannis, D., Slater, L., Yee, N., O'Brien, M., Hubbard, S. 2008. Spectral Induced Polarization and Electrodic Potential Monitoring of Microbially Mediated Iron Sulfide Transformations. *Journal of Geophysical Research*, **113**. G02020. doi:10.1029/2007JG000614.

Press, W.H., Teukolsky, S.A., Vetterling, W.T., Flannery, B.P. 1992. Numerical Recipes in C. The Art of Scientific Computing. 2nd Edition. Cambridge University Press, U.S.A.

Rajani, B., Kleiner, Y. 2003. Protection of Ductile Iron Water Mains against External Corrosion: Review of Methods and Case Histories. *Journal of the American Water Works Association*, **95(11)**:110-125.

Revil, A., Glover, P.W.J. 1998. Nature of Surface Electrical Conductivity in Natural Sands, Sandstones, and Clays. *Geophysical Research Letters*, **25(5)**:691-694.

Revil, A., Titov, K., Doussan, C., Lapenna, V. 2004. Applications of the Self-Potential Method to Hydrological Problems. In: "Applied Hydrogeophysics". (Ed). Vereecken, H., Binley, A., Cassiani, G., Revil, A., Titov, K. NATO Science Series IV: Earth and Environmental Sciences – Vol 71. Springer. Netherlands.

Revil, A., Mendoca, C.A., Atekwana, E.A., Kulessa, B., Hubbard, S.S., Bohlen, K.J. 2010. Understanding Biogeobatteries: Where Geophysics Meets Microbiology. *Journal of Geophysical Research*, **115**:G00GG02. doi: 10.1029/2009JG001065.

Revil, A., Florsch, N. 2010. Determination of Permeability from Spectral Induced Polarization in Granular Media. *Geophysical Journal International*, **181**:1480-1498.

Revil, A. 2012. Spectral Induced Polarization of Shaly Sand: Influence of the Electric Double Layer. *Water Resources Research*, **48** W02517. doi: 10.1029/2011/WR011260.

Reynolds, J.M. 2011. An Introduction to Applied and Environmental Geophysics. 2nd Edition. John Wiley & Sons Ltd. Chichester, U.K.

Richter, S., Thorarinsdottir, R, I., Jonsdottir, F. 2007. On-line Corrosion Monitoring in Geothermal District Heating Systems. II. Localized corrosion. *Corrosion Science*, **49(4)**:1907-1917.

Ricker, R.E. 2010. Analysis of Pipeline Steel Corrosion Data from NBS (NIST) Studies Conducted between 1922 – 1940 and Relevance to Pipeline Management. *Journal of Research of the National Institute of Standards and Technology*, **115(5)**:373-392.

Ridsdill-Smith, T.A., Dentith, M.C. 1999. The Wavelet Transform in Aeromagnetic Processing. *Geophysics*, **64(4)**:1003-1013.

Riley, J. 2005. Charge in colloidal systems. In: "Colloid Science Principles, Methods and Applications". (Ed) Cosgrove, T. Blackwell Publishing, Oxford, U.K.

Rim-rukeh, A., Awatefe, J.K. 2006. Investigation of Soil Corrosivity in the Corrosion of Low Carbon Steel pipe in Soil Environment. *Journal of Applied Sciences Research*, **2(8)**:466-469.

Roberge, P.R. 2000. Handbook of Corrosion Engineering. McGraw-Hill, U.S.A.

Robinson, W. 1993. Testing Soil for Corrosiveness. *Materials Performance*, **32(4)**:56-58.

Romanoff, M. 1957. Underground Corrosion. National Bureau of Standards Circular 579.

Roy, A., Apparao, A. 1971. Depth of Investigation in Direct Current Methods. *Geophysics*, **36**:943-959.

References

Roy, A. 1972. Depth of Investigation in Wenner, Three-Electrode and Dipole-Dipole DC Resistivity Methods. *Geophysical Prospecting*, **20**:329-340.

Ruffet, C., Darot, M., Gueguen, Y. 1995. Surface Conductivities in Rocks: A Review. *Surveys in Geophysics*, **16**:83-105.

Sadiq, R., Rajani, B., Kleiner, Y. 2004. Fuzzy-Based Method to Evaluate Soil Corrosivity for Prediction of Water Main Deterioration. *Journal of Infrastructure Systems*, **10(4)**:149-156.

Sammis, C.G. 1987. Methods of Experimental Physics Volume 24 – Part B. Geophysics Field Measurements. Academy Press, Inc. Florida, U.S.A.

Sass, O., Viles, H.A. 2010. Wetting and Drying of Masonry Walls: 2D-Resistivity Monitoring of Driving Rain Experiments on Historic Stonework in Oxford, UK. *Journal of Applied Geophysics*, **70**:72-83.

Sathiyanarayanan, S., Natarajan, P., Saravanan, K., Srinivasan, S., Venkatachari, G. 2006. Corrosion Monitoring of Steel in Concrete by Galvanostatic Pulse Technique. *Cement and Concrete Composites*, **28(7)**:630-637.

Sato, M., Mooney, H.M. 1960. The Electrochemical Mechanism of Sulphide Self Potentials. *Geophysics*, **25**:226-249.

Schaetzl, R.J., Anderson, S. 2005. Soils Genesis and Geomorphology. Cambridge University Press. New York, U.S.A.

Schlegel, M.L., Bataillon, C., Blanc, C., Pret, D., Foy, E. 2010. Anodic Activation of Iron Corrosion in Clay Media under Water saturated Conditions at 90°C: Characterization of the Corrosion Interface. *Environmental Science and Technology*, **44**:1503-1508.

Schmutz, M., Revil, A., Vaudelet, P., Batzie, M., Vinao, P.F., Werkema, D.D. 2010. Influence of Oil Saturation upon Spectral Induced Polarization of Oil-Bearing Sands. *Geophysical Journal International*, **183(1)**:211-224.

Schon, J.H. 1996. Physical Properties of Rocks – Fundamentals and Principles of Petrophysics (Seismic Exploration Series, No 18). Pergamon Press. New York, U.S.A.

Schwartz, N., Huisman, J.A., Furman, A. 2012. The Effect of NAPL on the Electrical Properties of Unsaturated Porous Media. *Geophysical Journal International*, **188**:1007-1011.

Scott, J.B.T., Barker, R.D. 2005. Characterization of Sandstone by Electrical Spectroscopy for Stratigraphical and Hydrogeological Investigations. *Quarterly Journal of Engineering Geology and Hydrogeology*, **38**:143-154.

Seabrook, B.C., Boadu, F.K. 2002. Relating Electrical Response and Petrophysical Properties Subjected to Stress Changes. *Journal of Environmental and Engineering Geophysics*, **7(2)**:88-99.

Sen, P.N., Scala, C., Cohen, M.H. 1981. A Self-Similar Model for Sedimentary Rocks with Application to the Dielectric Constant of Fused Glass Beads. *Geophysics*, **46**:781-795.

Seica, M.V., Packer, J.A., Grabinsky, M.W.F., Adams, B.J. Evaluation of the Properties of Toronto iron Water Mains and Surrounding Soil. *Canadian Journal of Civil Engineering*, **29**:222-237.

Seidel, K., Lange, G. 2007. Electromagnetic Methods. In: 'Environmental Geology. Handbook of Field Methods and Case Studies'. (Eds) Knodel, K., Lange, G., Voigt, H.-J. Springer-Verlag. Berlin, Germany.

Seigel, H.O. 1959. Mathematical Formulation and Type Curves for Induced Polarization. *Geophysics*, **24(3)**:547-565.

Slater, L.D., Lesmes, D. 2002. IP Interpretation in Environmental Investigations. *Geophysics*, **67(1)**:77-88.

Slater, L., Binley, A. 2003. Evaluation of Permeable Reactive Barrier (PRB) Integrity Using Electrical Imaging Methods. *Geophysics*, **68(3)**:911-921.

Slater, L.D., Ntarlagiannis, D., Wishart, D. 2006. On the Relationship between Induced Polarization and Surface Area in Metal-Sand and Clay-Sand Mixtures. *Geophysics*, **71(2)**:A1-A5.

Slater, L., Ntarlagiannis, D., Personna, Y.R., Hubbard, S. 2007. Pore-Scale Spectral Induced Polarization Signatures Associated with FeS Biomineral Transformations. *Geophysical Research letters*, **34**:L21404. doi: 10.1029/2007GL031840.

Scully, J.R. 2000. 2000. Polarization Resistance Method for Determination of Instantaneous Corrosion Rates. *Corrosion*, **56(2)**:199-218.

Sharma, P.V. 1997. Environmental and Engineering Geophysics. Cambridge University Press. Cambridge, U.K.

Shipilov, S.A., May, I.L. 2006. Structural Integrity of Aging Pipelines Having Cathodic Protection. *Engineering Failure Analysis*, **13(7)**:1169-1176.

Silva, S., Dick, L.F.P. 2008. EIS Study of Soil Corrosivity. *ECS Transactions*, **11(18)**:35-40.

Smith, C.A. 1981. Soil in the Corrosion Process: A Review of the Role of Soil Conditions on the Corrosion of Underground Pipes. *Anti-Corrosion Methods and Materials*, **28(2)**:4-8.

So, H-S., Millard, S.G. 2007. Assessment of Corrosion rate of Reinforced Steel in Concrete Using galvanostatic Pulse Transient Technique. *International Journal of Concrete Structures and Materials*, **1(1)**:83-88.

Soleymani, H.R., Ismail, M.E. 2004. Comparing Corrosion Measurement Methods to Assess the Corrosion Activity of Laboratory OPC and HPC Concrete Specimens. *Cement and Concrete Research*, **34**:2037-2044.

Soupios, P.M., Georgakopoulos, P., Papadopoulos, N., Saltas, V., Andreadakis, A., Vallianatos, F., Sarris, A., Makris, J.P. 2007. Use of Engineering Geophysics to Investigate a Site for a Building Foundation. *Journal of Geophysics and Engineering*, **4**:94-103.

Stansbury, E.E., Buchanan, R.A. 2000. Fundamentals of Electrochemical Corrosion. ASM International. Materials Park, U.S.A.

Stein, C.M. 1981. Estimation of the Mean of a Multivariate Normal Distribution. *The Annals of Statistics*, **9(6)**:1135-1151.

Stott, J.F.D., John, G. Corrosion in Soils. In: "Shreir's Corrosion. Volume 2". (Ed). Cottis, R.A., Graham, M.J., Lindsay, R., Lyon, S.B., Richardson, J.A., Scantlebury, J.D., Stott, F.H. Academic Press, Elsevier. Amsterdam, Netherlands.

Sultan, S.A., Mansour, S.A., Santos, F.M., Helaly, S. 2009. Geophysical Exploration for Gold and Associated Minerals, Case Study: Wadi El Beida Area, South Eastern Desert, Egypt. *Journal of Geophysics and Engineering*, **6(4)**:345-356.

Sumner, J.S. 1976. Principles of Induced Polarization for Geophysical Exploration. Elsevier Scientific Publishing Company. Amsterdam, Netherlands.

Szalai, S., Novak, A., Szarka, L. 2009. Depth of Investigation and Vertical Resolution of Surface Geoelectric Arrays. *Journal of Environmental and Engineering Geophysics*, **14(1)**: 15-23.

Szalai, S., Novak, A., Szarka, L. 2011. Which Geoelectric Array Sees the Deepest in a Noisy Environment? Depth of Detectability Values of Multielectrode Systems for Two-Dimensional Models. *Physics and Chemistry of the Earth, Parts A/B/C*, **36(6)**:1398-1404.

Tabbagh, A., Dabas, M., Hesse, A., Panissod, C. 2000. Soil Resistivity: A Non Invasive Tool to map Soil Structure Horizonation. *Geoderma*, **97(3-4)**:393-404.

Tavouraki-Papafotiou, B., Tsokas, G.N., Tsurlos, P. 2005. Wavelet Denoising of Magnetic Prospecting Data. *Journal of Balkan Geophysical Society*, **8(2)**:28-36.

Telford, W.M., Geldart, L.P., Sheriff, R.E. 1990. Applied Geophysics. 2nd Edition. Cambridge University Press. New York, U.S.A.

Tilley, R.J.D. 2004. Understanding Solids: the Science of Materials. John Wiley & Sons Ltd. Chichester, England.

Titov, K., Komarov, V., Tarasov, V., Levitski, A. 2002. Theoretical and Experimental Study of the Time Domain Induced Polarization in Water-Saturated Sands. *Journal of Applied Geophysics*, **50**:417-433.

To, A.C., Moore, J.R., Glaser, S.D. 2009. Wavelet Denoising Techniques with Applications to Experimental Geophysical Data. *Signal Processing*, **89**:144-169.

Uhlig, H.H. 1981. Corrosion and Corrosion Control: An Introduction to Corrosion Science and Engineering. 2nd Edition. Wiley, New York. U.S.A.

Ulrich, C., Slater, L.D. 2004. Induced Polarization Measurements on Unsaturated, Unconsolidated Sands. *Geophysics*, **69(3)**:762-771.

Vane, L.M., Zang, G.M. 1997. Effect of Aqueous Phase Properties on Clay Particle Zeta Potential and Electro-Osmotic Permeability: Implications for Electrokinetic Soil Remediation Processes. *Journal of Hazardous Materials*, **55(1-3)**:1-22.

Vanhala, H., Soininen, H. 1995. Laboratory Technique for Measurement of Spectral Induced Polarization Response of Soil Samples. *Geophysical Prospecting*, **43**:655-676.

Vanhala, H. 1997. Mapping Oil-Contaminated Sand and Till with the Spectral Induced Polarization (SIP) method. *Geophysical Prospecting*, **45(2)**:303-326.

Vaudelet, P., Schmutz, M., Pessel, M., Franceschi, M., Guerin, R., Atteia, O., Blondel, A., Ngomseu, C., Galaup, S., Rejiba, F., Begassat, P. 2011. Mapping of Contaminated Plumes with Geoelectric Methods. A case Study in Urban Context. *Journal of Applied Geophysics*, **75(4)**:738-751.

Viezzoli, A. Cull, J.P. 2005. Electrical Methods for Detection and Discrimination of Saline Groundwater in Clay-Rich Sediments in Northern Victoria. *Exploration Geophysics*, **36**:294-300.

Viezzoli, A. 2006. Advances in Complex impedance for Environmental Applications. PhD Thesis, School of Geosciences. Monash University, Australia.

Vinegar, H.J., Waxman, M.H. 1984. Induced Polarization of Shaly Sands. *Geophysics*, **49**:1267-1287.

Volkman, J., Klitzsch, N. 2010. Frequency-Dependent Electric Properties of Microscale Rock Models for Frequencies from One Millihertz to ten Kilohertz. *Vadose Zone Journal*, **9**:858-870.

Wait, J.R. 1982. Electromagnetic Response of a Medium Loaded with Coated Conductive Particles. *IEEE Transactions on Geoscience and Remote Sensing*, **GE-20(4)**:500-504.

Wanfang, Z., Beck, B.F., Stephenson, J.B. 1999. Investigation of Groundwater Flow in Karst Areas Using Component Separation of Natural Potential Measurements. *Environmental Geology*, **37(1-2)**:19-25.

Ward, S.H., Fraser, D.C. 1967. Conduction of Electricity in Rocks. In: "Mining Geophysics". (Ed). Hansen, D.A., Heinrichs, W.E., Holmer, R.C., MacDougall, R.E., Rogers, G.R., Sumner, J.S., Ward, S.H. The Society of Exploration Geophysicists. Tulsa, U.S.A.

Waxman, M.H., Smits, L.J.M. 1968. Electrical Conductivities in Oil-Bearing Shaley Sands. *Society of Petroleum Engineers Journal*, **8(2)**:107-122.

Weller, A., Borner, F.D. 1996. Measurements of Spectral Induced Polarization for Environmental Purposes. *Environmental Geology*, **27(4)**:329-334.

Wong, J., Strangway, D.W. 1981. Induced Polarization in Disseminated Sulfide Ores Containing Elongated Mineralization. *Geophysics*, **46(9)**:1258-1268.

Wu, Y.H., Liu, T.M., Luo, S.X., Sun, C. 2010. Corrosion Characteristics of Q235 Steel in Simulated Yingtan Soil Solutions. *Materials Science and Engineering Technology*, **41(3)**:142-146.

Xiaodan, F., Mingqui, L., Hongmei, X., Yongqiang, L., Duochang, C. 2007. Influence of Soil Humidity on Corrosion Behaviour of X70 Steel in Yellow Pebble Soil. *Corrosion Science and Protection Technology*, **19(1)**:35-37.

Yahaya, N., Lim, K.S., Noor, N.M., Othman, S.R., Abdullah, A. 2011. Effects of Clay and Moisture Content on Soil Corrosion Dynamic. *Malaysian Journal of Civil Engineering*, **23(1)**:24-32.

Yuanhui, W., Cheng, S., Shuquan, Z., DuoChang, C., Guohua, L., Xia, L. 2005. Influence of Soil Humidity on Corrosion Behaviour of X70 Pipeline Steel in Saline Soils of Qinghai Salt Lake Region. *Corrosion Science and Protection Technology*, **17(2)**:87-90.

Yukselen, Y., Kaya, Abidin. 2003. Zeta Potential of Kaolinites in the Presence of Alkali, Alkaline earth and Hydrolyzable Metal Ions. *Water, Air, and Soil Pollution*, **145**:155-168.

Yungul, S.H. 1996. Electrical methods in Geophysical Exploration of Deep Sedimentary Basins. 1st Edition. Chapman & Hall. London, U.K.

Zeyen, H., Pessei, M., Ledesert, B., Hebert, R., Bartier, D., Sabin, M., Lallemant, S. 2011. 3D Electrical Resistivity Imaging of the Near-Surface Structure of Mud-Volcano Vents. *Tectonophysics*, **509(3-4)**:181-190.

Zhang, X.L., Jian, Z.H., Yao, Z.P., Song, Y., Wu, Z.D. 2009. Effects of Scan Rate of the Potentiodynamic Polarization Curve Obtained to Determine the Tafel Slopes and Corrosion Current Density. *Corrosion Science*, **51**:581-581.

Zhdanov, M. 2008. Generalized Effective Medium Theory of Induced Polarization. *Geophysics*, **73(5)**:F197-F211.

Zimmermann, E., Kemna, A., Berwix, J., Glaas, W., Munch, H.M., Huisman, J.A. 2008. A High-Accuracy Impedance Spectrometer for Measuring Sediments with Low Polarizability. *Measurement Science and Technology*, **19**:105603-105611.

APPENDIX A.1   Summary of Synthetic Soil Samples

Table A.1. Summary for the synthetic soil samples and the designation used in this thesis.

Sample Designate	pH	Sand Content (%)	Clay Content (%)	Electrolyte	Electrolyte Content (% w/w)[*]
A5	5.0	95	5	DI	20
A10	4.7	90	10	DI	25
A15	4.6	85	15	DI	30
A20	4.5	80	20	DI	35
A25	4.5	75	25	DI	40
B5	4.8	95	5	0.01M NaCl	20
B10	4.6	90	10	0.01M NaCl	25
B15	4.6	85	15	0.01M NaCl	30
B20	4.5	80	20	0.01M NaCl	35
B25	4.5	75	25	0.01M NaCl	40
C5	4.7	95	5	0.1M NaCl	20
C10	4.5	90	10	0.1M NaCl	25
C15	4.3	85	15	0.1M NaCl	30
C20	4.3	80	20	0.1M NaCl	35
C25	4.2	75	25	0.1M NaCl	40

DI = deionized water. * - to attain complete saturation.

Table A.2. Particle size distribution of the kaolin clay used in this work after Viezzoli (2006).

< particle size (μm)	Composition (%)
2	68
5	81
10	88
20	95
30	98
75	100

APPENDIX A.2   THE LEVENBERG-MARQUARDT ALGORITHM

For least squares curve fitting of nonlinear functions, the Levenberg-Marquardt Algorithm (LMA) provides a numerical solution to minimizing the objective function iteratively. This objective function is the chi-square function which takes up the form given by Eq. A.1.

$$\chi^2(\mathbf{p}) = \sum_{i=1}^{N}\left[\frac{1}{\sigma_i^2}\left(y_i - \mathbf{f}(x_i;\mathbf{p})\right)^2\right] \tag{A.1}$$

Where,

N = number of data points,

σ_i^2 = the variance of each data point resulting from measurement error,

y_i = experimental data point,

$\mathbf{p}$ = the parameter(s) being optimized, and

$\mathbf{f}(x_i;\mathbf{p})$ = the model curve.

In most experiments, the variance σ_i^2 associated with y_i is not known. In the event that such measurement errors can be assumed to be mainly arising from instrumental errors, it can be safely assumed that σ_i^2 is consistent amongst all data point, thus $\sigma_i^2 = \sigma_n^2$. Under such cases, the weighting in Eq. A.1 is not required and the chi-square distribution can be given by:

$$\chi^2(\mathbf{p}) = \sum_{i=1}^{N}\left[\left(y_i - \mathbf{f}(x_i;\mathbf{p})\right)^2\right] \tag{A.2}$$

The LMA technique continuously switches between the Gauss-Newton Algorithm (GNA) and the method of Gradient Descent (GD) [see Bevington & Robinson, 1992; Press *et*. a*l*., 1992] to solve for the optimized parameter(s). In vector notation, it can be shown through some linearization that:

$$\chi^2(\mathbf{p} + \delta) \approx \left\|y - \mathbf{f}(\mathbf{p}) - \mathbf{J}\delta\right\|^2 \tag{A.3}$$

where, $\mathbf{J}$ is the Jacobian matrix and δ is a small perturbation. The δ which minimizes χ^2 is then evaluated from $\frac{\partial}{\partial\delta}\chi^2(\mathbf{p} + \delta) = 0$, resulting in:

$$\left(\mathbf{J^T J}\right)\delta = \mathbf{J^T}\left[y - \mathbf{f}(\mathbf{p})\right] \tag{A.4}$$

where, $\left(\mathbf{J^T J}\right)$ is the approximate Hessian matrix. Levenberg (1944) modified the above expression to include a positive parameter, λ resulting in:

$$\left(\mathbf{J^T J} + \lambda\mathbf{I}\right)\delta = \mathbf{J^T}\left[y - \mathbf{f}(\mathbf{p})\right] \tag{A.5}$$

where, $\mathbf{I}$ is the identity matrix. The parameter λ is adjusted for every iteration to reduce the misfit between the observed and modeled values. Note, if λ is adaptively reduced in every iteration, the algorithm behaves like the GNA and if λ is increased it behaves like the GD method. However, Levenberg's modified algorithm suffers from the drawback that if λ is very high, the term $\left(\mathbf{J}^\mathbf{T}\mathbf{J} + \lambda\mathbf{I}\right)$ is not used. Marquardt (1963) realized this and suggested a further modification to Levenberg's algorithm, by replacing the identity matrix $\mathbf{I}$ with the diagonal elements of the matrix $\left(\mathbf{J}^\mathbf{T}\mathbf{J}\right)$; thus providing the Levenberg-Marquardt algorithm expressed in Eq. A.6.

$$\left(\mathbf{J}^\mathbf{T}\mathbf{J} + \lambda\,\mathbf{diag}\left(\mathbf{J}^\mathbf{T}\mathbf{J}\right)\right)\delta = \mathbf{J}^\mathbf{T}\left[y - \mathbf{f}(\mathbf{p})\right] \tag{A.6}$$

In LMA, the choice of λ is very important. It should lie between an intermediate value in order to take advantage of the analytical solution as well as being able to decrease during iterations [Bevington & Robinson, 1992]. The initial starting values for $\lambda = \lambda_o$ can be estimated through several trial runs. The pseudocode given below provides an aid in understanding the LMA [Press *et al.*, 1992].

1) Calculate $\chi^2(\mathbf{p})$.

2) Start the iteration initially with a suitable value of $\lambda = \lambda_o$, say $\lambda = 0.01$.

3) Calculate $\delta\mathbf{p}$ and $\chi^2(\mathbf{p} + \delta\mathbf{p})$ with this initial choice of λ.

4) If $\chi^2(\mathbf{p} + \delta\mathbf{p}) > \chi^2(\mathbf{p})$, increase λ by a factor of 10. Go back to step **3)**.

5) If $\chi^2(\mathbf{p} + \delta\mathbf{p}) < \chi^2(\mathbf{p})$, decrease λ by a factor of 10. Update the trial solution to $\mathbf{p}^{'} = (\mathbf{p} + \delta\mathbf{p})$ and return to step **3)** replacing $\mathbf{p}$ by $\mathbf{p}^{'}$.

The algorithm stops when a solution is found, or when some given criterion has been reached (number of iterations, tolerance *etc.*). When minimization is successful and the chi-square minimization is carried out with the weights of the data points included, the covariance matrix $\mathbf{C}$ at the end of the iteration can be expressed by Eq. A.7.

$$\mathbf{C} = \left(\mathbf{J}^\mathbf{T}\mathbf{W}^\mathbf{T}\mathbf{W}\,\mathbf{J}\right)^{-1}, \tag{A.7}$$

where $\mathbf{W}$ is a diagonal matrix consisting of the reciprocal of variances in the data. In this case the square-root of the *j*-th diagonal element of $\mathbf{C}$ is proportional to the standard error associated with the *j*-th parameter. In some situations, the weighting of the data points are unknown. This arises especially when data acquisition is conducted using electronic instruments. Here, the $\mathbf{C}$ matrix can be written as:

$$C = \left(J^T J\right)^{-1} \tag{A.8}$$

To obtain errors in the parameters from C, further scaling is required. In this instance, the difference between the measured and modeled data can be used to map the variances in the final estimated parameters. Thus the standard errors in the final estimated parameters can be computed from Eq. A.9 [see Menke, 1989; Press *et*. *al*., 1992].

$$\sigma_k = \sqrt{\frac{SSE}{N-p}} \times \sqrt{diag\left(J^T J\right)^{-1}} = \sqrt{\frac{SSE}{N-p}} \times \sqrt{C_{kk}^{-1}} \tag{A.9}$$

where, SSE is the sum of squared errors and provides an unbiased estimate of noise in the data, N is the number of data points, p is the number of parameters. The quantity $(N - p)$ represents the degree of freedom, ν. It follows that when $N \gg p$,

$$\sqrt{\frac{SSE}{N-p}} \approx \sqrt{\frac{SSE}{N}} = RMSE \tag{A.10}$$

where RMSE is the root-mean-square-error. Hence, in the event that ν is very high, Eq. A.10 can be substituted into Eq. A.9 to provide estimates of errors in the final estimated parameters.

APPENDIX A.3　　BLOCK DIAGRAM FOR THE GALVANOSTATIC PULSE CURVE FITTING ROUTINE

The curve fitting routine consists of several subVI's which operate in unison to achieve the required function. Most of these subVI's are available in NI standard library functions. The block diagram for the main routine in shown in Fig. A.1. Explanatory notes are provided where necessary to aid in understanding the data flow and program execution. Some important subVI's developed as part of this work (employing other standard subVI's) is also highlighted. These subVI's are further expanded in Fig. A.2 and A.3.

MAIN ROUTINE
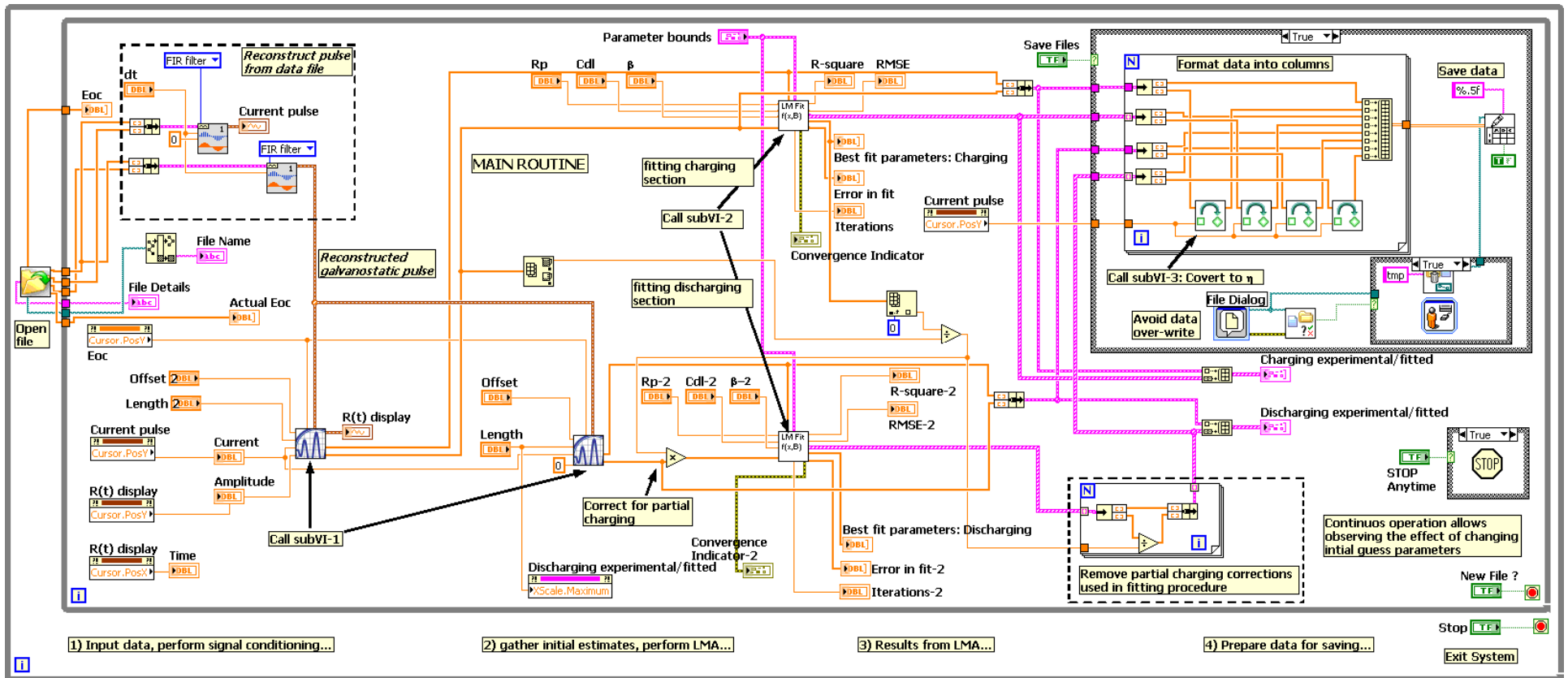
Figure A.1. Block diagram of the curve fitting routine. Note annotations provided in order to understand the data flow and program execution.

SubVI-1

After reconstruction of the pulse from the data file, the overpotential data is transformed to R(t)-response for the entire duration and is displayed. The charging and discharging sections are also extracted from the pulse and are passed onto subVI-2 and subVI-3 respectively for least squares fitting. The block diagram for the subVI-2 is shown in Fig. A.2. Note the difference in the use of this subVI for extracting the charging and discharging sections; these require different values for offset and length of the pulse, which are input in the main routine. Also, the charging section has to be corrected for the 'jump' in the pulse at $\Delta t = 1$ due to $i_{app} R_{\Omega}$.
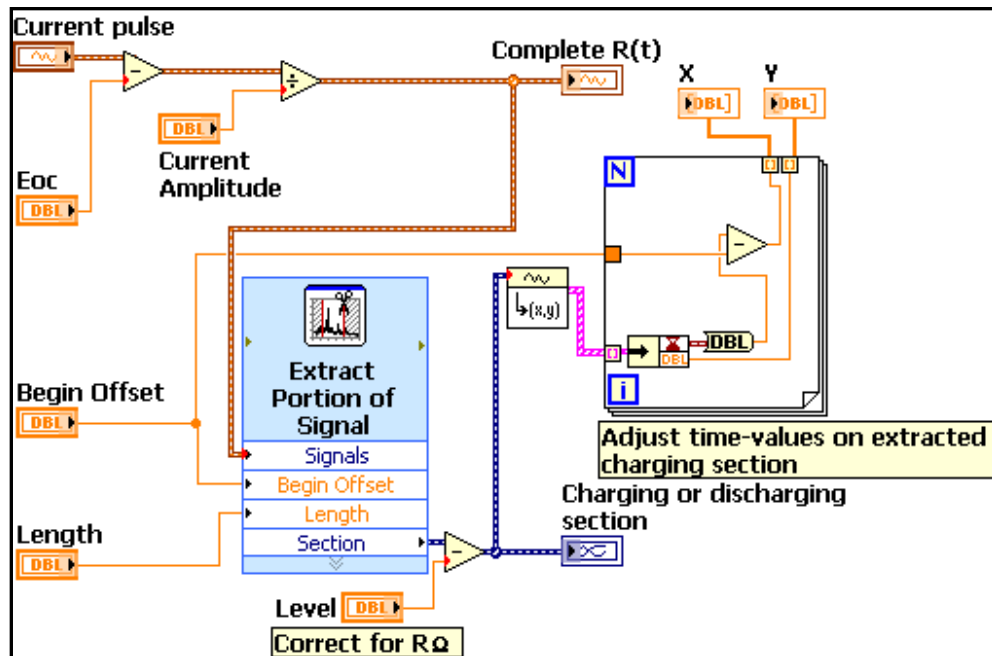
Figure A.2. Block diagram of subVI-2 used for displaying the complete R(t)-response, as well as for extracting charging or discharging sections.

SubVI-2

The subVI-2 fitting sub-routine implements the nonlinear least squares curve fitting process utilizing the NI's constrained *Nonlinear Curve Fit LM bound* subVI as shown in Fig A.3. For both charging and discharging curve analysis the same subVI is called, and the respective data is passed onto these sub-routines. The *Nonlinear Curve Fit LM bound* subVI utilizes the LMA to find the optimal parameters describing the data using a specified reference model function. Since the model function describing the charging and discharging processes are different, they were implemented as separate subVI's, each referenced as per required. These implemented model functions are respectively shown in Fig. A.3b and A.3c.
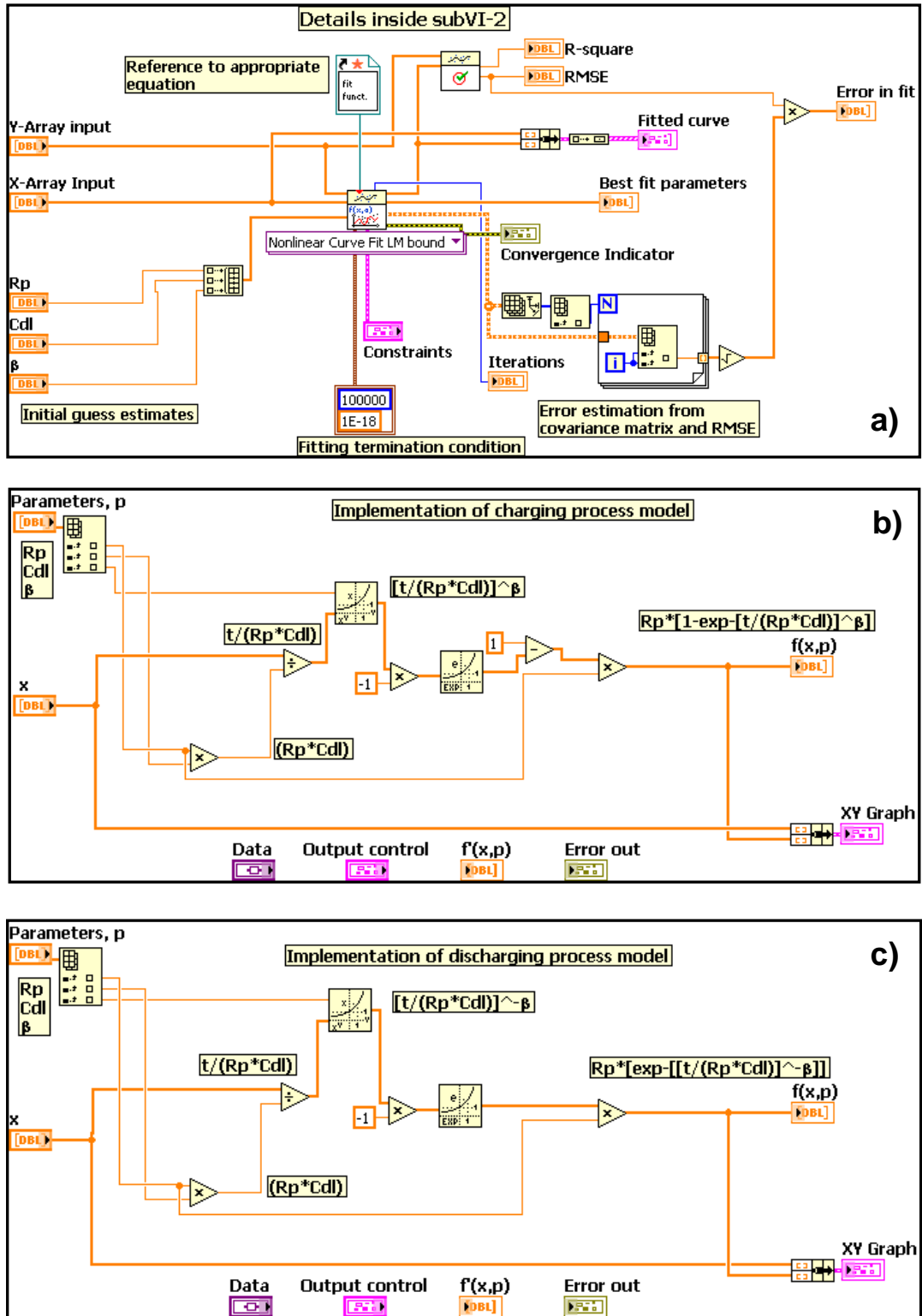
Figure A.3. **a)** Block diagram of the sub-routine implementing NI's *Nonlinear Curve Fit LM bound* subVI. Reference to the model equations for the charging and discharging processes were implemented as separate subVI's as shown in **b)** and **c)** respectively.

The fitting process is started by the user providing the initial estimates and defining the maximum and minimum bounds for the parameters. For both cases (charging and discharging), the misfit function given by the chi-square is minimized iteratively by the LMA. The block diagram for *Nonlinear Curve Fit LM bound* subVI is accessible, which shows the implementation of the actual LMA technique. The LMA stops when a) the maximum number of iterations is reached, or b) the tolerance falls below the minimum specified value, indicating optimal parameter values are found. Different starting values of $\lambda = \lambda_o$ were tested during this work. No significant differences in estimated parameters were observed for $\lambda_o = 0.01, 0.1, 1,$ and 10. For successive iterations, λ is either increased or decreased by a default factor of 10. The errors in the measured data are not known, however any such errors are believed to be equal for each data point and mainly attributed to consistent instrumental errors. Thus, in this particular case[*], the final covariance matrix at the end of the iteration from *Nonlinear Curve Fit LM bound* subVI is given by:

$$\mathbf{C} = \left[\mathbf{J}^\mathbf{T} \mathbf{J} \right]^{-1} \tag{A.10}$$

To compute the uncertainty in the *j*-th final estimated parameter the square-root of the *j*-th diagonal element in C is multiplied by the root-mean-square-error (RMSE) [see Appendix A.2] *i.e.*,

$$\sigma = RMSE \times \sqrt{\mathbf{diag}\left(\left[\mathbf{J}^\mathbf{T} \mathbf{J} \right]^{-1} \right)} \tag{A.11}$$

Note in this case the number of parameters, $p(3) \ll N$ (number of data points >250), in which case the degrees of freedom, ν is very high.

---

[*] The default values for the weights (inverse of σ^2) in NI's *Nonlinear Curve Fit LM bound* subVI is equal to 1. Thus, chi-minimization in this case proceeds with equal weighting to the data points, since the errors are unknown and assumed to be equal in each data point.

APPENDIX A.4   SAMPLE CALCULATION FOR THE DETERMINATION OF CORROSION PARAMETERS

For the purpose of demonstration, the calculation performed here is for the cast iron-B10 system during Day 1 measurements. The weighted means and standard deviations are based on the concept that a given a set of N measurements for a parameter A accompanied with different errors $[(A_1 + \sigma_1), (A_2 + \sigma_2), (A_3 + \sigma_3), \ldots, (A_N + \sigma_N),]$, provides a mean μ which should be weighted inversely as the square of its own error [Knoll, 2000; Deo, 2005]. Thus,

$$\mu = \left(\frac{\dfrac{A_1}{(\sigma_1)^2} + \dfrac{A_2}{(\sigma_2)^2} + \dfrac{A_3}{(\sigma_3)^2} + \ldots + \dfrac{A_N}{(\sigma_N)^2}}{\dfrac{1}{(\sigma_1)^2} + \dfrac{1}{(\sigma_2)^2} + \dfrac{1}{(\sigma_3)^2} + \ldots + \dfrac{1}{(\sigma_N)^2}} \right) \tag{A.12}$$

Likewise, the weighted standard deviation can then be estimated by:

$$\sigma = \left(\frac{1}{\dfrac{1}{(\sigma_1)^2} + \dfrac{1}{(\sigma_2)^2} + \dfrac{1}{(\sigma_3)^2} + \ldots + \dfrac{1}{(\sigma_N)^2}} \right) \tag{A.13}$$

For each galvanostatic pulse measurement, the estimations of the three corrosion parameters, *viz.*, R_p, C_{dl}, and β were accompanied by their respective errors projected from the covariance matrix and RMSE. Thus, the weighted scheme was applied to each of the three sets of estimations from the charging and the discharging curves (except for Day 7). This was done as follows.

<u>Charging Curve:</u>

From the three repeated measurements on the cast iron-B10 system:

$R_{p1} = (107 \pm 3.45)\ \Omega, \quad R_{p2} = (116 \pm 4.3)\ \Omega, \quad R_{p3} = (95.5 \pm 2.82)\ \Omega$

$C_{dl1} = (1.26 \pm 0.0024) \times 10^{-2}\ \text{F}, \quad C_{dl2} = (1.32 \pm 0.00315) \times 10^{-2}\ \text{F}, \quad C_{dl3} = (1.20 \pm 0.00206) \times 10^{-2}\ \text{F}$

$\beta_1 = 0.949 \pm 0.009, \quad \beta_2 = 0.902 \pm 0.008, \quad \beta_3 = 0.991 \pm 0.01$

Applying Eqs. A.12 and A.13, the weighted mean and standard deviations for the above measurements from the charging section are:

$R_p = (103 \pm 1.95)\ \Omega$

$C_{dl} = (1.24 \pm 0.0014) \times 10^{-2}\ \text{F}$

$\beta = 0.943 \pm 0.005$

APPENDIX

Discharging Curve:

From the three repeated measurements on the cast iron-B10 system:

$R_{p1} = (111 \pm 0.199)\ \Omega, \quad R_{p2} = (119 \pm 0.211)\ \Omega, \quad R_{p3} = (100 \pm 0.179)\ \Omega$

$C_{dl1} = (2.00 \pm 0.00105) \times 10^{-2}\ \text{F}, C_{dl2} = (1.85 \pm 0.001) \times 10^{-2}\ \text{F}, \quad C_{dl3} = (2.18 \pm 0.00113) \times 10^{-2}\ \text{F}$

$\beta_1 = 0.634 \pm 0.001, \qquad \beta_2 = 0.641 \pm 0.001, \qquad \beta_3 = 0.647 \pm 0.002$

Applying Eqs. A.12 and A.13, the weighted mean and standard deviations for the above measurements from the discharging section are:

$$R_p = (109 \pm 1.13)\ \Omega$$
$$C_{dl} = (1.99 \pm 0.001) \times 10^{-2}\ \text{F}$$
$$\beta = 0.641 \pm 0.001$$

Equations A.12 and A.13 are then again applied to both the weighted means and standard deviations from the charging and discharging curves to produce the overall weighted means and standard deviations. Hence, the overall weighted means and standard deviations for the cast iron-B10 system during Day 1 is:

$$R_p = \underline{(109 \pm 0.112)\ \Omega}$$
$$C_{dl} = \underline{(1.88 \pm 0.000552) \times 10^{-2}\ \text{F}}$$
$$\beta = \underline{0.649 \pm 0.0008}$$

The above scheme was applied for the calculation of corrosion parameters from all Day 1 measurements. For Day 7 measurements, only the charging sections were utilized and their weighted means and standard deviations were calculated. Further discussion is provided in the thesis.

APPENDIX A.5   PARAMETER ESTIMATES FROM CURVE FITTING ANALYSIS OF GALVANOSTATIC PULSES

The estimated parameters following the curve fitting exercise are given in this Appendix. Each metal/soil electrolyte was measured at least three times (unless shown otherwise by a '-') and the respective corrosion parameters (E_{CORR}, R_Ω, R_p, C_{dl}, β) for each measurement are given. The specific electrolyte in which a metal was placed is referred to by the sample designate, as discussed in the thesis and is also given in Appendix A.1. For convenience, the analyses of the charging and/or discharging curves are separately shown for each metal-soil system. Note that Rs corresponds to the Ohmic drops, R_Ω. For each of the parameters, R_p, C_{dl}, and β, the optimum or 'fitted" values from the curve fitting analysis are stated together with the standard deviations (Std Dev). As discussed in the thesis, E_{CORR} and R_Ω are manually determined from the user-interactive curve fitting routine GUI. Other parameters (R_p, C_{dl}, β) are determined from the constrained Levenberg-Marquardt nonlinear curve fitting algorithm.

MILD STEEL-SOIL SYSTEM – DAY 1

Electrolyte	Iapp (A)	M1 Ecorr (-V)	M1 Rs (Ω)	M1 Rp (Ω) Fit	M1 Rp (Ω) Std Dev	M1 C (F) Fit	M1 C (F) Std Dev	M1 β Fit	M1 β Std Dev	M2 Ecorr (-V)	M2 Rs (Ω)	M2 Rp (Ω) Fit	M2 Rp (Ω) Std Dev	M2 C (F) Fit	M2 C (F) Std Dev	M2 β Fit	M2 β Std Dev	M3 Ecorr (-V)	M3 Rs (Ω)	M3 Rp (Ω) Fit	M3 Rp (Ω) Std Dev	M3 C (F) Fit	M3 C (F) Std Dev	M3 β Fit	M3 β Std Dev
A5	4.00E-04	0.724	6.87E+02	2.37E+02	4.01E+00	1.20E-02	3.00E-05	1.000	0.595	0.724	6.87E+02	1.90E+02	2.17E+00	1.11E-02	2.60E-05	1.000	0.573	0.724	6.87E+02	1.69E+02	1.47E+00	1.06E-02	2.20E-05	1.000	0.524
A10	2.00E-04	0.734	3.54E+02	4.27E+02	4.41E+00	4.85E-03	1.10E-05	1.000	1.210	0.734	3.54E+02	4.02E+02	3.30E+00	4.73E-03	8.75E-06	1.000	1.060	0.734	3.54E+02	3.88E+02	2.56E+00	4.64E-03	7.34E-06	1.000	0.919
A15	2.00E-04	0.735	2.49E+02	2.66E+02	4.15E+00	9.19E-03	2.46E-05	1.000	0.824	0.736	2.49E+02	3.13E+02	1.86E+01	9.52E-03	1.84E-04	0.977	0.007	0.736	2.50E+02	4.79E+02	1.79E+01	9.78E-03	3.14E-05	1.000	0.991
A20	2.00E-04	0.736	2.06E+02	3.59E+02	3.06E+00	6.03E-03	1.00E-05	1.000	0.766	0.736	2.08E+02	4.00E+02	5.81E+00	6.19E-03	1.52E-05	1.000	1.120	0.736	2.08E+02	3.91E+02	5.00E+00	6.10E-03	1.38E-05	1.000	1.040
A25	2.00E-04	0.740	1.75E+02	2.91E+02	3.32E+00	7.54E-03	1.66E-05	1.000	0.812	0.74	1.74E+02	2.85E+02	8.69E+00	7.42E-03	8.83E-05	0.989	0.005	0.740	1.74E+02	2.75E+02	7.98E+00	7.31E-03	8.25E-05	0.998	0.005
B5	2.00E-04	0.721	3.35E+02	2.04E+02	3.13E+00	9.13E-03	3.24E-05	1.000	1.010	0.721	3.35E+02	1.88E+02	2.23E+00	9.00E-03	2.75E-05	1.000	0.905	0.721	3.34E+02	1.75E+02	1.56E+00	8.56E-03	2.24E-05	1.000	0.777
B10	2.00E-04	0.731	2.17E+02	3.35E+02	2.25E+00	5.40E-03	8.64E-06	1.000	0.798	0.731	2.18E+02	3.55E+02	3.43E+00	5.54E-03	1.16E-05	1.000	1.030	0.731	2.18E+02	3.45E+02	2.82E+00	5.45E-03	1.02E-05	1.000	0.927
B15	2.00E-04	0.736	1.77E+02	3.00E+02	9.97E-01	7.73E-03	1.07E-04	0.959	0.005	0.736	1.79E+02	2.62E+02	2.40E+00	7.32E-03	1.49E-05	1.000	0.759	-	-	-	-	-	-	-	-
B20	2.00E-04	0.723	1.47E+02	2.66E+02	1.99E+00	6.26E-03	1.28E-05	1.000	0.832	0.724	1.43E+02	2.76E+02	5.89E+00	6.33E-03	6.40E-05	0.971	0.004	-	-	-	-	-	-	-	-
B25	2.00E-04	0.736	1.25E+02	2.81E+02	2.72E+00	7.24E-03	1.47E-05	1.000	0.769	0.736	1.23E+02	2.70E+02	6.24E+00	6.99E-03	6.90E-05	0.984	0.004	0.736	1.25E+02	2.81E+02	2.52E+00	7.03E-03	1.37E-05	1.000	0.756
C5	2.00E-04	0.699	8.08E+01	1.80E+02	3.59E+00	7.64E-03	9.46E-05	0.932	0.005	0.699	8.08E+01	1.73E+02	3.44E+00	7.48E-03	9.25E-05	0.941	0.006	-	-	-	-	-	-	-	-
C10	2.00E-04	0.702	5.64E+01	1.83E+02	3.90E+00	7.97E-03	9.35E-05	0.960	0.005	0.702	5.64E+01	1.76E+02	4.00E+00	7.83E-03	9.69E-05	0.974	0.006	0.702	5.64E+01	1.72E+02	3.87E+00	7.79E-03	9.35E-05	0.985	0.006
C15	2.00E-04	0.715	5.19E+01	2.50E+02	4.55E+00	6.06E-03	5.36E-05	0.990	0.004	0.715	5.19E+01	2.45E+02	1.47E+00	6.01E-03	1.08E-05	1.000	0.774	0.714	5.18E+01	2.64E+02	5.41E+00	6.23E-03	6.28E-05	0.970	0.004
C20	2.00E-04	0.717	5.49E+01	3.64E+02	1.06E+00	3.05E-03	1.78E-05	1.000	0.947	0.717	5.48E+01	3.71E+02	2.66E+00	3.05E-03	1.68E-05	0.988	0.002	0.717	5.48E+01	3.67E+02	2.78E+00	3.01E-03	1.72E-05	1.000	0.003
C25	2.00E-04	0.705	4.12E+01	1.91E+02	4.44E+00	8.23E-03	1.07E-04	0.941	0.005	0.705	4.12E+01	1.79E+02	3.75E+00	7.98E-03	9.24E-05	0.961	0.005	0.705	4.12E+01	1.78E+02	3.77E+00	7.96E-03	9.22E-05	0.965	0.005

Table A.3. Computed corrosion parameters from curve fitting exercise on charging curves for mild steel exposed to different electrolytes on Day 1.

Electrolyte	Iapp (A)	M1 Ecorr (-V)	M1 Rs (Ω)	M1 Rp (Ω) Fit	M1 Rp (Ω) Std Dev	M1 C (F) Fit	M1 C (F) Std Dev	M1 β Fit	M1 β Std Dev	M2 Ecorr (-V)	M2 Rs (Ω)	M2 Rp (Ω) Fit	M2 Rp (Ω) Std Dev	M2 C (F) Fit	M2 C (F) Std Dev	M2 β Fit	M2 β Std Dev	M3 Ecorr (-V)	M3 Rs (Ω)	M3 Rp (Ω) Fit	M3 Rp (Ω) Std Dev	M3 C (F) Fit	M3 C (F) Std Dev	M3 β Fit	M3 β Std Dev
A5	4.00E-04	0.724	6.87E+02	2.32E+02	2.50E-01	8.21E-03	2.77E-05	0.726	0.001	0.724	6.87E+02	1.93E+02	2.13E-01	9.36E-03	2.90E-05	0.696	0.001	0.724	6.87E+02	1.75E+02	1.85E-01	1.01E-02	3.00E-05	0.686	0.001
A10	2.00E-04	0.734	3.54E+02	4.28E+02	2.57E-01	1.09E-02	1.63E-05	0.815	0.001	0.734	3.54E+02	4.05E+02	2.41E-01	1.16E-02	1.71E-05	0.812	0.001	0.734	3.54E+02	3.86E+02	2.31E-01	1.22E-02	1.82E-05	0.808	0.001
A15	2.00E-04	0.735	2.49E+02	2.75E+02	2.14E-01	1.58E-02	3.08E-05	0.819	0.001	0.736	2.49E+02	3.21E+02	2.34E-01	1.36E-02	2.46E-05	0.821	0.001	0.736	2.50E+02	5.03E+02	3.61E-01	8.77E-03	1.56E-05	0.804	0.001
A20	2.00E-04	0.736	2.06E+02	3.67E+02	2.40E-01	1.26E-02	2.05E-05	0.815	0.001	0.736	2.08E+02	4.13E+02	2.52E-01	1.14E-02	1.73E-05	0.804	0.001	0.736	2.08E+02	4.05E+02	2.52E-01	1.15E-02	1.80E-05	0.803	0.001
A25	2.00E-04	0.740	1.75E+02	3.02E+02	2.13E-01	1.49E-02	2.66E-05	0.786	0.001	0.740	1.74E+02	2.92E+02	2.11E-01	1.53E-02	2.81E-05	0.784	0.001	0.740	1.74E+02	2.82E+02	2.00E-01	1.58E-02	2.84E-05	0.785	0.001
B5	2.00E-04	0.721	3.35E+02	2.06E+02	2.02E-01	9.30E-03	2.45E-05	0.767	0.001	0.721	3.35E+02	1.91E+02	1.86E-01	1.00E-02	2.62E-05	0.762	0.001	0.721	3.34E+02	1.74E+02	1.61E-01	1.10E-02	2.84E-05	0.765	0.001
B10	2.00E-04	0.731	2.17E+02	3.38E+02	2.16E-01	1.21E-02	1.95E-05	0.831	0.001	0.731	2.18E+02	3.63E+02	2.19E-01	1.16E-02	1.75E-05	0.823	0.001	0.731	2.18E+02	3.53E+02	2.20E-01	1.19E-02	1.86E-05	0.830	0.001
B15	2.00E-04	0.736	1.77E+02	3.06E+02	2.07E-01	1.40E-02	2.43E-05	0.783	0.001	0.736	1.79E+02	2.71E+02	1.85E-01	1.58E-02	2.75E-05	0.790	0.001	-	-	-	-	-	-	-	-
B20	2.00E-04	0.723	1.47E+02	2.72E+02	1.75E-01	1.06E-02	1.73E-05	0.859	0.001	0.724	1.43E+02	2.79E+02	1.78E-01	1.03E-02	1.67E-05	0.856	0.001	-	-	-	-	-	-	-	-
B25	2.00E-04	0.736	1.25E+02	2.91E+02	1.97E-01	1.52E-02	2.61E-05	0.802	0.001	0.736	1.23E+02	2.75E+02	1.90E-01	1.61E-02	2.81E-05	0.802	0.001	0.736	1.25E+02	2.87E+02	1.98E-01	1.55E-02	2.70E-05	0.798	0.001
C5	2.00E-04	0.699	8.08E+01	1.90E+02	1.84E-01	6.75E-03	1.69E-05	0.837	0.001	0.699	8.08E+01	1.84E+02	1.79E-01	6.93E-03	1.75E-05	0.829	0.001	-	-	-	-	-	-	-	-
C10	2.00E-04	0.702	5.64E+01	1.89E+02	1.67E-01	7.91E-03	1.76E-05	0.883	0.001	0.702	5.64E+01	1.80E+02	1.73E-01	8.24E-03	1.98E-05	0.897	0.001	0.702	5.64E+01	1.77E+02	1.95E-01	8.40E-03	2.29E-05	0.918	0.001
C15	2.00E-04	0.715	5.19E+01	2.56E+02	1.73E-01	9.37E-03	1.58E-05	0.882	0.001	0.715	5.19E+01	2.53E+02	1.78E-01	9.43E-03	1.66E-05	0.889	0.001	0.714	5.18E+01	2.71E+02	1.76E-01	8.78E-03	1.43E-05	0.878	0.001
C20	2.00E-04	0.717	5.49E+01	3.67E+02	2.81E-01	9.45E-03	3.64E-06	0.904	0.001	0.717	5.48E+01	3.76E+02	2.75E-01	9.34E-03	1.29E-05	0.895	0.001	0.717	5.48E+01	3.69E+02	2.72E-01	9.49E-03	1.33E-05	0.901	0.001
C25	2.00E-04	0.705	4.12E+01	1.95E+02	1.67E-01	7.66E-03	1.64E-05	0.908	0.001	0.705	4.12E+01	1.84E+02	1.73E-01	8.04E-03	1.87E-05	0.920	0.001	0.705	4.12E+01	1.82E+02	1.86E-01	8.13E-03	2.04E-05	0.929	0.001

Table A.4. Computed corrosion parameters from curve fitting exercise on discharging curves for mild steel exposed to different electrolytes on Day 1.

MILD STEEL-SOIL SYSTEM – DAY 7

Electrolyte	Iapp (A)	Measurement 1								Measurement 2								Measurement 3							
		Ecorr (-V)	Rs (Ω)	Rp (Ω)		C (F)		β		Ecorr (-V)	Rs (Ω)	Rp (Ω)		C (F)		β		Ecorr (-V)	Rs (Ω)	Rp (Ω)		C (F)		β	
				Fit	Std Dev	Fit	Std Dev	Fit	Std Dev			Fit	Std Dev	Fit	Std Dev	Fit	Std Dev			Fit	Std Dev	Fit	Std Dev	Fit	Std Dev
B5	4.00E-08	0.025	1.02E+07	1.51E+06	3.15E+04	1.39E-07	1.00E-09	0.770	0.007	0.027	1.01E+07	1.45E+06	9.22E+03	1.56E-07	2.00E-09	0.756	0.011	0.027	9.78E+06	1.44E+06	1.10E+04	1.80E-07	2.50E-09	0.765	0.011
B10	2.00E-08	-0.048	2.85E+06	1.32E+06	1.07E+04	1.96E-07	3.00E-09	0.742	0.011	-0.047	2.91E+06	1.39E+06	1.25E+04	2.14E-07	3.44E-09	0.744	0.011	-0.046	2.99E+06	1.39E+06	2.34E+04	2.22E-07	1.10E-09	0.724	0.005
B15	4.00E-08	-0.024	1.48E+06	4.98E+05	3.38E+03	5.05E-07	6.41E-09	0.760	0.010	-0.023	1.54E+06	4.98E+05	8.30E+03	5.05E-07	2.70E-09	0.768	0.005	-	-	-	-	-	-	-	-
B20	1.00E-07	-0.023	6.75E+05	1.64E+05	1.10E+03	1.44E-06	1.86E-08	0.752	0.011	-0.022	6.93E+05	1.63E+05	1.07E+03	1.42E-06	1.84E-08	0.754	0.011	-0.022	6.96E+05	1.64E+05	2.91E+03	1.41E-06	8.30E-09	0.767	0.006
B25	2.00E-06	0.017	1.07E+05	1.54E+04	1.10E+02	5.25E-05	1.20E-07	0.779	0.003	0.017	1.07E+05	1.54E+04	1.07E+02	5.20E-05	1.15E-07	0.784	0.003	0.017	1.07E+05	1.54E+04	1.08E+02	5.15E-05	1.12E-07	0.791	0.003
C5	2.00E-07	0.060	1.62E+06	1.08E+05	6.40E+02	1.84E-06	2.35E-08	0.744	0.011	0.080	1.55E+06	1.02E+05	6.14E+02	1.96E-06	2.54E-08	0.744	0.011	0.060	1.52E+06	9.98E+04	6.38E+02	2.03E-06	2.77E-08	0.736	0.012
C10	4.00E-06	0.010	1.02E+05	1.32E+04	5.37E+02	1.03E-04	4.83E-06	0.722	0.010	0.010	1.02E+05	1.30E+04	4.68E+02	1.02E-04	4.12E-06	0.732	0.009	0.010	1.02E+05	1.24E+04	4.02E+02	9.76E-05	3.56E-06	0.741	0.009
C15	4.00E-06	0.023	9.09E+04	9.78E+03	8.90E+01	3.47E-05	5.21E-07	0.762	0.010	0.023	9.03E+04	9.78E+03	1.23E+02	3.63E-05	1.21E-07	0.805	0.004	0.023	9.03E+04	9.78E+03	1.24E+02	3.68E-05	1.22E-07	0.810	0.004
C20	4.00E-06	0.040	7.32E+04	5.94E+03	1.00E+02	4.83E-05	2.56E-04	0.715	0.005	0.037	7.41E+04	5.94E+03	5.56E+01	4.80E-05	8.40E-07	0.718	0.011	0.037	7.42E+04	5.94E+03	1.01E+02	4.75E-05	2.53E-07	0.721	0.005
C25	8.00E-06	0.088	4.46E+04	3.75E+03	5.03E+01	1.06E-04	2.46E-06	0.704	0.010	0.088	4.47E+04	3.73E+03	4.95E+01	1.04E-04	2.41E-06	0.704	0.010	0.090	4.47E+04	3.73E+03	5.30E+01	1.04E-04	4.19E-07	0.705	0.004

Table A.5. Computed corrosion parameters from curve fitting exercise on charging curves for mild steel exposed to different electrolytes on Day 7.

CAST IRON-SOIL SYSTEM – DAY 1

Electrolyte	Iapp (A)	Measurement 1								Measurement 2								Measurement 3							
		Ecorr (-V)	Rs (Ω)	Rp (Ω) Fit	Rp Std Dev	C (F) Fit	C Std Dev	β Fit	β Std Dev	Ecorr (-V)	Rs (Ω)	Rp (Ω) Fit	Rp Std Dev	C (F) Fit	C Std Dev	β Fit	β Std Dev	Ecorr (-V)	Rs (Ω)	Rp (Ω) Fit	Rp Std Dev	C (F) Fit	C Std Dev	β Fit	β Std Dev
A5	4.00E-04	0.643	4.55E+02	2.32E+02	3.43E+01	2.36E-02	2.57E-04	1.000	1.410	0.643	4.55E+02	2.69E+02	5.47E+01	2.35E-02	3.03E-04	1.000	1.680	-	-	-	-	-	-	-	-
A10	4.00E-04	0.660	2.74E+02	1.07E+02	8.26E+00	2.61E-02	3.01E-04	1.000	1.270	0.660	2.74E+02	1.10E+02	6.63E+00	2.16E-02	2.29E-04	1.000	1.380	-	-	-	-	-	-	-	-
A15	2.00E-04	0.654	2.23E+02	1.52E+02	4.40E+00	8.89E-03	8.40E-05	1.000	2.710	0.654	2.23E+02	1.82E+02	2.02E+01	9.60E-03	6.37E-04	0.905	0.022	0.654	2.23E+02	1.55E+02	4.70E+00	8.99E-03	8.70E-05	1.000	2.730
A20	4.00E-04	0.654	1.71E+02	9.73E+01	1.98E+00	1.34E-02	9.40E-05	1.000	1.320	0.654	1.71E+02	1.33E+02	1.21E+01	1.56E-02	9.34E-04	0.851	0.015	0.654	1.71E+02	9.20E+01	4.72E+00	1.28E-02	3.66E-04	0.999	0.017
A25	4.00E-04	0.660	1.67E+02	9.59E+01	1.18E+00	1.47E-02	5.70E-05	1.000	0.671	0.660	1.67E+02	8.75E+01	9.46E-01	1.40E-02	5.60E-05	1.000	0.709	0.660	1.67E+02	8.37E+01	7.96E-01	1.35E-02	5.20E-05	1.000	0.687
B5	4.00E-04	0.653	3.08E+02	9.41E+01	1.43E+00	1.44E-02	7.20E-05	1.000	0.876	0.653	3.08E+02	9.21E+01	3.57E+00	1.44E-02	3.81E-04	0.907	0.010	0.653	3.08E+02	8.20E+01	3.08E+00	1.42E-02	3.17E-04	0.979	0.012
B10	4.00E-04	0.657	1.93E+02	1.07E+02	3.45E+00	1.26E-02	2.41E-04	0.949	0.009	0.657	1.93E+02	1.16E+02	4.30E+00	1.32E-02	3.15E-04	0.902	0.008	0.657	1.93E+02	9.55E+01	2.82E+00	1.20E-02	2.06E-04	0.991	0.010
B15	4.00E-04	0.650	1.52E+02	1.20E+02	4.19E+00	1.25E-02	2.55E-04	0.934	0.008	0.650	1.52E+02	1.04E+02	2.96E+00	1.17E-02	1.88E-04	0.985	0.009	0.650	1.52E+02	1.15E+02	3.85E+00	1.23E-02	2.46E-04	0.938	0.008
B20	4.00E-04	0.663	1.32E+02	8.27E+01	3.07E+00	1.45E-02	3.05E-04	0.990	0.012	0.663	1.32E+02	8.38E+01	3.17E+00	1.46E-02	3.17E-04	0.981	0.011	0.663	1.32E+02	1.26E+02	9.00E+00	1.85E-02	8.73E-04	0.835	0.013
B25	2.00E-04	0.663	1.18E+02	1.26E+02	1.63E+00	1.07E-02	3.05E-04	1.000	1.010	0.663	1.18E+02	1.32E+02	5.34E+00	1.08E-02	2.39E-04	0.966	0.010	0.663	1.18E+02	1.29E+02	5.01E+00	1.07E-02	2.21E-04	0.980	0.010
C5	4.00E-04	0.669	6.79E+01	7.13E+01	1.72E+00	1.99E-02	3.05E-04	0.919	0.006	0.669	6.79E+01	6.81E+01	1.81E+00	1.99E-02	3.01E-04	0.962	0.007	0.669	6.79E+01	7.26E+01	1.72E+00	2.01E-02	2.92E-04	0.925	0.006
C10	4.00E-04	0.671	5.42E+01	9.23E+01	2.68E+00	2.01E-02	3.82E-04	0.867	0.005	0.671	5.42E+01	8.37E+01	2.24E+00	1.86E-02	3.03E-04	0.917	0.006	0.671	5.42E+01	8.51E+01	2.11E+00	1.88E-02	2.91E-04	0.904	0.005
C15	4.00E-04	0.661	4.72E+01	9.30E+01	2.07E+00	1.65E-02	2.60E-04	0.871	0.005	0.661	4.72E+01	6.71E+01	1.02E+00	1.31E-02	1.35E-04	0.997	0.007	0.661	4.72E+01	9.57E+01	2.28E+00	1.64E-02	2.64E-04	0.881	0.005
C20	4.00E-04	0.667	4.20E+01	1.18E+02	2.43E+00	1.43E-02	1.81E-04	0.900	0.004	0.667	4.20E+01	1.08E+02	2.07E+00	1.36E-02	1.54E-04	0.938	0.005	0.667	4.20E+01	1.10E+02	1.97E+00	1.36E-02	1.47E-04	0.927	0.004
C25	4.00E-04	0.662	3.65E+01	6.37E+01	1.58E+00	2.12E-02	3.71E-04	0.892	0.006	0.662	3.65E+01	5.92E+01	1.41E+00	2.05E-02	3.34E-04	0.922	0.007	0.662	3.65E+01	6.93E+01	1.92E+00	2.21E-02	4.41E-04	0.867	0.006

Table A.6. Computed corrosion parameters from curve fitting exercise on charging curves for cast iron exposed to different electrolytes on Day 1.

Electrolyte	Iapp (A)	Measurement 1								Measurement 2								Measurement 3							
		Ecorr (-V)	Rs (Ω)	Rp (Ω) Fit	Rp Std Dev	C (F) Fit	C Std Dev	β Fit	β Std Dev	Ecorr (-V)	Rs (Ω)	Rp (Ω) Fit	Rp Std Dev	C (F) Fit	C Std Dev	β Fit	β Std Dev	Ecorr (-V)	Rs (Ω)	Rp (Ω) Fit	Rp Std Dev	C (F) Fit	C Std Dev	β Fit	β Std Dev
A5	4.00E-04	0.643	4.55E+02	2.31E+02	1.18E+00	1.10E-02	1.60E-04	0.660	0.005	0.643	4.55E+02	2.65E+02	1.46E+00	8.82E-03	1.43E-04	0.630	0.005	-	-	-	-	-	-	-	-
A10	4.00E-04	0.660	2.74E+02	1.21E+02	6.49E-01	2.84E-02	4.64E-04	0.569	0.005	0.660	2.74E+02	1.21E+02	7.42E-01	2.08E-02	4.20E-04	0.504	0.004	-	-	-	-	-	-	-	-
A15	2.00E-04	0.654	2.23E+02	1.64E+02	7.05E-01	1.07E-02	1.26E-04	0.729	0.004	0.654	2.23E+02	1.89E+02	8.07E-01	9.26E-03	1.09E-04	0.728	0.004	0.654	2.23E+02	1.67E+02	7.20E-01	1.04E-02	1.24E-04	0.732	0.004
A20	4.00E-04	0.654	1.71E+02	1.06E+02	3.47E-01	2.16E-02	2.11E-04	0.613	0.003	0.654	1.71E+02	1.38E+02	4.72E-01	1.64E-02	1.66E-04	0.620	0.003	0.654	1.71E+02	9.89E+01	3.28E-01	2.28E-02	2.23E-04	0.628	0.003
A25	4.00E-04	0.660	1.67E+02	1.07E+02	2.37E-01	2.19E-02	1.57E-04	0.523	0.001	0.660	1.67E+02	9.74E+01	2.20E-01	2.28E-02	1.68E-04	0.519	0.001	0.660	1.67E+02	9.17E+01	2.04E-01	2.43E-02	1.75E-04	0.524	0.001
B5	4.00E-04	0.653	3.08E+02	9.76E+01	2.62E-01	2.49E-02	2.06E-04	0.573	0.002	0.653	3.08E+02	9.33E+01	2.48E-01	2.63E-02	-2.16E-04	0.575	0.002	0.653	3.08E+02	8.64E+01	2.29E-01	2.88E-02	2.33E-04	0.580	0.002
B10	4.00E-04	0.657	1.93E+02	1.11E+02	1.99E-01	2.00E-02	1.05E-04	0.634	0.001	0.657	1.93E+02	1.19E+02	2.11E-01	1.85E-02	9.60E-05	0.641	0.001	0.657	1.93E+02	1.00E+02	1.79E-01	2.18E-02	1.13E-04	0.647	0.002
B15	4.00E-04	0.650	1.52E+02	1.24E+02	1.78E-01	1.74E-02	6.80E-05	0.749	0.001	0.650	1.52E+02	1.08E+02	1.60E-01	1.99E-02	8.00E-05	0.763	0.002	0.650	1.52E+02	1.18E+02	1.77E-01	1.80E-02	7.30E-05	0.770	0.002
B20	4.00E-04	0.663	1.32E+02	8.91E+01	2.13E-01	2.81E-02	2.05E-04	0.586	0.002	0.663	1.32E+02	8.83E+01	2.10E-01	2.75E-02	1.97E-04	0.597	0.002	0.663	1.32E+02	1.27E+02	3.09E-01	1.90E-02	1.39E-04	0.604	0.002
B25	2.00E-04	0.663	1.18E+02	1.32E+02	2.45E-01	1.63E-02	8.20E-05	0.747	0.002	0.663	1.18E+02	1.33E+02	2.50E-01	1.60E-02	8.10E-05	0.757	0.002	0.663	1.18E+02	1.29E+02	2.44E-01	1.65E-02	8.30E-05	0.772	0.002
C5	4.00E-04	0.669	6.79E+01	7.61E+01	1.09E-01	2.70E-02	1.15E-04	0.619	0.001	0.669	6.79E+01	7.48E+01	1.04E-01	2.75E-02	1.17E-04	0.579	0.001	0.669	6.79E+01	7.87E+01	1.07E-01	2.59E-02	1.07E-04	0.593	0.001
C10	4.00E-04	0.671	5.42E+01	1.01E+02	1.35E-01	2.33E-02	9.60E-05	0.575	0.001	0.671	5.42E+01	9.20E+01	1.15E-01	2.42E-02	9.50E-05	0.567	0.001	0.671	5.42E+01	9.38E+01	1.25E-01	2.43E-02	1.00E-04	0.570	0.001
C15	4.00E-04	0.661	4.72E+01	1.02E+02	1.16E-01	1.84E-02	6.30E-05	0.616	0.001	0.661	4.72E+01	7.40E+01	8.60E-02	2.48E-02	8.60E-05	0.615	0.001	0.661	4.72E+01	1.07E+02	1.13E-01	1.73E-02	5.60E-05	0.595	0.001
C20	4.00E-04	0.667	4.20E+01	1.25E+02	1.01E-01	1.77E-02	3.90E-05	0.736	0.001	0.667	4.20E+01	1.15E+02	8.86E-02	1.92E-02	4.10E-05	0.725	0.001	0.667	4.20E+01	1.16E+02	9.86E-02	1.90E-02	4.40E-05	0.743	0.001
C25	4.00E-04	0.662	3.65E+01	7.19E+01	1.04E-01	2.53E-02	1.12E-04	0.591	0.001	0.662	3.65E+01	6.68E+01	1.00E-01	2.73E-02	1.23E-04	0.605	0.001	0.662	3.65E+01	7.44E+01	1.10E-01	2.42E-02	1.08E-04	0.610	0.001

Table A.7. Computed corrosion parameters from curve fitting exercise on discharging curves for cast iron exposed to different electrolytes on Day 1.

CAST IRON-SOIL SYSTEM – DAY 7

Electrolyte	Iapp (A)	Measurement 1								Measurement 2								Measurement 3							
		Ecorr (-V)	Rs (Ω)	Rp (Ω) Fit	Std Dev	C (F) Fit	Std Dev	β Fit	Std Dev	Ecorr (-V)	Rs (Ω)	Rp (Ω) Fit	Std Dev	C (F) Fit	Std Dev	β Fit	Std Dev	Ecorr (-V)	Rs (Ω)	Rp (Ω) Fit	Std Dev	C (F) Fit	Std Dev	β Fit	Std Dev
A5	1.00E-06	-0.153	9.32E+05	2.96E+04	7.36E+02	2.37E-05	8.83E-07	0.696	0.011	-0.167	9.02E+05	3.48E+04	5.93E+02	1.30E-05	3.13E-07	0.795	0.01369	-0.175	8.92E+05	4.85E+04	7.16E+02	1.10E-05	2.28E-07	0.764	0.009
A10	1.00E-06	-0.115	5.15E+05	3.39E+04	5.75E+02	1.55E-05	4.16E-07	0.711	0.010	-0.115	4.93E+05	4.02E+04	6.63E+02	1.49E-05	3.50E-07	0.739	0.00875	-0.115	4.88E+05	3.86E+04	7.14E+02	1.59E-05	4.24E-07	0.733	0.009
A15	1.00E-06	0.324	7.14E+04	2.37E+03	1.09E+01	7.18E-05	7.97E-07	0.773	0.012	0.324	7.27E+04	2.47E+03	1.17E+01	6.59E-05	7.85E-07	0.759	0.01209	0.324	7.34E+04	2.35E+03	9.83E+00	6.38E-05	7.40E-07	0.776	0.013
A20	2.00E-05	0.136	6.63E+04	2.01E+03	2.47E+02	1.24E-03	3.05E-04	0.495	0.016	0.136	6.48E+04	1.32E+03	1.22E+01	3.11E-04	4.30E-06	0.784	0.00817	0.136	6.46E+04	1.33E+03	6.99E+00	2.55E-04	1.93E-06	0.867	0.007
A25	3.00E-05	0.482	2.19E+04	8.88E+02	7.45E+00	8.87E-04	4.58E-06	1.000	1.100	0.482	2.27E+04	1.24E+03	2.48E+01	8.96E-04	7.33E-06	1	1.1	0.482	2.35E+04	1.42E+03	2.23E+01	7.11E-04	5.13E-06	1.000	1.100
B5	1.00E-05	0.194	7.38E+05	5.83E+03	6.62E+01	1.06E-04	1.40E-06	0.836	0.007	-	-	-	-	-	-	-	-	-	-	-	-	-	-	-	-
B10	8.00E-06	0.018	1.22E+05	2.97E+03	3.40E+01	1.02E-04	2.24E-06	0.690	0.011	0.018	1.23E+05	3.10E+03	4.90E+01	1.17E-04	3.53E-06	0.657	0.01187	0.018	1.26E+05	3.27E+03	4.00E+01	9.86E-05	2.17E-06	0.707	0.012
B15	8.00E-05	0.425	7.11E+03	4.00E+02	1.50E+01	5.32E-03	3.90E-05	1.000	1.000	0.425	7.09E+03	5.18E+02	3.54E+01	4.17E-03	5.60E-05	1	1.3	-	-	-	-	-	-	-	-
B20	1.00E-04	0.425	1.88E+04	2.50E+02	4.22E+00	4.90E-03	1.25E-04	0.910	0.022	0.425	1.87E+04	2.60E+02	4.15E+00	5.04E-03	1.33E-04	0.915	0.022	-	-	-	-	-	-	-	-
B25	5.00E-04	0.487	3.16E+03	3.66E+01	1.99E-01	1.15E-02	8.17E-05	1.000	0.672	0.487	3.06E+03	2.79E+01	8.26E-02	1.06E-02	6.30E-05	1	0.464	-	-	-	-	-	-	-	-
C5	2.00E-05	0.018	1.48E+05	2.00E+03	4.20E+01	4.54E-04	2.89E-06	0.948	0.010	0.018	1.45E+05	2.00E+03	4.20E+01	4.56E-04	3.20E-06	0.878	0.00928	-	-	-	-	-	-	-	-
C10	1.00E-04	0.395	4.74E+03	2.46E+02	1.60E+00	3.41E-03	6.00E-06	0.953	0.003	0.391	4.81E+03	2.42E+02	3.40E+00	3.00E-03	3.80E-05	0.917	0.00767	0.391	4.86E+03	2.26E+02	2.82E+00	2.76E-03	3.68E-06	0.874	0.008
C15	4.00E-04	0.469	1.27E+03	6.12E+01	1.90E-01	7.03E-03	2.83E-05	1.000	0.637	0.469	1.30E+03	5.91E+01	3.54E-01	7.06E-03	4.60E-05	0.998	0.00801	0.469	1.31E+03	5.88E+01	3.95E-01	7.17E-03	5.36E-05	0.973	0.008
C20	4.00E-04	0.471	7.72E+02	5.82E+01	8.25E-01	1.28E-02	1.66E-04	0.906	0.007	0.469	7.88E+02	6.14E+01	7.20E-01	1.14E-02	1.16E-04	0.948	0.00704	-	-	-	-	-	-	-	-
C25	5.00E-04	0.459	5.45E+02	4.00E+01	5.77E-01	1.44E-02	2.32E-04	0.868	0.010	0.459	5.47E+02	4.00E+01	5.60E-01	1.34E-02	2.22E-04	0.861	0.01039	-	-	-	-	-	-	-	-

Table A.8. Computed corrosion parameters from curve fitting exercise on charging curves for cast iron exposed to different electrolytes on Day 7.

WROUGHT IRON-SOIL SYSTEM – DAY 1

Electrolyte	Iapp (A)	Ecorr (-V)	Rs (Ω)	Rp (Ω) Fit	Rp (Ω) Std Dev	C (F) Fit	C (F) Std Dev	β Fit	β Std Dev	Ecorr (-V)	Rs (Ω)	Rp (Ω) Fit	Rp (Ω) Std Dev	C (F) Fit	C (F) Std Dev	β Fit	β Std Dev	Ecorr (-V)	Rs (Ω)	Rp (Ω) Fit	Rp (Ω) Std Dev	C (F) Fit	C (F) Std Dev	β Fit	β Std Dev
		Measurement 1								Measurement 2								Measurement 3							
A5	2.00E-04	0.677	5.75E+02	3.97E+02	1.93E+01	8.76E-03	5.01E-05	1.000	1.920	0.677	5.75E+02	2.72E+02	6.57E+00	7.99E-03	3.76E-05	1.000	1.630	0.677	5.75E+02	2.42E+02	4.22E+00	7.62E-03	3.09E-05	1.000	1.440
A10	2.00E-04	0.686	2.94E+02	1.85E+02	1.62E+00	6.20E-03	2.14E-05	1.000	1.360	0.686	2.94E+02	1.96E+02	2.19E+00	6.49E-03	2.56E-05	1.000	1.520	0.686	2.94E+02	1.93E+02	1.87E+00	6.41E-03	2.25E-05	1.000	1.360
A15	2.50E-04	0.696	2.19E+02	1.40E+02	2.32E+00	1.10E-02	5.22E-05	1.000	1.130	0.696	2.19E+02	1.33E+02	4.72E+00	1.04E-02	2.11E-04	0.959	0.009	0.696	2.19E+02	1.43E+02	5.44E+00	1.09E-02	2.38E-04	0.935	0.009
A20	2.50E-04	0.687	1.77E+02	1.43E+02	1.15E+00	8.64E-03	2.51E-05	1.000	0.836	0.687	1.77E+02	1.54E+02	3.91E+00	8.92E-03	1.27E-04	0.967	0.007	0.687	1.77E+02	1.44E+02	3.50E+00	8.70E-03	1.14E-04	0.996	0.007
A25	2.50E-04	0.687	1.50E+02	1.65E+02	2.62E+00	7.50E-03	6.90E-05	0.975	0.005	0.687	1.50E+02	1.78E+02	3.23E+00	7.81E-03	8.30E-05	0.953	0.005	0.687	1.50E+02	1.87E+02	3.38E+00	7.98E-03	8.60E-05	0.932	0.004
B5	2.80E-04	0.673	3.22E+02	1.16E+02	1.84E+00	9.11E-03	8.81E-05	0.995	0.006	0.673	3.22E+02	1.22E+02	2.14E+00	9.49E-03	1.01E-04	0.974	0.006	0.673	3.22E+02	1.21E+02	8.50E-01	9.67E-03	2.62E-05	1.000	0.688
B10	2.50E-04	0.695	2.00E+02	2.22E+02	5.42E+00	7.76E-03	8.82E-05	0.977	0.005	0.695	2.00E+02	1.87E+02	1.05E+00	7.00E-03	1.35E-05	1.000	0.694	0.695	2.00E+02	2.26E+02	5.31E+00	7.63E-03	9.24E-05	0.950	0.005
B15	2.50E-04	0.683	1.51E+02	1.60E+02	3.30E+00	8.47E-03	9.20E-05	0.990	0.006	0.683	1.51E+02	1.73E+02	3.62E+00	8.76E-03	9.93E-05	0.957	0.005	0.683	1.51E+02	1.68E+02	3.56E+00	8.64E-03	9.84E-05	0.968	0.005
B20	2.50E-04	0.686	1.35E+02	2.09E+02	9.94E-01	5.85E-03	1.03E-05	1.000	0.746	0.686	1.35E+02	2.27E+02	3.39E+00	6.04E-03	5.02E-05	0.968	0.004	0.686	1.35E+02	2.43E+02	3.66E+00	6.23E-03	5.30E-05	0.944	0.004
B25	2.50E-04	0.694	1.14E+02	1.81E+02	3.84E+00	9.44E-03	1.03E-04	0.951	0.004	0.694	1.14E+02	1.73E+02	3.85E+00	9.21E-03	1.00E-04	0.977	0.005	0.694	1.14E+02	1.84E+02	4.15E+00	9.43E-03	1.07E-04	0.955	0.005
C5	4.20E-04	0.675	6.44E+01	9.36E+01	1.59E+00	1.45E-02	1.89E-04	0.863	0.004	0.675	6.44E+01	1.04E+02	1.65E+00	1.42E-02	1.91E-04	0.883	0.005	0.675	6.44E+01	9.25E+01	1.65E+00	1.44E-02	1.89E-04	0.879	0.005
C10	5.00E-04	0.682	4.81E+01	8.94E+01	1.80E+00	1.65E-02	2.22E-04	0.896	0.005	0.682	4.81E+01	9.41E+01	1.87E+00	1.69E-02	2.29E-04	0.877	0.004	0.682	4.81E+01	9.12E+01	1.72E+00	1.65E-02	2.10E-04	0.888	0.004
C15	5.40E-04	0.703	4.17E+01	8.55E+01	1.49E+00	1.75E-02	2.10E-04	0.884	0.004	0.703	4.17E+01	8.55E+01	1.49E+00	1.75E-02	2.10E-04	0.884	0.004	0.703	4.17E+01	7.85E+01	1.23E+00	1.67E-02	1.78E-04	0.910	0.004
C20	4.00E-04	0.685	4.03E+01	1.20E+02	1.88E+00	1.15E-02	1.17E-04	0.916	0.004	0.685	4.03E+01	1.16E+02	1.79E+00	1.13E-02	1.13E-04	0.927	0.004	0.685	4.03E+01	1.18E+02	1.87E+00	1.15E-02	1.18E-04	0.921	0.004
C25	2.40E-04	0.694	4.07E+01	1.93E+02	3.31E+00	7.75E-03	7.50E-05	0.949	0.004	0.694	4.07E+01	1.95E+02	3.23E+00	7.77E-03	7.43E-05	0.938	0.004	0.694	4.07E+01	1.94E+02	3.36E+00	7.74E-03	7.70E-05	0.941	0.004

Table A.9. Computed corrosion parameters from curve fitting exercise on charging curves for wrought iron exposed to different electrolytes on Day 1.

Electrolyte	Iapp (A)	Ecorr (-V)	Rs (Ω)	Rp (Ω) Fit	Rp (Ω) Std Dev	C (F) Fit	C (F) Std Dev	β Fit	β Std Dev	Ecorr (-V)	Rs (Ω)	Rp (Ω) Fit	Rp (Ω) Std Dev	C (F) Fit	C (F) Std Dev	β Fit	β Std Dev	Ecorr (-V)	Rs (Ω)	Rp (Ω) Fit	Rp (Ω) Std Dev	C (F) Fit	C (F) Std Dev	β Fit	β Std Dev
A5	2.00E-04	0.677	5.75E+02	4.52E+02	8.30E-01	5.40E-03	2.84E-05	0.658	0.002	0.677	5.75E+02	2.92E+02	5.16E-01	8.46E-03	4.27E-05	0.662	0.002	0.677	5.75E+02	2.57E+02	4.46E-01	9.82E-03	4.91E-05	0.652	0.002
A10	2.00E-04	0.686	2.94E+02	2.04E+02	4.25E-01	1.23E-02	8.04E-05	0.552	0.002	0.686	2.94E+02	2.20E+02	4.45E-01	1.20E-02	7.66E-05	0.552	0.002	0.686	2.94E+02	2.16E+02	4.40E-01	1.23E-02	7.85E-05	0.552	0.002
A15	2.50E-04	0.696	2.19E+02	1.59E+02	4.31E-01	1.74E-02	1.61E-04	0.472	0.002	0.696	2.19E+02	1.48E+02	4.02E-01	1.91E-02	1.79E-04	0.463	0.002	0.696	2.19E+02	1.57E+02	4.25E-01	1.74E-02	1.61E-04	0.468	0.002
A20	2.50E-04	0.687	1.77E+02	1.56E+02	2.12E-01	1.83E-02	7.58E-05	0.573	0.001	0.687	1.77E+02	1.65E+02	2.26E-01	1.73E-02	7.20E-05	0.580	0.001	0.687	1.77E+02	1.53E+02	2.07E-01	1.83E-02	7.46E-05	0.586	0.001
A25	2.50E-04	0.687	1.50E+02	1.90E+02	1.70E-01	1.50E-02	4.20E-05	0.557	0.001	0.687	1.50E+02	2.01E+02	1.85E-01	1.45E-02	4.14E-05	0.559	0.001	0.687	1.50E+02	2.07E+02	1.84E-01	1.40E-02	3.85E-05	0.564	0.001
B5	2.80E-04	0.673	3.22E+02	1.18E+02	1.48E-01	2.18E-02	8.10E-05	0.628	0.001	0.673	3.22E+02	1.24E+02	1.57E-01	2.08E-02	7.69E-05	0.636	0.001	0.673	3.22E+02	1.29E+02	1.78E-01	2.06E-02	8.50E-05	0.607	0.001
B10	2.50E-04	0.695	2.00E+02	2.36E+02	2.07E-01	1.29E-02	3.32E-05	0.627	0.001	0.695	2.00E+02	1.92E+02	1.79E-01	1.54E-02	4.20E-05	0.632	0.001	0.695	2.00E+02	2.38E+02	2.09E-01	1.31E-02	3.42E-05	0.600	0.001
B15	2.50E-04	0.683	1.51E+02	1.75E+02	1.61E-01	1.53E-02	4.22E-05	0.600	0.001	0.683	1.51E+02	1.86E+02	1.75E-01	1.38E-02	3.90E-05	0.600	0.001	0.683	1.51E+02	1.79E+02	1.66E-01	1.44E-02	3.93E-05	0.618	0.001
B20	2.50E-04	0.686	1.35E+02	2.26E+02	1.32E-01	1.51E-02	2.45E-05	0.672	0.001	0.686	1.35E+02	2.40E+02	1.47E-01	1.42E-02	2.50E-05	0.678	0.001	0.686	1.35E+02	2.56E+02	1.49E-01	1.32E-02	2.20E-05	0.682	0.001
B25	2.50E-04	0.694	1.14E+02	1.90E+02	1.37E-01	1.77E-02	3.60E-05	0.663	0.001	0.694	1.14E+02	1.83E+02	1.37E-01	1.83E-02	3.85E-05	0.668	0.001	0.694	1.14E+02	1.96E+02	1.37E-01	1.74E-02	3.42E-05	0.658	0.001
C5	4.20E-04	0.675	6.44E+01	1.13E+02	1.33E-01	1.55E-02	6.48E-05	0.443	0.001	0.675	6.44E+01	1.14E+02	1.44E-01	1.56E-02	7.20E-05	0.433	0.001	0.675	6.44E+01	1.08E+02	1.23E-01	1.70E-02	6.50E-05	0.492	0.001
C10	5.00E-04	0.682	4.81E+01	1.05E+02	1.10E-01	2.09E-02	7.32E-05	0.495	0.001	0.682	4.81E+01	1.08E+02	1.16E-01	2.02E-02	7.23E-05	0.499	0.001	0.682	4.81E+01	1.04E+02	1.13E-01	2.11E-02	7.60E-05	0.506	0.001
C15	5.40E-04	0.703	4.17E+01	1.04E+02	1.29E-01	1.96E-02	8.90E-05	0.421	0.001	0.703	4.17E+01	1.04E+02	1.29E-01	1.96E-02	8.90E-05	0.421	0.001	0.703	4.17E+01	9.58E+01	1.17E-01	2.13E-02	9.47E-05	0.428	0.001
C20	4.00E-04	0.685	4.03E+01	1.31E+02	1.22E-01	1.57E-02	4.33E-05	0.620	0.001	0.685	4.03E+01	1.29E+02	1.11E-01	1.59E-02	4.07E-05	0.613	0.001	0.685	4.03E+01	1.32E+02	1.09E-01	1.55E-02	3.83E-05	0.603	0.001
C25	2.40E-04	0.694	4.07E+01	2.12E+02	1.55E-01	1.25E-02	2.68E-05	0.631	0.001	0.694	4.07E+01	2.09E+02	1.57E-01	1.25E-02	2.74E-05	0.641	0.001	0.694	4.07E+01	2.13E+02	1.48E-01	1.28E-02	2.62E-05	0.624	0.001

Table A.10. Computed corrosion parameters from curve fitting exercise on discharging curves for wrought iron exposed to different electrolytes on Day 1.

WROUGHT IRON-SOIL SYSTEM – DAY 7

Electrolyte	Iapp (A)	Measurement 1								Measurement 2								Measurement 3							
		Ecorr (-V)	Rs (Ω)	Rp (Ω) Fit	Rp (Ω) Std Dev	C (F) Fit	C (F) Std Dev	β Fit	β Std Dev	Ecorr (-V)	Rs (Ω)	Rp (Ω) Fit	Rp (Ω) Std Dev	C (F) Fit	C (F) Std Dev	β Fit	β Std Dev	Ecorr (-V)	Rs (Ω)	Rp (Ω) Fit	Rp (Ω) Std Dev	C (F) Fit	C (F) Std Dev	β Fit	β Std Dev
A5	3.00E-07	-0.117	1.05E+06	7.59E+04	3.82E+02	2.72E-06	2.84E-08	0.783	0.010	-0.115	1.04E+06	7.46E+04	3.53E+02	2.66E-06	2.69E-08	0.798	0.011	-0.115	1.04E+06	7.47E+04	3.33E+02	2.60E-06	2.50E-08	0.791	0.010
A10	1.00E-06	-0.136	3.31E+05	2.96E+04	2.54E+02	2.74E-05	7.90E-08	0.743	0.003	-0.136	3.32E+05	2.30E+03	2.39E+02	2.11E-05	5.30E-08	0.814	0.004	-0.136	3.32E+05	2.00E+04	2.14E+02	2.28E-05	3.29E-07	0.824	0.009
A15	3.00E-06	-0.136	1.97E+05	1.23E+04	2.21E+02	5.01E-05	2.87E-07	0.640	0.006	-0.136	1.96E+05	1.28E+04	4.11E+02	4.81E-05	2.64E-06	0.655	0.014	-0.136	1.97E+05	1.27E+04	3.66E+02	4.91E-05	2.14E-06	0.706	0.014
A20	2.00E-06	-0.088	1.45E+05	1.15E+04	3.40E+01	1.76E-05	1.11E-07	0.903	0.009	-0.088	1.44E+05	1.19E+04	4.30E+01	1.87E-05	1.30E-07	0.867	0.009	-0.088	1.44E+05	1.20E+04	1.77E+02	1.91E-05	8.60E-08	0.875	0.005
A25	2.00E-05	0.109	5.35E+04	9.37E+02	1.25E+01	5.14E-04	7.90E-06	1.000	0.000	0.109	5.34E+04	1.02E+03	1.30E+01	4.85E-04	6.84E-06	1.000	0.000	0.102	5.37E+04	1.22E+03	2.05E+01	4.91E-04	7.80E-06	1.000	0.000
B5	2.00E-06	-0.108	3.29E+05	1.36E+04	5.38E+02	9.42E-05	3.57E-06	0.793	0.010	-0.108	3.27E+05	1.31E+04	2.94E+02	6.58E-05	1.42E-06	0.858	0.009	-0.108	3.26E+05	1.33E+04	2.97E+02	6.31E-05	1.33E-06	0.869	0.010
B10	2.00E-06	-0.108	2.03E+05	1.15E+04	1.00E+02	3.40E-05	4.36E-07	0.800	0.008	-0.105	2.05E+05	1.30E+04	2.00E+02	3.89E-05	9.33E-07	0.721	0.009	-0.105	2.06E+05	1.40E+04	1.08E+02	5.90E-05	1.54E-07	0.765	0.003
B15	5.00E-06	-0.034	1.30E+05	9.00E+03	6.60E+01	2.11E-04	1.42E-06	0.658	0.003	-0.030	1.31E+05	8.25E+03	6.30E+01	1.88E-04	1.07E-06	0.648	0.003	-0.030	1.31E+05	9.14E+03	6.33E+02	2.00E-04	1.99E-05	0.616	0.012
B20	6.00E-06	0.061	4.93E+04	5.29E+03	3.30E+01	2.27E-04	7.11E-07	0.783	0.003	0.061	4.94E+04	5.33E+03	1.84E+02	2.31E-04	8.00E-06	0.783	0.009	0.061	4.93E+04	4.83E+03	3.30E+01	2.12E-04	5.71E-04	0.817	0.003
B25	5.00E-06	0.244	1.64E+04	1.02E+03	6.78E+00	3.53E-03	1.15E-05	1.000	0.000	0.244	1.64E+04	1.02E+03	7.28E+00	4.52E-03	1.93E-05	1.000	0.000	0.244	1.63E+04	1.02E+03	7.56E+00	4.95E-03	2.38E-05	1.000	0.000
C5	1.00E-05	-0.015	1.18E+05	4.88E+03	2.38E+02	3.06E-04	1.89E-05	0.677	0.010	-0.015	1.17E+05	4.44E+03	1.68E+02	2.56E-04	1.23E-05	0.704	0.010	-0.015	1.16E+05	5.37E+03	2.90E+02	2.96E-04	2.10E-05	0.666	0.011
C10	4.00E-06	0.037	4.58E+04	2.80E+03	1.12E+02	4.79E-04	2.39E-05	0.694	0.009	0.037	4.56E+04	2.65E+03	9.50E+01	4.12E-04	2.02E-05	0.680	0.010	0.037	4.55E+04	2.78E+03	1.23E+02	4.69E-04	2.65E-05	0.686	0.010
C15	2.00E-05	0.113	1.50E+04	8.11E+02	3.30E+01	1.58E-03	7.87E-05	0.699	0.010	0.113	1.49E+04	8.10E+02	3.10E+01	1.53E-03	7.36E-05	0.701	0.010	0.113	1.49E+04	7.56E+02	2.21E+01	1.39E-03	4.94E-05	0.731	0.009
C20	8.00E-05	0.275	3.16E+03	3.39E+02	6.20E+00	2.25E-03	4.44E-05	0.831	0.009	0.275	3.17E+03	3.39E+02	2.52E+00	2.24E-03	4.70E-06	0.844	0.003	0.275	3.17E+03	3.44E+02	6.20E+00	2.24E-03	4.36E-05	0.828	0.008
C25	2.00E-04	0.356	1.04E+03	1.42E+02	1.70E+00	4.11E-03	5.20E-05	0.879	0.008	0.357	1.04E+03	1.42E+02	1.20E+00	4.18E-03	8.30E-06	0.874	0.003	0.357	1.04E+03	1.39E+02	1.52E+00	4.01E-03	4.80E-05	0.886	0.008

Table A.11. Computed corrosion parameters from curve fitting exercise on charging curves for wrought iron exposed to different electrolytes on Day 7.

APPENDIX A.6   CURVE FITTING RESULTS FOR REPEATED MEASUREMENTS
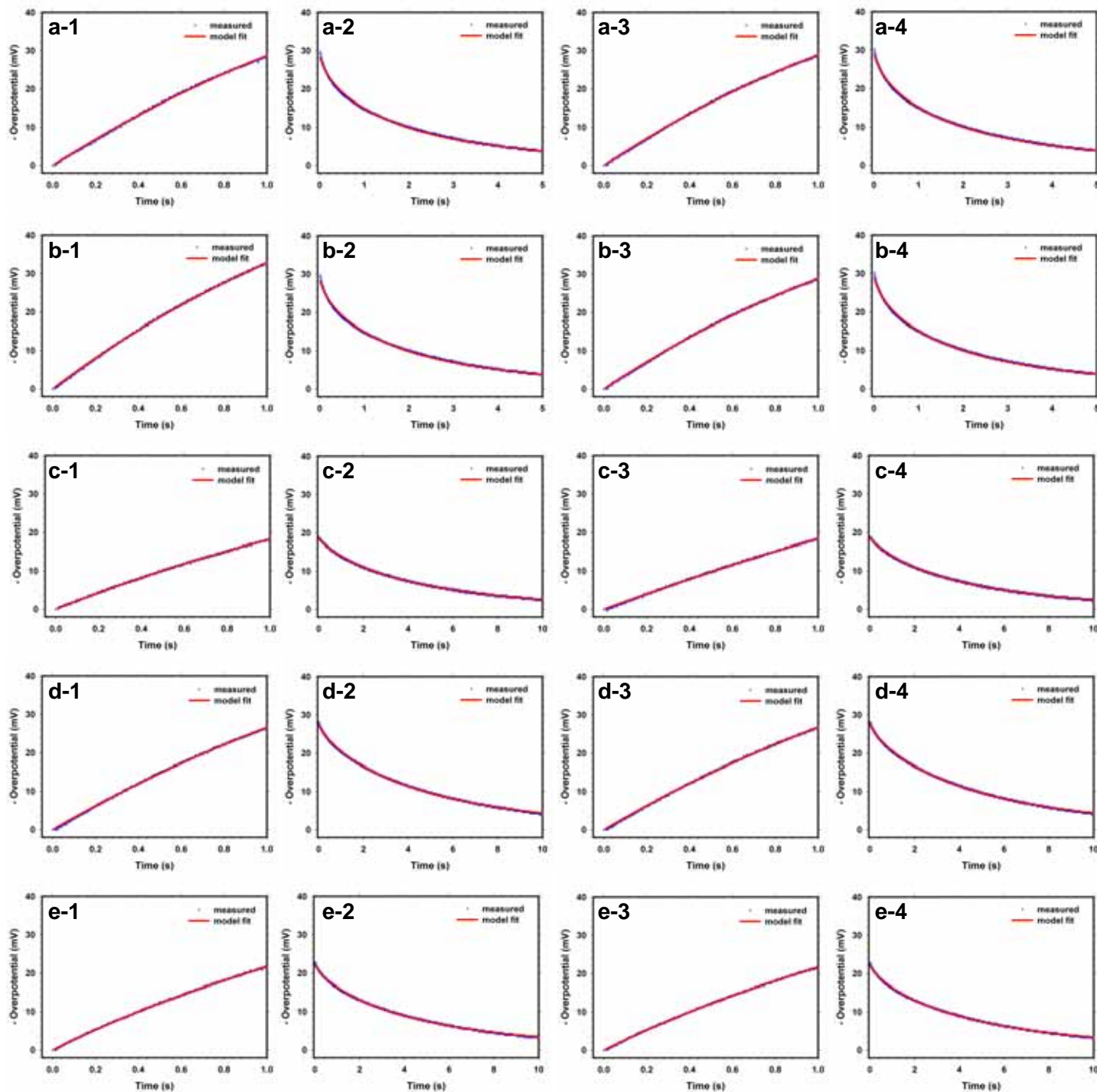
Figure A.4. Curve fitting of repeated short galvanostatic pulse measurements for mild steel in different clay content electrolytes saturated with deionized water measured on Day 1. The labels **a**, **b**, **c**, **d**, and **e** correspond to clay contents of 5%, 10%, 15%, 20%, and 25% respectively. The labels **1**, and **2** correspond to curve fitting of the charging and discharging curves respectively of the 2nd set of measurement while **3**, and **4** represent the curve fitting of the charging and discharging curves respectively of the 3rd set of measurement.
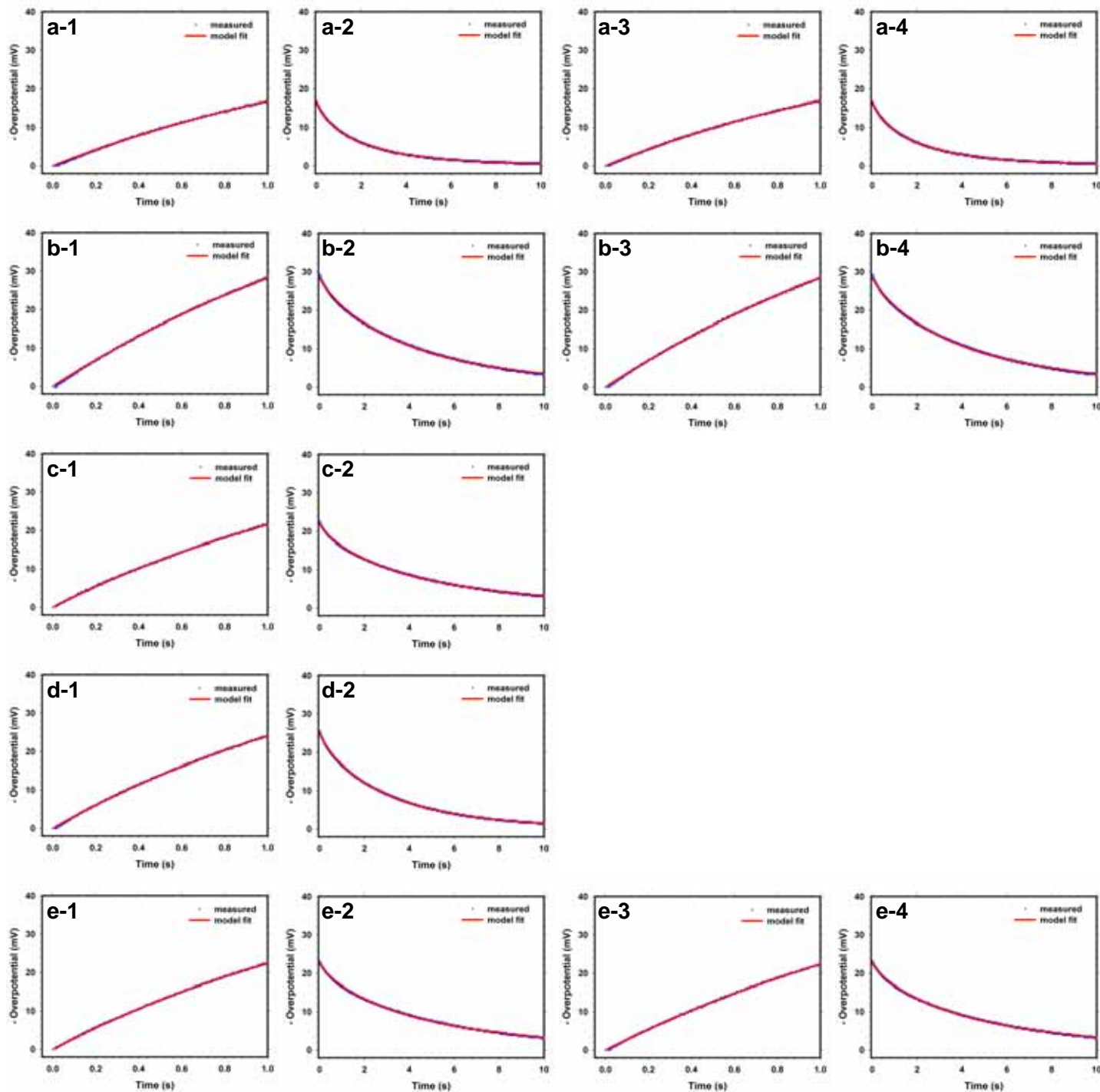
Figure A.5. Curve fitting of repeated short galvanostatic pulse measurements for mild steel in different clay content electrolytes saturated with 0.01M NaCl measured on Day 1. The labels **a**, **b**, **c**, **d**, and **e** correspond to clay contents of 5%, 10%, 15%, 20%, and 25% respectively. The labels **1**, and **2** correspond to curve fitting of the charging and discharging curves respectively of the 2nd set of measurement while **3**, and **4** (where available) represent the curve fitting of the charging and discharging curves respectively of the 3rd set of measurement.
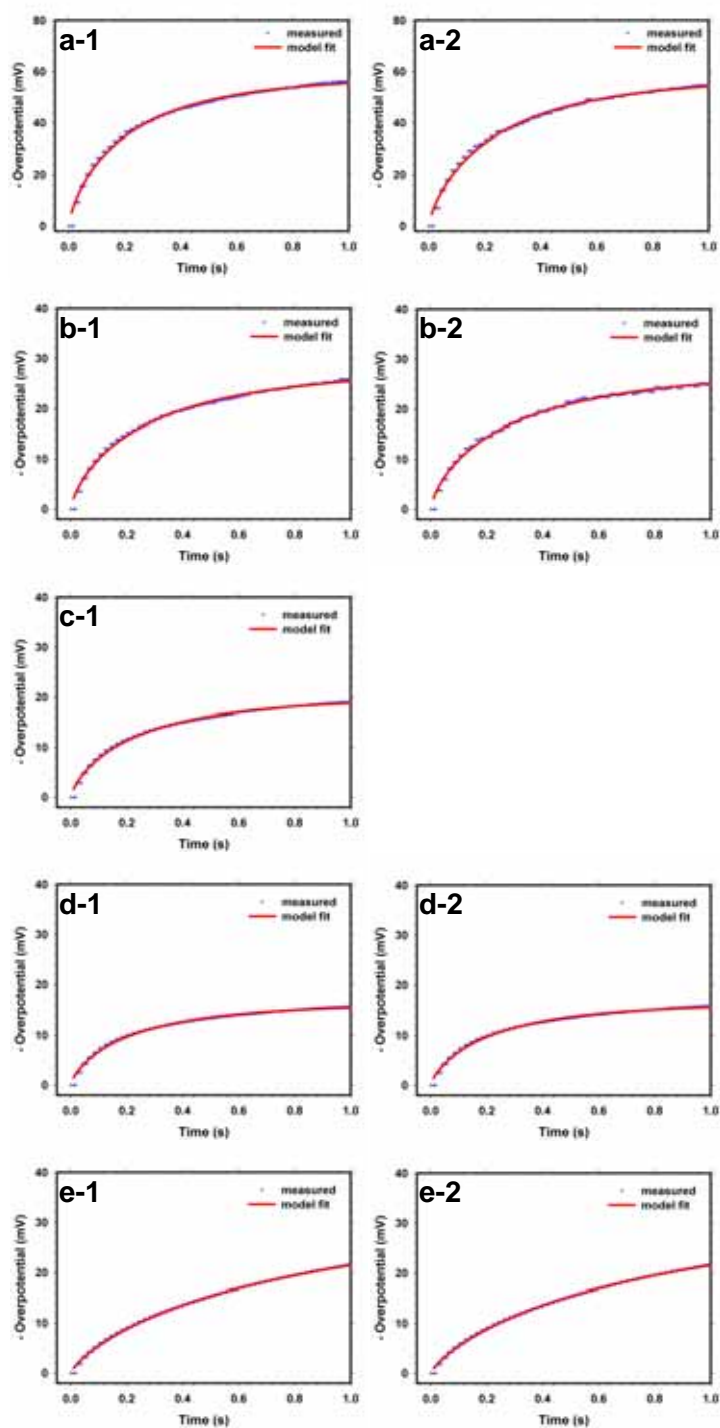
Figure A.6. Curve fitting of repeated short galvanostatic pulse measurements for mild steel in different clay content electrolytes initially saturated with 0.01M NaCl measured on Day 7. The labels **a**, **b**, **c**, **d**, and **e** correspond to clay contents of 5%, 10%, 15%, 20%, and 25% respectively. The labels **1**, and **2** (where available) correspond to curve fitting of the charging curves from the 2nd and 3rd set of measurement respectively.
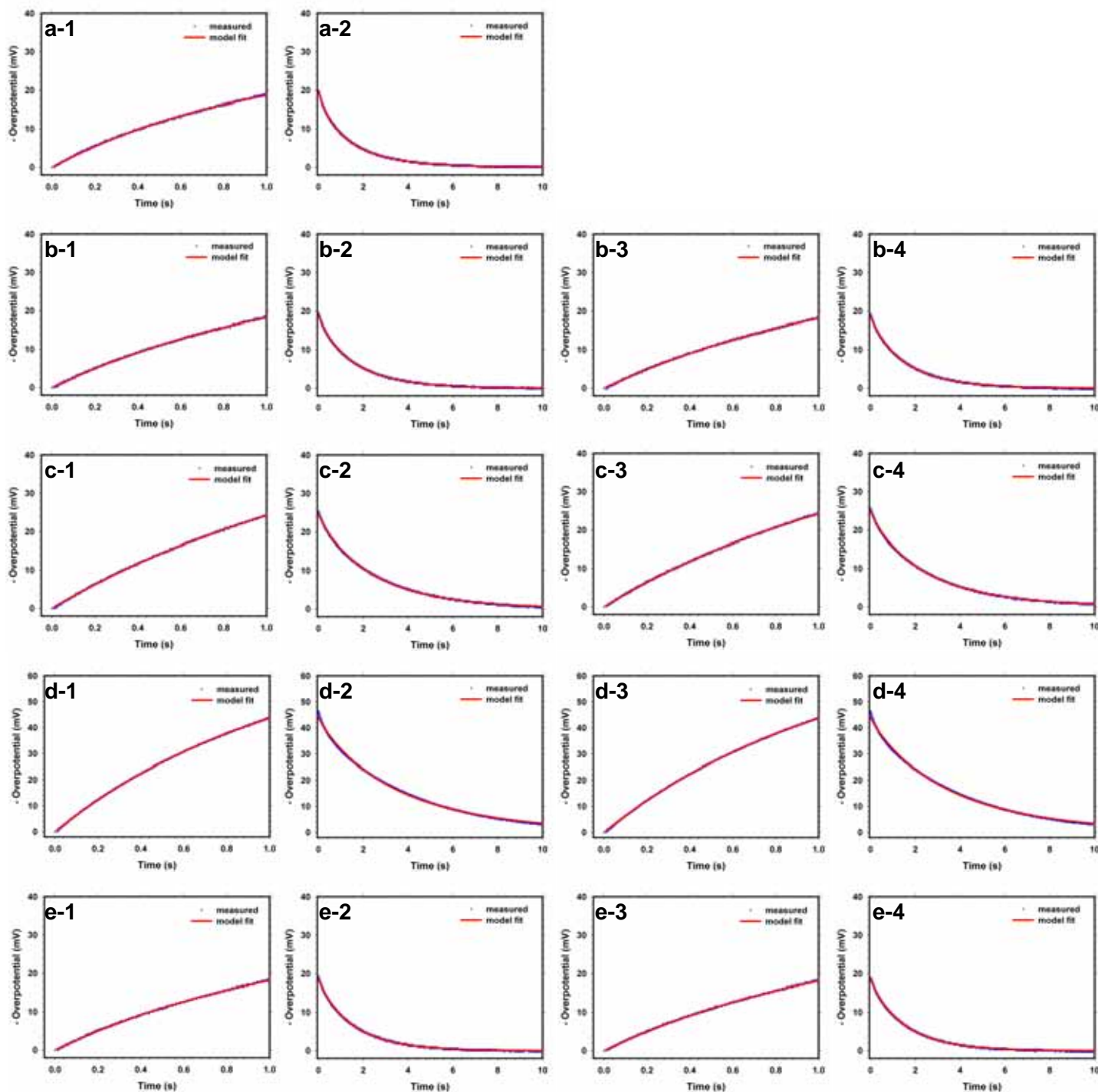
Figure A.7. Curve fitting of repeated short galvanostatic pulse measurements for mild steel in different clay content electrolytes saturated with 0.1M NaCl measured on Day 1. The labels **a**, **b**, **c**, **d**, and **e** correspond to clay contents of 5%, 10%, 15%, 20%, and 25% respectively. The labels **1**, and **2** correspond to curve fitting of the charging and discharging curves respectively of the 2nd set of measurement while **3**, and **4** (where available) represent the curve fitting of the charging and discharging curves respectively of the 3rd set of measurement.

Figure A.8. Curve fitting of repeated short galvanostatic pulse measurements for mild steel in different clay content electrolytes initially saturated with 0.1M NaCl measured on Day 7. The labels **a**, **b**, **c**, **d**, and **e** correspond to clay contents of 5%, 10%, 15%, 20%, and 25% respectively. The labels **1**, and **2** correspond to curve fitting of the charging curves from the 2nd and 3rd set of measurement respectively.
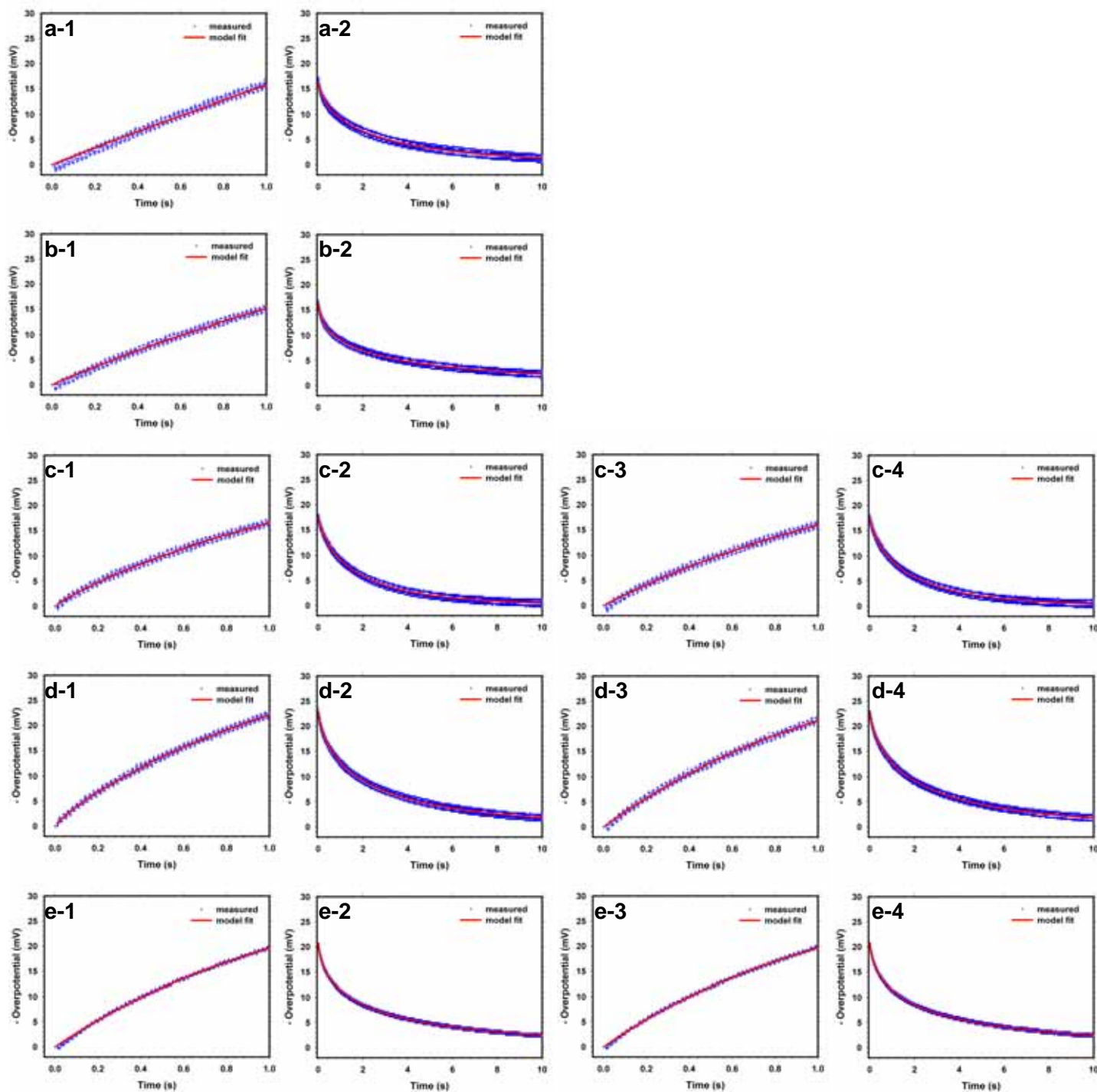
Figure A.9. Curve fitting of repeated short galvanostatic pulse measurements for cast iron in different clay content electrolytes saturated with deionized water measured on Day 1. The labels **a**, **b**, **c**, **d**, and **e** correspond to clay contents of 5%, 10%, 15%, 20%, and 25% respectively. The labels **1**, and **2** correspond to curve fitting of the charging and discharging curves respectively of the 2nd set of measurement while **3**, and **4** (where available) represent the curve fitting of the charging and discharging curves respectively of the 3rd set of measurement.

Figure A.10. Curve fitting of repeated short galvanostatic pulse measurements for cast iron in different clay content electrolytes initially saturated with deionized water measured on Day 7. The labels **a**, **b**, **c**, **d**, and **e** correspond to clay contents of 5%, 10%, 15%, 20%, and 25% respectively. The labels **1**, and **2** correspond to curve fitting of the charging curves from the 2nd and 3rd set of measurement respectively.
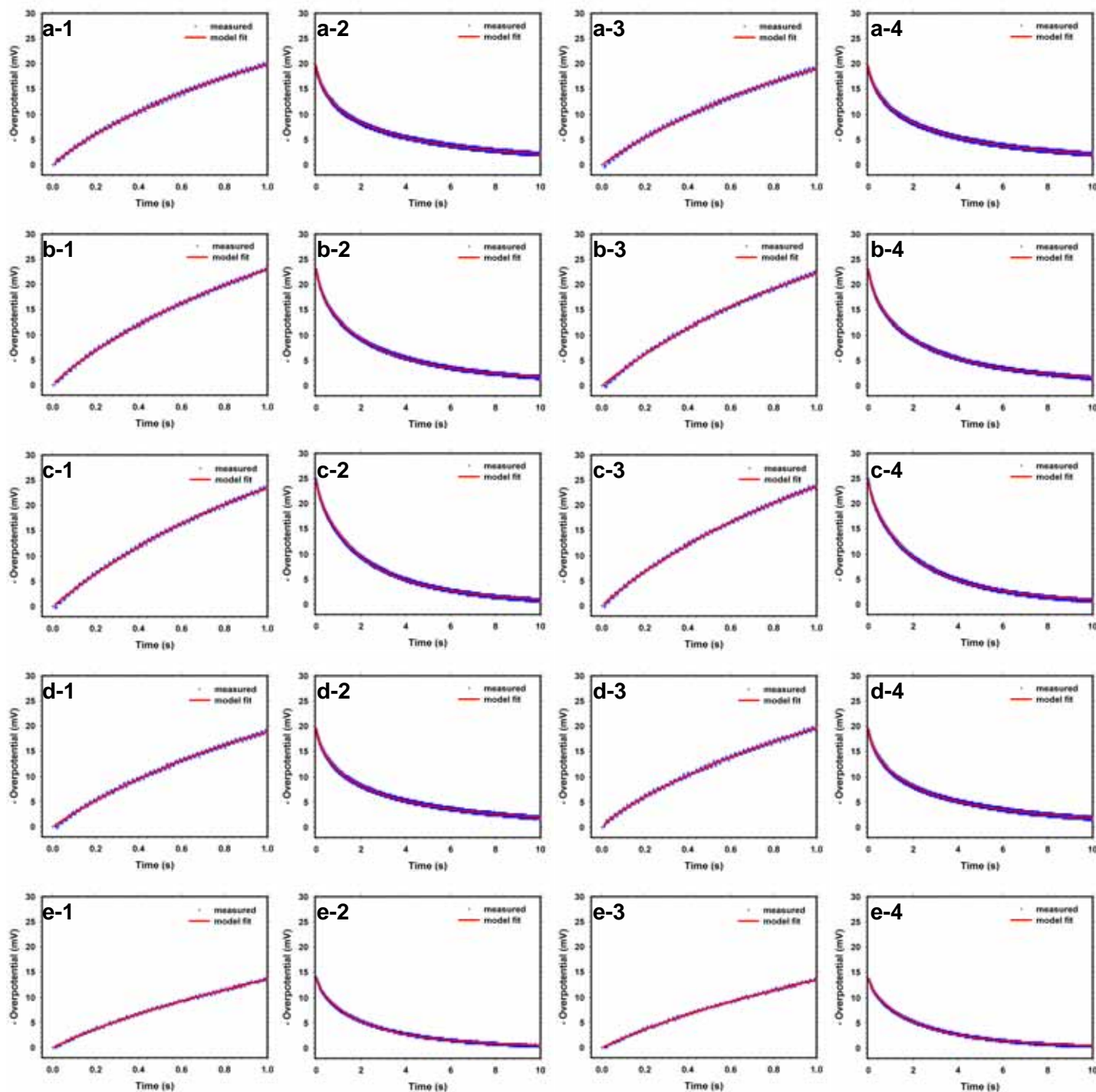
Figure A.11. Curve fitting of repeated short galvanostatic pulse measurements for cast iron in different clay content electrolytes saturated with 0.01M NaCl measured on Day 1. The labels **a**, **b**, **c**, **d**, and **e** correspond to clay contents of 5%, 10%, 15%, 20%, and 25% respectively. The labels **1**, and **2** correspond to curve fitting of the charging and discharging curves respectively of the 2nd set of measurement while **3**, and **4** represent the curve fitting of the charging and discharging curves respectively of the 3rd set of measurement.
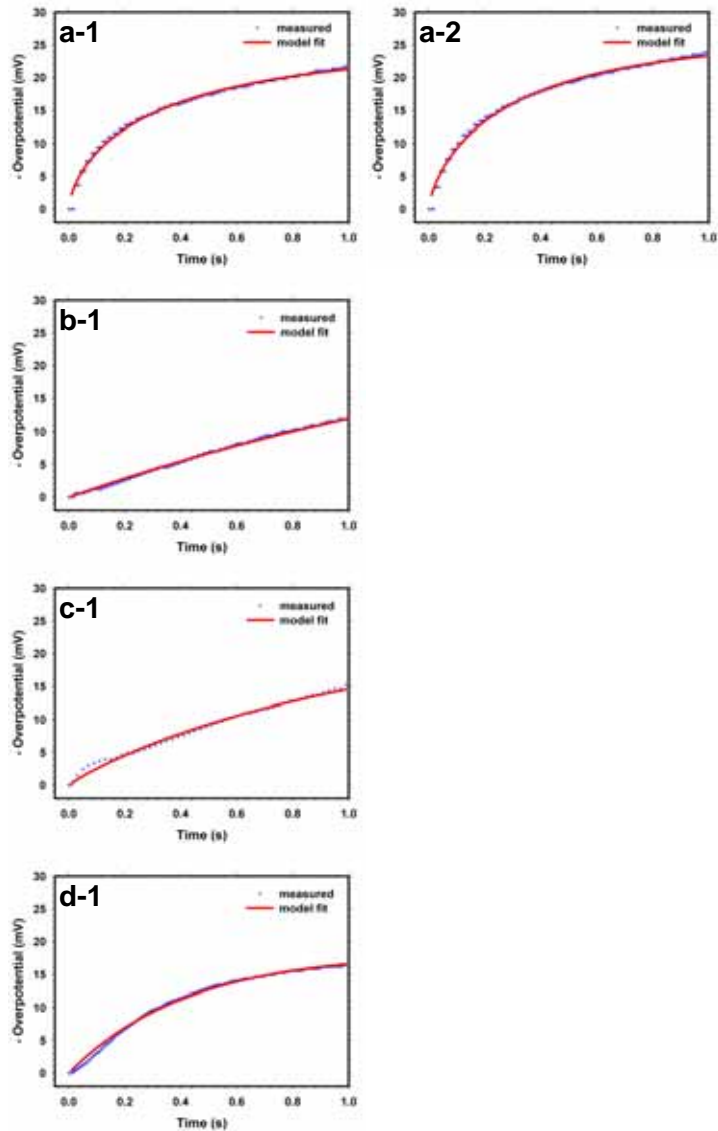
Figure A.12. Curve fitting of repeated short galvanostatic pulse measurements for cast iron in different clay content electrolytes initially saturated with deionized water measured on Day 7. The labels **a**, **b**, **c**, and **d** correspond to clay contents of 10%, 15%, 20%, and 25% respectively. The labels **1**, and **2** (where available) correspond to curve fitting of the charging curves from the 2nd and 3rd set of measurement respectively.
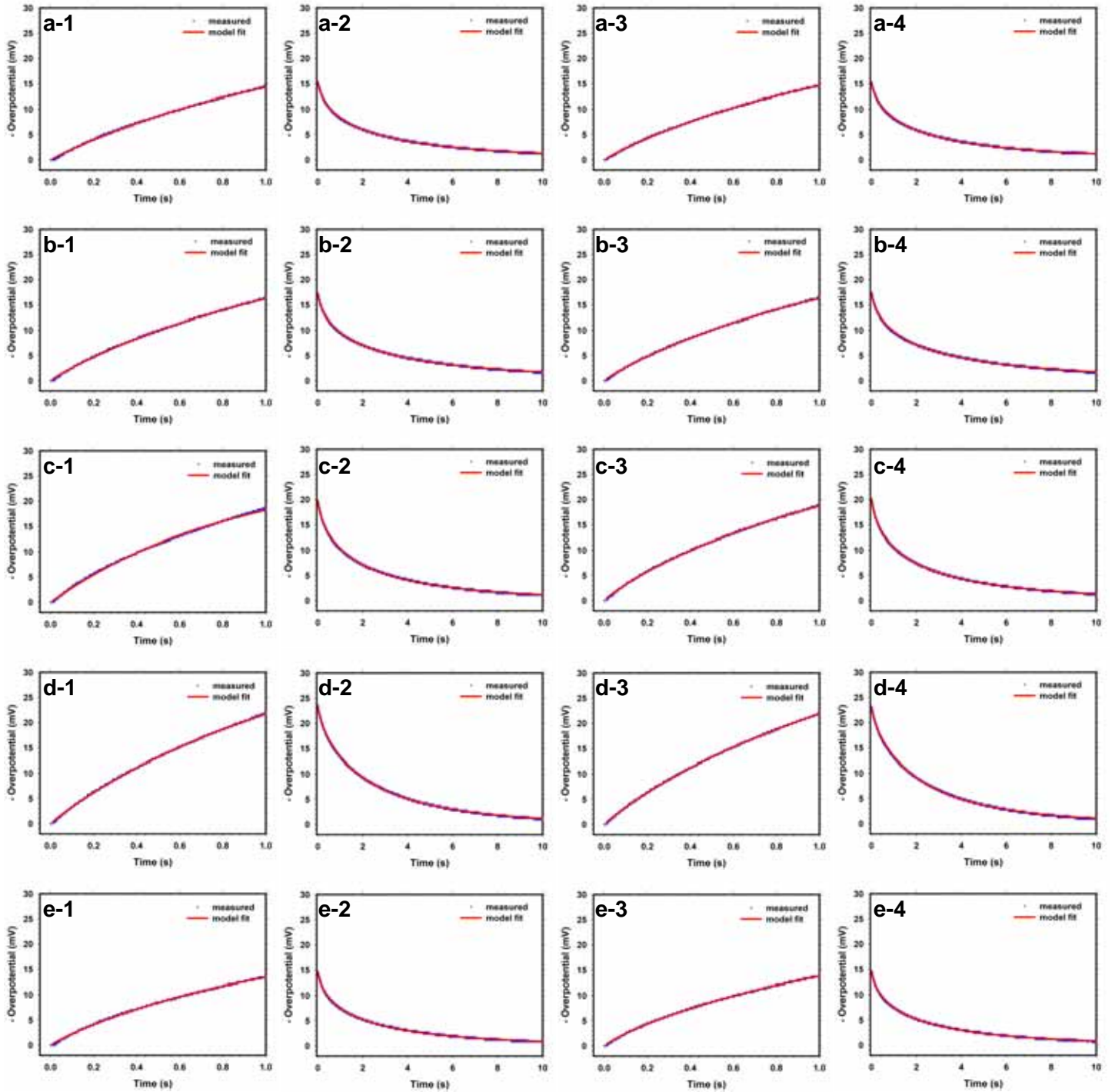
Figure A.13. . Curve fitting of repeated short galvanostatic pulse measurements for cast iron in different clay content electrolytes saturated with 0.1M NaCl measured on Day 1. The labels **a**, **b**, **c**, **d**, and **e** correspond to clay contents of 5%, 10%, 15%, 20%, and 25% respectively. The labels **1**, and **2** correspond to curve fitting of the charging and discharging curves respectively of the 2nd set of measurement while **3**, and **4** represent the curve fitting of the charging and discharging curves respectively of the 3rd set of measurement.
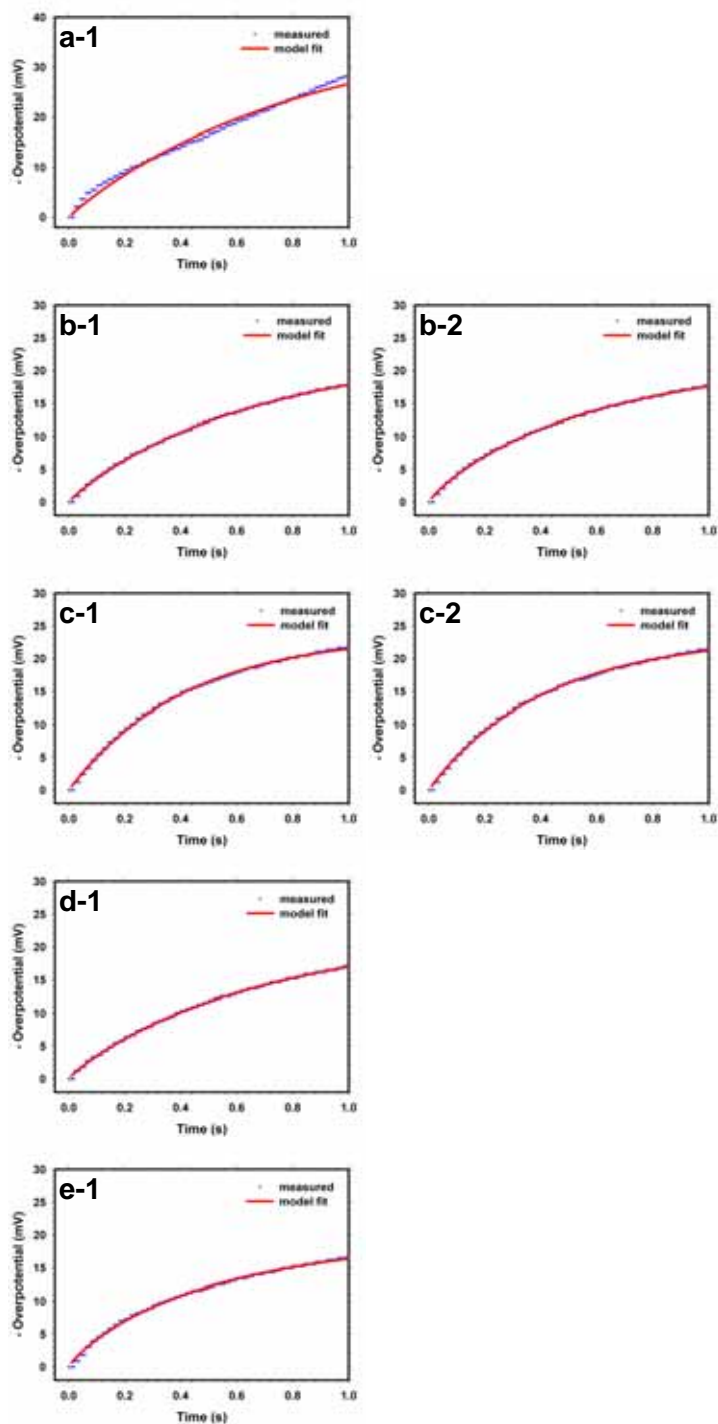
Figure A.14. Curve fitting of repeated short galvanostatic pulse measurements for cast iron in different clay content electrolytes initially saturated with 0.1M NaCl measured on Day 7. The labels **a**, **b**, **c**, **d**, and **e** correspond to clay contents of 5%, 10%, 15%, 20%, and 25% respectively. The labels **1**, and **2** (where available) correspond to curve fitting of the charging curves from the 2nd and 3rd set of measurement respectively.
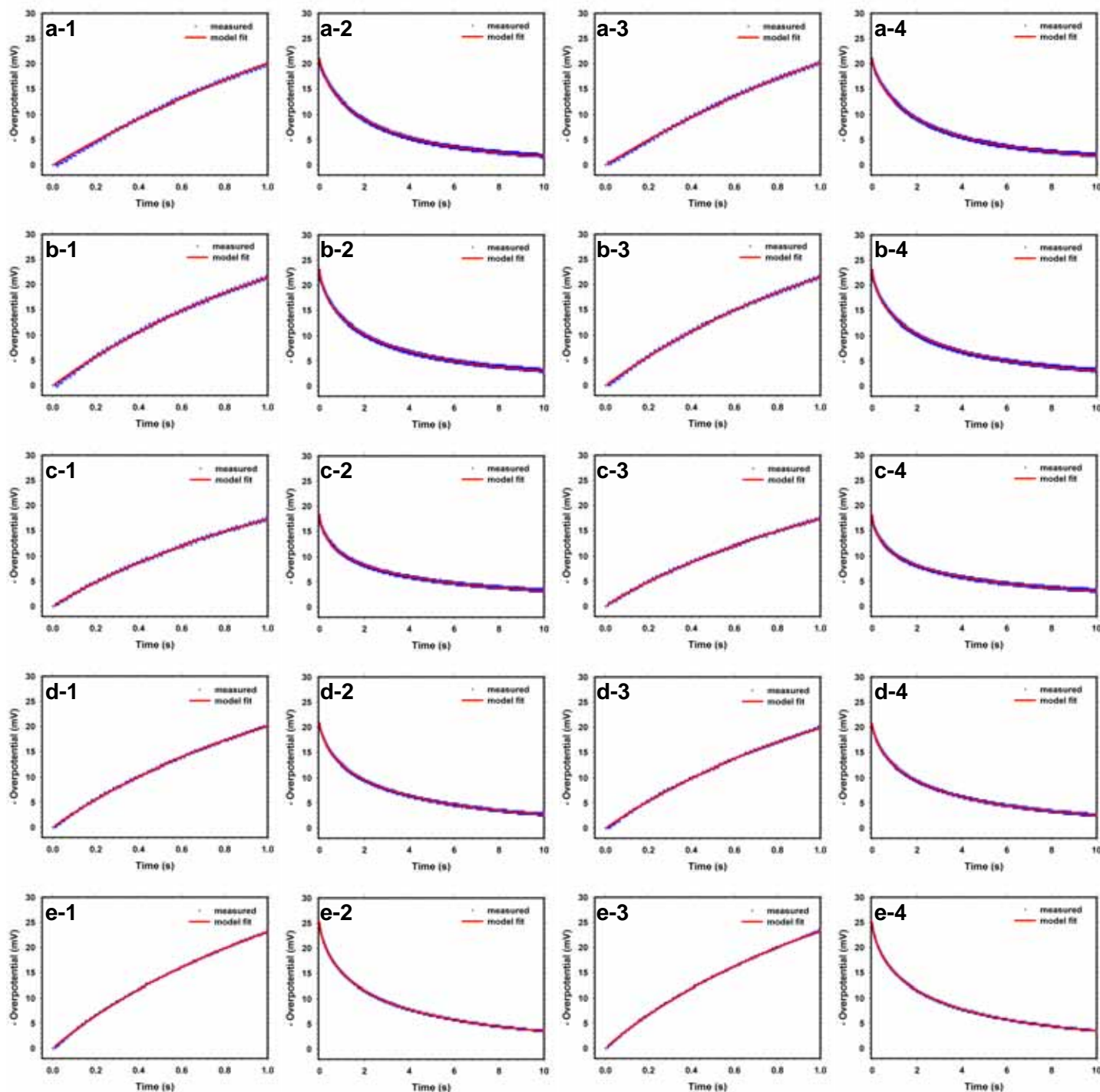
Figure A.15. Curve fitting of repeated short galvanostatic pulse measurements for wrought iron in different clay content electrolytes saturated with deionized water measured on Day 1. The labels **a**, **b**, **c**, **d**, and **e** correspond to clay contents of 5%, 10%, 15%, 20%, and 25% respectively. The labels **1**, and **2** correspond to curve fitting of the charging and discharging curves respectively of the 2nd set of measurement while **3**, and **4** represent the curve fitting of the charging and discharging curves respectively of the 3rd set of measurement.

Figure A.16. . Curve fitting of repeated short galvanostatic pulse measurements for wrought iron in different clay content electrolytes initially saturated with deionized water measured on Day 7. The labels **a**, **b**, **c**, **d**, and **e** correspond to clay contents of 5%, 10%, 15%, 20%, and 25% respectively. The labels **1**, and **2** correspond to curve fitting of the charging curves from the 2nd and 3rd set of measurement respectively.
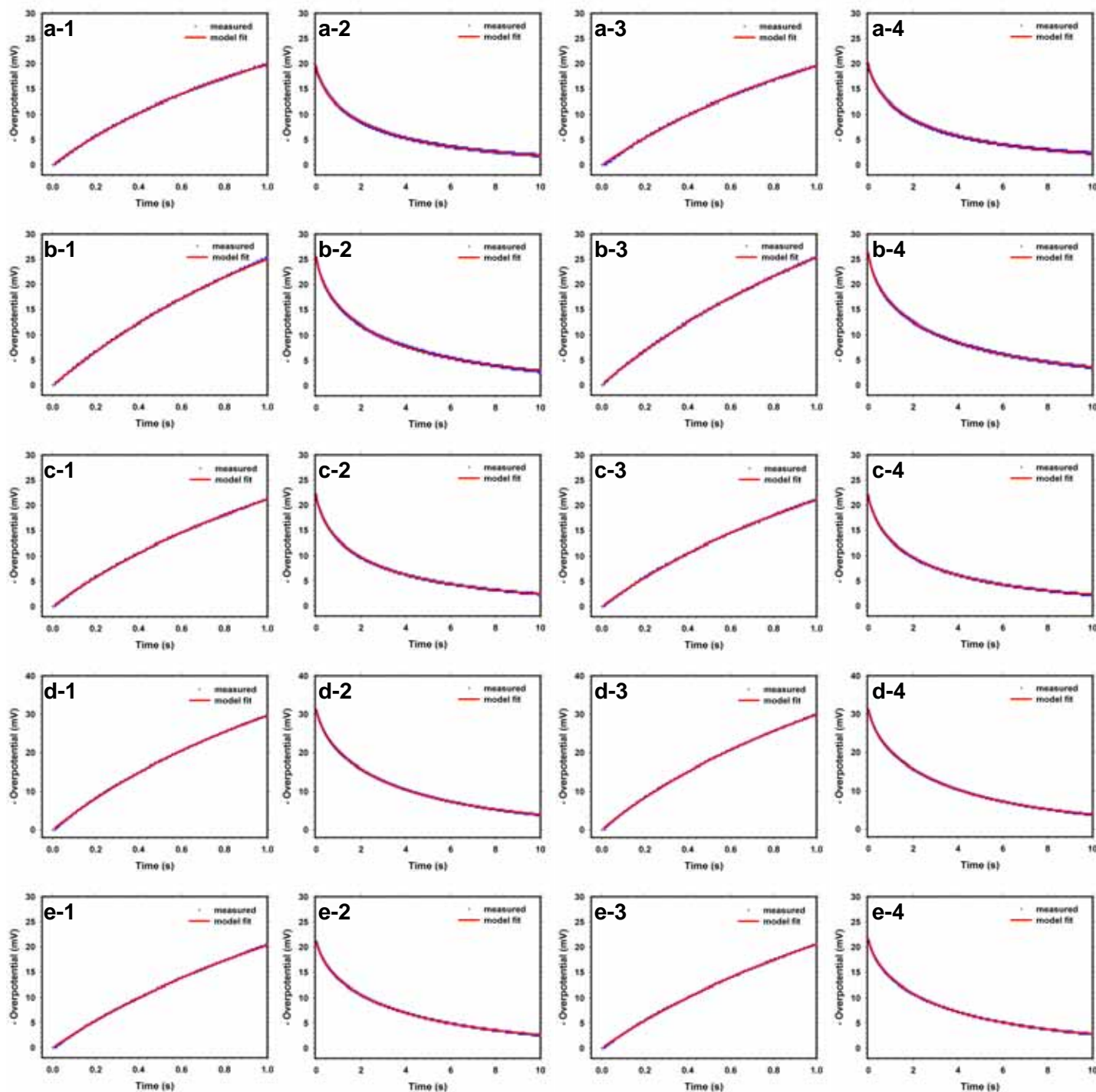
Figure A.17. Curve fitting of repeated short galvanostatic pulse measurements for wrought iron in different clay content electrolytes saturated with 0.01M NaCl measured on Day 1. The labels **a**, **b**, **c**, **d**, and **e** correspond to clay contents of 5%, 10%, 15%, 20%, and 25% respectively. The labels **1**, and **2** correspond to curve fitting of the charging and discharging curves respectively of the 2nd set of measurement while **3**, and **4** represent the curve fitting of the charging and discharging curves respectively of the 3rd set of measurement.

Figure A.18. Curve fitting of repeated short galvanostatic pulse measurements for wrought iron in different clay content electrolytes initially saturated with 0.01M NaCl measured on Day 7. The labels **a**, **b**, **c**, **d**, and **e** correspond to clay contents of 5%, 10%, 15%, 20%, and 25% respectively. The labels **1**, and **2** correspond to curve fitting of the charging curves from the 2nd and 3rd set of measurement respectively.

Figure A.19. Curve fitting of repeated short galvanostatic pulse measurements for wrought iron in different clay content electrolytes saturated with 0.1M NaCl measured on Day 1. The labels **a**, **b**, **c**, **d**, and **e** correspond to clay contents of 5%, 10%, 15%, 20%, and 25% respectively. The labels **1**, and **2** correspond to curve fitting of the charging and discharging curves respectively of the 2nd set of measurement while **3**, and **4** represent the curve fitting of the charging and discharging curves respectively of the 3rd set of measurement.
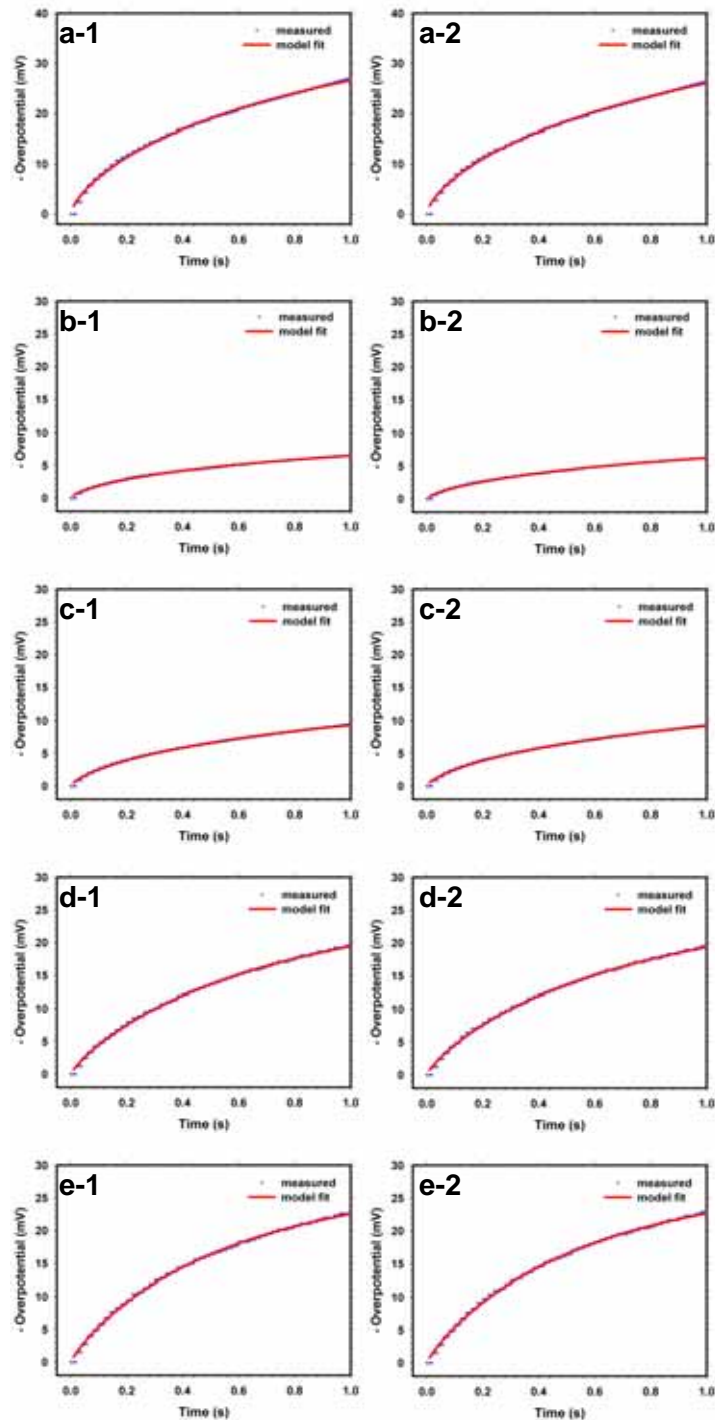
Figure A.20. Curve fitting of repeated short galvanostatic pulse measurements for wrought iron in different clay content electrolytes initially saturated with 0.1M NaCl measured on Day 7. The labels **a**, **b**, **c**, **d**, and **e** correspond to clay contents of 5%, 10%, 15%, 20%, and 25% respectively. The labels **1**, and **2** correspond to curve fitting of the charging curves from the 2nd and 3rd set of measurement respectively.

APPENDIX B.1   BLOCK DIAGRAM FOR THE SIP-IS MEASUREMENT AND CONTROL PROGRAM

The measurement and control program is based on several data acquisition and signal processing functions, which are available in NI LabVIEW as standard functions. The block diagram for the main program developed in this work is shown in Fig. B.1. Annotations are provided where necessary to aid in understanding the data flow and program execution.
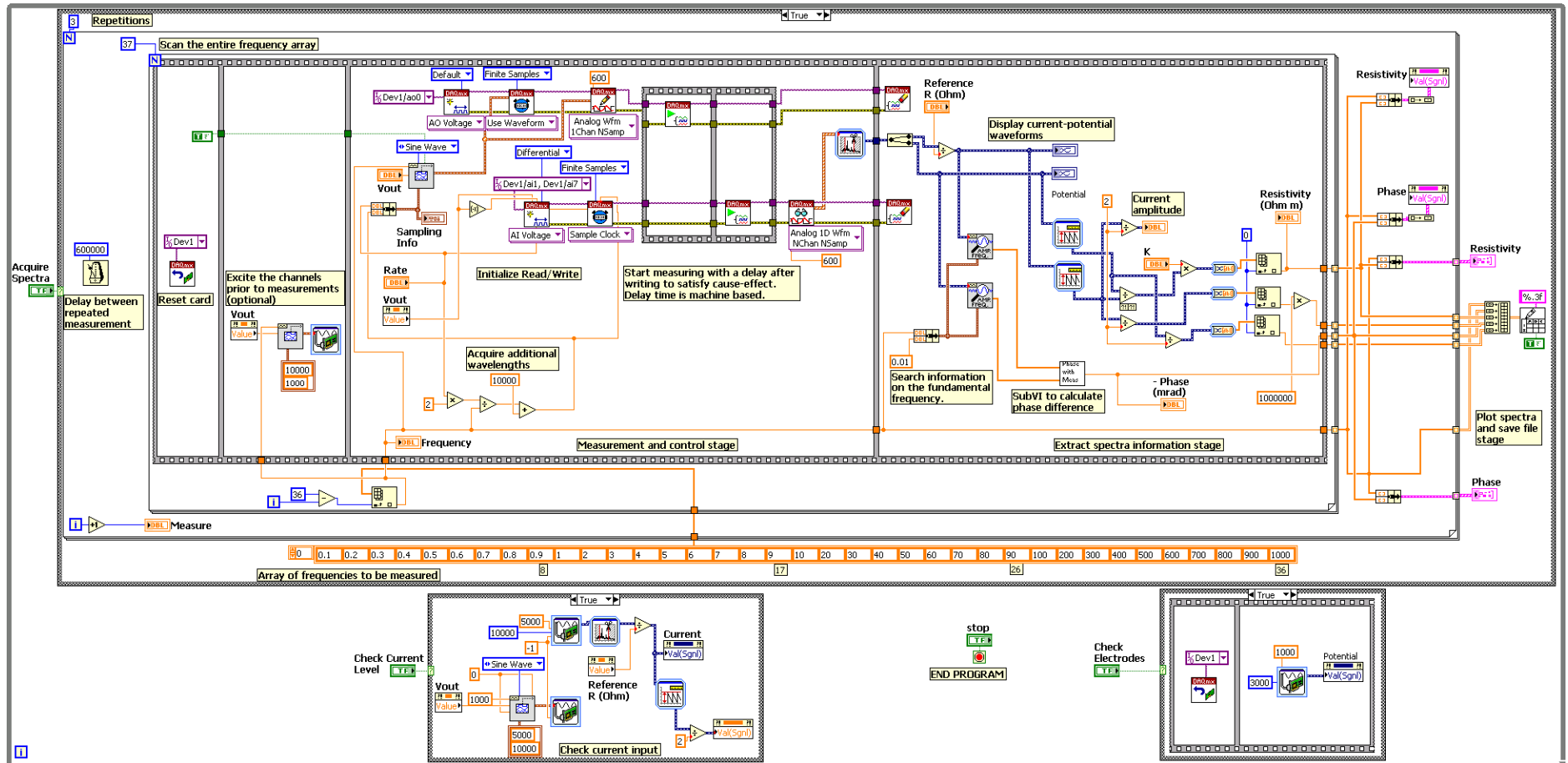
Figure B.1. Block diagram of the program for the measurement and control of the SIP-IS system.

APPENDIX B.2   BLOCK DIAGRAM FOR THE INVERSION OF PHASE SPECTRA PROGRAM

The block diagram for the complete program is shown in Fig. B.2 Explanatory notes are provided where necessary to aid in understanding the data flow and program execution.
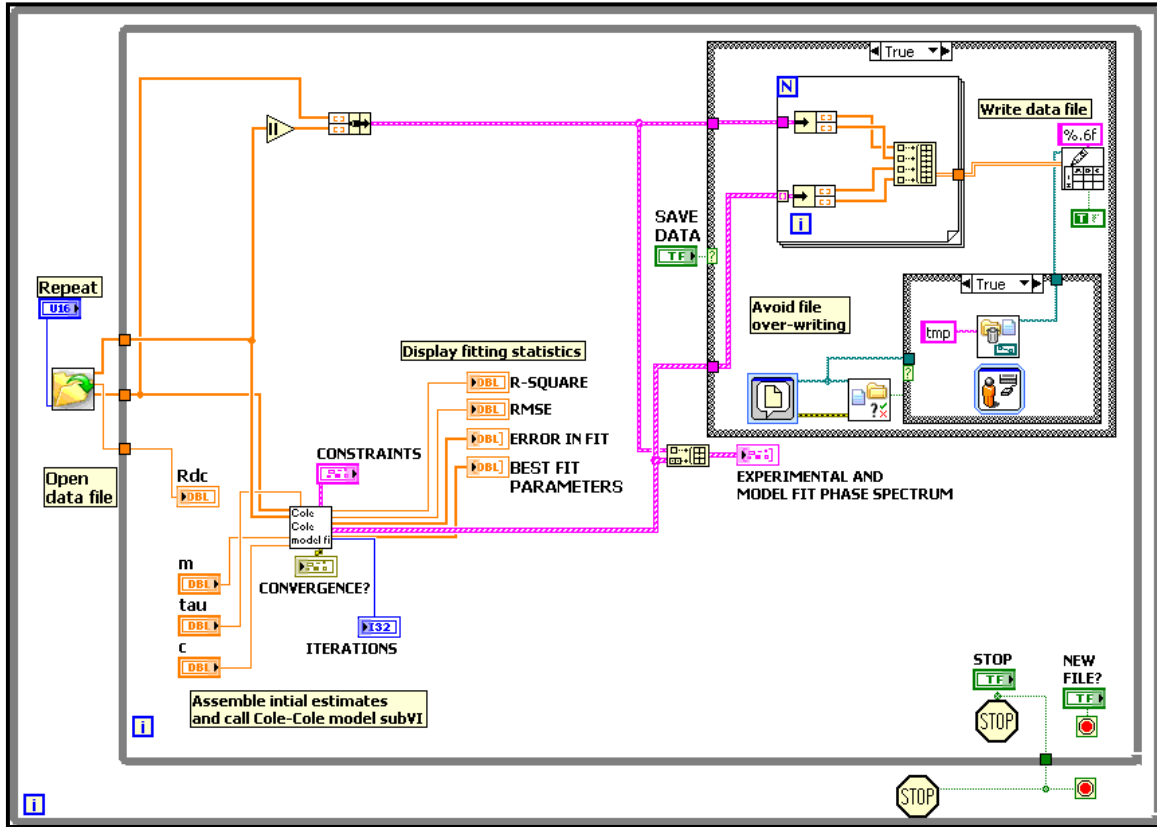
Figure B.2. Block diagram for inversion of ϕ-spectra. Note the annotations given.

The Cole-Cole model fit subVI in Fig. B.2 implements NI's constrained *Nonlinear Curve Fit LM bound* subVI as shown in Fig B.3. The model function implementing the complex Cole-Cole model is shown in Fig. B.4. Note that the ϕ value is extracted after computing the complex resistivity using complex to polar transformations. In this manner, only the experimental ϕ-spectra can be utilized for inversion and determination of the Cole-Cole parameters.
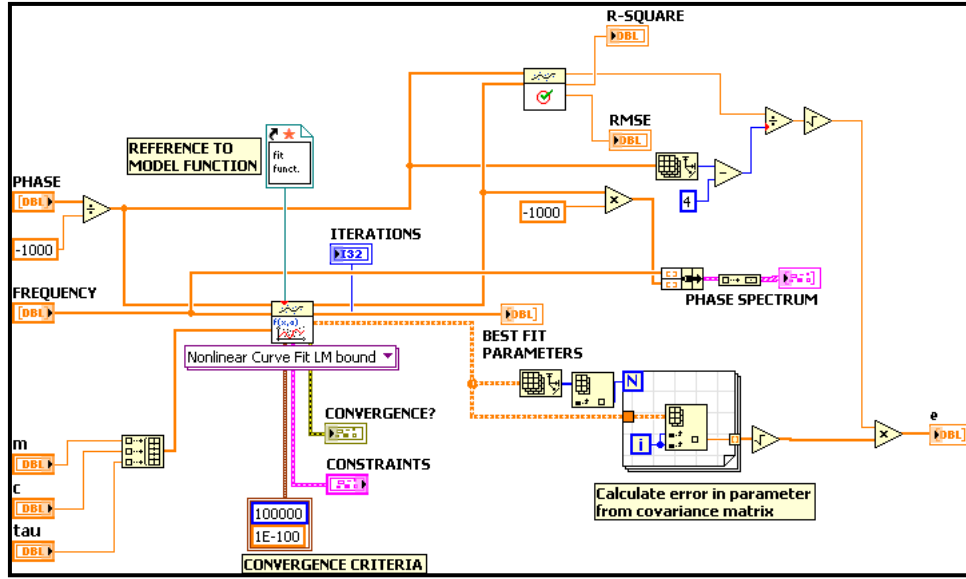
Figure B.3. Implementation of the Cole-Cole model fit subVI.
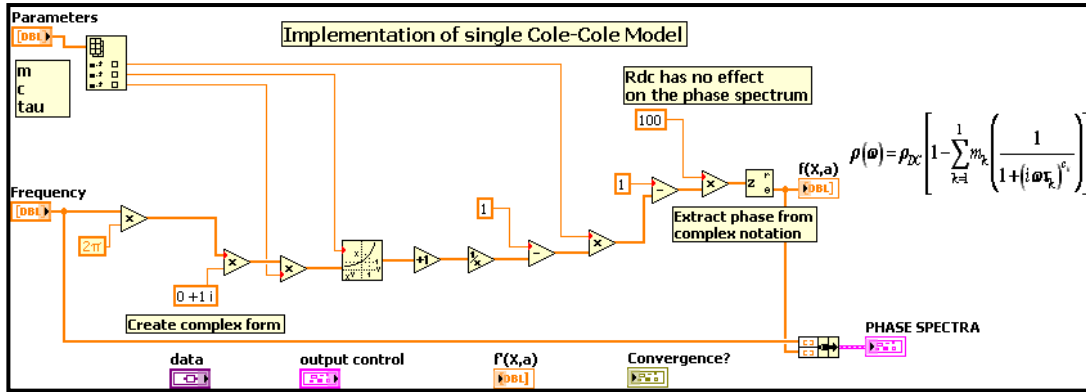
Figure B.4. Implementation of the single Cole-Cole model in complex form for extraction of ϕ.

Different starting values of $\lambda = \lambda_o$ was also tested during this work. For successive iterations, λ is either increased or decreased by a default factor of 10. Inversion of ϕ-spectra does not depend on ρ_{DC}, thus it can be given an arbitrary value in the model implementation. However, for coherency this value was changed according to the ρ_{DC} value (ρ at 0.1 Hz) of the sample being analyzed. Uncertainty in the j-th parameters is calculated from the square-root of the diagonal elements in the final covariance matrix, whereby the j-th term corresponds to error in the j-th parameter, multiplied by the square-root of the error variance as given by Eq. B.1.

$$\sigma = \left(\sqrt{\frac{\mathbf{SSE}}{N-3}} \right) \times \sqrt{\mathbf{diag}\left(\left[\mathbf{J^T J} \right]^{-1} \right)} \tag{B.1}$$

266

APPENDIX B.3   SYNTHETIC SOILS SPECTRAL DATA

Means (μ) and standard deviations (σ) for phase and resistivities computed from repeated measurements (M1, M2, and M3) are given. Note, all phase values are negative.

Table B.1. Spectral data for soil sample A5.

Frequency (Hz)	Phase (mrad)			Resistivity (Ω m)			Phase (mrad)		Resistivity (Ω m)	
	M1	M2	M3	M1	M2	M3	μ	σ	μ	σ
0.1	0.44	0.52	0.47	114.49	114.04	113.89	0.48	0.04	114.14	0.31
0.2	0.44	0.48	0.49	114.81	115.12	114.09	0.47	0.03	114.67	0.53
0.3	0.50	0.54	0.61	115.46	114.92	114.37	0.55	0.06	114.92	0.55
0.4	0.48	0.57	0.68	115.66	115.09	113.58	0.58	0.10	114.78	1.07
0.5	0.71	0.62	0.79	116.03	115.55	114.92	0.71	0.09	115.50	0.56
0.6	0.54	0.48	0.51	115.06	115.04	114.67	0.51	0.03	114.92	0.22
0.7	0.67	0.76	0.72	115.59	114.93	115.22	0.72	0.04	115.25	0.33
0.8	0.64	0.74	0.63	115.08	115.37	114.72	0.67	0.06	115.05	0.32
0.9	0.58	0.64	0.67	116.02	115.06	114.24	0.63	0.04	115.11	0.89
1	0.51	0.70	0.50	115.60	114.91	114.57	0.57	0.11	115.03	0.52
2	1.13	0.77	0.96	115.51	116.10	115.00	0.95	0.18	115.53	0.55
3	1.08	1.05	1.08	116.10	115.61	114.91	1.07	0.02	115.54	0.59
4	0.92	1.31	1.12	114.97	115.91	114.83	1.12	0.20	115.24	0.59
5	1.55	1.39	1.25	116.46	116.09	115.26	1.40	0.15	115.94	0.62
6	1.38	1.52	1.47	115.56	115.90	114.50	1.46	0.07	115.32	0.73
7	1.57	1.81	1.72	116.48	115.71	114.75	1.70	0.12	115.65	0.87
8	1.83	1.73	1.57	115.70	115.73	114.96	1.71	0.13	115.47	0.44
9	1.89	1.91	1.92	116.47	115.95	115.13	1.91	0.02	115.85	0.68
10	1.81	1.72	1.72	115.55	115.66	115.51	1.75	0.05	115.57	0.08
20	2.48	2.57	2.37	115.82	116.03	115.06	2.47	0.10	115.63	0.51
30	2.90	3.58	3.80	115.15	115.66	114.29	3.43	0.47	115.03	0.69
40	3.36	3.98	4.14	115.55	115.93	115.33	3.83	0.41	115.60	0.30
50	3.98	3.12	4.27	116.09	114.63	114.90	3.79	0.60	115.21	0.78
60	4.27	4.30	4.33	115.69	115.37	114.52	4.30	0.03	115.20	0.60
70	5.55	5.56	5.51	116.05	115.47	114.88	5.54	0.02	115.47	0.59
80	3.89	3.76	3.69	116.03	115.52	114.64	3.78	0.10	115.40	0.70
90	4.33	5.97	4.49	115.53	115.48	115.13	4.93	0.90	115.38	0.21
100	4.07	5.32	6.22	115.80	115.50	114.30	5.20	1.08	115.20	0.79
200	5.38	5.04	5.57	115.20	114.29	114.61	5.33	0.27	114.70	0.46
300	4.92	5.72	6.82	114.96	115.13	114.12	5.82	0.96	114.73	0.54
400	8.20	5.59	7.07	114.56	114.22	113.73	6.95	1.31	114.17	0.42
500	5.64	5.90	5.76	114.60	113.22	112.45	5.77	0.13	113.42	1.09
600	8.62	7.16	7.21	114.47	113.38	113.75	7.66	0.83	113.86	0.56
700	6.85	6.66	7.42	114.28	114.48	113.32	6.98	0.39	114.03	0.62
800	7.42	6.94	5.27	113.46	113.29	113.73	6.54	1.13	113.49	0.22
900	8.62	8.52	8.90	113.60	114.47	113.31	8.68	0.19	113.79	0.60
1000	7.84	8.10	6.34	113.50	112.38	112.36	7.43	0.95	112.75	0.65

Table B.2. Spectral data for soil sample A10.

Frequency (Hz)	Phase (mrad)			Resistivity (Ω m)			Phase (mrad)		Resistivity (Ω m)	
	M1	M2	M3	M1	M2	M3	μ	σ	μ	σ
0.1	0.38	0.31	0.37	68.25	67.90	67.50	0.35	0.03	67.88	0.38
0.2	0.46	0.43	0.45	68.33	68.06	67.67	0.44	0.01	68.02	0.33
0.3	0.49	0.49	0.49	68.37	68.03	67.62	0.49	0.00	68.01	0.38
0.4	0.51	0.52	0.56	68.53	68.19	67.67	0.53	0.03	68.13	0.44
0.5	0.57	0.61	0.61	68.66	68.21	67.84	0.59	0.02	68.24	0.41
0.6	0.57	0.63	0.63	68.64	68.10	67.91	0.61	0.03	68.22	0.38
0.7	0.64	0.69	0.56	68.44	68.28	67.89	0.63	0.07	68.20	0.28
0.8	0.69	0.76	0.60	68.50	68.10	67.91	0.68	0.08	68.17	0.30
0.9	0.72	0.44	0.68	68.58	68.20	67.73	0.61	0.15	68.17	0.43
1	0.80	0.67	0.79	68.55	68.42	67.72	0.75	0.07	68.23	0.45
2	0.97	0.96	1.03	68.70	68.31	67.94	0.98	0.04	68.32	0.38
3	1.11	1.06	1.08	68.71	68.43	67.81	1.08	0.03	68.32	0.46
4	1.36	1.39	1.17	68.58	68.14	68.04	1.31	0.12	68.25	0.29
5	1.45	1.48	1.43	68.43	67.85	67.99	1.45	0.03	68.09	0.31
6	1.59	1.60	1.52	68.48	68.34	68.02	1.57	0.04	68.28	0.24
7	1.78	1.62	1.74	68.70	68.43	67.84	1.71	0.08	68.32	0.44
8	1.69	1.90	1.83	68.69	68.36	68.04	1.81	0.10	68.36	0.32
9	2.00	1.85	2.11	68.78	68.17	67.90	1.99	0.13	68.28	0.45
10	1.97	2.18	2.01	68.53	68.30	68.04	2.05	0.11	68.29	0.25
20	3.52	3.29	2.83	68.46	68.23	68.03	3.21	0.35	68.24	0.22
30	4.10	4.01	3.89	68.50	68.10	67.92	4.00	0.11	68.17	0.30
40	4.67	4.32	4.76	68.45	68.15	67.95	4.58	0.23	68.18	0.25
50	4.52	4.33	4.54	68.09	68.28	67.85	4.46	0.11	68.07	0.21
60	5.78	4.41	4.19	68.45	68.28	67.93	4.79	0.86	68.22	0.27
70	4.38	6.86	4.39	68.21	68.12	67.75	5.21	1.43	68.03	0.24
80	5.17	4.51	5.25	68.44	67.99	67.77	4.98	0.41	68.07	0.34
90	7.72	5.40	7.72	68.18	68.21	67.69	6.95	1.34	68.03	0.29
100	8.31	8.31	8.31	68.42	68.19	67.82	8.31	0.00	68.14	0.30
200	6.88	6.77	6.73	68.14	67.99	67.55	6.79	0.08	67.89	0.31
300	6.29	6.46	7.84	68.18	67.79	67.25	6.86	0.85	67.74	0.47
400	5.90	9.45	9.01	67.98	67.72	67.39	8.12	1.93	67.70	0.30
500	7.32	10.26	6.33	67.86	67.37	66.97	7.97	2.05	67.40	0.45
600	7.43	7.12	7.89	67.36	67.71	63.48	7.48	0.39	66.18	2.35
700	8.54	8.21	7.89	67.84	67.59	67.05	8.22	0.32	67.49	0.40
800	9.12	9.20	9.82	67.88	68.76	66.81	9.38	0.38	67.82	0.98
900	6.84	7.82	8.23	67.93	67.47	67.21	7.63	0.71	67.54	0.37
1000	7.90	8.54	9.82	67.38	67.32	67.06	8.76	0.98	67.25	0.17

APPENDIX

Table B.3. Spectral data for soil sample A15.

Frequency	Phase			Resistivity			Phase		Resistivity	
(Hz)	(mrad)			(Ω m)			(mrad)		(Ω m)	
	M1	M2	M3	M1	M2	M3	μ	σ	μ	σ
0.1	0.31	0.45	0.45	47.77	47.59	47.38	0.40	0.08	47.58	0.19
0.2	0.48	0.47	0.50	47.77	47.57	47.41	0.48	0.01	47.58	0.18
0.3	0.53	0.52	0.54	47.83	47.65	47.45	0.53	0.01	47.64	0.19
0.4	0.57	0.58	0.57	47.84	47.68	47.49	0.57	0.00	47.67	0.18
0.5	0.60	0.64	0.62	47.87	47.66	47.42	0.62	0.02	47.65	0.22
0.6	0.65	0.68	0.58	47.84	47.54	47.47	0.64	0.05	47.62	0.20
0.7	0.66	0.66	0.65	47.79	47.64	47.44	0.65	0.01	47.62	0.17
0.8	0.74	0.69	0.73	47.88	47.64	47.52	0.72	0.03	47.68	0.18
0.9	0.44	0.70	0.70	47.86	47.62	47.47	0.61	0.15	47.65	0.19
1	0.75	0.74	0.77	47.90	47.66	47.50	0.75	0.02	47.69	0.20
2	1.09	1.04	1.12	47.85	47.65	47.49	1.08	0.04	47.66	0.18
3	1.30	1.22	1.17	47.83	47.63	47.45	1.23	0.07	47.64	0.19
4	1.49	1.53	1.33	47.86	47.62	47.49	1.45	0.10	47.66	0.19
5	1.65	1.73	1.54	47.85	47.67	47.48	1.64	0.10	47.67	0.19
6	1.87	1.86	1.80	47.88	47.67	47.46	1.84	0.04	47.67	0.21
7	2.03	1.92	1.98	47.80	47.64	47.44	1.98	0.06	47.63	0.18
8	1.91	1.91	1.91	47.86	47.65	47.47	1.91	0.00	47.66	0.20
9	2.14	2.26	2.18	47.84	47.63	47.48	2.19	0.06	47.65	0.18
10	2.46	2.22	2.18	47.85	47.67	47.46	2.29	0.15	47.66	0.19
20	3.51	2.88	-8.38	47.83	47.60	47.44	-0.66	6.69	47.62	0.20
30	3.36	3.36	3.36	47.76	47.60	47.37	3.36	0.00	47.58	0.20
40	3.88	3.91	3.73	47.73	47.55	47.35	3.84	0.10	47.54	0.19
50	5.41	6.12	4.67	47.65	47.51	47.33	5.40	0.73	47.50	0.16
60	4.63	5.32	5.23	47.62	47.49	47.30	5.06	0.37	47.47	0.16
70	6.27	5.98	4.43	47.65	47.42	47.31	5.56	0.99	47.46	0.18
80	7.09	6.44	6.82	47.60	47.43	47.31	6.78	0.33	47.44	0.15
90	5.31	7.26	5.07	47.66	47.45	47.28	5.88	1.20	47.46	0.19
100	7.30	6.85	5.30	47.59	47.44	47.28	6.48	1.05	47.44	0.15
200	8.48	11.77	7.71	47.45	47.24	47.11	9.32	2.15	47.27	0.17
300	10.80	9.61	6.20	47.28	47.16	47.02	8.87	2.39	47.15	0.13
400	7.27	10.61	10.66	47.31	47.09	46.86	9.51	1.94	47.09	0.22
500	8.82	9.00	9.57	47.27	47.04	46.70	9.13	0.39	47.00	0.29
600	7.99	8.74	10.25	47.38	47.04	46.76	8.99	1.15	47.06	0.31
700	7.08	8.85	7.64	47.19	46.72	46.76	7.86	0.90	46.89	0.26
800	9.18	10.76	9.20	47.09	46.67	46.85	9.71	0.91	46.87	0.21
900	6.47	19.46	17.41	47.11	46.36	46.23	14.44	6.98	46.57	0.47
1000	10.51	8.13	8.68	46.80	46.75	46.55	9.11	1.25	46.70	0.13

Table B.4. Spectral data for soil sample A20.

Frequency (Hz)	Phase (mrad)			Resistivity (Ω m)			Phase (mrad)		Resistivity (Ω m)	
	M1	M2	M3	M1	M2	M3	μ	σ	μ	σ
0.1	0.31	0.31	0.31	38.25	38.13	37.99	0.31	0.00	38.12	0.13
0.2	0.41	0.43	0.44	38.28	38.13	37.98	0.43	0.01	38.13	0.15
0.3	0.47	0.47	0.49	38.28	38.16	38.00	0.48	0.01	38.15	0.14
0.4	0.56	0.54	0.56	38.30	38.13	38.01	0.55	0.01	38.15	0.14
0.5	0.59	0.60	0.61	38.27	38.14	38.00	0.60	0.01	38.14	0.13
0.6	0.67	0.65	0.65	38.28	38.14	38.00	0.66	0.01	38.14	0.14
0.7	0.71	0.66	0.72	38.26	38.15	38.04	0.69	0.03	38.15	0.11
0.8	0.72	0.73	0.68	38.25	38.15	38.04	0.71	0.03	38.15	0.11
0.9	0.78	0.79	0.76	38.29	38.18	38.03	0.78	0.01	38.17	0.13
1	0.77	0.81	0.78	38.30	38.17	38.03	0.79	0.02	38.17	0.13
2	1.13	1.08	1.15	38.29	38.16	38.01	1.12	0.04	38.15	0.14
3	1.27	1.29	1.27	38.27	38.16	38.01	1.28	0.01	38.15	0.13
4	1.52	1.51	1.59	38.26	38.15	38.01	1.54	0.05	38.14	0.13
5	1.79	1.78	1.82	38.30	38.14	38.01	1.80	0.02	38.15	0.14
6	1.85	1.94	1.78	38.29	38.13	38.00	1.86	0.08	38.14	0.14
7	1.92	1.91	1.90	38.25	38.14	37.99	1.91	0.01	38.12	0.13
8	2.32	2.23	2.03	38.25	38.10	38.00	2.19	0.15	38.12	0.12
9	2.19	2.19	2.19	38.24	38.12	37.99	2.19	0.00	38.12	0.13
10	2.35	2.70	2.27	38.24	38.14	37.99	2.44	0.23	38.12	0.12
20	4.21	3.44	3.13	38.21	38.07	37.95	3.59	0.56	38.08	0.13
30	4.73	4.78	4.81	38.17	38.08	37.94	4.77	0.04	38.06	0.12
40	4.67	5.39	4.55	38.15	38.03	37.91	4.87	0.45	38.03	0.12
50	5.38	4.20	4.13	38.14	38.00	37.88	4.57	0.70	38.01	0.13
60	5.00	5.92	4.46	38.14	37.99	37.87	5.13	0.74	38.00	0.14
70	4.66	4.69	4.88	38.10	37.95	37.83	4.74	0.12	37.96	0.13
80	6.89	6.89	5.05	38.06	37.99	37.83	6.27	1.06	37.96	0.12
90	7.96	6.38	6.50	38.04	37.93	37.81	6.95	0.88	37.92	0.12
100	8.90	6.55	6.23	38.03	37.92	37.82	7.23	1.46	37.92	0.10
200	10.97	8.80	7.34	37.91	37.85	37.71	9.04	1.83	37.82	0.11
300	9.00	9.62	8.74	37.89	37.71	37.59	9.12	0.45	37.73	0.15
400	11.21	6.86	8.19	37.74	37.72	37.55	8.75	2.23	37.67	0.10
500	9.61	10.24	7.61	37.67	37.52	37.54	9.15	1.37	37.57	0.08
600	10.56	14.09	12.10	37.80	37.35	37.47	12.25	1.77	37.54	0.23
700	12.19	12.73	12.87	37.52	37.56	37.24	12.60	0.36	37.44	0.18
800	9.70	12.01	13.49	37.56	37.55	37.13	11.73	1.91	37.41	0.24
900	14.97	12.45	11.12	37.75	37.59	37.46	12.85	1.96	37.60	0.15
1000	9.25	10.75	15.23	37.48	37.19	36.94	11.74	3.11	37.20	0.27

Table B.5. Spectral data for soil sample A25.

Frequency (Hz)	Phase (mrad)			Resistivity (Ω m)			Phase (mrad)		Resistivity (Ω m)	
	M1	M2	M3	M1	M2	M3	μ	σ	μ	σ
0.1	0.53	0.50	0.53	31.53	31.45	31.32	0.52	0.01	31.43	0.10
0.2	0.59	0.57	0.53	31.57	31.44	31.43	0.56	0.03	31.48	0.08
0.3	0.59	0.53	0.60	31.56	31.44	31.35	0.57	0.03	31.45	0.11
0.4	0.61	0.60	0.62	31.54	31.45	31.31	0.61	0.01	31.43	0.12
0.5	0.69	0.67	0.64	31.56	31.48	31.37	0.66	0.03	31.47	0.09
0.6	0.81	0.70	0.69	31.59	31.44	31.41	0.74	0.06	31.48	0.10
0.7	0.68	0.64	0.73	31.55	31.46	31.35	0.68	0.05	31.46	0.10
0.8	0.79	0.79	0.73	31.56	31.50	31.36	0.77	0.03	31.47	0.10
0.9	0.82	0.88	0.76	31.55	31.45	31.35	0.82	0.06	31.45	0.10
1	0.82	0.86	0.91	31.58	31.43	31.34	0.86	0.04	31.45	0.12
2	1.06	1.06	1.21	31.51	31.48	31.36	1.11	0.08	31.45	0.08
3	1.63	1.44	1.28	31.53	31.50	31.36	1.45	0.17	31.46	0.09
4	1.60	1.51	1.46	31.55	31.45	31.41	1.52	0.07	31.47	0.07
5	1.74	1.67	1.88	31.54	31.45	31.37	1.77	0.11	31.46	0.08
6	1.94	1.96	1.87	31.52	31.44	31.33	1.92	0.05	31.43	0.09
7	2.02	2.14	2.12	31.52	31.33	31.33	2.09	0.07	31.39	0.11
8	2.15	2.30	2.30	31.53	31.44	31.28	2.25	0.08	31.42	0.13
9	2.47	2.43	2.23	31.56	31.44	31.35	2.38	0.13	31.45	0.11
10	2.83	2.40	2.32	31.48	31.46	31.34	2.51	0.27	31.43	0.08
20	3.01	3.18	3.50	31.49	31.37	31.30	3.23	0.25	31.39	0.10
30	4.21	3.75	3.54	31.37	31.39	31.25	3.83	0.34	31.34	0.08
40	4.08	4.06	5.02	31.42	31.36	31.25	4.39	0.55	31.34	0.08
50	4.84	4.13	6.25	31.44	31.33	31.24	5.07	1.08	31.34	0.10
60	5.30	7.05	6.71	31.39	31.31	31.18	6.36	0.93	31.30	0.11
70	5.91	7.52	5.13	31.41	31.32	31.19	6.19	1.22	31.31	0.11
80	5.06	5.06	5.06	31.38	31.33	31.22	5.06	0.00	31.31	0.08
90	6.31	5.67	5.87	31.36	31.25	31.20	5.95	0.33	31.27	0.08
100	8.18	6.12	5.77	31.32	31.26	31.16	6.69	1.30	31.25	0.08
200	6.80	7.19	6.97	31.26	31.19	31.30	6.99	0.20	31.25	0.06
300	9.23	6.84	11.38	31.24	31.17	30.96	9.15	2.27	31.12	0.14
400	11.71	15.02	9.67	31.10	30.94	30.99	12.13	2.70	31.01	0.08
500	9.54	8.24	12.01	31.08	30.92	30.75	9.93	1.92	30.92	0.16
600	10.33	8.21	9.42	31.01	31.03	30.94	9.32	1.06	31.00	0.05
700	11.66	15.54	13.73	31.04	30.78	30.76	13.64	1.94	30.86	0.16
800	12.63	10.96	10.02	30.88	31.00	30.95	11.20	1.32	30.94	0.06
900	10.27	14.81	10.07	31.04	30.43	30.78	11.71	2.68	30.75	0.31
1000	9.22	10.86	13.98	30.87	30.93	30.34	11.35	2.42	30.71	0.32

Table B.6. Spectral data for soil sample B5.

Frequency (Hz)	Phase (mrad)			Resistivity (Ω m)			Phase (mrad)		Resistivity (Ω m)	
	M1	M2	M3	M1	M2	M3	μ	σ	μ	σ
0.1	0.32	0.32	0.31	43.53	43.45	43.34	0.32	0.01	43.44	0.09
0.2	0.30	0.30	0.31	43.47	43.47	43.35	0.30	0.01	43.43	0.07
0.3	0.30	0.29	0.27	43.53	43.48	43.32	0.29	0.01	43.44	0.11
0.4	0.32	0.32	0.33	43.50	43.49	43.41	0.32	0.01	43.47	0.05
0.5	0.29	0.23	0.31	43.54	43.49	43.32	0.28	0.04	43.45	0.11
0.6	0.28	0.31	0.33	43.53	43.44	43.37	0.31	0.02	43.45	0.08
0.7	0.25	0.29	0.29	43.52	43.47	43.33	0.28	0.02	43.44	0.10
0.8	0.31	0.29	0.34	43.50	43.46	43.38	0.31	0.02	43.45	0.06
0.9	0.36	0.34	0.34	43.58	43.51	43.34	0.35	0.01	43.48	0.12
1	0.25	0.34	0.38	43.55	43.51	43.38	0.32	0.07	43.48	0.09
2	0.39	0.38	0.39	43.53	43.51	43.39	0.39	0.00	43.48	0.07
3	0.42	0.48	0.44	43.51	43.38	43.39	0.45	0.03	43.43	0.07
4	0.51	0.52	0.45	43.56	43.45	43.37	0.49	0.04	43.46	0.10
5	0.58	0.58	0.56	43.51	43.41	43.39	0.57	0.01	43.44	0.06
6	0.58	0.55	0.55	43.48	43.47	43.39	0.56	0.02	43.44	0.05
7	0.72	0.66	0.66	43.54	43.47	43.39	0.68	0.03	43.47	0.08
8	0.69	0.70	0.73	43.52	43.49	43.37	0.71	0.02	43.46	0.08
9	0.70	0.67	0.64	43.51	43.49	43.36	0.67	0.03	43.45	0.08
10	0.79	0.77	0.75	43.49	43.49	43.37	0.77	0.02	43.45	0.07
20	0.99	1.26	1.23	43.53	43.46	43.32	1.16	0.15	43.44	0.11
30	1.27	1.20	1.44	43.46	43.46	43.36	1.30	0.12	43.42	0.06
40	1.69	1.39	1.46	43.53	43.45	43.35	1.52	0.16	43.44	0.09
50	1.98	1.65	1.69	43.48	43.40	43.34	1.77	0.18	43.41	0.07
60	1.90	1.73	1.65	43.48	43.40	43.35	1.76	0.12	43.41	0.07
70	1.93	1.89	1.67	43.42	43.46	43.35	1.83	0.14	43.41	0.06
80	2.61	2.17	2.96	43.44	43.46	43.37	2.58	0.39	43.42	0.04
90	2.28	2.85	2.77	43.41	43.39	43.33	2.63	0.31	43.38	0.05
100	1.85	2.01	2.30	43.41	43.51	43.31	2.05	0.23	43.41	0.10
200	2.23	2.31	2.54	43.33	43.35	43.25	2.36	0.16	43.31	0.05
300	3.29	3.54	3.99	43.29	43.28	43.23	3.60	0.36	43.27	0.04
400	4.02	3.96	4.20	43.29	44.80	43.21	4.06	0.12	43.76	0.90
500	3.64	3.20	3.82	43.38	43.25	43.12	3.55	0.32	43.25	0.13
600	3.97	3.84	4.64	43.26	43.23	43.16	4.15	0.43	43.22	0.05
700	3.46	3.31	3.18	43.27	43.22	43.06	3.32	0.14	43.18	0.11
800	4.38	4.06	3.83	43.18	43.24	43.22	4.09	0.27	43.22	0.03
900	2.98	3.68	2.89	43.23	43.19	43.13	3.18	0.43	43.18	0.05
1000	4.22	4.32	3.41	43.28	43.20	42.98	3.99	0.50	43.15	0.15

Table B.7. Spectral data for soil sample B10.

Frequency (Hz)	Phase (mrad)			Resistivity (Ω m)			Phase (mrad)		Resistivity (Ω m)	
	M1	M2	M3	M1	M2	M3	μ	σ	μ	σ
0.1	0.47	0.52	0.47	25.03	24.82	24.65	0.48	0.03	24.83	0.19
0.2	0.37	0.32	0.34	25.02	24.82	24.64	0.34	0.03	24.82	0.19
0.3	0.34	0.40	0.32	24.99	24.82	24.63	0.35	0.04	24.81	0.18
0.4	0.35	0.40	0.36	25.00	24.82	24.62	0.37	0.03	24.81	0.19
0.5	0.42	0.38	0.39	25.03	24.83	24.64	0.40	0.03	24.83	0.19
0.6	0.43	0.33	0.43	25.04	24.82	24.63	0.39	0.06	24.83	0.20
0.7	0.38	0.34	0.39	25.07	24.87	24.64	0.37	0.03	24.86	0.21
0.8	0.41	0.41	0.43	25.06	24.84	24.66	0.42	0.01	24.85	0.20
0.9	0.39	0.44	0.35	25.05	24.86	24.69	0.39	0.05	24.87	0.18
1	0.40	0.43	0.96	25.08	24.86	24.65	0.60	0.32	24.86	0.22
2	0.54	0.53	0.57	25.05	24.86	24.62	0.55	0.02	24.84	0.21
3	0.62	0.68	0.57	25.03	24.84	24.66	0.62	0.05	24.84	0.19
4	0.69	0.68	0.78	25.02	24.85	24.63	0.72	0.06	24.84	0.19
5	0.88	0.72	0.85	25.04	24.85	24.66	0.82	0.09	24.85	0.19
6	0.97	0.85	0.94	25.05	24.87	24.64	0.92	0.06	24.85	0.21
7	1.01	0.92	0.83	25.04	24.86	24.66	0.92	0.09	24.86	0.19
8	1.08	0.99	1.01	25.05	24.87	24.65	1.03	0.04	24.86	0.20
9	0.94	1.02	0.99	25.05	24.87	24.67	0.98	0.04	24.86	0.19
10	1.10	1.18	1.16	25.05	24.88	24.66	1.15	0.04	24.86	0.20
20	1.24	1.54	1.50	25.02	24.86	24.65	1.43	0.17	24.84	0.19
30	1.70	1.91	1.53	25.04	24.86	24.67	1.71	0.19	24.86	0.18
40	1.86	1.87	2.37	25.08	24.85	24.67	2.04	0.29	24.87	0.21
50	1.98	1.85	1.80	25.03	24.88	24.65	1.88	0.09	24.85	0.19
60	2.86	2.50	2.21	25.03	24.83	24.63	2.52	0.32	24.83	0.20
70	2.08	2.25	2.31	25.07	24.86	24.66	2.22	0.12	24.86	0.20
80	2.12	2.14	2.31	25.02	24.85	24.63	2.19	0.10	24.83	0.19
90	2.30	2.55	2.39	25.02	24.81	24.63	2.41	0.13	24.82	0.19
100	3.58	2.53	3.06	24.99	24.83	24.63	3.06	0.52	24.82	0.18
200	3.61	3.11	2.52	24.98	24.78	24.62	3.08	0.54	24.79	0.18
300	3.62	3.92	3.94	24.99	24.76	24.57	3.83	0.18	24.77	0.21
400	4.31	4.12	4.22	24.92	24.43	24.57	4.22	0.09	24.64	0.25
500	4.05	3.43	2.94	24.87	24.80	24.70	3.47	0.56	24.79	0.09
600	3.82	4.40	4.62	24.89	24.74	24.55	4.28	0.41	24.73	0.17
700	3.92	3.41	3.60	24.90	24.75	24.55	3.64	0.26	24.73	0.17
800	4.36	4.69	4.23	24.82	24.74	24.45	4.43	0.24	24.67	0.19
900	4.01	4.59	4.00	24.87	24.62	24.54	4.20	0.33	24.68	0.17
1000	3.81	4.49	3.78	24.85	24.70	24.54	4.03	0.40	24.70	0.16

APPENDIX

Table B.8. Spectral data for soil sample B15.

Frequency (Hz)	Phase (mrad)			Resistivity (Ω m)			Phase (mrad)		Resistivity (Ω m)	
	M1	M2	M3	M1	M2	M3	μ	σ	μ	σ
0.1	0.50	0.55	0.53	21.21	21.20	21.18	0.53	0.03	21.20	0.01
0.2	0.35	0.38	0.41	21.21	21.17	21.18	0.38	0.03	21.19	0.02
0.3	0.37	0.39	0.41	21.19	21.16	21.18	0.39	0.02	21.18	0.02
0.4	0.43	0.38	0.41	21.18	21.18	21.20	0.41	0.02	21.18	0.01
0.5	0.42	0.38	0.46	21.17	21.18	21.17	0.42	0.04	21.17	0.00
0.6	0.44	0.41	0.39	21.20	21.16	21.17	0.41	0.03	21.18	0.02
0.7	0.42	0.39	0.41	21.19	21.16	21.17	0.40	0.01	21.18	0.02
0.8	0.43	0.44	0.46	21.18	21.17	21.18	0.44	0.02	21.18	0.01
0.9	0.48	0.43	0.46	21.18	21.14	21.20	0.46	0.03	21.18	0.03
1	0.44	0.44	0.45	21.19	21.16	21.17	0.44	0.01	21.17	0.02
2	0.62	0.52	0.58	21.18	21.17	21.16	0.57	0.05	21.17	0.01
3	0.70	0.70	0.67	21.18	21.16	21.18	0.69	0.02	21.17	0.01
4	0.74	0.77	0.82	21.20	21.14	21.19	0.78	0.04	21.17	0.03
5	0.79	0.75	0.80	21.18	21.13	21.17	0.78	0.03	21.16	0.02
6	0.78	0.78	0.88	21.18	21.13	21.17	0.82	0.05	21.16	0.02
7	0.89	0.91	1.07	21.17	21.12	21.16	0.96	0.10	21.15	0.03
8	1.05	1.00	1.10	21.16	21.12	21.16	1.05	0.05	21.15	0.02
9	1.13	1.15	0.93	21.17	21.14	21.18	1.07	0.12	21.16	0.02
10	1.09	1.15	1.10	21.20	21.15	21.16	1.11	0.03	21.17	0.02
20	1.52	1.46	1.63	21.20	21.14	21.16	1.53	0.09	21.16	0.03
30	1.85	1.80	1.63	21.17	21.14	21.15	1.76	0.11	21.15	0.02
40	2.04	2.36	2.26	21.18	21.13	21.14	2.22	0.16	21.15	0.03
50	2.24	2.01	2.67	21.18	21.13	21.14	2.31	0.33	21.15	0.03
60	2.35	2.47	2.14	21.16	21.11	21.12	2.32	0.17	21.13	0.03
70	3.26	2.77	2.50	21.15	21.10	21.12	2.84	0.39	21.13	0.02
80	2.99	3.47	2.77	21.15	21.11	21.12	3.08	0.36	21.13	0.02
90	3.83	3.03	2.45	21.18	21.09	21.13	3.10	0.69	21.13	0.04
100	2.88	3.38	3.81	21.17	21.12	21.11	3.36	0.47	21.13	0.03
200	5.54	5.26	3.86	21.13	21.07	21.09	4.89	0.91	21.10	0.03
300	3.34	4.12	4.35	21.13	21.04	21.07	3.94	0.53	21.08	0.04
400	6.25	5.18	4.60	21.10	21.06	21.05	5.34	0.84	21.07	0.03
500	5.53	5.52	6.12	21.11	20.94	21.08	5.72	0.34	21.04	0.09
600	5.09	5.01	4.80	21.26	20.99	22.11	4.97	0.15	21.45	0.58
700	5.74	6.47	5.71	21.00	20.95	21.04	5.97	0.43	21.00	0.05
800	6.96	5.81	6.53	21.03	20.98	20.94	6.43	0.58	20.98	0.04
900	5.68	5.43	5.83	20.09	20.98	20.87	5.65	0.20	20.65	0.48
1000	6.20	5.62	5.29	21.10	20.99	20.96	5.70	0.46	21.02	0.08

Table B.9. Spectral data for soil sample B20.

Frequency (Hz)	Phase (mrad)			Resistivity (Ω m)			Phase (mrad)		Resistivity (Ω m)	
	M1	M2	M3	M1	M2	M3	μ	σ	μ	σ
0.1	0.64	0.65	0.63	17.89	17.85	17.82	0.64	0.01	17.85	0.04
0.2	0.52	0.49	0.51	17.86	17.85	17.82	0.51	0.02	17.84	0.02
0.3	0.49	0.53	0.55	17.86	17.86	17.84	0.52	0.03	17.85	0.01
0.4	0.51	0.56	0.57	17.85	17.83	17.80	0.55	0.03	17.82	0.03
0.5	0.48	0.59	0.49	17.86	17.82	17.83	0.52	0.06	17.84	0.02
0.6	0.50	0.54	0.62	17.85	17.85	17.80	0.55	0.06	17.83	0.02
0.7	0.50	0.42	0.51	17.85	17.83	17.80	0.48	0.05	17.83	0.02
0.8	0.42	0.50	0.46	17.85	17.83	17.80	0.46	0.04	17.83	0.02
0.9	0.59	0.57	0.53	17.85	17.85	17.84	0.56	0.03	17.85	0.01
1	0.54	0.49	0.45	17.83	17.84	17.78	0.49	0.04	17.82	0.03
2	0.75	0.56	0.66	17.87	17.82	17.79	0.66	0.10	17.83	0.04
3	0.71	0.75	0.79	17.85	17.81	17.80	0.75	0.04	17.82	0.03
4	0.81	0.87	0.72	17.84	17.81	17.78	0.80	0.08	17.81	0.03
5	0.96	0.89	0.84	17.84	17.83	17.79	0.90	0.06	17.82	0.03
6	0.95	1.01	0.94	17.83	17.82	17.81	0.97	0.03	17.82	0.01
7	0.98	0.95	1.03	17.85	17.82	17.78	0.99	0.04	17.82	0.04
8	1.09	1.15	1.09	17.84	17.82	17.78	1.11	0.04	17.81	0.03
9	1.21	1.27	1.06	17.83	17.83	17.79	1.18	0.11	17.82	0.02
10	1.16	1.17	1.11	17.82	17.82	17.78	1.15	0.03	17.81	0.03
20	1.60	1.58	1.49	17.83	17.80	17.77	1.55	0.06	17.80	0.03
30	1.92	1.89	2.22	17.80	17.78	17.78	2.01	0.18	17.79	0.02
40	2.90	2.09	2.60	17.81	17.83	17.78	2.53	0.41	17.81	0.03
50	1.89	2.65	2.31	17.82	17.80	17.73	2.29	0.38	17.79	0.05
60	3.22	2.76	3.37	17.79	17.78	17.75	3.12	0.31	17.77	0.02
70	2.31	2.80	3.37	17.80	17.78	17.73	2.82	0.53	17.77	0.03
80	3.05	2.45	2.45	17.80	17.78	17.74	2.65	0.35	17.77	0.03
90	2.49	3.07	3.38	17.79	17.76	17.75	2.98	0.45	17.77	0.02
100	4.15	2.94	2.57	17.77	17.78	17.75	3.22	0.83	17.77	0.02
200	3.57	4.67	4.70	17.78	17.75	17.72	4.31	0.65	17.75	0.03
300	5.35	5.80	4.44	17.72	17.70	17.70	5.20	0.70	17.71	0.01
400	4.14	4.64	3.68	18.32	17.70	17.71	4.15	0.48	17.91	0.35
500	4.72	5.58	5.46	17.69	17.60	17.65	5.25	0.47	17.65	0.04
600	4.46	4.59	4.42	17.71	17.68	17.48	4.49	0.09	17.62	0.13
700	5.94	4.46	3.72	17.69	17.75	17.66	4.70	1.13	17.70	0.04
800	5.70	4.17	3.48	17.69	17.66	17.65	4.45	1.13	17.67	0.02
900	4.99	5.89	6.47	18.44	17.59	17.67	5.78	0.74	17.90	0.47
1000	5.63	3.88	5.64	17.68	17.66	17.66	5.05	1.01	17.67	0.01

Table B.10. Spectral data for soil sample B25.

Frequency (Hz)	Phase (mrad)			Resistivity (Ω m)			Phase (mrad)		Resistivity (Ω m)	
	M1	M2	M3	M1	M2	M3	μ	σ	μ	σ
0.1	0.66	0.65	0.67	15.64	15.60	15.57	0.66	0.01	15.60	0.04
0.2	0.52	0.50	0.48	15.64	15.61	15.54	0.50	0.02	15.59	0.05
0.3	0.46	0.42	0.49	15.68	15.56	15.55	0.45	0.04	15.59	0.07
0.4	0.52	0.51	0.53	15.58	15.57	15.53	0.52	0.01	15.56	0.02
0.5	0.46	0.42	0.49	15.59	15.57	15.53	0.46	0.03	15.56	0.03
0.6	0.30	0.34	0.51	15.61	15.56	15.53	0.38	0.11	15.57	0.04
0.7	0.51	0.50	0.47	15.59	15.57	15.53	0.49	0.02	15.56	0.03
0.8	0.49	0.52	0.56	15.60	15.57	15.53	0.52	0.03	15.57	0.03
0.9	0.52	0.56	0.53	15.61	15.59	15.55	0.54	0.02	15.58	0.03
1	0.54	0.50	0.57	15.61	15.61	15.55	0.53	0.03	15.59	0.03
2	0.58	0.65	0.62	15.59	15.56	15.56	0.62	0.04	15.57	0.02
3	0.63	0.83	0.74	15.60	15.57	15.53	0.74	0.10	15.57	0.03
4	0.78	0.83	0.90	15.58	15.57	15.52	0.83	0.06	15.56	0.03
5	1.06	1.23	0.87	15.61	15.57	15.53	1.05	0.18	15.57	0.04
6	0.97	0.92	0.98	15.56	15.58	15.51	0.96	0.03	15.55	0.04
7	0.98	1.06	1.17	15.61	15.56	15.53	1.07	0.10	15.56	0.04
8	1.27	1.54	1.18	15.59	15.54	15.52	1.33	0.19	15.55	0.04
9	1.15	1.30	1.45	15.58	15.56	15.52	1.30	0.15	15.55	0.03
10	1.33	1.34	1.26	15.63	15.56	15.51	1.31	0.04	15.57	0.06
20	1.68	1.96	1.81	15.59	15.53	15.50	1.81	0.14	15.54	0.05
30	2.11	1.88	2.40	15.56	15.53	15.50	2.13	0.26	15.53	0.03
40	2.63	2.33	2.07	15.58	15.54	15.51	2.34	0.28	15.54	0.03
50	2.77	2.51	3.03	15.56	15.53	15.49	2.77	0.26	15.53	0.03
60	2.58	2.13	2.47	15.58	15.52	15.50	2.40	0.24	15.53	0.04
70	3.07	3.34	3.55	15.54	15.51	15.48	3.32	0.24	15.51	0.03
80	3.23	2.60	3.25	15.53	15.53	15.50	3.02	0.37	15.52	0.02
90	2.87	2.52	3.29	15.57	15.55	15.47	2.89	0.38	15.53	0.05
100	3.43	3.26	4.21	15.55	15.51	15.47	3.63	0.51	15.51	0.04
200	4.15	4.24	4.65	15.53	15.49	15.45	4.34	0.27	15.49	0.04
300	4.38	3.29	4.23	15.49	15.49	15.44	3.97	0.59	15.48	0.03
400	3.94	4.14	5.10	15.50	15.97	15.43	4.39	0.62	15.63	0.29
500	4.14	4.72	4.29	15.48	15.38	15.42	4.38	0.30	15.43	0.05
600	5.60	5.50	6.09	15.43	15.40	15.40	5.73	0.32	15.41	0.02
700	5.13	6.20	4.66	15.47	15.41	15.43	5.33	0.79	15.44	0.03
800	4.37	4.07	4.63	15.47	15.86	15.40	4.36	0.28	15.57	0.25
900	5.82	5.75	5.51	15.36	15.41	15.39	5.69	0.16	15.39	0.02
1000	5.82	6.75	5.16	15.05	15.42	15.14	5.91	0.80	15.20	0.20

Table B.11. Spectral data for soil sample C5.

Frequency	Phase (mrad)			Resistivity (Ω m)			Phase (mrad)		Resistivity (Ω m)	
(Hz)	M1	M2	M3	M1	M2	M3	μ	σ	μ	σ
0.1	0.74	0.73	0.88	6.44	6.43	6.40	0.78	0.08	6.42	0.02
0.2	0.81	0.73	0.68	6.42	6.39	6.41	0.74	0.07	6.41	0.01
0.3	0.81	0.73	0.88	6.45	6.40	6.41	0.81	0.08	6.42	0.03
0.4	0.47	0.56	0.71	6.39	6.39	6.42	0.58	0.12	6.40	0.02
0.5	0.50	0.69	0.68	6.38	6.39	6.38	0.62	0.11	6.38	0.01
0.6	0.60	0.48	0.58	6.39	6.39	6.39	0.55	0.06	6.39	0.00
0.7	0.56	0.63	0.55	6.44	6.38	6.39	0.58	0.05	6.40	0.03
0.8	0.47	0.51	0.49	6.39	6.38	6.40	0.49	0.02	6.39	0.01
0.9	0.42	0.75	0.37	6.41	6.39	6.39	0.51	0.21	6.39	0.01
1	0.49	0.36	0.26	6.40	6.38	6.38	0.37	0.12	6.39	0.01
2	0.39	0.44	0.26	6.38	6.37	6.37	0.36	0.09	6.37	0.01
3	0.37	0.22	0.20	6.38	6.38	6.36	0.26	0.09	6.37	0.01
4	0.28	0.07	0.39	6.38	6.37	6.37	0.25	0.16	6.37	0.01
5	0.36	0.27	0.14	6.37	6.39	6.36	0.26	0.11	6.37	0.02
6	0.20	0.14	0.41	6.39	6.38	6.38	0.25	0.14	6.39	0.01
7	0.38	0.22	0.23	6.39	6.36	6.35	0.28	0.09	6.37	0.02
8	0.29	0.26	0.49	6.40	6.37	6.38	0.35	0.12	6.38	0.02
9	0.23	0.23	0.46	6.39	6.37	6.36	0.31	0.13	6.37	0.01
10	0.24	0.23	0.13	6.38	6.36	6.35	0.20	0.06	6.37	0.02
20	0.25	0.30	0.36	6.41	6.37	6.38	0.30	0.06	6.38	0.02
30	0.34	0.26	0.28	6.38	6.38	6.35	0.29	0.04	6.37	0.02
40	0.28	0.33	0.26	6.40	6.37	6.36	0.29	0.04	6.38	0.02
50	0.49	0.41	0.47	6.39	6.37	6.35	0.45	0.04	6.37	0.02
60	0.50	0.52	0.47	6.39	6.36	6.34	0.50	0.02	6.36	0.02
70	0.47	0.51	0.34	6.38	6.39	6.35	0.44	0.09	6.37	0.02
80	0.51	0.57	0.67	6.41	6.36	6.35	0.58	0.08	6.37	0.03
90	0.48	0.50	0.59	6.39	6.37	6.38	0.52	0.06	6.38	0.01
100	0.57	0.72	0.63	6.38	6.38	6.36	0.64	0.07	6.37	0.02
200	0.68	0.69	0.70	6.40	6.36	6.34	0.69	0.01	6.37	0.03
300	0.60	0.63	0.73	6.37	6.48	6.37	0.65	0.07	6.41	0.07
400	1.00	0.73	0.84	6.40	6.35	6.38	0.86	0.14	6.37	0.02
500	0.55	0.66	0.71	6.40	6.39	6.35	0.64	0.08	6.38	0.03
600	1.02	0.71	0.73	6.41	6.37	6.36	0.82	0.18	6.38	0.03
700	0.93	0.87	0.91	6.39	6.36	6.35	0.90	0.03	6.37	0.02
800	0.82	0.96	0.94	6.39	6.38	6.04	0.91	0.08	6.27	0.20
900	0.98	0.99	1.11	6.39	6.36	6.33	1.03	0.07	6.36	0.03
1000	1.01	0.92	0.82	6.40	6.37	6.37	0.92	0.09	6.38	0.01

Table B.12. Spectral data for soil sample C10.

Frequency	Phase			Resistivity			Phase		Resistivity	
(Hz)	(mrad)			(Ω m)			(mrad)		(Ω m)	
	M1	M2	M3	M1	M2	M3	μ	σ	μ	σ
0.1	0.98	0.90	1.10	4.26	4.26	4.24	0.99	0.10	4.26	0.02
0.2	0.78	1.35	1.14	4.27	4.26	4.24	1.09	0.29	4.26	0.01
0.3	0.93	0.62	0.92	4.27	4.27	4.27	0.82	0.18	4.27	0.00
0.4	0.75	0.59	0.48	4.27	4.26	4.25	0.61	0.14	4.26	0.01
0.5	1.05	1.16	0.94	4.25	4.27	4.28	1.05	0.11	4.27	0.01
0.6	0.81	0.92	0.42	4.10	4.26	4.25	0.72	0.26	4.20	0.09
0.7	0.76	0.47	1.13	4.21	4.25	4.26	0.78	0.33	4.24	0.02
0.8	0.61	0.61	0.59	4.27	4.28	4.26	0.61	0.01	4.27	0.01
0.9	0.59	0.74	0.22	4.26	4.27	4.26	0.52	0.27	4.26	0.01
1	0.49	0.76	1.03	4.26	4.25	4.25	0.76	0.27	4.25	0.01
2	0.93	0.70	0.79	4.29	4.26	4.24	0.80	0.12	4.26	0.02
3	0.85	0.70	0.54	4.28	4.26	4.25	0.70	0.16	4.27	0.01
4	0.42	1.02	0.51	4.26	4.26	4.28	0.65	0.32	4.26	0.01
5	0.52	0.46	0.32	4.27	4.27	4.27	0.43	0.10	4.27	0.00
6	0.49	0.49	0.49	4.29	4.27	4.26	0.49	0.00	4.27	0.02
7	1.20	0.86	0.63	4.27	4.26	4.27	0.90	0.29	4.27	0.01
8	0.73	0.16	0.54	4.27	4.26	4.25	0.48	0.30	4.26	0.01
9	0.38	0.37	0.32	4.27	4.26	4.27	0.36	0.04	4.26	0.01
10	0.32	0.24	0.24	4.27	4.28	4.27	0.27	0.05	4.27	0.01
20	0.36	0.42	0.33	4.27	4.27	4.26	0.37	0.05	4.27	0.00
30	0.52	0.45	0.45	4.28	4.26	4.27	0.47	0.04	4.27	0.01
40	0.49	0.63	0.58	4.26	4.26	4.25	0.56	0.07	4.26	0.01
50	0.54	0.41	0.47	4.27	4.24	4.23	0.47	0.07	4.25	0.02
60	0.62	0.57	0.69	4.24	4.25	4.27	0.63	0.06	4.25	0.02
70	0.61	0.56	0.75	4.26	4.26	4.28	0.64	0.10	4.27	0.01
80	0.68	0.73	0.59	4.25	4.25	4.27	0.67	0.07	4.25	0.01
90	0.52	0.59	0.63	4.27	4.28	4.27	0.58	0.05	4.27	0.00
100	0.66	0.57	0.56	4.28	4.26	4.24	0.60	0.06	4.26	0.02
200	0.85	0.87	0.95	4.25	4.27	4.26	0.89	0.05	4.26	0.01
300	0.76	0.90	0.71	4.24	4.26	4.23	0.79	0.09	4.24	0.01
400	1.01	0.81	0.80	4.26	4.26	4.27	0.87	0.12	4.26	0.01
500	1.21	1.06	0.83	4.25	4.23	4.26	1.03	0.19	4.24	0.02
600	0.91	0.83	0.93	4.25	4.26	4.27	0.89	0.05	4.26	0.01
700	1.03	0.98	1.15	3.91	4.31	4.28	1.05	0.09	4.17	0.22
800	1.14	1.32	1.01	4.25	4.24	4.26	1.16	0.16	4.25	0.01
900	1.11	0.88	1.00	4.26	4.24	4.27	1.00	0.11	4.26	0.01
1000	0.93	1.12	1.40	4.22	4.26	4.26	1.15	0.24	4.25	0.02

Table B.13. Spectral data for soil sample C15.

Frequency (Hz)	Phase (mrad)			Resistivity (Ω m)			Phase (mrad)		Resistivity (Ω m)	
	M1	M2	M3	M1	M2	M3	μ	σ	μ	σ
0.1	1.23	1.10	1.02	4.02	4.03	4.03	1.12	0.10	4.02	0.01
0.2	0.94	1.09	1.30	4.02	4.02	4.01	1.11	0.18	4.02	0.01
0.3	1.00	1.05	1.11	4.01	4.02	4.01	1.05	0.05	4.01	0.00
0.4	0.84	1.12	1.16	4.01	4.01	4.02	1.04	0.18	4.01	0.01
0.5	0.71	0.88	1.18	4.00	4.01	4.01	0.92	0.24	4.00	0.01
0.6	0.92	0.89	0.88	4.00	4.00	3.99	0.89	0.02	4.00	0.00
0.7	0.46	0.19	0.49	4.01	4.00	4.01	0.38	0.16	4.01	0.01
0.8	0.69	0.67	0.81	4.00	4.01	4.00	0.72	0.07	4.00	0.00
0.9	0.62	0.66	0.69	4.00	4.01	4.01	0.66	0.04	4.01	0.00
1	0.56	0.62	0.65	4.00	3.99	4.01	0.61	0.05	4.00	0.01
2	0.44	0.56	0.47	4.00	3.99	4.00	0.49	0.06	3.99	0.00
3	0.80	0.48	0.42	3.99	4.00	3.99	0.57	0.20	3.99	0.00
4	0.56	0.53	0.78	4.00	4.00	3.99	0.62	0.14	3.99	0.00
5	0.68	0.39	0.46	4.00	4.00	3.99	0.51	0.15	4.00	0.01
6	0.13	0.23	0.26	4.00	3.99	3.99	0.20	0.07	4.00	0.01
7	0.23	0.30	0.27	4.00	4.01	4.00	0.27	0.04	4.00	0.01
8	0.44	0.23	0.21	3.99	3.99	3.99	0.29	0.13	3.99	0.00
9	0.34	0.20	0.30	4.01	3.99	3.98	0.28	0.07	3.99	0.01
10	0.51	0.32	0.28	4.00	3.99	3.99	0.37	0.12	3.99	0.01
20	0.24	0.16	0.29	4.01	4.00	3.98	0.23	0.07	4.00	0.01
30	0.25	0.23	0.33	4.00	3.99	3.98	0.27	0.05	3.99	0.01
40	0.38	0.26	0.32	4.00	4.00	3.98	0.32	0.06	3.99	0.01
50	0.45	0.49	0.38	3.99	3.99	3.99	0.44	0.06	3.99	0.00
60	0.43	0.28	0.38	3.99	4.02	3.99	0.36	0.08	4.00	0.02
70	0.60	0.63	0.67	4.00	4.00	3.98	0.63	0.04	3.99	0.01
80	0.51	0.34	0.51	3.99	3.99	3.99	0.45	0.10	3.99	0.00
90	0.35	0.41	0.41	4.00	4.00	3.98	0.39	0.03	3.99	0.01
100	0.62	0.51	0.57	4.01	4.00	3.98	0.57	0.05	3.99	0.01
200	0.68	0.58	0.41	4.00	4.00	3.99	0.56	0.14	4.00	0.00
300	0.72	0.77	0.66	3.99	3.99	3.98	0.72	0.06	3.99	0.00
400	0.75	0.61	0.78	3.94	3.99	3.99	0.71	0.09	3.97	0.03
500	1.15	1.21	1.13	4.01	3.99	3.99	1.17	0.04	4.00	0.01
600	1.31	1.21	0.98	4.00	3.99	3.99	1.17	0.17	3.99	0.01
700	0.98	1.32	0.83	3.99	3.99	4.08	1.05	0.25	4.02	0.05
800	1.43	0.85	1.21	3.99	3.98	3.99	1.16	0.30	3.98	0.00
900	0.95	1.23	0.69	3.98	3.99	3.98	0.95	0.27	3.98	0.01
1000	1.23	0.95	1.66	3.98	4.01	4.00	1.28	0.35	4.00	0.02

Table B.14. Spectral data for soil sample C20.

Frequency (Hz)	Phase (mrad)			Resistivity (Ω m)			Phase (mrad)		Resistivity (Ω m)	
	M1	M2	M3	M1	M2	M3	μ	σ	μ	σ
0.1	1.23	1.69	1.64	3.63	3.64	3.62	1.52	0.25	3.63	0.01
0.2	0.97	1.09	0.95	3.62	3.64	3.64	1.00	0.07	3.63	0.01
0.3	1.00	0.84	0.68	3.63	3.62	3.62	0.84	0.16	3.62	0.01
0.4	0.84	0.74	0.90	3.61	3.61	3.61	0.83	0.08	3.61	0.00
0.5	0.51	0.69	0.63	3.62	3.62	3.61	0.61	0.09	3.61	0.01
0.6	0.91	0.51	0.74	3.63	3.61	3.62	0.72	0.20	3.62	0.01
0.7	0.59	0.58	0.94	3.62	3.62	3.61	0.70	0.21	3.62	0.00
0.8	0.72	0.68	0.75	3.62	3.61	3.61	0.72	0.04	3.61	0.00
0.9	0.61	0.52	0.53	3.61	3.63	3.60	0.55	0.05	3.62	0.02
1	0.73	0.61	0.74	3.62	3.61	3.62	0.69	0.07	3.62	0.00
2	0.32	0.74	0.44	3.61	3.62	3.60	0.50	0.21	3.61	0.01
3	0.11	0.45	0.52	3.62	3.62	3.61	0.36	0.22	3.61	0.00
4	0.66	0.41	0.41	3.61	3.61	3.60	0.49	0.15	3.61	0.00
5	0.59	0.24	0.64	3.61	3.61	3.62	0.49	0.22	3.61	0.01
6	0.36	0.63	0.57	3.61	3.62	3.60	0.52	0.14	3.61	0.01
7	0.46	0.35	0.48	3.61	3.60	3.60	0.43	0.07	3.60	0.00
8	0.42	0.49	0.26	3.60	3.61	3.59	0.39	0.11	3.60	0.01
9	0.25	0.32	0.30	3.61	3.60	3.60	0.29	0.04	3.60	0.00
10	0.33	0.26	0.30	3.60	3.62	3.60	0.30	0.03	3.61	0.01
20	0.54	0.55	0.51	3.61	3.61	3.60	0.53	0.02	3.61	0.01
30	0.50	0.65	0.68	3.61	3.60	3.59	0.61	0.09	3.60	0.01
40	0.80	0.77	1.00	3.60	3.59	3.60	0.86	0.12	3.60	0.00
50	0.54	0.64	0.63	3.61	3.60	3.59	0.60	0.05	3.60	0.01
60	0.71	0.83	0.96	3.62	3.61	3.59	0.83	0.13	3.61	0.01
70	0.66	0.56	0.67	3.60	3.60	3.59	0.63	0.06	3.60	0.00
80	0.48	0.54	0.60	3.61	3.60	3.60	0.54	0.06	3.60	0.01
90	0.77	0.69	0.53	3.60	3.61	3.60	0.66	0.13	3.60	0.00
100	0.87	0.62	0.82	3.64	3.60	3.59	0.77	0.13	3.61	0.02
200	0.99	1.02	1.21	3.61	3.61	3.59	1.07	0.12	3.60	0.01
300	0.88	1.20	0.97	3.60	3.59	3.59	1.02	0.17	3.59	0.01
400	1.35	1.10	0.95	3.61	3.61	3.60	1.13	0.20	3.60	0.01
500	1.16	1.02	1.26	3.62	3.60	3.60	1.15	0.12	3.60	0.01
600	1.38	1.18	1.08	3.60	3.60	3.59	1.21	0.15	3.60	0.01
700	1.05	0.91	0.90	3.60	3.70	3.59	0.95	0.08	3.63	0.06
800	0.97	1.13	1.34	3.60	3.59	3.58	1.14	0.18	3.59	0.01
900	1.57	1.07	1.32	3.60	3.59	3.60	1.32	0.25	3.60	0.01
1000	1.13	0.93	1.49	3.60	3.59	3.60	1.18	0.29	3.60	0.01

Table B.15. Spectral data for soil sample C25.

Frequency (Hz)	Phase (mrad)			Resistivity (Ω m)			Phase (mrad)		Resistivity (Ω m)	
	M1	M2	M3	M1	M2	M3	μ	σ	μ	σ
0.1	1.64	1.44	1.56	3.21	3.21	3.21	1.54	0.10	3.21	0.00
0.2	0.97	1.28	1.42	3.21	3.22	3.21	1.23	0.23	3.22	0.01
0.3	0.97	1.06	1.42	3.21	3.21	3.21	1.15	0.24	3.21	0.00
0.4	1.23	1.04	1.17	3.21	3.20	3.20	1.15	0.10	3.20	0.00
0.5	1.10	1.23	0.84	3.20	3.20	3.20	1.05	0.20	3.20	0.00
0.6	1.08	1.36	1.01	3.20	3.20	3.21	1.15	0.18	3.21	0.01
0.7	1.14	0.78	0.86	3.20	3.20	3.20	0.93	0.19	3.20	0.00
0.8	0.96	0.95	1.06	3.20	3.20	3.20	0.99	0.06	3.20	0.00
0.9	0.97	0.80	0.87	3.20	3.20	3.21	0.88	0.08	3.21	0.00
1	0.75	0.71	0.77	3.20	3.22	3.19	0.74	0.03	3.20	0.01
2	0.71	0.61	0.65	3.20	3.20	3.20	0.66	0.05	3.20	0.00
3	0.56	0.60	0.55	3.19	3.19	3.20	0.57	0.02	3.20	0.00
4	0.25	0.39	0.35	3.19	3.20	3.19	0.33	0.07	3.19	0.00
5	0.51	0.50	0.68	3.20	3.20	3.19	0.56	0.10	3.20	0.00
6	0.47	0.58	0.47	3.20	3.20	3.19	0.51	0.06	3.20	0.01
7	0.28	0.46	0.46	3.19	3.19	3.19	0.40	0.10	3.19	0.00
8	0.64	0.65	0.27	3.19	3.19	3.20	0.52	0.22	3.19	0.01
9	0.53	0.46	0.43	3.19	3.20	3.19	0.47	0.05	3.19	0.00
10	0.43	0.49	0.43	3.20	3.21	3.20	0.45	0.03	3.20	0.01
20	0.67	0.42	0.56	3.21	3.19	3.19	0.55	0.13	3.19	0.01
30	0.51	0.59	0.63	3.20	3.19	3.19	0.57	0.06	3.20	0.01
40	0.66	0.49	0.48	3.20	3.19	3.19	0.54	0.10	3.19	0.00
50	0.56	0.50	0.62	3.20	3.19	3.19	0.56	0.06	3.19	0.01
60	0.88	0.74	0.66	3.19	3.19	3.18	0.76	0.11	3.18	0.01
70	0.70	0.75	0.82	3.20	3.19	3.19	0.75	0.06	3.19	0.00
80	0.80	0.72	0.91	3.20	3.19	3.19	0.81	0.09	3.19	0.01
90	0.61	0.46	0.62	3.19	3.20	3.17	0.56	0.09	3.19	0.01
100	0.69	0.82	0.89	3.19	3.19	3.19	0.80	0.10	3.19	0.00
200	0.81	0.72	0.98	3.19	3.18	3.19	0.84	0.13	3.19	0.00
300	0.67	0.99	1.12	3.19	3.19	3.19	0.93	0.23	3.19	0.00
400	0.86	1.00	0.90	3.20	3.19	3.19	0.92	0.07	3.19	0.01
500	1.07	1.27	1.44	3.20	3.19	3.18	1.26	0.18	3.19	0.01
600	1.64	1.89	1.15	3.19	3.18	3.18	1.56	0.38	3.19	0.01
700	0.90	1.59	1.50	3.19	3.18	3.19	1.33	0.38	3.19	0.00
800	1.19	1.33	1.64	3.20	3.18	3.19	1.39	0.23	3.19	0.01
900	1.42	1.56	2.08	3.19	3.19	3.17	1.69	0.34	3.19	0.01
1000	2.07	1.20	1.25	3.20	3.19	3.19	1.51	0.49	3.19	0.00

APPENDIX B.4   SUMMARY OF COLE-COLE PARAMETERS FROM REPEATED MEASUREMENTS

Table B.16. Cole-Cole parameters obtained from inversion of each single ϕ-spectra. Note each repeated measurement has been analyzed individually.

Sample	Measurement 1						Measurement 2						Measurement 3					
	m	Δm	c	Δc	tau μs	Δtau μs	m	Δm	c	Δc	tau μs	Δtau μs	m	Δm	c	Δc	tau μs	Δtau μs
A5	0.0467	0.0160	0.450	0.070	45.2	56.6	0.0419	0.0107	0.444	0.061	69.4	66.2	0.0294	0.0035	0.555	0.057	259	90.4
A10	0.0343	0.0020	0.474	0.027	150	96.7	0.0337	0.0038	0.588	0.058	269	83.3	0.0359	0.0049	0.559	0.061	224	89
A15	0.0335	0.0012	0.600	0.001	333	51	0.0458	0.0138	0.574	0.119	164	143	0.0454	0.0099	0.600	0.003	85	61.8
A20	0.0436	0.0061	0.595	0.065	218	84.2	0.0628	0.0195	0.497	0.071	59	61	0.0447	0.0016	0.600	0.001	150	1300
A25	0.0452	0.0063	0.561	0.053	153	63.9	0.0793	0.0661	0.466	0.132	25.9	73.7	0.0611	0.0197	0.501	0.076	62.1	66.3
B5	0.0165	0.0028	0.560	0.060	133.5	67.5	0.0177	0.0031	0.540	0.053	102.8	55.5	0.0145	0.0010	0.600	0.000	230	40
B10	0.0171	0.0016	0.561	0.041	214	58.4	0.0249	0.0051	0.461	0.046	56.6	41.8	0.0204	0.0041	0.481	0.060	110	76.3
B15	0.0261	0.0057	0.562	0.069	107	69	0.0225	0.0025	0.592	0.043	157	48.3	0.0289	0.0065	0.520	0.054	65.3	46.4
B20	0.0274	0.0065	0.493	0.063	80.1	64.5	0.0189	0.0100	0.600	0.010	252.7	38.3	0.0234	0.0059	0.510	0.083	130	108
B25	0.0295	0.0062	0.461	0.049	62.7	47.6	0.0254	0.0011	0.519	0.026	100	571	0.0218	0.0022	0.522	0.044	212	63.9
C5	0.0070	0.0077	0.422	0.175	19	78.2	0.0066	0.0009	0.400	0.000	21.5	13.2	0.0043	0.0017	0.516	0.126	104	122
C10	0.0056	0.0018	0.474	0.097	99.5	96	0.0069	0.0048	0.417	0.146	39.4	103	0.0070	0.0001	0.423	0.028	38	7.3
C15	0.0070	0.0002	0.507	0.042	30.7	5	0.0070	0.0002	0.500	0.000	24.5	4.5	0.0070	0.0002	0.487	0.063	24.7	6.1
C20	0.0069	0.0040	0.456	0.160	76.2	152	0.0074	0.0003	0.400	0.000	50	151	0.0080	0.0002	0.404	0.031	55.9	16.3
C25	0.0090	0.0003	0.440	0.052	28.2	7.8	0.0090	0.0002	0.475	0.040	31.3	5.8	0.0090	0.0002	0.469	0.036	39	7.6

APPENDIX C.1   WAVELET TRANSFORM

In this section the basics of wavelet transform for denoising purposes will be given briefly. The purpose here is to provide background continuity to the terminologies used in the thesis regarding wavelet based denoising methods. For detailed discussions see Daubechies (1992), Donoho & Johnstone (1995), Jansen (2001), and Mallat (2009).

Let $\psi_{a,b}(x)$ be a family of child wavelets defined as:

$$\psi_{a,b}(t) = \frac{1}{\sqrt{|a|}} \psi^* \left(\frac{t-b}{a} \right), \quad a,b \in \mathbb{R}, \, a > 0 \tag{C.1}$$

where, a and b are the dilation and translation parameter respectively, and $\psi^*(t)$ is the complex conjugate of the analysing wavelet function $\psi(t)$, also referred to as the mother wavelet. It follows that any wavelet has to satisfy the following set of criterion:

$$\int_{-\infty}^{\infty} \psi(t) \, dt = 0 \quad, \tag{C.2}$$

$$\int_{-\infty}^{\infty} |\psi(t)|^2 \, dt < \infty \quad, \tag{C.3}$$

$$C = \int_{-\infty}^{\infty} \frac{|\Psi(\omega)|^2}{|\omega|} d\omega < \infty \quad, \tag{C.4}$$

where, $\Psi(\omega)$ is the Fourier transform of $\psi(t)$, C is the admissibility constant dependent upon the chosen wavelet, and Eq. C.4 is known as the admissibility condition. In principle, there is a range of mother wavelets which can be utilized to perform the wavelet transform. Some of these are the Haar, Daubechies, Coiflets, Symlet, Biorthogonal, and *etc* [see Daubechies, 1992; Jansen, 2001]. In the present work, the Haar wavelet has been utilized due to its similarity with TDIP signals and hence description will be limited to this only. The Haar wavelet's mother function is described by:

$$\psi(t) = \begin{cases} 1, & 0 \leq t < 0.5; \\ -1, & 0.5 \leq t < 1; \\ 0, & \text{otherwise.} \end{cases} \tag{C.5}$$

The Haar wavelet is the simplest possible wavelet and as noted is discontinuous. Another important feature defining any wavelet is its scaling function, $\varphi(t)$. The $\varphi(t)$ for the Haar wavelet is given by:

$$\varphi(t) = \begin{cases} 1, & 0 \leq t < 1; \\ 0, & \text{otherwise.} \end{cases} \tag{C.6}$$

For a time-varying signal *f*(t), the continuous wavelet transform (CWT) is defined as:

$$\mathrm{CWT}(a,b) = \int_{-\infty}^{\infty} f(t)\psi_{a,b}\ dt \tag{C.7}$$

In other words, the CWT of a function is the convolution of the function with a set of child wavelets generated by the mother wavelet. These wavelets continuously dilate and translate the function over the whole time series. Provided that the admissibility criterion is satisfied, the original function can be obtained from Eq. C.7 by:

$$f(t) = \frac{1}{C}\int_{-\infty}^{\infty}\int_{0}^{\infty}\psi\left(\frac{t-b}{a}\right)\mathrm{CWT}(a,b)\frac{da}{a^2}db \tag{C.8}$$

In practice, however, all signals are acquired at discrete time intervals. Hence, the discrete wavelet transform (DWT) is commonly utilized. Implementation of DWT is achieved by restrictions on the values of a, and b such that:

$$a = \alpha_o^m\ , \tag{C.9}$$

and,

$$b = n\beta_o\alpha_o^m\ , \tag{C.10}$$

where, $n, m \in \mathbb{Z}$ and control the dilation and translation effects respectively. Usually, the values of α_o and β_o are fixed to 2 and 1 respectively [see Daubechies, 1992]. In essence, wavelet transform involves convolution of the input signal by a distribution of low and high pass filters, whereby the scaling function provides the former effect and the wavelet function the latter. In this regard, the scaling function provides the approximate coefficients, while the wavelet function provides the detail coefficients. The approximate coefficients in each level are further worked upon in each successive level by another combination of low and high pass filters. The drawback with DWT is that it has poor translation-invariance properties due to the down-sampling and up-sampling schemes it employs in each decomposition and reconstruction level respectively. This is overcome by the undecimated wavelet transform (UWT). UWT does not perform down-sampling of the approximate and detail coefficients at each level thereby maintaining the same length as the original signal. Instead, UWT up-samples the coefficients of the low-pass and high-pass filters at each level [Coifman & Donoho, 1995].

Of course, the intention with these wavelet transforms is to perform signal denoising, which is carried out as follows. The denoising of the input signal is achieved in decomposition phase by thresholding the noisy wavelet coefficients. Here two types of thresholding are possible: a) soft, and b) hard. Soft thresholding [see Donoho & Johnstone, 1995] shrinks the wavelet coefficients towards zero by a threshold value, λ, if the former is greater than the latter, and sets all wavelength coefficients $\leq\lambda$ to

zero. This approach generally results in less artefacts and preserves smoothness in the data. On the contrary, in hard thresholding the wavelet coefficients below λ are made zero while those $\geq\lambda$ remain unchanged. For treatment of TDIP data in the present work soft thresholding has been utilized. The choice of λ is very important and there are several algorithms, which can be used for its estimation. Some of these are based on the Stein's Unbiased Risk Estimator (SURE), Hybrid, Universal, and Minimax algorithms [see Ogden, 1997]. For denoising in the TDIP system, the SURE algorithm in wavelet analysis worked by Donoho & Johnstone (1995) after Stein (1981) is utilized. This is available as an in-built algorithm in LabVIEW. Moreover, λ can either be kept constant or varied at each level of the wavelet decomposition level. For the TDIP system, the noise variances are estimated from the wavelet coefficients in the first level.

Once the thresholding has been applied, the signal is reconstructed using the inverse UWT to yield the denoised signal.

APPENDIX D.1   FURTHER DETAILS ON SELF POTENTIAL SURVEYING

D.1.1 Ag|AgCl Electrode Assembly and Verifications

The time consuming task in SP surveying is usually the cleaning and routine cross-calibration of common field worthy non-polarizable electrodes, resulting in low turnover, especially if a significant waiting period is required prior to taking measurements. Several studies have demonstrated that the ECG medical Ag|AgCl electrodes can be used for geoelectrical applications in different environments and structures [*e.g.*, Sass & Viles, 2010; Consentino *et*. *al*., 2011]. Also, the use of these electrodes has been demonstrated in Chapter 5, where they were utilized as potential electrodes for SIP studies of synthetic laboratory soils. For the SP study reported in Chapter 7, the 3M™ Red Dot™ Ag|AgCl electrodes were utilized as the non-polarizable electrodes. This was achieved in the following manner. Eight sets of hollow PVC tubes with a flanged base were constructed allowing the Ag|AgCl electrodes to be snapped onto a metallic contact on the base. This was then connected to an insulated copper wire running inside the hollow tube, as shown schematically in Fig. D.1.
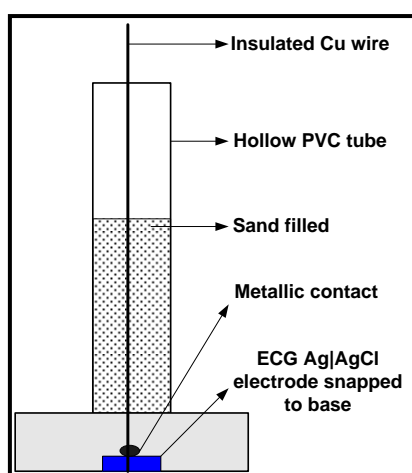
Figure D.1. Schematic of the ECG Ag|AgCl electrode based assembly for self potential surveying work carried out in the thesis.

To provide stability to the assembly, a sand fill was added into the hollow PVC as counterweight. The important feature here is the robust manner in which the disposable Ag|AgCl electrodes can be replaced from the assembly, allowing relatively quicker set-up in field when changing stations. Consistency amongst random Ag|AgCl electrodes was verified in the laboratory by placing the complete assemblies in close proximity on saturated mixtures of sand/clay and recording the potential differences between them. This cross-calibration was repeated for several new sets of electrodes. Integrity of these sensors in terms of their laboratory calibrations are presented in Fig. D.2.
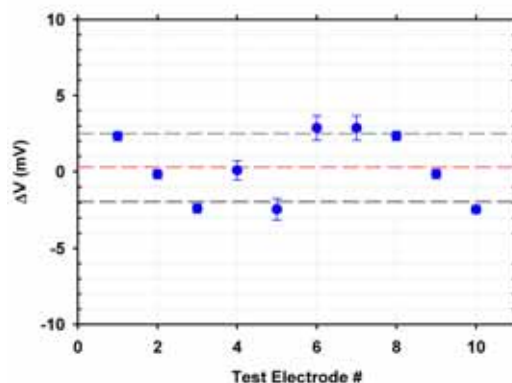
Figure D.2. Cross-calibration of Ag|AgCl medical electrodes. The error bars correspond to one standard deviation from the mean (blue dots), after continuous monitoring of ~10 mins. The dashed red and black lines represent the mean and standard deviation respectively of the observed variability amongst all test electrodes.

Each test electrode has been measured continuously with respect to a single Ag|AgCl electrode, adopted as a reference, over periods ranging from 10 – 15 mins. In this manner, Fig. D.2 illustrates the variabilities amongst each of the easily available electrodes. Generally, they agree within $\pm$ ~2 mV of each other, which is within the acceptable limit for field deployment. An important requirement for the use of these electrodes, however, is that the soil surface should be just wet enough such that a proper electrical contact can be established. If the surface is muddy with excess water, then the performance of these electrodes is poor. However, such situations were not encountered during field deployment. The ground preparations needed for efficient use of these electrode assemblies, as well as further details on SP measurements conducted for the study in Chapter 7 are described in next section.

D.1.2 Ground Preparations and Measurements

Prior to conducting SP measurements, the ground surface at each marked station was cleared of vegetation and an area of 10 cm $\times$ 10 cm was dug out to a depth of about 5 cm, exposing firm surface soils. The freshly exposed surfaces were then wet with fresh water providing a clean contact for the potential electrode assembly. Due to this local wetting, the contact impedance was generally <3 kΩ. An identical ground preparation was carried out for 7 stations at any time, allowing 7 electrode assemblies to be placed at each station ahead of the subsequent gradient scheme measurements. Fixed-base measurements were collected at each station relative to an 8th electrode assembly placed at the base station. A waiting period of 15-20 mins after placing the potential electrode assemblies was generally used before recording any data. Potentials were measured (after stable readings were achieved) using a high input-impedance (10 MΩ) Voltmeter. To ensure consistent polarity for each pair of electrodes the negative lead of the Voltmeter was always connected to whichever electrode was closest to the marker A at SITE 1, while at SITE 2

it was connected to the electrode closest to marker C. For fixed-base measurements, the negative lead was always connected to the base station electrode.

After acquiring the data, the Ag|AgCl electrode was removed from each assembly (including the base) and replaced by new sets. These were then advanced to the next set of 7 stations and measurements were resumed. This procedure was carried out for the entire transect length at both sites. Acquiring data from multiple stations in this manner minimizes delays due to waiting periods, which can be significant if single gradient measurements are conducted for each successive pair immediately after installation. It is to be noted here that fixed-base measurements at SITE 1 were performed a day after conducting the gradient measurements, while at SITE 2 both were conducted simultaneously. As part of data integrity management, potential differences amongst a pair of electrode assemblies placed side by side in the field were also randomly measured and were generally found to be very small (<2 mV).

Although these electrodes have been successfully utilized in the study, an important requirement is that significant ground preparations are necessary in order to carry out efficient measurements. The size of these electrodes requires that the ground surface is well levelled and free from excess water. Nevertheless once these conditions are met, the measurements procedure becomes faster.

APPENDIX D.2 DESIGN AND CALIBRATION OF FIELD CU|CUSO$_4$ ELECTRODES

For measurement of induced voltages in field, it is preferred to use non-polarizable electrodes. For the work reported in Chapter 7, a pair of non-polarizable Cu|CuSO$_4$ electrodes were created in the laboratory and verified prior to its use in the field. Each electrode consisted of a 30 cm long polycarbonate tube, with an inner diameter of 4 cm, consisting of the saturated CuSO$_4$ solution. A porous plug, made of Plaster of Paris, was affixed at the bottom allowing electrical continuity between the copper rod inside and the surface it is placed on. The tubular electrode consists of a solid PVC screw top-plug with BNC terminals to allow connections to the TDIP system. To increase the "life-time" of the electrode for continuous usage, a thin plastic cylindrical disk with a small concentric hole (diameter = 5 mm), acting as a channel for electrolyte flow, was fixed on top of the porous plug inside the tube. In this manner, the rate of discharge of the saturated CuSO$_4$ solution through the porous end-plug was minimized. The schematic of the potential electrode is given in Fig. D.3a. Prior to field use, the pair of potential electrodes were calibrated against each other in a low salinity water bath as shown in Fig. D.3b, and as well as in a salty slurry of sand and clay. The potential across the pair were monitored for ~20 hrs in each case.
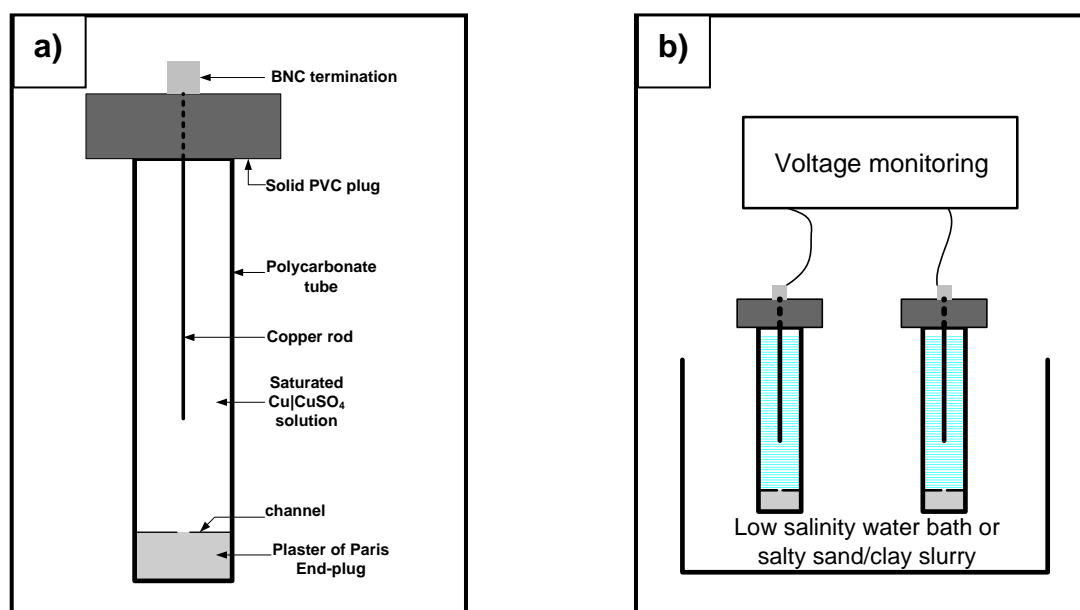
Figure D.3. Schematic of **a)** the non-polarizable Cu|CuSO$_4$ electrode, and **b)** cross-calibration procedure of the pair of electrodes. Voltage monitoring was automated and recorded every 1 s over a period of ~20 hrs.

The calibration results are shown in Fig. D.4, whereby a small mean potential difference (<1 mV) is observed between the two in the different mediums. It is also worthy to note that the design of a channelled electrolyte flow ensures good longevity of the electrodes. For example, in this case the

electrodes were left unattended over ~20 hrs, during which time it suffered relatively small electrolyte loss.
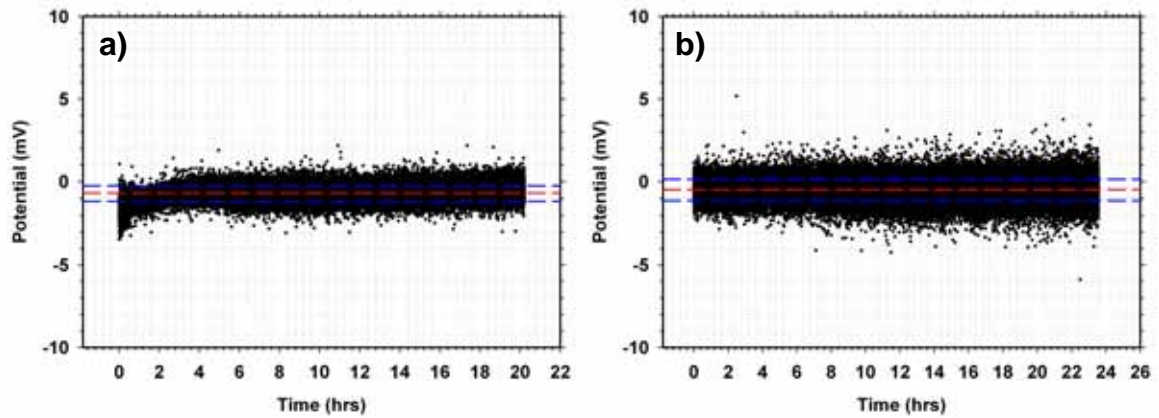
Figure D.4. Potential difference between the two non-polarizable Cu|CuSO$_4$ electrodes in **a)** a low salinity water bath, and **b)** in a salty sand/clay slurry when placed alongside each other. In both cases, the dashed red lines are the mean potential difference, while the blue dashed line shows the region bounded by ±σ from the mean.

The maximum difference between the two electrodes are generally <5 mV, which is a common value for the Cu|CuSO$_4$ electrodes [Butler, 2005]. Overall, the cross-calibration ensures it is feasible for the geophysical work reported in Chapter 7.

APPENDIX D.3 DC-TDIP PROFILING DATA FOR SITE 1 AND SITE 2

Table D.1. Geophysical profiling dataset for SITE 1. Note '-' indicates TDIP analysis could not be performed due to very poor SNR as described in the thesis.

STATION	a-spacing = 1 m			a-spacing = 3 m		
	M_a (mV/V)	ρ_a (Ω m)	MN (mS m^{-1})	M_a (mV/V)	ρ_a (Ω m)	MN (mS m^{-1})
1	16.44	76.27	0.216	7.41	17.99	0.412
2	19.16	86.81	0.221	7.53	23.35	0.322
3	5.09	63.01	0.081	9.06	21.13	0.429
4	4.27	28.68	0.149	11.09	16.75	0.662
5	6.93	31.01	0.223	15.69	17.22	0.911
6	4.27	24.08	0.177	16.28	14.58	1.116
7	4.59	18.91	0.243	15.55	15.04	1.034
8	3.85	19.15	0.201	20.87	13.78	1.514
9	4.38	16.01	0.274	12.04	13.81	0.872
10	2.71	14.59	0.186	10.33	12.69	0.813
11	2.69	16.09	0.167	24.09	10.38	2.321
12	3.59	9.29	0.387	-	10.65	-
13	3.33	7.68	0.433	23.78	7.39	3.217
14	3.2	11.41	0.28	15.87	6.31	2.516
15	3.38	20.92	0.162	39.83	7.92	5.028
16	2.88	14.03	0.205	25.83	6.43	4.017
17	2.29	10.28	0.223	23.90	6.57	3.639
18	2.64	9.67	0.273	30.29	6.53	4.642
19	4.22	8.45	0.5	16.02	6.27	2.556
20	3.52	9.65	0.365	11.31	6.52	1.734
21	3.66	7.36	0.498	23.11	6.1	3.791
22	7.75	8.61	0.9	12.54	7.90	1.587
23	7.58	20.07	0.378	20.76	7.06	2.941
24	8.18	19.89	0.411	9.64	7.93	1.215
25	6.43	14.26	0.451	22.29	7.4	3.011
26	9.74	20.35	0.479	20.49	7.53	2.723
27	-	16.34	-	17.37	8.07	2.152
28	-	18.44	-	11.88	6.71	1.771
29	-	18.12	-	19.89	7.62	2.609
30	19.16	16.33	1.173	13.64	7.36	1.854
31	6.15	20.5	0.3	18.31	7.82	2.340
32	16.82	12.82	1.312	7.70	8.17	0.943
33	6.26	11.75	0.533	15.39	9.42	1.634
34	6.79	28.12	0.242	11.38	10.06	1.132
35	5.83	21.33	0.273	10.53	10.79	0.976
36	9.55	23.17	0.412	11.81	11.65	1.014
37	2.64	25.04	0.105	11.1	10.69	1.038
38	3.25	22.83	0.142	9.96	12.57	0.792
39	3.99	25.25	0.158	9.34	11.59	0.806
40	2.48	35.91	0.069	12.88	14.26	0.903
41	2.86	64.25	0.045	8.07	14.75	0.547
42	1.69	76.32	0.022	7.08	15.53	0.456

Table D.2. Geophysical profiling dataset for SITE 2. Note '-' indicates TDIP analysis could not be performed due to very poor SNR as described in the thesis.

STATION	a-spacing = 3 m			STATION	a-spacing = 3 m		
	M_a (mV/V)	ρ_a (Ω m)	MN (mS m^{-1})		M_a (mV/V)	ρ_a (Ω m)	MN (mS m^{-1})
1	-	5.74	-	29	-	24.67	-
2	-	5.44	-	30	-	26.43	-
3	-	6.16	-	31	-	30.89	-
4	22.39	6.26	3.578	32	-	29.01	-
5	-	8.04	-	33	-	29.54	-
6	-	6.09	-	34	-	31.92	-
7	-	6.91	-	35	-	25.54	-
8	21.92	6.95	3.157	36	-	27.51	-
9	--	6.95	-	37	-	25.23	-
10	25.36	8.74	2.901	38	-	29.54	-
11	20.28	11.2	1.811	39	-	28.43	-
12	-	15.4	-	40	-	32.36	-
13	10.67	18.29	0.583	41	-	25.88	-
14	7.12	22.01	0.323	42	-	26.14	-
15	16.28	16.36	0.995	43	-	31.3	-
16	11.44	24.7	0.463	44	14.19	26.22	0.541
17	14.15	18.43	0.768	45	-	27.08	-
18	24.36	18.3	1.331	46	-	29.08	-
19	11.97	28.57	0.419	47	11.44	31.71	0.361
20	16.05	20.37	0.788	48	-	24.54	-
21	15.62	33.23	0.47	49	19.19	26.19	0.733
22	21.46	26.43	0.812	50	13.48	22.91	0.588
23	18.58	34.91	0.532	51	12.53	22.44	0.559
24	23.29	25.98	0.896	52	4.88	31.26	0.156
25	12.81	32.63	0.392	53	-	18.76	-
26	-	28.57	-	54	7.45	37.29	0.2
27	-	28.12	-	55	19.81	20.55	0.964
28	-	32.05	-				

APPENDIX D.4   SPECTRAL DATA OF FIELD SAMPLES

Means (μ) and standard deviations (σ) for phase and resistivities computed from repeated measurements (M1, M2, and M3) are given. Note, all phase values are negative

Table D.3. Spectral data for soil sample from Station 1.

Frequency (Hz)	Phase (mrad)			Resistivity (Ω m)			Phase (mrad)		Resistivity (Ω m)	
	M1	M2	M3	M1	M2	M3	μ	σ	μ	σ
0.1	3.9	3.9	3.9	92.8	92.5	93.0	3.9	0.1	92.8	0.2
0.2	4.6	4.2	4.5	92.9	92.9	92.7	4.4	0.2	92.8	0.1
0.3	4.9	4.9	4.7	93.2	92.9	93.1	4.8	0.1	93.1	0.1
0.4	5.3	5.2	5.2	93.1	92.7	92.6	5.2	0.0	92.8	0.3
0.5	5.4	5.3	5.5	92.7	92.8	92.9	5.4	0.1	92.8	0.1
0.6	5.2	5.8	5.7	93.0	92.7	92.8	5.6	0.3	92.8	0.2
0.7	5.5	6.0	6.0	93.1	93.1	92.9	5.8	0.2	93.0	0.1
0.8	6.2	6.1	5.5	93.1	92.7	92.9	5.9	0.4	92.9	0.2
0.9	6.3	6.4	6.4	92.9	92.8	93.0	6.4	0.1	92.9	0.1
1	6.5	6.5	6.5	92.9	93.0	92.6	6.5	0.0	92.8	0.2
2	7.7	7.6	7.5	92.6	92.5	92.8	7.6	0.1	92.6	0.2
3	8.5	8.2	8.5	92.1	92.3	92.6	8.4	0.2	92.3	0.2
4	8.8	9.2	8.9	92.3	92.0	91.9	8.9	0.2	92.0	0.2
5	9.2	9.3	9.4	92.0	92.0	91.8	9.3	0.1	91.9	0.1
6	10.1	9.9	9.7	91.7	92.0	91.9	9.9	0.2	91.9	0.2
7	9.9	9.8	9.7	91.7	91.6	91.9	9.8	0.1	91.7	0.1
8	10.2	10.4	10.4	92.2	91.6	91.9	10.3	0.1	91.9	0.3
9	11.0		10.5	92.0	91.9	91.9	10.8	0.4	91.9	0.1
10	11.1	10.5	10.4	92.0	91.7	92.0	10.7	0.4	91.9	0.2
20	11.5	11.5	11.8	91.5	91.3	91.5	11.6	0.2	91.4	0.1
30	12.7	13.4	13.6	91.3	91.1	90.6	13.2	0.5	91.0	0.3
40	12.5	15.3	13.9	90.7	90.8	90.7	13.9	1.4	90.7	0.1
50	13.4	13.6	15.1	90.7	90.4	90.4	14.0	0.9	90.5	0.1
60	13.1	16.3	13.0	90.7	90.4	90.4	14.1	1.9	90.5	0.2
70	14.6	16.7	14.0	90.3	90.4	90.3	15.1	1.4	90.3	0.1
80	15.3	14.0	14.2	89.3	90.2	89.9	14.5	0.8	89.8	0.4
90	15.7	13.5	13.8	89.7	90.4	90.1	14.3	1.2	90.1	0.3
100	14.0	15.6	15.1	89.9	89.8	89.7	14.9	0.8	89.8	0.1
200	15.8	16.0	18.9	89.3	89.6	89.4	16.9	1.7	89.4	0.2
300		18.3	14.6	88.6	88.9	88.9	16.4	2.7	88.8	0.2
400	12.6	24.2	19.5	88.9	88.3	88.3	18.8	5.9	88.5	0.4
500	23.8	24.7	15.5	88.2	88.2	87.7	21.3	5.1	88.0	0.3
600	21.0	19.1	26.6	88.4	88.8	88.8	22.2	3.9	88.7	0.2
700	22.0	34.8	23.9	88.4	86.9	87.3	26.9	6.9	87.5	0.8
800	22.1	20.7	23.4	87.5	87.1	87.9	22.1	1.3	87.5	0.4
900	25.5	29.4	16.7	88.2	86.3	87.2	23.9	6.5	87.2	1.0
1000	18.8	34.9	22.2	87.5	85.5	87.1	25.3	8.5	86.7	1.0

Table D.4. Spectral data for soil sample from Station 3.

Frequency (Hz)	Phase (mrad)			Resistivity (Ω m)			Phase (mrad)		Resistivity (Ω m)	
	M1	M2	M3	M1	M2	M3	μ	σ	μ	σ
0.1	5.8	5.7	5.8	48.9	48.9	48.7	5.75	0.01	48.85	0.10
0.2	6.4	6.4	6.4	48.9	48.7	48.7	6.42	0.02	48.78	0.11
0.3	6.9	6.5	6.9	48.9	48.8	48.8	6.74	0.24	48.81	0.06
0.4	7.3	7.3	7.3	48.7	48.7	48.7	7.27	0.02	48.71	0.02
0.5	7.6	7.5	7.6	48.7	48.7	48.6	7.56	0.03	48.68	0.04
0.6	8.1	8.1	8.1	48.7	48.7	48.6	8.12	0.04	48.66	0.07
0.7	8.4	8.3	8.3	48.6	48.6	48.5	8.33	0.03	48.60	0.06
0.8	8.5	8.5	8.6	48.7	48.6	48.5	8.55	0.03	48.62	0.09
0.9	8.8	8.8	8.8	48.7	48.6	48.5	8.79	0.03	48.59	0.09
1	9.0	9.0	9.0	48.6	48.6	48.5	9.01	0.03	48.53	0.07
2	10.5	10.5	10.6	48.4	48.4	48.3	10.51	0.08	48.38	0.06
3	11.5	11.4	11.5	48.3	48.3	48.2	11.46	0.05	48.26	0.05
4	12.0	12.1	12.0	48.2	48.1	48.0	12.01	0.08	48.09	0.10
5	12.5	12.9	12.4	48.2	48.1	48.0	12.61	0.28	48.10	0.07
6	12.9	13.2	13.3	48.0	48.0	47.9	13.13	0.22	48.00	0.05
7	13.5	13.3	13.6	48.0	47.9	47.8	13.48	0.13	47.90	0.09
8	13.3	13.5	13.8	48.0	47.9	47.9	13.55	0.25	47.91	0.05
9	14.0	13.9	13.7	47.9	47.9	47.8	13.84	0.12	47.86	0.09
10	13.8	14.2	14.8	47.9	47.8	47.7	14.28	0.49	47.78	0.08
20	15.2	15.8	15.7	47.5	47.4	47.4	15.57	0.29	47.45	0.06
30	17.8	17.7	18.1	47.3	47.3	47.2	17.89	0.18	47.24	0.04
40	17.1	15.9	18.2	47.1	47.2	47.0	17.08	1.18	47.10	0.06
50	17.7	15.8	16.5	47.0	47.1	46.9	16.68	0.95	46.99	0.12
60	17.0	18.0	17.5	47.0	46.9	46.8	17.52	0.69	46.91	0.07
70	19.6	16.5	16.0	46.8	46.8	46.8	17.34	1.94	46.82	0.03
80	19.2	17.9	20.0	46.8	46.7	46.7	19.04	1.06	46.73	0.08
90	17.8	17.4	17.6	46.7	46.7	46.6	17.63	0.21	46.67	0.05
100	16.4	16.4	16.5	46.7	46.7	46.5	16.41	0.06	46.63	0.11
200	17.6	18.8	18.2	46.3	46.1	46.2	18.19	0.58	46.20	0.09
300	16.9	14.9	20.1	46.0	46.1	45.8	17.32	2.65	45.95	0.15
400	16.8	20.1	16.4	45.9	45.7	45.8	17.77	2.04	45.80	0.10
500	13.8	28.0	12.9	45.6	45.6	45.6	18.26	8.45	45.61	0.03
600	13.4	15.0	14.4	45.8	45.7	45.8	14.23	0.81	45.76	0.05
700	13.9	18.0	14.0	45.6	45.7	45.5	15.32	2.32	45.58	0.11
800	13.2	14.8	29.9	45.6	45.5	44.7	19.29	9.19	45.27	0.47
900	18.7	25.9	23.1	45.1	45.5	44.4	22.58	3.60	45.02	0.56
1000	31.8	21.7	12.0	45.4	45.5	45.3	21.83	9.87	45.40	0.14

Table D.5. Spectral data for soil sample from Station 5.

Frequency (Hz)	Phase (mrad)			Resistivity (Ω m)			Phase (mrad)		Resistivity (Ω m)	
	M1	M2	M3	M1	M2	M3	μ	σ	μ	σ
0.1	4.5	4.5	4.4	29.1	29.0	28.9	4.48	0.06	28.97	0.11
0.2	5.2	5.2	5.2	29.1	29.0	28.9	5.22	0.02	28.96	0.10
0.3	5.7	5.7	5.7	29.1	28.9	28.8	5.72	0.02	28.94	0.11
0.4	6.1	6.1	6.1	29.0	28.9	28.8	6.07	0.01	28.92	0.11
0.5	6.3	6.3	6.3	29.0	28.9	28.8	6.31	0.03	28.88	0.11
0.6	6.9	6.8	6.8	29.0	28.8	28.8	6.81	0.04	28.88	0.10
0.7	7.0	7.0	7.1	29.0	28.8	28.7	7.05	0.01	28.84	0.12
0.8	7.3	7.3	7.3	29.0	28.8	28.8	7.28	0.01	28.86	0.10
0.9	7.4	6.2	7.5	28.9	28.9	28.8	7.04	0.73	28.85	0.09
1	7.7	6.3	7.6	28.9	28.8	28.7	7.17	0.79	28.82	0.10
2	9.0	9.0	9.0	28.9	28.7	28.6	9.01	0.03	28.74	0.12
3	9.8	10.1	9.9	28.8	28.7	28.6	9.91	0.13	28.67	0.11
4	10.6	10.4	10.7	28.7	28.6	28.5	10.56	0.16	28.62	0.10
5	11.0	11.3	11.3	28.7	28.6	28.5	11.20	0.16	28.58	0.07
6	11.4	11.5	11.4	28.6	28.5	28.4	11.46	0.06	28.55	0.10
7	11.9	11.7	11.8	28.6	28.5	28.4	11.79	0.09	28.52	0.10
8	12.1	12.0	12.4	28.6	28.5	28.4	12.20	0.20	28.49	0.10
9	12.8	12.2	12.7	28.6	28.4	28.4	12.58	0.31	28.47	0.12
10	12.5	12.3	12.6	28.6	28.5	28.4	12.48	0.17	28.46	0.10
20	14.6	13.9	14.0	28.4	28.3	28.2	14.20	0.37	28.28	0.09
30	15.2	15.6	14.3	28.3	28.2	28.0	15.08	0.66	28.18	0.14
40	16.9	15.5	15.0	28.2	28.1	28.0	15.81	0.98	28.10	0.10
50	17.2	15.0	15.0	28.1	28.1	27.9	15.73	1.24	28.04	0.09
60	17.2	17.5	16.5	28.0	28.0	27.9	17.05	0.52	27.97	0.08
70	15.3	18.6	15.5	28.0	27.9	27.9	16.46	1.83	27.94	0.10
80	18.1	16.5	15.6	28.0	27.9	27.8	16.74	1.27	27.89	0.12
90	15.8	14.9	16.8	28.0	27.9	27.7	15.82	0.94	27.86	0.12
100	17.8	18.2	17.0	28.0	27.8	27.7	17.67	0.58	27.83	0.16
200	19.3	18.8	19.9	27.7	27.5	27.5	19.29	0.56	27.58	0.09
300	18.8	25.1	20.9	27.6	27.3	27.3	21.63	3.23	27.40	0.14
400	18.3	25.0	17.9	27.4	27.3	27.3	20.39	4.01	27.32	0.09
500	15.8	22.1	17.6	27.3	27.3	27.0	18.51	3.28	27.19	0.14
600	19.6	17.2	25.9	27.3	27.2	27.0	20.89	4.46	27.14	0.15
700	17.0	19.5	17.9	27.3	27.3	27.2	18.14	1.22	27.25	0.08
800	17.0	19.2	26.1	27.3	27.0	27.2	20.76	4.75	27.16	0.14
900	22.8	19.4	20.9	27.3	27.2	26.8	21.07	1.69	27.10	0.30
1000	24.6	22.7	19.8	27.3	27.1	27.1	22.38	2.39	27.17	0.11

Table D.6. Spectral data for soil sample from Station 7.

Frequency (Hz)	Phase (mrad)			Resistivity (Ω m)			Phase (mrad)		Resistivity (Ω m)	
	M1	M2	M3	M1	M2	M3	μ	σ	μ	σ
0.1	6.0	6.0	6.0	41.1	41.0	40.9	5.98	0.01	40.99	0.06
0.2	6.9	6.9	7.0	41.0	40.9	40.9	6.94	0.03	40.92	0.04
0.3	7.1	7.6	7.6	40.9	40.9	40.8	7.40	0.27	40.87	0.07
0.4	8.0	8.1	8.1	40.9	40.8	40.8	8.08	0.04	40.85	0.08
0.5	8.4	8.4	8.5	40.9	40.8	40.7	8.43	0.02	40.81	0.08
0.6	9.1	9.1	9.0	40.9	40.7	40.7	9.05	0.03	40.77	0.07
0.7	9.3	9.3	9.4	40.8	40.7	40.6	9.34	0.02	40.71	0.08
0.8	9.7	9.6	9.6	40.8	40.7	40.6	9.65	0.02	40.70	0.09
0.9	9.8	9.9	9.8	40.8	40.7	40.6	9.86	0.06	40.69	0.08
1	10.1	10.1	10.2	40.7	40.7	40.5	10.12	0.05	40.66	0.11
2	12.3	11.9	12.0	40.6	40.5	40.4	12.07	0.18	40.49	0.07
3	13.1	13.3	13.0	40.4	40.4	40.3	13.15	0.15	40.35	0.07
4	14.1	13.9	13.9	40.3	40.3	40.2	13.97	0.15	40.25	0.09
5	14.9	14.9	14.7	40.3	40.1	40.1	14.84	0.14	40.17	0.07
6	15.8	15.4	15.7	40.2	40.1	40.0	15.64	0.21	40.09	0.08
7	15.3	15.4	15.5	40.2	40.1	40.0	15.40	0.08	40.06	0.09
8	16.0	16.0	16.6	40.1	40.0	39.9	16.22	0.36	39.98	0.07
9	16.5	16.7	16.5	40.0	40.0	39.9	16.58	0.08	39.95	0.06
10	16.4	17.5	16.3	39.9	39.9	39.8	16.74	0.65	39.88	0.05
20	20.1	19.6	19.4	39.7	39.6	39.5	19.71	0.37	39.60	0.09
30	21.4	19.1	20.1	39.5	39.4	39.4	20.19	1.15	39.39	0.07
40	20.0	21.9	20.7	39.3	39.2	39.2	20.89	0.97	39.24	0.08
50	20.1	19.5	20.2	39.1	39.1	39.1	19.92	0.41	39.11	0.03
60	19.6	19.9	19.6	39.1	39.0	38.9	19.74	0.17	39.02	0.07
70	24.3	23.5	20.6	39.0	38.9	38.9	22.78	1.96	38.91	0.07
80	20.1	20.2	22.6	39.0	38.9	38.8	20.98	1.39	38.88	0.13
90	21.1	23.8	20.4	38.9	38.8	38.8	21.77	1.81	38.82	0.08
100	21.7	21.7	24.2	38.8	38.7	38.6	22.54	1.48	38.69	0.09
200	21.2	19.0	20.8	38.5	38.4	38.5	20.36	1.16	38.43	0.05
300	22.0	18.9	18.7	38.2	37.9	38.0	19.85	1.84	38.02	0.12
400	24.9	24.5	17.3	37.9	37.5	37.7	22.24	4.24	37.70	0.17
500	18.9	24.3	16.9	37.9	37.1	37.7	20.02	3.84	37.54	0.43
600	17.1	24.8	28.4	37.6	37.3	37.4	23.42	5.79	37.45	0.16
700	24.3	16.6	26.8	37.0	37.6	37.2	22.56	5.32	37.30	0.30
800	18.5	28.2	19.3	37.6	36.8	37.7	22.00	5.41	37.36	0.45
900	19.1	28.6	20.4	37.8	37.8	37.7	22.71	5.14	37.72	0.05
1000	27.6	28.0	23.5	37.3	37.4	37.7	26.37	2.49	37.46	0.22

Table D.7. Spectral data for soil sample from Station 9.

Frequency (Hz)	Phase (mrad)			Resistivity (Ω m)			Phase (mrad)		Resistivity (Ω m)	
	M1	M2	M3	M1	M2	M3	μ	σ	μ	σ
0.1	6.2	6.4	6.3	32.1	32.0	31.9	6.32	0.07	31.99	0.08
0.2	7.3	7.3	7.0	32.0	31.9	31.8	7.22	0.17	31.90	0.06
0.3	7.8	7.8	7.8	32.0	31.9	31.8	7.84	0.01	31.86	0.10
0.4	8.2	8.3	8.3	31.9	31.8	31.8	8.26	0.03	31.84	0.07
0.5	8.5	8.6	8.5	31.9	31.8	31.8	8.54	0.04	31.82	0.06
0.6	9.2	9.2	9.2	31.9	31.8	31.8	9.17	0.01	31.81	0.05
0.7	9.5	9.5	9.4	31.9	31.8	31.7	9.45	0.05	31.76	0.10
0.8	9.7	9.7	9.7	31.8	31.7	31.7	9.71	0.01	31.73	0.04
0.9	9.5	9.8	9.9	31.8	31.7	31.7	9.72	0.23	31.70	0.07
1	10.1	10.1	10.1	31.8	31.7	31.6	10.11	0.04	31.70	0.07
2	11.7	11.6	11.5	31.6	31.5	31.5	11.61	0.12	31.53	0.06
3	12.7	12.4	12.5	31.6	31.5	31.4	12.52	0.13	31.48	0.07
4	13.2	13.2	13.0	31.5	31.4	31.3	13.13	0.12	31.40	0.06
5	13.9	13.5	13.7	31.4	31.4	31.3	13.70	0.20	31.34	0.06
6	14.1	14.0	13.7	31.4	31.3	31.2	13.94	0.19	31.30	0.09
7	14.3	14.6	14.1	31.3	31.2	31.2	14.29	0.26	31.24	0.07
8	14.7	14.4	14.5	31.3	31.2	31.2	14.52	0.15	31.21	0.07
9	15.2	14.5	15.2	31.2	31.1	31.1	14.98	0.42	31.14	0.09
10	15.1	15.5	15.3	31.2	31.2	31.1	15.32	0.19	31.16	0.09
20	16.6	16.0	16.0	31.0	30.9	30.9	16.17	0.33	30.92	0.07
30	17.6	17.8	16.3	30.9	30.8	30.7	17.25	0.81	30.81	0.08
40	17.9	16.3	16.9	30.7	30.7	30.6	17.04	0.78	30.70	0.06
50	19.3	17.2	17.4	30.7	30.6	30.6	17.96	1.16	30.62	0.05
60	18.4	17.6	17.0	30.6	30.5	30.5	17.68	0.68	30.55	0.05
70	19.2	16.6	16.6	30.6	30.5	30.5	17.46	1.55	30.52	0.04
80	18.7	17.2	17.4	30.5	30.4	30.4	17.77	0.80	30.45	0.06
90	18.7	17.1	16.2	30.5	30.4	30.4	17.32	1.28	30.42	0.04
100	19.5	17.5	19.0	30.4	30.4	30.2	18.63	1.06	30.33	0.13
200	15.2	16.0	17.6	30.3	30.1	29.9	16.25	1.20	30.09	0.19
300	21.8	19.7	14.6	30.0	29.9	30.0	18.67	3.70	29.94	0.04
400	18.8	16.5	17.1	29.9	29.9	29.8	17.47	1.21	29.86	0.06
500	19.8	17.8	17.0	29.4	29.7	29.7	18.21	1.47	29.63	0.16
600	19.3	13.2	14.4	29.7	29.9	29.7	15.62	3.28	29.73	0.11
700	18.4	14.2	19.9	29.5	29.8	29.5	17.52	2.96	29.57	0.19
800	19.3	21.9	19.6	29.5	29.7	29.7	20.28	1.42	29.62	0.12
900	20.7	19.1	21.5	29.4	29.6	29.2	20.44	1.24	29.41	0.21
1000	28.0	18.0	27.9	29.8	29.3	29.4	24.66	5.73	29.52	0.23

Table D.8. Spectral data for soil sample from Station 11.

Frequency (Hz)	Phase (mrad)			Resistivity (Ω m)			Phase (mrad)		Resistivity (Ω m)	
	M1	M2	M3	M1	M2	M3	μ	σ	μ	σ
0.1	4.0	4.0	4.0	22.0	22.0	22.0	4.02	0.02	22.00	0.03
0.2	4.5	4.7	4.7	22.0	22.0	21.9	4.61	0.13	21.96	0.04
0.3	4.7	5.1	5.1	22.0	21.9	21.9	4.96	0.25	21.95	0.04
0.4	4.9	5.0	5.5	22.0	21.9	21.9	5.11	0.31	21.93	0.04
0.5	5.7	5.7	5.7	21.9	21.9	21.9	5.70	0.01	21.91	0.04
0.6	6.1	6.1	6.2	21.9	21.9	21.9	6.15	0.02	21.90	0.03
0.7	6.4	6.4	6.4	21.9	21.9	21.9	6.39	0.03	21.88	0.03
0.8	6.6	6.6	6.6	21.9	21.9	21.8	6.62	0.02	21.88	0.03
0.9	6.8	6.8	6.8	21.9	21.9	21.8	6.78	0.01	21.87	0.03
1	7.0	7.0	7.0	21.9	21.9	21.8	7.00	0.02	21.86	0.03
2	8.4	8.4	8.4	21.8	21.8	21.8	8.38	0.02	21.79	0.04
3	9.4	9.2	9.3	21.8	21.7	21.7	9.29	0.09	21.75	0.03
4	10.2	10.0	9.8	21.7	21.7	21.7	10.00	0.18	21.71	0.02
5	10.4	10.4	10.7	21.7	21.7	21.6	10.49	0.17	21.67	0.03
6	10.9	9.9	10.9	21.7	21.7	21.6	10.55	0.59	21.65	0.03
7	11.0	11.4	11.1	21.7	21.6	21.6	11.17	0.18	21.63	0.04
8	11.7	11.3	11.4	21.7	21.6	21.6	11.48	0.19	21.61	0.05
9	11.7	12.1	11.6	21.6	21.6	21.6	11.78	0.29	21.59	0.03
10	10.6	12.3	12.0	21.6	21.5	21.5	11.64	0.91	21.57	0.04
20	13.6	13.0	13.1	21.5	21.5	21.4	13.26	0.34	21.45	0.04
30	13.7	14.2	15.0	21.4	21.4	21.3	14.30	0.63	21.38	0.04
40	14.3	15.6	16.1	21.4	21.3	21.3	15.34	0.97	21.31	0.04
50	14.9	14.3	14.1	21.3	21.3	21.2	14.42	0.43	21.27	0.03
60	14.1	16.5	14.6	21.3	21.2	21.2	15.09	1.28	21.23	0.04
70	14.9	16.0	17.6	21.2	21.2	21.1	16.19	1.35	21.19	0.05
80	17.9	17.7	14.6	21.2	21.1	21.1	16.74	1.86	21.16	0.03
90	14.4	15.9	14.4	21.2	21.1	21.1	14.89	0.90	21.14	0.03
100	18.1	14.2	15.5	21.1	21.1	21.1	15.94	2.00	21.10	0.02
200	17.7	16.2	16.2	21.0	21.0	20.9	16.70	0.86	20.96	0.02
300	18.6	13.1	18.8	20.8	20.9	20.8	16.81	3.25	20.83	0.07
400	16.6	23.4	23.4	20.9	20.7	20.8	21.13	3.89	20.79	0.09
500	22.8	20.3	24.6	20.5	20.7	20.4	22.56	2.15	20.56	0.17
600	16.0	25.1	17.8	20.8	20.6	20.6	19.64	4.83	20.67	0.13
700	25.1	22.1	19.8	20.8	20.7	21.1	22.35	2.64	20.85	0.21
800	22.6	23.9	17.8	20.5	20.0	20.7	21.46	3.20	20.37	0.37
900	25.6	27.9	22.3	20.5	20.3	20.3	25.28	2.84	20.37	0.14
1000	18.7	13.0	19.8	20.7	20.5	20.4	17.18	3.69	20.54	0.18

Table D.9. Spectral data for soil sample from Station 13.

Frequency (Hz)	Phase (mrad)			Resistivity (Ω m)			Phase (mrad)		Resistivity (Ω m)	
	M1	M2	M3	M1	M2	M3	μ	σ	μ	σ
0.1	1.4	1.4	1.2	7.7	7.7	7.6	1.32	0.09	7.65	0.01
0.2	1.4	1.5	1.5	7.7	7.6	7.6	1.45	0.02	7.65	0.01
0.3	1.5	1.5	1.6	7.6	7.6	7.6	1.54	0.02	7.65	0.00
0.4	1.6	1.7	1.6	7.7	7.6	7.6	1.64	0.02	7.64	0.01
0.5	1.7	1.7	1.7	7.6	7.6	7.6	1.70	0.01	7.64	0.00
0.6	1.8	1.8	1.8	7.6	7.6	7.6	1.78	0.01	7.64	0.00
0.7	1.8	1.9	1.9	7.6	7.6	7.6	1.87	0.02	7.64	0.00
0.8	1.9	1.9	1.9	7.6	7.6	7.6	1.91	0.01	7.64	0.01
0.9	1.9	2.0	2.0	7.6	7.6	7.6	1.97	0.03	7.64	0.00
1	2.1	2.0	2.1	7.6	7.6	7.6	2.04	0.02	7.64	0.00
2	2.4	2.4	2.4	7.6	7.6	7.6	2.39	0.03	7.63	0.01
3	2.7	2.7	2.7	7.6	7.6	7.6	2.68	0.01	7.62	0.01
4	2.9	2.9	2.9	7.6	7.6	7.6	2.88	0.02	7.62	0.00
5	3.1	3.0		7.6	7.6	7.6	3.02	0.07	7.62	0.00
6	3.1	3.1	3.2	7.6	7.6	7.6	3.15	0.02	7.62	0.01
7	3.3	3.3	3.3	7.6	7.6	7.6	3.29	0.04	7.61	0.00
8	3.5	3.5	3.4	7.6	7.6	7.6	3.44	0.07	7.61	0.00
9	3.3	3.3	3.4	7.6	7.6	7.6	3.36	0.04	7.61	0.00
10	3.5	3.5	3.4	7.6	7.6	7.6	3.47	0.04	7.61	0.00
20	3.9	4.1	4.1	7.6	7.6	7.6	4.03	0.13	7.60	0.01
30	4.4	4.2	4.1	7.6	7.6	7.6	4.24	0.18	7.59	0.00
40	5.1	4.2	4.2	7.6	7.6	7.6	4.51	0.49	7.58	0.00
50	5.3	5.2	4.4	7.6	7.6	7.6	4.97	0.53	7.58	0.00
60	5.1	4.6	4.9	7.6	7.6	7.6	4.89	0.24	7.57	0.00
70	4.7	4.9	4.7	7.6	7.6	7.6	4.79	0.08	7.57	0.01
80	5.3	4.4	4.7	7.6	7.6	7.6	4.81	0.43	7.57	0.00
90	4.7	4.3	5.7	7.6	7.6	7.6	4.90	0.71	7.56	0.00
100	5.3	4.9	4.5	7.6	7.6	7.6	4.87	0.41	7.56	0.00
200	4.5	4.9	5.5	7.6	7.6	7.5	4.97	0.51	7.56	0.03
300	4.2	5.5	4.9	7.5	7.5	7.5	4.89	0.67	7.53	0.01
400	5.0	6.7	6.0	7.5	7.5	7.5	5.91	0.81	7.52	0.01
500	7.0	5.3	5.4	7.6	7.5	7.5	5.91	0.98	7.53	0.05
600	5.0	4.8	4.4	7.5	7.5	7.5	4.73	0.28	7.51	0.00
700	4.8	5.7	5.8	7.5	7.5	6.8	5.43	0.53	7.27	0.38
800	6.5	8.6	8.6	7.5	7.5	7.5	7.92	1.21	7.50	0.02
900	4.9	5.4	4.4	7.5	7.0	7.5	4.90	0.52	7.34	0.30
1000	5.6	4.7	4.6	7.5	7.5	7.5	4.97	0.56	7.49	0.01

APPENDIX

Table D.10. Spectral data for soil sample from Station 15.

Frequency (Hz)	Phase (mrad)			Resistivity (Ω m)			Phase (mrad)		Resistivity (Ω m)	
	M1	M2	M3	M1	M2	M3	μ	σ	μ	σ
0.1	3.5	3.4	3.4	10.8	10.8	10.8	3.44	0.02	10.81	0.02
0.2	3.3	3.6	3.5	10.8	10.8	10.8	3.47	0.15	10.80	0.02
0.3	3.6	3.6	3.6	10.8	10.8	10.8	3.62	0.01	10.79	0.02
0.4	3.7	3.7	3.7	10.8	10.8	10.8	3.71	0.01	10.78	0.02
0.5	3.7	3.7	3.8	10.8	10.8	10.8	3.74	0.02	10.78	0.01
0.6	4.0	4.0	4.0	10.8	10.8	10.8	3.98	0.00	10.78	0.02
0.7	4.0	4.0	4.0	10.8	10.8	10.8	4.01	0.04	10.77	0.02
0.8	4.1	4.1	4.1	10.8	10.8	10.8	4.11	0.02	10.77	0.02
0.9	4.2	4.2	4.2	10.8	10.8	10.7	4.17	0.01	10.77	0.02
1	4.2	4.3	4.2	10.8	10.8	10.7	4.25	0.01	10.76	0.02
2	4.8	4.8	4.8	10.8	10.7	10.7	4.80	0.02	10.74	0.02
3	5.1	5.2	5.1	10.8	10.7	10.7	5.13	0.04	10.73	0.02
4	5.3	5.3	5.5	10.7	10.7	10.7	5.37	0.09	10.72	0.02
5	5.6	5.6	5.6	10.7	10.7	10.7	5.60	0.03	10.71	0.02
6	5.6	5.6	5.7	10.7	10.7	10.7	5.65	0.03	10.71	0.02
7	5.9	5.9	5.9	10.7	10.7	10.7	5.90	0.03	10.70	0.02
8	6.1	6.1	5.9	10.7	10.7	10.7	6.05	0.13	10.69	0.02
9	6.0	6.1	6.2	10.7	10.7	10.7	6.09	0.11	10.69	0.02
10	6.1	6.0	6.2	10.7	10.7	10.7	6.12	0.09	10.69	0.02
20	6.6	6.7	6.8	10.7	10.7	10.6	6.70	0.13	10.66	0.02
30	7.0	7.6	7.4	10.7	10.6	10.6	7.36	0.30	10.64	0.02
40	7.0	7.3	7.5	10.6	10.6	10.6	7.30	0.24	10.62	0.02
50	8.2	7.0	7.7	10.6	10.6	10.6	7.63	0.57	10.62	0.01
60	8.7	7.1	7.5	10.6	10.6	10.6	7.73	0.83	10.60	0.02
70	7.5	7.9	7.5	10.6	10.6	10.6	7.61	0.23	10.60	0.02
80	7.2	7.7	7.1	10.6	10.6	10.6	7.36	0.35	10.59	0.02
90	7.2	7.1	8.1	10.6	10.6	10.6	7.48	0.57	10.58	0.02
100	7.4	8.0	7.6	10.6	10.6	10.5	7.66	0.31	10.57	0.03
200	9.0	7.7	8.7	10.6	10.5	10.5	8.50	0.70	10.55	0.02
300	8.1	7.6	6.4	10.5	10.5	10.5	7.35	0.86	10.52	0.02
400	9.4	7.4	9.1	10.6	10.5	10.5	8.64	1.06	10.51	0.05
500	7.4	6.3	9.3	10.5	10.5	10.4	7.69	1.51	10.46	0.04
600	7.9	10.2	7.7	10.5	10.5	10.4	8.60	1.38	10.48	0.03
700	11.0	8.3	10.5	10.5	10.4	10.4	9.95	1.45	10.47	0.04
800	11.0	5.1	8.6	10.4	10.5	11.1	8.25	2.94	10.68	0.41
900	8.4	12.3	6.6	10.5	10.4	10.4	9.08	2.90	10.42	0.04
1000	8.2	8.3	8.9	10.5	10.5	10.4	8.44	0.38	10.45	0.06

Table D.11. Spectral data for soil sample from Station 17.

Frequency (Hz)	Phase (mrad)			Resistivity (Ω m)			Phase (mrad)		Resistivity (Ω m)	
	M1	M2	M3	M1	M2	M3	μ	σ	μ	σ
0.1	1.7	1.7	1.8	7.2	7.2	7.2	1.72	0.06	7.21	0.00
0.2	1.9	2.0	2.1	7.2	7.2	7.2	1.99	0.07	7.20	0.01
0.3	2.1	2.1	2.2	7.2	7.2	7.2	2.11	0.05	7.19	0.01
0.4	2.4	2.2	2.3	7.2	7.2	7.2	2.30	0.07	7.19	0.00
0.5	2.3	2.4	2.4	7.2	7.2	7.2	2.34	0.04	7.19	0.01
0.6	2.5	2.5	2.5	7.2	7.2	7.2	2.49	0.03	7.19	0.01
0.7	2.7	2.5	2.6	7.2	7.2	7.2	2.61	0.06	7.18	0.01
0.8	2.6	2.6	2.6	7.2	7.2	7.2	2.64	0.01	7.19	0.01
0.9	2.7	2.7	2.7	7.2	7.2	7.2	2.69	0.02	7.18	0.01
1	2.8	2.7	2.8	7.2	7.2	7.2	2.76	0.02	7.18	0.00
2	3.2	3.2	3.2	7.2	7.2	7.2	3.22	0.01	7.17	0.01
3	3.5	3.6	3.5	7.2	7.2	7.2	3.51	0.06	7.17	0.01
4	3.6	3.7	3.7	7.2	7.2	7.2	3.69	0.06	7.16	0.01
5	3.9	3.8	3.9	7.2	7.2	7.2	3.85	0.02	7.16	0.01
6	4.1	4.1	4.0	7.2	7.2	7.1	4.04	0.04	7.16	0.01
7	4.2	4.2	4.1	7.2	7.2	7.2	4.17	0.08	7.15	0.01
8	4.2	3.9	4.3	7.2	7.1	7.1	4.16	0.22	7.15	0.01
9	4.4	4.4	4.3	7.2	7.1	7.1	4.38	0.04	7.15	0.01
10	4.5	4.6	4.5	7.2	7.1	7.1	4.51	0.04	7.15	0.01
20	5.3	5.1	5.1	7.1	7.1	7.1	5.17	0.12	7.13	0.01
30	5.4	5.8	5.7	7.1	7.1	7.1	5.63	0.23	7.12	0.00
40	6.0	6.0	6.1	7.1	7.1	7.1	6.04	0.05	7.11	0.01
50	5.4	5.4	5.6	7.1	7.1	7.1	5.48	0.12	7.11	0.01
60	5.0	5.4	5.8	7.1	7.1	7.1	5.43	0.39	7.10	0.01
70	5.8	6.4	5.5	7.1	7.1	7.1	5.88	0.47	7.10	0.01
80	6.8	5.6	5.8	7.1	7.1	7.1	6.09	0.62	7.09	0.01
90	5.7	6.6	5.8	7.1	7.1	7.1	6.04	0.50	7.09	0.00
100	6.8	6.9	6.4	7.1	7.1	7.1	6.70	0.25	7.09	0.01
200	5.3	5.5	6.0	7.1	7.1	7.1	5.60	0.38	7.07	0.01
300	6.6	5.6	5.4	7.1	7.1	7.0	5.89	0.66	7.06	0.01
400	6.1	5.6	4.8	7.1	7.0	7.0	5.48	0.64	7.05	0.01
500	5.1	5.9	5.9	7.0	7.0	7.0	5.66	0.47	7.03	0.01
600	7.1	6.5	4.6	7.0	7.0	7.0	6.05	1.28	7.03	0.02
700	6.4	5.0	5.1	7.0	7.0	7.0	5.52	0.76	7.02	0.01
800	6.4	7.1	4.2	7.0	7.0	7.0	5.92	1.52	7.03	0.01
900	4.9	5.1	5.7	6.7	6.4	7.0	5.22	0.42	6.69	0.33
1000	5.5	5.8	5.1	7.0	7.0	7.0	5.47	0.33	7.02	0.02

APPENDIX

Table D.12. Spectral data for soil sample from Station 19.

Frequency (Hz)	Phase (mrad)			Resistivity (Ω m)			Phase (mrad)		Resistivity (Ω m)	
	M1	M2	M3	M1	M2	M3	μ	σ	μ	σ
0.1	3.1	3.2	3.2	9.2	9.2	9.2	3.17	0.02	9.21	0.01
0.2	3.4	3.4	3.4	9.2	9.2	9.2	3.38	0.02	9.21	0.01
0.3	3.5	3.5	3.5	9.2	9.2	9.2	3.51	0.03	9.20	0.01
0.4	3.6	3.6	3.6	9.2	9.2	9.2	3.62	0.01	9.19	0.01
0.5	3.7	3.7	3.7	9.2	9.2	9.2	3.70	0.01	9.19	0.01
0.6	3.9	3.9	3.9	9.2	9.2	9.2	3.90	0.01	9.18	0.01
0.7	4.0	4.0	4.0	9.2	9.2	9.2	3.98	0.03	9.18	0.01
0.8	3.8	4.1	4.0	9.2	9.2	9.2	3.98	0.16	9.18	0.01
0.9	4.1	4.1	4.1	9.2	9.2	9.2	4.13	0.01	9.17	0.01
1	4.2	4.2	4.2	9.2	9.2	9.2	4.19	0.01	9.17	0.01
2	4.7	4.7	4.8	9.2	9.2	9.1	4.71	0.05	9.16	0.01
3	5.1	5.1	5.0	9.2	9.1	9.1	5.07	0.05	9.14	0.01
4	5.2	5.2	5.2	9.1	9.1	9.1	5.22	0.02	9.13	0.01
5	5.4	5.4	5.5	9.1	9.1	9.1	5.42	0.03	9.13	0.01
6	5.6	5.8	5.6	9.1	9.1	9.1	5.63	0.11	9.12	0.01
7	5.8	5.6	5.1	9.1	9.1	9.1	5.51	0.38	9.12	0.01
8	6.0	5.8	5.8	9.1	9.1	9.1	5.86	0.12	9.11	0.01
9	6.1	6.0	5.9	9.1	9.1	9.1	5.99	0.08	9.11	0.01
10	6.1	6.3	6.0	9.1	9.1	9.1	6.10	0.16	9.11	0.01
20	6.6	6.7	6.7	9.1	9.1	9.1	6.69	0.08	9.08	0.01
30	7.4	7.2	7.1	9.1	9.1	9.1	7.24	0.17	9.06	0.01
40	7.6	7.6	7.4	9.1	9.1	9.0	7.54	0.12	9.05	0.01
50	8.3	7.0	7.7	9.0	9.0	9.0	7.68	0.65	9.05	0.00
60	6.9	8.6	6.8	9.1	9.0	9.0	7.41	0.99	9.04	0.01
70	6.9	7.8	7.4	9.0	9.0	9.0	7.38	0.42	9.03	0.01
80	7.2	8.4	7.1	9.0	9.0	9.0	7.53	0.73	9.02	0.01
90	9.3	8.7	7.4	9.0	9.0	9.0	8.48	0.98	9.02	0.01
100	8.2	8.1	7.0	9.0	9.0	9.0	7.75	0.69	9.01	0.01
200	8.4	8.6	9.2	9.0	9.0	9.0	8.72	0.42	8.98	0.01
300	7.5	7.9	8.0	9.0	9.0	9.0	7.82	0.29	8.96	0.01
400	9.1	7.6	8.1	8.9	8.9	8.9	8.27	0.74	8.94	0.01
500	10.7	7.3	10.2	8.9	8.9	8.9	9.41	1.87	8.91	0.03
600	7.3	8.7	8.4	8.9	8.9	8.9	8.13	0.73	8.93	0.01
700	10.3	8.0	11.2	9.0	9.8	8.9	9.84	1.62	9.24	0.52
800	11.1	9.1	9.1	8.7	8.9	8.9	9.76	1.13	8.83	0.11
900	5.9	7.5	8.4	8.9	8.9	8.9	7.27	1.30	8.91	0.02
1000	8.9	7.4	8.3	8.9	8.0	9.4	8.21	0.73	8.76	0.68

Table D.13. Spectral data for soil sample from Station 21.

Frequency (Hz)	Phase (mrad)			Resistivity (Ω m)			Phase (mrad)		Resistivity (Ω m)	
	M1	M2	M3	M1	M2	M3	μ	σ	μ	σ
0.1	1.3	1.3	1.3	5.2	5.2	5.2	1.32	0.01	5.16	0.01
0.2	1.3	1.3	1.3	5.2	5.2	5.1	1.29	0.01	5.15	0.00
0.3	1.3	1.3	1.3	5.2	5.2	5.2	1.31	0.01	5.15	0.00
0.4	1.3	1.3	1.3	5.2	5.2	5.1	1.32	0.02	5.15	0.01
0.5	1.3	1.3	1.3	5.2	5.1	5.1	1.29	0.02	5.15	0.00
0.6	1.4	1.4	1.4	5.2	5.1	5.1	1.37	0.01	5.15	0.00
0.7	1.4	1.4	1.4	5.2	5.1	5.1	1.39	0.02	5.15	0.01
0.8	1.4	1.4	1.4	5.2	5.1	5.1	1.40	0.01	5.15	0.00
0.9	1.3	1.4	1.5	5.2	5.1	5.1	1.39	0.08	5.15	0.01
1	1.4	1.4	1.5	5.2	5.1	5.1	1.44	0.01	5.15	0.01
2	1.6	1.6	1.6	5.2	5.1	5.1	1.58	0.01	5.14	0.01
3	1.7	1.7	1.7	5.1	5.1	5.1	1.70	0.01	5.14	0.01
4	1.8	1.8	1.7	5.1	5.1	5.1	1.75	0.04	5.14	0.00
5	1.9	1.8	1.8	5.1	5.1	5.1	1.83	0.06	5.14	0.01
6	1.9	1.9	1.9	5.1	5.1	5.1	1.89	0.03	5.14	0.01
7	1.8	1.9	1.9	5.1	5.1	5.1	1.88	0.03	5.14	0.00
8	2.0	2.0	2.0	5.1	5.1	5.1	1.97	0.01	5.14	0.00
9	2.0	1.9	2.0	5.1	5.1	5.1	1.98	0.03	5.14	0.01
10	2.1	2.1	2.0	5.1	5.1	5.1	2.06	0.04	5.14	0.01
20	2.3	2.2	2.3	5.1	5.1	5.1	2.28	0.07	5.13	0.00
30	2.4	2.4	2.4	5.1	5.1	5.1	2.41	0.02	5.13	0.01
40	2.4	2.6	2.5	5.1	5.1	5.1	2.49	0.09	5.13	0.01
50	2.5	2.6	2.7	5.1	5.1	5.1	2.62	0.10	5.12	0.01
60	2.6	2.4	2.5	5.1	5.1	5.1	2.52	0.08	5.12	0.00
70	2.8	3.2	2.9	5.1	5.1	5.1	2.96	0.18	5.12	0.00
80	2.9	2.9	2.7	5.1	5.1	5.1	2.83	0.08	5.12	0.01
90	3.0	2.9	2.8	5.1	5.1	5.1	2.88	0.11	5.12	0.01
100	2.8	2.5	2.8	5.1	5.1	5.1	2.68	0.17	5.12	0.01
200	2.7	2.6	3.1	5.1	5.1	5.1	2.79	0.23	5.11	0.01
300	3.1	3.6	3.4	5.1	5.1	5.1	3.36	0.25	5.10	0.01
400	3.9	3.4	3.0	5.1	5.1	5.1	3.42	0.44	5.10	0.01
500	3.5	3.0	3.8	5.1	5.1	5.1	3.44	0.41	5.10	0.01
600	2.3	3.2	3.4	5.1	5.1	5.1	2.95	0.55	5.10	0.01
700	2.7	3.6	3.2	5.2	5.1	5.1	3.15	0.43	5.15	0.07
800	3.0	2.8	3.0	5.1	5.1	5.1	2.92	0.14	5.10	0.01
900	2.8	2.9	2.6	5.1	5.6	5.1	2.75	0.17	5.27	0.30
1000	3.0	2.3	3.3	5.1	5.1	5.1	2.86	0.51	5.09	0.01

Table D.14. Spectral data for soil sample from Station 23.

Frequency (Hz)	Phase (mrad)			Resistivity (Ω m)			Phase (mrad)		Resistivity (Ω m)	
	M1	M2	M3	M1	M2	M3	μ	σ	μ	σ
0.1	3.2	3.4	3.4	16.5	16.5	16.5	3.31	0.09	16.49	0.02
0.2	3.4	3.6	3.6	16.5	16.5	16.5	3.51	0.08	16.47	0.02
0.3	3.7	3.7	3.7	16.5	16.4	16.4	3.70	0.02	16.45	0.02
0.4	3.8	3.8	3.8	16.5	16.4	16.4	3.82	0.01	16.45	0.02
0.5	3.9	3.9	3.9	16.5	16.4	16.4	3.90	0.03	16.44	0.02
0.6	4.1	4.2	4.1	16.4	16.4	16.4	4.13	0.02	16.43	0.02
0.7	4.2	4.2	4.2	16.5	16.4	16.4	4.20	0.01	16.42	0.04
0.8	4.3	4.3	4.3	16.4	16.4	16.4	4.28	0.01	16.42	0.02
0.9	4.3	4.4	4.4	16.4	16.4	16.4	4.36	0.01	16.42	0.02
1	4.5	4.4	4.4	16.4	16.4	16.4	4.43	0.02	16.41	0.03
2	5.1	5.0	5.1	16.4	16.4	16.4	5.05	0.03	16.38	0.02
3	5.4	5.4	5.4	16.4	16.4	16.3	5.40	0.04	16.37	0.02
4	5.7	5.7	5.6	16.4	16.3	16.3	5.65	0.03	16.34	0.01
5	5.9	5.8	5.9	16.4	16.3	16.3	5.89	0.06	16.34	0.02
6	5.9	6.1	6.0	16.3	16.3	16.3	6.00	0.08	16.32	0.02
7	6.2	6.1	6.2	16.3	16.3	16.3	6.13	0.04	16.32	0.02
8	6.4	6.4	6.3	16.3	16.3	16.3	6.35	0.04	16.31	0.02
9	6.3	6.3	6.6	16.3	16.3	16.3	6.40	0.14	16.30	0.02
10	6.8	6.4	6.8	16.3	16.3	16.3	6.68	0.21	16.30	0.03
20	7.3	7.6	7.5	16.3	16.2	16.2	7.45	0.15	16.24	0.02
30	7.8	8.1	7.3	16.2	16.2	16.2	7.77	0.40	16.21	0.03
40	7.6	7.5	7.8	16.2	16.2	16.2	7.66	0.15	16.19	0.03
50	8.6	8.1	8.6	16.2	16.2	16.1	8.42	0.26	16.17	0.02
60	8.2	7.6	7.9	16.2	16.1	16.2	7.94	0.31	16.16	0.02
70	7.9	7.8	8.6	16.2	16.1	16.1	8.11	0.44	16.14	0.02
80	9.5	8.1	7.9	16.1	16.1	16.1	8.49	0.84	16.13	0.02
90	8.6	8.5	8.3	16.1	16.1	16.1	8.46	0.17	16.12	0.03
100	9.4	8.1	8.2	16.1	16.1	16.1	8.55	0.70	16.11	0.02
200	8.6	8.4	8.7	16.1	16.0	16.0	8.55	0.18	16.04	0.02
300	8.7	7.7	8.4	16.0	16.0	16.0	8.24	0.51	16.00	0.02
400	9.5	7.1	8.1	16.0	15.9	16.0	8.22	1.21	15.95	0.03
500	8.3	8.3	8.7	15.9	15.9	15.9	8.44	0.22	15.91	0.02
600	7.7	7.7	7.7	15.9	16.0	15.9	7.69	0.00	15.92	0.05
700	7.0	7.9	10.5	15.9	15.9	15.8	8.48	1.81	15.90	0.05
800	9.2	9.1	9.7	15.9	15.9	15.9	9.33	0.31	15.89	0.03
900	8.5	7.9	11.0	15.7	15.8	15.8	9.12	1.62	15.77	0.03
1000	9.0	7.7	8.6	15.8	15.9	15.8	8.45	0.67	15.85	0.04

Table D.15. Spectral data for soil sample from Station 25.

Frequency (Hz)	Phase (mrad)			Resistivity (Ω m)			Phase (mrad)		Resistivity (Ω m)	
	M1	M2	M3	M1	M2	M3	μ	σ	μ	σ
0.1	2.7	2.7	2.7	13.1	13.1	13.1	2.66	0.01	13.11	0.02
0.2	2.9	2.9	2.9	13.1	13.1	13.1	2.87	0.01	13.10	0.02
0.3	3.0	3.0	3.0	13.1	13.1	13.1	3.03	0.01	13.09	0.01
0.4	3.1	3.2	3.1	13.1	13.1	13.1	3.15	0.01	13.08	0.02
0.5	3.3	3.3	3.2	13.1	13.1	13.1	3.25	0.01	13.08	0.02
0.6	3.4	3.4	3.4	13.1	13.1	13.1	3.42	0.02	13.08	0.02
0.7	3.5	3.5	3.5	13.1	13.1	13.1	3.51	0.02	13.07	0.02
0.8	3.5	3.6	3.6	13.1	13.1	13.0	3.56	0.06	13.07	0.02
0.9	3.7	3.7	3.7	13.1	13.1	13.0	3.68	0.00	13.07	0.02
1	3.7	3.6	2.3	13.1	13.1	13.0	3.22	0.82	13.07	0.02
2	4.3	4.3	4.3	13.1	13.0	13.0	4.30	0.03	13.04	0.02
3	4.6	4.5	4.6	13.1	13.0	13.0	4.57	0.05	13.03	0.03
4	4.8	4.9	4.9	13.0	13.0	13.0	4.85	0.07	13.01	0.02
5	5.1	4.9	5.0	13.0	13.0	13.0	5.02	0.11	13.01	0.02
6	5.2	5.2	5.2	13.0	13.0	13.0	5.18	0.02	13.00	0.02
7	5.3	5.4	5.2	13.0	13.0	13.0	5.30	0.08	13.00	0.02
8	5.4	5.6	5.6	13.0	13.0	13.0	5.54	0.11	12.99	0.03
9	5.5	5.4	5.6	13.0	13.0	13.0	5.49	0.08	12.99	0.02
10	5.6	5.9	5.8	13.0	13.0	13.0	5.78	0.12	12.98	0.02
20	6.6	6.2	6.2	13.0	13.0	12.9	6.31	0.24	12.95	0.02
30	7.4	6.7	6.8	12.9	12.9	12.9	6.98	0.39	12.92	0.03
40	6.8	7.0	6.7	12.9	12.9	12.9	6.81	0.18	12.91	0.02
50	6.7	7.0	6.6	12.9	12.9	12.9	6.74	0.22	12.90	0.02
60	6.8	7.4	8.1	12.9	12.9	12.9	7.46	0.66	12.88	0.03
70	8.3	7.1	7.4	12.9	12.9	12.9	7.59	0.63	12.88	0.02
80	7.7	7.7	8.4	12.9	12.9	12.9	7.95	0.42	12.87	0.02
90	8.1	8.1	9.1	12.9	12.9	12.8	8.43	0.56	12.87	0.03
100	7.0	7.8	8.9	12.9	12.9	12.8	7.89	0.97	12.86	0.03
200	7.1	8.5	9.0	12.8	12.8	12.8	8.20	1.02	12.81	0.03
300	8.1	7.9	8.1	12.8	12.7	12.8	8.05	0.10	12.77	0.03
400	8.5	8.5	8.0	12.8	12.8	12.7	8.33	0.30	12.76	0.02
500	8.7	7.3	7.2	12.7	12.7	12.7	7.75	0.83	12.69	0.02
600	8.3	8.6	8.1	12.8	12.7	12.7	8.34	0.25	12.73	0.04
700	8.5	10.3	10.3	12.7	12.8	12.7	9.66	1.03	12.73	0.07
800	8.3	10.7	10.0	12.8	12.7	12.6	9.67	1.20	12.71	0.06
900	11.2	11.4	10.3	12.7	12.6	14.1	10.95	0.62	13.14	0.81
1000	10.7	10.3	8.1	12.7	12.7	12.7	9.67	1.40	12.71	0.03

Table D.16. Spectral data for soil sample from Station 27.

Frequency (Hz)	Phase (mrad)			Resistivity (Ω m)			Phase (mrad)		Resistivity (Ω m)	
	M1	M2	M3	M1	M2	M3	μ	σ	μ	σ
0.1	1.0	1.0	1.0	14.3	14.3	14.3	1.01	0.02	14.27	0.02
0.2	0.9	1.2	1.2	14.3	14.3	14.3	1.09	0.16	14.27	0.02
0.3	1.3	1.3	1.3	14.3	14.3	14.3	1.33	0.01	14.27	0.01
0.4	1.4	1.4	1.4	14.3	14.3	14.2	1.41	0.00	14.26	0.01
0.5	1.5	1.5	1.5	14.3	14.3	14.2	1.49	0.01	14.27	0.02
0.6	1.5	1.6	1.6	14.3	14.3	14.3	1.58	0.03	14.26	0.01
0.7	1.7	1.7	1.7	14.3	14.3	14.2	1.67	0.01	14.26	0.01
0.8	1.7	1.7	1.7	14.3	14.3	14.2	1.72	0.02	14.26	0.02
0.9	1.8	1.6	1.8	14.3	14.3	14.2	1.73	0.10	14.26	0.02
1	1.8	1.9	1.9	14.3	14.3	14.2	1.85	0.02	14.25	0.02
2	2.2	2.2	2.2	14.3	14.2	14.2	2.23	0.02	14.24	0.01
3	2.6	2.5	2.5	14.3	14.2	14.2	2.54	0.02	14.23	0.02
4	2.7	2.8	2.7	14.3	14.2	14.2	2.75	0.07	14.23	0.02
5	2.9	3.0	2.9	14.2	14.2	14.2	2.93	0.04	14.22	0.02
6	3.0	3.1	3.0	14.3	14.2	14.2	3.05	0.07	14.22	0.03
7	3.1	3.1	3.2	14.2	14.2	14.2	3.14	0.05	14.21	0.02
8	3.3	3.3	3.3	14.2	14.2	14.2	3.28	0.02	14.21	0.02
9	3.6	3.3	3.4	14.2	14.2	14.2	3.40	0.17	14.20	0.02
10	3.4	3.3	3.5	14.2	14.2	14.2	3.41	0.08	14.20	0.02
20	4.1	4.2	4.0	14.2	14.2	14.2	4.09	0.10	14.19	0.01
30	4.8	4.5	4.5	14.2	14.2	14.1	4.58	0.17	14.16	0.01
40	4.4	5.2	5.5	14.2	14.1	14.1	5.04	0.53	14.15	0.02
50	4.6	5.8	4.8	14.2	14.1	14.1	5.05	0.66	14.14	0.02
60	4.8	5.0	5.0	14.2	14.1	14.1	4.93	0.09	14.13	0.03
70	5.4	5.0	4.7	14.1	14.1	14.1	5.04	0.31	14.12	0.02
80	5.7	5.3	5.2	14.1	14.1	14.1	5.38	0.29	14.11	0.01
90	5.8	4.9	6.8	14.1	14.1	14.1	5.82	0.95	14.10	0.01
100	5.2	5.6	7.0	14.1	14.1	14.1	5.94	0.92	14.11	0.02
200	5.9	5.1	6.2	14.1	14.1	14.1	5.70	0.58	14.06	0.01
300	7.4	6.1	7.5	14.1	14.0	14.0	7.01	0.82	14.05	0.01
400	5.0	5.2	5.9	14.1	14.0	14.0	5.40	0.47	14.03	0.03
500	7.2	5.3	4.9	14.0	14.0	14.0	5.79	1.26	14.03	0.02
600	7.8	6.5	4.6	14.0	14.0	14.0	6.27	1.62	14.01	0.01
700	7.3	4.8	5.4	14.0	14.0	14.0	5.82	1.29	14.01	0.03
800	8.3	9.2	6.1	14.1	14.0	14.0	7.84	1.61	14.04	0.03
900	7.7	8.4	8.0	14.0	14.0	14.0	8.01	0.37	14.04	0.01
1000	7.3	6.5	7.0	14.1	14.0	14.0	6.92	0.37	14.03	0.03

Table D.17. Spectral data for soil sample from Station 29.

Frequency (Hz)	Phase (mrad)			Resistivity (Ω m)			Phase (mrad)		Resistivity (Ω m)	
	M1	M2	M3	M1	M2	M3	μ	σ	μ	σ
0.1	2.1	2.1	2.1	18.1	18.2	18.2	2.07	0.01	18.15	0.01
0.2	2.4	2.4	2.4	18.1	18.1	18.1	2.40	0.01	18.14	0.00
0.3	2.6	2.1	2.6	18.1	18.1	18.1	2.44	0.26	18.13	0.01
0.4	2.7	2.2	2.8	18.1	18.1	18.1	2.55	0.33	18.13	0.01
0.5	2.9	2.9	2.9	18.1	18.1	18.1	2.88	0.01	18.12	0.00
0.6	3.1	3.1	3.1	18.1	18.1	18.1	3.08	0.01	18.11	0.01
0.7	3.2	3.1	3.2	18.1	18.1	18.1	3.16	0.01	18.11	0.00
0.8	3.3	3.1	3.3	18.1	18.1	18.1	3.22	0.10	18.11	0.01
0.9	3.3	3.3	3.3	18.1	18.1	18.1	3.32	0.01	18.10	0.00
1	3.4	3.4	3.4	18.1	18.1	18.1	3.39	0.02	18.10	0.01
2	4.0	4.0	4.0	18.1	18.1	18.1	4.02	0.01	18.07	0.01
3	4.4	4.4	4.4	18.1	18.0	18.1	4.42	0.05	18.05	0.01
4	4.8	4.6	4.8	18.0	18.0	18.0	4.71	0.10	18.04	0.01
5	4.9	4.9	4.9	18.0	18.0	18.0	4.86	0.00	18.03	0.01
6	5.1	5.0	5.1	18.0	18.0	18.0	5.06	0.05	18.02	0.01
7	5.2	5.3	5.3	18.0	18.0	18.0	5.26	0.03	18.01	0.01
8	5.6	5.3	5.4	18.0	18.0	18.0	5.41	0.14	18.00	0.00
9	5.8	5.4	5.8	18.0	18.0	18.0	5.69	0.21	17.99	0.01
10	5.7	5.6	5.7	18.0	18.0	18.0	5.66	0.03	17.99	0.01
20	6.3	6.3	6.5	17.9	18.0	17.9	6.36	0.11	17.94	0.01
30	7.3	6.8	6.7	17.9	17.9	17.9	6.92	0.33	17.91	0.02
40	6.8	7.0	6.9	17.9	17.9	17.9	6.89	0.06	17.88	0.01
50	7.6	8.4	8.1	17.9	17.8	17.8	8.03	0.41	17.85	0.01
60	7.8	8.5	7.2	17.8	17.8	17.8	7.86	0.66	17.84	0.01
70	9.2	9.0	9.1	17.8	17.8	17.8	9.09	0.13	17.82	0.01
80	8.5	7.6	9.9	17.8	17.8	17.8	8.66	1.11	17.81	0.01
90	8.0	9.6	9.0	17.9	17.8	17.8	8.86	0.85	17.83	0.06
100	9.8	7.3	10.5	17.9	17.8	17.8	9.21	1.69	17.82	0.06
200	9.8	9.3	9.4	17.7	17.7	17.7	9.51	0.28	17.72	0.01
300	8.4	10.2	9.3	17.7	17.7	17.8	9.29	0.90	17.70	0.06
400	9.7	9.3	8.6	17.6	17.7	17.6	9.17	0.54	17.63	0.03
500	8.2	10.0	8.9	17.6	17.6	17.5	9.04	0.88	17.58	0.03
600	8.9	8.6	9.4	17.5	17.6	17.6	8.98	0.42	17.60	0.05
700	9.2	9.1	10.1	17.6	18.7	17.4	9.44	0.55	17.92	0.69
800	11.1	10.7	9.1	17.4	17.6	17.6	10.29	1.08	17.55	0.11
900	10.2	9.5	9.8	17.5	17.5	17.6	9.80	0.34	17.54	0.03
1000	12.5	9.2	12.0	17.4	17.5	17.6	11.21	1.79	17.47	0.11

Table D.18. Spectral data for soil sample from Station 31.

Frequency (Hz)	Phase (mrad)			Resistivity (Ω m)			Phase (mrad)		Resistivity (Ω m)	
	M1	M2	M3	M1	M2	M3	μ	σ	μ	σ
0.1	3.1	3.1	3.2	9.4	9.4	9.4	3.12	0.04	9.37	0.01
0.2	3.1	3.4	3.4	9.4	9.4	9.4	3.30	0.19	9.36	0.01
0.3	3.5	3.5	3.6	9.4	9.4	9.3	3.54	0.02	9.36	0.01
0.4	3.7	3.7	3.7	9.4	9.3	9.3	3.66	0.00	9.35	0.01
0.5	3.7	3.7	3.7	9.4	9.3	9.3	3.70	0.01	9.34	0.01
0.6	3.9	3.9	3.9	9.4	9.3	9.3	3.91	0.01	9.34	0.01
0.7	4.0	4.0	4.0	9.3	9.3	9.3	3.99	0.01	9.34	0.01
0.8	4.0	4.0	4.0	9.3	9.3	9.3	4.03	0.01	9.34	0.01
0.9	4.1	4.1	4.1	9.3	9.3	9.3	4.13	0.01	9.33	0.01
1	4.2	4.1	4.2	9.3	9.3	9.3	4.17	0.02	9.33	0.01
2	4.7	4.7	4.6	9.3	9.3	9.3	4.66	0.04	9.31	0.01
3	4.9	4.9	4.9	9.3	9.3	9.3	4.92	0.01	9.30	0.01
4	5.1	5.2	5.1	9.3	9.3	9.3	5.15	0.06	9.29	0.01
5	5.3	5.4	5.3	9.3	9.3	9.3	5.35	0.03	9.28	0.01
6	5.6	5.4	5.4	9.3	9.3	9.3	5.49	0.10	9.28	0.01
7	5.7	5.6	5.7	9.3	9.3	9.3	5.67	0.03	9.28	0.01
8	5.9	5.7	5.8	9.3	9.3	9.3	5.80	0.08	9.27	0.01
9	5.8	6.0	5.8	9.3	9.3	9.3	5.86	0.12	9.27	0.01
10	6.0	6.1	6.1	9.3	9.3	9.3	6.09	0.05	9.27	0.01
20	6.4	6.4	6.9	9.3	9.2	9.2	6.55	0.27	9.24	0.01
30	7.4	7.4	7.0	9.2	9.2	9.2	7.27	0.19	9.22	0.01
40	6.9	7.2	7.2	9.2	9.2	9.2	7.10	0.14	9.21	0.01
50	7.4	6.9	6.7	9.2	9.2	9.2	7.01	0.37	9.21	0.01
60	7.4	7.1	7.6	9.2	9.2	9.2	7.37	0.23	9.20	0.01
70	7.4	7.0	7.4	9.2	9.2	9.2	7.25	0.21	9.19	0.01
80	7.1	7.2	7.2	9.2	9.2	9.2	7.17	0.07	9.18	0.01
90	8.6	8.3	8.3	9.2	9.2	9.2	8.38	0.18	9.17	0.01
100	7.1	7.9	7.2	9.2	9.2	9.2	7.41	0.44	9.17	0.01
200	8.9	6.8	7.6	9.1	9.1	9.1	7.78	1.07	9.14	0.01
300	8.3	7.1	6.9	9.1	9.1	9.1	7.42	0.73	9.12	0.01
400	7.3	6.1	8.5	9.1	9.1	9.1	7.28	1.18	9.11	0.01
500	8.0	6.5	8.7	9.1	9.1	9.1	7.76	1.11	9.08	0.01
600	8.8	8.4	6.8	9.1	9.0	9.1	8.03	1.06	9.08	0.03
700	8.6	7.4	8.1	9.1	9.1	9.0	8.04	0.60	9.06	0.01
800	8.6	8.1	6.3	9.1	9.1	9.1	7.66	1.23	9.07	0.02
900	9.1	11.0	9.3	9.1	9.0	9.0	9.79	1.05	9.04	0.02
1000	10.1	10.3	10.7	9.1	9.1	9.0	10.33	0.32	9.06	0.05

Table D.19. Spectral data for soil sample from Station 33.

Frequency (Hz)	Phase (mrad)			Resistivity (Ω m)			Phase (mrad)		Resistivity (Ω m)	
	M1	M2	M3	M1	M2	M3	μ	σ	μ	σ
0.1	3.6	3.4	3.5	17.4	17.4	17.4	3.52	0.12	17.36	0.01
0.2	3.8	3.5	3.4	17.4	17.3	17.3	3.57	0.20	17.35	0.01
0.3	4.0	4.0	4.0	17.3	17.3	17.3	3.98	0.02	17.33	0.01
0.4	4.1	4.2	4.1	17.4	17.3	17.3	4.12	0.03	17.33	0.02
0.5	4.2	4.3	4.2	17.3	17.3	17.3	4.25	0.03	17.32	0.01
0.6	4.5	4.5	4.5	17.3	17.3	17.3	4.50	0.02	17.30	0.02
0.7	4.6	4.6	4.6	17.3	17.3	17.3	4.61	0.01	17.29	0.02
0.8	4.8	4.7	4.7	17.3	17.3	17.3	4.74	0.01	17.30	0.03
0.9	4.8	4.8	4.8	17.3	17.3	17.3	4.83	0.00	17.28	0.02
1	4.9	4.9	4.9	17.3	17.3	17.3	4.94	0.01	17.29	0.02
2	5.8	5.7	5.7	17.3	17.3	17.2	5.74	0.08	17.25	0.01
3	6.2	6.1	6.2	17.2	17.2	17.2	6.19	0.04	17.22	0.02
4	6.8	6.7	6.5	17.2	17.2	17.2	6.67	0.15	17.21	0.01
5	7.0	7.1	6.8	17.2	17.2	17.2	6.95	0.16	17.19	0.02
6	7.1	7.2	7.1	17.2	17.2	17.2	7.14	0.09	17.19	0.01
7	7.3	7.6	7.3	17.2	17.2	17.1	7.41	0.19	17.16	0.02
8	7.5	7.7	7.5	17.2	17.2	17.1	7.55	0.10	17.16	0.01
9	8.0	7.6	7.8	17.2	17.1	17.1	7.78	0.19	17.14	0.02
10	7.8	7.9	8.0	17.1	17.2	17.1	7.91	0.10	17.14	0.02
20	8.8	9.4	8.8	17.1	17.1	17.1	9.03	0.35	17.07	0.02
30	9.9	9.6	9.4	17.0	17.0	17.0	9.65	0.24	17.03	0.01
40	9.7	9.5	9.8	17.0	17.0	17.0	9.65	0.13	17.00	0.01
50	10.6	9.7	10.3	17.0	17.0	17.0	10.20	0.49	16.99	0.01
60	10.7	10.5	11.6	17.0	17.0	16.9	10.91	0.59	16.96	0.02
70	10.4	10.2	10.7	17.0	16.9	16.9	10.42	0.22	16.96	0.04
80	11.2	10.9	10.8	16.9	16.9	16.9	10.95	0.26	16.92	0.01
90	11.8	11.0	10.9	16.9	16.9	16.9	11.22	0.49	16.92	0.02
100	13.4	12.6	10.2	16.9	16.9	16.9	12.09	1.68	16.88	0.01
200	11.1	13.2	12.0	16.8	16.8	16.8	12.11	1.02	16.80	0.01
300	13.8	11.2	11.6	16.7	16.8	16.7	12.23	1.42	16.75	0.02
400	13.6	17.5	13.4	16.9	16.7	16.7	14.84	2.33	16.73	0.13
500	12.1	13.0	11.5	16.6	16.5	16.6	12.19	0.78	16.56	0.07
600	15.8	11.9	13.9	16.7	16.7	16.7	13.86	1.95	16.70	0.01
700	10.2	12.2	12.0	16.6	16.7	16.6	11.47	1.12	16.63	0.04
800	11.1	14.0	12.1	16.5	16.6	16.5	12.43	1.49	16.51	0.07
900	15.0	12.5	14.6	16.7	16.6	16.6	14.05	1.33	16.63	0.02
1000	18.2	18.0	19.9	16.6	16.5	16.6	18.67	1.07	16.57	0.05

Table D.20. Spectral data for soil sample from Station 35.

Frequency (Hz)	Phase (mrad)			Resistivity (Ω m)			Phase (mrad)		Resistivity (Ω m)	
	M1	M2	M3	M1	M2	M3	μ	σ	μ	σ
0.1	1.6	1.6	1.6	23.4	23.4	23.4	1.58	0.01	23.43	0.03
0.2	1.7	1.7	1.8	23.4	23.4	23.4	1.74	0.02	23.42	0.03
0.3	1.8	1.8	1.8	23.5	23.4	23.4	1.84	0.02	23.42	0.03
0.4	1.9	1.9	2.0	23.4	23.4	23.4	1.94	0.01	23.41	0.00
0.5	2.0	2.0	2.0	23.4	23.4	23.4	2.01	0.02	23.42	0.02
0.6	2.2	2.2	2.2	23.4	23.4	23.4	2.17	0.02	23.41	0.01
0.7	2.2	2.2	2.3	23.4	23.4	23.4	2.24	0.02	23.40	0.01
0.8	2.3	2.3	2.3	23.4	23.4	23.4	2.33	0.00	23.40	0.02
0.9	2.4	2.4	2.4	23.4	23.4	23.4	2.38	0.00	23.39	0.01
1	2.5	2.4	2.4	23.4	23.4	23.4	2.43	0.04	23.40	0.03
2	2.9	2.9	2.3	23.4	23.4	23.3	2.69	0.36	23.37	0.03
3	3.3	3.2	3.3	23.4	23.4	23.3	3.26	0.05	23.36	0.02
4	3.5	3.5	3.5	23.4	23.3	23.3	3.51	0.05	23.34	0.03
5	3.7	3.6	3.7	23.4	23.3	23.3	3.68	0.05	23.34	0.02
6	3.9	3.9	3.8	23.3	23.3	23.3	3.89	0.06	23.33	0.01
7	4.0	4.0	3.9	23.3	23.3	23.3	3.96	0.03	23.32	0.02
8	4.1	4.1	4.3	23.3	23.3	23.3	4.17	0.08	23.31	0.01
9	4.2	4.3	4.3	23.3	23.3	23.3	4.26	0.04	23.31	0.01
10	4.5	4.4	4.3	23.3	23.3	23.3	4.40	0.06	23.31	0.02
20	4.9	5.0	4.9	23.3	23.2	23.2	4.97	0.07	23.25	0.02
30	6.2	5.3	5.6	23.2	23.2	23.2	5.69	0.46	23.22	0.01
40	5.9	5.5	5.7	23.2	23.2	23.2	5.74	0.22	23.20	0.03
50	6.8	6.7	6.7	23.2	23.2	23.1	6.74	0.03	23.17	0.03
60	7.0	6.1	7.5	23.2	23.2	23.1	6.88	0.75	23.16	0.02
70	6.9	6.4	6.1	23.2	23.1	23.1	6.45	0.40	23.13	0.02
80	6.8	7.2	6.0	23.1	23.1	23.1	6.67	0.61	23.13	0.02
90	6.6	6.7	6.6	23.1	23.2	23.1	6.64	0.09	23.13	0.04
100	6.3	6.1	6.4	23.1	23.1	23.1	6.25	0.15	23.11	0.02
200	8.0	6.2	7.2	23.1	23.1	23.0	7.14	0.89	23.04	0.02
300	8.3	9.0	7.9	23.2	22.9	23.0	8.36	0.57	23.03	0.11
400	9.8	8.0	9.0	22.9	23.5	22.8	8.90	0.91	23.08	0.34
500	8.2	7.7	8.1	22.9	22.8	22.9	7.99	0.28	22.89	0.05
600	7.1	10.4	8.6	22.9	22.8	22.9	8.70	1.62	22.88	0.04
700	8.2	9.5	10.2	22.8	22.8	22.8	9.31	1.05	22.81	0.03
800	7.3	7.8	8.5	23.1	23.3	22.8	7.87	0.62	23.04	0.26
900	9.4	7.8	8.8	22.7	22.8	22.7	8.67	0.81	22.75	0.05
1000	10.5	9.7	11.9	22.9	22.7	22.6	10.66	1.10	22.72	0.15

Table D.21. Spectral data for soil sample from Station 37.

Frequency (Hz)	Phase (mrad)			Resistivity (Ω m)			Phase (mrad)		Resistivity (Ω m)	
	M1	M2	M3	M1	M2	M3	μ	σ	μ	σ
0.1	1.9	1.9	2.0	31.6	31.6	31.6	1.95	0.00	31.61	0.04
0.2	2.2	2.2	2.2	31.6	31.5	31.5	2.23	0.01	31.56	0.07
0.3	2.4	2.4	2.5	31.6	31.6	31.5	2.44	0.04	31.58	0.07
0.4	2.5	2.6	2.6	31.7	31.5	31.5	2.55	0.01	31.58	0.07
0.5	2.6	2.7	2.7	31.6	31.6	31.4	2.63	0.04	31.52	0.08
0.6	2.9	2.9	2.8	31.7	31.6	31.6	2.85	0.04	31.60	0.05
0.7	2.9	2.9	3.0	31.7	31.5	31.5	2.93	0.03	31.57	0.07
0.8	3.1	3.0	3.0	31.6	31.6	31.5	3.04	0.03	31.53	0.07
0.9	3.1	3.1	3.1	31.6	31.5	31.5	3.10	0.02	31.56	0.05
1	3.2	2.7	3.2	31.6	31.6	31.5	3.03	0.28	31.57	0.08
2	3.5	3.8	3.7	31.6	31.5	31.5	3.69	0.13	31.55	0.05
3	4.2	4.2	4.1	31.6	31.5	31.5	4.17	0.06	31.53	0.03
4	4.4	4.5	4.4	31.6	31.5	31.5	4.42	0.08	31.49	0.05
5	4.6	4.6	3.7	31.5	31.5	31.4	4.31	0.51	31.47	0.07
6	4.8	4.8	4.9	31.5	31.5	31.4	4.83	0.05	31.46	0.06
7	4.9	4.8	4.9	31.5	31.4	31.4	4.88	0.04	31.43	0.08
8	5.0	5.0	5.0	31.5	31.4	31.4	5.00	0.02	31.44	0.06
9	5.2	5.5	5.3	31.4	31.4	31.4	5.35	0.17	31.40	0.03
10	5.4	5.4	4.8	31.5	31.4	31.4	5.19	0.35	31.42	0.04
20	6.2	5.9	6.3	31.4	31.3	31.2	6.13	0.17	31.32	0.08
30	6.2	6.8	6.6	31.3	31.3	31.2	6.55	0.30	31.25	0.03
40	7.4	6.5	7.9	31.3	31.2	31.2	7.26	0.70	31.21	0.04
50	8.3	6.8	7.7	31.3	31.2	31.2	7.60	0.76	31.21	0.05
60	7.0	8.4	7.1	31.3	31.2	31.1	7.50	0.75	31.19	0.07
70	8.8	7.2	7.8	31.2	31.1	31.1	7.93	0.77	31.14	0.06
80	8.4	9.5	8.3	31.2	31.1	31.1	8.75	0.67	31.14	0.05
90	8.8	7.3	7.8	31.2	31.2	31.0	7.97	0.78	31.13	0.10
100	9.2	7.4	8.0	31.2	31.1	31.0	8.20	0.90	31.10	0.07
200	7.1	8.3	8.0	31.0	30.9	30.9	7.80	0.60	30.94	0.08
300	10.1	9.3	10.5	30.9	30.9	30.8	9.98	0.59	30.88	0.06
400	7.4	9.4	6.7	30.9	30.9	30.8	7.83	1.44	30.89	0.04
500	12.0	8.5	8.6	30.6	30.7	30.7	9.74	2.00	30.66	0.02
600	9.3	6.9	9.1	30.8	30.8	30.8	8.44	1.36	30.79	0.03
700	8.1	9.4	12.2	30.8	30.8	30.6	9.88	2.08	30.72	0.10
800	6.7	9.8	7.8	30.7	30.8	30.7	8.12	1.56	30.74	0.02
900	12.9	12.3	14.0	30.4	30.5	30.6	13.09	0.83	30.48	0.11
1000	18.3	13.5	13.0	30.4	35.8	30.5	14.93	2.89	32.21	3.08

Table D.22. Spectral data for soil sample from Station 39.

Frequency (Hz)	Phase (mrad)			Resistivity (Ω m)			Phase (mrad)		Resistivity (Ω m)	
	M1	M2	M3	M1	M2	M3	μ	σ	μ	σ
0.1	1.2	1.4	1.4	32.9	32.9	32.8	1.35	0.09	32.86	0.04
0.2	1.6	1.6	1.6	32.9	32.8	32.8	1.61	0.02	32.84	0.08
0.3	1.8	1.7	1.8	32.9	32.9	32.8	1.76	0.03	32.87	0.05
0.4	1.9	1.9	1.9	32.9	32.9	32.8	1.89	0.02	32.88	0.05
0.5	2.0	2.0	1.9	32.9	32.9	32.9	1.95	0.02	32.89	0.04
0.6	2.1	2.1	2.1	32.9	32.8	32.8	2.09	0.01	32.86	0.06
0.7	2.2	2.2	2.2	32.9	32.9	32.8	2.17	0.02	32.86	0.04
0.8	2.2	2.3	2.2	32.9	32.9	32.8	2.24	0.02	32.85	0.04
0.9	2.1	2.3	2.3	32.9	32.9	32.8	2.26	0.10	32.86	0.07
1	2.4	2.4	2.3	32.9	32.9	32.8	2.34	0.03	32.86	0.10
2	2.9	2.9	2.8	32.9	32.8	32.8	2.86	0.05	32.83	0.06
3	3.2	3.2	3.2	32.9	32.8	32.8	3.18	0.01	32.82	0.04
4	3.4	3.4	3.5	32.9	32.8	32.7	3.42	0.05	32.79	0.06
5	3.5	3.7	3.5	32.9	32.8	32.8	3.57	0.07	32.80	0.05
6	3.8	3.9	3.8	32.8	32.8	32.7	3.84	0.05	32.77	0.05
7	3.8	3.8	4.0	32.8	32.7	32.7	3.90	0.13	32.76	0.06
8	4.2	4.2	4.0	32.8	32.8	32.7	4.13	0.14	32.74	0.08
9	4.1	4.2	4.2	32.7	32.7	32.6	4.16	0.07	32.69	0.05
10	4.3	4.2	4.3	32.8	32.7	32.7	4.28	0.03	32.74	0.04
20	5.2	5.4	5.2	32.7	32.6	32.6	5.27	0.11	32.66	0.06
30	5.8	5.8	6.1	32.6	32.6	32.6	5.90	0.20	32.61	0.04
40	5.5	5.8	5.7	32.6	32.6	32.6	5.66	0.18	32.58	0.02
50	6.5	5.9	5.8	32.6	32.6	32.5	6.07	0.34	32.54	0.07
60	6.3	5.8	6.1	32.6	32.6	32.5	6.06	0.27	32.56	0.04
70	6.8	6.9	7.3	32.6	32.5	32.5	7.03	0.28	32.54	0.03
80	7.5	7.0	6.8	32.5	32.5	32.5	7.11	0.32	32.49	0.03
90	8.7	7.4	7.1	32.5	32.5	32.4	7.73	0.84	32.46	0.06
100	6.3	6.6	7.2	32.4	32.4	32.4	6.71	0.47	32.43	0.01
200	8.0	8.6	10.0	32.4	32.4	32.3	8.86	0.99	32.36	0.07
300	8.2	8.7	7.6	32.4	32.3	32.2	8.17	0.54	32.28	0.07
400	9.7	10.9	10.6	32.3	32.2	32.1	10.40	0.80	32.21	0.12
500	8.7	9.0	11.3	32.2	32.0	32.0	9.70	1.44	32.06	0.15
600	8.7	9.8	9.4	32.2	32.1	32.1	9.30	0.56	32.14	0.07
700	8.8	7.8	8.6	32.0	32.1	32.3	8.41	0.54	32.14	0.19
800	9.5	9.5	8.9	32.3	32.1	32.1	9.29	0.35	32.15	0.10
900	10.4	10.8	9.2	32.1	31.9	31.8	10.10	0.41	31.95	0.16
1000	10.0	11.5	12.5	32.2	32.1	31.8	11.34	0.48	32.00	0.22

APPENDIX D.5 COLE-COLE PARAMETERS FROM SIP MEASUREMENTS OF FIELD SAMPLES

Table D.23. Cole-Cole parameters for soil samples collected from different stations. Note inversion of each repeated measurement (ϕ-spectra) has been performed separately. From these the weighted Cole-Cole parameters have been calculated.

Station	Measurement 1						Measurement 2						Measurement 3					
#	m	Δm	c	Δc	tau µs	Δtau µs	m	Δm	c	Δc	tau µs	Δtau µs	m	Δm	c	Δc	tau µs	Δtau µs
1	0.1457	0.0135	0.3	0.004	98	69	0.1658	0.0165	0.3	0.004	94	71	0.1539	0.0078	0.3	0.002	95.6	36
3	0.14	0.0056	0.3	0.003	721	276	0.1508	0.0053	0.3	0.003	406	131	0.1387	0.0189	0.307	0.044	763	472
5	0.1507	0.0038	0.3	0.002	235	51	0.1567	0.0176	0.309	0.028	179	105	0.1614	0.0052	0.3	0.002	140	36
7	0.1538	0.0101	0.331	0.024	859	242	0.183	0.0052	0.3	0.002	328	84	0.1604	0.0134	0.316	0.028	698	265
9	0.1565	0.0035	0.3	0.002	558	118	0.1387	0.0025	0.3	0.002	1200	203	0.1465	0.0042	0.3	0.002	691	190
11	0.1659	0.0071	0.3	0.002	83	26	0.1668	0.01	0.3	0.003	85	38	0.1577	0.0052	0.3	0.002	119	31
13	0.04	0.0038	0.332	0.028	340	152	0.0479	0.0022	0.3	0.001	118	41	0.0422	0.0085	0.324	0.051	187	186
15	0.0704	0.0018	0.3	0.001	386	91	0.0658	0.0022	0.3	0.001	601	190	0.0674	0.0015	0.3	0.001	544	114
17	0.0444	0.0027	0.337	0.021	693	179	0.0435	0.0024	0.342	0.019	769	177	0.0454	0.0008	0.3	0	807	142
19	0.0874	0.0165	0.248	0.036	123.2	145	0.0687	0.0038	0.288	0.016	539	73	0.0758	0.002	0.28	0.001	228	54
21	0.0245	0.0006	0.3	0.000	384	87.3	0.0256	0.0006	0.3	0	292	61	0.0246	0.0007	0.3	0	386	93
23	0.0713	0.0039	0.295	0.016	605	158	0.07	0.0031	0.283	0.013	702	148	0.0885	0.0019	0.25	0.001	171	38
25	0.0916	0.0032	0.25	0.001	49	15	0.0988	0.0029	0.250	0.001	30	9.6	0.0794	0.01	0.28	0.027	139	100
27	0.0608	0.0024	0.32	0.000	40	10	0.0563	0.014	0.305	0.045	53	72	0.0398	0.0042	0.383	0.036	328	145
29	0.0879	0.0124	0.287	0.027	70	57	0.0787	0.0019	0.3	0.001	126	24	0.0813	0.0025	0.3	0.001	118	28
31	0.0844	0.0017	0.25	0.000	131	26	0.0792	0.0028	0.25	0.001	194	70	0.0794	0.0023	0.25	0.001	203	61
33	0.1384	0.0340	0.256	0.038	32	51	0.1472	0.0089	0.25	0.001	21	9	0.1479	0.0094	0.25	0.001	18	8
35	0.08	0.0006	0.3	0.001	32	3.6	0.0799	0.0153	0.292	0.03	29	31	0.0857	0.0047	0.3	0.001	21	7
37	0.0953	0.0104	0.3	0.002	35	25	0.0855	0.0048	0.3	0.001	54	21	0.0904	0.0066	0.3	0.001	40	19
39	0.0764	0.0089	0.322	0.021	45	27	0.097	0.0057	0.3	0.001	13	4	0.0864	0.0204	0.318	0.036	26	32

APPENDIX D.6   CURVE FITTING RESULTS OF GALVANOSTATIC PULSES FOR CAST-IRON/SOIL SYSTEMS

Curve fitting of galvanostatic pulses for the different cast-iron/soil systems, which have been used to extract the corrosion related parameters presented in Appendix D.7, are presented herein. Each curve has been analyzed separately, as opposed to analyzing the mean curve from repeated measurements, in order to avoid diluting the edge associated with the onset of charging and discharging processes. Consequently, charging and discharging sections from all (3) repeated measurements (referred to as Batch 1 – 3 in the illustrations) are presented.
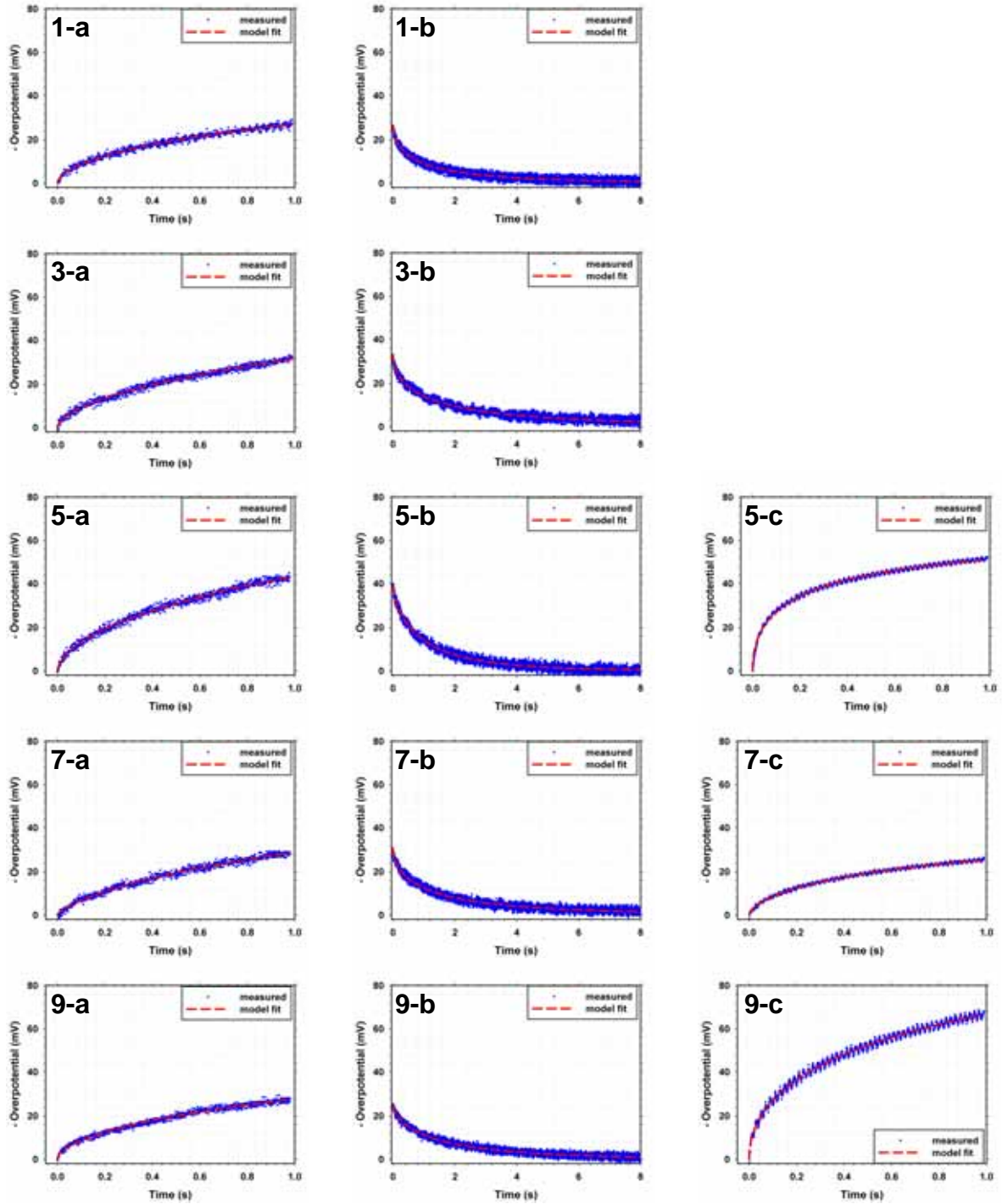
Figure D.5. Curve fitting for charging and discharging sections of the cast-iron/soil responses for Batch 1 measurements during Day 1 and Day 7. The labels are organized as such; the different soils are identified by the numericals, which correspond to the station number along the SITE 1 transect, while the labels **a** and **b** correspond to charging and discharging sections from Day 1 measurements, and **c** corresponds to the charging section from Day 7 measurements.
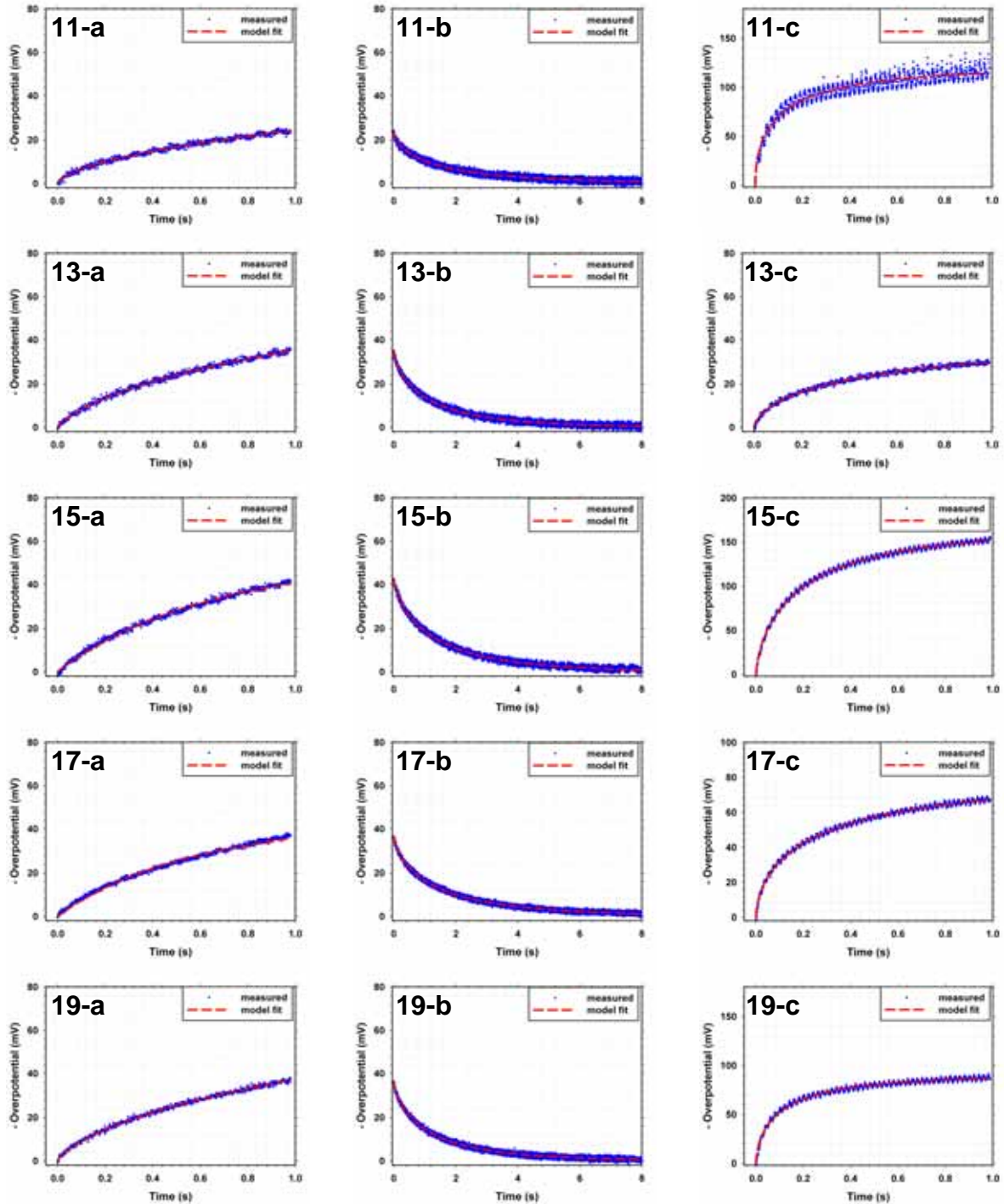
Figure D.6. Curve fitting for charging and discharging sections of the cast-iron/soil responses for Batch 1 measurements during Day 1 and Day 7. The labels are organized as such; the different soils are identified by the numericals, which correspond to the station number along the SITE 1 transect, while the labels **a** and **b** correspond to charging and discharging sections from Day 1 measurements, and **c** corresponds to the charging section from Day 7 measurements.

Figure D.7. Curve fitting for charging and discharging sections of the cast-iron/soil responses for Batch 1 measurements during Day 1 and Day 7. The labels are organized as such; the different soils are identified by the numericals, which correspond to the station number along the SITE 1 transect, while the labels **a** and **b** correspond to charging and discharging sections from Day 1 measurements, and **c** corresponds to the charging section from Day 7 measurements.
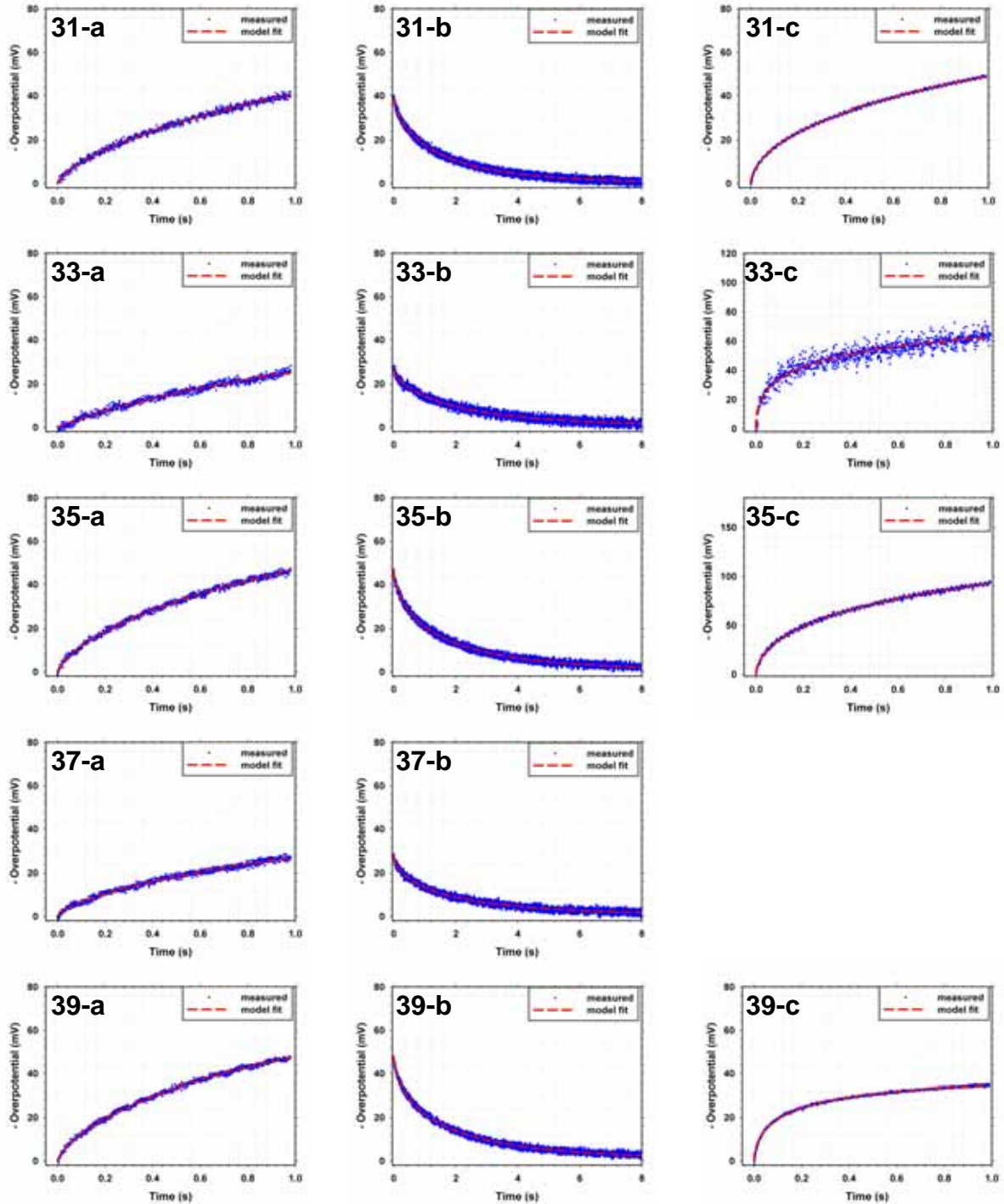
Figure D.8. Curve fitting for charging and discharging sections of the cast-iron/soil responses for Batch 1 measurements during Day 1 and Day 7. The labels are organized as such; the different soils are identified by the numericals, which correspond to the station number along the SITE 1 transect, while the labels **a** and **b** correspond to charging and discharging sections from Day 1 measurements, and **c** corresponds to the charging section from Day 7 measurements.
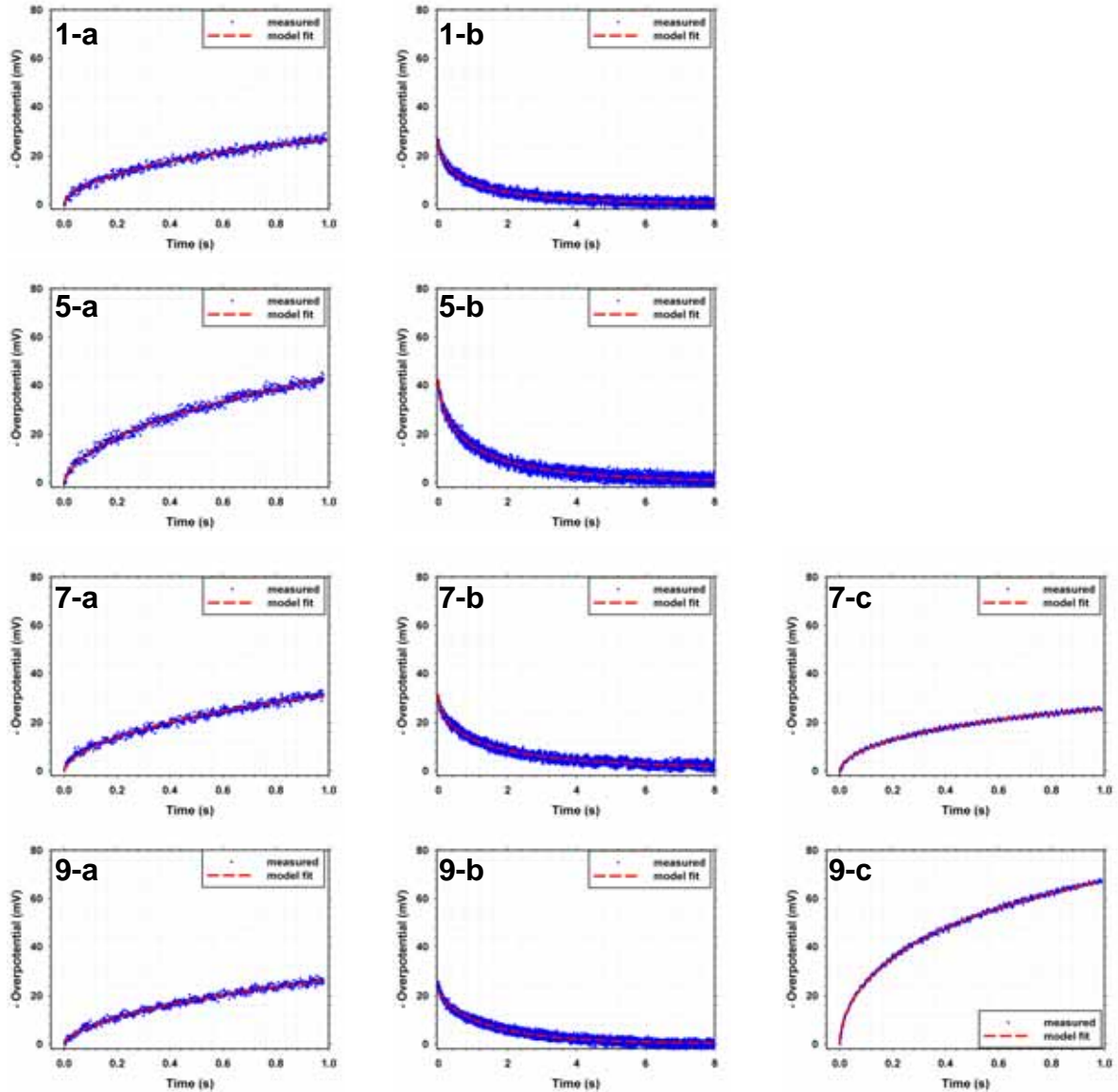
Figure D.9. Curve fitting for charging and discharging sections of the cast-iron/soil responses for Batch 2 measurements during Day 1 and Day 7. The labels are organized as such; the different soils are identified by the numericals, which correspond to the station number along the SITE 1 transect, while the labels **a** and **b** correspond to charging and discharging sections from Day 1 measurements, and **c** corresponds to the charging section from Day 7 measurements.
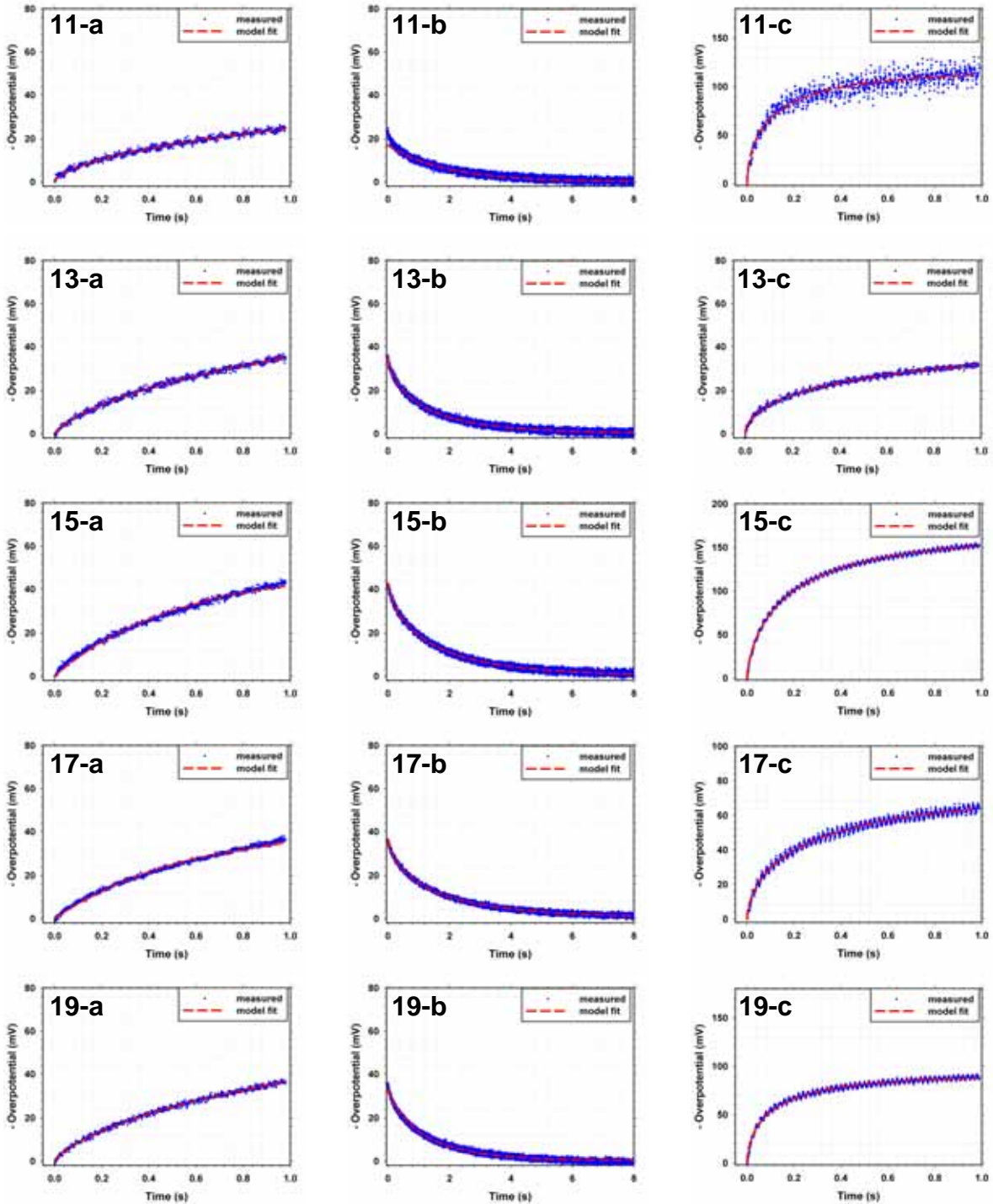
Figure D.10. Curve fitting for charging and discharging sections of the cast-iron/soil responses for Batch 2 measurements during Day 1 and Day 7. The labels are organized as such; the different soils are identified by the numericals, which correspond to the station number along the SITE 1 transect, while the labels **a** and **b** correspond to charging and discharging sections from Day 1 measurements, and **c** corresponds to the charging section from Day 7 measurements.
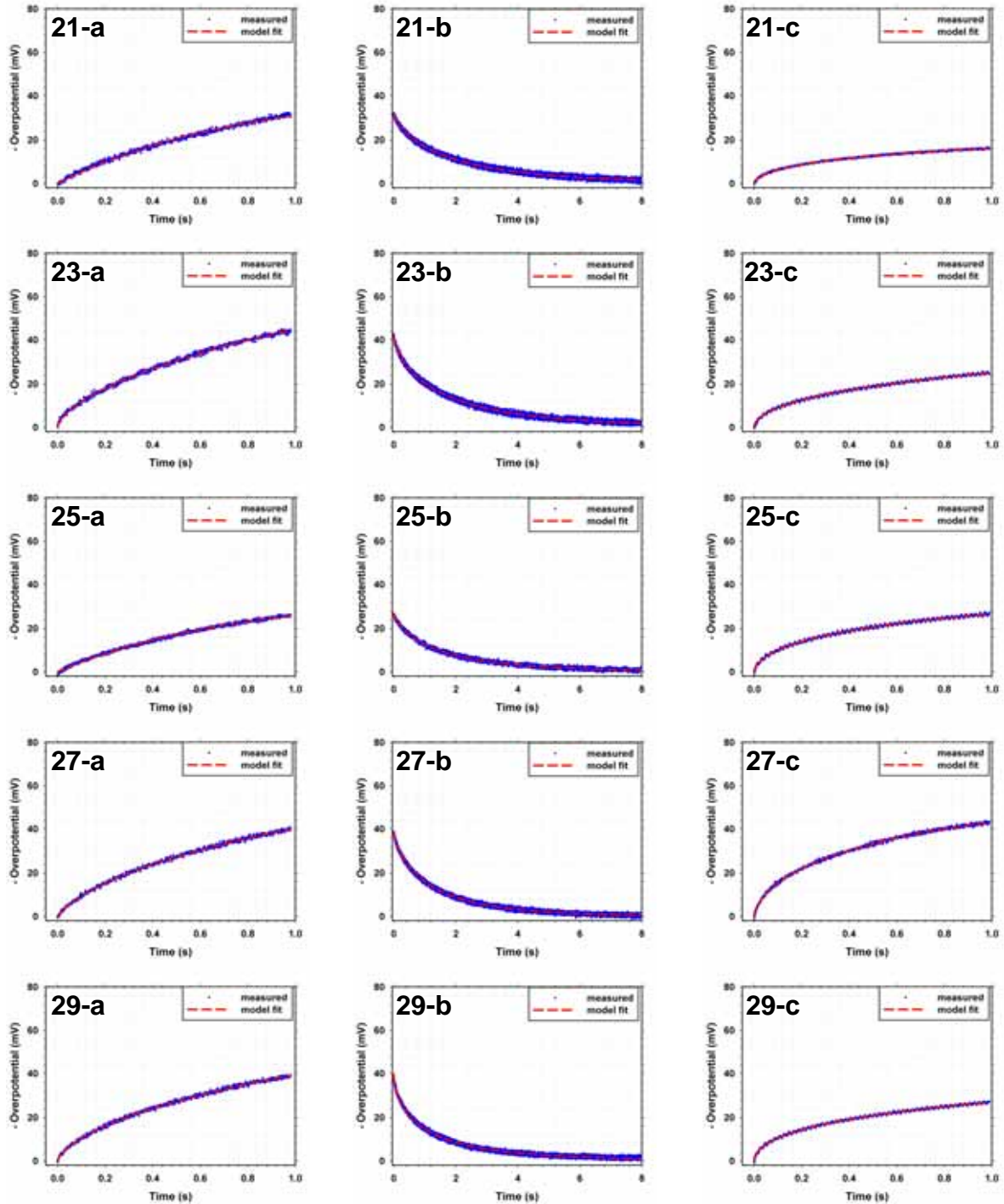
Figure D.11. Curve fitting for charging and discharging sections of the cast-iron/soil responses for Batch 2 measurements during Day 1 and Day 7. The labels are organized as such; the different soils are identified by the numericals, which correspond to the station number along the SITE 1 transect, while the labels **a** and **b** correspond to charging and discharging sections from Day 1 measurements, and **c** corresponds to the charging section from Day 7 measurements.
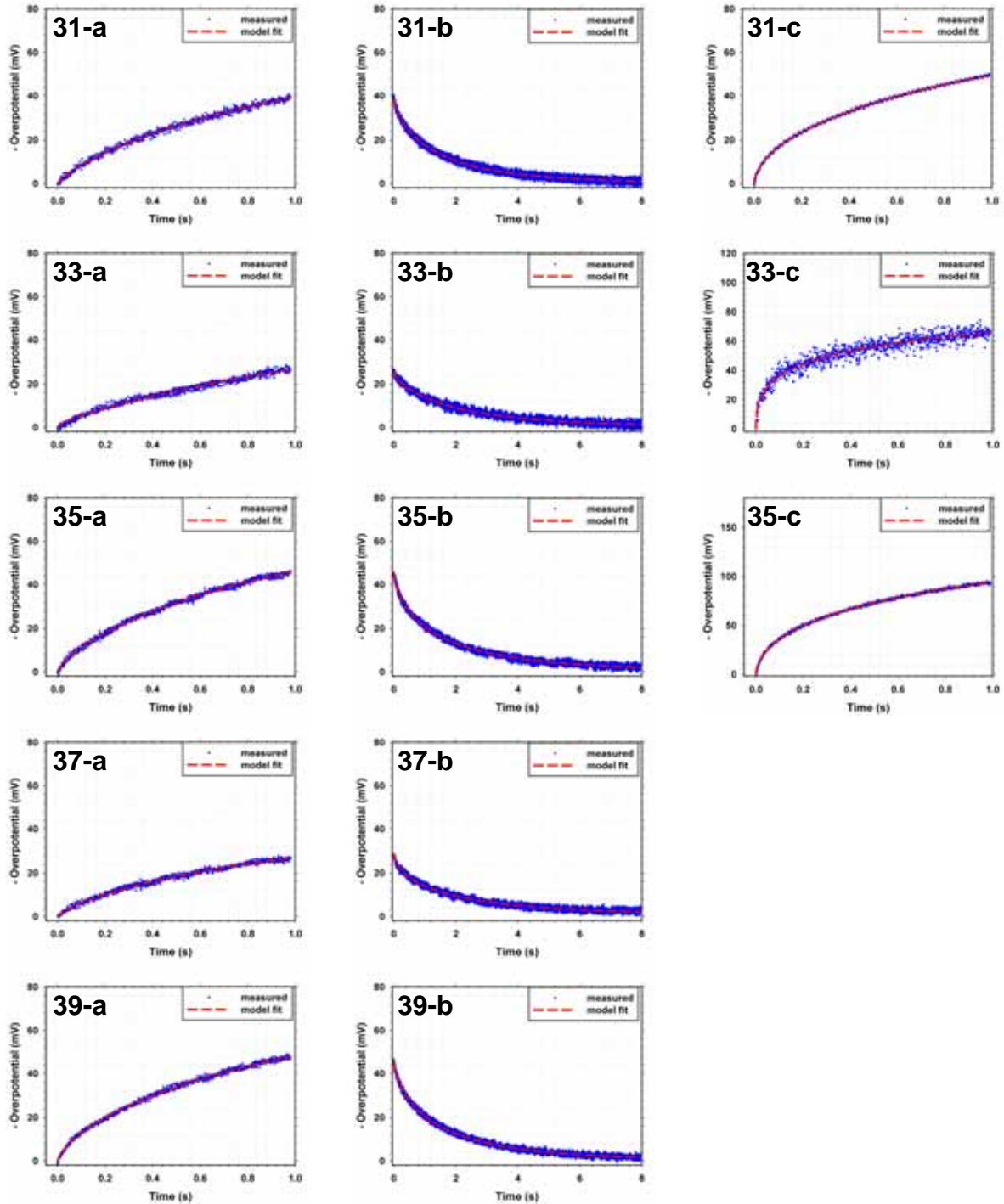
Figure D.12. Curve fitting for charging and discharging sections of the cast-iron/soil responses for Batch 2 measurements during Day 1 and Day 7. The labels are organized as such; the different soils are identified by the numericals, which correspond to the station number along the SITE 1 transect, while the labels **a** and **b** correspond to charging and discharging sections from Day 1 measurements, and **c** corresponds to the charging section from Day 7 measurements.
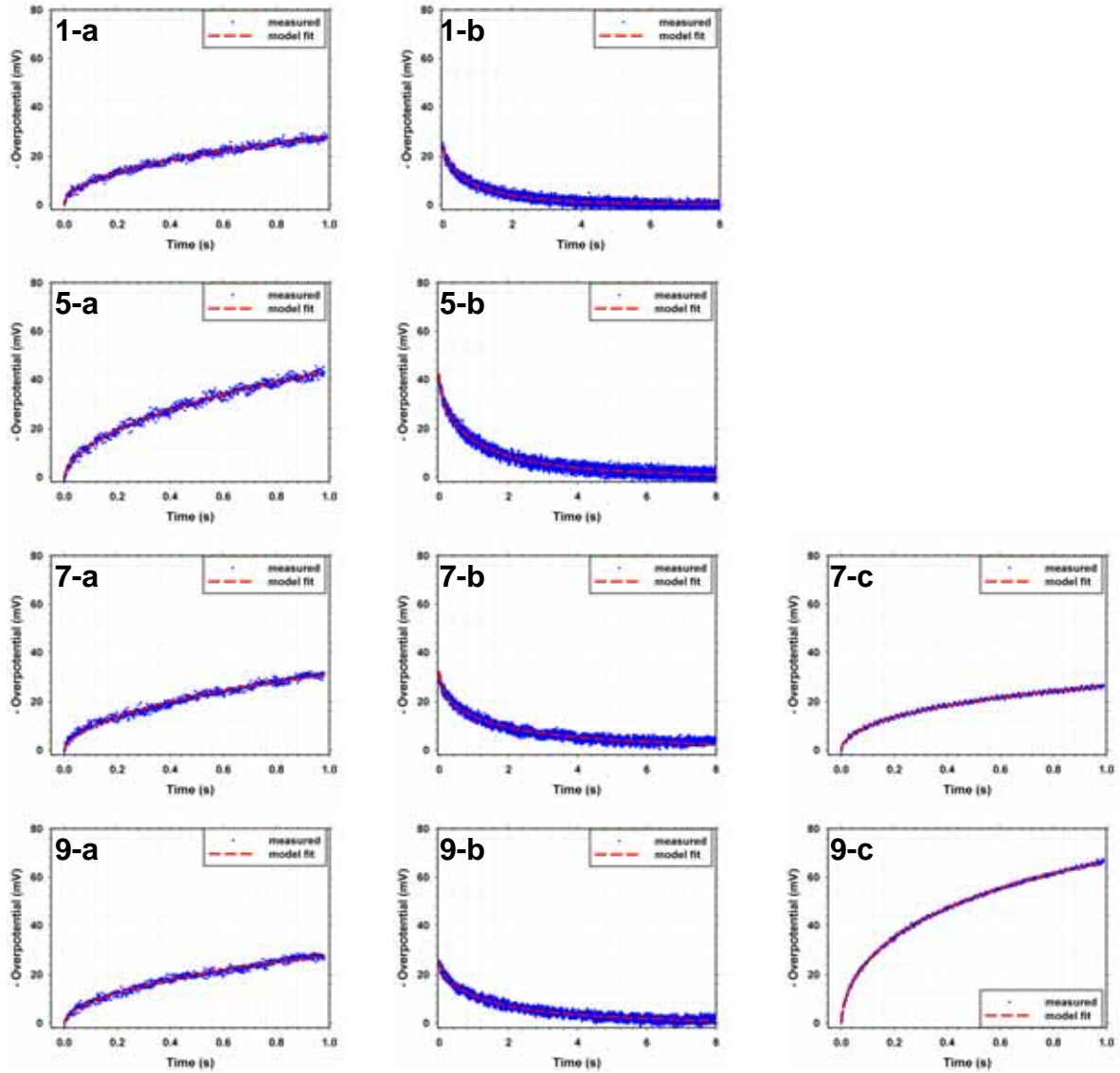
Figure D.13. Curve fitting for charging and discharging sections of the cast-iron/soil responses for Batch 3 measurements during Day 1 and Day 7. The labels are organized as such; the different soils are identified by the numericals, which correspond to the station number along the SITE 1 transect, while the labels **a** and **b** correspond to charging and discharging sections from Day 1 measurements, and **c** corresponds to the charging section from Day 7 measurements.

Figure D.14. Curve fitting for charging and discharging sections of the cast-iron/soil responses for Batch 3 measurements during Day 1 and Day 7. The labels are organized as such; the different soils are identified by the numericals, which correspond to the station number along the SITE 1 transect, while the labels **a** and **b** correspond to charging and discharging sections from Day 1 measurements, and **c** corresponds to the charging section from Day 7 measurements.

Figure D.15. Curve fitting for charging and discharging sections of the cast-iron/soil responses for Batch 3 measurements during Day 1 and Day 7. The labels are organized as such; the different soils are identified by the numericals, which correspond to the station number along the SITE 1 transect, while the labels **a** and **b** correspond to charging and discharging sections from Day 1 measurements, and **c** corresponds to the charging section from Day 7 measurements.

Figure D.16. Curve fitting for charging and discharging sections of the cast-iron/soil responses for Batch 3 measurements during Day 1 and Day 7. The labels are organized as such; the different soils are identified by the numericals, which correspond to the station number along the SITE 1 transect, while the labels **a** and **b** correspond to charging and discharging sections from Day 1 measurements, and **c** corresponds to the charging section from Day 7 measurements.

APPENDIX D.7   CORROSION RELATED PARAMETERS FROM GALVANOSTATIC PULSE MEASUREMENTS ON CAST-IRON/SOIL SAMPLES

Each cast-iron/soil system was measured at least three times (unless shown otherwise by a '-') and the respective corrosion parameters (E_{CORR}, R_{Ω}, R_p, C_{dl}, β) for each measurement is given. Note that electrochemical cells consisting of soil samples from Stations 1, 2 and 36 could not be analyzed after 7 days due to development of large Ohmic drops. The R_p and C_{dl} are stated here in their raw units (Ω and F respectively), while in the thesis they are transformed into their conventional units ($k\Omega$ cm^2 and μF cm^{-2} respectively) and presented.

DAY 1 MEASUREMENTS

STATION	Iapp (A)	M1 Ecorr (-V)	M1 Rs (Ω)	M1 Rp Fit	M1 Rp Std Dev	M1 C Fit	M1 C Std Dev	M1 β Fit	M1 β Std Dev	M2 Ecorr (-V)	M2 Rs (Ω)	M2 Rp Fit	M2 Rp Std Dev	M2 C Fit	M2 C Std Dev	M2 β Fit	M2 β Std Dev	M3 Ecorr (-V)	M3 Rs (Ω)	M3 Rp Fit	M3 Rp Std Dev	M3 C Fit	M3 C Std Dev	M3 β Fit	M3 β Std Dev
1	1.00E-04	0.700	1.19E+03	6.72E+02	7.00E+01	4.63E-03	7.03E-04	0.576	0.012	0.700	1.19E+03	6.91E+02	8.12E+01	4.85E-03	8.15E-04	0.577	0.013	0.700	1.17E+03	1.11E+03	2.46E+02	9.88E-03	3.24E-03	5.16E-01	1.23E-02
3	2.00E-04	0.687	5.76E+02	8.90E+02	2.84E+02	1.92E-02	6.83E-03	0.571	0.012	-	-	-	-	-	-	-	-	-	-	-	-	-	-	-	-
5	2.00E-04	0.692	3.70E+02	5.04E+02	3.80E+01	5.21E-03	5.45E-04	0.601	0.010	0.689	3.77E+02	4.23E+02	2.43E+01	4.14E-03	3.19E-04	0.641	0.010	0.689	3.68E+02	4.65E+02	3.05E+01	4.66E-03	4.23E-04	0.614	0.010
7	2.00E-04	0.697	5.26E+02	3.28E+02	3.04E+01	6.38E-03	5.79E-04	0.726	0.014	0.697	5.14E+02	3.50E+02	4.70E+00	6.56E-05	5.20E-05	0.619	0.003	0.697	5.18E+02	3.50E+02	4.70E+00	6.63E-03	5.30E-05	0.624	0.003
9	2.00E-04	0.709	4.30E+02	4.38E+02	7.00E+01	1.17E-02	2.12E-03	0.619	0.013	0.707	4.28E+02	4.40E+02	4.00E+00	1.19E-02	1.36E-04	0.579	0.003	0.709	4.28E+02	4.40E+02	3.84E+00	1.25E-02	1.42E-04	0.566	0.003
11	2.00E-04	0.705	2.77E+02	3.59E+02	4.60E+01	1.11E-02	1.58E-03	0.637	0.012	0.705	2.71E+02	4.00E+02	3.70E+00	1.26E-02	1.44E-04	0.609	0.003	0.705	2.71E+02	3.50E+02	3.10E+00	1.06E-02	9.00E-05	0.640	0.003
13	2.00E-04	0.693	1.00E+02	3.13E+02	1.04E+01	4.04E-03	1.36E-04	0.771	0.008	0.692	1.00E+02	3.11E+02	1.04E+01	4.00E-03	1.32E-04	0.781	0.009	0.692	1.00E+02	3.11E+02	1.04E+01	4.00E-03	1.32E-04	0.781	0.009
15	2.00E-04	0.680	1.41E+02	2.53E+02	1.20E+00	2.43E-03	9.10E-06	0.990	1.000	0.680	1.34E+02	2.43E+02	1.10E+00	2.11E-03	9.90E-06	0.990	1.000	0.680	1.35E+02	2.43E+02	1.10E+00	2.16E-03	1.00E-05	0.990	1.000
17	2.00E-04	0.702	8.63E+01	2.14E+02	9.70E-01	2.57E-03	1.10E-05	0.990	1.000	0.702	8.93E+01	2.15E+02	9.50E-01	2.69E-03	1.10E-05	0.990	1.000	0.703	8.22E+01	2.20E+02	4.20E+00	2.51E-03	5.30E-06	0.943	0.004
19	2.00E-04	0.688	1.16E+02	3.61E+02	1.09E+01	4.29E-03	1.36E-04	0.733	0.006	0.688	1.13E+02	3.26E+02	8.60E+00	3.89E-03	1.04E-04	0.771	0.007	0.687	1.19E+02	3.26E+02	8.60E+00	3.89E-03	1.05E-04	0.771	0.007
21	2.00E-04	0.691	6.41E+01	2.01E+02	1.20E+00	3.24E-03	1.45E-05	0.990	1.000	0.691	6.87E+01	2.21E+02	1.40E+00	3.65E-03	1.40E-05	0.990	1.000	0.691	6.87E+01	2.21E+02	1.40E+00	3.65E-03	1.40E-05	0.990	1.000
23	2.00E-04	0.701	2.03E+02	4.07E+02	1.07E+01	3.59E-03	9.10E-05	0.772	0.006	0.701	1.93E+02	6.86E+02	4.20E+01	6.07E-03	3.96E-04	0.648	0.006	0.701	2.01E+02	4.56E+02	1.48E+01	3.99E-03	1.29E-04	0.735	0.006
25	2.00E-04	0.699	1.66E+02	4.46E+02	3.50E+01	8.91E-03	6.07E-04	0.705	0.007	0.698	1.74E+02	1.80E+02	9.60E-01	4.29E-03	1.46E-05	0.990	1.000	0.698	1.67E+02	3.23E+02	1.67E+01	6.66E-03	2.72E-04	0.770	0.007
27	2.00E-04	0.699	1.82E+02	3.17E+02	4.96E+00	3.27E-03	4.90E-05	0.820	0.005	0.699	1.75E+02	3.42E+02	6.20E+00	3.42E-03	6.30E-05	0.780	0.005	0.698	1.79E+02	3.55E+02	6.98E+00	3.51E-03	7.00E-05	0.773	0.005
29	2.00E-04	0.698	2.38E+02	3.13E+02	5.20E+00	3.47E-03	6.20E-05	0.769	0.005	0.698	2.32E+02	3.76E+02	8.80E+00	4.10E-03	1.13E-04	0.698	0.005	0.698	2.34E+02	3.28E+02	6.00E+00	3.60E-03	7.44E-05	0.743	0.005
31	2.00E-04	0.690	1.79E+02	4.18E+02	1.75E+01	4.15E-03	1.77E-04	0.732	0.008	0.688	1.85E+02	3.33E+02	9.70E+00	3.44E-03	9.20E-05	0.821	0.008	0.686	1.93E+02	2.84E+02	6.84E+00	3.14E-03	6.20E-05	0.910	0.010
33	2.00E-04	0.688	2.24E+02	2.37E+02	1.58E+01	5.55E-03	2.28E-04	0.937	0.018	0.688	2.15E+02	7.64E+02	2.54E+02	1.19E-02	2.47E-03	0.739	0.015	0.688	2.16E+02	2.88E+02	2.40E+01	6.17E-03	3.51E-04	0.859	0.016
35	2.00E-04	0.684	3.29E+02	4.38E+02	1.35E+01	3.35E-03	1.15E-04	0.720	0.007	0.685	3.31E+02	3.90E+02	9.47E+00	2.98E-03	7.72E-05	0.764	0.007	0.686	3.31E+02	4.28E+02	1.23E+01	3.26E-03	9.80E-05	0.746	0.006
37	2.00E-04	0.692	4.29E+02	3.64E+02	3.80E+01	8.06E-03	8.18E-04	0.699	0.012	0.692	4.32E+02	2.44E+02	1.04E+01	5.33E-03	2.20E-04	0.783	0.011	0.692	4.27E+02	4.33E+02	4.80E+01	9.12E-03	1.04E-03	0.662	0.011
39	2.00E-04	0.699	4.51E+02	4.12E+02	8.90E+00	2.96E-03	7.50E-05	0.724	0.005	0.700	4.44E+02	4.27E+02	9.60E+00	3.04E-03	8.10E-05	0.711	0.005	0.700	4.44E+02	4.32E+02	9.90E+00	3.03E-03	8.20E-05	0.712	0.005

Table D.24. Computed corrosion parameters for Day 1 from charging curves of cast-iron/soil system.

STATION	Iapp (A)	M1 Ecorr (-V)	M1 Rs (Ω)	M1 Rp Fit	M1 Rp Std Dev	M1 C Fit	M1 C Std Dev	M1 β Fit	M1 β Std Dev	M2 Ecorr (-V)	M2 Rs (Ω)	M2 Rp Fit	M2 Rp Std Dev	M2 C Fit	M2 C Std Dev	M2 β Fit	M2 β Std Dev	M3 Ecorr (-V)	M3 Rs (Ω)	M3 Rp Fit	M3 Rp Std Dev	M3 C Fit	M3 C Std Dev	M3 β Fit	M3 β Std Dev
1	1.00E-04	0.700	1.19E+03	6.10E+02	3.54E+00	1.44E-03	2.58E-05	0.570	0.004	0.700	1.19E+03	6.02E+02	3.21E+00	1.48E-03	2.36E-05	0.610	0.004	0.700	1.17E+03	8.54E+02	4.46E+00	1.08E-03	1.55E-05	7.35E-01	4.80E-03
3	2.00E-04	0.687	5.76E+02	8.84E+02	4.06E+00	1.47E-03	2.14E-05	0.547	0.003	-	-	-	-	-	-	-	-	-	-	-	-	-	-	-	-
5	2.00E-04	0.692	3.70E+02	4.35E+02	1.57E+00	2.26E-03	2.26E-05	0.710	0.003	0.689	3.77E+02	3.94E+02	1.60E+00	2.42E-03	2.53E-05	0.617	0.003	0.689	3.68E+02	3.90E+02	1.50E+00	2.53E-03	2.74E-05	0.724	0.004
7	2.00E-04	0.697	5.26E+02	3.41E+02	1.60E+00	3.52E-03	5.00E-05	0.585	0.003	0.697	5.14E+02	3.30E+02	1.47E+00	3.79E-03	5.20E-05	0.575	0.003	0.697	5.18E+02	3.50E+02	1.00E+01	3.82E-03	9.80E-06	0.540	0.001
9	2.00E-04	0.709	4.30E+02	3.34E+02	1.30E+00	4.21E-03	4.42E-05	0.819	0.005	0.707	4.28E+02	3.72E+02	1.50E+00	3.89E-03	4.45E-05	0.680	0.004	0.709	4.28E+02	3.63E+02	1.40E+00	4.01E-03	4.30E-05	0.680	0.003
11	2.00E-04	0.705	2.77E+02	3.28E+02	1.20E+00	4.23E-03	4.50E-05	0.678	0.003	0.705	2.71E+02	2.57E+02	6.54E-01	7.25E-03	4.10E-05	0.990	0.140	0.705	2.71E+02	2.78E+02	1.10E+00	4.79E-03	4.80E-05	0.809	0.004
13	2.00E-04	0.693	1.00E+02	2.99E+02	7.16E-01	3.82E-03	2.60E-05	0.729	0.002	0.692	1.00E+02	2.92E+02	7.30E-01	3.93E-03	2.70E-05	0.745	0.002	0.692	1.00E+02	2.92E+02	7.30E-01	3.93E-03	2.70E-05	0.745	0.002
15	2.00E-04	0.680	1.41E+02	2.53E+02	4.67E-01	5.27E-03	2.60E-05	0.748	0.002	0.680	1.34E+02	2.31E+02	4.40E-01	5.82E-03	3.00E-05	0.746	0.002	0.680	1.35E+02	2.35E+02	4.52E-01	5.71E-03	3.00E-05	0.746	0.002
17	2.00E-04	0.702	8.63E+01	2.06E+02	3.50E-01	6.69E-03	3.20E-05	0.704	0.002	0.702	8.93E+01	2.08E+02	3.50E-01	6.72E-03	3.20E-05	0.704	0.002	0.703	8.22E+01	2.07E+02	3.40E-01	6.71E-03	3.10E-05	0.726	0.002
19	2.00E-04	0.688	1.16E+02	3.41E+02	6.59E-01	4.30E-03	1.82E-05	0.720	0.002	0.688	1.13E+02	2.88E+02	6.34E-01	4.03E-03	2.30E-05	0.833	0.003	0.687	1.18E+02	3.16E+02	6.30E-01	3.67E-03	2.10E-05	0.712	0.002
21	2.00E-04	0.691	6.41E+01	1.90E+02	3.20E-01	9.75E-03	4.40E-05	0.759	0.002	0.691	6.87E+01	2.14E+02	3.60E-01	8.66E-03	4.00E-05	0.757	0.002	0.691	6.87E+01	2.14E+02	3.60E-01	8.66E-03	4.00E-05	0.757	0.002
23	2.00E-04	0.701	2.03E+02	3.89E+02	6.00E+00	4.09E-03	1.74E-05	0.725	0.002	0.701	1.93E+02	6.39E+02	9.90E-01	2.49E-03	1.07E-05	0.710	0.001	0.701	2.01E+02	4.41E+02	7.00E-01	3.63E-03	1.61E-05	0.709	0.001
25	2.00E-04	0.699	1.66E+02	4.15E+02	7.30E-01	3.47E-03	1.66E-05	0.753	0.002	0.698	1.74E+02	1.82E+02	3.20E-01	8.01E-03	3.90E-05	0.743	0.002	0.698	1.67E+02	2.87E+02	5.30E-01	5.00E-03	2.50E-05	0.807	0.002
27	2.00E-04	0.699	1.82E+02	3.14E+02	4.50E-01	3.86E-03	1.52E-05	0.722	0.001	0.699	1.75E+02	3.19E+02	4.57E-01	3.77E-03	1.50E-05	0.761	0.001	0.698	1.79E+02	3.51E+02	5.30E-01	3.45E-03	1.40E-05	0.705	0.001
29	2.00E-04	0.698	2.38E+02	3.25E+02	6.40E-01	3.15E-03	1.80E-05	0.630	0.001	0.698	2.32E+02	3.77E+02	7.00E-01	2.72E-03	1.50E-05	0.638	0.001	0.698	2.34E+02	3.25E+02	5.80E-01	3.19E-03	1.65E-05	0.659	0.001
31	2.00E-04	0.690	1.79E+02	3.84E+02	8.10E-01	3.65E-03	2.10E-05	0.742	0.002	0.688	1.85E+02	3.12E+02	7.00E-01	4.50E-03	2.75E-05	0.747	0.002	0.686	1.93E+02	2.82E+02	6.40E-01	5.05E-03	3.20E-05	0.719	0.002
33	2.00E-04	0.688	2.24E+02	2.18E+02	7.30E-01	9.16E-03	8.30E-05	0.739	0.004	0.688	2.15E+02	6.73E+02	2.20E+00	2.85E-03	2.40E-05	0.773	0.004	0.688	2.16E+02	2.59E+02	8.80E-01	7.35E-03	6.60E-05	0.804	0.004
35	2.00E-04	0.684	3.29E+02	4.27E+02	9.00E-01	3.33E-03	2.00E-05	0.660	0.003	0.685	3.31E+02	3.83E+02	7.60E-01	3.78E-03	2.10E-05	0.676	0.002	0.686	3.31E+02	4.09E+02	7.70E-01	3.56E-03	1.90E-05	0.679	0.002
37	2.00E-04	0.692	4.29E+02	3.49E+02	1.10E+00	4.73E-03	4.40E-05	0.656	0.003	0.692	4.32E+02	2.51E+02	7.80E-01	6.79E-03	6.20E-05	0.640	0.003	0.692	4.27E+02	4.28E+02	1.20E+00	3.97E-03	3.40E-05	0.631	0.002
39	2.00E-04	0.699	4.51E+02	4.12E+02	7.50E-01	3.48E-03	1.86E-05	0.640	0.001	0.700	4.44E+02	3.97E+02	6.60E-01	3.55E-03	1.70E-05	0.703	0.002	0.700	4.44E+02	4.09E+02	6.60E-01	3.45E-03	1.60E-05	0.693	0.001

Table D.25. Computed corrosion parameters for Day 1 from discharging curves of cast-iron/soil system.

DAY 7 MEASUREMENTS

STATION	Iapp (A)	Measurement 1										Measurement 2										Measurement 3									
		Ecorr (-V)	Rs (Ω)	Rp (Ω)		C (F)		β				Ecorr (-V)	Rs (Ω)	Rp (Ω)		C (F)		β				Ecorr (-V)	Rs (Ω)	Rp (Ω)		C (F)		β			
				Fit	Std Dev	Fit	Std Dev	Fit	Std Dev					Fit	Std Dev	Fit	Std Dev	Fit	Std Dev					Fit	Std Dev	Fit	Std Dev	Fit	Std Dev		
1	-	-	-	-	-	-	-	-	-			-	-	-	-	-	-	-	-			-	-	-	-	-	-	-	-		
3	-	-	-	-	-	-	-	-	-			-	-	-	-	-	-	-	-			-	-	-	-	-	-	-	-		
5	4.00E-06	0.173	3.80E+04	1.56E+04	1.47E+02	2.06E-05	5.59E-07	0.480	0.005			-	-	-	-	-	-	-	-			-	-	-	-	-	-	-	-		
7	4.00E-06	-0.028	1.57E+04	1.03E+04	2.50E+02	1.01E-04	4.03E-06	0.618	0.006			-0.018	2.08E+04	1.08E+04	2.94E+02	1.10E-04	5.07E-06	0.591	0.006			-0.012	2.35E+04	1.19E+04	3.77E+02	1.24E-04	7.20E-06	0.551	0.006		
9	4.00E-05	-0.023	4.77E+03	3.22E+03	1.45E+02	5.85E-04	5.58E-05	0.491	0.007			0.058	6.07E+03	2.84E+03	3.99E+01	4.30E-04	1.17E-05	0.545	0.003			0.068	6.11E+03	2.77E+03	3.34E+01	4.25E-04	9.97E-06	0.546	0.003		
11	1.00E-04	0.002	3.88E+03	1.21E+03	1.20E+01	1.07E-04	3.20E-06	0.536	0.014			0.025	4.02E+03	1.17E+03	1.15E+01	1.14E-04	3.20E-06	0.573	0.015			0.052	4.11E+03	1.22E+03	1.47E+01	1.24E-04	4.22E-06	0.540	0.015		
13	4.00E-04	0.510	2.26E+02	1.00E+02	1.67E+00	5.79E-03	1.55E-05	0.618	0.003			0.510	2.22E+02	1.12E+02	2.10E+00	5.97E-03	2.35E-04	0.560	0.007			0.510	2.20E+02	1.12E+02	2.10E+00	5.89E-03	2.25E-04	0.570	0.007		
15	2.00E-05	0.117	6.74E+03	8.10E+03	2.45E+01	2.69E-05	1.78E-07	0.659	0.004			0.136	6.70E+03	8.05E+03	2.00E+01	2.59E-05	1.41E-07	0.657	0.003			0.149	6.92E+03	7.77E+03	1.70E+01	2.70E-05	1.31E-07	0.678	0.003		
17	4.00E-06	0.181	7.19E+03	1.97E+04	1.23E+02	1.61E-05	2.34E-07	0.575	0.004			0.179	8.03E+03	1.83E+04	1.88E+02	1.65E-05	3.76E-07	0.603	0.008			0.175	7.38E+03	1.89E+04	2.38E+02	1.59E-05	4.82E-07	0.563	0.009		
19	4.00E-05	0.279	2.79E+03	2.24E+03	7.10E+00	5.67E-05	5.21E-07	0.600	0.006			0.279	2.77E+03	2.28E+03	7.30E+00	5.58E-05	5.18E-07	0.592	0.006			0.292	2.71E+03	2.42E+03	1.24E+01	5.42E-05	8.08E-07	0.553	0.007		
21	4.00E-05	0.273	2.31E+03	6.09E+02	5.20E+00	1.34E-03	2.22E-05	0.571	0.003			0.265	2.36E+03	6.08E+02	9.60E+00	1.41E-03	4.40E-05	0.568	0.005			0.262	2.39E+03	6.04E+02	8.53E+00	1.35E-03	3.70E-05	0.573	0.004		
23	4.00E-06	0.118	2.68E+04	1.63E+04	1.07E+03	2.83E-04	3.44E-05	0.492	0.006			0.109	2.77E+04	1.43E+04	7.06E+02	1.95E-04	1.67E-05	0.531	0.006			0.110	2.78E+04	1.56E+04	8.58E+02	2.18E-04	2.20E-05	0.513	0.006		
25	4.00E-06	0.164	3.64E+04	1.12E+04	3.06E+02	1.04E-04	5.40E-06	0.553	0.006			0.165	3.71E+04	1.08E+04	2.55E+02	9.81E-05	4.40E-06	0.567	0.006			0.165	3.81E+04	1.12E+04	3.19E+02	1.04E-04	5.69E-06	0.551	0.006		
27	4.00E-06	0.144	2.42E+04	1.64E+04	1.70E+02	5.09E-05	9.64E-07	0.594	0.003			0.134	2.48E+04	1.56E+04	1.55E+02	4.91E-05	8.53E-04	0.621	0.003			0.134	2.46E+04	1.71E+04	2.06E+02	5.48E-05	1.21E-06	0.583	0.003		
29	4.00E-06	-0.013	1.85E+04	1.25E+04	3.69E+02	1.25E-04	7.34E-06	0.519	0.005			-0.013	1.89E+04	1.30E+04	4.08E+02	1.39E-04	8.64E-06	0.515	0.005			-0.016	1.73E+04	1.36E+04	5.07E+02	1.52E-04	1.14E-05	0.503	0.005		
31	4.00E-06	0.027	2.23E+04	2.68E+04	5.72E+02	8.93E-05	3.00E-06	0.566	0.003			0.027	2.26E+04	2.66E+04	5.38E+02	8.49E-05	2.70E-06	0.573	0.003			0.029	2.25E+04	2.69E+04	5.39E+02	8.36E-05	2.62E-06	0.574	0.003		
33	2.00E-05	0.112	1.98E+04	4.21E+03	2.19E+02	1.13E-04	1.88E-05	0.423	0.017			0.133	1.98E+04	4.59E+03	2.53E+02	1.23E-04	2.23E-05	0.407	0.016			0.146	2.01E+04	4.27E+03	1.66E+02	9.30E-05	1.19E-05	0.421	0.014		
35	2.00E-06	-0.046	4.72E+04	7.86E+04	1.56E+03	1.56E-05	5.95E-07	0.547	0.004			-0.028	6.45E+04	7.65E+04	1.07E+03	1.43E-05	3.88E-07	0.553	0.003			-0.013	8.02E+04	7.55E+04	1.00E+03	1.36E-05	3.51E-04	0.555	0.003		
37	2.00E-05	-	-	-	-	-	-	-	-			-	-	-	-	-	-	-	-			-	-	-	-	-	-	-	-		
39	2.00E-05	0.344	5.24E+03	1.89E+03	5.90E+00	1.00E-04	8.48E-07	0.542	0.003			0.320	4.88E+03	2.06E+03	6.20E+00	9.65E-05	7.82E-07	0.541	0.003			0.309	4.77E+03	2.17E+03	6.60E+00	9.38E-05	7.59E-04	0.543	0.003		

Table D.26. Computed corrosion parameters for Day 7 from charging curves of cast-iron/soil system.